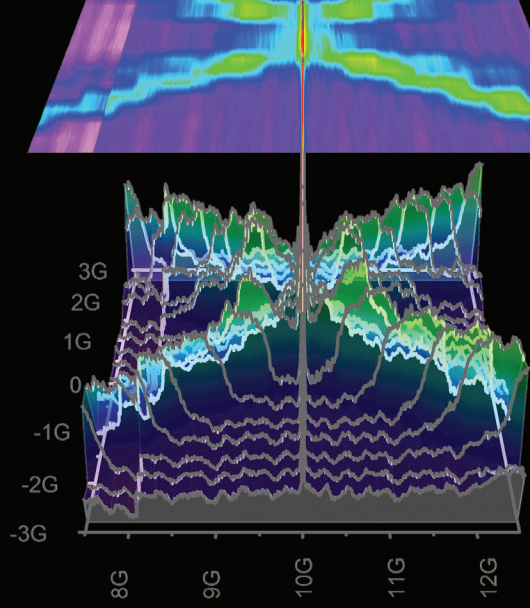

PhD DISSERTATION

NEW PHOTONIC ARCHITECTURES AND DEVICES FOR GENERATION AND DETECTION OF SUB-THz AND THz WAVES

Author: Ángel Rubén Criado Serrano
Supervisor: Pablo Acedo Gallardo

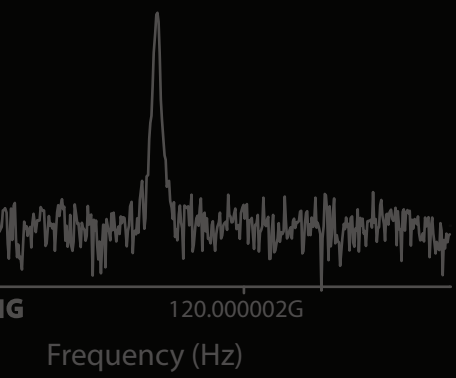

Universidad Carlos III de Madrid
April 2013

Universidad
Carlos III de Madrid

TESIS DOCTORAL

NEW PHOTONIC ARCHITECTURES AND DEVICES FOR GENERATION AND DETECTION OF SUB-THz AND THz WAVES

Autor:
Ángel Rubén Criado Serrano

Director:
Pablo Acedo Gallardo

DEPARTAMENTO DE TECNOLOGÍA ELECTRÓNICA

Leganés, abril de 2013

TESIS DOCTORAL

NEW PHOTONIC ARCHITECTURES AND DEVICES FOR GENERATION AND DETECTION OF SUB-THz AND THz WAVES

Autor: Ángel Rubén Criado Serrano

Director: Pablo Acedo Gallardo

Firma del Tribunal Calificador:

Firma

Presidente: (Nombre y apellidos)

Vocal: (Nombre y apellidos)

Secretario: (Nombre y apellidos)

Calificación:

Leganés, de de 2013

PhD DISSERTATION

NEW PHOTONIC ARCHITECTURES AND DEVICES FOR GENERATION AND DETECTION OF SUB-THz AND THz WAVES

Author: Ángel Rubén Criado Serrano
Supervisor: Pablo Acedo Gallardo

A Cristina y Ariadna

ACKNOWLEDGEMENT/ AGRADECIMIENTOS

A Pablo Acedo. Gracias por la oportunidad que me dio de entrar en el mundo de la investigación allá por 2007. Gracias por ser un gran ejemplo de dirección y supervisión, y por enseñarme muchas más cosas de las que se pueden aprender en un laboratorio. Espero seguir aprendiendo contigo en las etapas venideras.

A los compañeros del Grupo de Optoelectrónica y Tecnología Láser (GOTL). En especial a mis compañeros de laboratorio, Pedro y Estefanía; y a mis compañeros de despacho, Iago y Álvaro. Como no, también mención muy especial a los veteranos de la mesa óptica que aún quedan, Pablo Pedreira y Dani; y a los que se fueron, Rui y Vincent. Gracias por vuestros consejos dentro y fuera del laboratorio.

A los compañeros del departamento de Tecnología Electrónica. Especialmente a Carlos, Almudena y Ricardo.

Thanks to our German colleagues. From Erlangen: Gottfried H. Döhler (Max Planck Institute for the Science of Light), Stefan Malzer and Sascha Preu (Friedrich-Alexander-Universität Erlangen-Nürnberg). Thank you very much for our collaboration and the opportunity of using your great photomixers. And from Darmstadt: Hans L. Hartnagel and Peter Meissner (Technische Universität Darmstadt). Special thanks to Peter Meissner and the fruitful discussions about the contents of this dissertation.

I would like to thank Prof. Ian H. White for the opportunity of working at Centre for Photonic Systems, University of Cambridge, UK. Thanks to Adrian Wonfor, Vojtech Olle and especially Zhen Yang for making my visit a very nice, productive and unforgettable experience.

Me gustaría también darle las gracias a aquellos profesores que he tenido a lo largo de mi formación académica de primaria y secundaria y que me marcaron positivamente, de una forma u otra. Un profesor nunca debería olvidar que tiene un gran poder para motivar a un alumno, tanto académica como personalmente. Gracias a Manuela Garlito, Carmen Cid, Mariló Rivas (CEIP Andrés Manjón); Juan Antonio Muriel (IES Avalón), y aquellos cuyo nombre no recuerdo ahora: mi profesor de lengua de 3º de ESO y mis profesores de Educación Física y

Tecnología de 2º de ESO (IES Victoria Kent).

A mi amigo David, muchas gracias por estar siempre ahí.

A Fernando, Irene y Marta. Lo que Fourier ha unido que el tiempo no lo separe.

A mis padres. Gracias a ellos es posible que haya llegado aquí, y que sea la persona que soy a día de hoy. Gracias por ser un perfecto ejemplo de lo que deben ser unos padres, especialmente ahora, que me toca a mí. Nunca podré agradeceros suficientemente todo lo que habéis hecho por mí.

A mi hermano Tony: qué aburrida hubiera sido la infancia y la adolescencia sin ti, a pesar de esas tardes de no dejarme estudiar y llamarme gafotas. Gracias hermano. A mi hermana Inma. No dejes nunca de esforzarte por dedicarte a lo que te gusta (y por encontrarlo), al final siempre se cosecha lo que se siembra.

A Cristina. Gracias por estar en lo bueno, porque casi siempre eres causa de lo bueno; y por apoyarme en lo malo, donde casi siempre eres solución. No tendré en mi vida días suficientes para agradecerte y quererte todo lo que te mereces. Gracias por la familia que ya tenemos y por nuestra pequeña Ariadna (y los que estén por llegar).

CONTENTS

Chapter III
New architectures for photonic synthesis of low phase noise mm-Wave, sub-THz and THz Continuous Wave signals using multimode optical sources

Chapter IV
Detection: Heterodyne Electro-Optical detection of microwave, mm-Wave and Sub-THz signals

Chapter V
Results discussion. Conclusions

Chapter VI
Selected publications and preprints

Appendix I
THz history

Appendix II
mm-wave, sub-THz and THz technology. Sources and detectors: state-of-the-art (November, 2012)

Appendix III
On the basics of nonlinear optics

Appendix IV
Phase Noise measurement

Appendix V
Uncertainty

Appendix VI
Laser Characterization Platform

ABSTRACT

The development of high-quality and reliable devices in the THz frequency region to fill the existing technological gap has become a major concern. This is chiefly motivated by the need of a widespread exploitation of the extensive variety of identified applications in this frequency region by a wide range of users, including the non-scientific community. The photonic approaches used for these purposes offer important and exclusive advantages over other existing alternatives, which have as a main representative the all-electronic technology, especially in terms of frequency range coverage, possibility of photonic distribution using optical fibers, weight and Electromagnetic Interference (EMI) immunity. Nevertheless, the optical techniques have traditionally provided with worse performance in terms of phase noise, tunability and dynamic range (in generation), and conversion ratio (in detection) when compared to state-of-the-art all-electronic THz technology. The work accomplished in this thesis focuses on the design, development and validation of new photonic architectures and devices for both generation and detection of sub-THz and THz waves which overcome the drawbacks of optical techniques at this frequency region while maintaining all their advantages.

In this thesis, several photonic sub-THz and THz generation systems have been developed using Difference Frequency Generation (DFG) architectures in which the DFG source is provided by an Optical Frequency Comb Generator (OFCG) and optical mode selection. Different devices and techniques are investigated for each part of the system before arriving to the final high performance synthesizer. Passively Mode-Locked Laser Diodes (PMMLDs) are firstly evaluated as integrated OFCG. An improved design of the OFCG is achieved with a scheme based on a Discrete Mode (DM) laser under Gain-Switching (GS) regime and optical span expansion by the use of a single Electro-Optical (EO) phase modulator. As optical mode selection, both high selective optical filtering and Optical Injection Locking (OIL) are used and evaluated. A commercial 50 GHz photodiode (PD) and an n-i-pn-i-p superlattice THz photomixer are employed as photodetector for Optical to THz conversion.

The final reported system consists on an OFCG based on GS, OIL as mode selection strategy and an n-i-pn-i-p superlattice photomixer. This synthesizer offers a wide frequency range (60-140 GHz), readily scalable to a range between 10 GHz and values well above 1 THz. Quasi-continuous tunability is offered in the whole frequency range, with a frequency resolution of 0.1 Hz at 100 GHz that can be straightforwardly improved to 0.01 Hz at 100 GHz and 0.1

Hz at 1 THz. The measured FWHM at 120 GHz is <10 Hz, only limited by the measurement instrumentation. The system offers excellent frequency and power stability with frequency and power deviations over 1 hour of 5 Hz and 1.5 dB, respectively. These values are also limited by both the accuracy and uncertainty of the measurement setup.

The performance achieved by this photonic sub-THz and THz synthesizer for most figures of merit matches or even surpasses those of commercial state-of-the-art all-electronic systems, and overcomes some of their characteristics in more than one million times when compared to commercial state-of-the-art photonic solutions.

The detection part of this thesis explores the use of photonic architectures based on EO heterodyne receivers and the key devices that encompass these architectures: photonic Local Oscillators (LOs) and EO mixers. First results are developed at microwave frequencies (<15 GHz) using an Ultra-Nonlinear Semiconductor Amplifier (XN-SOA) as EO mixer and a GS based photonic LO. It is demonstrated how this LO device based on GS provides with a significant improvement in the performance of the overall EO receiver when compared to a traditional linearly modulated LO. Furthermore, this detection architecture is validated in an actual application (photonic imaging array), featuring scalability, flexibility and reasonable conversion ratios.

After this, an EO heterodyne receiver is demonstrated up to frequencies of 110 GHz. The photonic LO employed is the abovementioned photonic sub-THz synthesizer developed in this thesis, while the EO mixer is an np-i-pn quasi ballistic THz detector. The first fabricated sample of this novel device is used, which is optimized for homodyne/heterodyne detection. The resulting sub-THz EO heterodyne receiver has conversion ratios around -75 dB. It works under zero-bias conditions, which together with the photonic distribution of the LO offers a high potential for remote detection of sub-THz and THz waves.

In summary, new photonic architectures and devices are able to provide with state-of-the-art performance for generation of sub-THz and THz waves. In the case of EO heterodyne detection at sub-THz and THz frequency regions, photonic techniques are improving their performance and are closer to offer an alternative to all-electronic detectors.

RESUMEN

El desarrollo de dispositivos fiables y de alta calidad en el rango frecuencial de Terahercios (THz) con el fin de cubrir el actual vacío tecnológico se ha convertido en una importante inquietud científica. Esto está principalmente motivado por la necesidad de explotar el gran número de aplicaciones identificadas en esta región frecuencial por un gran número de usuarios, incluyendo a usuarios no científicos. El enfoque fotónico empleado para estos propósitos ofrece importantes y exclusivas ventajas sobre otras alternativas existentes, que tienen como principal representante a la tecnología electrónica, especialmente en términos de rango de frecuencia de funcionamiento, posibilidad de distribución fotónica con fibras ópticas, peso, e inmunidad electromagnética. No obstante, las técnicas fotónicas tradicionalmente han ofrecido peores prestaciones en términos de ruido de fase, sintonía y rango dinámico (en generación) y ratio de conversión (en detección) con respecto a la tecnología electrónica de THz en el estado del arte. El trabajo realizado en esta tesis se centra en el diseño, desarrollo y validación de nuevas arquitecturas y componentes fotónicos tanto para generación como detección de ondas de sub-THz y THz que permitan solucionar las desventajas de las técnicas ópticas manteniendo todas sus ventajas.

En esta tesis, varios sistemas de generación de sub-THz y THz han sido desarrollados utilizando arquitecturas Difference Frequency Generation (DFG) en las que la fuente DFG es proveída por un Optical Frequency Comb Generator (OFCG) y selección de modos ópticos. Diferentes dispositivos y técnicas son investigados para cada parte del sistema hasta conseguir un sintetizador de altas prestaciones. Passively Mode-Locked Laser Diodes (PMMLDs) son inicialmente evaluados como OFCG integrados. Un diseño mejorado del OFCG es conseguido mediante el uso de un esquema basado en un láser Discrete Mode (DM) bajo régimen Gain Switching (GS) y expansión del ancho de banda óptico mediante el uso de un modulador de fase Electro-Óptico (EO). Como estrategia de selección de modos ópticos, tanto filtrado óptico altamente selectivo como Optical Injection Locking (OIL) son usados y evaluados. Un fotodiodo comercial de ancho de banda 50 GHz y un fotomezclador de THz de superred n-i-pn-i-p son empleados.

El sistema de generación final que se presenta en esta tesis consiste en un OFCG basado en GS, OIL como técnica de selección de modos ópticos y un fotomezclador de THz de superred n-i-pn-i-p. Este sintetizador ofrece un rango de funcionamiento de 60 a 140 GHz, directamente escalable a un rango entre 10 GHz y valores más allá de un THz. Sintonía cuasi-continua es ofrecida en todo el rango de frecuencia de operación, con una resolución en frecuencia de 0.1 Hz a 100 GHz que puede ser directamente escalable a 0.01 Hz a 100 GHz

y 0.1 Hz a 1 THz. El ancho de línea a 3-dB de la señal a 120 GHz es menor de 10 Hz, solo limitada por la instrumentación de medida. El sistema ofrece una excelente estabilidad en potencia y frecuencia, con desviaciones sobre una hora de operación de 1.5 dB y 5 Hz, respectivamente. Estos valores también están limitados por la precisión e incertidumbre de la instrumentación de medida.

Las prestaciones conseguidas por este sintetizador fotónico de sub-THz y THz para la mayoría de figuras de mérito, igualan o superan aquellas de las mejores soluciones comerciales electrónicas en el estado del arte, y supera algunas de estas características en más de un millón de veces en el caso de soluciones fotónicas comerciales en el estado del arte.

La parte de detección de esta tesis explora el uso de arquitecturas fotónicas basadas en receptores EO heterodinos y los componentes clave que forman estas arquitecturas: Oscilador Local (OL) fotónico y mezcladores EO. Los primeros resultados son desarrollados en el entorno de microondas (<15 GHz) usando un amplificador de semiconductor óptico ultra no lineal (XN-SOA) como mezclador EO y un OL fotónico basado en GS. Se demuestra como este OL basado en GS ofrece una mejora significativa de las prestaciones del receptor con respecto al uso de OL fotónicos tradicionales basados en modulación lineal. Además, esta arquitectura de detección es validada en una aplicación real (imaging array fotónico), ofreciendo escalabilidad, flexibilidad y ratios de conversión razonables.

Tras esto, un receptor EO heterodino es demostrado hasta frecuencias de 110 GHz. El OL fotónico empleado es el sintetizador de altas prestaciones presentado en esta tesis, mientras que el mezclador EO es un nuevo detector de THz: el np-i-pn cuasi-balístico. La primera muestra fabricada de estos nuevos dispositivos, especialmente diseñados y optimizados para detección homodina y heterodina, es empleada. El receptor EO heterodino resultante ofrece ratios de conversión de -75 dB. Este dispositivo es capaz de trabajar sin alimentación, lo que unido a la distribución fotónica del OL, ofrece un gran potencial para detección remota de ondas de sub-THz y THz.

En resumen, las nuevas arquitecturas y dispositivos fotónicos presentados en esta tesis son capaces de ofrecer prestaciones en el estado del arte para generación de ondas de sub-THz y THz. En el caso de detectores EO heterodinos en frecuencias de sub-THz y THz, las técnicas fotónicas están mejorando sus prestaciones significativamente y están cada vez más cerca de ofrecer una alternativa a detectores electrónicos en el estado del arte.

SCIENTIFIC CONTRIBUTIONS LIST

Journal papers & letters included in this PhD thesis

1. Acedo, P., Carpintero, G., **Criado, A.R.,** De Dios, C., & Yvind, K. Photonic synthesis of continuous-wave millimeter-wave signals using a passively mode-locked laser diode and selective optical filtering. *Microwave and Optical Technology Letters*, *54*(6), 1416–1419 (2012). doi:10.1002/mop.26822.

2. **Criado, A. R.,** Acedo, P., Carpintero, G., de Dios, C. & Yvind, K. Observation of phase noise reduction in photonically synthesized sub-THz signals using a passively mode-locked laser diode and highly selective optical filtering. *Optics Express, 20*(2), 1253–1260 (2012). doi:10.1364/OE.20.001253.

3. **Criado, A.R.,** De Dios, C., Acedo, P., Carpintero, G., & Yvind, K. Comparison of Monolithic Optical Frequency Comb Generators Based on Passively Mode-Locked Lasers for Continuous Wave mm-Wave and Sub-THz Generation. *Journal of Lightwave Technology*, *30*(19), 3133–3141 (2012). doi:10.1109/JLT.2012.2211998.

4. **Criado, A. R.,** de Dios, C., Döhler, G. H., Preu, S., Malzer, S., Bauerschmidt, S., Lu, H., Gossard, A. C. & Acedo, P. Ultra narrow linewidth CW sub-THz generation using GS based OFCG and n-i-pn-i-p superlattice photomixers. *Electronics Letters* 48, 1425–1426 (2012). doi: 10.1049/el.2012.3158.

5. Davies, D. Inside View. *Electronics Letters*, *48*(22), 1376 (2012). doi:10.1049/el.2012.3593. **Interview.** doi: 10.1049/el.2012.3593.

6. **Criado, A. R.,** Dios, C. de, Prior, E., Döhler, G. H., Preu, S., Malzer, S., Lu, H., Gossard, A. C. & Acedo, P. Continuous wave sub-THz photonic generation with ultra-narrow linewidth, ultra-high resolution, full frequency range coverage and high long-term frequency stability. *Under review in IEEE Transactions on Terahertz Science and Technology* (12/2012).

7. **Criado, A.R.,** De Dios, C., & Acedo, P. Characterization of Ultra-Nonlinear SOA in a Heterodyne Detector Configuration With Remote Photonic Local Oscillator Distribution. *IEEE Photonics Technology Letters*, *24*(13), 1136–1138 (2012). doi:10.1109/LPT.2012.2196690.

8. Dios, C. de, **Criado, A.R.,** Prior, E., & Acedo, P. Enhancing the Performance of Electro-Optical Heterodyne Receivers using Gain

Switched Photonic Local Oscillators. *Journal of Lightwave Technology, 31*(8), 1331-1336, (2013). doi:10.1109/JLT.2013.2248121

9. **Criado, A.R.,** Montero-de Paz, J., De Dios, C., García, L. E., Segovia, D., & Acedo, P. Photonic Heterodyne Pixel for Imaging Arrays at Microwave and mm-Wave Frequencies. *Advances in Optical Technologies*, *2012*, 1–7 (2012). doi:10.1155/2012/792571.

Preprints included in this PhD thesis

A. **Criado, A.R.** et al. Sub-THz optoelectronic heterodyne receiver based on np-i-pn quasi-ballistic THz receiver and ultra-low phase noise sub-THz photonic Local Oscillator. *Preprint.*

B. **Criado, A.R.** et al. Zero-bias mm-wave optoelectronic heterodyne detection with np-i-pn THz detector and ultra-narrow linewidth sub-THz photonic Local Oscillator. *Preprint.*

Other contributions during the PhD thesis

Journal papers and letters

1. Arredondo, B., de Dios, C., Vergaz, R., **Criado, A.R**., Romero, B., Zimmermann, B., Würfel, U. Performance of ITO-free inverted organic bulk heterojunction photodetectors: Comparison with standard device architecture. *Under review in Solar Energy Materials and Solar Cells, (02/2013).*

2. Pedreira, P., Esteban, L., **Criado, A.R.,** Acedo, P., Sanchez, M., & Sanchez, J. Two color multichannel heterodyne interferometer set up for high spatial resolution electron density profile measurements in TJ-II. *Review of Scientific Instruments*, *81*(10), 10D517–3 (2010). doi:10.1063/1.3475729.

Conference contributions

1. Garcia-Muñoz, L.-E., Montero-de-Paz, J., Rivera-Lavado, A., Cámara-Mayorga, I., Güsten, R., Generalov, A., Lioubtchenko, D., Acedo, P., de Dios, C., **Criado, A.R.,** Ugarte-Muñoz, E., Räisänen, A. V., & Segovia-Vargas, Daniel. THz Antenna Array Based on Photomixers for Radioastronomy Applications. *EuCAP 2013, 7th European Conference on Antennas and Propagation,* (04/2013).

2. Arredondo, B., Romero, B., Dios, C. de, Vergaz, R., **Criado, A.R.,** & Sánchez-Pena, J. M. Thickness dependence of organic photodetector bandwidth. *9th Spanish Conference on Electron Devices,* (02/2013).

3. **Criado, A.R.,** Dios, C. de, Acedo, P., & Hartnagel, H. L. New concepts for a Photonic Vector Network Analyzer based on THz heterodyne phase-coherent techniques. *European Microwave Week 2012,* (10/2012).

4. Dios, C. de, **Criado, A. R.,** Döhler, G. H., Preu, S., Malzer, S., Bauerschmidt, S., García, L. E., Acedo, P. & Segovia, D. Sub-THz and THz Photonic Generation with Continuous Tunability Using Gain Switching based Optical Frequency Comb Generators and n-i-p-n-i-p Superlattice Photomixers. in *International Topical Meeting on Microwave Photonics. MWP 2012* (09/2012).

5. **Criado, A.R.,** Montero-de-Paz, J., Dios, C. de, García, L. E., Acedo, P., & Segovia, D.. Optoelectronic imaging array for microwave and mm-wave frequency range. *XXVII Simposio Nacional de la URSI*

(Unión Científica Internacional de Radio), (09/2012).

6. Acedo, P., Carpintero, G., **Criado, A.R.,** & Yvind, K. Photonic Synthesis of sub-THz Signals Using Mode-Locked Single QW Lasers and Tunable Fabry-Perot Fiber Filters. *EuMC 2011. 41st European Microwave Conference 2011* (pp. 1253–1256). Manchester Central, Manchester, UK, (10/2011).

7. **Criado, A.R.,** Acedo, P., García, L. E., Montero-de-Paz, J., Andrés-García, B., Carpintero, G., & Segovia, D. Heterodyne mm-wave pixel detector using photonic mixer and photonic local oscillator. *URSI 2011. 26th Simposium Nacional Unión Científica Internacional de Radio* (pp. 1–4). Leganés, Madrid, Spain, (09/2011).

8. Pedreira, P., **Criado, A.R.,** Acedo, P., Esteban, L., & Sánchez, M. Determination of spatial resolution for electron density profile measurements using a two color expanded-beam multichannel heterodyne interferometer in TJ-II. In E. P. Society (Ed.), *37th European Physical Society Conference on Plasma Physics*. Dublin, Ireland (06/2010).

9. Pedreira, P., Esteban, L., **Criado, A.R.,** Acedo, P., Sánchez, M., & Sánchez, J. First results from the two color multichannel heterodyne interferometer for high spatial resolution electron density profile measurements in TJ-II. *18th Topical Conference on High-Temperature Plasma Diagnostics*. : Wildwood, New Jersey, United States of America (05/2010).

Preprints

A. Yang, Z., Wonfor, A., **Criado, A.R.,** Dijk, F. van, Acedo, P., Penty, R. V., & White, I. H. Chirp-Enhanced Direct Modulation of a Monolithically Integrated Tunable Dual Laser Sub-Terahertz Transmitter (2013).

B. **Criado, A.R.,** Montero-de-Paz, J., Ugarte-Muñoz, E., Dios, C. de, García, L. E., Acedo, P., Segovia, D. & Hartnagel, H. L. Heterodyne photonic receiving antenna in the microwave and millimeter regime. (2012).

I

Introduction

1

Some background: The "THz gap"

At the end of 19th century, Hertz[1], Tesla[2] and Torres Quevedo[3] demonstrated the possibility of using the electromagnetic waves, theoretically described some years before by Maxwell[4], to carry out wireless transmissions in the radio frequency range. Their experiments were the inception of the whole development of the radio frequency region accomplished up to nowadays. Surprisingly, they were not aware of the huge consequences of their findings, as Hertz stated:

"It's of no use whatsoever[...] this is just an experiment that proves Maestro Maxwell was right—we just have these mysterious electromagnetic waves that we cannot see with the naked eye. But they are there"[5]

However, their research work opened this frequency range to the world. Basically, any technological field we know today wouldn´t be possible without the work of these pioneers: telephony, internet, smartphones, wireless communications or medical instrumentation and therapies, among others.

Some years later, at the beginning of the 20th century, the development of the quantum theory by Planck[6] and Einstein[7], among many other scientists[8], laid the foundations for the development of another frequency range: the optical or photonic range. However, the explosion of the applications in the photonic range would begin with the appearance of a high quality optical source several years later, in 1960: the laser[9,10]. This high quality source permitted the actual realization of most of the applications predicted for this frequency range and many others developed afterwards whose number is still growing today, such as biomedicine, optical communications, industrial manufacturing or spectroscopy, among many others.

This progress of the different regions of the electromagnetic (EM) spectrum during the last century is represented in Figure 1, where the development of the Radiofrequency (RF) and optical parts of the EM spectrum are shown. In this Figure 1, and despite the great research effort in the last century, we can see that there is still a great frequency region almost unexplored in the middle of the EM spectrum: the Terahertz (THz) range. This frequency range covers approximately

from millimeter waves (mm-waves) to Far Infrared (FIR) (60 GHz to 30 THz). This is the reason why this region is widely known as the "THz gap"[11–13]. Maybe the uncharted characteristic of the THz region could have been a reason itself for the first experiments carried out in this frequency range during the beginning of the 20th century. A detailed infography about THz history and main findings during the last century is included at the end of this document in *Appendix I. THz* history.

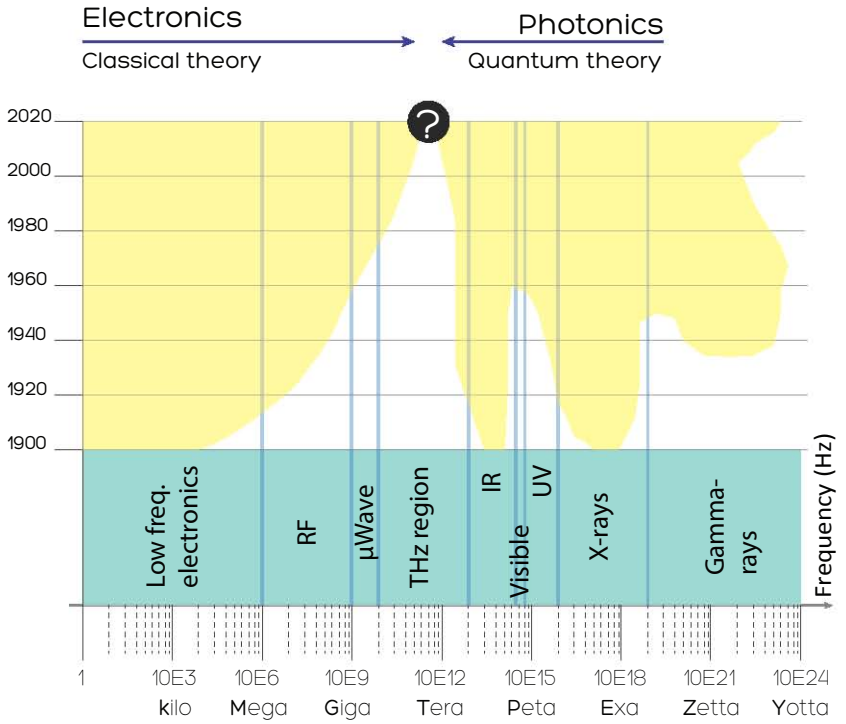

Figure 1 Electromagnetic spectrum. Evolution in the last century of the technology development (yellow region) in the different frequency regions. RF: radiofrequency; µWave: microwave; IR: infrared; UV: ultraviolet. Adapted from Zomega´s Terahertz Wave eBook[14]

In the last decades, we have witnessed an increase of the interest on this frequency range (THz) chiefly leaded by the potential features identified in the sub-THz and THz regions. These unique features of THz waves can be summarized in four key points:

- **Contactless identification of hidden objects and materials**[15]**.** Most nonpolar dielectric materials (basically dry and non-metallic) such as wood, plastic, cardboard or textiles are transparent to THz waves. This permits to see through these materials and identify hidden objects and materials like weapons, drugs or explosives.

- **Molecular resonances**[11,16]**.** The rotational and/or vibrational modes of a significant number of molecules are allocated in the sub-THz and THz regions. Moreover, some intermolecular effects can be also identified in this range. This permits to identify several compounds like drugs, explosives or biomolecules that have their fingerprint (absorption lines) in this frequency region and could not be identified using another frequency range.

- **Non-ionizing radiation**[13,14,16]. The energy associated with the THz radiation (around 1 meV at 240 GHz) is not able to ionize (i.e. harm) biological tissue. This is especially relevant for inspection and identification in homeland security and biomedical applications.

- **Atmospheric absorption**. Maybe one of the most significant features of THz waves is the huge absorption coefficient they have in ambient air due to water absorption. This is represented in Figure 2, where it can be seen how the attenuation dramatically increases for frequencies above 60-70 GHz[17]. However, it has been used as an advantage in some applications, like short range secure communications, where the information modulated in sub-THz and THz waves can be only received within a limited range, thus the interception of critical information becomes not feasible out of the secured area[18].

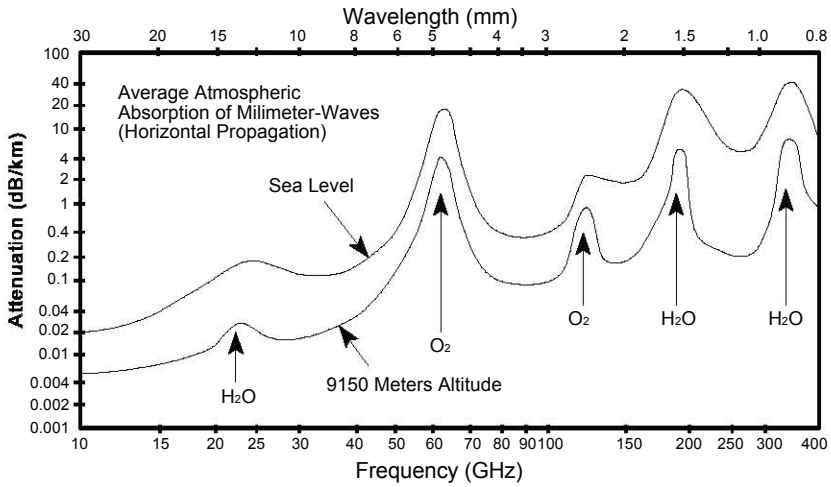

Figure 2 Atmospheric absorption at mm-wave and sub-THz ranges. Extracted from the Electronic Warfare and Radar Systems Engineering Handbook (open resource)[17]. Significant absorption peaks are located at around 60 GHz, 120 GHz, 200 GHz and 350 GHz.

This set of features provided by the THz radiation can be compared to those offered by other frequency ranges, such as photonics, microwave or

X-rays[13]. The presence of these frequency ranges in today´s applications is huge in a wide range of disciplines, hence, the comparison of their characteristics can provide an estimation of the magnitude of the potential of the THz range in the following years. As a reference for this discussion, the frequency, energy and wavelength ranges of each region are depicted in Figure 3.

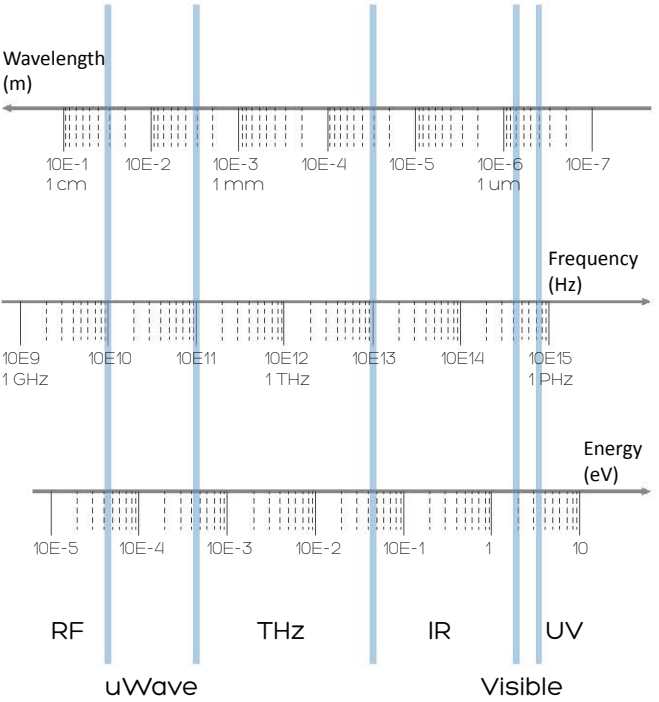

Figure 3 Energy, wavelength and frequency conversion chart around THz region.

The sub-THz and THz waves have the ability of penetrating through dielectrics and being able to identify hidden objects, what is shared with microwave and X-ray regions, but not with the optical signals, where the penetration depth is not high enough. The microwave radiation is also non-ionizing, as THz waves, but due to its longer wavelength; the spatial resolution provided in imaging applications is much lower. This is a clear advantage for THz waves in security imaging, but especially in biomedical imaging, where the resolution is one of the most critical factors. The X-ray region provides opposite characteristics to microwaves in this aspect. The spatial resolution is much higher than any of the others regions (with the exception of Gamma rays), but it is a harmful radiation, both for the subject under study and for the operator. Due to this fact, the maintenance policies and costs are much higher. Moreover, X-rays systems are very expensive and bulky.

Although all these four frequency domains offer non-contact identification or imaging of the sample, there is an important factor that is the capability of providing spectroscopic information of the sample. In this sense, X-rays provide

worse performance, due to much lower frequency sweep capabilities[13].

Another disadvantage of X-rays is the energy consumption. As the generation of X-rays is very inefficient, they need very high voltage values across the generation tubes (20 to 150 kV)[19]. Meanwhile, the great technology development of photonic and microwave regions has resulted in the availability of energy efficient sources and detectors. In the THz range, although the energy consumption is much lower than in X-ray domain, there is still great room for improvement. This is basically caused by a much less developed technology.

In Table I1, the abovementioned aspects and additional ones are summarized, in order to provide a clear comparison of the features of the different frequency regions.

Technology	Advantages	Disadvantages
Microwave	High sensitivity Good penetration in many materials Not hazardous No contact with sample	Low resolution
Infrared	High sensitivity 2D arrays real-time available Designs based on optical techniques Good resolution Not hazardous No contact with the sample	Low penetration in the materials
X-rays	High sensitivity 2D array available Highest penetration Excellent resolution No contact with sample	Hazardous Strict maintenance policies No spectroscopic information (no functional imaging)
Terahertz	Good resolution Good penetration in many materials Good sensitivity Not hazardous No contact with the sample	Low scan time Limited dynamic range

Table I1 Performance summary of different technologies available through the EM spectrum. Adapted from Redo-Sanchez *et al.*[13]

After the previous discussion, the question would be why this late development of the applications in the THz domain. The explanation is found in the delayed development of the THz technology when compared to other regions. Available THz detectors provide reasonable sensitivities at room-temperature operation, but worse than in other frequency ranges where the technology is largely developed. This, together with the limited power that compact THz sources can provide nowadays, make that currently available THz systems present worse dynamic ranges than in other frequency regions.

Nevertheless, the great research effort to improve THz technology, together with its unique combination of features, foretell a great potential of the THz range in the following years.

2

Interest in the "THz gap": Applications

The characteristics and unique features of the sub-THz and THz ranges, already introduced in the previous section, have as a consequence the existence of a great number of applications identified in this frequency range, which are maximizing the investment on THz research and development from some years to now.

Some of these applications were identified even before the existence of suitable generation and detection technology. This is the case of fusion plasma diagnostics based on THz[11,20] and especially THz astronomy[11,21], which appeared in 1970´s and drove the development of the THz technology during decades. Nevertheless, the vast majority of applications have arisen with the availability of better THz generation and detection systems.

In a first step, the applications of the sub-THz and THz ranges can be classified in three fields: communications, spectroscopy and imaging. It must be noted that spectroscopy and imaging are overlapped in most cases, as it can be seen in Figure 4, where this classification is represented for the main THz application fields. Additionally, a number of techniques used in other frequency ranges that have been successfully demonstrated in the THz region are also included in this Figure 4. In this section, the main applications of the THz range are briefly described following this classification.

Communications in the sub-THz and THz ranges are able to provide very high bandwidth, especially if photonic generation is used, where modulation in the optical domain can be accomplished[22]. Current communication systems use carrier frequencies in the lower range of THz region, i.e. mm-wave (below 140 GHz). Although at these frequency ranges the atmospheric absorption is very high[18], it is lower than at higher THz frequencies (see Figure 2), allowing short-range links[23]. Actually, this short range is as limited as a few meters.

Despite this short-range, there are three reasons why the communication links at sub-THz carriers are nowadays a prolific research field[18,22,24,25]. The first one is the absence of regulations in several bands within the sub-THz range[21]. The second is the high data rates that can be achieved[23]. The third is the possibility

of using this high absorption as a security resource for secure links, in which the transmitted data cannot be intercepted at distances greater than a few meters; and also for frequency reuse.

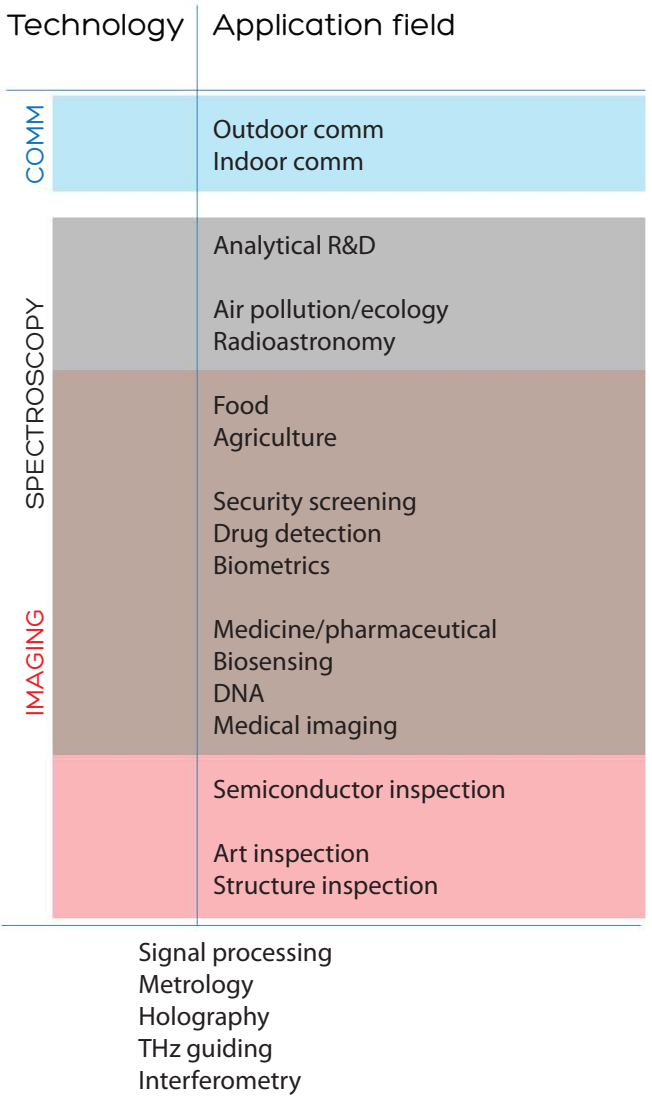

Figure 4 Applications in the THz range, classified in COMM (communications), SPECTROSCOPY, IMAGING or a combination of these latter two.

As previously said, a great number of resonance peaks of molecular and intermolecular vibrational modes are allocated in this frequency range. This makes spectroscopy one of the main application fields in the THz range. Moreover, if combined with imaging, not only the location, but also the composition of a sample or part of it can be identified. This sets up a powerful tool for a great

number of applications, such as security, atmospheric and air observation, biomedical imaging or fundamental molecular analysis, among others.

Although today there are much more applications pushing THz development, it was astronomy which firstly leaded this THz research in 1970´s. Several of the sources and detectors available today owe their existence to astronomy[26], and even several major branches of astronomy are still reliant on a further development of THz technology[27]. The interest of astronomy and astrophysics in the THz radiation is threefold[27]:

- Low temperature collisions of diffuse molecules have their vibrational and rotational modes in the THz regime.
- The blackbody spectrum (4-100 K) is allocated in the THz range.
- Some particles, such as graphite grains are transparent to THz frequencies.

The importance of the identification and study of astronomical processes at THz frequencies is key in the path to understand how galaxies are formed or even how Big Bang was originated[27].

Today, major astronomical observatories like HIFI on the Herschel Space Observatory, or GREAT on SOFIA[21] are equipped with THz telescope systems. It is worth saying that due to the attractive of remote LO distribution for THz generation and detection, photonic techniques are becoming a promising technology for astronomy, especially at lower THz frequencies (< 1 THz), where they can now provide high performance[28].

The spectroscopy applications extend down to atmosphere levels, especially to analyze the composition of the air, study molecular processes[21] and identify eventual dangerous substances[21]. In this sense, the identification of air pollutants is of especial interest for agriculture industries. Moreover, another THz application in agriculture is the quantification of the humidity of fruits and vegetables to identify the optimum collection times.

The fusion plasma diagnostics is also one of the first application fields of the sub-THz and THz technology, basically focused on electron density profile measurements as a function of time and position in the plasma core[11]. These measurements are accomplished by using heterodyne interferometry[29] and Thomson scattering techniques and measurement of Electron Cyclotron Emission (ECE) from the plasma. Typical values of ECE in Tokamak systems are in the range 100-150 GHz. Moreover, frequency sweep capabilities allow different penetration depths in the plasma, thus achieving 2D imaging systems for the representation of the plasma[11].

The spectroscopy features of THz waves are a valuable resource for fundamental analysis in a significant number of research fields, for example, detection of alcohol and sugar[30], monitoring of composition of CH-plasma during

diamonds CVD process[31], or even application of the supersonic molecular beams for analytical investigations[32]. The non-contacting spectroscopy applications are also applied to food and pharmaceutical industries[33–36], not only for compound control but also for packaging evaluation and non-desired dielectric materials identification[37] (e.g. plastics or metals inside the package).

But maybe the most popular application in the mm-wave range is imaging for homeland security purposes[15,38,39]. These systems are already commercially available and can be found in a great number of international airports, also known as T-rays scanners. In an equivalent way as X-rays scanners, they permit the visualization of hidden objects, but without harming biological tissues and allowing for the identification of compounds, like drugs or explosives through non-contacting detection[40]. The development of the THz technology is expected to provide in a few years with more compact and low cost scanners that will allow directly identifying almost in real time the composition of hidden materials, without ionizing radiation.

Asides from the already mentioned, non-destructive inspection have wide application in the semiconductors field[37], art conservation[21], or even building structure inspection. This is basically due to the capabilities of identifying structural defects such as cracks or voids, measure thickness and inspect corrosion effects[14,38].

Medical imaging is a major research field within the THz region[16,41] due to its features in terms of resolution (although much lower than X-rays) and especially non-ionizing properties[34,36,41–43]. As it is the case for security screening, in the following years we can expect an advent of compact, less expensive and high performance THz systems that will permit an efficient and not-hazardous identification and visualization of human tissues for biomedical purposes. The imaging of human structures has been also studied for biometric identification applications[37]. Also applications in biosensing have been reported. Examples that can be highlighted are analysis of exhaled air[44,45], remote heart-rate monitoring[46] or even analysis of DNA[47].

The number of applications in the THz is still growing today. Several techniques widely used in other frequency regions (microwave, RF) have been already reported in the THz region, what can be also seen as a clear indicator of the appearance in a near future of further applications at THz frequencies related to these techniques, such as signal processing[48–54], metrology[55–60], holography[61,62], THz guiding[63–73] or interferometry[74–76].

3

Building systems in the "THz gap": sub-THz and THz technology

The great number of applications for the sub-THz and THz regions identified in previous paragraphs are to be implemented through the different technologies developed for these frequency ranges. In this section, a brief revision of the state-of-the-art of mm-wave, sub-THz and THz technology is presented. This review is mainly focused on the generation and detection technologies with more capabilities and potential in terms of compactness and performance, which are the main current research trends for the new generations of THz technologies. A brief discussion about THz optics (especially guiding THz optics) is also included. For the interested reader, a much more extensive review about THz generation and detection technology can be found in *Appendix II. mm-wave, sub-THz and THz technology. Sources and detectors: state-of-the-art (November,* 2012). In this appendix almost all existing sources and detectors are described and their state-of-art performance and characteristics as November of 2012 are listed for each device/technology.

When dealing with THz systems and technologies, it is important to differentiate between the two basic types of THz systems: pulsed and Continuous Wave (CW). Figure 5 represents the temporal and frequency domain characteristics of both pulsed and CW radiation. The concept follows the same idea as pulsed and CW waves in any other frequency range. CW signals appear as a sinusoid in temporal domain, and as a tone in the frequency domain (Figure 5). Alternatively, pulsed signals are time-limited waveforms in the temporal domain and cover a very wide range in the frequency domain, inversely proportional to the temporal width of the pulse. These two types of systems offer different capabilities and their use depends on the final application. A summary of their main features is shown in Table I2.

CW systems are used for applications requiring narrow-band signals, such as communications and high-resolution spectroscopy. These systems are

also used when high sensitivity is required, as they can be used in heterodyne schemes. Concerning frequency response measurements, they are able to achieve much higher frequency resolution, but sweeping is required, thus being slower than their pulsed counterparts. For these applications, CW systems are commonly used under the framework of Fourier Transform Spectroscopy (FTS)[21] schemes.

Pulsed systems provide with broadband signals that allow for direct spectral measurements. These spectral measurements are much faster than in CW systems, but they have much less resolution. The pulsed systems are mainly associated to Time Domain Spectroscopy (TDS)[21].

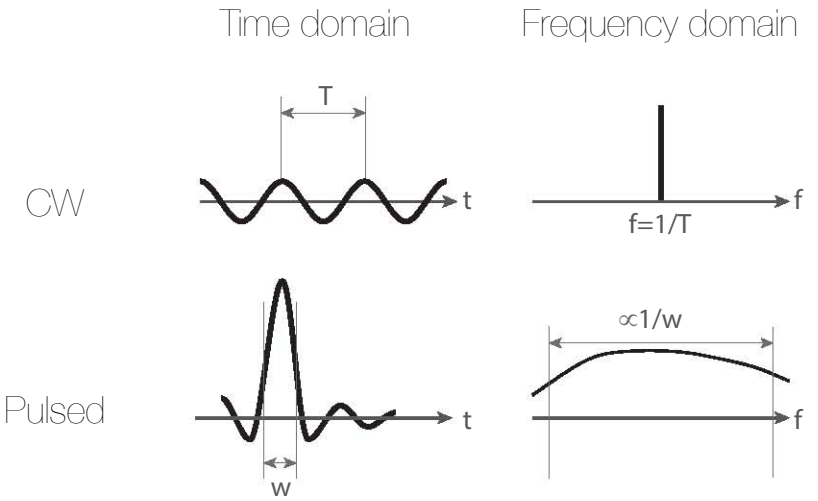

Figure 5 Representation of continuous Wave (CW) and pulsed radiation. Temporal and frequency domains

CW	Pulsed
Narrowband	Broadband
Sweeping required for spectral data	Direct measurement of spectral data
High power density (per Hz) available	Lower power densities (per Hz)
Coherent detection available (amplitude and phase information)	Coherent detection available (amplitude and phase information)
Heterodyne systems available (higher sensitivity)	Depth/thickness information (time of flight)

Table I2 Main characteristics of CW and pulsed THz radiation for spectroscopy applications

This thesis focuses on CW systems. For this reason, the technology summary of this section emphasizes CW systems versus pulsed ones, although these will be also listed in order to provide a global view of the current THz technology scenario. Furthermore, the previously mentioned appendix (*Appendix II. mm-wave, sub-THz and THz technology. Sources and detectors: state-of-the-art (November,* 2012)*)*, includes extensive information of both CW

and pulsed systems.

3.1 Sub-THz and THz sources

The THz technology has been growing and improving for several years now due to the effort of numerous research groups trying to translate all the unique features of the THz radiation to valuable applications for the real world. However, there is still a lack of THz systems with the required characteristics to offer an easy exploitation of all the identified applications in this frequency region by a wider range of users, including non-scientific users. The main reason for this is still the need of a high quality, low cost, compact and easy to operate source that would allow this, as in the past the laser did for the photonic domain.

The generation of sub-THz and THz signals can be accomplished using three different approaches. The first one tries to push the limits of electronics to higher frequencies. The second one relies on the conversion of optical signals down to frequencies in the sub-THz and THz ranges. The last approach is the direct generation of sub-THz and THz signals using a single specific device.

Direct generation is the approach commonly found in other frequency regions. However, this approach has had very limited potential in the THz region, being this the main reason for the traditional lack of available technology in the THz range (see Figure 1). This bottleneck in the development of THz systems has been partially overcome by further progresses on the other two approaches: frequency multiplication from the microwave region, and downconversion from the optical domain. Nowadays, most THz technology development (with some exceptions) is accomplished from these two approaches, which are able to provide with high performance THz generation systems.

One of the possible classifications of the existing sub-THz and THz sources can be based on this criterion, as it is represented in Figure 6. In this figure, almost all existing sources are listed and classified in these three main groups depending on the approach employed for generation. Furthermore, the ability of producing CW and/or pulsed radiation is also depicted in this Figure 6.

The review of sub-THz and THz signals generation of this section includes a brief summary of almost all the available sources, both pulsed and CW, that are represented in Figure 6. After this, a technology mapping of the sources able to provide with CW radiation, which is the focus of this work, is presented. In a third step, a criterion to select and compare the generation technologies with the highest potential is presented. This criterion is used to identify the most promising sources for the development of THz technology in the short and intermediate future.

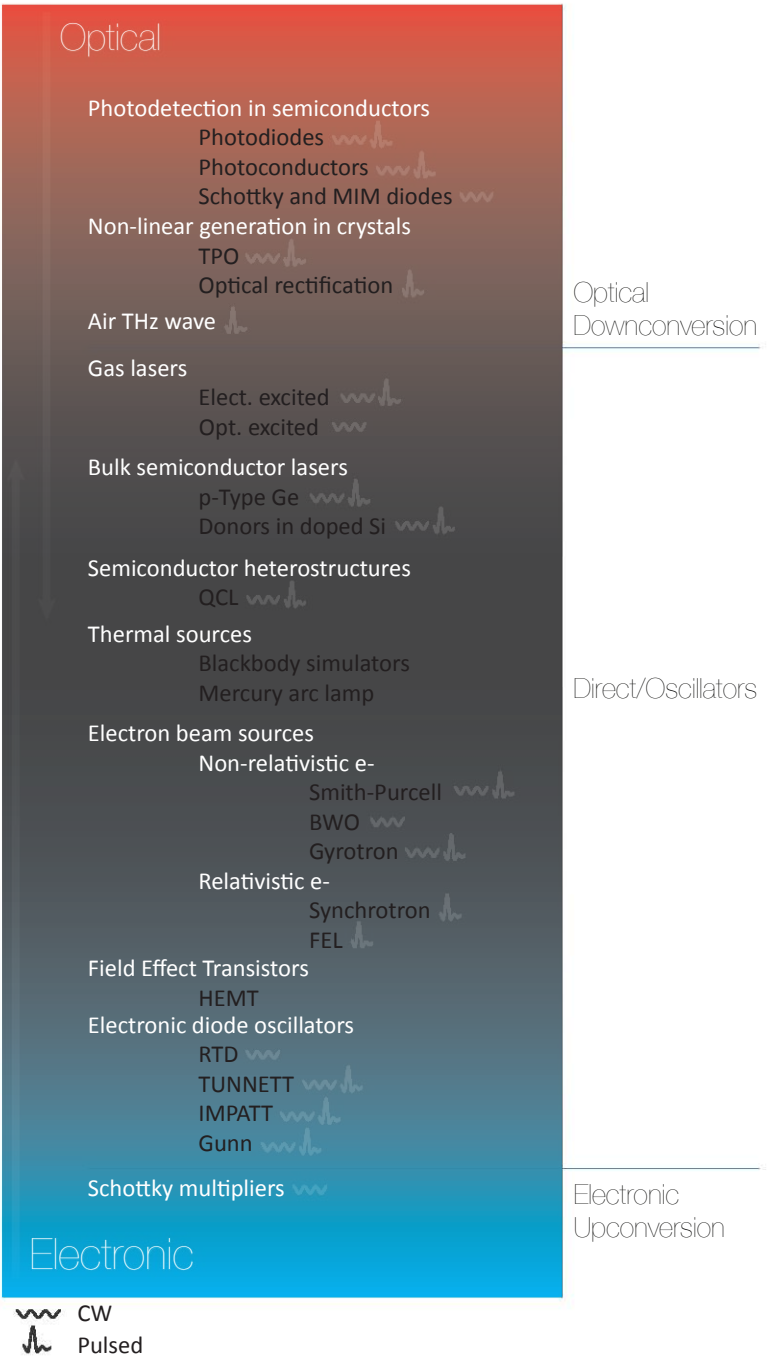

Figure 6 sub-THz and THz generation technology chart. The sources are classified as a function of the approach employed: electronic upconversion, direct generation and optical downconversion. Furthermore, the CW and pulsed generation capabilities of each source are shown

Generation based on electronic upconversion is carried out using **Schottky multipliers.** This is one of the most extended technologies for sub-THz and THz generation, mainly due to the high performance they can provide[77].

Despite of having less performance than electronic upconversion or optical downconversion systems, there are several approaches for sub-THz and THz direct generation. They can be allocated in seven groups, also represented in Figure 6: electronic diode oscillators, Field Effect Transistors (FETs), electron beam sources, thermal sources, THz Quantum Cascade Lasers (THz-QCL), semiconductor bulk THz lasers and gas lasers.

- **Electronic diode oscillators**. These sources are based on microwave frequency diode oscillators that are designed and implemented for higher frequency operation. Between the variety of topologies based on diodes that have been reported, we can mention: Gunn diodes[78], Impact Ionization Avalanche Transit-Time (IMPATT) diodes[78], Tunnel Injection Transit-Time (TUNNETT) diodes[79] or Resonant Tunneling Diodes (**RTD**)[80,81], being RTDs the most promising technology nowadays for the direct generation of THz signals below 1-2 THz.

- **FETs**. Although FETs have been demonstrated as oscillators (even amplifiers) in the low THz frequency region (mainly below 500 GHz)[82–84], they have proven much more potential as detectors, as it will be shown later in the section devoted to review THz detection[83,85,86].

- **Electron beam sources.** They can be divided into two subgroups: non-relativistic and relativistic. The first ones use an electron beam for the generation of THz signals. **Smith-Purcell** sources[87], **Backward Wave Oscillators** (BWO)[88] and **gyrotrons**[21,89,90] are included in this subgroup. Relativistic sources, such as synchrotrons[91] and Free Electron Lasers (FEL)[92] also make use of electron beams, accelerating them close to the speed of light. Because of this, they are extremely huge systems, some as big as a whole building. Among these electron beam-based sources, maybe only Smith-Purcell sources and BWOs meet enough requirements to be suitable sources for wide use, at least in terms of size.

- **Thermal sources.** They were the first employed THz sources (e.g. mercury arc lamp)[93]. They emit incoherent radiation in a wide range of frequencies, even up to UV. Their emission spectrum is similar to the blackbody spectrum[94]. They are mainly used for calibration purposes[21].

- **THz-QCLs (Terahertz Quantum Cascade Lasers)**. They are semiconductor heterostructures that have revolutionized both

optics[95] and THz fields[96]. They provide with very high power levels (around 140 mW), but they hardly work below 2 THz[21] and require cryogenic cooling[97] to operate within the THz range.

- **Bulk semiconductor lasers.** In these devices, the active medium consists on a bulk material (not a heterostructure). Standard semiconductor laser structures are of no application at THz frequencies as the smallest bandgaps in materials are above 18 THz[21]. However, with the aid of proper doping techniques, some bulk lasers emitting pulsed and multiline THz radiation have been demonstrated: p-Type Germanium lasers[98] and Silicon-doped optically excited lasers[99].

- **Gas lasers**. They were the first THz sources used in 1970´s for astronomy and fusion plasma diagnostics purposes[29], and are still widely used today for these applications. They are bulky devices, but provide high power levels (around 600 mW for electrically excited gas lasers and around 100 mW for optically excited ones)[21]. They can operate under pulsed or quasi-CW (multiline) operation.

When discussing optical downconversion techniques we can identify three main groups:

- **THz wave air photonics.** This is a recent technology for the generation and detection of pulsed THz radiation. Its main advantage is the high frequency that can be achieved, as high as 60 THz[100–103]. The operation principle relies on the creation of a gas plasma region by optical excitation trough an ultrafast pulse. Emission of THz pulsed radiation from frequency components contained in the optical excitation mixed in air plasma is due to non-linear processes (i.e. ponderomotive force or Four-Wave Mixing (FWM))[100–102].

- **THz generation in non-linear crystals.** This group includes THz Optical Parametric Oscillators (THz OPO or TPO)[104,105] and optical rectification (or Electro-Optical Sampling, EOS) in non-linear crystals[106]. Both approaches are mainly used under pulsed operation in TDS setups, although TPOs are also able to provide CW signals using CW pump lasers[21]; and some CW systems based on EOS have been also reported.

- **Photodetection in semiconductors.** The process of optical to (mm-wave) THz conversion in a photodetector is also known as Difference Frequency Generation (**DFG**)[21,107] or Optical Heterodyne Generation (OHG)[108]. It is based in the detection of two optical frequencies spaced by the desired sub-THz or THz frequency. The photodetector detects the power of this dual-

mode optical signal, thus detecting the difference frequency term (i.e. THz signal). As mixer element, diodes like Schottky[109] or Metal-Insulator-Metal (MIM)[21] have been used. However, the vast majority DFG systems employ photodetectors such as **Photoconductors** (PC)[108,110,111] **or Photodiodes** (PD)[112–116]. DFG in photodetectors, especially in PDs is one of the most promising generation technologies below 1 THz.

Among the sources from Figure 6, those being able to provide CW radiation are mapped as a function of size, power and frequency range in Figure 7 and Figure 8. These maps permit a general view of currently available CW THz generation technology at a glance.

The first map (Figure 7) shows the relative position of each CW generation technology as a function of their size and their output power at around 1 THz. The desired region is bottom-right, i.e., small size (even with integration capabilities) and high output power. Furthermore, the size of each source can give an approximated idea of the magnitude of its cost.

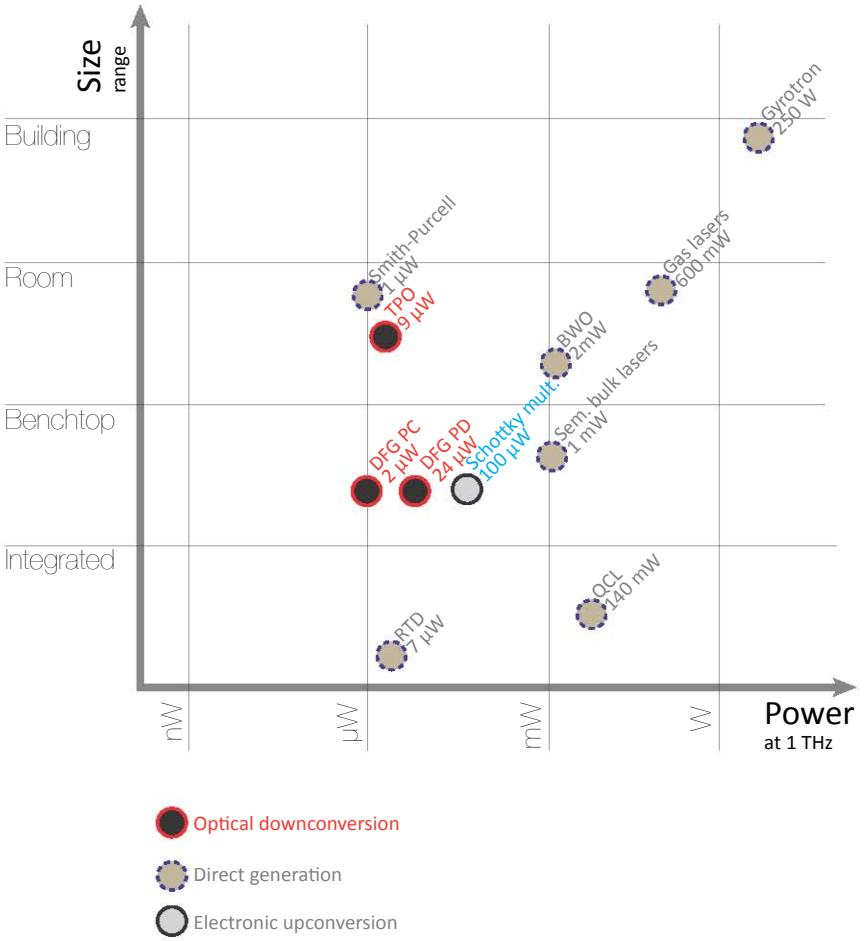

Figure 7 CW THz generation technology map. Size vs. power. References of the data in the figure are provided in the extended review included as *Appendix II. mm-wave, sub-THz and THz technology. Sources and detectors: state-of-the-art (November,* 2012)

Figure 8 shows the map of these sources as a function of their frequency coverage and output power at 1 THz. Wide frequency coverage regions and high output power (i.e. wider vertical coverage and right position) are the ideal features.

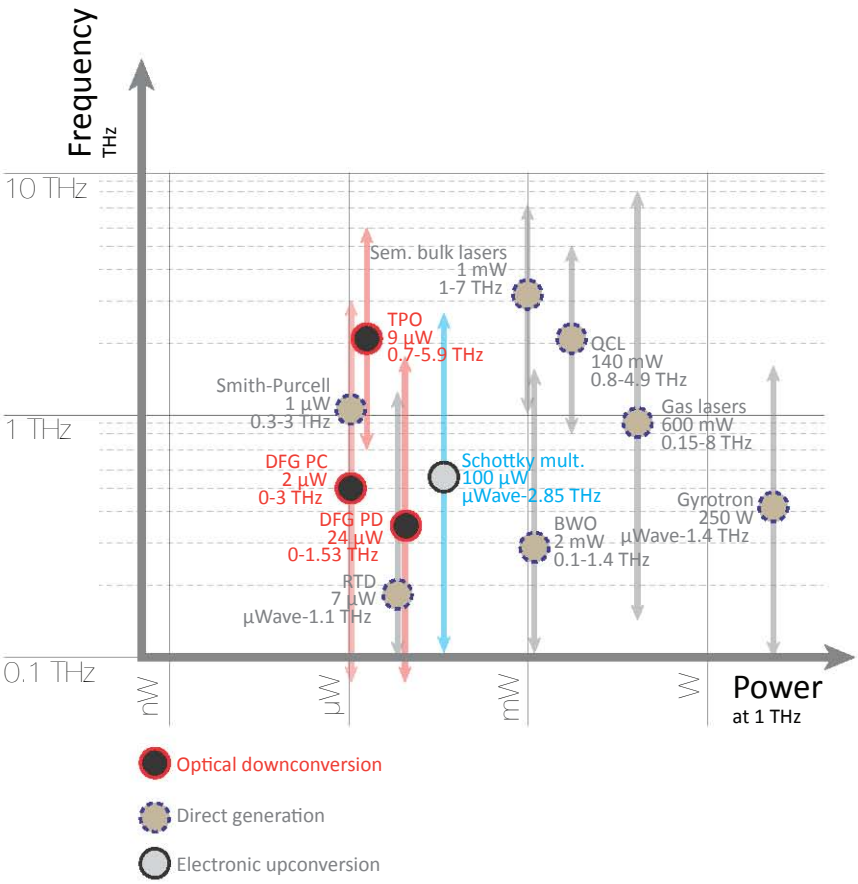

Figure 8 CW THz generation technology map. Frequency coverage vs. power. Each symbol text contains: name of the device (line 1), maximum power at 1 THz (line 2), and frequency coverage (line 3). References of the data in the figure are provided in the extended review included as *Appendix II. mm-wave, sub-THz and THz technology. Sources and detectors: state-of-the-art (November,* 2012)

In order to compare these technologies and to identify the ones with the highest potential for next generation THz sources, we are going to define a criterion based on figures of merit. Moreover this criterion will be biased by current trends of THz generation, which are basically driven by users and market needs. The selected figures of merit that build up this criterion cover basically all characteristics of a generation system:

- Maximum power. Maximum output power demonstrated for a given technology.
- Frequency range. Frequency range in which it is possible to generate signals.
- Tunability. Tunability capabilities around the center frequency.

Also tunability characteristics (continuous or discrete) are considered.

- Minimum spectral FWHM. Minimum Full Width at Half Maximum (FWHM) of the generated CW signals demonstrated with the analyzed technology. Because of the difficulty of measuring phase noise at high frequencies, most investigations only report on the FWHM as an indicator of the phase noise performance.

- Minimum size. Minimum size in which the given technology has been implemented.

- Coherent/incoherent. Coherent sources are defined here as those having a significant degree of both temporal and spatial coherence in the generated signals. Further details on temporal and spatial coherence of EM waves can be found in Born & Wolf[117].

- Cooling requirements. Room temperature (RT) operation is defined here for those systems where no cooling is needed, or just Thermo Electric Coolers (TEC), heatsinks or thermal pads are enough.

A complete review of these figures of merit for all available sources (Figure 6) is included in *Appendix II. mm-wave, sub-THz and THz technology. Sources and detectors: state-of-the-art (November,* 2012). It is important to note that this appendix review is based in the state-of-the-art performance of these figures of merit rather than in an exhaustive description of the theoretical background behind the different approaches.

After the evaluation of the abovementioned figures of merit, those with a highest potential for reliable, compact and cost efficient THz generation are presented below with more detail, including a discussion of each one based on the mentioned figures of merit. These technologies are: electronic upconversion using Schottky diodes, RTDs, QCLs, DFG using PCs and DFG using PDs. It must be noted that the focus of this evaluation is placed on the frequency range 0.1 to 2 THz approximately, which is the one of interest for this work.

- Electronic upconversion is carried out by multiplying a reference in the microwave or mm-wave region to higher frequencies. Schottky multipliers are used to implement doublers, triplers or a chain of them, ending up with benchtop size sources. Maybe this is the highest performance commercially available coherent source nowadays, and it is widely used for applications below 2 THz. They provide with reasonable power levels (around 100 μW at 1 THz)[118], frequency values up to 2.85 THz[119] and coherent signals under RT operation. An important inconvenient of multiplication processes is that it translates into a multiplication

of frequency instability and phase noise[120]. However, as high performance microwave references can be used, FWHM and frequency resolution values in the Hz range can be obtained[118]. One of the main disadvantages is the operation bandwidth, which is limited by the metallic waveguides used to a few hundreds of GHz in the better cases (higher frequencies). Because of this, several branches working at different bands are required to have full frequency range coverage.

- One of the most promising direct generators at THz frequencies below 1 THz is the RTD. This is basically because of its planar integration capabilities, low cost potential and room temperature operation. Operation frequencies up to 1.1 THz[81] have been reported, although operation up to 2-3 THz in a short-term future is expected[121]. They are also coherent sources that have demonstrated output powers around 7 μW at 1 THz[81]. However its signal quality is not very high, with linewidths (i.e. FWHM) in the order of 10 MHz[122], and they offer a very limited tunability range over the center frequency (around 4%)[80].

- Another of the selected technologies here is the THz-QCL. The main advantage is the output power they are able to provide, with impressive values in the order of 140 mW[21]. They are also very interesting in size (planar/integrated size) and cost. Nevertheless, there are three main drawbacks associated to THz-QCLs. The first one is that they need to be cryogenically cooled in order to properly operate at THz frequencies[97]. The closest approach to RT operation in the THz range requires mixing the emission of the QCL with an injected IR laser in the QCL itself, producing a THz output at RT in the nW range[123] The second is that their tunability is very limited. The main tunability methods require mechanical means[124], using MEMs[125] and wire-lasers[126], with record values around 8.6% of Center Frequency (CF)[125]. Very narrow tunability (10 GHz) can be obtained with current or temperature control. Finally, the generated frequencies are basically above 2 THz for practical devices, reaching about 4.9 THz[96]. Applying external magnetic fields, operation down to 0.8 THz has been achieved[21]. Due to its characteristics, the THz-QCL is an excellent candidate for some applications above 2 THz, like THz astronomy, but these drawbacks, especially the need of cryogenic cooling, can hardly be sustained in wide spread commercial applications.

- The two last technologies are DFG using PCs[110,127–130] and PDs[112–116] as photodetectors that perform the optical to THz downconversion. They have output power values lower than electronic upconversion, their main competitor. Using PCs,

values around 2 μW at 1 THz[108] have been achieved. The use of PDs provide with higher output powers, up to 24 μW at 1.06 THz[108], which is one of their main advantages over PCs. However, in terms of maximum operation frequency, the opposite occurs. PCs present bandwidths up to 3 THz[21], while PDs offer frequencies up to 1.53 THz[131]. A more extensive description of reported PCs and PDs characteristics will be described in later sections of this work.

The tunability capabilities and the quality of the signals in terms of FWHM depend on the optical source employed for these optical downconversion schemes. With some of them, like the one developed in this PhD work, FWHM in the Hz range and frequency resolution around 0.1 Hz at 1 THz can be obtained[132]. Our optical source is able to dramatically increase the signal performance in DFG systems, matching or even surpassing the linewidth and frequency resolution of the best electronic upconversion systems. However, when using optical sources like those employed by commercially available solutions[129,133], these values are around a few MHz. Further description of the optical sources that can be used in DFG schemes will be treated in later sections.

DFG-based schemes can provide with similar cost, size and RT cooling characteristics as Schottky multipliers. The main advantage of DFG is that it is able to offer full frequency band coverage with the same source (using adequate optical architectures[132]). Additionally, they can provide a unique feature that is the capability of remote THz generation and optical signal distribution using optical fiber, what is a great advantage in terms of losses, Electromagnetic Interference (EMI) immunity and weight. The optical fiber distribution has two additional and significant advantages. The first one is the capability of using Commercial Off-The-Shelf (COTS) optical components in the telecom range that provides with high performance, wide range and low cost devices. The second one is the possibility of using signal processing techniques inherited from the Microwave Photonics field[50].

Thus, after this evaluation, electronic upconversion using Schottky diodes and DFG using PDs are identified as the two technologies that nowadays have the highest potential for the development of the next generation of sub-THz and THz sources. Electronic upconversion is more mature as commercial solution, but DFG using PDs offers promising capabilities due to the remote photonic distribution of the signal. The work presented in this PhD dissertation is based on DFG using PDs, which will be more deeply described later in this document (chapter II).

3.2 Sub-THz and THz detectors

In the previous section, THz generation technologies were firstly classified depending on the generation approach (see Figure 6). For this overview of the THz detection technologies, we are going to classify the detectors depending on the pulsed or continuous temporal characteristics of the incoming THz wave, as it is represented in Figure 10.

Moreover, a receiver scheme can be also classified from other points of view. One of them is whether the detection is coherent or incoherent. In most cases, when the coherence concept is applied on detection, it refers to temporal rather than spatial coherence. In a coherent receiver, the detected signal is phase-correlated with the emitted signal, thus, there is a coherent superposition of both fields (they have a constant relative phase). Coherent receivers allow measuring not only amplitude, but also the phase changes of the received signal with respect to a reference.

Furthermore, a receiver can work under direct and/or heterodyne detection. In direct detection, the THz signal measured (Measurement signal, M) is detected without converting its frequency to a different frequency band. Usually, as it is the case of rectifiers, a DC signal proportional to the power is obtained from the device, what can be also seen as a conversion to DC.

In heterodyne detection, the THz detector is used as mixer. Two signals, the THz radiation (or measurement signal, M) and a Local Oscillator (LO) of different frequency are mixed to obtain an Intermediate Frequency (IF) signal at lower frequencies, as depicted in Figure 9. This is accomplished by multiplying the M signal with a LO, producing a sum and a difference term. However, a device performing this ideal multiplication does not exist, as actual mixers produce several additional and non-desired terms. There exist basically two types of mixing devices: nonlinear mixers (i.e. square law detectors) and switching mixers.

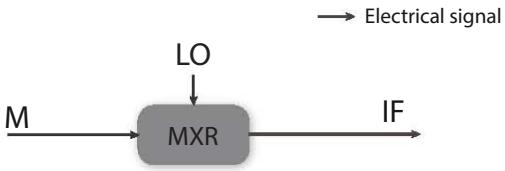

Figure 9 Sub-THz and THz CW heterodyne detection schemes: all electronic mixing

The nonlinear mixers take advantage of the nonlinear relationship between the generated current and detector bias voltage, i.e. V-I curve, to perform the mixing process in a controlled region of the nonlinear V-I region. The V-I curve of a nonlinear device can be expressed as[21]:

$$I(V) = k_0 + k_1 V + k_2 V^2 + \ldots = \sum_{i=0}^{\infty} k_i V^i \quad (1)$$

where the third term in the right part of (1) (i.e. second order term) is the one of interest, as it contains the difference term. In square-law detectors, this term is dominant ($k_2 >> k_i;\ i \neq 2$). If the whole equation (1) is expanded, frequency terms at $|nf_{LO} \pm mf_M|$ will appear, although with much less power in the case of a square-law detector. The squared input voltage V^2 can be written as follows:

$$V^2 = {V_M}^2 + {V_{LO}}^2 + 2V_M V_{LO} \quad (2)$$

The two first terms of the right hand side of equation (2) will give DC terms, and terms at frequencies $2f_M$ and $2f_{LO}$. The third term of the right hand side gives the sum and difference terms.

The nonlinear detector is sensitive to the total power of the sum of both M and LO signals (V_M and V_{LO}), but not to the individual fields as it is not fast enough to follow both fields, i.e. it has enough bandwidth for the IF signal but not for responding directly to the LO or M fields[21].

The second type of mixers are those able to react to the individual fields M and LO. They are called switch mixers[21]. In this case, the LO signal is a square signal that switches the phase of the M signal from 0º to 180º and viceversa in each half period of LO. The equation describing this process consists on the multiplication of the M signal with a square LO signal with 50% duty cycle, which is expressed according to its Fourier decomposition, (3):

$$\begin{aligned} V_{OUT} &= V_M V_{LO} = \\ &V_{M,0} \sin\left(2\pi f_M t\right) \\ &\times \left[V_{LO,0} \left(\frac{4}{\pi} \sin\left(2\pi f_M t\right) - \frac{4}{3\pi} \sin\left(2\pi 3 f_M t\right) \right.\right. \\ &\left.\left. + \frac{4}{5\pi} \sin\left(2\pi 5 f_M t\right) - \ldots \right) \right] \end{aligned} \quad (3)$$

being $V_{M,0}$ and $V_{LO,0}$ the voltage amplitude of the M and LO voltages, respectively. It is important to notice that a LO with a large amplitude can be seen as a square signal, as it will saturate the mixer. The IF power has a component proportional to the product of M and LO amplitudes. However, this multiplicative component tends to be very low at THz frequencies, like in Schottky diodes, but can be higher (desired scenario) in some state-of-the-art FET mixers[134]. Other switch mixers are SIS mixers[21]. As the IF power will depend in the mixing

components, a higher multiplicative term is much convenient than lower multiplicative terms or additive terms in order to provide higher mixer input (basically through higher LO power) and higher sensitivity in the receiver[134].

The importance of heterodyne schemes, as it is in any other frequency range, is given basically by two key advantages. Firstly, a LO with higher power than the M signal can be used to improve the sensitivity, as the IF term depends on both M and LO signal power values. Secondly, the IF signal frequency can be chosen in a range where very high sensitivity instrumentation is available, for instance MHz range, where Electrical Spectrum Analyzers (ESA) provide with very good sensitivity features. These advantages can dramatically improve the overall sensitivity of the system, as well as the dynamic range.

Homodyne detection is closely related to the heterodyne concept as it is basically a special case of heterodyne detection. In a homodyne setup, the source signal is split in two paths. One of them will be the M signal and the other one the LO. As they come from the same source, the frequency is the same and the IF signal frequency is 0 Hz (DC).

As it has been previously said in section 3.1, all compact THz generation technologies below 2 THz, especially the photonic ones, have a common bottleneck associated to the limited output power they can provide. This is a limiting factor for the dynamic range of the whole THz system. In order to overcome this, extensive work has been (and will be) made in order to increase the power in generation. Nevertheless, another approach is focused in the improvement of the sensitivity in the receiver. Less attention has been paid to this approach, especially in photonic THz systems, but nowadays is becoming a major research trend[135,136]. The main method to attain this higher sensitivity is the use and optimization of heterodyne systems, which are EO heterodyne systems in the case of using photonic THz LOs.

Another future aspect to improve is related to the coherent detection in these heterodyne EO systems. Coherent pump-probe systems with high quality have been demonstrated [137], but the coherence in EO heterodyne systems will need further and extensive study[138].

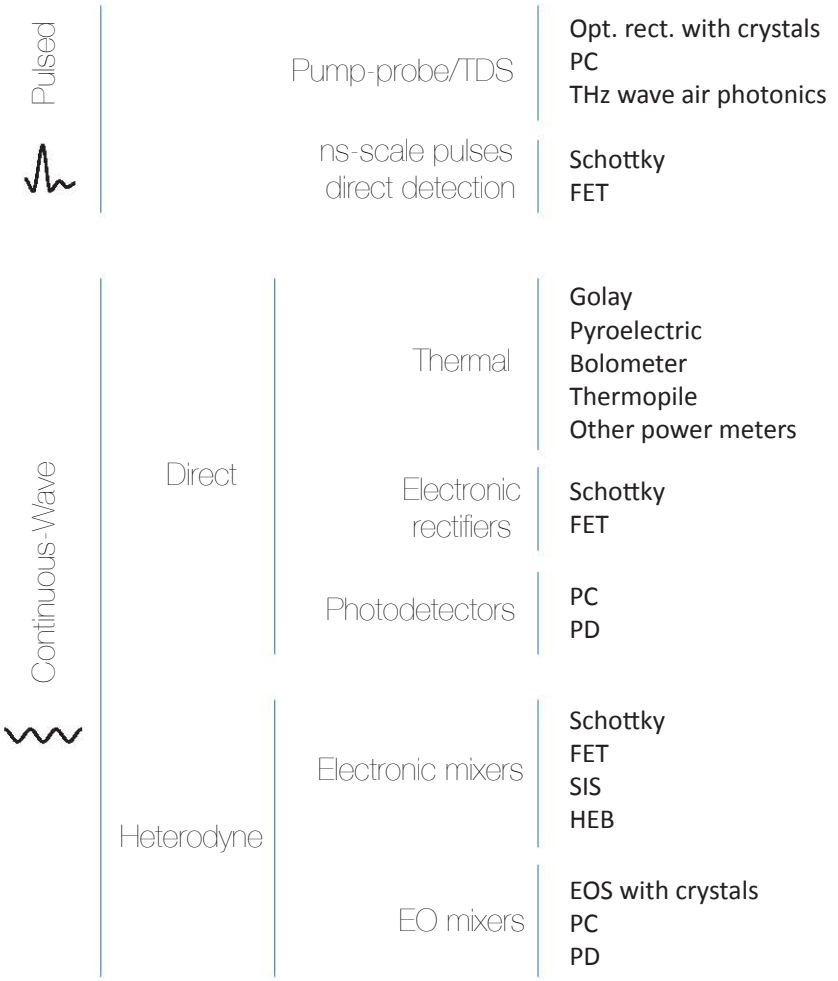

Figure 10 sub-THz and THz detection technology chart. The detectors are classified in pulsed and CW. Additionally, direct and heterodyne detection is included for CW receivers

In a similar way as the sub-THz and THz generation review of section 3.1, as a first step almost all existing detectors, both pulsed and CW, are listed here to illustrate the technologies currently available for THz detection. Then, the devices able to detect CW sub-THz and THz waves are mapped as a function of several figures of merit. Finally, a discussion about those having a highest potential for high performance receiver systems is included. Concerning the general sub-THz and THz detection overview, which is represented in Figure 10, it must be noted that some devices have been allocated in several groups as they can be used in various detection schemes. It is worth mentioning that an extended review of sub-THz and THz detection is included in the already mentioned *Appendix II. mm-wave, sub-THz and THz technology. Sources and detectors: state-of-the-art*

(November, 2012).

The two main groups of detectors that are found for pulsed THz radiation are:

- **Coherent detection of THz pulses of fs-ps width using pump-probe schemes.** This is the case of TDS measurement systems[107,139], where optical rectification in crystals (mainly $LiTaO_3$ or ZnTe)[21,107,140], PCs[107,140–142] or THz wave air photonics techniques[100,102] are employed for detection.
- **Direct incoherent detection of ns-scale THz pulses**, like those obtained from macropulses bunches in relativistic electron beam THz sources[143]. Schottky diodes[144,145] and FETs[146] have been also used for these purposes.

For CW THz detectors classification, direct and heterodyne detection is differentiated. Thermal detectors, electronic rectifiers and photodetectors can be employed as direct detectors. For the case of heterodyne operation, both electronic and Electro-Optical (EO) mixers have been reported (Figure 10).

- CW direct detection:
  - **Thermal detectors**. In these detectors, the radiation absorbed heats the device and some variation in the device physical properties is measured. They are characterized by a wide detection frequency range (usually covering both THz and far-IR regions) and very slow operation at room temperature, although it can be increased by cryogenic cooling[21]. They were the first devices used for detection (see Appendix I. THz history) and are still widely used for power measurement in this frequency range. In this group are included: Golay cells[21,147,148], pyroelectric detectors[21,147,149], bolometers[21,149,150] and thermopiles[21,151,152].
  - A **rectifier** is a device that is able to generate a DC current from an AC excitation. Due to a nonlinear relationship between the bias voltage and the generated current, the AC excitation is downconverted to DC due to self-mixing mechanisms. In this sense, a rectifier can also be used as mixer for downconversion to an intermediate frequency (IF) in a heterodyne system[21]. **Schottky diodes**[153–156]and **FETs**[157–162]. have been largely used as rectifiers in the microwave region for decades, and one of the main approaches for THz detection is the extension of these devices to higher frequencies.

- **Photodetectors** are devices that do not respond to thermal variations, as is the case of thermal detectors, but to the interaction of photons with electrons in the material[21]. This is why they are also known as quantum detectors[147]. There are two kinds of photodetectors that have been used for direct detection in the sub-THz range: **PCs**[130,163] and **PDs**[164].

- CW heterodyne detection:

  - **Electronic mixers**. This is the approach most widely used and with better performance. Some of them present two inputs, one for each signal (M and LO), like some three-terminal **FETs**[134,165,166], and other have only one input (two-terminal devices), thus M and LO signals have to be coupled before entering the mixer. The latter is the case of Schottky diodes[21,167,168], for instance. Other electronic mixers widely used in the THz region are: Superconductor-Insulator-Superconductor (**SIS**)[21,77,167,169] mixers and Hot Electron Bolometers (**HEB**)[21,167,170].

  - In **Electro-Optical mixers** (EO mixers, or optoelectronic mixers[171]), the M signal in the THz domain is mixed with a LO modulated onto an optical carrier, i.e. a photonic LO. As photodetectors, EO mixers are sensitive to the power term of the two optical fields, thus they detect the difference term, i.e. THz signal (DFG process, see chapter II), which is the process used in generation. As mixers, they are able to mix the received THz field with the field generated by DFG of the two incoming optical fields. The great advantage of these schemes is the possibility of LO remote distribution using optical fibers. This is the receiver approach on which this PhD work is focused. It offers great scalability, flexibility, light weight and cost reduction in the receiver design.

    In this sense, it is worth saying that theoretically, both PDs and PCs are photodetectors sensitive to the power (not the field) of the incoming optical signal, thus they are able to accomplish DFG. On the other hand, only PCs are expected to work as photomixers as they multiply the THz signal generated by DFG (usually LO) with the incoming THz field. Nevertheless, as it will be shown, PDs have been experimentally demonstrated to work as photomixers, although no clear theoretical explanation on this phenomena has been reported yet.

Electro-Optical mixing has been reported in few works for the THz frequency region, mainly due to the very few EO mixers reported for the THz domain and due to their high conversion losses. Between these works on EO heterodyne detection, some of them use **PCs**[55–57,59,60,138], and only three groups (including ours) have used **photodiode-like structures**[164,171,172]. Additionally, an experiment about CW heterodyne detection using optical rectification in crystals has been also reported[56]. In this thesis a new device for EO heterodyne THz mixing (np-i-pn quasi-ballistic THz detector[173–175]) is described and will be discussed with detail.

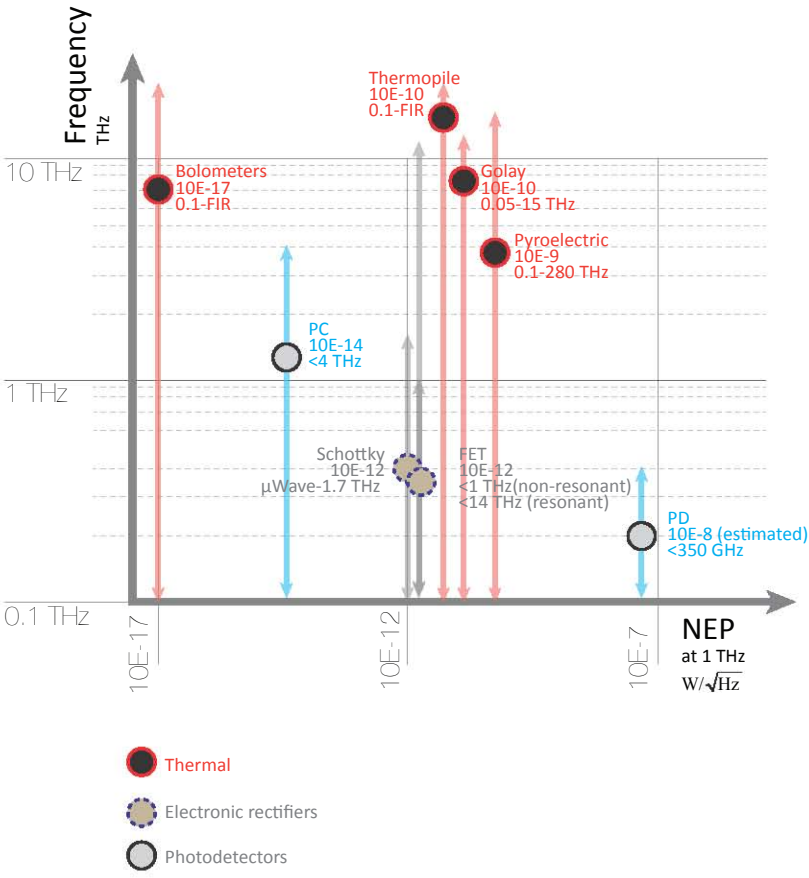

Figure 11 sub-THz and THz direct detection technology map. Frequency coverage vs. NEP. Each symbol text contains: name of the device (line 1), NEP value at 1 THz (line 2, W/sqrt(Hz)), and frequency coverage (line 3). References of the data in the figure are provided in the extended review included as Appendix II. mm-wave, sub-THz and THz technology. Sources and detectors: state-of-the-art (November, 2012)

In Figure 11 the detectors able to directly detect CW signals are mapped as a function of frequency working region and Noise Equivalent Power (NEP). The NEP is defined as the signal power that is required at the input to obtain a Signal-to-Noise Ratio (SNR) equal to unity at the output of a detector in 1 Hz bandwidth[21]. Thus, it is related to SNR rather than just noise in the detector. It is important to note that a more convenient figure of merit to describe detector performance is Detectivity, which is just the NEP normalized by the detector active area[21]. Nevertheless, most literature report just on NEP values and for this reason is the parameter chosen for the map shown in Figure 11. In this figure, lower NEP and larger frequency coverage are preferred. We can see in this figure that several thermal detectors have a bandwidth beyond the usual requirements for THz applications.

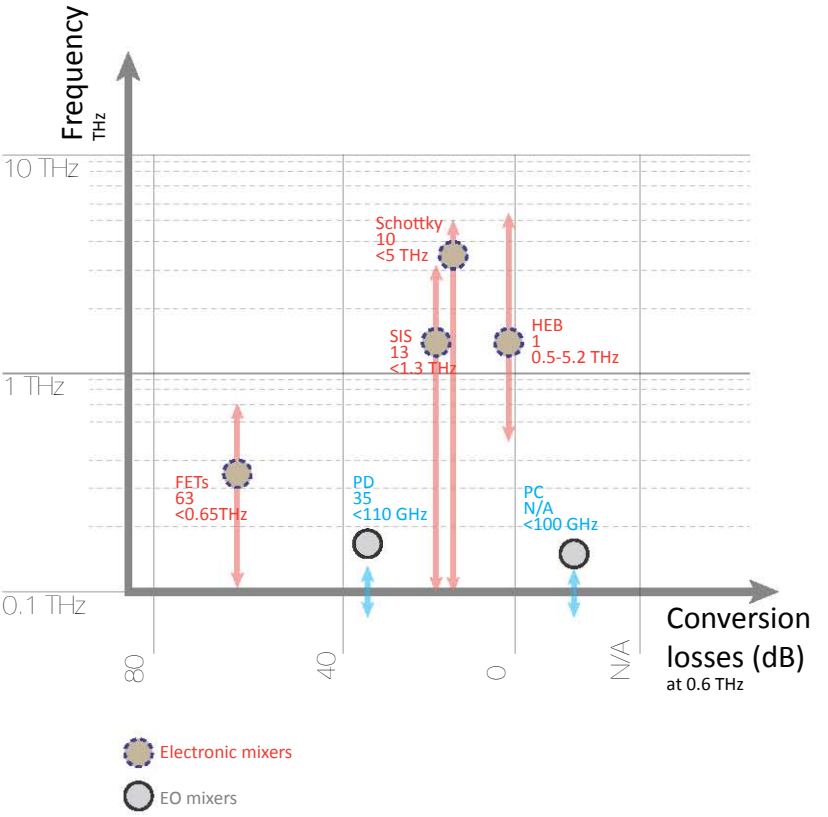

Figure 12 sub-THz and THz heterodyne detection technology map. Frequency coverage vs. conversion losses. Each symbol text contains: name of the device (line 1), Conversion losses at 0.6 THz or maximum demonstrated frequency (line 2, dB) and maximum frequency demonstrated (line 3). References of the data in the figure are provided in the extended review included as *Appendix II. mm-wave, sub-THz and THz technology. Sources and detectors: state-of-the-art (November,* 2012)

Figure 12 contains a technological map of the performance under heterodyne operation of those detectors capable of working as mixers. They are mapped as a function of the frequency range of the M sub-THz/THz signal and the conversion losses (dB). The conversion losses are defined here following the definition usually employed in other frequency ranges, i.e. the ratio of the IF output signal power to the M input signal power[21]. Figure 12 shows how electronic mixers provide with much higher performance than EO mixers in terms of frequency range and conversion losses. However, EO mixers have the unique capability of remote distribution of the LO through optical fiber, with all the advantages related to this already mentioned in section 3.1.

From the discussion above, it can be concluded that THz detection development has a certain technological delay over generation. This causes that well-established detection technologies like Schottky diodes, SIS or HEBs are still far to be replaced. EO heterodyne detection technologies are yet to provide commercial and reliable systems, and their development has a long path to go, as it can be seen from Figure 12.

3.3 Sub-THz and THz optics: free space optics and waveguides

Although sub-THz and THz optics are not one of the research topics in this work, a brief discussion about them is presented for a better understanding of the technology employed in this frequency region. Sub-THz and THz optics techniques can be divided into two basic groups: free space optics and waveguides.

For THz frequencies (approximately above 500 GHz), free space optics are typically used. In this case, quasi-optic components and quasi-optics design are used[21]. Further details on optics, materials and components for free-space transmission of THz waves can be found in Bründermann[21] and Lee[176]. It is important to note that although the water absorption lines present in air can results in high losses (see Figure 2), dry air can be almost lossless[64]. Free space optics schemes are typical for example in TDS spectroscopy systems and stand-off imaging applications.

On the other hand, a wide variety of THz waveguides have been theoretically and experimentally reported.

The most commonly used waveguide is the metallic rectangular waveguide inherited from the microwave region, and it is basically the only one commercially available. Rectangular waveguides have been traditionally fabricated at microwave frequencies from metals like Cu or Ag. This technology follows some of the principles applied to metallic waveguides at microwave

frequencies and tries to push the design and fabrication to higher frequencies. The most widely used nomenclature for waveguides dimensions is given by the already ceased organization Electronic Industries Alliance (EIA), whose standards are now under maintenance by Electronic Components Industry Association (ECIA). The waveguides following this standard are defined with the prefix WR. The waveguide with the highest bandwidth demonstrated is the WR-0.34, which works from 2.2 to 3.25 THz[177]. Specifications are only available up to WR-0.51: 1.4 to 2.2 THz, internal dimensions of 0.130 x 0.065 mm and losses about 0.3-0.5 dB/mm, assuming conductivity of gold, and a surface roughness factor of 1.5[178]. However, and despite the available fabrication techniques, further miniaturization has become an important bottleneck, as the roughness and polishing requirements are extremely high[21].

A significant number of dielectric waveguides have been also reported with promising results in terms of losses and frequency bandwidth[63]. Among dielectric waveguides, some follow the designs of rectangular waveguides[179], like Dielectric Rod Waveguides (DRW) made from Si that work up to frequencies of 325 GHz[180,181], or low-loss waveguides fabricated from Sapphire in the 75-110 GHz frequency range[68].

Finally, optical fibers and plastic optical fibers (POF) have been also extrapolated down to the THz range. Although some of the proposed developments are solid-core fibers (like those typically used in the optical region), most of them try to use the low losses associated to dry air THz transmission to create fibers with hollow-core and microstructured designs[63–65,72], like those applied in Photonic Crystal Fibers (PCF) in the optical domain. This way, the target is to confine the THz waves in a waveguide, but obtaining losses close to free-space transmission. Some materials commonly used in these designs are high-density polyethylene (HDPE) or polymethylmethacrylate (PMMA), but also some materials like Teflon, Zeonex® or Topas® have been employed[63]. State-of-the-art losses of 0.05 mm^{-1} (0.217 dB/mm) for a frequency range of 0.2-3.0 THz, and 0.009 mm^{-1} (0.039 dB/mm) for 0.2-1.5 THz have been reported[63].

4

Thesis framework and objectives

The work developed in this PhD dissertation has been carried out under the framework of NeoImag-THz project (TEC2009-14525-C02-02), founded by the Spanish Ministry of Science and Technology. NeoImag-THz aimed to develop a heterodyne Electro-Optical (EO) receiver in an array configuration at 100-120 GHz, mainly focused for imaging applications. The main objectives of the project are the following ones:

- To develop a high quality (low phase noise) photonic Local Oscillator at frequencies in the range of 100-120 GHz.
- To develop an Electro-Optical heterodyne detector at frequencies in the range of 100-120 GHz.
- The extension of this receiver to an array configuration.

The first two objectives of NeoImag-THz are associated to this thesis work. Thus, we can clearly divide the contributions of this dissertation in two parts: THz photonic generation (chapter III) and THz photonic heterodyne detection (chapter IV).

A photonic architecture for low phase noise sub-THz and THz generation is to be proposed, developed and validated. The technology chosen for this architecture is optical downconversion using DFG techniques. Although DFG architectures will be described in detail in chapter II, we can briefly introduce here the specific DFG scheme that has been selected to be used through the generation part of this thesis work.

The proposed DFG scheme is schematically represented in Figure 13, and consists on the following devices: a multimode optical source (i.e. Optical Frequency Comb Generator, OFCG), an optical mode selection stage and a photodetector. The process of how signals are processed through the setup to finally generate the desired THz frequency is also depicted in this Figure 13: two optical frequencies spaced by the desired THz frequency are selected from

the multimode optical source and then mixed in the photodetector, where the difference term (i.e. the desired THz signal) is provided at its output.

Two different DFG generation systems based on this architecture are presented in this thesis. The first one uses a Passively Mode-Locking Laser Diode (PMLLD) as OFCG, high selective optical filtering with Fabry-Perot filters to select the two required optical modes and a 50 GHz commercial photodiode as photodetector device. The second implementation is the result of the optimization of each part of the first system, and it encompasses a Gain-Switched based OFCG (with an additional optical span expansion stage), a selection stage using Optical Injection Locking (OIL) and an n-i-pn-i-p superlattice THz photomixer. An overview of these two systems is presented in chapter III, along with the summary of the corresponding reported scientific results.

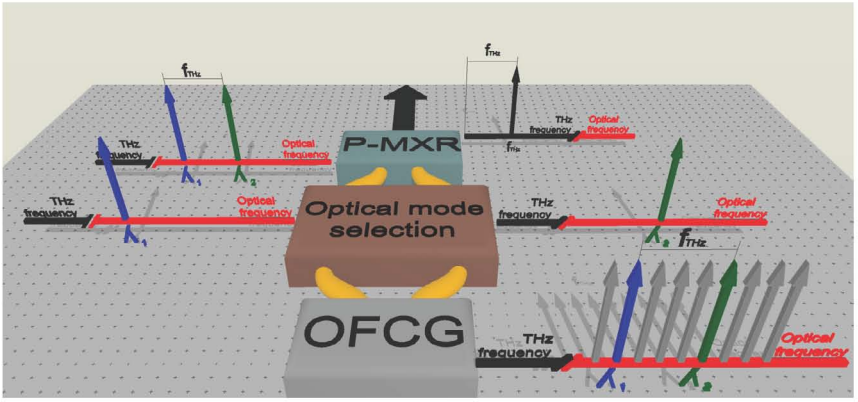

Figure 13 Sub-THz generator block diagram. OFCG: Optical Comb Frequency Generator; P-MXR: photodetector. The frequency graphs depict how the frequencies are generated and selected in the optical domain and downconverted to the THz range

With respect to the detection part of the thesis, the photonic architecture that is selected to be implemented and studied is a heterodyne receiver in Electro-Optical (EO) configuration. The schematic view of this detection architecture is depicted for THz frequencies in Figure 14. The received signal (M) is downconverted with a Local Oscillator (LO) modulated onto an optical carrier (i.e. photonic LO). The difference term (Intermediate Frequency, IF) is provided at the output of the EO mixer. In some EO heterodyne receiver architectures, such as the one developed in this thesis work for microwave frequencies, the IF signal is delivered modulated onto an optical carrier (photonic signal), rather than an electronic one. In the view of this Figure 14, we can see that this EO heterodyne receiver architecture has two key devices: photonic LO and EO mixer.

This detection architecture is firstly proposed and implemented at microwave frequencies, using an Ultra Nonlinear Semiconductor Optical Amplifier (XN-SOA) as EO mixer. Two different photonic LO are employed: a linearly modulated (small signal modulation) semiconductor DFB laser, and a Gain Switched (GS) semiconductor DFB laser. Both LO approaches are compared

through the evaluation of several figures of merit of microwave EO heterodyne receivers. Further information is provided in chapter IV.

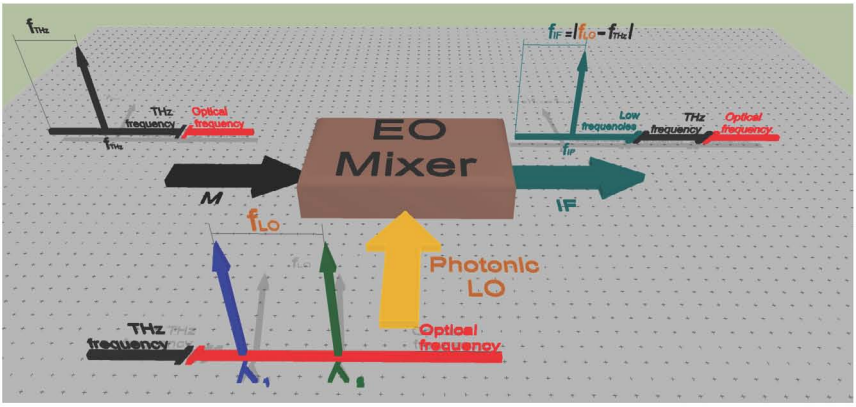

Figure 14 EO heterodyne receiver diagram. LO: photonic Local Oscillator; M: measurement signal; EO Mixer: Electro-Optical Mixer; IF: Intermediate frequency

The availability of a device suitable to operate as EO mixer at THz frequencies, the np-i-pn quasi-ballistic detector, permits the validation of this photonic detection architecture of Figure 14 at sub-THz frequencies. In this case, the photonic LO is the low phase noise photonic sub-THz generator developed in this thesis work. The details on this system can be also found in chapter IV.

II

Photonic Continuous Wave (CW) sub-THz and THz technology: Difference Frequency Generation (DFG) and detection using photomixers

1

Introduction

The use of photonic technology to generate sub-THz and THz frequency signals (optical downconversion) and to process them at optical domain has become a major research field. This has not occurred by chance. The capabilities of generating and processing signals in the electric domain using photonic technologies have been extensively used and validated at microwave frequencies (Microwave Photonics and Radio over Fiber[182,183] techniques). Thus, the extension of the techniques used in Microwave Photonics to sub-THz and THz frequencies seems a natural path to take advantage of the high potential and wide range of advantages offered by the photonic technology.

Photonic technologies at microwave, sub-THz and THz frequencies permit the use of optical components in the telecom range (wavelength range around 1550 nm), where there are a large range of Commercial Off-The-Shelf (COTS) and high performance devices. The energy consumption is also significantly lower, which is very important as the energy efficiency and low energy system design are becoming a major concern[184]. Other advantage is the use of optical fiber and its associated benefits, as light weight, very low losses (around 0.2 dB/km), compactness and cost. Also, working at optical frequencies allows EMI immunity and high bandwidth capabilities[182,183].

Moreover, these techniques allow for remote distribution of signals using low-loss optical fibers. This is a especially interesting feature at sub-THz and THz domains, where the transmission is characterized by very high losses; due to atmospheric attenuation in free space propagation, and due to guiding losses when using metallic and dielectric waveguides (see I.3.3). This apprach has found great potential applications at microwave frequencies requiring long distances distribution, e.g. radar, sensing, communications and astronomical applications[28].

The attainment of a high-quality photonic generator at sub-THz frequencies is the mainobjective of this work, both for its use as generator, and also for its use as photonic LO in EO sub-THz heterodyne receivers. Among the different technologies for sub-THz and THz generation presented in Chapter

I, the one to be used in this thesis work is the optical downconversion using Difference Frequency Generation (DFG). The detection part of this thesis is accomplished using photomixers in EO heterodyne detection schemes. This chapter is devoted to present with more detail such schemes.

Section 2 of this chapter describes the principle of operation of DFG-based sub-THz and THz generators. The generation process is described and their theoretical foundations are presented, along with different DFG architectures and photodetectors (see Figure 15, left). Specifically, the two most widely used DFG architectures are detailed: two single mode lasers, and a multimode optical source (such as an Optical Frequency Comb Generator (OFCG)) with the use of optical mode selection.

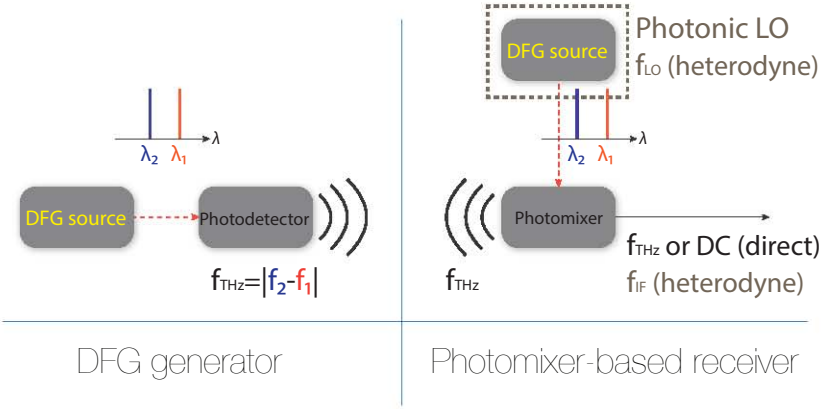

Figure 15 Photomixer-based sub-THz and THz generation and detection. DFG generation (left); and photomixer receiver (right), both direct and heterodyne

In section 3, a discussion of the different detection schemes based on photomixers in the sub-THz and THz range is included (see Figure 15, right). As explained later, a photomixer is a photodetector with mixing capabilities. The discussion is focused on Electro-Optical (EO) heterodyne receiver schemes using photoconductors (PCs) and photodiodes (PDs), along with their operation principles and current state-of-the-art performance.

2

Difference Frequency Generation (DFG) of CW sub-THz and THz signals

2.1 Principle of operation

THz CW generation based on DFG consists on the detection of the power associated with two CW signals at optical frequencies separated by the desired THz frequency, as it is represented in Figure 16, a. This power detection can take place in several kinds of photosensitive devices, such as Schottky[109] or Metal-Insulator-Metal (MIM)[21] diodes. However, the vast majority of DFG systems employ photodetectors: Photoconductors (PCs)[108,110,111] or Photodiodes (PDs)[112–116]. These photodetectors convert optical power to electrical current. After the detection, the power of each field and the difference term are generated. The difference term is the important one in DFG as it contains the CW signal with a frequency equal to the difference between the two optical frequencies (i.e. f_{THz} in Figure 16). This frequency spacing is chosen to be at THz frequencies within the bandwidth of the photodetector, in order to obtain the required THz CW signal at the output of the photodetector (Figure 16, b).

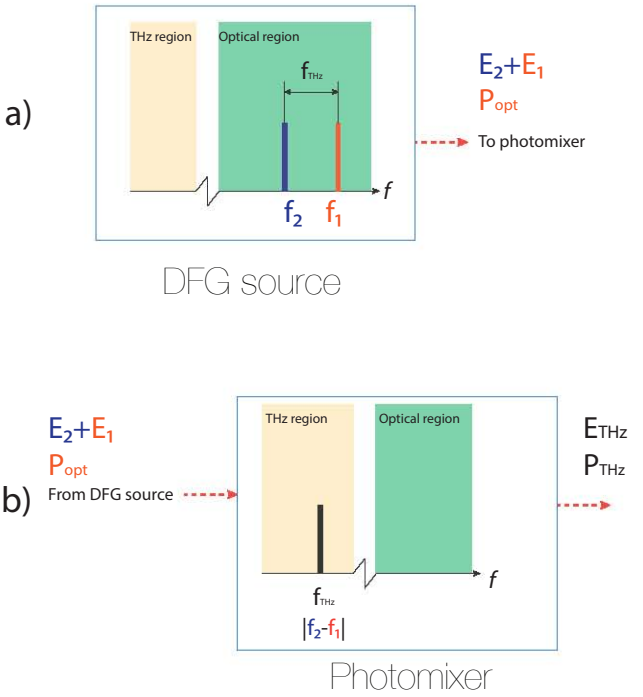

Figure 16 DFG generation process: a) Two frequencies in the optical domain are mixed in a photodetector device. The frequency spacing between both CW optical signals is equal to the desired THz frequency. b) The difference term at THz region is delivered at the output of the photomixer

If the spatial phase modulation of the optical beam is not taken into account, what is a common assumption for PCs and PDs (in which the illumination area is much smaller than the THz wavelength[116]), the analysis is simplified assuming the same direction of the wave vectors[116]. The total optical field (E_{opt}) at the input of the photomixer is described according to equation (4).

$$E_{opt}(t) = E_1 \exp\left[i\left(2\pi f_1 t + \phi_{01}\right)\right] + E_2 \exp\left[i\left(2\pi f_2 t + \phi_{02}\right)\right] \quad (4)$$

where E_1 and E_2 are the amplitudes of the optical signals(see Figure 16), f_i is the frequency of the signal i and ϕ_{0i} its initial phase.

The optical power associated to the total optical field E_{opt} (P_{opt}) is given by (5).

$$P_{opt} = E_{opt} \cdot E_{opt}^{*} = \left|E_1\right|^2 + \left|E_2\right|^2 + E_1 E_2 \exp\left[i\left(2\pi\left(f_1 - f_2\right)t + \left(\phi_{01} - \phi_{02}\right)\right)\right] + E_1 E_2 \exp\left[i\left(2\pi\left(f_2 - f_1\right)t + \left(\phi_{02} - \phi_{01}\right)\right)\right] \quad (5)$$

If only positive frequencies are taken into account, the optical power P_{opt} can be expressed according to (6).

$$P_{opt} = E_1^2 + E_2^2 + E_1 E_2 \cos\left[2\pi\left(f_{THz}\right)t + \left(\phi_{02} - \phi_{01}\right)\right] \quad (6)$$

As it can be seen from equation (6), the optical power P_{opt} is modulated in amplitude by the THz frequency. To generate the THz signal, this optical power is detected using semiconductor structures where holes and electrons are generated by the photos. Electrons and holes in a photodetector are separated, either by an external field (i.e. DC bias in PCs) or using p-i-n structures (i.e. PDs). This way, the generated current has a component at the same THz frequency as the modulation of the optical beam.

In a photodetector, the generated THz current (I_{THz}) and the optical power (P_{opt}) at low frequencies (where roll-off terms can be omitted) are related by the responsivity of the photodetector ($\Re$).

$$I_{THz} = \Re P_{opt} \quad (7)$$

$$\Re = \frac{\eta e}{h f_{opt}} \quad (8)$$

Where η is the quantum efficiency (conversion efficiency of photons to electrons), e is the electron charge, h is the Planck´s constant and f_{opt} the frequency of the optical beam.

Finally, the THz emitted power (9), is given by the antenna resistance (R_A). An important conclusion from (7) and (9) is that the THz power is proportional to the squared optical power.

$$P_{THz} \leq \frac{1}{2} R_A I_{THz}^{\ 2} \quad (9)$$

At this point, it is important to discuss the phase noise of the optical fields (E_1 and E_2) in equation (6). In Figure 17a, two optical fields are shown

that have deterministic phases (the phase ϕ has a time evolution perfectly linear, or equivalently, the frequency is a constant value), thus the phase difference is a constant value as well. This is the ideal case that results in a perfect CW optical power signal. However, an actual signal has not a constant phase ϕ (or equivalently, frequency f) but a randomly variable one due to the noise present in any real signal. This case is shown in Figure 17b, where the optical fields E_1 and E_2 present a time fluctuation given by δT_1 and δT_2, respectively. Thus, the phase difference ϕ_2-ϕ_1 term of equation (6) has also a random fluctuation that produces a certain amount of phase noise in the optical power P_{opt}, hence in the generated THz signal which will not be a pure CW signal anymore.

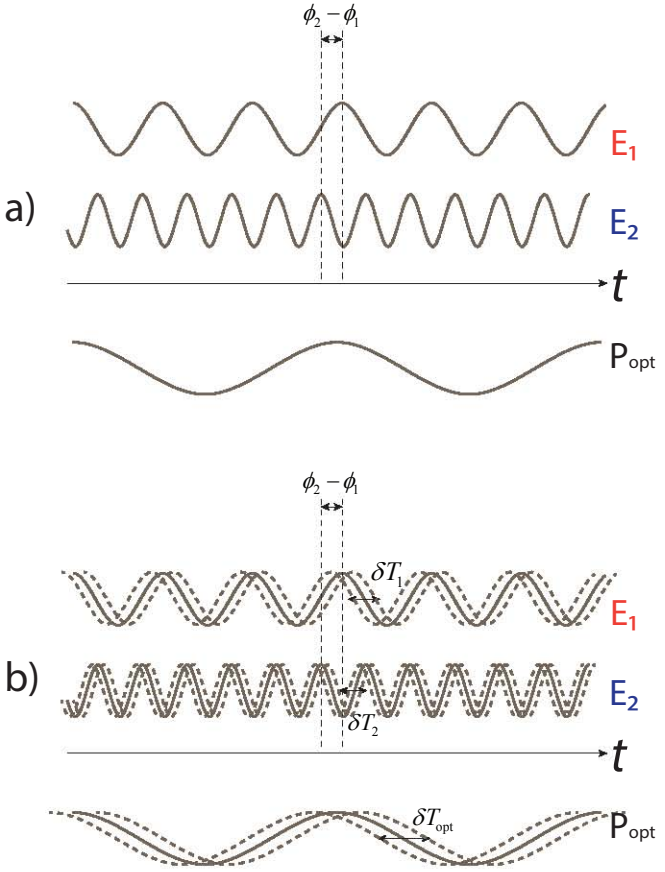

Figure 17 Optical fields phase coherence in the temporal domain: a) fixed phase relationship between optical fields E_1 and E_2 gives a pure CW optical power signal P_{opt}; b) random temporal fluctuations (i.e. timing jitter) in both optical fields E_1 and E_2 results in phase noise in the detected signal generated by DFG

Due to the importance of phase noise as a main figure of merit in signal generation, let us now discuss more deeply these phase fluctuations associated to any actual signal and the effects translated to the sum of two of them, both in the

temporal and frequency domains.

The phase noise spectrum originates from the phase fluctuations, which are equivalent to time fluctuations, and also equivalent to frequency fluctuations. The phase and time variations are equivalent magnitudes related by (10):

$$\delta T(t) = \frac{1}{2\pi f_o}\delta\phi(t) \tag{10}$$

where δT is the timing jitter (i.e. time fluctuations), f_0 is the center frequency of the signal under consideration and $\delta\phi(t)$ the phase deviation from the ideal linear phase. These fluctuations are translated to the frequency domain as frequency variations, as phase and frequency are parameters related by (11).

$$\phi(t) = 2\pi \int_{t-\tau}^{t} f(t')dt' \tag{11}$$

Thus, the phase deviation $\delta\phi(t)$ from the ideal linear phase can be expressed by (12):

$$\begin{aligned}\delta\phi(t) &= 2\pi \int_{t-\tau}^{t} \left(f(t') - f_0\right)dt' = \\ 2\pi &\int_{t-\tau}^{t} \left(\delta f(t')\right)dt' = \phi(t) - \phi(t-\tau)\end{aligned} \tag{12}$$

This is represented in Figure 18, where the instantaneous frequency and phase fluctuations are schematically represented. This phase noise given by phase (frequency) fluctuations produces a broadening of the frequency spectrum, which will be wider as the fluctuations increase.

The basic mathematical model describing the phase (frequency) noise spectrum of an EM signal is to be presented here. It must be noted that no amplitude noise is considered as it is not the focus of this work. An alternative derivation of the noise spectrum of a signal including amplitude noise can be found in *Appendix IV. Phase Noise measurement*.

The phase fluctuations (or equivalently frequency fluctuations) are a consequence of noise in the system, and they are commonly treated as a random variable modeled with a stochastic process, with different probability density functions depending on the nature of the noise that is present in the system. The origin of this noise significantly depends on the source generating the EM signal. A brief discussion of this origin for the case of lasers will be presented later in this chapter.

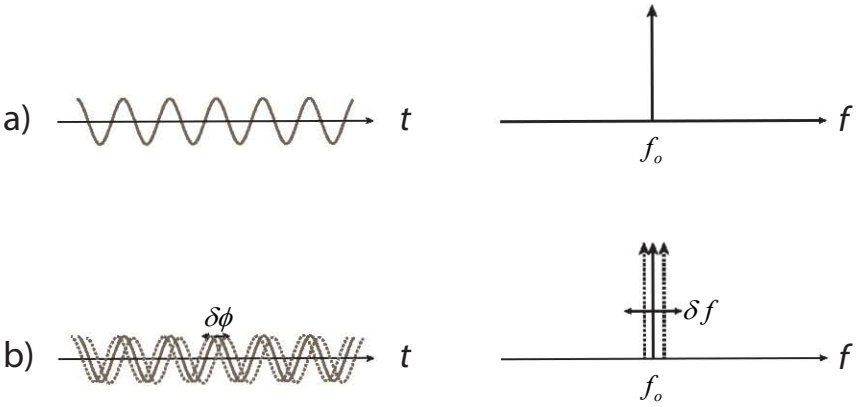

Figure 18 CW signal in temporal (left column) and frequency (right column) domains: a) ideal CW signal with deterministic phase (equivalent to Figure 17a) is a pure tone in the frequency domain; b) actual signal with random phase fluctuations (equivalent to Figure 17b) translates to the frequency domain as a tone with frequency fluctuations

Thus, an EM signal with phase (frequency) noise can be expressed using a random variable for the phase fluctuations $\delta\phi(t)$, if this noise is expressed in terms of phase; or equivalently using a random variable for the frequency $f(t)$, if the phase(frequency) noise is expressed in terms of frequency fluctuations, (13).

$$E(t) = E_0 \exp\left[i\left(2\pi f_0 t\right)\right]\exp\left[i\delta\phi\left(t\right)\right] = E_0 \exp\left[i\left(2\pi f\left(t\right)\right)\right]\exp\left[i\left(\phi_{00}\right)\right] \tag{13}$$

In order to discuss the influence of the term $f(t)$ in the signal generated by DFG, we have to provide ourselves with several tools. First, the power spectral density (PSD) of a signal is defined as (14) by the Wiener-Khintchine theorem[185,186].

$$S\left(f\right) = \mathfrak{F}T\left\{G\left(\tau\right)\right\} \tag{14}$$

This equation defines the power spectrum $P(f)$ of a signal $E(t)$ as the Fourier transform of its autocorrelation function $G(\tau)$, which is mostly determined by the random variables contained in the signal. Moreover, the phase noise spectrum is commonly represented by the Single Sideband (SSB) noise-to-carrier power ($\mathscr{L}(f)$, see equation (87) in *Appendix IV. Phase Noise measurement*). The different kind of noises of the system will be related to a certain slope f^n of the phase (frequency) noise spectrum (in logarithmic units), as depicted in Figure 19. Thus, the fitting of the experimental measurements to different slopes allows us to identify the different kinds of phase (frequency) noises the signal has. Further details on this can be found on *Appendix IV. Phase Noise measurement*.

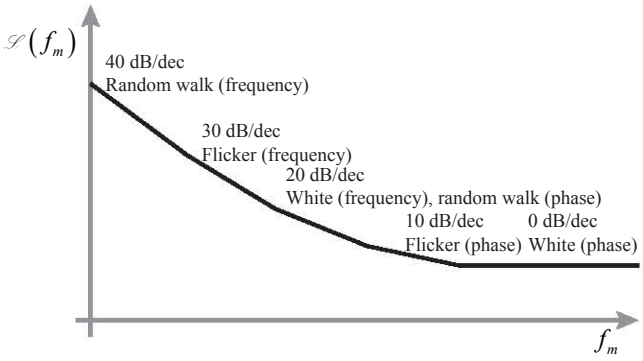

Figure 19 Classification of phase and frequency noise sources from the slopes of the Single Sideband Noise to Carrier Ratio $\mathscr{L}(f)$

In order to follow with our mathematical description of the phase (frequency) noise spectrum, we have to choose a mathematical model for the phase (frequency) fluctuations. The question is what process better define this noise in an actual signal, or equivalently, what is the probability density function (pdf) of the phase $\phi(t)$ and frequency fluctuations $f(t)$. An exhaustive model containing all the different kinds of phase and frequency noises that can be experimentally found (see Figure 19) is implausible. One of the most complete models only covers two kinds of frequency noises (Flicker frequency noise, f^{-1}; and Gaussian frequency deviations (equivalent to a random walk phase term), f^{-2}). This model, developed by Herzel[187], results in the convolution of a Gaussian noise spectrum (given by the Flicker frequency noise distribution) and a Lorentzian noise spectrum (given by the Gaussian frequency noise distribution). The final noise spectrum is called a Voigt line profile, and there is no analytical expression for this function[187,188].

Because of the complexity associated to the analysis, most theoretical works only treat the f^{-2} noise of the phase noise spectrum depicted in Figure 19, having very good agreement with most experimental results[186,189]. This f^{-2} noise means that the frequency fluctuations have a Gaussian pdf. As the phase $\phi(t)$ is related with the frequency according to (11), we know that it follows a Wiener process, also known as random walk, or Brownian process. This is due to the property that the integral of a Gaussian random variable follows a random walk. This can be also seen in the opposite direction: the instantaneous value of a variable following a Brownian process has a Gaussian pdf (the frequency is the derivative of the phase with respect to time). It must be noted that a Wiener distribution is not-stationary, but if we consider the difference between two phase terms, i.e. phase deviations $\delta\phi(t)$, the resulting distribution is Gaussian and it is stationary[189].

This way, expressing all phase (frequency) fluctuations of the signal under the frequency term, (13), the frequency is defined as a random variable following a Gaussian pdf with f_0 mean and a variance of σ_f^2, as shown in (15).

$$f(t) \sim N\left(f_0, {\sigma_f}^2\right) \tag{15}$$

This is translated to the frequency domain as a Lorentzian shaped phase noise spectrum with Full Width at Half Maximum (FWHM) equal to the variance σ_f^2. A comprehensive and complete derivation of this noise spectrum can be found in Podesta[189]. Thus, the PSD of the signal *E(t)* is finally given by (16), where it can be seen how the statistical characteristics (σ_f^2) of the frequency noise appear directly related to the phase noise spectrum.

$$S(f) = {E_0}^2 \frac{{\sigma_f}^2}{\left(\frac{{\sigma_f}^2}{2}\right) + 2\pi\left(f - f_0\right)} \tag{16}$$

Through this work, the FWHM will be used as the figure of merit of the phase noise of both THz and optical signals. This is because the FWHM is the parameter usually employed to quantify the noise spectrum of an optical signal. In the case of THz signals, the measurement instrumentation limitations and the limited power result in limited dynamic range of the measured spectrum. Under these conditions, a fair comparison of the phase noise performance between THz signals is given by using the FWHM rather than the Single Side Band (SSB) carrier-to-noise spectrum. This is discussed in Criado *et al*[190] with further details.

At this point, it has been stated how the phase noise of a signal can be effectively modeled using a Wiener process as pdf for the phase fluctuations, what is completely equivalent to frequency fluctuations following a Gaussian pdf. This model translates to the frequency domain as a Lorentzian function around the center frequency, instead of just a delta function that is found in the ideal case. Moreover, it has been show how the variance associated to the frequency fluctuations σ_f^2 (which in turn are directly related to the phase fluctuations[189]) define the FWHM or linewidth of the signal spectrum.

Now, the next step is to find out the noise spectrum of the power signal associated to the sum of two fields, as that it the case for DFG systems. The power of the sum of two EM signals is given by (17). As in previous steps, we express all phase random fluctuations (modeled as a Wiener process) as frequency random fluctuations (modeled as a Gaussian process). Thus, we will have a signal containing the difference between two Gaussian processes ($f_1(t)$ and $f_2(t)$).

$$P_{opt} = \left|E_1\right|^2 + \left|E_2\right|^2 + E_1 E_2 \exp i\left[2\pi\left(f_2(t) - f_1(t)\right)t + \left(\phi_{02} - \phi_{01}\right)\right] \tag{17}$$

Where ϕ_1 and ϕ_2 are constants, and $f_1(t)$ and $f_2(t)$ are random variables following Gaussian processes with f_1 and f_2 mean, and ${\sigma_{f1}}^2$ and ${\sigma_{f2}}^2$ variance, respectively, (18),(19).

$$f_1(t) \sim N\left(f_1, {\sigma_{f1}}^2\right) \tag{18}$$

$$f_2(t) \sim N\left(f_2, {\sigma_{f2}}^2\right) \tag{19}$$

The difference of these two Gaussian processes that has been defined as $f_{THz}(t)$ in DFG systems, is given by equation (20):

$$f_{THz}(t) \sim N\left(f_2 - f_1, {\sigma_{f1}}^2 + {\sigma_{f2}}^2 - 2\sigma_{f1f2}\right) \tag{20}$$

being σ_{f1f2} the covariance between $f_1(t)$ and $f_2(t)$.

As conclusion from equation (20), it can be highlighted that the resulting difference signal, i.e. the signal at THz frequencies in this case, will have a spectral width given by a FWHM value of ${\sigma_{f1}}^2 + {\sigma_{f2}}^2 - \sigma_{f1f2}$. The covariance term is given by the phase (frequency) noise correlation between both signals, which in the view of (20) has a dramatic effect over the spectral FWHM. This result is of key importance in our work as it will be discussed later.

2.2 DFG architectures

The two optical frequencies spaced by a THz frequency that are required in a DFG system (Figure 16, a) can be provided by several DFG architectures. Such schemes are key for the quality of the generated signal in terms of phase noise, and also for the frequency coverage, resolution and tunability, as they depend on the actual architecture chosen. The phase noise and linewidth of the THz signal is given by the phase (frequency) noise correlation between the two mixed optical modes and their optical FWHM, as represented by equation (20). This THz FWHM can be lowered by a higher correlation (σ_{f1f2}), or by narrower optical FWHMs (${\sigma_{f1}}^2$ and ${\sigma_{f2}}^2$). The frequency tunability and resolution is given by the characteristics of the optical source(s).

There exist basically four DFG architectures that are represented graphically in Figure 20.

The incoherent DFG sources have been reported few times[191] and are not very usual due to the poor phase performance they offer. They are based on optically filtering of two slides of an Amplified Spontaneous Emission (ASE) source (Figure 20, a)[191].

The most usual scheme is the use of two single-mode optical sources (Figure 20, b)[129,133]. In order to provide tunability, at least one of these sources

has to be tunable to select the frequency spacing between modes (f_{THz}). This is a simple scheme and maybe the one with lowest cost, although the FWHM performance they offer is not very good, as the two modes are provided by independent sources with no correlation between them. Complex Optical Phase Locked Loops (OPLLs) schemes are required to achieve a certain correlation between them[192,193].

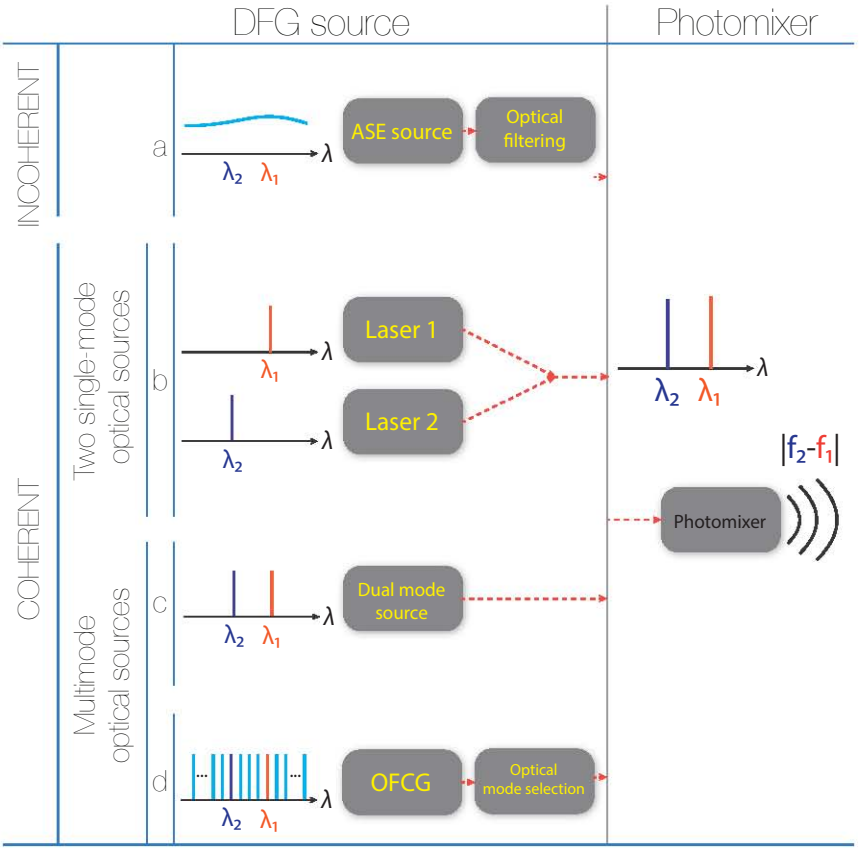

Figure 20 Optical architectures for DFG of CW THz signals: a) ASE source + optical filtering; b) two single-mode optical sources; c) dual mode optical source; d) OFCG + optical mode selection

The other two strategies to provide the two required optical modes are based in a single multimode optical source.

The use of a dual-mode optical source[194] (Figure 20, c) overcomes the problem associated to the phase coherence between the optical modes of the previous DFG sources. As two optical modes are generated in the same device, high mode correlation can be achieved, thus narrow THz FWHM values. Additional features are the low cost associated to these sources and the potential for integration. However, the main issue of this approach, and basically the

reason why is not very often used, is the non-existent or very limited tunability of the generated THz frequency, as the spacing between modes is fixed by the device structure.

Another approach based on multimode optical sources is the use of a multimode optical source such as GHz-rate OFCGs and an optical mode selection stage to extract the two required modes (Figure 20, d)[131,132,195]. This is a more complex alternative than in turn can provide with very high mode correlation, thus a very narrow THz FWHM (in the Hz range). Most OFCG have fixed repetition frequency, both benchtop-sized commercial systems[196] and integrated ones[197]. Thus, in principle, the optical mode selection stage allows for tunability in discrete steps equal to the frequency spacing between optical modes (in the GHz range).

The most important among these four DFG schemes are the use of two single mode semiconductor lasers (Figure 20, b) and an OFCG plus optical mode selection (Figure 20, c). These two are presented with more detail in the following sections.

2.3 DFG architectures based on two single-mode semiconductor lasers

2.3.1 Principle of operation

The use of two single-mode semiconductor lasers as DFG source is the most widely used, and also the only available nowadays as a commercial solution[129,133]. It consists on coupling the output of two independent single mode lasers that are separated by a frequency in the sub-THz or THz range, as depicted in Figure 20, b. In this section, the characteristics and performance provided by this DFG source are discussed. Nevertheless, as a first step to understand how this DFG source works, some basic concepts about semiconductor diode laser devices are presented. Further details on semiconductor lasers can be found in Agrawal & Dutta[198] or Coldren & Corcine[199].

A diode laser is an optical oscillator based on semiconductor heterostructures. Laser emission (i.e. stimulated emission) occurs in one or several cavity modes (i.e. longitudinal modes) that are within the gain bandwidth of the laser (Δf_g), and only if a current above the threshold current is applied to the laser (see Figure 21).

The threshold current is the current above which stimulated emission is predominant. This means that the photons are generated and emitted coherently

in the gain medium, thus with the same phase, frequency, polarization and direction. The gain bandwidth of a laser (Δf_g) is the frequency region in which the gain exceeds the losses of the laser. The frequency of the allowed cavity modes is determined, as shown in equation (21), by L (the cavity length) and μ (the refractive index of the active layer). In this equation (21), m is an integer number and c the speed of light. Moreover, the frequency spacing between these cavity modes (Δf_m) is shown in (22). In this equation, μ_g, which is the group refractive index, includes the frequency dependence of μ. For instance, a InGaAsP based semiconductor laser with a Fabry-Perot cavity of L=4 mm, will have a Δf_m of around 10 GHz.

$$f_m = \frac{mc}{\mu 2L} \tag{21}$$

$$\Delta f_m = \frac{c}{\mu_g 2L} \tag{22}$$

When the gain bandwidth is smaller than the cavity modes spacing ($\Delta f_g < \Delta f_m$), the gain of the laser basically affects only one of the cavity modes, and single mode emission occurs (Figure 21, a). On the other hand, when the gain bandwidth is greater than the cavity modes spacing ($\Delta f_g > \Delta f_m$), multimode emission appears, as shown in Figure 21, b. It is worth saying that this is a basic description of how single mode emission is obtained, as there exist a number of techniques to attain it[199].

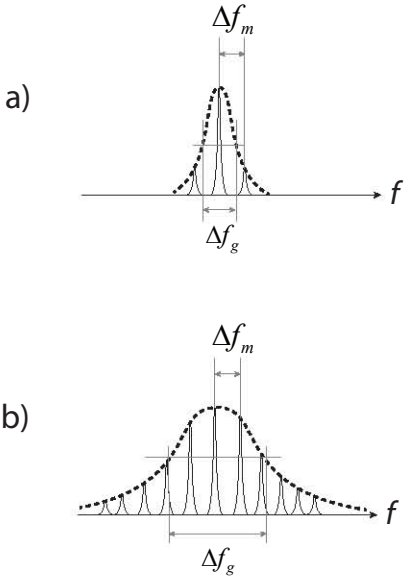

Figure 21 Frequency (optical) spectra of a laser output. a) Single cavity mode emission from a laser; b) multiple cavity mode emission from a laser

An interesting conclusion, obtained from the simple expression given by (22), is that the frequency spacing between optical modes Δf_m can be changed by two parameters: the cavity length and the refractive index. The first is determined by fabrication in semiconductor lasers (without an external cavity), while the latter can be varied by the temperature of the laser.

Then, the output electric field of a laser can be represented as a sum of the emitted cavity modes fields, according to equation (23), where no spatial distribution is considered for simplicity reasons.

$$E(t) = \sum_m A_m \exp i\left[2\pi\left(f_0 + m\Delta f_m\right)t + \phi_m\right] \tag{23}$$

A_m is the field amplitude of the mth cavity mode, f_0 the center frequency, Δf_m the frequency spacing between cavity modes and ϕ_m the temporal phase of the mth cavity mode.

The dynamic behavior of a semiconductor laser is given by the rate equations, which define the relationship between the carrier density, *n*, and the density of photons, *S*. A representation of the rate equations for a single mode laser (only one term *m* considered in (23)) and without taking into account spatial distribution is given by equations (24) and (25). The rate equations are the basis to understand a wide variety of processes in semiconductor lasers[199].

$$\frac{dn}{dt} = \frac{j(t)}{ed} - \Gamma g\left(n - n_t\right)\upsilon_g S - \frac{n}{\tau_s} \tag{24}$$

$$\frac{dS}{dt} = \Gamma g\left(n - n_t\right)\upsilon_g S - \frac{S}{\tau_{ph}} + \frac{\beta\Gamma n}{\tau_s} \tag{25}$$

where n is the carrier density, n_t the transparency density, S the density of photons, $j(t)$ the current density, e the electron charge, d the active layer thickness, τ_s the carrier lifetime, Γ the fraction of the optical power confined in the active volume, g_0 is the optical gain per unit length, υ_g the group velocity, τ_{ph} the photon lifetime and β the coupling factor of the spontaneous emission into the lasing mode.

The photon lifetime τ_{ph} is defined as shown in (26), where α_m and α_i are the mirror and internal loss, respectively[200].

$$\tau_{ph} = \frac{1}{\upsilon_g\left(\alpha_m + \alpha_i\right)} \tag{26}$$

Moreover, the output optical power emitted by the laser diode will be

given by (27):

$$P_0 = \left(\frac{\alpha_m}{\alpha_m + \alpha_i} \right) \frac{V}{\Gamma} \frac{Shf_0}{\tau_{ph}} \tag{27}$$

where f_0 is the emitted frequency and h is the Planck´s constant.

Let us now to briefly describe the phase (frequency) noise spectrum of the optical signal (optical modes) generated by a laser (Figure 21) and compare it with the general model for an EM signal that has been previously presented.

The most simple model to study the noise of a laser is derived from the analysis of the noise produced by spontaneous emission of photons within the cavity of the laser, without taken into account other sources of noise (Langevin terms). It is demonstrated how this noise produces a phase (frequency) noise spectrum with a Lorentzian shape centered in the emission frequency $f_{0,}$ what completely agrees with the general case for a EM signal presented previously[199]. Moreover, the FWHM of this Lorentzian shape in the most general case is a term known as the Schawlow-Townes (ST) limit ($\sigma^2_{f\,ST} = \Delta f_{ST}$)[199], given by (28):

$$\sigma_{f\,ST}^{\,2} = \Delta f_{ST} = \upsilon_g \frac{hf_0 g n_{sp} \alpha_m}{4P_0} \tag{28}$$

where n_{sp} is the spontaneous emission factor[201]. The expression shown in (28) is considered a limit, as it only takes into account the spontaneous emission and experimentally the optical FWHM is always higher than this value. Actually, Henry demonstrated in 1982 that this limit cannot be directly applied to semiconductor lasers, as in these devices more effects have to be taken into account, namely, the variations induced in the refraction index when the carrier density varies in the active region of the cavity[202,203]. Then, Henry included a term in the definition of the ST linewidth for a semiconductor laser diode, known as Alpha factor or Henry factor (α), to define a modification over the ST limit that can be applied to semiconductor lasers ($\Delta f_{ST\text{-}H}$)[199], (29).

$$\Delta f_{ST-H} = \Delta f_{ST} \left(1 + \alpha\right) \tag{29}$$

2.3.2 Characteristics and performance

2.3.2.1 Characteristics

Once the fundamentals on the characteristics of the optical field emitted by diode lasers have been presented, we can continue with the discussion about the characteristics and performance of the DFG architectures based on two single-mode lasers. In chapter I, we established several figures of merit to evaluate THz sources. Among them, our work is focused on the following ones: frequency range, tunability and FWHM (phase noise).

The maximum synthesized THz frequency when using two single mode lasers as DFG architecture is given by the center frequency of the employed lasers and their tunability range, as it can be understood from Figure 16. In terms of laser tunability, the emitted center frequency (f_0) of a semiconductor laser is basically governed by carrier and thermal effects[204] that change the refraction index of the cavity. This change in the refraction index produces the variation of the emitting frequency according to (21). When no modulation is applied, or it is below 10 MHz, the thermal effect is dominant because of the large time constant[205]. The thermal effect is controlled by the laser current and especially by the temperature of the laser (usually controlled by a Thermoelectric Cooler (TEC)).

The tunability of the THz signal is determined by the tunability of the frequency spacing between both lasers. As a single mode lasers allows for a continuous tunability of its emitting frequency, this DFG architecture also offers a continuous tunability of the THz signal. As previously mentioned, the tunability in most semiconductor lasers is governed by its current and temperature. The laser current allows little tunability capability (i.e. low wavelength to current detuning ratio) and its change also affects the output power according to the Power-Current (P-I) curve. A current increment causes a higher temperature in the cavity, changing the refraction index μ, and the frequency increases, or equivalently, the wavelength decreases, (21). Usually, temperature control using TEC is employed for tuning, as the wavelength to temperature detuning ratio is much larger than in the case of current control, and this allows for a larger tuning range. Thus, the tunability range of the laser is basically given by temperature rather than current control, and is determined by the temperature range in which the laser can operate properly that uses to be about 0-40 ºC. The tunability resolution of the center wavelength determines the frequency resolution of the generated sub-THz or THz signal, and is governed by the laser characteristics and both the current and temperature resolution of the laser controller employed. As the wavelength detuning is very low using current control, in this case the highest resolution is achieved by current control. The temperature and current resolution of laboratory-grade laser controllers are around 0.01ºC and 50 μA, respectively[206].

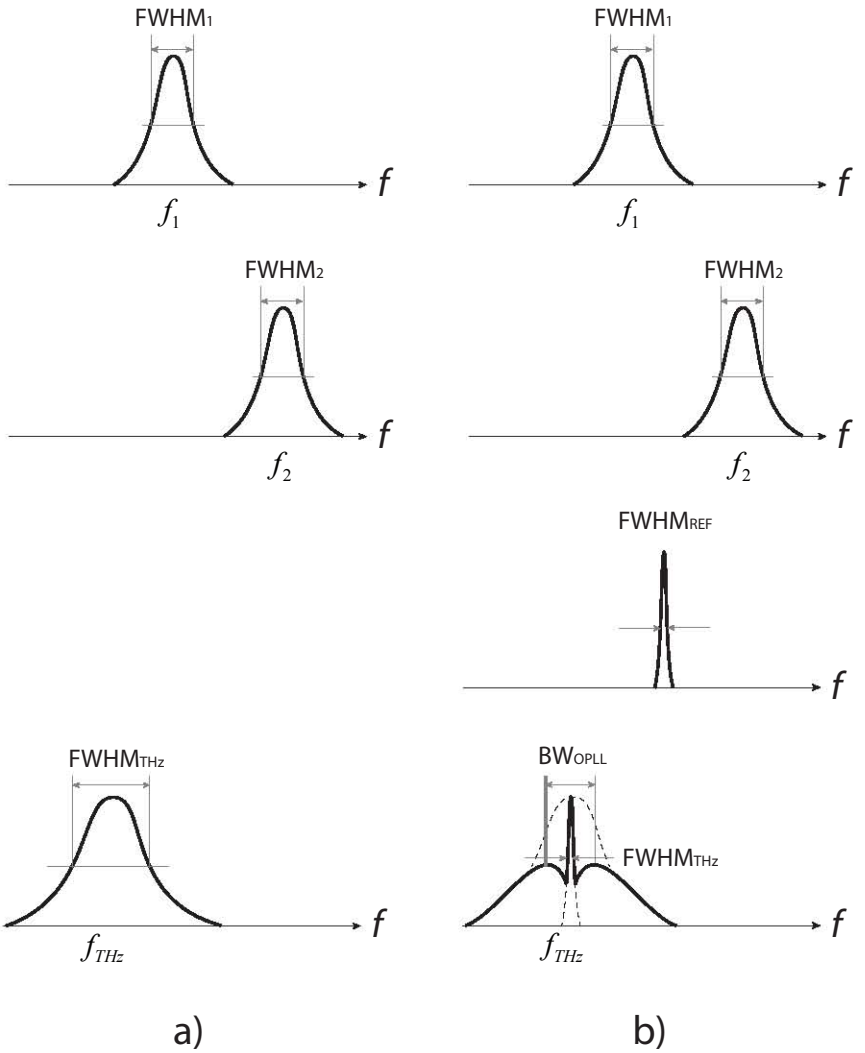

Figure 22 FWHM of a THz signal generated by a DFG architecture based on two semiconductor lasers: a) typical case, two independent sources results in a THz signal with a FWHM equal to the sum of the FWHMs of the sources; b) the use of a OPLL allows to reduce the FWHM to that of a reference, however, it has a limited BW, and the phase noise of the THz signal beyond this BW will be high as there is no correlation between the noise

The FWHM of the generated THz is given by equation(20). As two independent lasers are used, the covariance term σ_{f1f2} is 0, and the variance of the resulting distribution is just the sum of the variance of the two optical fields, σ_{f1}^2 and σ_{f2}^2. Thus, the resulting phase noise spectrum will be a Lorentzian with a FWHM equal to the sum of the FWHMs of the lasers. This case is shown in Figure 22a. An alternative way to come to the same conclusion is considering that the multiplicative term between both fields that we are considering (equation (6)) can

be solved in the frequency domain as a convolution of both signal spectra shown in Figure 22a (first and second row). It is important to note that conclusion only applies if they are independent signals, as in this case. For the case of correlated sources (treated below), the usual convolution properties do not apply, and much more complex mathematics are involved in the convolution process[207].

In order to reduce the FWHM of the THz signal when using two independent sources for DFG generation, the two lasers can be locked to introduce phase coherence between them ($\sigma_{f1f2} > 0$, if they are positive correlated, i.e. the fluctuations vary in the same direction). This can be accomplished by Optical Phase Locked Loops (OPLLs)[192], where the lasers are locked to an external RF reference or to an optical absolute reference (atom gas transition or Fabry-Perot cavity with very high Q factor)[193,208]. Usually, the feedback loop follows a Pound-Drever-Hall scheme[208,209]. This feedback loop has a bandwidth limited by the electronics used. This way, the phase fluctuations can be only locked if they are slow enough to be followed by the electronic circuit (in practical cases, OPLLs have bandwidth below a few GHz), and out of this bandwidth the phase noise of the THz signal is again determined by the uncorrelated noise (FWHM of the optical sources) and not by the reference of the OPLL. An illustrative example is shown in Figure 22b, where it is represented how the frequency fluctuations are locked to an external reference. The resulting signal will have the frequency fluctuations of the reference, but only within the BW of the OPLL, where the noise of the two optical fields is now correlated. The use of an OPLL results in a significant increment of complexity and cost of the system. For these reasons, OPLLs are not usually offered as commercial solutions.

2.3.2.2 Performance

The most commonly employed lasers for DFG are Distributed Feedback (DFB) lasers as they provide low cost and high performance. Moreover, they are available in compact and fiber-pigtailed packaging, such as 14-pin butterfly package, with center wavelengths in the telecom range. Their free-running optical FWHM uses to be in the MHz range, which is a good value among semiconductor lasers, but translates to a THz beating with a FWHM value of several MHz. Although these values are sufficient for a range of applications, they are not suitable for high-quality sub-THz and THz generation, such as LO or high-resolution spectroscopy[132]. The wavelength to current detuning ratio and the wavelength to temperature detuning ratio are about 0.0005 nm/mA and 0.05 nm/ºC, respectively[210]. These values give a tunability range of around 250-500 GHz for a standard DFB laser, thus 0.5-1 THz for a DFG source consisting in two DFBs. It must be noted that this tunability range can be readily extended using several lasers[211]. The tunability resolution (i.e. frequency resolution) is barely 60 MHz with TEC control and 3 MHz with current control. In terms of power, DFB lasers have output power values (fiber coupled) in the range from a few mWs to tens of mWs[210].

Another possibility for dual-source DFG architectures is the use of

External Cavity Lasers (ECL). They provide very narrow optical linewidth (around 100 kHz), very large tunability range given by the external cavity (>100 nm, or equivalently >12 THz) and output power in the range of DFB´s. However, they are not a popular option as they are bulky and with a cost around one order of magnitude higher than DFBs. Moreover, the wavelength resolution is 2 pm (around 250 MHz of frequency resolution).

A recent kind of semiconductor lasers that can also be used are Discrete Mode (DM) lasers[212]. Their tunability range, frequency resolution and output power are similar to those of DFBs, as well as their cost and packaging. Furthermore, their great advantages are that they present a very narrow linewidth comparable to that of ECLs (below 100 kHz), and a high bandwidth under direct modulation (>20 GHz)[213].

2.4 DFG architectures based on multimode optical source and optical mode selection

When a multimode optical source (i.e. OFCG) and optical mode selection is used as DFG architecture, two optical modes from the multimode optical source spaced by a frequency value within the sub-THz or THz range, are selected, giving the desired output that appears in Figure 20, d. In this sense, this DFG scheme consists basically of two key parts: an OFCG and an optical mode selection scheme.

This section is devoted to the description of such DFG architectures, and it is divided in three parts. The first one describes in detail the principles of operation of OFCGs as multimode source and the usually required optical span expansion, as well as the existing techniques to implement them. The second part describes the existing techniques to select the two required optical modes from the multimode source. Finally, the last part refers to the characteristics and state-of-the-art performance provided by these DFG architectures.

2.4.1 Multimode optical sources: Optical Comb Frequency Generators

2.4.1.3 Principle of operation

OFCGs have been used for years as a tool within several research

fields. In 2005, Glauber, Hall and Hänsch won the Nobel Prize in Physics for their contribution to optical coherence and spectroscopy, in part due to the development of the optical comb technique[214]. Since that year, OFCGs popularity and research effort have grown exponentially, becoming a powerful technique in a wide range of applications, including metrology[57], spectroscopy[215] and from a few years to now, THz generation[132,195].

The frequency spectrum (i.e. optical spectrum) of an ideal OFCG is depicted in Figure 20d. This ideal OFCG consists on a train of delta functions both in frequency and time domains, i.e. a perfect pulsed source. The actual spectra of OFCGs are far from this ideal case, as it will be explained later in this section.

Firstly, it is important to enumerate the main characteristics of an OFCG. That can be summarized as follows:

1. Coherence between optical modes (i.e. phase noise correlation). This will determine the phase noise performance of the synthesized signal, as it can be inferred from equation (20).

2. Repetition frequency (f_{rep}), or frequency spacing between modes and its tunability range (if any, see Figure 23).

3. Center wavelength. We would prefer the center frequency to be in the telecom range (around 1550 nm), to take advantage of the wide range, low cost and high performance COTS optical devices available at these wavelengths.

4. Optical span (δf), also known as frequency span, frequency bandwidth or optical bandwidth. Usually it is measured at 3 dB, although sometimes is specified at 10 or 20 dB (see Figure 23).

5. Spectrum flatness. The flatness is defined by the maximum amplitude deviation between the different modes amplitudes in the desired wavelength. A high flatness is desirable for a range of applications, especially for Wavelength-Division Multiplexing (WDM).

The requirements for each of these characteristics are determined by the final application of the OFCG. In the case of THz generation using DFG, the critical aspects are those enumerated above in points 1 to 4: high coherence between optical modes, an adequate repetition frequency (and the tunability associated), an operation wavelength centered in the telecom range with a sufficient optical span.

Figure 23 describes the temporal and spectral characteristics of OFCGs. As a starting point, Figure 23a shows a short (optical) pulse of duration $\delta\tau_{FWHM}$. The FWHM of the temporal pulse ($\delta\tau$) is inversely proportional to the FWHM of the frequency domain curve (δf_{FWHM}), as they are related by Fourier transform[216].

Thus, the narrower the temporal pulse, the wider the optical span The relationship between both parameters is given by the Time Bandwidth Product (TBP), as shown in (30) and Figure 23a.

$$TBP = \delta f_{FWHM} \cdot \delta \tau_{FWHM} \tag{30}$$

Depending on the function that better fits the temporal pulse, this TBP has a theoretical minimum value (e.g. 0.44 for Gaussian shaped temporal pulse)[200,217,218]. When the measured TBP is close to this minimum value, it is said that the pulse is Fourier-limited, or TBP-limited, which is the optimum case. Thus, how close the TBP is from its limit can be used as a figure of merit of the quality of a pulsed optical source, or equivalently, an OFCG.

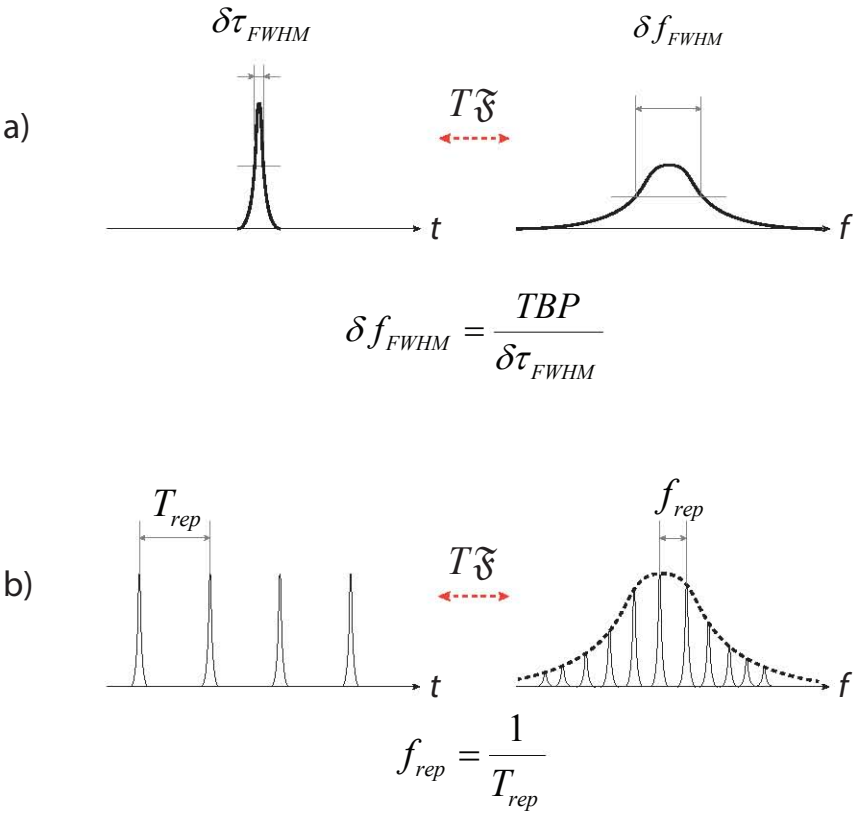

Figure 23 a) Individual temporal pulse and frequency domain representation. The temporal width of the pulse is inversely proportional to the frequency width (i.e. bandwidth, optical span); b) temporal pulse train and frequency domain representation. The frequency domain envelope, i.e. bandwidth or optical span is determined by the temporal width of the pulse as explained in a). The train is also translated as a train in the frequency domain. The repetition rate is inversely proportional to the repetition frequency

The output of an OFCG does not consist of an individual pulse (Figure 23a), but a pulse train, as depicted in Figure 23b. In this case the temporal pulse train is translated to the frequency domain to also a set of frequencies with an envelope (i.e. multiplied in amplitude) corresponding to the Fourier transform of the individual pulse shape depicted in Figure 23a. Equivalently, the shape of these pulses on the frequency domain is the Fourier transform of the envelope of the temporal pulse train. The separation between pulses is given by the repetition period in the temporal domain (T_{rep}), this is, the repetition frequency (f_{rep}) in the frequency domain. Both are related according to equation (31).

$$f_{rep} = \frac{1}{T_{rep}} \tag{31}$$

It is important to note that changes in the temporal characteristics translate to the frequency domain. In this sense, a temporal pulse compression is equivalent to optical span expansion, so, narrow temporal pulses are desired to obtain wide optical spans, (30).

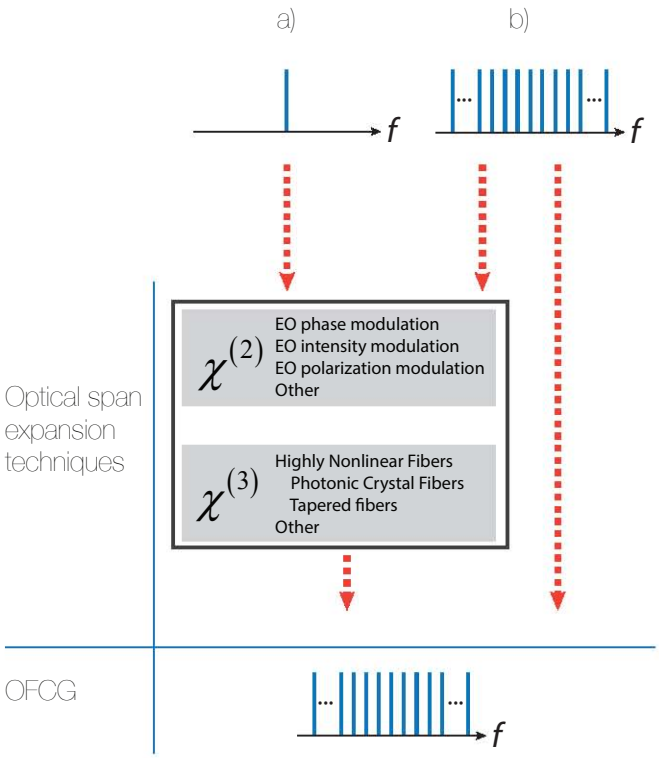

Figure 24 OFCG implementation strategies. There exist two main strategies. a) single wavelength source + span expansion techniques; b): OFCG direct generation (additional optical span expansion stages can be used)

The implementation of an OFCG is usually done in two different ways. One of the most widely used techniques is to employ a single mode laser as optical seed of an optical span expansion stage, which can be in cascade[219] or ring configurations[220] (Figure 24a). This converts the CW laser into an optical pulsed source, i.e. an OFCG. The second way is the direct generation of an optical pulsed source, thus direct generation of an OFCG. In this latter approach, also further expansion techniques (i.e. pulse compression) can be used to increase the optical span of the OFCG (Figure 24b). Due to the interest for this thesis work, we will focus on this second approach.

2.4.1.4 OFCG direct generation techniques

Direct generation of OFCGs is based on pulsed optical sources. There exist four techniques to induce pulsed operation in a laser: Superradiance (SR), Q-switching, Mode-Locking (ML) and Gain Switching (GS). This pulsed operation can be either externally induced, directly related to the laser structure, or both. When it is related to the laser structure, multimode spectral operation of the optical source is required (Figure 21b). We briefly describe here the basic concepts on pulsed optical sources, for a specific bibliography we refer to Vasil´ev[200].

Although SR is a phenomenon already reported by Dicke in 1954[221], its application to semiconductor lasers is beginning to be understood during the very last years[222–224]. SR is defined as the cooperative radiative recombination in an ensemble of quantum oscillators[224]. This way, the emission is not caused by the individual interaction between atoms, but because of a cooperative spontaneous emission, resulting in spatial and temporal coherence, anisotropic radiation pattern and afterpulse ringing oscillations[224]. The pulse width that can be obtained are about hundreds of fs and the repetition rates around a few MHz[223]. Out of the four techniques to obtain pulses from semiconductor lasers, SR is the less mature, less predictable and maybe the most difficult to achieve, being hardly dependent on the laser structure and design.

Q-switching is based on the modulation of the Q factor of the optical cavity (resonator) of the laser. When a high Q factor is used, the cavity present low losses, below the gain, and stimulated emission occurs. Alternatively, if a low Q factor is induced, the losses increase above the gain, making stimulated emission (i.e. lasing) not possible. The pulses appear when the Q-switch is modulated in a specific way. At low Q, the energy is stored in the cavity, building up a population inversion in the active medium. When the carrier density n saturates, the Q factor is suddenly changed from low to high. The stored energy is transferred to lasing as a pulse that uses to have high peak powers[200].

The Q factor modulation can be done by modulating a specific section of the laser with an external signal (active Q-switching) or by the insertion of a saturable absorber in the cavity (passive Q-switching). A saturable absorber is a material that presents high loss at low power levels and when the optical intensity

in the cavity grows and the losses saturate, it presents low losses and induces a high-Q-factor in the cavity. There exist several techniques and materials for the implementation of saturable absorbers[200], and they are widely used both in passive Q-switching and passive ML devices.

The repetition rate (frequency spacing in the optical domain) is basically determined by the amplitude of the injected current, in active Q-switching; and by the DC bias applied to the saturable absorber, in passive Q-switching. Although a few ps pulse widths and GHz rate have been achieved, commonly obtained values are in the order of several tens of ps for pulse widths and several MHz for the repetition rates[200]. As this mechanism depends on the modulation of the Q factor but not on the cavity length, the repetition frequency of the pulses can be tuned in a wide range. Q-switching lasers are currently much less used than ML, as they need specially fabricated devices while offering wider optical pulses[200].

Mode-Locking (ML) short pulse generation relays on introducing somehow coherence between the cavity modes of a semiconductor laser structure. If a fixed phase and amplitude relationship (equations (32) and (33)) between cavity modes is achieved in a multimode laser (Figure 25), the resulting output electric field will be a train of pulses similar to that represented in Figure 23b and given by equation (34). This is proven by substituting (32) and (33) in equation (23) [200,225].

$$\phi_m - \phi_{m-1} = \Delta\phi \approx \text{constant} \tag{32}$$

$$\begin{aligned} &A_m \exp i\left[2\pi\left(f_0 + m\Delta f_m\right)t + \phi_m\right] = \\ &A_0 \exp i\left[2\pi f_0 t + \phi_{00}\right] \exp i\left[m\left(\Delta f_m t + \Delta\phi\right)\right] \end{aligned} \tag{33}$$

$$E(t) = A_0 \left\{ \frac{\sin\left[2\pi\left(k+\frac{1}{2}\right)\Delta f_m t_1\right]}{\sin\left(2\pi\Delta f_m t_1/2\right)} - \frac{1}{2} \right\} \exp i\left[2\pi f_0 t + \phi_{00}\right] \tag{34}$$

$$t_1 = t + \frac{\Delta\phi}{2\pi\Delta f_m} \tag{35}$$

Where k is the number of longitudinal optical modes considered.

Under this assumption, the temporal behavior of the temporal output of a ML laser along the field distribution of with some of its cavity modes are depicted in Figure 25. A pulse appears only at the output if the cavity modes are coherently

superposed in phase[203], that also implies a high degree of coherence between longitudinal optical modes.

To obtain such ML behavior, the required phase coherence between the cavity modes can be achieved in three ways: Active Mode-Locking (AML), Passive Mode-Locking (PML) and Hybrid Mode-Locking (HML).

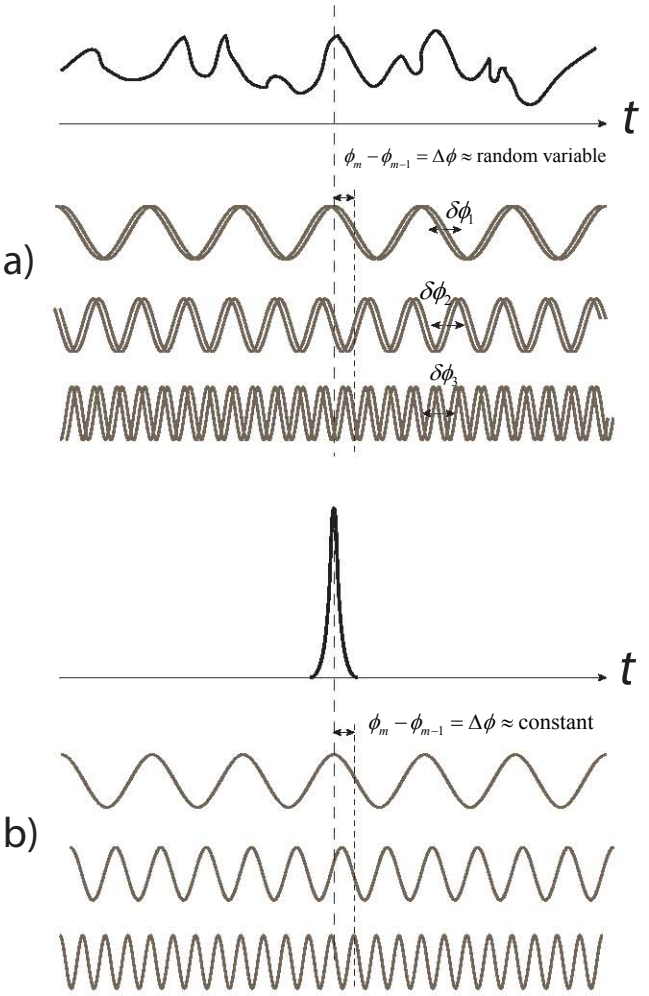

Figure 25 Mode Locking operation. Temporal representation of different cavity modes electric fields: a) random phase fluctuations between modes give as a result a random laser output signal; b) fixed phase between modes gives as a result a pulsed laser output signal. Adapted from de Dios[203]

AML requires the modulation of the gain or losses of the cavity with a frequency equal to Δf_m, defined in equation (22). Due to this modulation, each cavity mode will present sidebands that lock the adjacent cavity modes. In AML the repetition frequency is locked to an external reference, hence the coherence

between modes is very high and the FWHM of the optical modes signal can be very narrow (Hz range).

In PML, a loss region, usually a saturable absorber, is introduced inside the cavity. The loss remains higher than the gain except near the peak of the pulse travelling by the cavity. At this moment, the optical power passing through the saturable absorber grows producing a sudden reduction of the losses induced by the absorber. When the losses reduce below the gain, net gain is translated to the pulse. The pulse is shortened in every round trip due to the combined effect of gain and loss saturation until steady state is achieved. This process is represented in Figure 26.

The operation principle is similar to that of Q-switching, but in this case the repetition frequency does not depend on the current amplitude but is fixed by the cavity length[218].No external reference is used, just DC bias is needed to obtain pulsed operation. The coherence between modes is much lower than in AML and the FWHM of the photodetected signal much higher[226]. Sometimes, a modulation is applied to the saturable absorber, what is known as HML, where performance similar to AML, in terms of the coherence between modes, can be obtained.

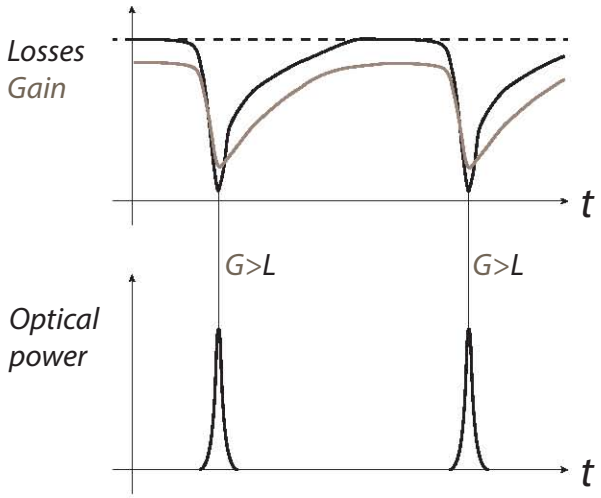

Figure 26 Passive Mode-locking steady-state operation. Temporal representation of the loss and gain inside the optical cavity and the output optical power. Adapted from Vasil´ev[200]

For all ML lasers, the repetition frequency is fixed by the frequency spacing between cavity modes (22), thus it is determined by the cavity length. This is an important drawback of ML, as the repetition frequency cannot be tuned (or the tunability is very limited), and depends on the design and fabrication of the device, not on an external current (or other electrical paramenter) that can be easily varied.

Among the four mechanisms to obtain pulsed operation of lasers, ML is the one that provides with the shortest pulses, reaching pulse widths of a few fs[218], thus widest optical spans; and highest repetition frequencies, above 100 GHz[218].

The most usual ML lasers are fiber ML lasers and integrated ML lasers. The first ones are benchtop-sized and because of their cavity lengths, they have repetition frequencies around tens of MHz. Higher repetition frequencies can be achieved by harmonic ML, in which several pulses travel simultaneously trough the cavity. However, this requires additional mechanisms to synchronize the pulses, resulting in more complex systems[227]. Integrated ML allow for repetition frequencies even above 100 GHz. Although significant advances have been reported in Photonic Integrated Circuits (PIC), the manufacturing processes are not still mature enough to offer repeatability and efficiency in this kind of active devices[228].

Gain Switching (GS) is based in the quick change of gain in the active medium of the optical resonator, which is forced to enter and to exit from stimulated operation in each period. In a semiconductor laser, this is achieved through current modulation. When a semiconductor laser is turned on from below or around its threshold current with a large signal, the output power presents a transient second order response characterized by a relaxation oscillation with frequency higher than the rise time of the current (see Figure 27a). This transient is given by equation (36).

$$\frac{d^2(\delta N)}{dt^2}+2\sigma\frac{d(\delta N)}{dt}+2\pi f_R^2\delta N=0 \tag{36}$$

Being f_R the relaxation oscillation frequency, and 2σ the damping factor which are given by the following expressions:

$$f_R=\frac{1}{2\pi}\left(\frac{\Gamma v_g a_0}{qV}\eta_i\left(I-I_{th}\right)\right)^{1/2} \tag{37}$$

$$2\sigma=\Gamma v_g a_0 S_b+\frac{1}{\tau_{ph}} \tag{38}$$

where Γ is the fraction of the optical power confined in the active volume, υ_g the group velocity, a_0 the differential gain, q the electron charge, V the volume of the active area, η_i the internal quantum efficiency and I_{th} the threshold current. τ_{ph} is the photon lifetime and S_b the average photon density.

In GS, this relaxation frequency is used to produce an optical pulsed output. If a pulsed current is applied from around or below the threshold, the density of photons, thus the optical power, will have a pulsed response, as shown

in Figure 27b. The key advantage of GS is that the width of the generated optical pulse is shorter than the width of the applied pulsed current. A large sinusoidal current modulation can also be used instead of a pulsed current[200].

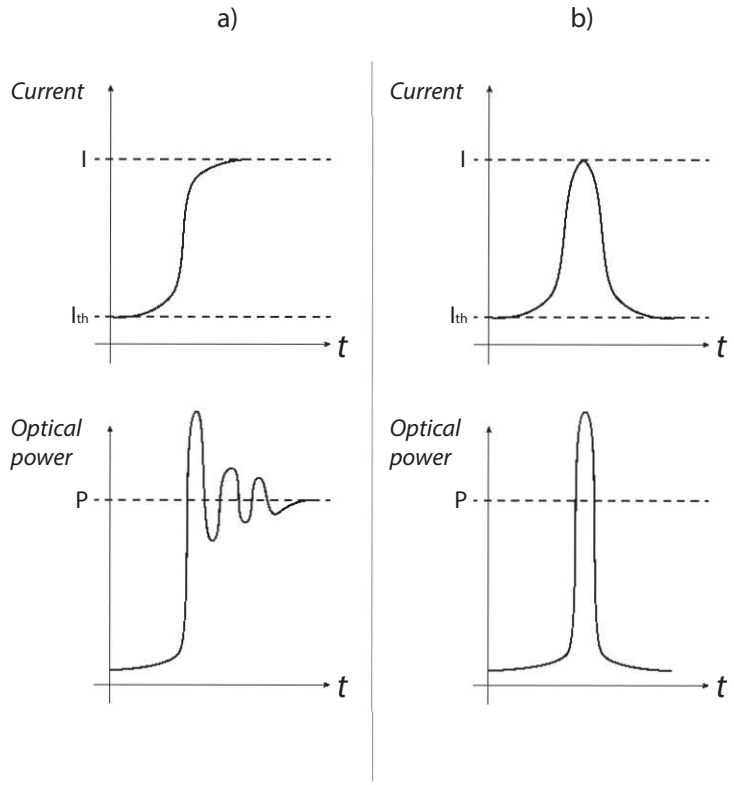

Figure 27 Gain Switching operation. Temporal representation of injected current and optical power: a) rapid switch-on of a diode laser and relaxation frequencies induced in the optical power due to underdamping; b) pulsed current modulation and optical pulse generation derived from the associated relaxation frequencies. Adapted from de Dios[203]

The operation principle of GS can be also explained from the point of view of the rate equations ((24) and (25)). The current bias and modulation are chosen so the device enters to laser operation only in a small time gap within the period. The high frequency switch-on due to the current injection makes the carrier density to rapidly grow from below to above the threshold carrier density (n_{th}). As the carrier density exceeds the threshold value, stimulated emission (i.e. laser operation) occurs and the carrier density n decreases very quickly due to generated photons, producing a pulsed optical output (i.e. density of carriers S). This is represented in Figure 28.

The pulse widths achieved with this technique is in the order of several ps or tens of ps[203], and the repetition frequency can have a very wide range, from MHz to several tens of GHz, only limited by the bandwidth of the laser. It must be

noted that the repetition frequency only depends on the bandwidth of the device and the injection current, so it is independent to the laser structure.

As no special fabrication or design are required for GS operation, it provides with a very simple technique to obtain optical pulses from a COTS laser, what is one of its main advantages. Nevertheless, when comparing with ML, GS offer wider temporal pulses, with more limited peak powers and with worse jitter performance[203].

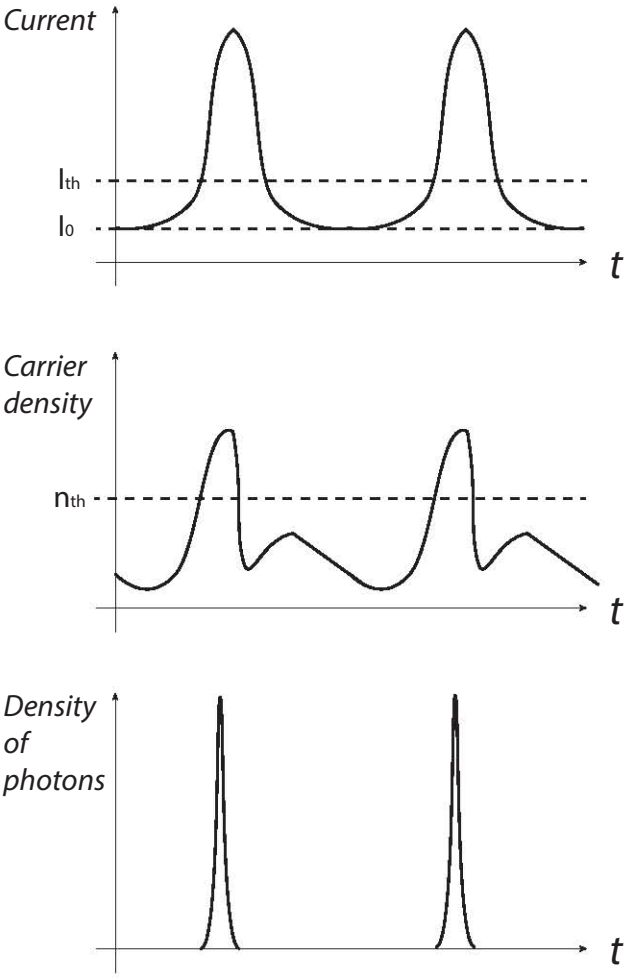

Figure 28 Gain Switching operation. Rate equations temporal representation: current $j(t)$, carrier density n and density of photons S. Adapted from Vasil´ev[200]

2.4.1.5 Optical span expansion techniques

As mentioned before, and to obtain wider combs spans, pulsed laser

sources are usually combined with optical span expansion techniques. Optical span expansion techniques are basically based on nonlinear optical processes. In any case, and before starting the description of the different nonlinear processes used for comb expansion, some preliminary discussion is needed. A comprehensive definition of optical nonlinearity is given by Saleh & Teich[229], where the characteristics of a linear optical media are summarized in several key points:

- The optical properties such as refractive index and absorption coefficients are independent of light intensity.
- The principle of superposition holds.
- The frequency of light cannot be altered by its passage through the medium.
- Light cannot interact with light. Two optical beams in the same region cannot have any effect on each other, thus, light cannot control light.

Thus, a nonlinear optical media is a media that violates one or several of the abovementioned characteristics of a linear media.

Typical span expansion techniques relies on pulse compression, according to Fourier theory and the explanation given in Figure 23a, pulse compression is translated to the optical domain as a widening of the optical span. Nevertheless, this is only true if a pulse with no dispersion is considered, thus not all pulse compressions are translated as a widening of the optical span. To illustrate this, let us firstly define dispersion and how it affects the pulse.

The propagation of a pulse (or any signal containing more than one frequency component) through an optical fiber leads to dispersion effects[230], which consists on the propagation of the different frequency components at different velocities due to the frequency dependence of the refractive index n of the medium. These are linear effects, as they arise from a frequency dependence of the refraction index n, which is still independent of the intensity of the field (at low powers).

Dispersion is translated to the temporal domain as a widening of the temporal pulse, but the optical spectra remains the same. At a first glance, this does not agree with the Fourier theory explained before. However, this is because not only amplitude, but phase has to be considered in the Fourier transform. Figure 29a represents an optical pulse with no dispersion. All its frequency components (Figure 29a, first row) propagate with no phase difference. In this ideal case, the TBP is equal to its limit or, in other words, the pulses are Fourier-limited or TBP-limited. The case of an optical pulse that has been affected by dispersion is depicted in Figure 29b. In this case, due to the frequency dependence of the refraction index, the frequency components propagate at different velocities, having a phase difference between them, as shown in the first row of Figure 29b.

Although there are no new frequency components, this phase difference (i.e. chirping) causes a broadening of the temporal pulse, represented in the second row of Figure 29, b.

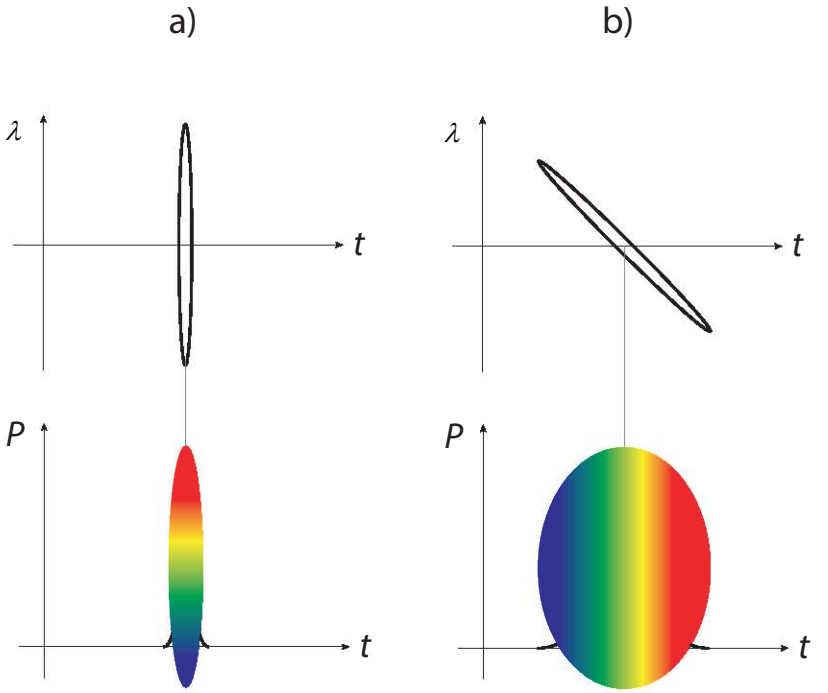

Figure 29 Linear broadening of an optical pulse due to dispersion. First line represents propagation of the different frequency components in the time domain. Second row represents the optical power of the pulse in the temporal domain: a)all frequency components propagate with the same phase (no dispersion), TBP limited optical pulse; b) the frequency components propagate with the a phase difference due to dispersion, leading to a broadening of the temporal pulse that is no longer close to its TBP limit. Adapted from de Dios[203]

When a pulse has been broadened due to dispersion, it can be compressed using linear pulse compression techniques, such as propagation along standard and compensating fibers with the adequate length. The compression limit in this case is fixed by the TBP limit[203], see equation (30). If this is the case, pulse compression does not lead to optical spectrum expansion as the optical frequencies present are the same.

Nevertheless, in this work we are interested in the case where the pulse compression leads to optical span expansion. In this case, the compression techniques are necessarily nonlinear. This is due to the violation of several of the characteristics of a linear media: new frequencies appear, two optical beams in the same region interact on each other and the refractive index of the media depends on the light intensity.

Nonlinear techniques use nonlinear phenomena. Some theoretical background on nonlinear optics is included in *Appendix III. On the basics of nonlinear optics* in order to provide a basic understanding of the physical mechanisms behind the different optical span expansion techniques presented here. The nonlinear phenomena are given by the susceptibility terms of the media with an order equal or higher than two. Although orders higher than three can be experimentally found[231], they are related to very specific applications, and most nonlinearities can be included in either second ($\chi^{(2)}$) or third order ($\chi^{(3)}$) susceptibilities.

In the process of broadening of the optical span of an OFCG, both linear and nonlinear techniques are used. The first ones are usually needed to have a good quality pulse, Fourier-limited, to start with; and the second ones to effectively extend the optical span of the OFCG.

a Second order susceptibility expansion techniques

Nonlinear processes associated to second order susceptibility $\chi^{(2)}$ used for OFCG expansion appear basically in crystals. Depending on the values of the input frequencies (f_i and f_j in equation (70), *Appendix III. On the basics of nonlinear optics),* they can be divided in several phenomena that depend on the frequency value of the new generated frequency component f_m: Electro Optical (EO) linear effect (Pockels effect); optical rectification (EO rectification, EOR); and three wave mixing processes such as Second Harmonic Generation (SHG), Sum Frequency Generation (SFG) and Difference Frequency Generation (DFG)[231]. The corresponding frequency components are shown in (39):

$$\begin{aligned} & \chi^{(2)}\left(f_m; f_i, f_j\right) = \chi^{(2)}\left(f_m = f_i + f_j\right) \\ Linear\ EO\,(Pockels) \quad & \chi^{(2)}\left(-f_m; f_m, 0\right) \\ EOR \quad & \chi^{(2)}\left(0; f_m, -f_m\right) \\ SHG \quad & \chi^{(2)}\left(2f_m; f_m, f_m\right) \\ SFG \quad & \chi^{(2)}\left(f_1 + f_2; f_1, f_2\right) \\ DFG \quad & \chi^{(2)}\left(f_1 - f_2; f_1, -f_2\right) \end{aligned} \tag{39}$$

Concerning optical span expansion techniques, the most important from these processes is the EO linear effect, also known as Pockels effect, which is the phenomenon associated to EO optical modulators.

An EO modulator can modulates phase, intensity or polarization. In this case, the input frequency *f* does not refer to the optical signal entering the modulator, but to the frequency of the electrical signal applied to the crystal (i.e. the modulating signal). This modulating signal changes the refraction index of

the crystal proportionally to the electric field of the modulating signal (see (74), *Appendix III. On the basics of nonlinear optics)*, thus the index ellipsoid, which in turn governs the propagation of an optical signal through the crystal[232]. The new generated frequencies are given by phase or amplitude modulation, in an equivalent way as it happens in other frequency regions.

As an example, phase modulators based on the abovementioned effect are one of the most typical components used for OFCG expansion. A phase modulator changes the phase of the optical field passing through them, according to (40), where L is the length of the EO crystal, ϕ_0 is the initial phase, λ_0 the center wavelength, $k_{Pockels}$ the EO coefficient associated to the Pockels effect, E_m the electric field applied to the EO crystal (i.e. the modulating signal), V_m the voltage amplitude of the modulating signal and V_π the half-wave voltage, which is the voltage needed to produce a phase retardation equal to π [231].

$$\varphi = \varphi_0 - \pi \frac{n^3 L}{\lambda_0} k_{Pockels} E_m = \varphi_0 - \pi \frac{V_m}{V_\pi} \tag{40}$$

When the modulating signal E_m (input to the electrical port of the modulator) is a sinusoidal signal, the amplitude of the optical field at the output of the EO is:

$$E_{out} = E_0 \sum_{n=-\infty}^{\infty} J_n \left(\pi \frac{V_m}{V_\pi} \right) \exp i2\pi \left(f - nf_m \right) t \tag{41}$$

where J_n is the Bessel function of first order, and E_0 the amplitude of the input optical field. Thus, a phase modulation will produce new sidebands in the spectrum (i.e. new generated frequencies), expanding the frequency span as a function of the applied modulation index given by the amplitude of the modulation signal V_m. A higher V_m. produces the appearance of more sidebands, thus a wider frequency span[232].

b Third order susceptibility expansion techniques

The third order susceptibility effects $\chi^{(3)}$ used for OFCG expansion basically appear in optical fibers. Optical fibers are mostly made of silica, which is a symmetric molecule. Thus, second order susceptibility $\chi^{(2)}$ phenomena do not originates in optical fibers[230], but those related to the phenomena associated to the real part of third order susceptibility $\chi^{(3)}$: Self Phase Modulation (SPM), Cross-Phase Modulation (XPM), Four Wave Mixing (FWM), Degenerate Four Wave Mixing (DFWM), and Third Order Generation (THG). The effects related to the imaginary part of $\chi^{(3)}$ are Stimulated Raman Scattering (SRS) and Stimulated Brillouin Scattering (SBS). Depending on the frequency values involved in the $\chi^{(3)}$ phenomena, they can be classified[231] as shown in (42), where

only those related to the real part appear, as they are the significant ones for the optical span expansion techniques.

$$\chi^{(3)}\left(f_m; f_i, f_j, f_k\right) = \chi^{(3)}\left(f_m = f_i + f_j + f_k\right)$$

$$\begin{aligned} &\textit{Quadratic EO (Kerr) SPM} && \chi^{(3)}\left(f_m; f_m, f_m, -f_m\right) \\ &\textit{XPM} && \chi^{(3)}\left(f_1; f_1, f_2, -f_2\right) \\ &\textit{FWM} && \chi^{(3)}\left(f_i + f_j + f_k; f_i, f_j, f_k\right) \\ &\textit{THG} && \chi^{(3)}\left(3f_m; f_m, f_m, f_m\right) \\ &\textit{DFWM} && \chi^{(3)}\left(f_m; f_m, -f_m, f_m\right) \end{aligned} \quad (42)$$

Self Phase Modulation (SPM) which is given by the quadratic EO effect (Kerr effect), can be seen as a self phase modulation of the optical signal. In this case, the change of refractive index is quadratic with respect to the electric field (as shown in (74) and Figure 78, *Appendix III. On the basics of nonlinear optics)*. XPM is a similar effect that originates from the same physical principle. However, in XPM two optical beams are involved in the process, and they produce a phase modulation on each other.

FWM consists in the appearance of a new frequency that is the sum of three optical frequencies present in the nonlinear media. When the frequencies are the same, a third harmonic is generated (THG). DFWM is a special case of FWM where a signal at the same frequency, but propagating in the opposite direction is generated[231].

It is important to highlight that these processes depend on the power of the input optical field and in parameters of the fiber. A regular silica optical fiber would require very high input powers to achieve significant $\chi^{(3)}$ effects, as it associated nonlinear refractive index n_2 (see (74), *Appendix III. On the basics of nonlinear optics)* is low[230]. For this reason, and when these processes are desired, specialty optical fibers with high nonlinear refractive indexes n_2 are used. These fibers are microstructured fibers such as Photonic Crystal Fibers (PCF) or tapered fibers. The highly nonlinear fibers are typically used as optical span expansion technique. The generated frequencies using these fibers originate basically from FWM that is also combined with SPM, XPM and SRS effects[230].

2.4.2 Optical mode selection strategies

As mentioned before, multimode source based DFG architectures rely on an OFCG and an optical selection stage. Two different strategies for the selection of the two required optical modes are found in the literature. The first one is based on optical filtering and the second one in Optical Injection Locking (OIL).

One of the most widely used methods to select the two required optical modes from a multimode source in DFG schemes is to use selective filtering. This can be accomplished with Arrayed Waveguided Gratings (AWGs)[195], or high-selective Fabry-Perot Tunable Filters (FPTF)[132,190,228,233]. It must be noted that FPTF are able to provide with really high Q factors (>3000[190]), thus narrow filter bandwidths (few GHz); however, AWGs have higher potential for integration in Photonic Integrated Circuits (PIC)[234].

In Optical Injection Locking (OIL)[235], the desired optical mode from the source (OFCG, master) is injected to a slave laser, which acts as both filter and amplifier, in the sense that it is able to filter the injected mode and to provide with optical gain at the same time. As the optical gain is only applied to the selected optical mode, better values of noise floor and Side Mode Suppression Ratio (SMSR) are achieved[213].

2.4.3 Characteristics and performance

2.4.3.6 Characteristics

As with the discussion about the DFG architecture based on two semiconductor lasers, we are now to analyze the figures of merit related to DFG architectures based on OFCG and optical selection. These figures of merit were included in the comparison of THz generation technologies of chapter I: frequency range, tunability, and FWHM (phase noise) of the THz signal.

The frequency range of the OFCG source is upper limited by the optical span of the OFCG, as it determines the maximum frequency separation (i.e. THz frequency) between the two optical fields that are selected. Eventually, also the optical selection stage can have influence on this highest generated frequency, as it has to properly work along the complete optical span of the OFCG. The spectrum flatness is important, but it is not as critical as in communication applications (i.e. WDM), especially when using Optical Injection Locking (OIL) as optical mode selection technique[213].

The tunability aspects associated to the THz signal in this DFG architecture are more complex than in other DFG schemes. Most OFCGs present a fixed repetition frequency (i.e. optical mode frequency spacing), as it is the case of MLL-based OFCG. This is translated to the THz signal as tunability in discrete steps equal to the repetition frequency, determined by the two optical modes of the OFCG that are selected. Traditionally, this has been one of the main disadvantages of this DFG architecture compared to those based on two optical sources. As we will discuss later in this thesis work, it is demonstrated how the use of a OFCG design with a tunable repetition frequency allows to build up a system where the combination of discrete tunability (given by the optical selection stage) and tunability of the repetition frequency of the OFCG permits a quasi-continuous tunability of the synthesized THz frequency. In this

case, the optical selection stage gives a discrete gross tuning, while the OFCG provides the continuous fine tunability[132]. With respect to the lower limit, this is determined by the repetition frequency of the OFCG, and corresponds to the case of selecting two adjacent optical modes of the OFCG.

Thus, the frequency resolution for a fixed-rate OFCG is the repetition frequency (usually in the GHz range for OFCGs used in DFG systems); while the frequency resolution for a tunable rate OFCG is given by $m{\cdot}f_{RES\_REF}$, where m is the separation between the two selected optical fields expressed in number of modes, and f_{RES_REF} is the frequency resolution of the reference, that can be as low as 1 mHz in state-of-the-art commercial RF synthesizers[236].

The frequency spacing is important when using optical filters to select the optical modes, because it has to be greater than the bandwidth of the filters (around >6 GHz for high selective optical filters[190]). When using OIL the spacing is not as critical as using optical filtering, but it is also desirable to have frequency spacing at GHz rate, in order to allow for easier locking procedures. It is also highly desirable a wide tuning range of the frequency spacing. It is very convenient to use telecom wavelengths (around 1550 nm) because of the reasons already discussed. Moreover, if PDs are the photodetectors to be used, this is a requirement as they only work at these wavelengths.

As discussed before, phase noise is associated to the mutual coherence of the optical modes used to synthesize the THz signal. This is the main advantage of this DFG architecture over the use of two single mode lasers, as high coherence between optical modes can be achieved. The resulting FHWM of the THz signal can be even in the Hz range when using an external reference in the OFCG.

In order to discuss this improvement in FWHM, let us going back to equation (20), where the phase noise of the THz signal is a function of the noise of the two optical fields. As the optical modes are originated in the same device, these have a certain phase correlation between them. This means that the covariance term σ_{f1f2} will have a positive value (as the frequency fluctuations of the optical modes will vary in the same direction), and the variance of (20), which is directly the noise spectrum FWHM, is reduced proportionally to this factor. The amount of uncorrelation between the optical modes will determine the FWHM of the THz signal.

In the case of perfect correlation (i.e. coherence), the correlation function ρ_{f1f2} (defined in (43)) will have a value of 1.

$$\rho_{f1f2} = \frac{\sigma_{f1f2}}{\sigma_{f1}\sigma_{f2}} \tag{43}$$

Thus, using (20) and (43), the distribution of the frequency fluctuations of the THz signal under perfectly correlated noise of the optical signals is:

$$f_{THz}(t) \sim N\left(f_2 - f_1, \left(\sigma_{f1} - \sigma_{f2}\right)^2\right) \tag{44}$$

If we now assume that the optical fields generated inside the OFCG have the same FWHM, the THz frequency will not have any fluctuation, and will become a constant value, what corresponds to a delta function in the frequency domain, i.e. an ideal CW signal with no noise.

Of course, a perfect correlation cannot be achieved in actual systems, but it can be close to it. In the case of OFCGs that use an external RF reference to lock the optical modes, such as AMLL or GS-based OFCGs, the amount of uncorrelated noise is that of the reference RF signal. As nowadays very low phase noise RF synthesizers are available, this amount of uncorrelated noise is very low, and the correlation factor ρ_{f1f2} is close to 1. This is translated to the THz signal spectra as a phase noise spectrum inherited from the RF reference (Figure 30).

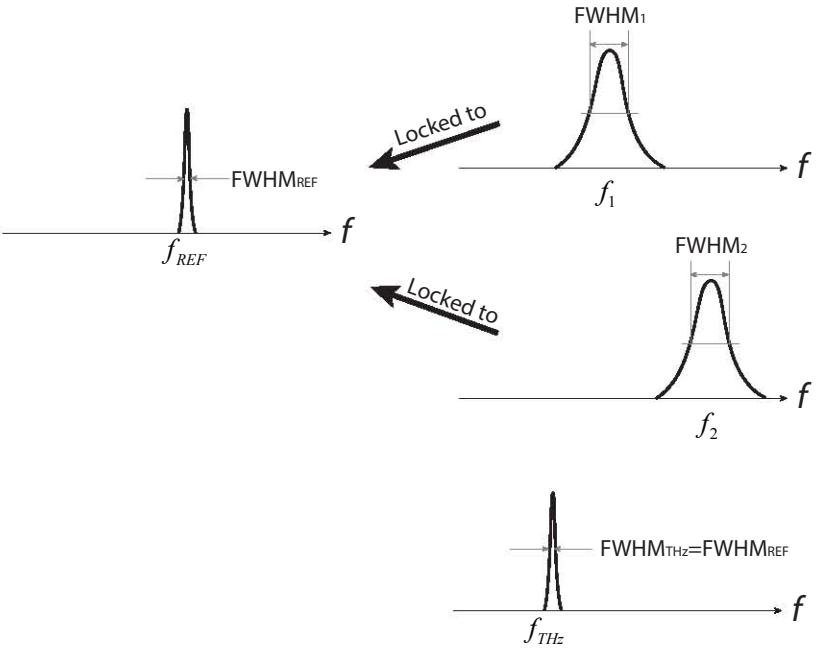

Figure 30 Two optical modes from an OFCG (signals 1 and 2), which uses an RF reference (REF). The RF reference imposes a high correlation between the noise spectra of the optical fields. The optical power resulting from the sum of both (i.e. THz field), has the noise spectrum of the reference

Let us now to go a little bit further in the analysis of the phase noise for the case of OFCGs comparing our model with a well known used model specified for AMLL and PMLL that is given by Eliyahu *et al.*[186,237]. Their analysis, carried out in the temporal domain, claims that the use of an RF reference bounds the phase fluctuations of both optical fields to a certain upper limit, so these fluctuations

do not follow a random walk anymore as the external reference acts as a restoring force of these fluctuations[186]. Moreover, this upper bound is given by the noise of the RF reference[186].

We can readily apply their initial assumptions to any pulsed source, or even more, to any CW signal where an external reference is applied. The mean value of the difference between the timing jitter δT at two time points t_1 and t_2 of a signal is given by equations (45) and (46) for the cases of using an external reference and no reference (i.e. passive locking), respectively.

$$E\left[\left(\delta T\left(t_2\right)-\delta T\left(t_1\right)\right)^2\right]=2\left[G_{REF}\left(0\right)-G_{REF}\left(\left|t_2-t_1\right|\right)\right] \quad (45)$$

$$E\left[\left(\delta T\left(t_2\right)-\delta T\left(t_1\right)\right)^2\right]=2E\left[\Delta T^2\right]\frac{\exp\left(-T/\tau_t\right)}{\left[1-\exp\left(-T/\tau_t\right)\right]^2}\cdot \left[\left|t_2-t_1\right|\frac{1-\exp\left(-2T/\tau_t\right)}{2\exp\left(-T/\tau_t\right)}-1+\exp\left(-\left|t_2-t_1\right|T/\tau_t\right)\right] \quad (46)$$

Being T the period of the signal, τ_t the coherence time of the timing jitter δT in a given time value, $G_{REF}(\tau)$ the autocorrelation function of the external reference (related with the noise spectrum as given by (14)) and ΔT the fluctuation of the period T. These equations, especially (46) are detailed models that include the amount of coherence between the noises at two temporal points.

From previous discussions, we know that the timing jitter is directly related to the phase fluctuations by (10). We also know that the phase fluctuations describe (generally) a random walk defined by a Wiener process. The derivative of the phase is the frequency as given by (11), so the difference between the timing jitter δT at two time points t_1 and t_2 of (45) and (46), can be seen as a parameter directly related to the frequency fluctuations.

Following this analogy, equation (45) states that when an external reference is used, the fluctuations are bounded by the external reference noise spectrum (given by $G_{REF}(\tau)$) as it can be seen in Figure 31a.

For the case when no external reference is used, (46), two limit cases appear depending on the ratio between the coherence time τ_t, and the period T. The first one occurs when the coherence time is much lower than the period. In this case the noises (i.e. jitter) between adjacent periods is basically uncorrelated. In this case, (46) follows a quadratic function as shown in Figure 31b, this is, the random walk that we have assumed for the phase, or equivalently, the time fluctuations, as they have been directly related by (10) in our previous discussions. The case when the noises between periods are highly correlated (but no external reference is used), is given when the coherence time is much greater

than the period. In this case, also shown in Figure 31b, the fluctuations have an unbounded linear trend.

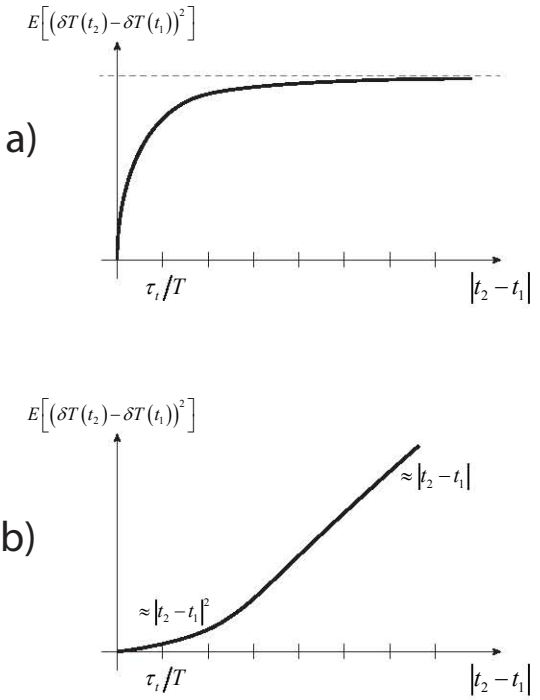

Figure 31 Average value of the timing jitter difference between two time instants t_1 and t_2 as a function of the separation between these time values. The s axis is given as a function of the coherence time of the jitter with respect to the period of the signal: a) the use of an external reference acts as a restoring force and the timing jitter between two time values is bounded by the reference noise; b) when no reference is used, this timing jitter difference follows a random walk when the correlation time of the timing jitter is much lower than the period (uncorrelated timing jitter between different periods) and a linear trend when the timing jitter pdfs overlap from period to period

In summary, a THz signal with very low phase noise can be obtained in a DFG system from two optical signals with relatively large optical FWHM, given a high correlation between the noise of these optical signals, i.e. a high phase coherence between optical modes in the OFCG. In practical cases, the correlation will not be perfect, but can be very high if the OFCG uses a high quality RF signal, and in this case the THz field will have the noise spectrum of that reference, which is the only source of uncorrelated noise in the process. Thus, the phase noise of the THz signal generated with this DFG architecture is independent of that of each optical mode when these are highly correlated (e.g. OFCG using an RF reference). It is important to note that if the phase noise (optical FWHM) of each optical mode is independently measured, we will not see any FWHM reduction due to the reference, as it only appears in the THz signal generated in the DFG process (see Figure 30).

At this point, another question arises in the view of Figure 22b and Figure 30: Why the phase noise spectra of the THz signal is different in this case when compared to the use of an OPLL, if both use a reference to lock the optical modes? The answer is straightforward: in the case of an OPLL, an external electronic circuitry is employed to lock the optical modes to a reference (RF or optical). In this latter case, the optical fields have to follow the reference through the feedback loop, which has a limited BW given by the electronics. Thus, the feedback loop will not be fast enough to lock very fast variations, and the phase noise at high frequency offsets will be uncorrelated. In the case presented in this section, when an OFCG uses a reference (ML or GS-based), there is no feedback loop: the RF reference is modulating the optical source directly. The optical fields do not have to follow a reference, the optical fields (i.e. photons) are modulated within the device and thus they are generated with a phase correlation between them given by this modulation signal (RF reference).

2.4.3.7 Performance

The range of OFCGs suitable for DFG generation is extensive. From simple schemes including a OFCG with a few hundreds GHz, which can be used to generate signals in the mm-wave and sub-THz range[132]; to OFCGs with optical span values of 3.64 THz (28 nm or 365 lines) within a 3.5 dB[238] power variation. Impressively flatted OFCGs with 1 dB-bandwidth of 750 GHz have been also reported[219].

Among the strategies for the implementation of an OFCG shown in Figure 24, the direct generation of an OFCG allows for a saving in component count, cost, energy consumption and physical dimensions of the DFG source. This is an important advantage over the use of a single mode laser and optical span expansion.

From the OFCG direct generation techniques presented in 2.4.1.2, SR is not a completely understood technique when applied to semiconductor lasers, it is difficult to implement and requires of special manufactured devices. Q-switching also requires special design and manufacturing, and provides broader pulses than the other techniques. Although ML also requires special design and fabrication as SR and Q-switching, it is able to offer very narrow pulses, thus very wide optical spans. This is the reason why ML is the most widely used technique for the direct generation of an OFCG. GS generates wider pulses than ML, but better than Q-switching. Moreover, GS can be implemented in COTS lasers and the repetition frequency can be widely tuned, which is a significant advantage over ML which repetition frequency is fixed by fabrication.

ML is able to offer very narrow pulses (down to around 5 fs), thus optical span values of several THz, and very high repetition frequencies (i.e. frequency spacing between modes) up to a few hundreds of GHz. However, this repetition rate is fixed, so the DFG source provides only discrete tunability with a resolution equal to the repetition frequency. If PML is used, the device works as a pulsed

source with just DC bias, giving minimum THz FWHM values in the order of kHz. When AML or HML is used, the laser is locked to an external RF reference (equal to the repetition frequency), having very high coherence between modes and THz FWHM in the Hz range.

The capability of GS to provide a simple, compact and reliable pulsed source that in addition is able to offer GHz repetition rates widely tunable has caused that some recent approaches for the direct generation of OFCG rely on these optical sources[239,240], as it is the case of part of the work presented in this thesis[132]. As a RF reference is used in the GS process, in this case also the modes are locked, with high phase correlation between them, and Hz-range THz FWHM can be attained.

As mentioned before, when further optical span is needed, expansion techniques are implemented. The main approaches for the expansion of the optical span (i.e. nonlinear pulse compression techniques) are the EO modulation (both phase and intensity) and the use of nonlinear optical fibers.

2.5 Photodetectors for DFG

At this point, it is important to clarify the nomenclature employed in this document to refer to both photodetectors and photomixers. A photodetector is a device that senses the optical power and converts it to electrical current (i.e. photocurrent). If two optical fields are detected, DFG occurs (without any mixing process, just optical power detection). On the other hand, a photomixer is a device that is able to act as photodetector, but also can offer mixing capabilities to mix the DFG-generated signal with an incoming one (within its electrical bandwidth). Hence, we refer to photodetectors to those employed in generation in DFG systems, and photomixers to those employed in Electro-Optical heterodyne detection. PCs and PDs are employed as photodetectors. It is worth saying that in the literature, the term photomixer is indistintively used for photodetectors on DFG systems.

As mentioned before and shown in Figure 16, a DFG system consists of a dual optical frequency source, already discussed above, and a photodetector, which is the device that converts the optical power to a THz wave. The equations of this conversion for photodetectors (neglecting the roll-off terms, i.e. at frequencies lower than the device bandwidth), (7) and (9), are reproduced here again for clarity.

$$I_{THz} = \Re P_{opt} \tag{47}$$

$$P_{THz} \leq \frac{1}{2} R_A I_{THz}^{\ 2} \tag{48}$$

In this section, the photodetectors used for DFG generation, photoconductors (PCs) and photodiodes (PDs), are presented, as well as a brief review of their main characteristics and current state-of-the-art performance. It is important to note that in usually employed photodetectors, such as most PCs and PDs, the illumination area (several μm) is much smaller than the THz wavelength, and the generation mechanism of the THz radiation comes from the collective contribution of all the generated carriers. In this situation, the direction of the generated THz waves is perpendicular to the illuminated surface[116].

2.5.1 Photoconductors (PC)

They can be classified as intrinsic and extrinsic. In the intrinsic detectors, the photon energy has energy greater than the gap between the valence and the conduction band of the semiconductor. When the photon reaches the detector, an electron is excited from the valence to the conduction band and a hole is created in the valence band, thus increasing the conductivity in the device and producing in last term a current flow. If the energy of the photon is not higher than the energy gap, impurities can be added to the semiconductor, close to the valence and conduction bands so that a photon can excite an electron from a donor state or into an acceptor state[21]. Due to the energy of the photons at THz range, almost all THz photoconductor receivers are extrinsic. Photoconductors have been used since 1960´s, for THz detection. During decades, InSb and Ge detectors have been used down to 2 THz. In the case of Ge, several impurities were used: Ge:Sb, GeAs. Ge:P, Ge:In…[21].

The THz generation by photomixing in PCs can be pulsed, using fs-range pulsed optical sources; and also CW, using DFG. In the pulsed case, the maximum achievable frequency depends on both the optical pulse width and the photoconductor carrier lifetime[116].

The most suitable and widely used material to implement PCs is the Low Temperature Grown GaAs (LT-GaAs)[116]. The LT-GaAs is used with optical sources in the 800 nm range, such as fs Ti:Sapphire lasers[108] or Er-doped fiber lasers[241] for pulsed THz generation, and near infrared CW lasers, such as 850 nm CW laser diodes, for CW THz generation[242–244].

However, it is especially interesting the pursue of the operation in the telecom range wavelength, in order to take advantage of the great number of compact, low cost and high performance COTS optical devices. With this motivation, photoconductors operating in the 1500 nm range have been recently developed. These photoconductors are made of LT InGaAs/InAlAs on InP multilayer quantum wells[110,127–130].

To better understand the operation of these devices, the equivalent AC circuit of a PC photomixer with a coupled antenna is represented in Figure 32, being V_b the bias voltage applied to the PC, $G(t)$ the conductance of the PC, C_{pm} its capacitance, and R_A the antenna resistance[245].

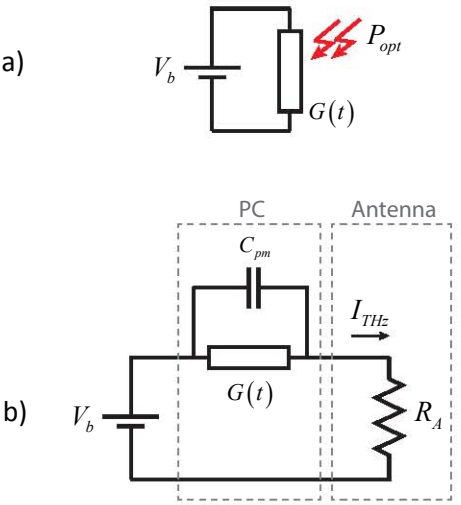

Figure 32 a) Schematic representation of a PC; b) simplified equivalent AC circuit of a PC photomixer and coupled antenna

Equation (48) defines the maximum THz power P_{THz} that can be generated in a photodetector. In PCs, this term is defined according to equation (49):

$$P_{THz}(f) = \frac{I_{THz}{}^2 R_A}{2}\eta_{t,PC}(f_{THz})\eta_{RC}(f_{THz}) = \frac{I_{THz}{}^2 R_A}{2}(g)^2 \frac{1}{1+(f_{THz}/f_{rec})^2}\frac{1}{1+(f_{THz}/f_{RC})^2} = \frac{I_{THz}{}^2 R_A}{2}\left(\frac{\tau_{rec}}{\tau_{tr}}\right)^2 \frac{1}{1+(f_{THz}/f_{rec})^2}\frac{1}{1+(f_{THz}/f_{RC})^2} \quad (49)$$

where τ_{rec} is the electron-hole recombination time, f_{rec} the 3-dB frequency of the electron-hole recombination time ($1/(2\pi\tau_{rec})$), τ_{tr} the transit time (carrier lifetime) and g the photoconductive gain[116]. The term $\eta_{t,PC}(f_{THz})$ is associated to the nonideal carrier transport, and it is approximated as g^2 for low frequencies and as $f_{THz}{}^{-2}$ for high frequencies. Thus, the dependence on the recombination time is overcome. The parameter f_{RC} is related to the RC circuit encompassing the antenna resistance R_A and the device capacitance C_{pm}, according to (50).

$$f_{RC} = \frac{1}{2\pi R_A C_{pm}} \tag{50}$$

In the view of this equation (49), it is clear that the frequency response of a PC is limited by a RC roll-off and attenuated by a factor dependent on both recombination and transit times (τ_{rec} and τ_{tr}). A low value of C_{pm} leads to a higher RC frequency bandwidth[116]. The carrier recombination time τ_{rec} can be reduced by reducing the distance gap between the electrodes or by applying a higher bias voltage[246].

The generated THz current I_{THz} was also defined for an ideal photodetector in equation (47). We can specify this I_{THz} for a PC photomixer as follows[116]:

$$I_{THz} = G(t)V_b \tag{51}$$

It can be seen how the PC is equivalent to a variable resistance with a conductance *G(t)*. This conductance value depends on the optical power of the incident field and can be expresses according to equation (52).

$$G(t) = G_0\left(1+\frac{2kE_1E_2\sin\left(2\pi f_{THz}t+\phi\right)}{\left(E_1^{\,2}+E_2^{\,2}\right)\sqrt{1+\left(2\pi f_{THz}\tau_{rec}\right)^2}}\right) = G_0\left(1+\frac{2k\sqrt{P_1P_2}\sin\left(2\pi f_{THz}t+\phi\right)}{\left(P_1+P_2\right)\sqrt{1+\left(2\pi f_{THz}f\tau_{rec}\right)^2}}\right) \tag{52}$$

Where *k* is a mixing efficiency factor ranging from 0 to 1 associated to the spatial overlap of the optical fields, not dependent on the device[107]. An illustrative representation of the generated THz current I_{THz} as a function of the bias voltage V_b in a PC is shown in Figure 33.

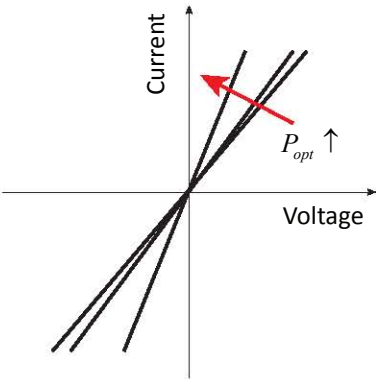

Figure 33 V-I curve for a typical PC. The optical power delivered to the PC changes the curve slope

The current state-of-the-art performance summary of PCs for sub-THz and THz generation based on DFG appears in Table II1.

Parameter	Photodetection in photoconductors
Pulsed/CW	Pulsed/CW
Maximum power (CW)/ Pulse energy (pulsed)	2 μW at 1 THz[108]
Frequency range (THz)	0-3 THz[21]
Tunability	Dependent on optical source. Can be very wide and continuous
Minimum FWHM (CW)	Dependent on optical source. Can be very narrow (Hz range)[132]
Minimum size (range)	Integrated. Compact devices packaged in cm[110,111]
Coherent/Incoherent	Coherent
Cooling	RT

Table II1 Performance summary of THz generation based on photodetection in PCs

PCs are able to provide with a high bandwidth, up to 3 THz. However, the output power is lower than PDs, achieving a maximum reported value of 2 μW at 1 THz. The coherence of the DFG source allows a coherent emission of THz waves. PCs are compact and can be integrated as planar devices. Moreover, they work at RT.

2.5.2 Photodiodes (PD)

The THz current I_{THz} is given by equation (47) for a p-i-n PD. Further explanation on the origin of the photocurrent in PDs and their limitations (especially UTC structures) can be found in Feiginov[247]. The relationship between current I_{PD} and bias voltage V_b in a PD is expressed according to equation (53) that is illustrated in Figure 34.

$$I_{PD} = I_0 \left[\exp\left(\frac{qV}{k_B T} \right) - 1 \right] + I_{THz} \tag{53}$$

Being I_0 the dark current, k_B the Boltzmann constant, T the temperature and q the electron charge. At negative bias voltage values, the first term of the right part of (53), associated to the dark current is very low and usually much lower than the generated photocurrent, i.e. I_{THz}

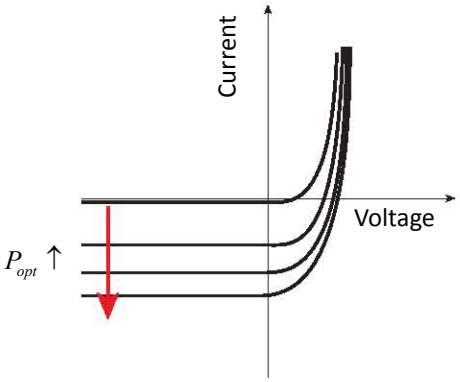

Figure 34 V-I curve for a typical PD. The optical power increases the reverse current when the PD is biased with a reverse voltage

In Figure 35 it is shown the equivalent AC circuit of a PD. In this case, the PD consists on a p-i-n structure that is modeled as a current source delivering the THz current I_{THz}.

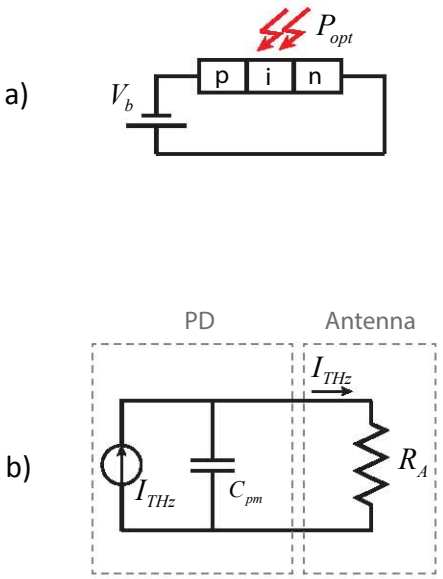

Figure 35 a) Schematic representation of a PD (including p-i-n junction); b) simplified equivalent AC circuit of a PD photodetector and coupled antenna

As with PCs, we can define the specific THz power P_{THz} emitted by a PD with a coupled antenna (54)[116].

$$P_{THz}(f) = \frac{{I_{THz}}^2 R_A}{2} \eta_{t,PIN}(f_{THz}) \eta_{RC}(f_{THz}) = \frac{{I_{THz}}^2 R_A}{2} \frac{1}{1+(f_{THz}/f_{tr})^2} \frac{1}{1+(f_{THz}/f_{RC})^2} \quad (54)$$

The parameter f_{tr} is the frequency at 3 dB associated with the transit time (carrier lifetime) τ_{tr}, given by $f_{tr} \sim 1/(2\tau_{tr})$. In the case of PDs there exist two main roll-offs: transit time and RC. This is one of the main differences of PDs and PCs concerning frequency response. The value of C_{pm} can be lowered down (even down to a few fF) to increase the RC frequency bandwidth. Another way to increase this frequency is reducing the antenna resistance R_A, however, this causes a reduction of the THz power. However, the reduction of C_{pm} has associated a degradation of the transit time frequency. Thus, in the case of PDs, there exist a trade-off between these two roll-offs that limits the maximum usable frequency.

In conclusion, the maximum frequency of PCs is limited by the carrier lifetime (transit time) associated to the photodetector. At high frequencies, the

frequency response is affected by to two factors in p-i-n diodes: transit time and RC roll-offs[107,116], existing a trade-off between both[107]. These two roll-offs contribute to the frequency response above the 3-dB bandwidth proportionally to f^{-2} each one[116]. This is the main reason of the lower maximum frequency of p-i-n photodiodes when compared to photoconductors.

However, photodiodes present several advantages over photoconductors that make them a promising technology for THz generation: first, they have higher gain (ideal unity-gain responsivity at sufficiently low frequencies); second, they need lower applied voltage between contacts; and third, the thermal effects are lower, thus higher optical power can be applied and higher THz power can be obtained[116]. Furthermore, they mostly work in the telecom wavelength range.

There exist basically three kinds of devices based on p-i-n structures[116]:

- p-i-n diodes. They have a limited bandwidth, thus having low output power even at intermediate frequencies. They are surface illuminated devices, where the optical signal is perpendicular to the generated current. An improved design of p-i-n diodes are the Travelling-Wave (TW) PDs. These are edge-illuminated devices with a waveguide structure where optical and electronic signals travel in the same direction. As the waveguide can be designed as lumped elements, it can be matched to the output impedance, and the RC frequency bandwidth is greatly improved[248].

- Photodiodes with electron transport only. In these diodes, the photocurrent is basically generated only by electrons. As the velocity of the holes is less than that of electrons, higher frequencies can be achieved. This operation principle is followed by the Uni-Travelling Carrier Photodiode (UTC-PD)[113,114], Travelling-Wave Uni-Travelling Carrier Photodiode (TW-UTC-PD)[112], and n-i-pn-i-p superlattice photomixers[115,116]. Also by other modifications over UTC-PD: Near-Ballistic UTC (NBUTC)[249] and Modified UTC (MUTC)[250]. The main advantage of the UTC structures is that they are able to provide a higher maximum output power[247].

- Ballistic transport p-i-n structures. The electrons are accelerated trough a large region, obtaining higher carrier velocities. This is the case of n-i-pn-i-p superlattice photomixers[115,116], where the trade-off between transit time and RC roll-offs is overcome by the use of superlattice structures, allowing for independent design of both[116], what is a promising result for the development of higher frequency photodiodes.

As the limited THz output power is one of the main concerns in compact THz technology, great effort is currently placed in photodiodes, as they are expected to generate higher THz power. In this sense, 24 μW at 1.06 THz has been

achieved[112] and around 300 μW is theoretically predicted with the limitations of space charge effects and heating of the device[247].

It must be noted that PDs have been successfully integrated with planar antennas, both resonant[112] and broadband (i.e. log-periodic[112], log-spiral[116]). In the first case, they have higher output power but tunability around 20% of the center frequency, while in the latter case they are able to cover the whole range[21]. Moreover, they have also been integrated in InP substrates[251], in this case achieving lower bandwidth values around 100 GHz.

The current state-of-the-art performance summary of PDs for sub-THz and THz generation is included below in Table II2.

Parameter	Photodetection in p-i-n photodiodes
Pulsed/CW	Pulsed[252]/CW
Maximum power (CW)/ Pulse energy (pulsed)	24 μW at 1.06 THz[108]
Frequency range (THz)	0-1.6 THz[131]
Tunability	Dependent on optical source. Can be continuous and covering the whole range[21]
Minimum FWHM (CW)	Dependent on optical source. Can be very narrow (Hz range)[132]
Minimum size (range)	Integrated. Compact devices packaged in cm[116]
Coherent/Incoherent	Coherent
Cooling	RT

Table II2 Performance summary of THz generation based on photodetection in p-i-n PDs

In this Table II2 it can be seen how the maximum generated power is 24 μW at 1 THz, which is around one order of magnitude higher than in the case of PCs. However, as mentioned above, the operation frequency is lower, with maximum reported frequencies of 1.6 THz. As PCs, they are also compact devices with integration potential in planar structures and RT operation.

3

Sub-THz and THz signal detection with photomixers

3.1 Principle of operation

As discussed in Chapter I, sub-THz and THz signal detection has been traditionally carried out using electronic and thermal devices. Both thermal detectors and electronic rectifiers have been extensively used in direct detection, while electronic and thermal mixers such as Schottky diodes, Superconductor-Insulator-Superconductor (SIS) mixers and Hot Electron Bolometers (HEB) have been the preferred options for heterodyne detection, as these kinds of detectors are able to offer nowadays a high performance and low conversion losses in the case of using them as mixers.

The use of photonic architectures and devices for sub-THz and THz detection has been motivated by the appearance and establishment of the optical techniques in the sub-THz and THz range, especially for generation. However, the use of optical approaches for detection of CW signals is less extended, although is becoming a prolific research field in the last years. Nowadays, the use of photonic receivers in the THz range is almost only used in coherent, pulsed systems, basically employed in TDS schemes. Both PCs and EO crystals are used for this purpose.

This interest in CW sub-THz and THz detection using photonic techniques is highly led by the possibility of using remote distribution with optical fiber of photonic sub-THz and THz LO with very low losses, allowing for both remote generation and heterodyne detection of sub-THz and THz signals. Due to the advantages of heterodyne receiver operation, already mentioned in

chapter I, and those associated to photonic distribution of a LO, the pursuit for Electro-Optical heterodyne receivers in the sub-THz and THz range is becoming a key aspect in the photonic THz field[136]. The EO heterodyne detection scheme appears in Figure 36. It encompasses a photonic LO and an EO mixer. The M signal is delivered to the mixer as an electrical signal, while the LO is delivered as an optical signal. The LO and M signals are mixed and the difference term (IF) is obtained at the output of the mixer.

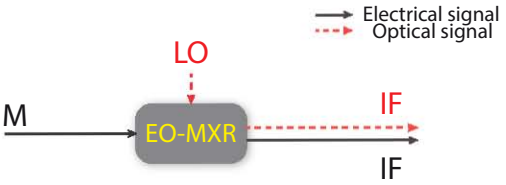

Figure 36 Sub-THz and THz CW heterodyne detection schemes: Electro-Optical mixing

The EO heterodyne detection at sub-THz and THz regions is much less developed than the traditional all-electronic heterodyne schemes and the performance in terms of Conversion Ratio (CR) is nowadays much worse. Most photodetectors used in CW generation have been also used in CW detection (PCs and PDs) as photomixers, however, some are specifically designed for operation as receivers, as the one used in this work (the np-i-pn quasi-ballistic THz detector). PCs are typical photomixers, however, it will be shown how a PD can act as photomixer even when they are not supposed to have mixing capabilities. In the following sections, the characteristics and state-of-the-art performance of photomixers, i.e. PCs and PDs, for detection of CW sub-THz and THz signals are presented, especially for EO heterodyne detection.

It is important to note that as a mixer performs a multiplication of both M and LO signals, the phase noise of the IF signal will be determined by the two input signals, according to the discussion previously presented for DFG systems, which can be also applied to this case. Thus, the phase noise of the IF signal can be describe according to equation (20).

3.2 Photomixers for sub-THz and THz detection

3.2.1 Photoconductors (PC)

The THz detection with photoconductors below 2 THz began with GaAs devices. GaAs is sensitive to near infrared optical wavelengths (around 800

nm). The appearance of Low Temperature grown GaAs (LT-GaAs), was a major advance for THz technology, given the short carrier lifetime of this material that made it especially suitable for THz detection and generation[107].

CW THz receivers using LT-GaAs photoconductors (i.e. using wavelength around 800-850 nm) have been extensively reported[243,244]. Nevertheless, the CW detection was introduced later than pulsed operation. This is because the differences between pulsed and CW radiation. If the same average optical power is considered, fs pulses with MHz range repetition rates have much higher peak power values, but also the semiconductor has much more time to recover from the excited into dark state, given the repetition rate. This is the main reason why the CW detection with photoconductors was delayed until the technology was developed[163].

The advent of the telecom technologies in the optical domain has driven the development of PCs for operation with optical wavelengths at 1550 nm. Also PCs at 1550 nm have appeared with decades of delay given the problems associated to the behavior of PCs made from InP or InGaAs (i.e. sensitive to 1550 nm radiation). The main problem is that in these materials the dark conductivity is much greater, reducing dramatically the performance. Only in the last years some feasible solutions to this problem have been reported. One of them, (reported in 2010) is the introduction of Fe impurities in the InGaAs (Fe:InGaAs)[253]. However, poor power performance in emission is achieved[163]. The other solution (2009), combines the introduction of Be acceptors and a multilayer structure with InAlAs thin layers.[127]. PCs at 1550 nm for CW operation are already commercially available[130], some of them based in the latter cited solution to overcome the high dark conductivity[128,133].

It is worth to briefly explain the operation behavior of a PC in reception operation. If we consider the equivalent circuit of a PC shown in Figure 32, the M signal will be received in the antenna and it will be seen by the PC as a change in the bias voltage. At the same time, optical illumination is applied to the PC, modulating its conductance *G(t)*. In the case of direct detection, the optical signal acts as a switch, allowing for current flow in the equivalent circuit. In heterodyne EO schemes, the optical illumination comes from a DFG architecture, and consists of two optical modes. This causes the conductance *G(t)* to be modulated at the LO frequency given by the DFG optical illumination.

Figure 37 is an illustrative scheme (adapted from Sartorius[163]) of this process and how the photocurrent is generated in reception. In the view of equation (51), under optical illumination, no photocurrent is generated if there is no bias voltage V_b across the terminals of the PC, i.e. THz radiation illuminating the antenna. When both optical and THz illumination impinge the PC, a photocurrent proportional to the product of the optical power and the THz field is generated. As the photoconductor does not work unbiased, the THz illumination is able to produce the required bias voltage to generate the photocurrent. Thus, PCs can be seen as a switching mixer. Actually, PCs are also known as photoconductive switches[21].

It is important to say that if the same optical illumination signal is used in generation and detection, the receiver allows for a coherent detection of the THz signal under an homodyne scheme[254,255].

Table II3 contains a performance summary of state-of-the-art direct detection with PCs. It can be seen that operation bandwidths up to 4 THz in direct CW detection have been achieved. The NEP values are very good, but they are referred to LT-GaAs PCs operating with optical pumping at around 800 nm. The frequency bandwidth is in the MHz range, although it is basically limited by the output terminal design of the PC.

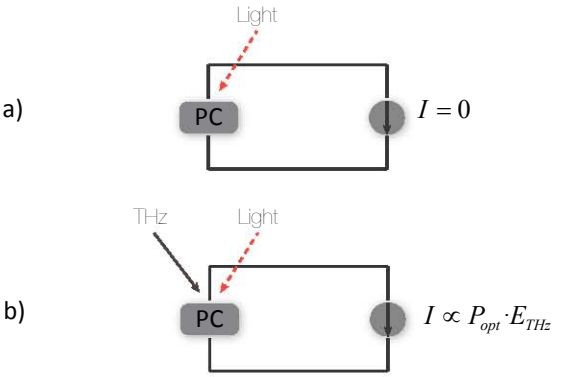

Figure 37 Detection operation of a PC: a) only light impinges; b) both light and THz radiations impinge. Adapted from Sartorius *et al.*[163]

Parameter	PC (CW operation)
Frequency range (THz)	Up to 4 THz[130,163]
Coherent/Incoherent	Coherent[163,256]
Minimum size (range)	Planar, antenna coupled[127]
NEP (W/(Hz)$^{1/2}$)	$4{\cdot}10^{-14}$ with GaAs[21]
Frequency bandwidth (Hz)	50 MHz[21]
Cooling	RT, but cooling can improve performance of some materials[21]

Table II3 Performance summary of CW THz direct detection based on PCs

Among the limited number of work on EO THz heterodyne detection nowadays, PCs are the most usually employed devices. They have been used for heterodyne detection demonstrating coherent capabilities[138], and also in metrology applications with OFCGs[55–57,59,60] (Table II4).

Parameter	PC (CW operation)
Frequency range (THz)	Demonstrated up to 100 GHz[55–57,59,60,138]
Coherent/Incoherent	Coherent[138]
Minimum size (range)	Planar, antenna coupled[138]
Frequency bandwidth (Hz)	Around 830 MHz[138]
Conversion losses (dB)	N/A
Noise temperature	N/A
Cooling	RT[138]

Table II4 Performance summary of CW THz heterodyne detection based on PCs

Up to now, PCs have been demonstrated in sub-THz heterodyne receivers with M signals in the order of 100 GHz[55–57,59,60,138]. The IF signal with higher frequency reported is around 850 MHz[138]. Besides this, higher M frequencies should be readily achievable at the expense of higher conversion losses, and also higher IF frequencies should be achieved by proper IF output design (bias-Tee, coaxial IF output). It must be noted that the conversion losses associated to a PC working as an EO heterodyne detector are not clearly analyzed in the literature.

3.2.2 Photodiodes (PD)

Between the several p-i-n structures reported for THz emission (section II.2.5.2), up to now, only two have been successfully used for detection: TW-UTC-PD[171,172] and UTC-PD[164]. UTC-PD[164] has been reported to work as both a direct detector (forward biased, square-law detector) and as homodyne detector (reverse biased). TW-UTC-PD[171,172] has been reported in EO heterodyne detection, working with a reverse bias voltage. In this thesis work, a new p-i-n structure detector is reported to properly work for EO heterodyne detection: the np-i-pn quasi-ballistic THz detector (see chapter IV).

As seen on section II.2.5.2, generation based on PDs provides much higher power than photoconductors, so they use to be the preferred choice for state-of-the-art THz generation schemes based on DFG on semiconductors[25,163]. However, in detection, PCs are preferred for direct detection. The reason for this needs the understanding of the behavior of a PD as detector. If we attend to the VI curve of a PD represented in Figure 34, we can see that the device will work as a PD with negative bias voltage values V_b, and as a diode for positive voltage values V_b. According to the discussion of section 2.5, PDs can only properly generate a photocurrent I_{THz}, when they operate reverse-biased. The schemes reported for EO heterodyne and homodyne detection with PDs are in this bias region[171,172164].

When they are forward-biased, they have a certain range of the VI curve

with a quadratic behavior (Figure 34), so they can be used in this bias range as square-law detectors for direct detection. This scheme has been only reported by Nagatsuma *et al.*[164]. However, this last scheme has high conversion losses, as the second order nonlinear parameter k_2 (associated to the quadratic term) is not the dominant one in the nonlinear behavior of the PD and the noise current is high. Moreover, a coherent detection scheme is implausible in this bias region (direct detection)[163]. A simplified explanation of this is given by Sartorius *et al.*[127,163] and is represented in Figure 38. A PC needs a bias voltage to generate a photocurrent I_{THz}, while a PD generates photocurrent even without an external bias voltage. If we remember that the THz field detected by the antenna is seen by the photomixer as a change in the bias voltage, or a bias modulation[257], in direct detection in a PC, the detected photocurrent is proportional to the product of the optical power and the THz field. In the case of a PD, the photocurrent due to the optical CW illumination adds to the current due to voltage variations caused by the detected THz field (see equation (53)). In the view of equation (53) and Figure 34, the first photocurrent is much higher than that generated by the THz field. Thus, the latter is very difficult to detect as high noise currents due to the optical illumination are expected[127,163]. Then, a coherent detection with PD only seems to be possible using them as mixers in homodyne[164] or heterodyne schemes[171,172], although this path in still almost unexplored and has not been reported yet.

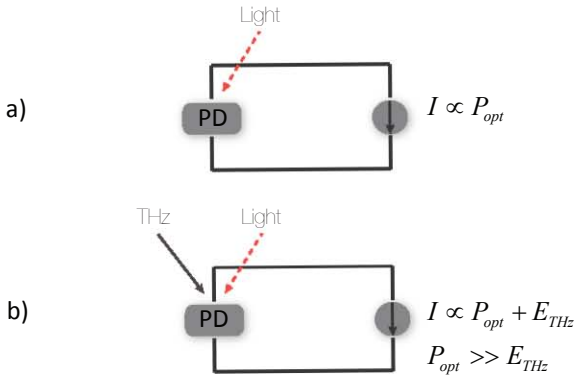

Figure 38 Detection operation of a PD: a) only light impinges; b) both light and THz radiation impinge. Adapted from Sartorius *et al.*[163]

Electro-Optical (EO) heterodyne detection in a PD has not a clear explanation yet and at the time of writing this document, there is no theoretical model to these mixing phenomena that occurs in the PD. It is known from the discussion above that the received THz field produces a bias modulation in the PD. In EO heterodyne detection, the optical illumination will contain the LO frequency. As the PD is biased with a negative voltage, a photocurrent at LO frequency is generated. This photocurrent containing the LO is added to the current generated by a variation in the bias voltage, see equation (53). Thus, we have the sum of both currents, and at a first glance we do not have any multiplicative term that could give the heterodyne detection. Nevertheless, it has

been experimentally demonstrated that there exists a mixing term, although with very high conversion losses[171,172].

The performance summary of direct detection with PDs is contained in Table II5. As already said, the maximum frequency achieved in direct detection with PDs corresponds to the only reported case (350 GHz), from which also a NEP value of $4.7 \cdot 10^{-8}$ is estimated from the data reported by the authors. The frequency bandwidth is expected to be around several GHz, although it is not explicitly reported.

Parameter	PD (CW operation)
Frequency range (THz)	Up to 350 GHz[164]
Coherent/Incoherent	Incoherent[163]
Minimum size (range)	Planar, antenna coupled[164]
NEP (W/(Hz)$^{1/2}$)	NA, estimated NEP from reported noise values $\leq 4.7 \cdot 10^{-8}$ [164]
Frequency bandwidth (Hz)	NA.
Cooling	RT[164]

Table II5 Performance summary of CW THz direct detection based on PDs

Some of the first results of EO mixing in a PD are from late 90´s[258]. All them use the M signal for modulating the bias of the photodiode, thus producing a mixing between the M signal and the optical LO that enters the PD. In the following years, basically three groups reported this bias-modulation scheme in a PD at higher frequencies (up to 10 GHz) [249,250,257,259].

The use of this scheme with M signals in the THz region was firstly reported in 2010, using a UTC-PD in a homodyne receiver up to 420 GHz[164]. After that, extensive work of Rouvalis, Seeds and coworkers on this topic has been also reported, in this case using a TW-UTC-PD[171,172] in heterodyne detection at 100 GHz with IF signals in the order of 50 kHz.

Parameter	PD (CW operation)
Frequency range (THz)	Demonstrated up to 420 GHz (homodyne detection)[164], and 110 GHz (heterodyne detection)(Chapter IV)
Coherent/Incoherent	Coherent[211]
Minimum size (range)	Planar, antenna coupled[138]
NEP (W/(Hz)$^{1/2}$)	NA, estimated NEP $\leq 4.7 \cdot 10^{-8}$ [164,172]
Frequency bandwidth (Hz)	Around 1 MHz (Chapter IV)
Conversion losses (dB)	32 dB[172]

Noise temperature	N/A
Cooling	RT[211]

Table II6 Performance summary of CW THz heterodyne detection based on PDs

4

Conclusions

In this chapter, the fundamentals of CW THz generation using optical downconversion systems based on DFG have been presented. Moreover, two main DFG architectures have been analyzed with more details: two single mode semiconductor lasers, and multimode optical source (OFCG) with optical mode selection stage. The work of this thesis focuses in the latter DFG architecture, thus it has been discussed with further details, including OFCG fundamentals and generation, OFCG expansion techniques and different strategies to select the required optical modes. The characteristics of the available photodetectors for DFG generation (PCs and PDs) have been also presented, along with the current state of the art for both kinds of photodetectors.

The use of photomixers (PCs and PDs) for detection has been analyzed; both in direct detection and EO heterodyne detection schemes. The principles of detection operation for each particular kind of photomixer have been discussed. Finally, the current state of the art for both photomixers operating as receivers has been summarized.

III

New architectures for photonic synthesis of low phase noise mm-Wave, sub-THz and THz Continuous Wave signals using multimode optical sources

1

Introduction

This third chapter of the thesis introduces the actual author´s contributions to the development of sub-THz photonic generation architectures based on Difference Frequency Generation (DFG). This chapter presents an overview of the work developed. Further details are given in the corresponding publications included in chapter VI.

Chapters I and II have already introduced that the sub-THz generation technology to be used in this thesis is Difference Frequency Generation (DFG). A DFG architecture is based on a DFG source and a photodetector. Specifically, we will focus on DFG schemes based on Optical Frequency Comb Generators (OFCG, multimode sources) and optical mode selection (section II.2.4).

Two DFG photonic architectures based on multimode optical sources and optical mode selection have been proposed, implemented and studied. The first one, presented in section 2 of this chapter, uses Passively Mode Locked Laser Diodes (PMLLDs) as OFCG, high selective optical filtering as optical selection strategy and a commercial 50 GHz bandwidth Photodiode (PD). The second one, which is discussed in section 3, employs a Gain Switching (GS) based OFCG along with an OFCG span expansion stage, Optical Injection Locking for the required optical modes selection and a n-i-pn-i-p superlattice THz photomixer for sub-THz generation.

2

mm-wave and sub-THz Continuous Wave generation using Passively Mode Locking Laser Diodes

2.1 Passively Mode Locking Laser Diodes for Difference Frequency Generation

The first DFG architecture proposed during this work explores the use of different kinds of PMLLDs as multimode sources for sub-THz generation.

Two different PMLDDs designs are employed for the work covered in this chapter. First, a PMLLD with a Fabry-Perot cavity is used (Figure 39a). We have three available samples of this design, developed in the framework of the Epixnet Network of Excellence. After the complete characterization of each one and its comparison (see *Appendix VI. Laser Characterization Platform)*, we select the one with best performance for our purposes.The second design is based on a ring cavity (Figure 39b) developed at COBRA, Technische Universiteit Eindhoven. A chip containing eight modifications on the main design is available. As with the previous design, all these devices are characterized prior to the selection of the best one to work with.

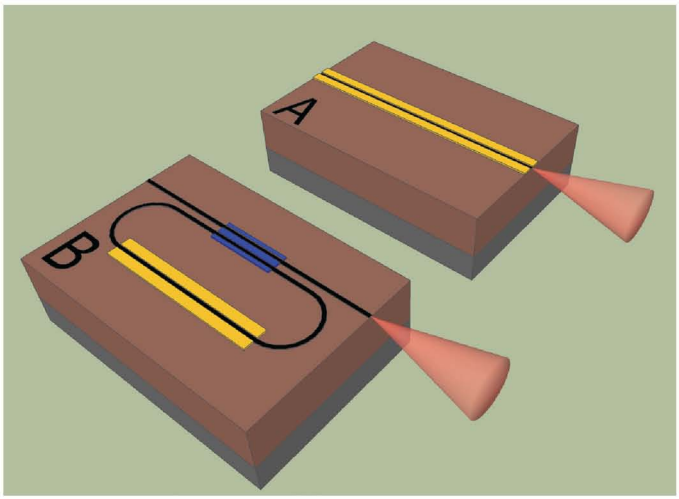

Figure 39 Schematic view of a Fabry-Perot laser cavity (A), and ring laser cavity (B). Yellow: gain regions and saturable absorber; blue: multimode interference (MMI) coupler[228]

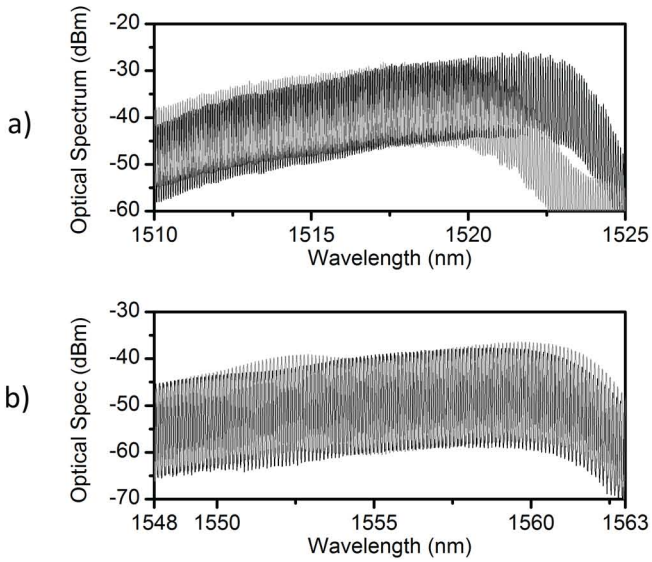

Figure 40 Optical span of the OFCGs under two different operation conditions: a) Fabry-Perot cavity; b)ring cavity[228]

The maximum optical power provided by the FP and ring cavity PMLLDs is 2 mW and 0.15 mW, respectively. These FP and ring cavity PMLLDs have a measured temporal pulse width of about 6 and 9 ps, respectively. Neither linear compression (i.e. chirping compensation) nor nonlinear compression stages (i.e. optical span expansion) are incorporated to improve the optical span of

the multimode source. The optical span that these devices are able to provide with is about 0.8 and 1.2 THz, respectively. The optical spectra for both devices under two different operation conditions are shown in Figure 40. The operation conditions correspond to the selected as optimum voltage-current (V-I) point for overall device performance (black traces) and to the V-I point where the optical span is maximum (grey traces).

As all Passive Mode-Locking (PML) lasers, the repetition frequency of these devices is fixed by the cavity length and cannot be tuned. Furthermore, and as a reminder, these PMLLDs work under DC bias, and they are not locked to an external RF reference, as it is the case for Active Mode-Locking (AML) lasers. The OFCG based on a Fabry-Perot cavity has frequency spacing between modes (i.e. repetition frequency) of 10 GHz, while the one based on a ring cavity features a repetition frequency of 15 GHz. These mode spacing values are shown in the optical spectra of Figure 40.

2.2 Description of DFG experimental setup

The experimental setup is shown in Figure 42, where the main blocks (i.e. DFG scheme and photomixer) are itemized. The different PMLLDs used as multimode source (OFCG) are placed in the probe station (Figure 41). After amplification with an Erbium Doped Fiber Amplifier (EDFA1), the optical signal containing the OFCG enters the optical mode selection stage, where it is divided into two branches (C2). Each branch has a Fabry Perot Tunable Filters (FPTF1 and FPTF2) to select one of the two required optical frequencies typical for DFG sources. Both branches are coupled again (C3). This spectrum is eventually amplified and pass-band filtered (to remove Amplified Spontaneous Emission (ASE) noise of the amplification stages) before delivering it to the photomixer (50 GHz bandwidth PD). As previously mentioned, no optical span extension stages are employed for these studies.

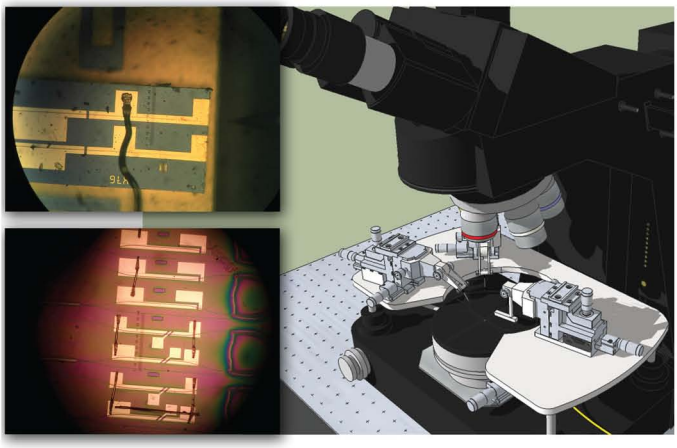

Figure 41 Pictures of the chips containing the two employed PMLLDs. Fabry-Perot cavity (top) and ring cavity (bottom)[228]

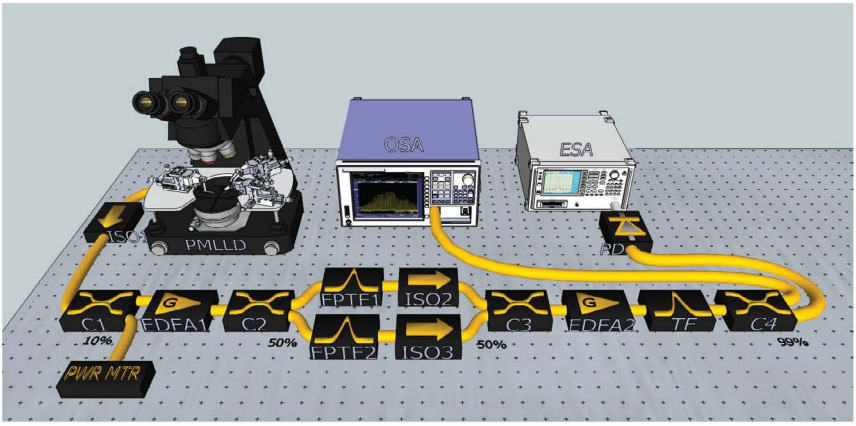

Figure 42 Experimental setup used in the work presented in this section[190,228,233]. PMLLD: Passively Mode-Locked Laser Diode; C: optical coupler; PWR MTR: power meter; EDFA: Erbium Doped Fiber Amplifier; FPTF: Fabry-Perot Tunable Filter; ISO: optical isolator; TF: tunable band pass optical filter; OSA: Optical Spectrum Analyzer; ESA: Electrical Spectrum Analyzer[190]

Besides the characteristics of the multimode source (i.e. PMLLD) the optical mode selection stage is the core of the DFG architecture. The employed filters are high-selective FTPFs featuring a Finesse parameter of 3000. This is translated to the optical domain (at 1550 nm) to a 3-dB bandwidth of around 6 GHz. Due to this high Finesse, the required DC voltage control must have high resolution (below 1 mV) and stability. Two examples of the optical spectra at the output of the optical mode selection stage are shown in Figure 43, where the two selected optical modes of each spectrum can be seen. These optical signals to be delivered to the photomixer have a frequency spacing between the two selected

modes of 60 GHz (solid trace) and 90 GHz (dashed trace). Traces corresponding to both FP (black trace) and ring cavity (grey trace) PMLLDs are represented.

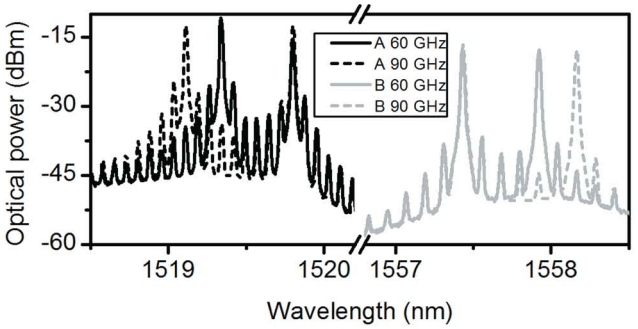

Figure 43 Optical selection stage output for both OFCGs: a) Fabry-Perot cavity, repetition frequency is 10 GHz; b)ring cavity, repetition frequency is 15 GHz[228]

Thus, the tunability of this DFG source, then of the generated sub-THz signal, is controlled by the optical mode selection stage. This tunability is discrete, with a resolution equal to the repetition frequency of the OFCG (10 and 15 GHz for the FP and ring cavity PMLLDs, respectively).

Finally, the photomixer used was a COTS 50 GHz bandwidth TW-PD. Due to its RC roll-off, it has been possible to use it for sub-THz generation up to 140 GHz. However, the losses above 100 GHz have significantly limited the dynamic range of the measurements obtained using this setup[190].

2.3 Results

An example of the sub-THz signals generated with this DFG architecture can be seen in Figure 44. In this case, the PMLLD based on a Fabry-Perot cavity is employed. This figure shows the optical spectra containing the two selected optical frequencies delivered to the photomixer (Figure 44, left) for different frequency spacing values between 20 and 120 GHz. In the same figure, the sub-THz signals at the output of the photomixer that are generated with these optical spectra (Figure 44, right) are also shown. These results are fully discussed in Criado et al. Observation of phase noise reduction in photonically synthesized sub-THz signals using a passively mode-locked laser diode and highly selective optical filtering. *Optics Express* **20(2),** 1253–1260 (2012)[190].

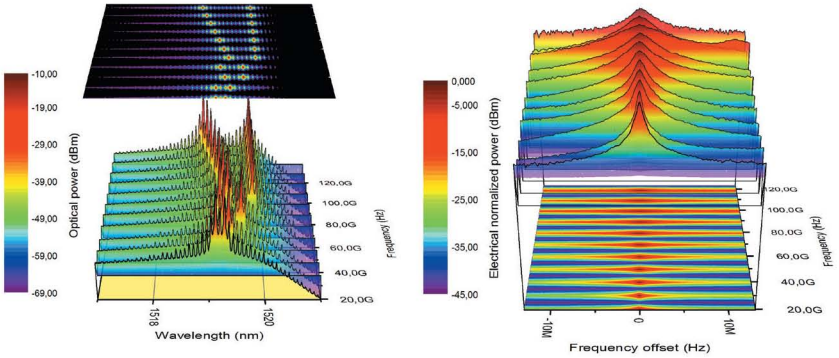

Figure 44 DFG generation using a FP PMLLD up to 120 GHz. Optical spectra (left) and corresponding sub-THz signals (right)[190]

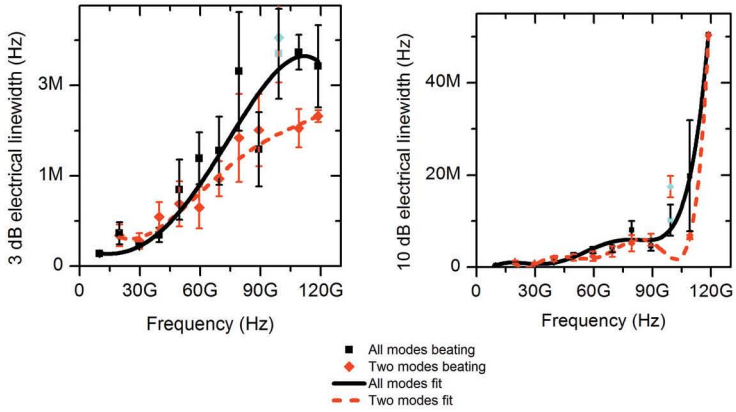

Figure 45 Comparison between all-modes-beating (direct harmonic generation) and two-mode-beating of the 3-dB linewidth (left) and the 10-dB linewidth (right)[190]

As mentioned before, one of the main objectives of this thesis is to achieve a high quality (low phase noise) performance. For this reason, this is for us a main figure of merit (phase noise) that has to be studied. The phase noise performance exhibited by these sub-THz signals, based on the evaluation of the 3-dB and 10-dB spectral FWHM, is analyzed for the synthesized signals taking as a reference the electrical signals obtained with direct harmonic generation. Direct harmonic generation consists on the photomixing of all the optical modes from the OFCG (not only two). No significant differences are observed below 50 GHz, but from this frequency onwards, it can be appreciated in Figure 45 a linewidth reduction trend that becomes greater as the frequency increases, reaching reductions of 35% at 110 GHz and 25% at 120 GHz. These results suggest that the approach selecting the two required modes provides a phase noise (thus FWHM) reduction in the sub-THz generated signal when compared to direct harmonic generation. This result is discussed in detail in the publication: Criado et al. Observation of phase noise reduction in photonically synthesized sub-THz signals using a

passively mode-locked laser diode and highly selective optical filtering. *Optics Express* **20(2),** 1253–1260 (2012)[190].

Furthermore, an exhaustive comparison of the two PMLLDs designs previously cited (Fabry-Perot and ring cavities) as DFG sources is carried out in Criado et al. Comparison of Monolithic Optical Frequency Comb Generators based on Passively Mode-Locked Lasers for Continuous Wave mm-Wave and sub-THz generation. *Journal of Lightwave Technology* **30(19),** 3133-3141 (2012)[228]. They are analyzed and evaluated both as OFCG (see Figure 46) and for the OFCG application of sub-THz generation using our photonic synthesis DFG architecture (Figure 47). Figure 46 shows part of the characterization accomplished to compare both integrated OFCGs and includes the voltage-current mapping of several figures of merit, namely, optical power, central wavelength, optical FWHM, first harmonic electrical power, repetition frequency and electrical FWHM (first harmonic).

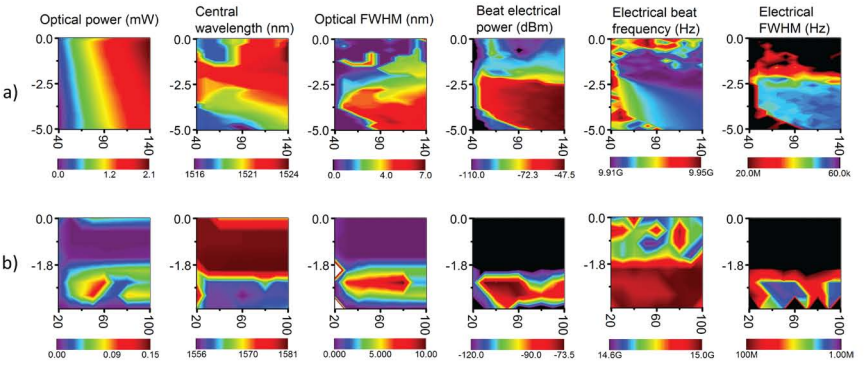

Figure 46 Detail of the characterization as OFCG of the employed PMLLDs: a) Fabry-Perot cavity; b) ring cavity[228]

The sub-THz signals generated using both PMLLDs, with the optical signals shown in Figure 43, can be seen below in Figure 47. The output power at 90 GHz is around -35 dBm for the FP PMLLD and -65 dBm for the PMLLD based on a ring cavity, using optical amplification as shown in Figure 42 to deliver around 10 dBm of optical power to the PD. The FWHM values for the signal at 90 GHz generated by the FP and ring-cavity based DFG sources are around 2 and 32 MHz, respectively. The FWHM values experiment a degradation as the frequency increases, due to the absence of an external reference in the OFCG, what it is explained with detail in the selected publications included in this thesis: Acedo et al. Photonic synthesis of continuous-wave millimeter-wave signals using a passively mode-locked laser diode and selective optical filtering. *Microwave and Optical Technology Letters* **54(6),** 1416–1419 (2012)[233], Criado et al. Observation of phase noise reduction in photonically synthesized sub-THz signals using a passively mode-locked laser diode and highly selective optical filtering. *Optics Express* **20(2),** 1253–1260 (2012)[190] and Criado et al. Comparison of Monolithic Optical Frequency Comb Generators based on Passively Mode-Locked Lasers

for Continuous Wave mm-Wave and sub-THz generation. *Journal of Lightwave Technology* **30(19),** 3133-3141 (2012)[228].

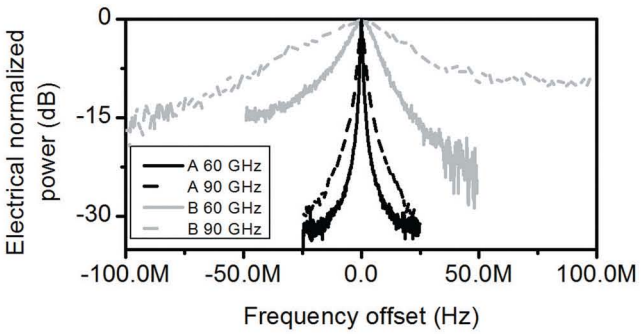

Figure 47 Generated sub-THz signals (60 and 90 GHz) after photomixing the spectra of Figure 43: a) Fabry-Perot cavity; b) ring cavity[228]

In conclusion, the proposed DFG generation architecture along with the use of the PMLLDs described above has allowed us to:

- Validate the proposed DFG architecture and to demonstrate sub-THz generation with this scheme.
- Evaluate the phase noise of the sub-THz signals photonically synthesized with this DFG architecture. It has been demonstrated a phase noise reduction with this scheme when compared to direct harmonic generation (photomixing all the modes of the OFCG).
- Develop a platform to perform systematic characterizations and to deeply compare integrated OFCGs, both as generic OFCGs and for their application in DFG architectures.

3

mm-wave and sub-THz Continuous Wave ultra-low phase noise photonic generation using a Gain Switching based Optical Frequency Comb Generator and n-i-pn-i-p superlattice photomixers

3.1 Gain Switching techniques for Difference Frequency Generation

The DFG architecture in which the work of section III.2 is based on has already been validated. The next step is to improve the devices that encompass this architecture (i.e. multimode source, optical selection stage and photomixer), in order to achieve a low phase noise photonic sub-THz generator with optimum performance using this DFG architecture.

The PMLDDs used for the first DFG architecture previously presented in this chapter provide with potentially integrated OFCGs for DFG architectures. However, they present several disadvantages, namely, lack of tunability of the repetition frequency (thus the tunability of the sub-THz signal is limited to discrete steps equal to the repetition frequency), low optical output power (that in turns reduce the integration potential as external optical amplifiers are needed) and a phase noise performance worse than electronic approaches.

We focus then on an OFCG design that would be able to solve these issues. Traditional fiber based OFCGs could have been the solution, but they are bulky and expensive. The expertise of our group in Gain Switching techniques, along with the work on OFCGs of the group of Anandarajah[240] give us the key to the design of a compact, tunable and cost-effective OFCG based on COTS components: the Gain Switched OFCG (GS-OFCG).

In chapter II, it was introduced that an optical pulsed source can be seen as an OFCG. Among the strategies used to directly generate an OFCG, we described Gain Switching (GS) as a technique that is able to provide with a pulsed optical output using any Commercial Off-The-Shelf (COTS) semiconductor laser. The semiconductor laser is forced to enter and to exit from stimulated operation in each period by the use of an external pulsed modulation, producing temporal pulses narrower than the modulation introduced to the laser. It was also described how this pulsed modulation can be replaced by a large signal sine modulation (use of a RF reference).

Thus, the GS approach permits a wide tunability range of the repetition frequency, given by the external RF reference, which also forces a high coherence between optical modes (see discussion in chapter II). Furthermore, the use of COTS lasers allows having an OFCG with higher optical power, as they use to provide with higher output power than MLLDs. Therefore, the identified issues of PMLLDs can be overcome with the use of a GS based OFCG. Nevertheless, GS sources feature wider temporal pulses than their ML counterparts that translate in narrower optical spans. For this reason, the GS based OFCGs require additional optical span expansion stages using the techniques presented in chapter II.

Concerning the other two main parts of the DFG architecture, it will be shown in this chapter how they have been optimized by the use of Optical Injection Locking (OIL) as optical selection stage; and by the availability of a high performance THz photomixer: the n-i-pn-i-p superlattice photomixer.

3.2 Description of DFG experimental setup

The DFG architecture developed in this section is schematically presented in Figure 48, where the three main parts of the scheme are shown: GS-OFCG, optical mode selection stage and photomixer (n-i-pn-i-p). In this figure, also the DFG process in the frequency domain is depicted.

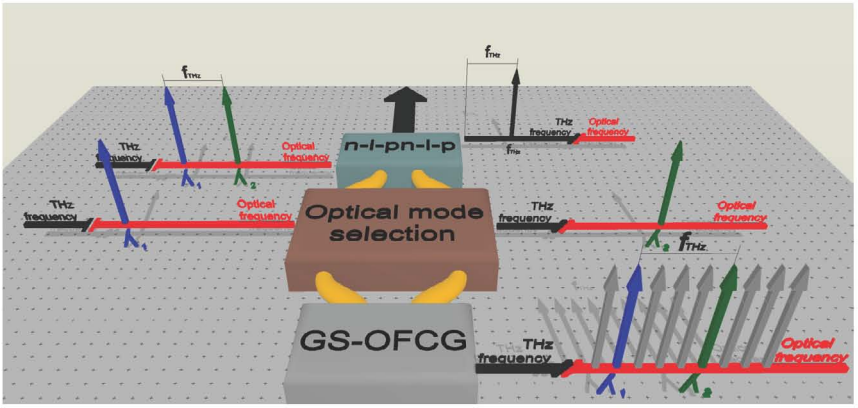

Figure 48 A schematic view of how the frequencies are generated and processed through the setup[132,135]

The experimental arrangement of this GS-OFCG (block named as GS-OFCG in Figure 48) is detailed below in Figure 49.

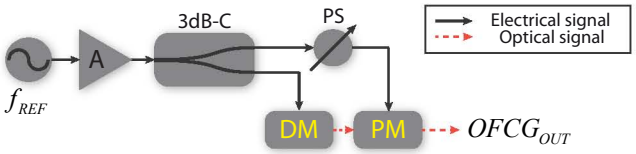

Figure 49 GS-OFCG basic scheme. A: electrical amplifier; 3dB-C: 3-dB coupler; DM: Discrete Mode Laser; PS: electrical phase shifter; PM: optical phase modulator (optical span expansion stage)[132]

The employed laser is a Discrete Mode (DM) laser, which was already introduced in chapter II. DM lasers are Fabry-Perot semiconductor lasers that achieve single-mode emission by the introduction of a small number of etched features distributed along the ridge waveguide. They are low cost devices and their structure allow them to offer very narrow optical FWHM (below 100 kHz) and high Side Mode Suppression Ratio (SMSR) values[260].

The GS-OFCG (Figure 49) has a wide tuning range of the repetition frequency, around 6-12 GHz in our design, but potentially scalable to about 4-18 GHz. As previously commented, a drawback of this approach is that the optical span provided by the laser under GS is not very high (around 80 GHz, see Figure 50, center trace). For this reason, an optical span expansion stage is employed, based only on a single Electro-Optical (EO) Phase Modulator (PM). The provided optical spectra at different points of the setup depicted in Figure 49 are shown in Figure 50. From bottom to top: DM laser output without modulation, DM laser under GS regime and DM laser under GS regime and span expansion stage.

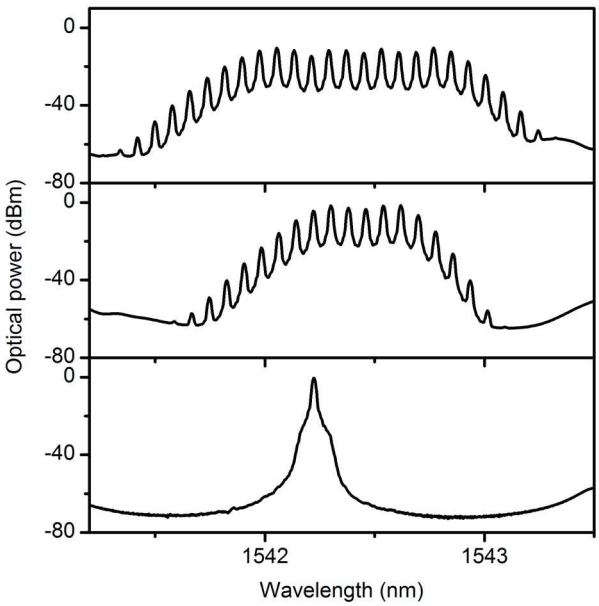

Figure 50 Optical spectra of the GS-OFCG. Bottom trace: DM laser without modulation; center trace: DM laser under GS regime; top trace: OFCG output[213]

The maximum optical span provided by this GS-OFCG is determined by several parameters, being the modulation power one of the most important. The evolution of the optical span with the modulation power can be seen in Figure 51, where about 230 GHz of optical span is achieved for a modulation power of 32 dBm. Further optical span expansion can be straightforwardly obtained using the techniques described in chapter II.

Regarding the optical mode selection stage, selective filtering using FPTFs provided us with good results in the scheme described in previous sections in the sense that they do not add phase noise to the generated sub-THz system and they offer an efficient use of the maximum average input power to the photomixer (more details in Criado *et al.*[190]). Nevertheless, the resolution and stability of the voltage control results in a poor long term stability[213]. Moreover, additional optical amplification is needed due to the insertion losses of the filters and to provide higher optical power to the photomixer. The solution for the first issue could be a complex feedback loop that would require extremely precise electronics given the low voltage values needed to tune the FPTFs. The second issue has a hard solution at a first glance.

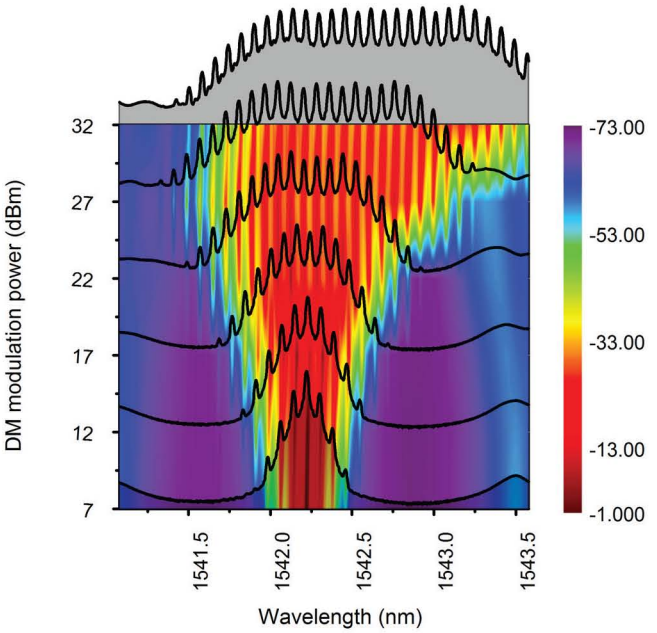

Figure 51 OFCG optical spectra (Z axis: optical power (dBm)). Evolution with the modulation power (GS and EO PM)[213]

In this sense, we decide to explore Optical Injection Locking (OIL) as a technique that could be used to accomplish a "clean" filtering of the optical modes, thus the optical mode selection stage. Theoretically, OIL would allow for filtering and amplification in the same process, a higher SMSR, and especially higher stability. The comparison between the performances provided by these two optical mode selection techniques is represented in Figure 52, where it is shown how OIL provides better SMSR (thus better SNR) and optical mode power.

A final improvement of this setup from the previously used DFG architecture with PMLLDs is the use of a new photomixer. A high performance THz photomixer would arrive under the collaboration we started with G. H. Döhler (Max Planck Institute for the Science of Light, Erlangen, Germany), S. Malzer and S. Preu (Friedrich-Alexander-Universität Erlangen-Nürnberg, Erlangen, Germany). This photomixer, a n-i-pn-i-p superlattice photomixer, has an operation bandwidth in excess of 1 THz, but what it is more important, it is able to provide independent optimization of both transit and RC roll-offs, thus overcoming the trade-off usually present in most high-bandwidth PDs[115]. Figure 53 shows both the GS-OFCG (bottom-left) and the n-i-pn-i-p superlattice photomixer (packaged version, top right).

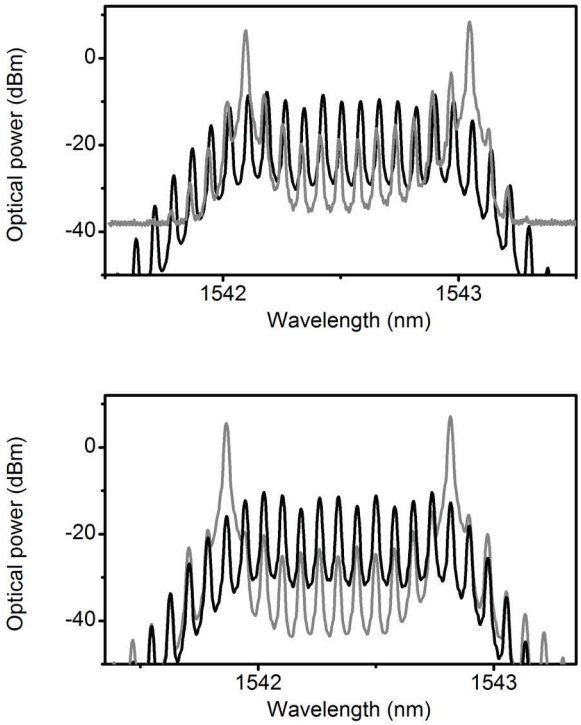

Figure 52 Optical mode selection stage output. Based on selective optical filtering using FPTF (top trace), and base on OIL (bottom trace)[213]

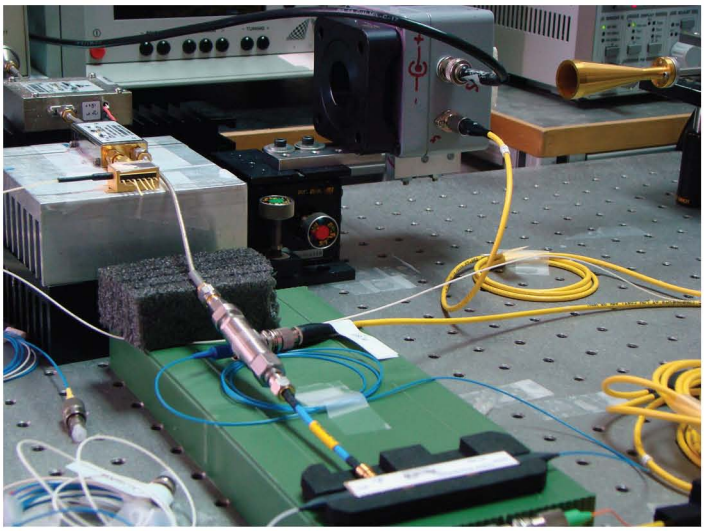

Figure 53 GS-OFCG (bottom-left) and n-i-pn-i-p superlattice photomixer (packaged version) with receiving horn antenna (top-right)

The frequency response for 90-140 GHz and for the whole operation range of the photomixer (inset) are shown in Figure 54.

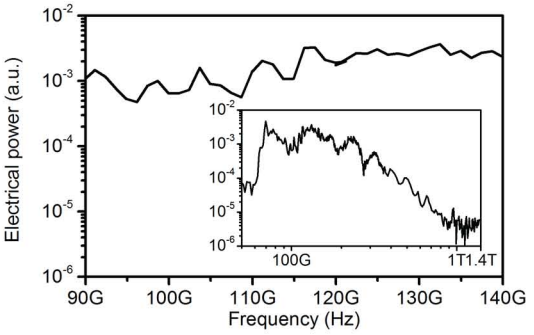

Figure 54 Frequency response and generated photocurrent of the employed n-i-pn-i-p superlattice photomixer (packaged version)[213]

3.3 Results

An example of the signals generated after photomixing the optical spectra in Figure 52 in the n-i-pn-i-p superlattice photomixer is shown in Figure 55. The optical power of the signal generated at 120 GHz is around -55 dBm. It must be noted that in this case, free space propagation without optical system is used, so the expected losses are high[132]. The minimum allowable values for span (2.1 kHz) and Resolution Bandwidth (RBW, 10 Hz) are used. FWHM values below the measurement limits (<10 Hz) are obtained. These results suggest that the achieved coherence between the optical modes of the GS-OFCG is very high, and the phase noise of the sub-THz signal is basically that of the employed RF reference. Further details are included in Criado et al. Ultra narrow linewidth CW sub-THz generation using GS based OFCG and n-i-pn-i-p superlattice photomixers. *Electronics Letters* **48(22),** 1425–1426 (2012)[132].

The tunability of the system is achieved by the combination of two mechanisms. The first one is the optical mode selection that is the only one traditionally used in this kind of DFG architectures and permits a frequency resolution equal to the repetition frequency of the OFCG. This was the tunability mechanism used in the previous work presented in section III.2. The second is the tunability provided by the GS-OFCG over the repetition frequency that allows fine tunability. The joint control of these two parts of the DFG scheme has allowed us to reach to a system with full frequency range coverage with quasi-continuous tunability and excellent linearity. An example of tunability in a narrow range of 1.5 kHz (at 120 GHz) is shown in Figure 56. The coefficient of

determination (R^2) of the data with a linear fit is between 1 and 0.99985 for the different tunability spans, what demonstrates an almost perfect linearity of the frequency tunability.

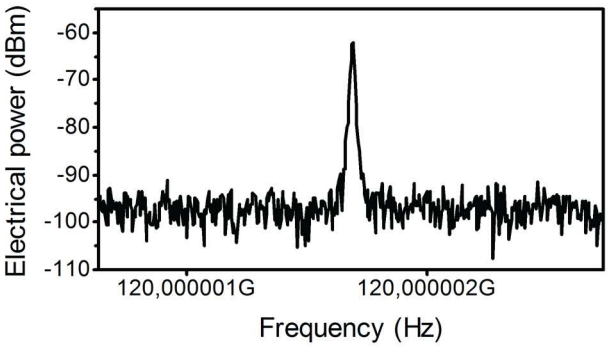

Figure 55 Sub-THz generated signal at 120 GHz. Span = 2.1 kHz, RBW = 10 Hz, sweep time = 63 s[132,213]

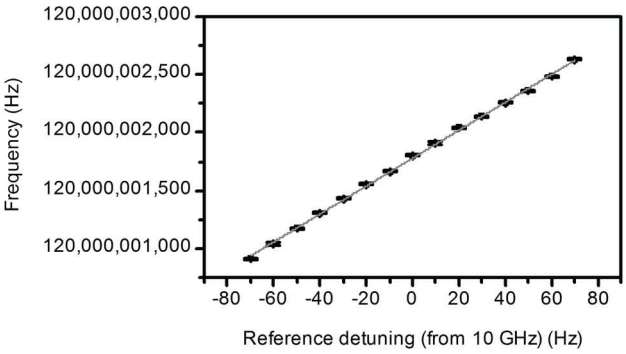

Figure 56 Fine tunability, 120 Hz steps of f_{THz} (f_{REF} = 10 GHz). X axis: detuning of f_{REF}; Y axis: THz output frequency, f_{THz}. Measured data (average values: black dots; standard deviation: black caps); and linear fit (grey trace). Electrical spectra measurement parameters: span = 2.1 kHz, RBW = 30 Hz, sweep time = 7 s[213]

The long-term stability over one hour of the generated signals is shown in Figure 57. The frequency and power deviations are around 5 Hz and 1.5 dB, respectively. As with the FWHM measurements, in this case also the measured values are in the measurement limits of the instrumentation used, thus the actual values could be better. This stability is basically given by the optical selection stage based on OIL[213] and the RF reference. The complete discussion on these results is included in Criado et al.Continuous wave sub-THz photonic generation with ultra-narrow linewidth, ultra-high resolution, full frequency range coverage and high long-term frequency stability. *Under review in IEEE Transactions on Terahertz Science and Technology* (2012)[213]).

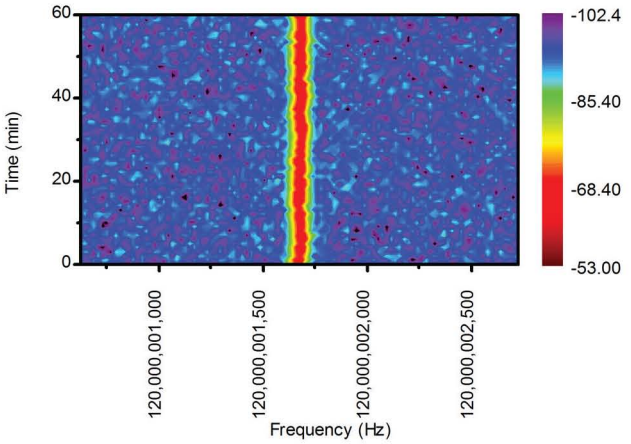

Figure 57 Sub-THz generated signal at 120 GHz. Evolution with time. (Z axis: electrical power (dBm)). Electrical spectra measurement parameters: span = 2.1 kHz, RBW = 30 Hz, sweep time = 7 s[213]

Finally, it is important to highlight the scalability associated to this DFG design. In terms of frequency range, the upper frequency can be readily extended beyond 1 THz with just re-designing the optical span expansion stage with the techniques already discussed in chapter II and in Criado et al.[213]. The lower frequency can be as low as the repetition frequency (a few GHz) if the RF electronics of the GS-OFCG are optimized for a wider bandwidth (e.g. 4-18 GHz). With respect to the frequency resolution, it basically depends on the RF reference resolution and the number of optical modes of separation between the two selected modes. Thus, the use of a state-of-the-art RF reference with 1 mHz of frequency resolution[236] would permit a frequency resolution of the THz signal of 10 mHz at 100 GHz, and 100 mHz at 1 THz. The optical output power of the system can be incremented by using higher power lasers in the OIL stage, thus avoiding the need of optical amplification, which can be also a complementary way of offering higher output power. The advantage of using just OIL for obtaining higher power is that no noise associated to optical amplifiers is added to the system.

The results demonstrated with this optimized DFG architecture for sub-THz and THz CW generation using a GS-OFCG can be summarized in four points:

- Generation of ultra-low phase noise sub-THz signals, with a FWHM below our measurement limits (< 10 Hz).
- Quasi-continuous tunability of the sub-THz signal through the whole frequency range of operation (60-140 GHz), with a frequency resolution of 0.1 Hz at 100 GHz.

- Stability. The system achieves a high long-term power and specially frequency stability, with 1.5 dB and 5 Hz deviations over one hour, respectively, at 120 GHz. These values are also limited by the measurement instrumentation.
- Scalability. The developed system permits a straightforward improvement of frequency range (both lower and upper frequencies), frequency resolution and output power.

IV

New architectures and devices for Heterodyne Electro-Optical detection of microwave, mm-Wave and Sub-THz signals

1

Introduction

The use of photonic heterodyne architectures for detection has been already demonstrated at microwave frequencies, showing the potential of the approach in terms of remote signal distribution and scalability, without sacrificing all the advantages associated to the optical techniques. The potential and functionalities of photonic (Electro-Optical, EO) heterodyne detection are now to be scaled up to THz frequencies, where the remote signal distribution becomes even more important due to the high losses associated to sub-THz and THz signals, both under guided transmission and free space propagation. EO heterodyne detection at sub-THz frequencies has been reported few times, using photoconductors (PCs) and also photodiodes (PDs), as it has been already discussed in both chapters I and II.

In this fourth chapter we describe two different schemes and components for EO heterodyne detection. The first one (section IV.2) is a novel EO heterodyne detector scheme at microwave frequencies that makes use of an Ultra Nonlinear Semiconductor Optical Amplifier (XN-SOA) as EO mixer and a Gain Switching (GS) LO as photonic LO. The second one (section IV.3) presents an EO heterodyne sub-THz receiver comprising a sub-THz mixer and a photonic sub-THz LO. The EO mixer is a new THz detector especially designed for homodyne/heterodyne operation: the np-i-pn quasi ballistic detector. The photonic sub-THz LO is that developed in this thesis and already presented in chapter III.

The contents of this chapter are an overview of the work developed on photonic detection for the sub-THz and THz frequency ranges. Further details can be found in the selected publications and preprints included in chapter VI.

2

Electro-Optical Heterodyne Detection of Microwave signals based on an Ultra Non Linear Electro-Optical receiver

2.1 Semiconductor Optical Amplifiers for Electro-Optical heterodyne detection at microwave frequencies

As it has been highlighted through this document, the use of an EO heterodyne receiver offers several advantages related to the possibility of remote photonic distribution of Local Oscillators (LO) and Intermediate Frequencies (IF). The investigation of EO (photonic) heterodyne receivers in the microwave range is an important field as these EO architectures are potential candidates for the implementation of scalable and flexible solutions for Microwave Photonics heterodyne receivers. Thus, the study and development of their two key components, i.e. photonic LO and EO mixer, is fundamental to attain an optimum performance in these architectures.

In the last years, Semiconductor Optical Amplifiers (SOAs) have been proposed as EO mixers. They are versatile, compact and reliable low cost optical devices. The mixing process using a SOA can be accomplished in all optical or Electro-Optical (EO) configuration. In the EO mixing, which is the one of interest for our work, only one of the electrical signals, the local oscillator (LO) or the radio-frequency (RF), is modulated on an optical carrier. The other electrical

signal modulates the SOA bias voltage. Both downconversion and upconversion have been reported with this EO scheme, considering an electrical LO. Further details on the reported configurations of a SOA for EO mixing can be found in Criado et al.[261].

In the work presented in this section, we present a novel scheme for microwave EO heterodyne detection using an Ultra Nonlinear SOA (XN-SOA) as EO mixer, trying to take advantage of the additional nonlinearities of this device. Furthermore, we also present an optimization of the EO heterodyne receiver performance by the use of a Gain Switched photonic LO instead of a traditional linearly modulated photonic LO.

2.2 Electro-Optical heterodyne receiver experimental setup

The EO heterodyne receiver diagram is shown in Figure 58, where it is also represented the remote distribution by optical fiber of both LO and IF signals. An optical signal containing the LO frequency is mixed in the XN-SOA with an RF frequency, given through the electrical port of the XN-SOA. At the optical output of the mixer, the mixing components appear, being the difference term IF the one of interest. The EO mixing approach in a SOA is not very usual, as most literature only pays attention to the all-optical mixing. For this reason, only a few publications have been reported about this EO heterodyne architecture at microwave frequencies using a SOA as EO mixer (see Criado et al.[261]).

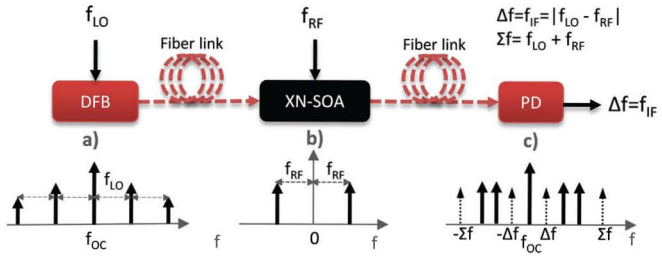

Figure 58 EO mixing concept using an Ultra Non Linear SOA: a)optical output of GS DFB laser; b)electrical signal modulating the XN-SOA bias; c)optical output of the XN-SOA (only sum and difference terms are represented)[261]

The two key devices of the EO architecture can be also identified in Figure 58: photonic LO and EO mixer. The photonic LO encompasses a semiconductor laser, in this case a Distributed Feedback (DFB) laser, and the LO modulation signal (f_{LO}). We evaluate two different photonic LOs. The first one is a linearly modulated DFB, which is the usually employed scheme for photonic LOs.

The second one is a DFB under GS modulation. The comparison of both LO approaches allows us to investigate the effects of the use of a GS based LO in the performance of the overall EO heterodyne receiver when compare to the typical linearly modulated LO. The optical spectra of both photonic LOs for a modulation frequency of 12 GHz are shown in Figure 59.

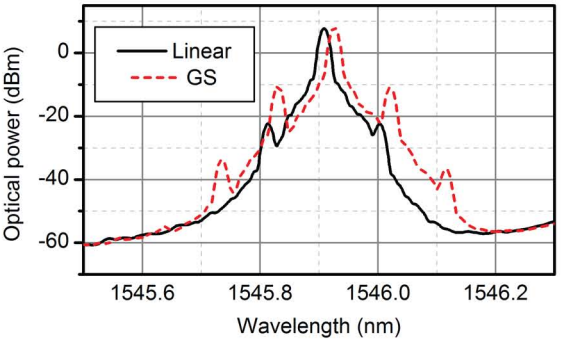

Figure 59 GS and linear photonic LO. Optical spectra of the DFB under linear and GS modulation[262]

As EO mixer, we use a non-conventional SOA, an Ultra Non-Linear SOA (XN-SOA), to try to take advantage of the additional nonlinearities it provides in the mixing process. As it can be seen in Figure 58, the XN-SOA receives the photonic LO at its optical input, while the received RF signal is applied to the bias port of the EO-mixer. As the bias port of the XN-SOA features a SMA 50 Ω input, the RF signal can be directly applied without impedance matching circuits. The resulting IF term is generated at the optical output port of the XN-SOA as a photonic signal that can be distributed to a remote signal processing stage where it is downconverted from the optical to the electrical domain using a high bandwidth photodiode (PD).

2.3 Results

The evaluation of this EO heterodyne receiver is accomplished for frequencies much higher than the 3-dB bandwidth of the two key devices of the architecture (photonic LO and EO mixer), around 2 GHz, and it features an operation bandwidth of 2-15 GHz.

Previous to discuss the results, it is important to define the Conversion Ratio (CR) which is the main figure of merit chosen to evaluate the EO mixer. This parameter can be alternatively expressed as its opposite (in dB units) or inverse value (in natural units), known in this case as Conversion Losses. The

CR receives two different definitions depending on the experimental framework. For EO-mixers at microwave frequencies, it is common to define the CR as the ratio between the electrical power of the downconverted signal at f_{IF} (output of the photodiode) and the electrical power of the RF signal present after mixing at f_{RF} (output of the photodiode)[263]. For electronic mixers and also for EO-mixers at sub-THz frequencies, the typical definition of CR is mostly employed, which is computed as the ratio of the power of the IF signal at the output of the mixer (f_{IF}) to the power of the RF (or Measurement signal, M) signal at the input of the mixer[264]. According to this, we use the first definition in the results presented in this section, and the second definition in the following section of this chapter (section 3) where an EO heterodyne receiver at sub-THz frequencies is introduced.

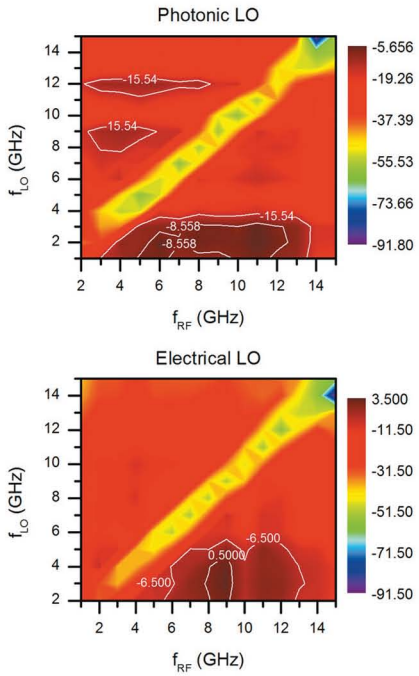

Figure 60 Down-conversion ratios in dB for the EO mixer based on XN-SOA. Contour lines represent 3dB and 10dB bandwidth[261]

The CR map of the XN-SOA used as EO mixer in the experimental setup of Figure 58 is shown in Figure 60. A GS based photonic LO is employed to evaluate the mixer performance. In this Figure 60 it can be seen that the operation frequency range of both the RF and the LO signals is as wide as 2-15 GHz. Maximum CRs of around -8 dB are obtained. The optimum regions are those where the photonic LO shows a better modulation response: below its bandwidth (around 2 GHz), and for a modulation frequency of 12 GHz (transmission line adapted for this frequency value). It can be seen how for IF signals below 2 GHz the performance dramatically decreases, mainly due to the frequency response

of the RF Low Noise Amplifier (LNA) at the output of the PD (2-40 GHz). These results are included in the publication Criado et al. Characterization of Ultra-Nonlinear SOA in a Heterodyne Detector Configuration With Remote Photonic Local Oscillator Distribution. *IEEE Photonics Technology Letters* **24(13),** 1136–1138 (2012)[261]).

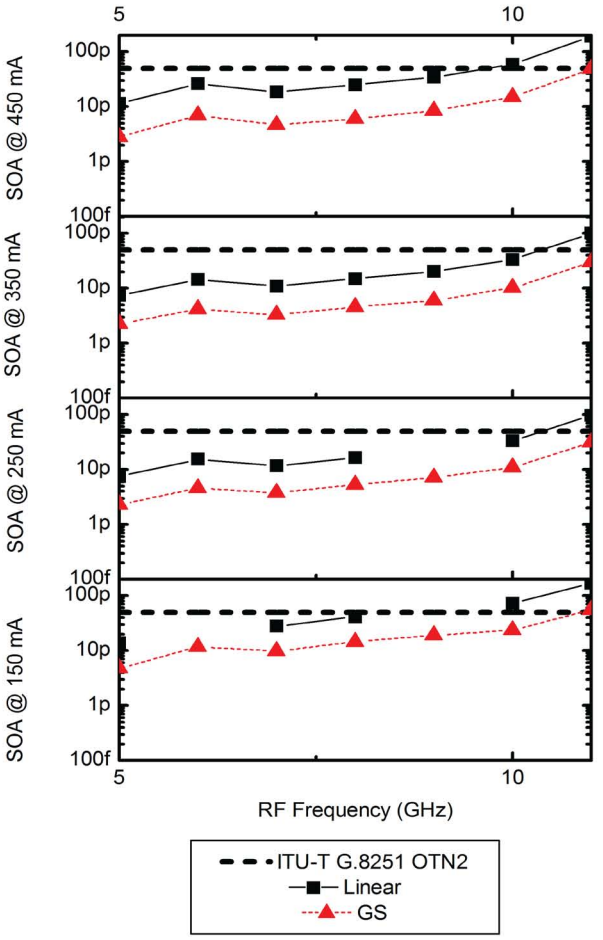

Figure 61 RMS jitter (s) integrated over the band 20 kHz-80 MHz (OTN2 protocol) for both linear and GS LO under different bias point of the Ultra Non Linear SOA[262]

As mentioned before, different photonic LOs are used in this EO scheme. In order to compare performance, the figures of merit that are selected are the following ones: CR (already described above), linearity and phase noise. The linearity is referred to the change of the IF power when the RF power is changed. The phase noise, in this case, is evaluated through the root mean square

(RMS) integrated jitter in a wide frequency range (20 kHz-80MHz). This is made because one of the objectives of this work is to identify if the additional nonlinearities of the proposed devices (GS and XN-SOA) degrade the noise performance, and this is better represented by integrating a wide frequency range of the noise spectrum rather than just evaluate the FWHM (very narrow range of the noise spectrum). For this analysis, the LO frequency is fixed at 12 GHz. This comparison is included in Dios et al. Enhancing the Performance of Electro-Optical Heterodyne Receivers using Gain Switched Photonic Local Oscillators. *Journal of Lightwave Technology,* **31(8),** 1331-1336 , (2013)[262]).

The results conclude that the overall performance (CR and phase noise) is greatly improved when using a GS LO instead of a traditionally modulated LO, although the linearity of the receiver is the same for both LO devices. As an example of these results, in Figure 61 it is represented the noise performance comparison through the RMS integrated jitter for several working conditions (RF frequency and bias current of the XN-SOA), showing how this parameter is improved using GS-LO versus linear LO.

After the complete evaluation of this EO heterodyne receiver (both architecture and devices), we moved forward to validate its performance in real applications. For this reason, an imaging array configuration using this EO heterodyne receiver as pixel element is carried out under collaboration with the Radiofrequency Group of Universidad Carlos III de Madrid. It provides with a flexible and scalable solution for systems requiring a remote distribution of both LO and IF signals. Moreover, the system offers robustness, EMI immunity and cost efficiency due to the low number of components that the receiver encompasses under the proposed architecture.

Basic imaging results are accomplished and presented for a 1x3 array. Figure 62 shows the experimental arrangement of the 1x3 array, which was firstly designed for 9 elements. The employed antennas are Linear Tapered Slot Antipodal Antennas (LTSA) with an operation frequency range of 7-20 GHz and a gain of 9-10 dB. Additional details on this imaging array can be found in the corresponding publication (Criado et al. Photonic Heterodyne Pixel for Imaging Arrays at Microwave and MM-Wave Frequencies. *Advances in Optical Technologies* **2012,** 1–7 (2012)[265]).

Figure 62 Implemented 3x3 array. Linear Tapered Slot Antipodal Antennas (LTSA)[265]

Figure 63 and Figure 64 represents the employed target and the imaging results, respectively. The simple cross used as target is approximately recovered using this array, as depicted in Figure 64. It can be seen how the recovered image is blurred, what is explained because of the spatial resolution of the system (the spot size is around 10 cm of diameter).

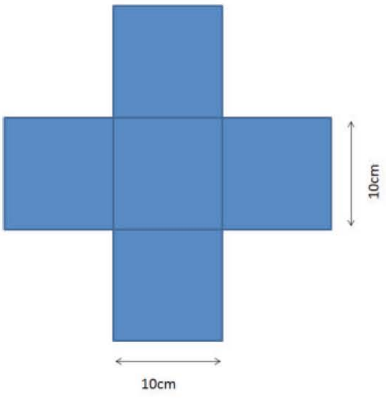

Figure 63 Target for imaging experiment[265]

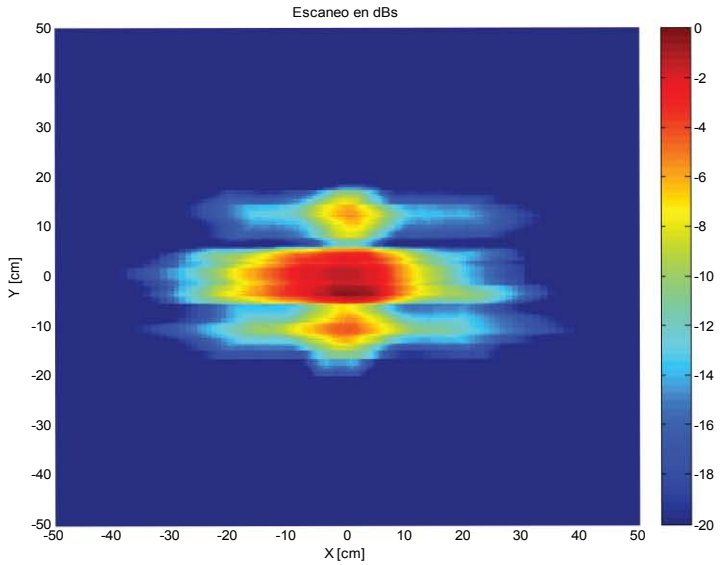

Figure 64 Imaging results with the target of Figure 63 using EO heterodyne receiver pixel based on XN-SOA mixer[265]

The presented results related to this EO heterodyne receiver at microwave frequencies (both architecture and devices) can be summarized in the following points:

- The EO mixer based on a XN-SOA works properly over a wide frequency range (2-15 GHz).
- A comparison between linear photonic LO and GS-based photonic LO is accomplished, showing a significant performance enhancement using the latter.
- The EO heterodyne receiver is demonstrated to be a potential pixel element for array applications. The use of the receiver in an imaging array is demonstrated.

3

Electro-Optical Heterodyne Detection of sub-THz signals with an ultra-low noise photonic sub-THz Local Oscillator and np-i-pn quasi-ballistic THz detectors

3.1 Electro-Optical heterodyne receivers at THz frequencies

As already mentioned, one of the main contributions for the complete development of THz photonic technology would be the development of a heterodyne receiver at sub-THz frequencies under an EO scheme. In order to attain it, two components are needed, a high-quality photonic sub-THz generator (already discussed in chapter III) and a device with working capabilities as EO mixer at sub-THz frequencies.

Both PCs and PDs have been demonstrated to work as THz EO mixers, but both present significant drawbacks for their use for this application. PCs provide with low performance when using optical pumping at 1550 nm (i.e. high dark current), and the conversion efficiency is very low[116] (see Chapter II). On the other hand, the only kind of PDs that have been reported to work as EO mixer are Uni Travelling Carrier (UTC) PDs, both with[172] and without[164] Travelling Wave (TW) structure. However, the physical mechanism behind their operation as mixers is not clear, and the Conversion Ratio (CR) is still low (-32 dB), although higher than in PCs[172].

Thus, the development of a new sub-THz photomixer featuring an improved EO mixing operation is needed. The target is to surpass the very low conversion ratios currently associated to EO heterodyne receivers in the sub-THz range, while keeping all the advantages of EO receivers schemes. During the last year, the group of G. H. Döhler (Max Planck Institute for the Science of Light, Erlangen, Germany), S. Malzer and S. Preu (Friedrich-Alexander-Universität Erlangen-Nürnberg, Erlangen, Germany) have been working on a new device, the np-i-pn quasi-ballistic THz detector, especially optimized for its use in homodyne/heterodyne detection. It is fabricated in collaboration with the group of A. C. Gossard, University of California Santa Barbara (UCSB). In the framework of the collaboration between both groups, in this section we show the first results of such structures from the first available samples, which have been implemented under an EO heterodyne receiver architecture using our DFG sub-THz generator as photonic LO.

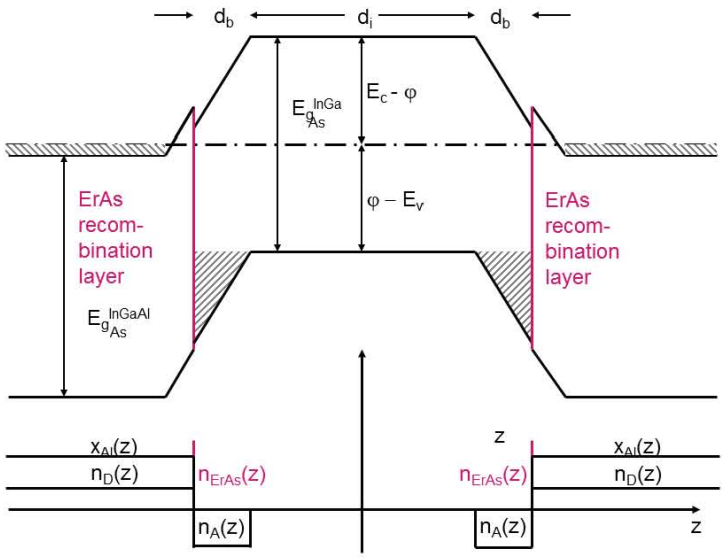

Figure 65 Layer structure diagram of the np-i-pn quasi-ballistic THz detector

3.2 The np-i-pn quasi-ballistic THz detector

The np-i-pn quasi-ballistic THz detector is based on a new design concept

by G. Döhler *et al.* This detector, whose design is specifically made for THz EO heterodyne and homodyne detection, is fabricated from a symmetric n+p+-i-p+n+ In0.53(Ga1-x Alx)0.47As-layer structure that is shown in Figure 65.

We can briefly summarize its key design features as follows:

- The layer thickness and the acceptor density in the p+-layers are chosen such that the Fermi level in the central i-InGaAs is near midgap, resulting in a low dark detector conductance.
- Due to the symmetric design at zero bias the central i-InGaAs layer is field-free. Under illumination the photo-generated electrons escape symmetrically into the n+layers by diffusion on the sub-ps scale.
- The thin barrier resulting from the p-doping in combination with the ErAs layer enables fast tunneling recombination of the photo-generated holes with electrons from the n+-layers on the ns scale. Hence, the photocurrent at zero bias should be zero.
- At low applied voltage the additional drift favors escape of the electrons in field direction, yielding a photocurrent saturating corresponding to the full electron generation rate a few 100 mV. This implies high responsivity up to high frequencies.
- If the optical power and the applied voltage are modulated at THz frequencies f_1 and f_2, respectively, the amplitude of the signal observed at the difference frequency $f_{IF} = f_1 - f_2$ is proportional to the product of the amplitudes of the two signals.

A picture of the first fabricated chip containing the np-i-pn detectors is shown in Figure 66.

All the devices contained in this chip (around 150) are characterized in terms of voltage-current curves (V-I) for three different optical illumination powers: no optical illumination, optical power 1 and optical power 2 (~2 times optical power 1). As an example, the VI curves of one of the devices are shown in Figure 67. It can be seen that the curves are not symmetric (as expected from the design). Moreover, the slope of the curve depends on the optical power that illuminates the device, what shows some similarities of this photomixer with the behavior of PCs under detection (see discussion in chapter II).

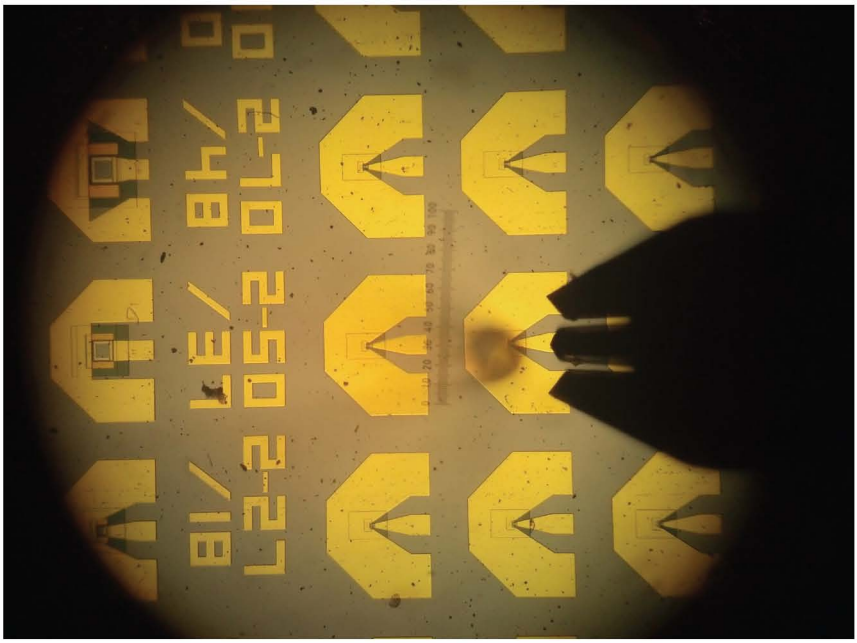

Figure 66 Detail of the chip sample containing several np-i-pn quasi-ballistic detectors. In the picture, a Ground-Signal-Ground (GSG) RF probe and a vertical lightwave probe are placed in one of the devices

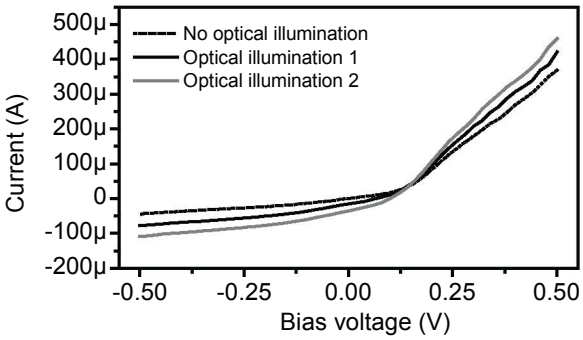

Figure 67 Current-Voltage characterization of np-i-pn quasi ballistic THz detector (ID 111122B_A3-2x)

3.3 Electro-Optical heterodyne receiver experimental setup

The EO heterodyne receiver scheme employed at sub-THz frequencies was already introduced in chapter I (Figure 14), and is reproduced here for clarity purposes in Figure 68. The two key devices of this architecture, as it has been already said, are the photonic LO and the EO mixer. The photonic LO to be used in this EO heterodyne receiver has been developed in this thesis and has been presented in chapter III.

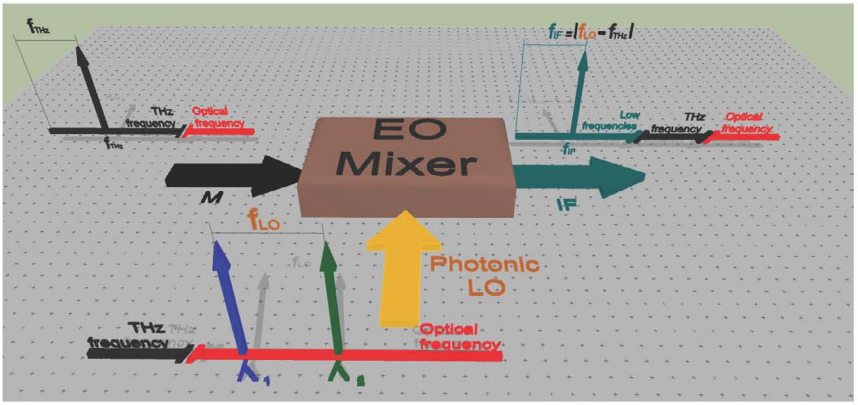

Figure 68 EO heterodyne receiver diagram. LO: photonic Local Oscillator; M: measurement signal; EO Mixer: Electro-Optical Mixer; IF: Intermediate frequency

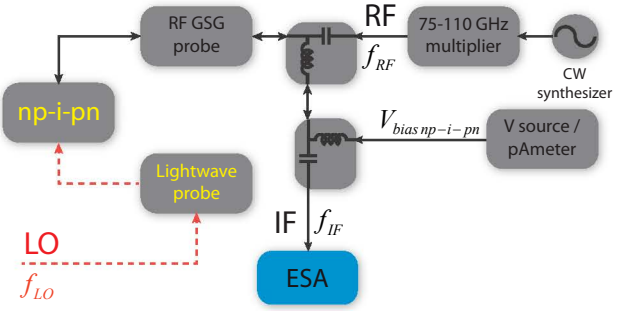

Figure 69 Sub-THz EO heterodyne detection scheme. LO: photonic LO of Fig. 2; Lightwave probe: vertical lensed fiber lightwave probe; np-i-pn: np-i-pn quasi-ballistic THz detector; RF GSG probe: 50 GHz RF GSG probe (125 um pitch); BT1: 75 kHz-40 GHz bias-tee; BT2: 7 kHz-12.5 GHz bias-tee; ESA: electrical spectrum analyzer[173]

In order to evaluate the described the np-i-pn detector as sub-THz EO mixer, the experimental setup of Figure 69 is used. The optical signal from the photonic LO is delivered to the active area of the np-i-pn mixer, which is placed

in a probe station (Figure 70), by the use of lightwave probe. From the picture of Figure 66, it can be noticed that the available np-i-pn devices only have one electronic port that has to be used for three functions: M signal delivering, IF signal retrieval and DC biasing. This is accomplished using the experimental arrangement of Figure 69. A Ground-Signal-Ground (GSG) RF probe is connected to the terminals of the EO mixer. A bias-tee with a lower cutoff frequency of 75 kHz (BT1) diplex the signal into two branches: M (input), and DC (input)-IF (output). Another bias-tee (BT2) is placed in the DC-IF path, in this case with a lower cutoff frequency of 7 kHz. This BT2 permits to separate the DC signal from the IF signal. The M signal is provided by a CW synthesizer (RF synthesizer using mm-wave multipliers above 50 GHz). The voltage is provided by a voltage source/picoammeter. The IF is monitored in an Electrical Spectrum Analyzer (ESA).

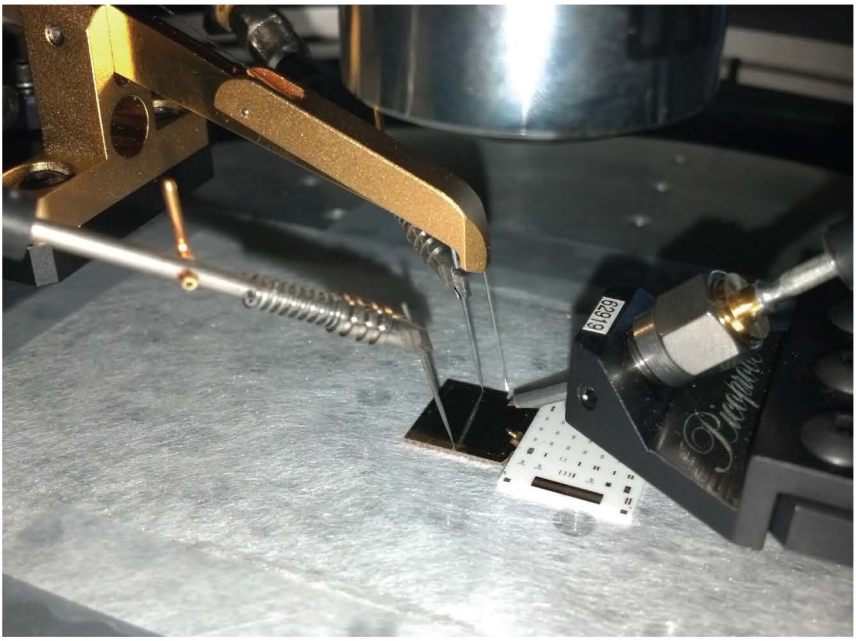

Figure 70 Detail of the experimental setup. Probe station with the sample chip, a calibration chip substrate (white chip), lightwave probe (left) and GSG RF probe (right). Two DC probes are used to fix the chip to the probe station. This setup seen at the microscope is the one shown in Figure 66

The first experiments with this sub-THz EO heterodyne receiver are carried out at 50 GHz, which is the bandwidth of the measurement instrumentation employed (bias-tee, RF probe, coaxial cables). Later experiments at 110 GHz are also accomplished with the same experimental arrangement. In both cases, the losses associated to the paths of IF and M signals are calibrated and corrected.

3.4 Results

After the preliminary characterization of the np-i-pn detectors (see Figure 67), EO heterodyne detection is demonstrated. The main figure of merit employed to evaluate the performance of these devices as EO mixers in the proposed sub-THz EO heterodyne receiver architecture is the Conversion Ratio (CR). It is important to remind the discussion held in section 2 of this chapter, where the different definitions of the CR are explained, and it is clarified that the CR for THz EO mixers follows the traditional definition, i.e. ratio of the IF output power to the M input power to the mixer.

Heterodyne detection is achieved with this detection architecture and devices, although with very low CR (around -75 dB). An example of an IF signal at 5 MHz retrieved when an M signal at 50 GHz is detected is shown in Figure 71. The used span is 2 kHz, and the RBW is the minimum allowed by the ESA (10 Hz). Despite the fact that the mixed signals, photonic LO and RF synthesizer (M), share the same 10 MHz reference, there is still an amount of uncorrelated noise between them that is translated to the IF signal as additional phase noise, as it can be seen in Figure 71. This is explained according to the discussion of chapter II (equation (20)) where it is detailed the relationship between the phase noise of a signal generated by the multiplication of other two signals, and the correlation between the noise of these two.

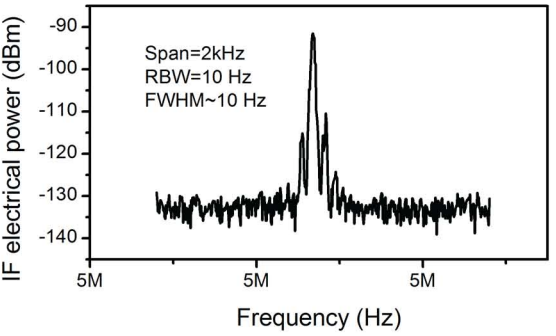

Figure 71 IF detected electrical signal. LO~50 GHz. Span= 2 kHz, RBW=10 Hz, sweep time=60 s[173]

At 50 GHz, the np-i-pn has been evaluated as sub-THz EO mixer in terms of CR as a function of bias voltage and optical LO power, retrieved IF power as a function of bias voltage and M power, linearity in terms of the power of M signal, and generated photocurrent as a function of the optical LO power. Moreover, it has been also tested when only a photonic LO signal is applied to it, working in this case as a photomixer in generation.

As an example, the map representing the CR as a function of both LO optical power and bias voltage of the EO mixer is depicted in Figure 72. This device has not a strong dependence on the bias voltage, but it has with respect to the optical LO power. For the maximum LO optical power (2.4 mW), a maximum CR value of -75 dB is obtained. It can be noticed how the tested device actually works at even zero-bias voltage.

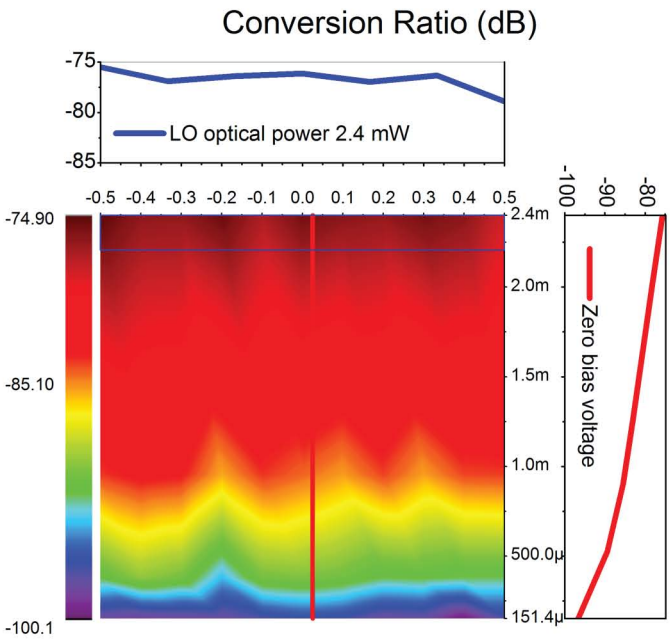

Figure 72 Z-axis: Conversion ratio (dB). X-axis: bias voltage of the np-i-pn (V). Y-axis: LO optical power (W). Top inset: cut of the map at maximum LO optical power (2.4 mW). Right inset: cut of the map at zero bias voltage[173]

The linearity of the sub-THz EO heterodyne receiver as a function of the power of M signal is evaluated at zero bias voltage, as shown in Figure 73. It features an excellent linear performance, with a slope of 1.01 for the average of the measured values. The perfect linear behavior (slope of 1) is within the uncertainty bars of the measurements. A detailed analysis of these results is shown in Criado et al. Zero-bias mm-wave optoelectronic heterodyne detection with np-i-pn THz detector and ultra-narrow linewidth sub-THz photonic Local Oscillator. *Preprint* (2012)[173].

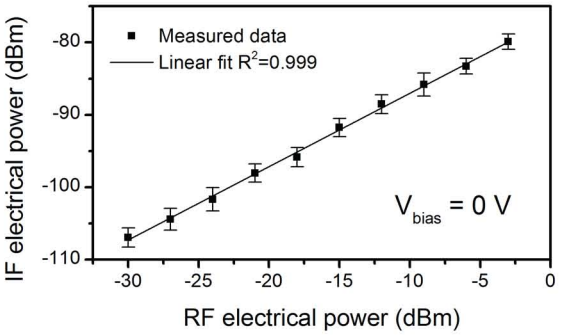

Figure 73 IF electrical power as a function of M electrical power. Uncertainty bars represent random uncertainty of the measurement set. Bias voltage np-i-pn is 0 V. IF electrical power linear fit (slope=1.01 dBm/dBm, R2=0.998)[173]

Also EO heterodyne detection at 110 GHz is obtained, despite the losses due to the bandwidth of the available measurement setup (50 GHz) as high as 42 dB for the path of M signal. In this case a different device contained in the same sample chip is used. The obtained IF signal at 1 MHz, in this case with an M signal at 110 GHz, can be found in the inset of Figure 74. The IF spectrum shown in Figure 74 (inset) corresponds to the average of 55 traces measured with a RBW of 100 Hz. It can be appreciated a slight broadening of the IF signal with respect to the results obtained at 50 GHz (Figure 71). This is directly explained following the argument of the previous paragraph. In this case, the signals to mix are the photonic LO and the M signal, however, in this case the M signal is not provided by an RF synthesizer, but by an mm-wave multiplier that uses as source this RF synthesizer and multiplies it by a factor of 6. Thus, although a 10 MHz reference is shared between the photonic LO and the RF synthesizer, the frequency noise associated to the remaining uncorrelated noise is multiplied by a factor of 6, translated to the IF signal as an increment of the phase noise.

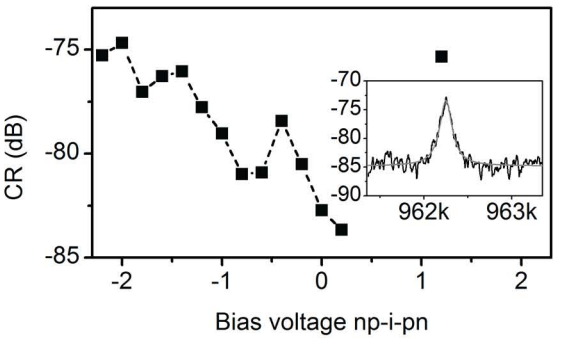

Figure 74 Conversion Ratio of the optoelectronic downconversion as a function of np-i-pn bias voltage. Inset: IF electrical spectrum. RBW:100 Hz, Span: 2 kHz, 55 traces average[175]

For the operation at 110 GHz, the EO receiver performance has been evaluated in terms of the CR, Signal to Noise Ratio and noise floor, all of them as a function of the bias voltage applied to the np-i-pn detector. Figure 74 represents the CR associated to this heterodyne receiver at 110 GHz, using an IF frequency around 1 MHz. The maximum conversion ratio obtained is also around -75 dB for the tested device. The retrieved IF signal is also shown in Figure 74, inset, as previously commented. Furthermore, the noise floor and the SNR as a function of the bias voltage are analyzed. This is shown in Figure 75. It is shown how the tested device has a stronger dependence on the bias voltage than the one tested at 50 GHz. In this case, the CR and SNR have better values at reverse bias voltages. A maximum SNR of 16 dB is achieved at -2 V. Also zero bias operation is achieved, but in this case with a degraded performance (SNR value of only 5 dB) as the noise floor (dark current) increases with the bias voltage (Figure 75). The complete details of these results at 110 GHz can be found in Criado et al. Sub-Thz optoelectronic heterodyne receiver based on np-i-pn quasi-ballistic THz receiver and ultra-low phase noise sub-THz photonic Local Oscillator. *Preprint* (2012)[175].

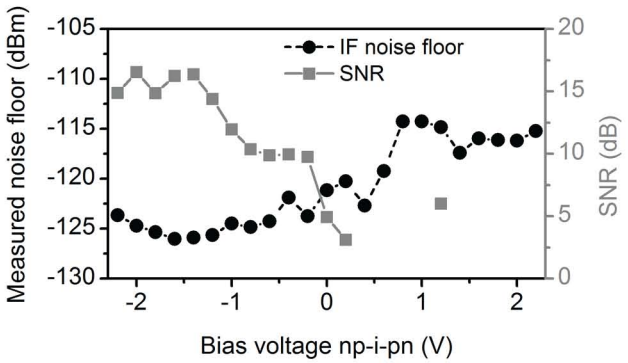

Figure 75 Measured noise floor and SNR of the IF signal as a function of np-i-pn bias voltage[175]

The results achieved with this sub-THz EO heterodyne receiver architecture and the devices that comprise it, can be summarized as follows:

- Demonstration of the functionality of the EO heterodyne receiver architecture, using the np-i-pn quasi ballistic THz detector as EO mixer and the low phase noise photonic sub-THz synthesizer presented in chapter III as photonic LO. The frequencies used for the M signal are 50 GHz (within the bandwidth of the employed instrumentation) and 110 GHz (using the experimental setup out of its 50 GHz bandwidth, with estimated losses of 42 dB in the M path).
- Characterization of the overall performance of the EO heterodyne receiver as a function of the photonic LO and M powers.

- Characterization of the Conversion Ratio (CR), Signal to Noise Ratio (SNR) and linearity of the sub-THz EO mixer.
- Demonstration of zero bias operation of the np-i-pn mixer under the sub-THz EO heterodyne detection architecture presented.

V

Results discussion. Conclusions

1

Results discussion

1.1 mm-wave and sub-THz generation

Several photonic Local Oscillators (LO) have been conceived, designed, implemented and tested in this thesis for the development of high quality (low phase noise) tunable sub-THz and THz sources. All of them are based on Difference Frequency Generation (DFG) architectures using two key elements: a DFG source and a photomixer. The DFG source is based on an optical multimode source (Optical Frequency Comb Generator, OFCG) and an optical mode selection stage. The different approaches implemented for the devices of this DFG architecture are discussed below.

The first implemented DFG structure is based on the use of integrated OFCGs based on Passively Mode Locked Laser Diodes (PMLLDs), high selective filtering using Optical Fabry-Perot filters to select the required optical modes, and a commercial 50 GHz-bandwidth photodiode. This implementation offers discrete tunability with frequency steps corresponding to the repetition rate of the PMLLD employed (10 GHz and 15 GHz in this work), hence having a maximum frequency resolution of 10 GHz. The demonstrated frequency range for the generated signals covers from 10 to 120 GHz. The best Full Width at Half Maximum (FWHM) obtained for the synthesized signals is around 2 MHz at 90 GHz. The optical source offers a limited output power, around 500 μW and the optical filters introduce a significant amount of losses. For these reasons, several optical amplification stages (up to three) are required to provide to the photomixer an optical average power around 10 mW.

Although PMLDDs (and in general, MLLDs) provide a potentially integrated OFCG, they present several issues hard to overcome to accomplish the objective of a high quality sub-THz oscillator. Firstly, they offer low average optical power. This makes the use of optical amplification such as Semiconductor

Optical Amplifiers (SOAs) or preferably Erbium Doped Fiber Amplifiers (EDFAs) necessary. This has two important drawbacks: the integration potential is dramatically reduced if several external amplification stages are need at the output; and the use of several amplification stages reduces the Signal to Noise Ratio (SNR) as Amplified Spontaneous Emission (ASE) (i.e. Noise Figure) is added in each stage.

A second important drawback is related to the availability of the devices and the repeatability of their performance. There already exist fully functional Photonic Integrated Circuit (PIC) platforms, such as JePPIX[266] or III-V Labs (Thales), and much effort is being placed in this research field. However, photonic integration is not mature enough nowadays to provide repeatability, efficient production and cost affordable manufacturing, at least for active devices. This point is also related to the previous one, as the integration of several SOA sections in the PIC is not easy and the obtained amplification performance is worse than external amplification using EDFAs, mainly because SOAs have a lower saturation output power. Moreover, MLLDs offer none or very limited tunability in the frequency spacing between longitudinal modes. Because of this, the tunability of the sub-THz system is restricted to discrete steps (equal to the repetition frequency).

In the view of the performance offered by the DFG architecture based on PMLLDs (summarized in Table V1), several points are to be improved in order to attain a high quality sub-THz photonic source. The main ones are the need of better tunability features and a better phase noise performance. To achieve these objectives, the devices that comprise the DFG architecture are replaced in order to optimize it.

An OFCG based in a state-of-the-art design and Commercial Off-The-Shelf (COTS) components is designed and implemented, providing a compact and cost-effective multimode optical source with high coherence between optical modes, as it employs an external RF reference. This OFCG is based on a Gain Switched (GS) Discrete Mode (DM) laser and a span expansion stage comprising a single Electro-Optical Phase Modulator. As optical mode selection strategy, optical filtering with Fabry Perot tunable filters is used. Nevertheless, a new approach based on Optical Injection Locking (OIL) is also implemented, allowing for both filtering and amplification in a single stage with better performance. As photomixer, we use an n-i-pn-i-p superlattice photomixer with an operation bandwidth in excess of 1 THz, which is designed and implemented by our colleagues from Max Planck Institute for the Science of Light (Erlangen, Germany) and Friedrich-Alexander-Universität Erlangen-Nürnberg (Erlangen, Germany). The fabrication of the device is made in collaboration with the group of A. C. Gossard, University of California Santa Barbara (UCSB).

This final system offers a frequency range coverage from 60 to 140 GHz, in which the joint operation of optical selection stage and tunable OFCG allows a quasi-continuous tunability covering the whole frequency range. The lower frequency can be decreased down to a few GHz (repetition frequency) by the use

of higher bandwidth (around 4-18 GHz) RF electronics in the GS-OFCG. On the other hand, the upper frequency can be straightforwardly increased well above 1 THz including additional optical span expansion stages implemented with the techniques described in this document (chapter II). The current frequency resolution is 0.1 Hz at 100 GHz, but it can be readily improved to 0.01 Hz at 100 GHz and 0.1 Hz at 1 THz replacing the RF reference of the GS-OFCG with a commercially available state-of-the-art RF synthesizer featuring a frequency resolution of 1 mHz[236]. It must be highlighted that the tunability of this system features an almost perfect linearity. The system delivers to the photomixer an average optical power of 10 mW with no need of optical amplification stages, such as EDFAs or SOAs. Moreover, this output power can be increased with slight changes in the design (i.e. OIL components) and without using optical amplifiers. The FWHM of the generated signal at 120 GHz is below 10 Hz, what is the measurement limit of the available instrumentation. The system also presents an excellent long-term power and especially frequency stability, with variations over one hour of 1.5 dB and 5Hz, respectively, at 120 GHz. These reported values are also limited by the measurement instrumentation, and their actual values could be better.

Parameter	PMLLD+FPTF	GS-OFCG+OIL
Pulsed/CW	CW	CW
Optical average output power (W) without optical amplification	Below 500 μW	Around 10 mW
Frequency range (THz)	Around 0.8-1.2 THz for the analyzed devices.	Currently 230 GHz, readily scalable beyond 1 THz.
Tunability	Discrete, around 10 GHz steps. Frequency resolution around 10 GHz.	Whole range tunability, 0.1 Hz resolution at 100 GHz. Scalable down to 0.01 Hz at 100 GHz
Minimum FWHM (CW)	Around 2 MHz at 120 GHz	<10 Hz at 120 GHz
Power stability. Expressed as deviation over one hour operation (dB)	N/A	1.2 dB
Frequency stability. Expressed as deviation over one hour operation (Hz)	N/A	5 Hz
Minimum size (range)	Benchtop	Benchtop
Coherent/Incoherent	Coherent	Coherent
Cooling	RT	RT

Table V1 Performance summary of THz generation systems implemented during this thesis work. References for the table values can be found in chapter III

The performance summary of the two DFG systems conceived and implemented in this thesis work is shown in Table V1.

The performance offered by the photonic architecture and devices for sub-THz and THz generation developed in this thesis matches or even surpasses the phase noise performance and tunability of the best all-electronic THz generation systems commercially available[118], and surpass these parameters in more than one million times for the case of the best commercially available photonic THz generation systems[133]. Furthermore, it maintains all the exclusive advantages associated to the photonic techniques for THz generation, such as low losses, remote distribution, EMI immunity and light weight.

1.2 mm-wave and sub-THz EO detection

Two photonic receivers based on Electro-Optical (EO) heterodyne detection architectures have been conceived, designed, implemented and tested in this thesis. The first one is a microwave EO heterodyne receiver that uses a GS photonic LO and an Ultra-Non Linear SOA (XN-SOA) as EO mixer. The second is a sub-THz heterodyne receiver that employs the low phase noise sub-THz photonic source developed in this thesis as photonic LO and a np-i-pn quasi ballistic detector as EO mixer.

The EO heterodyne detection is firstly demonstrated at microwave frequencies (<15 GHz). The resulting scheme is a compact, cost effective and flexible receiver which offers reasonable Conversion Ratios (CR, up to -8 dB). The two devices that encompass the EO heterodyne detection architecture, i.e. the photonic LO and the EO mixer, are evaluated and optimized. A XN-SOA, rather than a conventional SOA, is used as EO mixer in order to take advantage of the additional nonlinearities of this device to optimize the mixing process. The performance of this EO mixer is evaluated trough the frequency mapping of the CR as a function of both RF and LO frequencies. Furthermore, the use of a GS based photonic LO is also investigated and compared to the case in which a traditionally linearly modulated photonic LO is used. In order to do this, the overall performance of the receiver is evaluated through the CR, linearity and phase noise as a function of RF frequency and XN-SOA bias current conditions. It is demonstrated how the use of this GS-LO provides with a significant improvement of the analyzed figures of merit.

Although the CR offered by this EO heterodyne receiver is much lower than electronic mixers and lower than state-of-the-art EO mixers at microwave frequencies[261], it has great potential for applications requiring scalability and remote distribution of the LO and Intermediate Frequency (IF) signals. This is

why it has been integrated in a real application: a photonic imaging array that has been implemented in collaboration with the Radiofrequency Group of Universidad Carlos III de Madrid. This array is implemented with three pixel elements and imaging results of a defined target are demonstrated at 12 GHz.

After these results at microwave frequencies, the EO heterodyne architecture is implemented in the sub-THz range, giving rise to the second EO detection architecture presented in this thesis. The two key devices of this architecture, i.e. photonic LO and EO mixer, are implemented with the low phase noise photonic generator developed in this thesis and with a np-i-pn quasi-ballistic detector, respectively. This np-i-pn detector is based in a new design concept optimized for THz homodyne/heterodyne detection, and it is designed and developed by our colleagues from Max Planck Institute for the Science of Light (Erlangen, Germany) and Friedrich-Alexander-Universität Erlangen-Nürnberg (Erlangen, Germany). The fabrication of the device is made in collaboration with the group of A. C. Gossard, University of California Santa Barbara (UCSB). The results presented in this thesis are obtained with the first implementation of this detector.

The sub-THz EO heterodyne receiver architecture is firstly tested at 50 GHz with an IF of 5 MHz, mainly due to the bandwidth of the available instrumentation (50 GHz). A detailed study of this sub-THz heterodyne receiver at 50 GHz is performed, evaluating several parameters and figures of merit such as CR as a function of optical LO power and bias voltage, IF received power as a function of the optical LO power and measurement signal (M) power, linearity of IF with respect to M, and generated photocurrent with respect to the LO optical power received. The mixer performance does not show a significant dependence with respect to the bias voltage and it works at zero bias. The maximum CR, -75 dB, is achieved at maximum LO optical power (2.4 mW). To the best of our knowledge, this is the first EO heterodyne receiver at sub-THz frequencies capable of working unbiased.

The same scheme is also validated at 110 GHz with an IF signal at 1 MHz despite of the high losses associated to the limited bandwidth of the available instrumentation (50 GHz, giving 42 dB of losses in the sub-THz path at 110 GHz). In this experiment, the performance characterization is limited to the analysis of the CR, Signal-to-Noise Ratio (SNR) and noise floor, all of them as a function of the bias voltage. In this case, a different detector from the same chip is used, showing higher dependence on the bias voltage. The device features best performance at reverse voltage values. The better CR value (-75 dB) is achieved at -2 V. Nevertheless, the achieved conversion ratio with the first available samples of these new THz detectors is still far from the state of the art performance in EO THz heterodyne receivers, achieved by Rouvalis *et al.* in a Travelling-Wave Uni-Travelling-Carrier Photodiode (TW-UTC-PD) with a CR of -32 dB at 100 GHz. Nevertheless, further improvement of the device, along with integration with antenna will increase the performance.

2

Conclusions

In this thesis, and through the development of new photonic architectures and the evaluation of new photonic devices, it has been shown that photonic technologies are an alternative for both generation and detection at sub-THz and THz frequency ranges.

The use of these new photonic architectures and devices has allowed us to develop THz synthesizers matching or even surpassing the performance of the best state-of-the-art commercially available electronic based THz generation systems, and surpassing in more than one million times most figures of merit of state-of-the-art commercial photonic THz synthesizers. In this sense, we are in the position to fully incorporate these developments to commercial THz generation systems that would allow benefit from the number of exclusive advantages associated to the optical approaches.

Also photonic receiver architectures based on Electro-Optical (EO) heterodyne detection are feasible at sub-THz and THz frequencies as it has been demonstrated. Nevertheless, in this case, in spite of using state-of-the-art photonic devices (both photonic LOs and sub-THz EO mixers), the achievable performance is still far from that offered by all-electronic and thermal THz heterodyne receivers. Therefore, further effort has to be placed in the following years in the development of new devices for these EO heterodyne detection architectures in order to achieve similar performance than their all-electronic counterparts and bring to the THz receivers all the benefits of photonic techniques.

Finally, these photonic architectures and devices, especially those developed for sub-THz and THz CW ultra low phase noise generation, are now to be demonstrated in actual applications, like imaging, high resolution spectroscopy or LO distribution, e.g. for radioastronomy purposes.

VI

Selected publications and preprints

1

Wiley, Microwave and Optical Technology Letters (published 06/2012)

Selected publication 1	
Citation	P. Acedo, G. Carpintero, **A. R. Criado**, C. de Dios, and K. Yvind, "Photonic synthesis of continuous-wave millimeter-wave signals using a passively mode-locked laser diode and selective optical filtering," Microwave and Optical Technology Letters, vol. 54, no. 6, pp. 1416–1419, Jun. 2012.
JCR impact factor	0.618
Submitted	09/08/ 2011
Published	06/2012
Comments	Copyright 2012 Wiley Periodicals, Inc.

Table VI-1 Selected publication 1. Summary of publication information

CHAPTER VI

PHOTONIC SYNTHESIS OF CONTINUOUS-WAVE MILLIMETER-WAVE SIGNALS USING A PASSIVELY MODE-LOCKED LASER DIODE AND SELECTIVE OPTICAL FILTERING

P. Acedo,[1] G. Carpintero,[1] A.R. Criado,[1] C. de Dios,[1] and K. Yvind[2]
[1] Department of Electronics Technology, Universidad Carlos III de Madrid, Leganés, Madrid 28911 Spain; Corresponding author: pag@ing.uc3m.es
[2] DTU Fotonik, Department of Photoniks Engineering, Technical University of Denmark, Lyngby DK-2800 Denmark

Received 9 August 2011

ABSTRACT: *We report a photonic synthesis scheme for continuous wave millimeter-wave signal generation using a single passively mode-locked laser diode (PMLLD), optical filtering and photomixing in a fast photodiode. The phase noise of the photonically synthesized signals is evaluated and inherits the characteristics of the PMLLD electrical power spectrum.* © 2012 Wiley Periodicals, Inc. Microwave Opt Technol Lett 54:1416–1419, 2012; View this article online at wileyonlinelibrary.com. DOI 10.1002/mop.26822

Key words: *millimeter-wave photonic generation; mode-locked lasers; photomixing; phase noise*

1. INTRODUCTION

The lack of suitable generation and detection technology above 120 GHz, and most notably in the THz band is lagging the widespread use of signals in this frequency range within important fields of application such as security, biology, medicine [1], and wireless communications [2]. The development of such sources and detectors has motivated huge research efforts in this field over the last years, and now several techniques for continuous wave (CW) millimeter-wave and THz generation are available [3]. Among these, photonic techniques are potentially advantageous for producing low cost, compact, and room temperature operation components given the recent advances in photonic integrated circuits [4].

The most promising photonic millimeter-wave and THz generation technique is based on the combination (mixing) of two input wavelengths, producing a signal with a frequency equal to the difference between them. The mixing takes place either in a nonlinear media (i.e., difference frequency generation) or in a photomixing device (i.e., optical heterodyne photomixing, OHP), such as a photoconductive antenna or a photodiode [3].

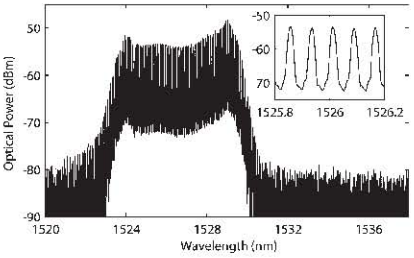

Figure 1 Optical spectrum of the QW PMLLD (40 nm span, A in Fig. 2). Inset: detailed span (0.4 nm)

The usual schemes for OHP use either two optical frequencies from different laser sources, achieving a great frequency range and continuous tunability at the expense of complex optical phase locked loops (OPLL) schemes [5]; or two modes filtered from an optical frequency comb generator (OFCG), where additional devices such as phase modulators, RF synthesizers, nonlinear optical fiber, and complex optical filters are usually needed to implement the OFCG, generate the electrical signal, and maintain the continuous tunability [6].

In this article, we present a straightforward OHP setup for millimeter-wave and sub-THz signal generation based on three key elements: a single passively mode-locked laser diode (PMLLD) acting as OFCG, two high selectivity Fabry Perot fiber filters to select two of the optical modes from the OFCG, and a fast photodiode as the photomixing element. These elements present a great integration potential, then the presented OHP scheme could be translated into a photonic integrated circuit. The use of a PMLLD allows not only the implementation of a monolithic OFCG based on a single device but also takes advantage of the low phase noise performance demonstrated by this kind of devices without the use of an OPLL or external RF references [7]. The frequency range of the electrical signal that can be synthesized with this setup is only limited by the optical bandwidth of the optical comb generated by the PMLDD (640 GHz in our case) and the bandwidth of the photodiode device, that can be close to 1 THz, as it is the case of the traveling-wave uni-traveling carrier photodiode technology [8].

2. PASSIVELY MODE-LOCKED LASER DIODE AS MONOLITHIC OPTICAL FREQUENCY COMB GENERATOR

The PMLLD used in this study has a two contact structure comprised of a saturable absorber and a gain section, of 85 μm and 3915 μm length, respectively [9]. The active region contains one InGaAsP/AlGaInAs quantum-well (QW) emitting at a central wavelength of 1527 nm. Longitudinal confinement of the optical field is achieved by the formation of a 2-μm width ridge waveguide structure. The facet at the absorber end is HR coated (95% reflection) and the output facet is as cleaved.

Passive mode-locking regime is achieved with a reverse DC voltage on the saturable absorber. Figure 1 shows the optical spectrum of the laser in this regime when the reverse bias applied to the saturable absorber is -2.7 V and the drive current is 55 mA. The main trace shows the complete spectrum on a 40-nm span. The inset presents the modes around 1527 nm, where the spacing between modes corresponds to the repetition rate of the PMLLD ($f_{ml} = 9.92$ GHz).

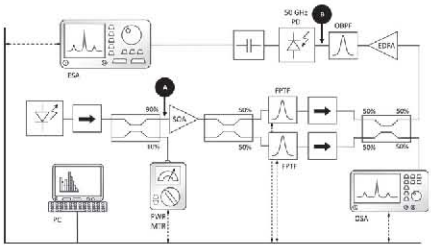

Figure 2 Experimental setup

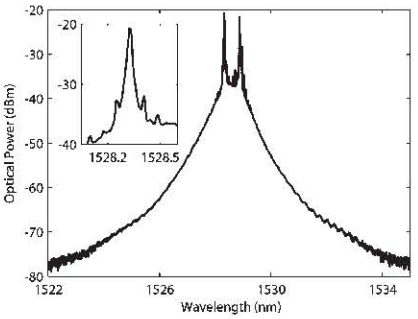

Figure 3 Processed optical signal prior to photomixing stage (B in Fig. 2). Inset, detail of one of the modes

3. CW MILLIMETER-WAVE AND SUB-THz PHOTONIC SYNTHESIS SYSTEM DESCRIPTION

The experimental setup of the millimeter-wave and sub-THz signal photonic generation scheme presented in this work is shown in Figure 2. The PMLLD chip is on a thermoelectric controlled stage and the light at the output facet is coupled to a single mode fiber. An optical isolator is included at this point to avoid back reflections from the following elements of the setup, such as the 90:10 split ratio directional coupler placed to monitor the optical output power.

The 90% output of this splitter is then amplified using an erbium doped fiber amplifier and divided in two branches, each with a Fabry Perot tunable filter (FPTF). These filters have a very high selectivity (Finesse = 3000, that is, 3-dB bandwidth = 50 pm) that corresponds to a 3-dB bandwidth of 6.43 GHz at 1527 nm and allow us to filter one mode from the complete optical spectrum (Fig. 1) independently on each branch. The filters are followed by another optical isolator to prevent reflections. The two filtered wavelengths that exhibit the desired frequency difference are then recombined in a 50:50 optical directional coupler to obtain an optical signal comprising the two selected modes. One of the outputs of the 50:50 coupler is directly connected to an optical spectrum analyzer to track the spectrum and the mode spacing. Figure 3 shows the spectrum of the optical signal after filtering and recombination. In this figure, the detailed optical spectrum of one of the filtered modes is shown, demonstrating a side mode suppression ratio of 12 dB. It is important to note that the high selectivity of these filters requires a fine control and stabilization of their control voltages, as small drifts or voltage amplitude noise would translate into associated amplitude variations in the final synthesized signal.

The other coupler output is sent to another amplification stage with a linear semiconductor optical amplifier (SOA QPhotonics QSOA-1550). This stage is needed to increase the optical power and make it possible to clearly detect the beat note signal at the photodetector output. The SOA output is then sent to an optical band-pass filter to reduce the amplified spontaneous emission of the spectrum outside the bandwidth of interest, hence increasing the signal-to-noise ratio. The filtered modes beat on a fast photodiode (u2t XPDV2020R), used as photomixing element, which offers a 3-dB bandwidth of 50 GHz. The generated electrical signal, with a frequency given by the frequency difference between the optical modes is observed on an electrical spectrum analyzer (ESA).

It is worth to mention that the tunability of the presented photonic synthesis covers the millimeter-wave to sub-THz signals ranges by tuning of one of the filters to the peak wavelength of one mode and subsequent application of a variable voltage to the other filter to select the desired second mode, spaced from the first one a frequency equal to the desired synthesized electrical signal. The frequency step is 9.92 GHz, determined by the repetition rate of the PMLLD (f_{ml}).

4. EXPERIMENTAL RESULTS

The study of the CW millimeter-wave synthesized signal is carried out by evaluating its electronic spectral characteristics after the mixing of the selected optical modes in the fast photodiode, separated by a frequency equal to $4{\cdot}f_{ml}$. The experimental study has been centered to this frequency range ($4{\cdot}f_{ml}$ = 39.73 GHz) to guarantee a negligible contribution of the sum of the side residual optical modes after filtering (inset of Fig. 3), while maintaining the frequency within the detection limits (limited only by the photodiode and the ESA).

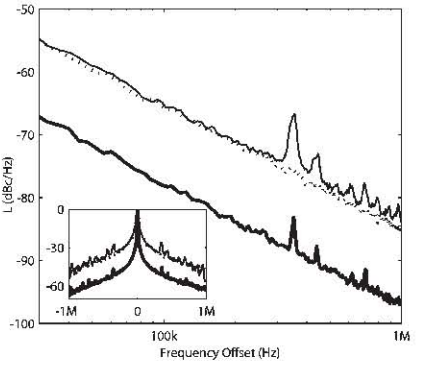

Figure 4 SSB noise-to-carrier power ratio ($L(f)$) versus frequency offset. Thick black line, fundamental harmonic (f_{ml} = 9.92 GHz); dotted black line, fourth harmonic ($4{\cdot}f_{ml}$ = 39.73 GHz); thin black line, photonically synthesized signal ($4{\cdot}f_{ml}$ = 39.73 GHz). Inset, power normalized spectra

The phase noise performance, important for applications such as wireless communications, is evaluated measuring the single side band (SSB) noise and the full width at half maximum (FWHM) of the electrical spectrum. To understand its characteristics, these results are compared with those found studying the electrical signal directly obtained from the PMLLD by harmonic generation (i.e., optical to electrical conversion of the PMLLD output (Fig. 1) in the fast photodiode without mode filtering). In this case, the two filtering branches are replaced by a tunable optical attenuator to have the same noise and spectral contribution of the optical amplification stages and properly compare the spectra.

Figure 4 shows the SSB noise-to-carrier power ratio ($L(f)$) of the signals under study. The analysis of the phase noise of the signal obtained by harmonic generation from the PMLDD shows a difference between the fundamental and the fourth harmonic of $\approx$12 dB that is in well agreement with the increment associated to frequency multiplication, given by $20\cdot\log(N)$, where N is the harmonic number. The SSB noise of the photonically synthesized signal at $4\cdot f_{\mathrm{ml}}$ is similar to that of the corresponding harmonic of the PMLLD signal. Nevertheless, the SSB noise of the synthesized signal exhibits a set of frequency peaks present in the fundamental harmonic that are not observed at the fourth harmonic of the source signal. This demonstrates that the SSB noise of the synthesized signal, although having a general behavior similar to that associated to the harmonic at the same frequency, inherits phase noise characteristics directly from the fundamental harmonic associated with the repetition rate of the PMLLD. This implies a clear advantage of the synthesized signal over the PMLDD direct harmonic generation signal when maximum deliverable power is a concern. The maximum electrical power offered by a photodiode is limited by its maximum input optical power. Generating an electrical signal using only two modes (synthesized signal) instead of all modes (PMLLD harmonic signal) means that only the optical power at the required frequency is mixed in the photodiode, maximizing its electrical power with no degradation of the phase noise, only at the expense of further optical amplification of the selected longitudinal modes.

The normalized spectra of the generated signals are represented in the inset of Figure 4. Considering the electrical spectra of the PMLLD signal, the measured FWHM of the fundamental harmonic is 8.77 kHz, while the value for the fourth harmonic is 24.58 kHz. Using the fundamental harmonic FWHM as reference, the values have an almost linear dependence with the frequency, as it has been described for these optical sources [10]. Observing the synthesized signal, we obtain a FWHM of 27.42 kHz. As this measure is similar to that obtained for the fourth harmonic of the PMLLD signal and also matches the linear dependence described above, this would allow us to predict the FWHM for signals synthesized at higher frequencies [11].

It is important to note that the eventual contribution to the SSB noise given by amplitude jitter associated to possible drifts of the central frequency of the FPTFs will be negligible compared to the contribution of the timing jitter to the SSB noise as demonstrated in Ref. 11. That is another advantage of our setup over more complex systems that rely on OPLL for sub-THz signal generation, where phase instabilities in the loop are directly translated to timing jitter and, therefore, to SSB noise.

5. CONCLUSIONS

In this work, we have presented a compact and straightforward system for photonic synthesis of CW millimeter-wave and sub-THz signals using a QW PMLLD, tunable Fabry Perot fiber filters, and photomixing in a fast photodiode. The use of a single QW PMLLD to serve as OFCG presents a great integration potential for the system, while offering very low phase noise performance inherent to this kind of devices. Other advantages of the system include a negligible phase noise degradation related to eventual drifts at the Fabry Perot filters, and a higher deliverable electrical power as only optical power at the required frequency difference is mixed (synthesized signal, two modes) and not at other nondesired frequencies (direct harmonic generation, all modes).

With this setup, millimeter-wave, and sub-THz signals at integer multiples of that associated to the repetition rate of the PMLLD (9.92 GHz in this case) can be obtained through selective filtering of the optical spectrum emitted by the laser and photomixing in a fast photodiode, with a highest frequency to be synthesized only limited by the optical spectrum of the OFCG and the photodiode bandwidth.

A photonically synthesized signal at 39.73 GHz has been generated with this setup and analyzed, reporting performance for both SSB noise and FWHM similar to that of the corresponding harmonic at the same frequency of the QW PMLLD. Moreover, some spectral characteristics (i.e., frequency peaks in the SSB noise) from the fundamental harmonic that are not observed at the fourth harmonic are directly inherited to the synthesized signal at 39.73 GHz, offering a system that translates to the generated millimeter-wave signal the noise characteristics of the OFCG used.

REFERENCES

1. P.H. Siegel, Terahertz technology in biology and medicine, IEEE Trans Microwave Theor Tech 52 (2004), 2438–2447.
2. A.J. Seeds and K.J. Williams, Microwave photonics, J Lightwave Technol 24 (2006), 4628–4641.
3. T. Nagatsuma, Generating millimeter and terahertz waves, IEEE Microwave Mag 10 (2009), 64–74.
4. D. Saeedkia and S. Safavi-Naeini, Terahertz photonics: Optoelectronic techniques for generation and detection of terahertz waves, J Lightwave Technol 26 (2008), 2409–2423.
5. H. Ito, T. Furuta, F. Nakajima, K. Yoshino, and T. Ishibashi, Photonic generation of continuous THz wave using uni-traveling-carrier photodiode, J Lightwave Technol 23 (2005), 4016–4021.
6. S. Ho-Jin, N. Shimizu, T. Furuta, K. Suizu, H. Ito, and T. Nagatsuma, Broadband-frequency-tunable sub-terahertz wave generation using an optical comb, AWGs, optical switches, and a uni-traveling carrier photodiode for spectroscopic applications, J Lightwave Technol 26 (2008), 2521–2530.
7. G. Carpintero, M.G. Thompson, R.V. Penty, and I.H. White, Low noise performance of passively mode-locked 10-GHz quantum-dot laser diode, IEEE Photonics Technol Lett 21 (2009), 389–391.
8. E. Rouvalis, C.C. Renaud, D.G. Moodie, M.J. Robertson, and A.J. Seeds, Traveling-wave uni-traveling carrier photodiodes for continuous wave THz generation, Opt Exp 18 (2010), 11105–11110.
9. K. Yvind, D. Larsson, L.J. Christiansen, J. Mork, J.M. Hvam, and J. Hanberg, High-performance 10 GHz all-active monolithic mode-locked semiconductor lasers, Electron Lett 40 (2004), 735–737.
10. J. Bureau International des Poids et Measures (BIPM), Evaluation of measurement data—guide to the expression of uncertainty in measurement, (BIPM). JCGM, 2008.
11. D. Eliyahu, R.A. Salvatore, and A. Yariv, Effect of noise on the power spectrum of passively mode-locked lasers, J Opt Soc Am B: Opt Phys 14 (1997), 167–174.

CHAPTER VI

2

OSA, Optics Express (published 01/2012)

Selected publication 2	
Citation	**A. R. Criado**, P. Acedo, G. Carpintero, C. de Dios, and K. Yvind, "Observation of phase noise reduction in photonically synthesized sub-THz signals using a passively mode-locked laser diode and highly selective optical filtering," Optics Express, vol. 20, no. 2, pp. 1253–1260, Jan. 2012.
JCR impact factor	3.587
Submitted	24/11/ 2011
Published	16/01/2012
Comments	

Table VI-2 Selected publication 2. Summary of publication information

CHAPTER VI

Observation of phase noise reduction in photonically synthesized sub-THz signals using a passively mode-locked laser diode and highly selective optical filtering

A. R. Criado,[1,*] P. Acedo,[1] G. Carpintero,[1] C. de Dios,[1] and K. Yvind[2]

[1]*Electronics Technology Department, Universidad Carlos III de Madrid, Butarque 15, Leganés, Madrid 28911, Spain*

[2] *DTU Fotonik, Department of Photonics Engineering, Technical University of Denmark, Ørsteds Plads 343, 2800-Kgs. Lyngby, Denmark*

[*]*acriado@ing.uc3m.es*

Abstract: A Continuous Wave (CW) sub-THz photonic synthesis setup based on a single Passively Mode-Locked Laser Diode (PMLLD) acting as a monolithic Optical Frequency Comb Generator (OFCG) and highly selective optical filtering has been implemented to evaluate the phase noise performance of the generated sub-THz signals. The analysis of the synthesized sub-THz signals up to 120 GHz gives as a result an effective reduction of the electrical linewidth when compared to direct harmonic generation that begins at 50 GHz and becomes greater as the frequency increases. The phase noise reduction offered by the setup, along with its integration potential, cost and bandwidth, make it a promising candidate to the development of an integrated and high performance low phase noise local oscillator in the sub-THz range.

OCIS codes: (140.4050) Mode-locked lasers; (190.2620) Harmonic generation and mixing; (250.5960) Semiconductor lasers; (350.4010) Microwaves.

References and links

1. P. H. Siegel, "Terahertz technology," IEEE Trans. Microwave Theory Tech. **50**(3), 910–928 (2002).
2. C. Jansen, S. Wietzke, O. Peters, M. Scheller, N. Vieweg, M. Salhi, N. Krumbholz, C. Jördens, T. Hochrein, and M. Koch, "Terahertz imaging: applications and perspectives," Appl. Opt. **49**(19), E48–E57 (2010).
3. J. Capmany and D. Novak, "Microwave photonics combines two worlds," Nat. Photonics **1**(6), 319–330 (2007).
4. S. Ristic, A. Bhardwaj, M. Rodwell, L. Coldren, and L. Johansson, "An Optical Phase-Locked Loop Photonic Integrated Circuit," J. Lightwave Technol. **28**, 526–538 (2009).
5. X. Leijtens, "JePPIX: the platform for Indium Phosphide-based photonics," IET Optoelectron. **5**(5), 202–206 (2011).
6. H.-J. Song, N. Shimizu, T. Furuta, K. Suizu, H. Ito, and T. Nagatsuma, "Broadband-Frequency-Tunable Sub-Terahertz Wave Generation Using an Optical Comb, AWGs, Optical Switches, and a Uni-Traveling Carrier Photodiode for Spectroscopic Applications," J. Lightwave Technol. **26**(15), 2521–2530 (2008).
7. H. Ito, T. Furuta, F. Nakajima, K. Yoshino, and T. Ishibashi, "Photonic generation of continuous THz wave using uni-traveling-carrier photodiode," J. Lightwave Technol. **23**(12), 4016–4021 (2005).
8. P. Acedo, H. Lamela, S. Garidel, C. Roda, J. P. Vilcot, G. Carpintero, I. H. White, K. A. Williams, M. Thompson, W. Li, M. Pessa, M. Dumitrescu, and S. Hansmann, "Spectral characterisation of monolithic modelocked lasers for mm-wave generation and signal processing," Electron. Lett. **42**(16), 928–929 (2006).
9. P. Acedo, G. Carpintero, A. R. Criado, and K. Yvind, "Photonic Synthesis of sub-THz Signals Using Mode-Locked Single QW Lasers and Tunable Fabry-Perot Fiber Filters," in European Microwave Week EuMIC11-4, Paris, France (2011).
10. P. Vasil'ev, *Ultrafast Diode Lasers: Fundamentals and Applications* (Artech House Publishers, 1995).
11. K. Yvind, D. Larsson, L. J. Christiansen, J. Mork, J. M. Hvam, and J. Hanberg, "High-performance 10 GHz all-active monolithic modelocked semiconductor lasers," Electron. Lett. **40**(12), 735–737 (2004).
12. G. Carpintero, M. G. Thompson, R. V. Penty, and I. H. White, "Low Noise Performance of Passively Mode-Locked 10-GHz Quantum-Dot Laser Diode," IEEE Photon. Technol. Lett. **21**(6), 389–391 (2009).
13. D. Linde, "Characterization of the noise in continuously operating mode-locked lasers," Appl. Phys. B **39**(4), 201–217 (1986).

14. D. Eliyahu, R. A. Salvatore, and A. Yariv, "Effect of noise on the power spectrum of passively mode-locked lasers," J. Opt. Soc. Am. B **14**(1), 167–174 (1997).
15. E. Rouvalis, C. C. Renaud, D. G. Moodie, M. J. Robertson, and A. J. Seeds, "Traveling-wave Uni-Traveling Carrier photodiodes for continuous wave THz generation," Opt. Express **18**(11), 11105–11110 (2010).
16. E. Sooudi, G. Huyet, J. G. McInerney, F. Lelarge, K. Merghem, R. Rosales, A. Martinez, A. Ramdane, and S. P. Hegarty, "Injection-Locking Properties of InAs/InP-Based Mode-Locked Quantum-Dash Lasers at 21 GHz," IEEE Photon. Technol. Lett. **23**(20), 1544–1546 (2011).
17. S. Gee, F. Quinlan, S. Ozharar, and P. Delfyett, "Two-mode beat phase noise of actively modelocked lasers," Opt. Express **13**(11), 3977–3982 (2005).

1. Introduction

Today, the pursue for integrated and cost-effective generation and detection technologies that could allow a widespread access to the potential applications in the sub-THz and THz frequencies has become one of the most active fields of research [1, 2]. A narrow linewidth of the sub-THz signals, in addition to cost and compactness of the proposed solutions, is needed for some of the applications, such as high resolution spectroscopy [2] or broad bandwidth communications [3]; but especially towards the development of heterodyne receivers in this frequency band, where a good quality Local Oscillator (LO) signal is mandatory.

Signal generation by downconversion from the optical domain appears as a promising technology for filling the THz gap mainly because of its integration potential [4, 5] and its good performance [6]. The photonic generation of sub-THz Continuous Wave (CW) signals is carried out by beating in a photomixing device two optical frequencies with a frequency difference equal to that of the electrical signal to be generated. These two optical frequencies can be obtained from two independent lasers, requiring external Optical Phase Locked Loops (OPLL), but providing continuous tunability [7]; or from a single source, like dual-mode devices [8] or Optical Frequency Comb Generators (OFCG), which usually requires additional components as phase modulators or external RF references and offers discrete tunability [6].

In this paper, a compact setup for CW sub-THz photonic synthesis using an OFCG and highly selective optical filtering [9] is employed to study the phase noise performance of the signals synthesized with this scheme and to compare them with those obtained by direct harmonic generation. In this setup, two optical modes are filtered from a Passively Mode-Locked Laser Diode (PMLLD), which is employed as OFCG, and then mixed in a fast photodiode to generate an electrical signal with a frequency equal to the frequency spacing between the two optical modes selected.

Photonic synthesis of electrical signals up to 120 GHz has been accomplished. The analysis of the phase performance of these signals when compare to direct harmonic generation gives as a result an electrical linewidth reduction that becomes more remarkable as the frequency increases. No reduction seems to exist at lower frequencies (less than 50 GHz), but a narrowing in the electrical linewidth begins to appear for frequencies greater than 50 GHz. From this point onwards, the reduction increases as the frequency gets higher, reaching narrowing values of 35% at 110 GHz and 25% at 120 GHz with respect to direct harmonic generation. The reported phase noise improvement of CW sub-THz signals synthesized with this setup along with its integration potential, cost and bandwidth capabilities make it a promising candidate to the development of an integrated and high performance local oscillator in the sub-THz range.

2. Mode-locked laser diode as optical frequency comb generator

A mode-locked laser diode (MLLD) is a source of short optical pulses in the picosecond or subpicosecond range. As a semiconductor device, is compact and can be fully integrated on an InP substrate with a central wavelength in the 1550 nm range, that makes it fully compatible with fiber Commercially available Off-The-Shelf (COTS) telecom components. In addition, Photonic Integrated Circuits (PIC) are available to extend integrability to monolithic integrated circuits or transceivers [4, 5].

A mode-locked device can operate in active, passive or hybrid regime. In the three cases, the longitudinal optical modes are phase-locked and an optical comb is generated. but they are different in nature and the phenomena behind their operation are also distinct, what translates in a dissimilar behavior at all levels [10]. In the passive operation, usually only a saturable absorber (SA) region is used in the device to lock the phase of the optical modes. The passive mode-locked device is completely functional with a DC current signal for the gain section and a DC voltage for the SA region, without the need of a RF reference or any additional external device. Moreover, the phase noise performance in this mode of operation can be extremely good, reaching sub-kHz RF linewidth in the electrical signal associated with the mode-locking repetition rate [11, 12]. Alternatively, under active mode-locking operation, the optical pulses are synchronized to an external RF reference at the mode-locked frequency of the device (or subharmonics). In this case, the pulsed signal can exhibit the phase noise performance of the external reference that could be in the Hz range [13].

It should be noticed that the electrical noise spectra of the beat signal generated under active and passive operation are essentially different. In passive operation, the timing jitter fluctuation appears as a non-stationary process that is unbounded as the spacing between pulses becomes greater, leading to a noise spectra that fits to a curve between Lorentzian and Gaussian depending on the device characteristics. The timing jitter fluctuation associated to active mode-locking is a stationary process, which is externally restored with the RF reference that keep this timing jitter bounded to a value that remains constant independently of the separation between pulses. This is translated to the noise spectrum as a narrow spike (determined by the external reference, i.e. the timing jitter bound) on top of a shape similar to the one that appears in the passive operation [14].

The device used in this work is a Passively Mode-Locked Laser Diode (PMLLD) that has a two contact structure comprised of a SA section of 85 µm length and a gain section of 3915 µm length. The active region contains one InGaAsP/AlGaInAs Quantum Well (QW) emitting at a central wavelength of 1518 nm. Longitudinal confinement of the optical field is achieved by the formation of a 2 µm width ridge waveguide structure. The facet at the absorber end is HR coated (95% reflection) and the output facet is as cleaved [11].

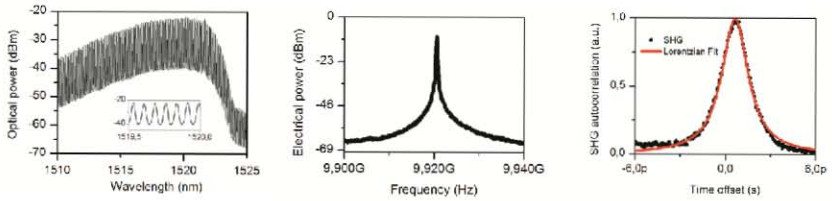

Fig. 1. Optical spectrum (left) and detailed optical spectrum (left inset); electrical spectrum of the fundamental mode-locked frequency (center); and SHG autocorrelation trace with Lorentzian fit (right).

The operation point of the device has been chosen to be within the mode-locking region of the dynamics map of the device. This point corresponds to a current of 115 mA in the gain section and a voltage value of –2.6 V for the SA section. In Fig. 1 the behavior of the device under these conditions is shown. In the leftmost figure the optical spectrum of the device is represented, which exhibits an optical bandwidth of 3 nm (~390 GHz) at 3 dB and 10 nm (~1.3 THz) at 10 dB. The inset details the frequency separation between optical modes (~10 GHz). In Fig. 1 (center) the fundamental beat signal associated with the repetition rate of the device (f_{ML} = 9.92 GHz) is represented, while the rightmost graph of Fig. 1 contains the Second Harmonic Generation (SHG) autocorrelation trace and its Lorentzian fit. The decorrelated temporal pulses of the device feature a temporal Full Width at Half Maximum (FWHM) of 1 ps, thus having a Time-Bandwidth Product (TBP) equal to 0.39.

3. Continuous wave sub-THz photonic synthesis setup

The experimental setup of the CW sub-THz photonic synthesis scheme [9] is shown in Fig. 2. The output of the PMLLD, which is placed in a probe station, is coupled using a lensed fiber that is followed by an optical isolator (ISO1) to prevent back reflections to the device. At this point, 10% of the signal is coupled out for power monitoring purposes (C1), while the rest is optically amplified using an Erbium Doped Fiber Amplifier (EDFA1) after which it is divided in two filtering branches (C2). Each filtering branch allows independent filtering of a selected optical mode of the OFCG through the use of a high Finesse Fabry Perot Tunable fiber Filter (FPTF1-2) that exhibits a 3-dB bandwidth of 6.5 GHz at 1520 nm. An optical isolator (ISO2-3) is also used at each filter output to prevent reflections. Then, both filtering branches are coupled (C3) to obtain a signal containing the two filtered optical modes with a frequency difference equal to the desired CW sub-THz signal. This signal is amplified again with an EDFA (EDFA2) and filtered using a wider bandwidth (130 GHz) tunable optical band pass filter (TF) for ASE suppression in the region outside the bandwidth of interest. After that, a 99:1 optical coupler (C4) allows the monitoring with an Optical Spectrum Analyzer (OSA) of the signal to be photomixed in a fast photodiode (PD, 50 GHz 3-dB bandwidth). Finally, the electrical signal generated in the photodiode with a frequency equal to the difference between the two optical modes is observed in an Electrical Spectrum Analyzer (ESA).

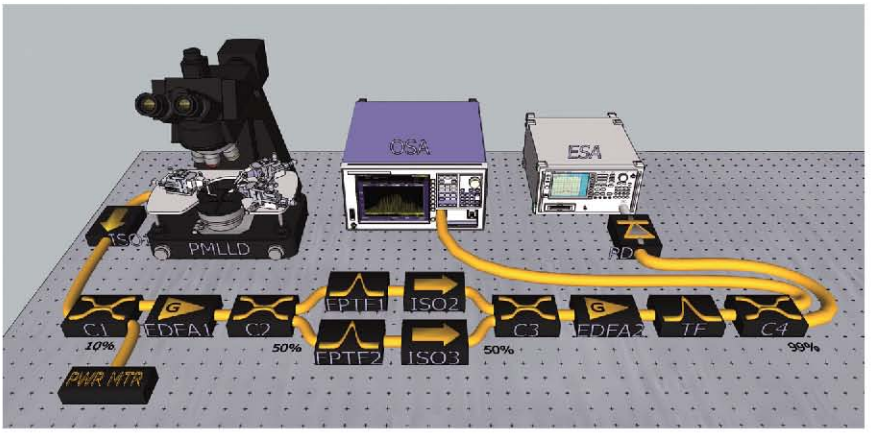

Fig. 2. CW Sub-THz Photonic Synthesis setup. See text for details.

The operation wavelength of the setup around the 1550 nm range allows taking advantage of high performance COTS telecom fiber components. This approach has potential for integration as a Photonic Integrated Circuit (PIC) [4] for a future monolithic implementation of the setup based on the basic building blocks defined on current generic foundry platforms providing active/passive integration [5]. Based on these building blocks, the mode locked source can be implemented in a ring laser structure, while multiple options are available for the optical filters (from rings to array waveguide gratings) and the couplers (from Y-couplers to multimode interference couplers).

4. Experimental results

4.1 Direct harmonic generation

The most straightforward way of obtaining a mm-wave with an OFCG is the direct harmonic generation, where all the optical modes of the OFCG are photomixed directly generating an electrical comb signal that contains all the harmonics of the fundamental frequency ($N \cdot f_{ML}$, being N the harmonic number). The characteristics of a signal generated this way are well known [13, 14], and for that reason a directly harmonic-generated signal will serve us as a

reference to evaluate the performance of the photonically synthesized electrical signals with our setup.

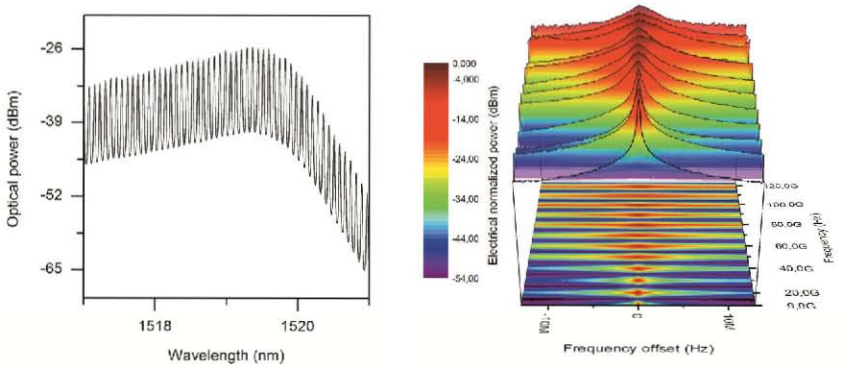

Fig. 3. Direct harmonic generation. Optical spectrum (left) before photomixing, and the generated electrical spectrum after photomixing (right, RBW = 30 kHz), observed at all the harmonics frequencies (fundamental frequency of the PMLL is f_{ML} = 9.92 GHz).

In Fig. 3 (left) the optical spectrum that is photomixed for direct harmonic generation is depicted. This optical spectrum (PMLLD spectrum without mode filtering) generates an electrical signal containing all the harmonics frequencies (Fig. 3, right). The electrical power of the represented electrical spectra is peak normalized. Nevertheless, the reduction in dynamic range given by both the losses of the measurement scheme and the decreasing peak power as the frequency increases can be seen in Fig. 3 (right).

4.2 Photonic synthesis of CW sub-THz signals

The spectra of the photonically synthesized signals using the setup from Fig. 2 are shown in Fig. 4. In Fig. 4 (left) it is depicted the selected optical modes employed to synthesize each of the electrical signals represented in Fig. 4 (right). It can be seen that only two optical modes with a frequency separation equal to the desired electrical signal are present in each optical spectrum before detection due to the high selective filtering employed in the setup, which allows to achieve a Side-Supression Ratio (SSR) of ~11 dB. These optical spectra generate the corresponding electrical signals appearing in Fig. 4 (right) after photomixing, each of them containing only the frequency represented in the graph, i.e., the required synthesized RF signal. Values for the peak power of the electrical signals of Fig. 4 (corrected for harmonic mixers losses when they are used) as well as the measured noise floor at each synthesized frequency are represented in Fig. 5.

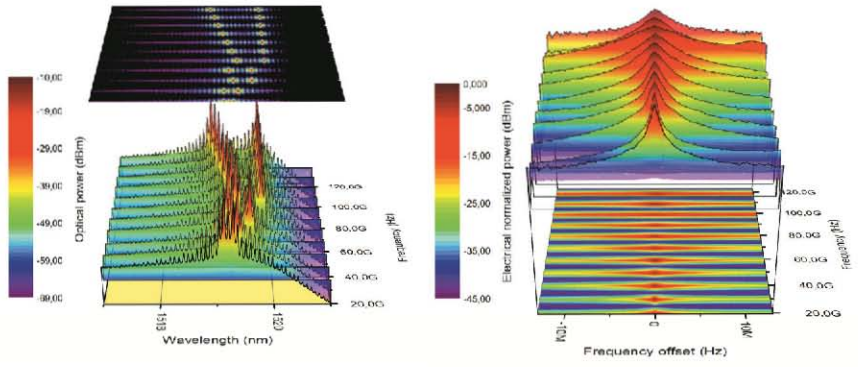

Fig. 4. Photonic synthesis. Optical spectra (left) before photomixing, and the corresponding generated electrical spectra after photomixing (right, RBW = 30 kHz)) for signals between 20 GHz and 119 GHz.

At this point it is important to note that the optical power introduced into the photodiode for the photonic synthesis setup contains only the optical power associated to the two modes separated by the desired frequency. This translates into an optimized use of the optical to electrical conversion compared to direct harmonic generation, where the complete optical spectrum enters the detector to generate an electrical signal that contains power related to all harmonic frequencies. This is important as the maximum output power of the generated electrical signals is limited by the maximum optical input power of the photomixing device, which is low for any photomixing device, but it is better for photodiodes than for photoconductors, especially for improved photodiode structures like Travelling Wave photodiodes (TW PD) or Uni-Travelling-Carrier photodiodes (UTC PD) [15]. So, this scheme allows an optimized use of the available photodetector RF output power.

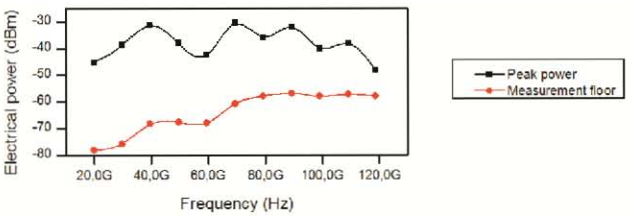

Fig. 5. Electrical peak power (black squares) and measurement floor (red circles) of the electrical signals synthesized with our CW THz photonic synthesis setup.

We should note that the maximum frequency of the synthesized signals is limited both by the bandwidth of the OFCG (1.3 THz of 10-dB bandwidth for our OFCG) and by the photodiode bandwidth. The photodiode used in this experiment has a maximum optical input power of 20 mW and a 3-dB bandwidth of 50 GHz and it is clearly limiting the performance above 100 GHz regardless the high bandwidth available associated to our OFCG. However, state of the art detectors can reach values up to 1 THz in the case of UTC PDs [7] and Travelling Wave Uni-Travelling-Carrier photodiodes (TW-UTC PD) [15]. Hence, the proposed scheme can be readily scaled to synthesize higher RF frequencies. Regarding the frequency resolution of the signals the system can synthesize, there are stabilization techniques, as optical injection, that could offer tuning of the mode-locked frequency up to 270 MHz [16]. This could be the subject for future studies, but it lays beyond the scope of the present work.

4.3 Electrical linewidth reduction of the synthesized signals

Once the generation of sub-THz signals using both direct harmonic generation and photonic synthesis is accomplished, we proceed to evaluate the phase noise characteristics of the synthesized signals using as a reference the directly harmonic generated signals. This analysis is done using the 3-dB and 10-dB electrical bandwidth. The losses introduced by the 50 GHz-bandwidth photodiode and the harmonic mixers of the ESA at higher frequencies result in measurements with very limited dynamic range at high frequencies, i.e. ~10 dB for 120 GHz, as it can be seen in Fig. 5. This makes the comparison using the Single Side-Band (SSB) noise unfair when comparing across all the required frequency range (20-120 GHz), being this the reason to establish the 3-dB and 10-dB bandwidths as parameters for comparison. The optical amplification stages are the same in both direct harmonic generation (all optical modes) and photonic synthesis (two optical modes) in order to have the same phase noise contribution given by the optical amplifiers, in case it exists. The optical spectrum of the all-modes signal is optically attenuated before photomixing to obtain an electrical signal with a similar power in the frequency of interest for both cases. This allows us to have the same dynamic range in the electrical signals that are compared thus allowing a fair comparison in terms of phase noise and electrical linewidth.

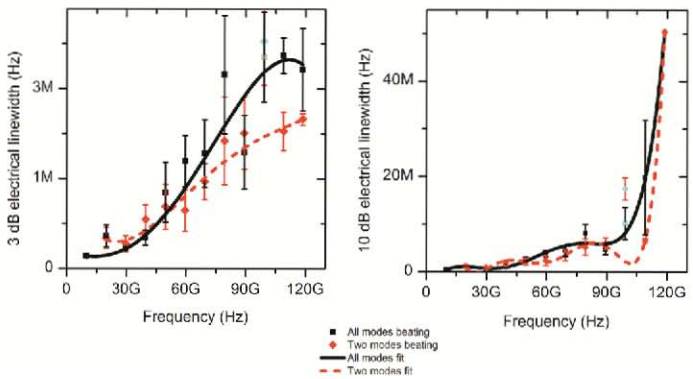

Fig. 6. Comparison between all-modes-beating and two-mode-beating of the 3-dB linewidth (left) and the 10-dB linewidth (right).

The electrical linewidths of the generated electrical signals are represented in Fig. 6. It can be seen for both 3-dB (left) and 10-dB (right) figures that the electrical linewidth of the synthesized signals generated filtering two optical modes is very close to that of the signals generated using all optical modes for frequencies below 50 GHz. For frequencies greater than 50 GHz, the linewidths related with the photonic synthesis using two modes begin to be smaller than those related to direct harmonic generation, and this difference between them seems to increase as the frequency of the synthesized signal gets higher, reaching a 25% reduction for the maximum frequency synthesized (120 GHz) and exhibiting a reduction of 35% for 110 GHz.

The experimental results suggest that under passive mode-locking regime, the photomixing of a greater number of modes may lead to an eventual degradation in the phase noise performance compared to just two-mode beating because of the unbounded behavior of the timing jitter fluctuations under passive operation which follow a random walk trend [14], and whose addition could worsen the total timing jitter and thus the phase noise. This is just opposite to the expected in the active case, where the contribution of more modes should improve the phase noise of the generated signals [17], as the timing jitter fluctuations are always bounded by an external reference [14].

The trend of this reduction is not followed by the signals generated at 99 GHz, what can be caused by an anomalous behavior of the device at this point, generating an additional spurious signal separated ~1MHz, as represented in the right graphs of Fig. 3 and Fig. 4. It must be noticed also that the comparison for the 119 GHz signals is significantly affected by the dynamic range of the measurement scheme at this frequency (~10 dB, see Fig. 5) resulting in a broader 10-dB linewidth for the synthesized signal that does not follow the trend observed before this point.

Finally, it is important to remark that the amplitude jitter associated to possible drifts of the central frequency of the FPTFs will have no significant contribution to the SSB noise, even in the case of strong amplitude fluctuations. Under passive mode-locking operation, the SSB noise is expected to be basically caused only by the timing jitter as demonstrated in [14]. This can be considered as an advantage of our setup over more complex systems that rely on OPLL for sub-THz signal generation where phase instabilities in the loop are directly translated to timing jitter and therefore to SSB noise.

5. Conclusions

A compact and straightforward setup for Continuous Wave (CW) sub-THz photonic synthesis has been implemented and experimentally studied. The scheme proposed is based on the selective filtering of longitudinal optical modes from a Passively Mode-Locked Laser Diode (PMLLD), which acts as an Optical Frequency Comb Generator (OFCG), and their photomixing in a fast photodiode with the objective of studying the phase noise characteristics of the generated signal. In order to do this, the synthesized signal has been compared to the signal generated after the mixing of all the optical modes of the OFCG, whose characteristics are well known. This scheme does not need an Optical Phase Lock Loop (OPLL), as it is based on the use of a PMLLD as OFCG, which in addition does not need any RF signal or phase modulation. Hence, this scheme is cost-effective and potentially integrated as a PIC based on the current basic building blocks that are made available on generic foundry platforms.

Photonic synthesis of CW electrical signals up to 120 GHz using a 50GHz photodiode has been experimentally achieved using this scheme. The phase noise performance it exhibits, based on the evaluation of the 3-dB and 10-dB electrical linewidths, has been analyzed for the synthesized signals taking as a reference the electrical signals obtained with direct harmonic generation. No significant differences have been observed below 50 GHz, but from this frequency onwards, it can be appreciated a linewidth reduction trend that becomes greater as the frequency increases, reaching reductions of 35% at 110 GHz and 25% at 120 GHz.

The reported phase noise improvement of CW sub-THz signals synthesized with this setup along with its integration potential, cost and bandwidth capabilities make it a promising candidate to the development of an integrated and high performance local oscillator in the sub-THz range.

Acknowledgments

Work supported by the Spanish Ministry of Science and Technology through the project TEC2009-14525-C02-02 and by the European Commission FP7 iPHOS Project. The work by A.R. Criado has been supported by the Spanish Ministry of Science and Technology under the FPI Program, Grant# BES2010-030290.

3

IEEE/OSA, Journal of Lightwave Technology (published 10/2012)

Selected publication 3	
Citation	**A. R. Criado**, C. de Dios, P. Acedo, G. Carpintero, and K. Yvind, "Comparison of Monolithic Optical Frequency Comb Generators Based on Passively Mode-Locked Lasers for Continuous Wave mm-Wave and Sub-THz Generation," Journal of Lightwave Technology, vol. 30, no. 19, pp. 3133–3141, Oct. 2012.
JCR impact factor	2.784
Submitted	04/05/ 2012
Published	01/10/2012
Comments	Copyright (c) 2012 IEEE. Personal use of this material is permitted. However, permission to use this material for any other purposes must be obtained from the IEEE by sending a request to pubs-permissions@ieee.org.

Table VI-3 Selected publication 3. Summary of publication information

CHAPTER VI

Comparison of Monolithic Optical Frequency Comb Generators based on Passively Mode-Locked Lasers for Continuous Wave mm-Wave and sub-THz generation

A.R. Criado, *Student Member, IEEE*, C. de Dios, P. Acedo, *Member, IEEE*, G. Carpintero, *Member, IEEE* and K. Yvind

***Abstract*—. In this paper, two different Passive Mode-Locked Laser Diodes (PMLLD) structures, a Fabry-Perot cavity and a ring cavity laser are characterized and evaluated as monolithic Optical Frequency Comb Generators (OFCG) for CW sub-THz generation. An extensive characterization of the devices under study is carried out based on an automated measurement system that systematically evaluates the dynamic characteristics of the devices, focusing on the figures of merit that define the optimum performance of a pulsed laser source when considered as an OFCG. Sub-THz signals generated with both devices at 60 GHz and 90 GHz are presented and analyzed in terms of electrical linewidth to compare such components for mm-Wave and sub-THz photonic generation. This work offers a systematic comparison of PMLLD devices for OFCG operation and provides reference information of the performance of two different device topologies that can be used for the implementation of photonic integrated sub-THz CW generation.**

***Index Terms*— mm-wave and THz photonic synthesis, optical filtering, Optical Frequency Comb, optical heterodyne photomixing, passively mode-locked lasers.**

I. Introduction

During the last decade, there has been a great research effort centered in the development of suitable generation and detection technologies to satisfy the needs of the frequency region known as the "THz gap" [1, 2]. This is mainly because of the great number of potential applications identified in this region, namely, imaging for security [3, 4] or biomedicine [5], spectroscopy [6] or short-range high data rate communications [7], among others. For some of them, even commercial room-temperature solutions for generation and/or detection are already available.

Nevertheless, there exists yet an important and increasingly need for even more compact, low cost and versatile solutions [8] that would allow complete exploitation of the THz domain with a more affordable technology This next generation of THz technology should be also energy-efficient, following the trend of all technology development nowadays, where the power consumption has become one of the main concerns [9, 10].

The Research and Development of technology for the THz region is being accomplished from two main approaches. The first one aims to push the frequency limits of electronic devices to cover the sub-THz and THz regions [11], while the second one is based on the downconversion from the optical domain [12]. Several schemes and technologies have been proposed and developed in the last years following both trends, but in terms of potential integration, compactness, performance and cost-effectiveness, which are the requirements for the next generation of THz technology; the main candidates nowadays are Resonant Tunneling Diodes (RTDs) for the electronic approach [13], and optical heterodyning using two optical frequencies for the photonic technology [14]. Both present advantages and disadvantages with respect to each other, but the optical heterodyning appears as a good candidate mainly because of two key aspects: a higher available bandwidth, both in generation [14] and detection [15]; and the integration potential as Photonic Integrated Circuit (PICs) using generic foundry platforms already available [16, 17].

Optical heterodyning relies on the combination in a photomixer device of two optical frequencies to generate an electrical signal with a frequency equal to the frequency spacing between both optical modes [14]. This electrical frequency must be within the bandwidth of the photomixer to properly achieve generation (highest output power). Suitable photomixer devices include Photoconductive Antennas (PCA) [15], Uni-Travelling-Carrier Photodiodes (UTC-PD) [18], Travelling-Wave Uni-Travelling-Carrier Photodiodes (TW-UTC-PD) [19] or n-i-pn-i-p superlattice photomixers [20]. The

Manuscript received May 4, 2012. Work supported by the Spanish Ministry of Science and Technology through the project TEC2009-14525-C02-02. The work by A.R. Criado has been supported by the Spanish Ministry of Science and Technology under the FPI Program, Grant# BES2010-030290.

A. R. Criado, C. de Dios P. Acedo and G. Carpintero are with the Electronics Technology Department, Universidad Carlos III de Madrid, Leganés, Madrid 28911 Spain (e-mail: acriado@ing.uc3m.es).

K. Yvind is with DTU Fotonik, Department of Photonics Engineering, Technical University of Denmark, Ørsteds Plads 343, 2800-Kgs. Lyngby, Denmark

two optical frequencies can be provided by two different sources (lasers) or by a single optical source. When two sources are used, continuous tunability is provided, but to obtain good phase noise characteristics of the generated signal complex Optical Phase Locked Loops (OPLL) are needed to correlate the noise from both sources and attain a stable THz signal. In the case of using one source, this can be a dual-mode structure [21], where very limited tunability is offered, or a multimode optical source (Optical Frequency Combs), where discrete tunability (multiples of the fundamental repetition frequency) is provided using high selective optical filtering [22] or Optical Injection Locking (OIL) [23] to select two modes from the optical spectrum. As the optical modes used for the THz signal generation are phase-locked and a narrow optical linewidth can be used, extremely low noise and narrow THz signals can be generated. Because of this, multimode sources are preferred for the development of high performance and compact THz generation technology.

Typical multimode sources are based on Optical Frequency Comb Generators (OFCG) implemented as benchtop devices using phase modulators, non-linear fibers, RF generators and other external devices [18, 23, 24]. Nevertheless there are other devices, with much higher integration potential, that can be used as OFCG as are Mode-Locked Laser Diodes (MLLD) [22] or more recently, high-Q silicon-nitride spiral resonators [25]. While the latter resonators don´t offer good phase noise characteristics and are not mature enough for integration, MLLDs are devices that can be integrated as PICs and are able to offer extremely low phase noise at less than 1 MHz offset from the carrier both under passive [26] regime and specially under active or hybrid regime [26]. Another advantage they offer is that the influence of mode partition noise is negligible because of the strong coherence that exists among the longitudinal modes emitted [27].Thus, nowadays MLLDs are largely the best option for integrated GHz-rate OFCGs. Potential applications of these OFCG would include integrated systems requiring a fixed mm-wave carrier, as it is the case of automotive radars [28]; LO for integrated heterodyne receivers in the mm-wave and sub-THz region [29] or integrated OFCG for metrology [30].

When dealing with photonic generation of mm-wave and sub-THz signals, one of the fundamental parameter that has to be taken into account is Phase Noise. The electrical phase noise performance and linewidth of the sub-THz signals generated by Actively Mode-Locked Laser Diode (AMLLD) or Hybrid Mode-Locked Laser Diodes (HMLLD) are inherited from the external RF reference used, that acts as a restoring force of the timing fluctuations, thus achieving extremely low phase noise and linewidths in the Hz range [26, 31]. In the case of Passively Mode-Locked Laser Diodes (PMLLD), also low noise performance is achieved, with linewidths below 1 kHz [26], but not as good as in the case of AMLLD or HMLLD [26, 32]. However, as no external RF reference is needed in the case of PMLLDs, just DC bias current for the gain section and DC reverse bias voltage for the saturable absorber, they make up a complete monolithic OFCG that in addition offers a dramatically reduction of power consumption, being the most efficient OFCG in terms of energy saving. In this sense, PMLLDs used as OFCG are great candidates for the development of the next generation of photonic THz transmitters technology that should be able to provide high performance and energy efficiency in an integrated and cost effective device.

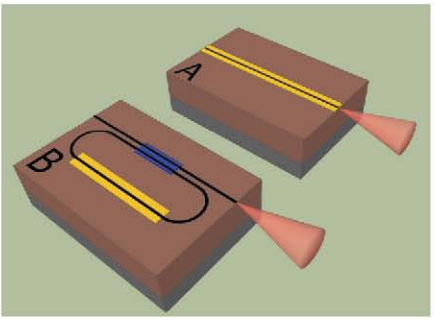

Fig. 1. Schematic view of a Fabry-Perot laser cavity (A), and ring laser cavity (B). Yellow: gain regions and saturable absorbers; black: optical waveguides; blue: MMI optical coupler.

The monolithic integration of PMLLD is a mature and fruitful field of study. The architecture most commonly considered is based on a travelling wave Fabry-Perot cavity (Fig. 1, A). In its simpler configuration, a Fabry-Perot PMLLD includes a gain section and an absorber section, though more complex and advanced structures have also been reported. Quantum Well, Quantum Dot and Quantum Dash mode-locked lasers have been manufactured using this design. As an alternative to those, monolithic devices based on ring cavity structures are being developed (Fig. 1, B). They provide with two important advantages over Fabry-Perot cavities. First, the length of the cavity can be more accurately controlled; and second, its output is coupled to a Multimode Interference (MMI) coupler also integrated in the substrate, allowing higher integration potential in PIC devices.

In this paper, and with the objective of experimentally identifying the optimum PMLLD structure for sub-THz integrated photonic generation, two different structures, a Fabry-Perot cavity (FP) PMLLD and a ring cavity PMLLD, are characterized and evaluated as monolithic OFCG for CW sub-THz generation. Both structures share the same material technology (InP) and are based on Quantum Well (QW) active regions. Systematic comparison of different operation parameters for both PMLLD devices is carried out to characterize them for optimum OFCG operation.

Generation of sub-THz signals using both devices at ~60 GHz and ~90 GHz is accomplished with the help of a photonic synthesis scheme based on the optical filtering of two modes

from a multimode source and its photomixing in a high bandwidth photodiode [22]. The synthesized signals are evaluated in terms of electrical linewidth and compared to the reference information of the two different PMLLD topologies. The methodology described in this paper as well as the results on the comparison of both devices can be used to optimize PMLLD structures for the implementation of integrated sub-THz CW photonic generators.

II. Characterization of Monolithic Optical Frequency Comb Generators based on Passively Mode-Locked Lasers

A. Description of the devices

The two PMLLDs structures that are to be evaluated in this work are represented in Fig. 1. As previously mentioned, the study will be centered only in PMLLDs given their potential features for the integration of CW THz transmitters. Both are Quantum Well (QW) based devices. The first one has Fabry-Perot cavity (Fig. 1 A) with a fundamental frequency set by the cavity round-trip time of f_A=9.92 GHz (Device A, Fig. 2 top). The second one features a ring cavity structure (Fig. 1 B) whose length gives a repetition rate of f_B=14.99 GHz (Device B, Fig. 2 bottom).

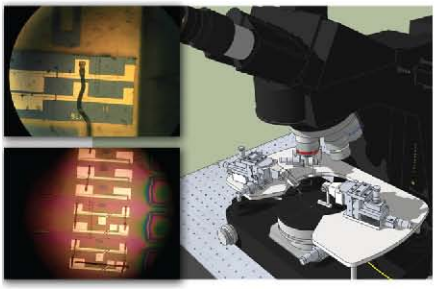

Fig. 2. Picture of the chips containing the devices under test. PMLLD A (top) and PMLLD B (bottom) and their placement on the probe station.

The device A is a PMLLD that has been previously described in [33]. It has a two contact structure comprised of a Saturable Absorber (SA) section of 85 µm length and a gain section of 3915 µm length. The active region contains one InGaAsP/AlGaInAs Quantum Well (QW) emitting at a central wavelength of 1519 nm. Longitudinal confinement of the optical field is achieved by the formation of a 2 µm width ridge waveguide structure. The facet at the absorber end is HR coated (95% reflection) and the output facet is as cleaved [33].

Device B has been fabricated on an InP technology platform based on active/passive integration [16]. The active areas of the chip consist of four strained QWs embedded in 500 nm InGaAsP (Q1.25) waveguiding layer. The passive areas are formed by selective etching and re-growth, with a 500 nm InGaAsP (Q1.25) waveguiding layer, with buttjoint coupling to the active ones. Both the active and passive layers are sandwiched between an n-doped InP substrate and a p-doped 1500 nm-thick InP cladding with a 300 nm contact layer. Shallow etching is used for the straight waveguides while the curved waveguides are deeply etched. The shallow waveguides are created by an etch depth of 100 nm into the guiding layer, having a ridge width of 2 µm. The deep etched waveguides on the other hand have a ridge width of 1.5 µm. The ring structure that was measured has a total cavity length of 5405 µm, with an active section of 750 µm length in which a 30 µm long saturable absorber is defined at its center. The resulting repetition rate of the device is f_B=14.99 GHz.

B. Characterization of the devices

In this section, a complete characterization of the two devices is presented, with emphasis on the parameters of interest for proper OFCG operation.

The experimental setup for the measurement of the devices is depicted in Fig. 3. The output of the laser is coupled to a lensed fiber followed by an optical isolator. A 10% of the signal is coupled out (Coupler1) for power monitoring, while the rest is divided by a 3-dB optical coupler (Coupler2). One of the outputs is monitored in an Optical Spectrum Analyzer (OSA). The second output is downconverted from optical to electrical domain using a high bandwidth photodiode (PD) (50 GHz 3-dB bandwidth) and monitored in an Electrical Spectrum Analyzer (ESA).

PMLLDs characterization and their qualitative analysis are presented in three steps using the data provided by the characterization platform described. The first step (1) aims for a general description of the performance of the devices based on six figures of merit (parameters) that are detailed in corresponding maps for the operational range of the devices defined by the bias current into the active region (I) and the reverse voltage in the saturable absorber (V). Then, in step (2), a detailed analysis for the optimum saturable absorber voltage (V) value obtained in step (1) is carried out. Finally, step (3), deals with the detailed characterization of the optimum V-I point for each device identified in steps (1) and (2).

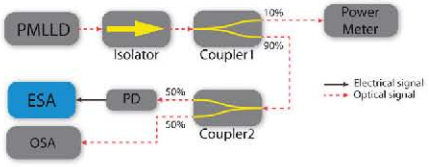

Fig. 3. Experimental setup for devices characterization.

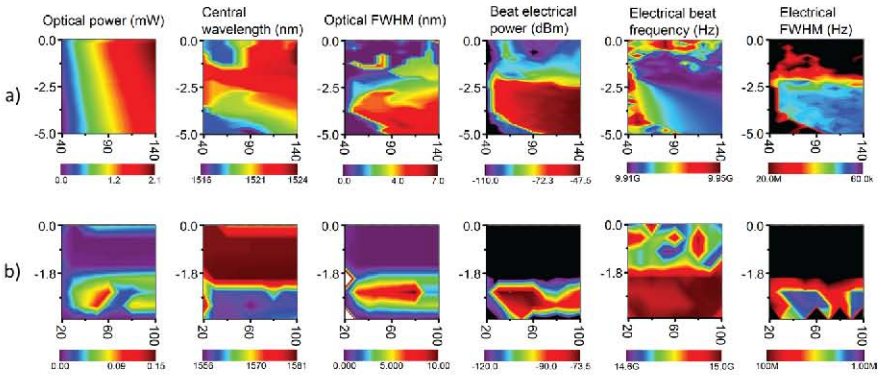

Fig. 4. V-I OFCG figure-of-merit maps for device A (top row) and device B (bottom row). Gain section current (I) is in mA (horizontal axis) and saturable absorber voltage (V) is in Volts (vertical axis). Z-axis scales: Optical power (linear), Central wavelength (linear), Optical FWHM (linear), Beat electrical power (logarithmic), Electrical beat frequency (linear), Electrical FWHM (logarithmic).

1) To proceed with the first characterization stage, the data maps for six OFCG figures of merit (parameters) are presented in Fig. 4. The measurements can be classified in two categories: optical domain characteristics and electrical domain characteristics. The optical parameters are measured using an Optical Spectrum Analyzer (OSA, Fig. 3) and those are the output optical power, the central wavelength and optical Full Width at Half Maximum (FWHM) values. The electrical domain measurements are measured using and Electrical Spectrum Analyzer (ESA, Fig. 3) connected at the output of the high speed photodiode used for detecting the optical signal from the devices. Those electrical parameters are the beat electrical power, beat electrical frequency and electrical FWHM. These six parameters are evaluated for several gain section currents (I) and saturable absorber voltages (V), within the safety limits of the devices, to obtain six maps that allow identification of the different working regions for each device (Fig. 4).

   The behavior of device A is depicted in Fig. 4a. From these results we can conclude that the behavior of the device used as OFCG improve when both current and reverse voltage increases, leading to a clear region located at the higher reverse voltage and current levels where the device offers a better performance (Fig. 4a). In the case of device B (Fig. 4b), there exists a more specific region, around -2.5 V and 50-90 mA, where the device features its best performance (i.e. higher power and optical FWHM and narrower electrical FWHM). In this case that region does not correspond to the lowest voltage and highest current values.

   The optical power output for device A reaches as much as 2 mW, increasing linearly as a function of the bias current. Device B has a much lower output power, showing a maximum of 0.1 mW for the operational region centered at 50 mA and -2.5 V. From the optical measurements, it can be seen that the threshold currents are approximately 40 mA and 20 mA for devices A and B, respectively.

   The wavelength of device A is slightly outside the telecom range (1550 nm), centered around 1520 nm, while in the case of the device B, we have two completely different regions of operation as far as for the central wavelength is concerned. Above -2 V the central wavelength is centered at 1580, while below this value, the optical spectrum "hops" into the 1556 nm region. The optical comb-like spectra reaches a FWHM value of around 6 nm (~0.8 THz) for device A, increasing as both current and reverse voltage increase; while the device B presents a FWHM value of around 9 nm (~1.2 THz) in the region below -1.8 V.

   The evolution of the electrical domain parameters evaluated follows a similar trend as the optical figures of merit. Device A presents a beat signal with a frequency around 9.92 GHz and with an electrical power that increases with current and reverse voltage. Device B has an electrical beat of a frequency around 14.99 GHz and a maximum power of -73 dBm that is observed in a small region centered over 50 mA and -2.5 V.

   With this first set of data we are able to identify the V-I operation regions where the devices will behave better as OFCGs. These regions would be the V-I region above 60 mA and below -2.5 V for PMLLD A; and above 25 mA and below -1.8 V for PMLLD B.

2) The mapping of the different figures of merit described above has allowed us to identify the optimum saturable absorber reverse voltage for both devices. Now in this second step, the saturable absorber voltages for both

devices are kept constant at the values where the previously described figures of merit present better values, this is, -4 V for PMLLD A and -2.5 V for PMLLD B. For further characterization of the devices, the above mentioned figures of merit are represented again in 2D graphs as a function of the bias current (Fig. 5) for those optimum voltage values. This gives a clearer and more comprehensive view of the performance offered by the devices at its optimum voltage point and permits the identification of the optimum bias current point.

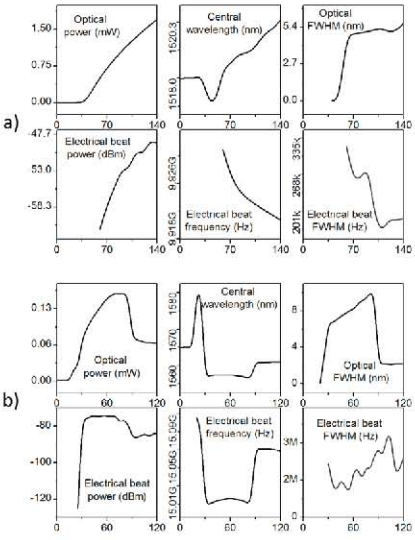

Fig. 5. Evolution of the electrical and optical figures of merit as a function of the bias current (horizontal axis, I, mA) for A and B for optimum saturable absorber voltages: -4 V and -2.5 V, respectively.

Fig. 5a presents the OFCG figures of merit for device A. It can be seen again that the optical output power has a linear dependence with the bias current after the threshold current, which has a translation in the electrical beat power that also increases with the current. In Fig. 6a the evolution with the bias current of the optical and electrical spectra are shown, where we can see a continuous tunability range between 1517.02 to 1520.4 nm for the central wavelength of the optical comb, and between 9.932 and 9.921 GHz for the beat frequency. The optical FWHM is almost constant after 70 mA within the range between 4.9 to 5.7 nm; while the electrical FWHM decreases when the current rises, to then stabilize for high current values (>100 mA), at around a minimum value of 185 kHz.

In Fig. 5b the merit figures for device B are represented. In this case, there is an increment of both optical and electrical beat power with the current below 70 mA. Above this point, the power saturates and begins to decrease, limiting the proper working region to 20-70 mA. Near this region (30-80 mA), a comb-like spectra centered at 1556 nm appears as dominant in the optical spectra, as it can be appreciated in Fig. 5b and in Fig. 6b. The beat frequency in this working range (30-80 mA) decreases to 14.99 GHz, remaining almost constant. The optical FWHM reaches 9 nm of maximum value and the electrical FWHM of the beat note has a minimum value of 1.5 MHz.

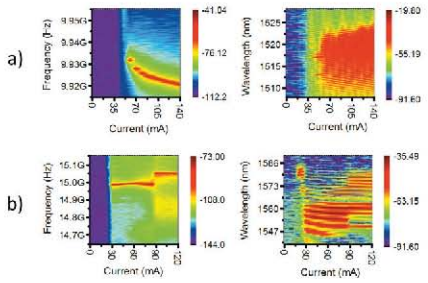

Fig. 6. Electrical and optical spectra evolution with bias current for devices A and B for optimum saturable absorber voltages: -4 V and -2.5 V, respectively. Z axis units are dBm.

3) Characterization steps 1) and 2) have allowed us to identify the optimum V-I working points for both devices that are -4V and 140 mA for device A and -2.5 V and 50 mA for device B. In this final characterization step, we proceed to fully evaluate the performance of both devices as OFCG for millimeter and sub-THz generation.

In this sense, the optical outputs from both devices at their optimum operation points are also characterized in terms of the temporal width of the generated pulses using a Second Harmonic Generation (SHG) autocorrelator. Given the low efficiency of the SHG process and the low output power of the devices, the optical output from both devices is amplified using an Erbium Doped Fiber Amplifier (EDFA) and filtered with Optical Band Pass Filters (OBPF) for ASE suppression. Due to the different emission wavelength presented by both devices, different EDFAs and optical filters had to be used to perform the measurements. The results are shown in Fig. 7. The optical spectra under these conditions and the generated electrical beat after photomixing are also displayed, along with the autocorrelation trace for comparison (Fig. 7).

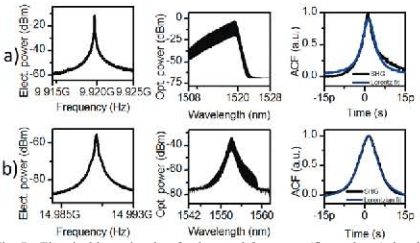

Fig. 7. Electrical beat signal at fundamental frequency (first column), band-pass filtered optical spectra (second column) and SHG autocorrelation trace (third column) for device A (a) and device B (b).

The temporal traces obtained from the fitting of the autocorrelation traces with the autocorrelation of Lorentzian functions (Fig. 7) provides temporal FWHM values of 5.8 ps for device A and 8.57 ps for device B. The values for the Time-Bandwidth Product (TBP) are computed using the bandwidth determined by the ASE suppression filtering stages and are shown in Table I. A summary on other electrical and optical characteristics of both devices in their optimum V-I point is presented in Table I. In this Table I, also the absolute higher values of both optical power and optical FWHM are included.

TABLE I
FIGURES OF MERIT. SUMMARY

PARAMETER/DEVICE	A	B
OPTIMUM V-I POINT, OPTICAL AMPLIFYING + FILTERING (FIG. 7) FIGURES OF MERIT VALUES		
Central wavelength (nm)	1520	1558
Optical FWHM (without filtering) (nm/GHz)	5.7/740	7.7/952
Optical FWHM (with filtering) (nm/GHz)	1.5/195	1/124
Beat signal frequency (Hz)	9.92G	14.99G
Electrical beat power (dBm)	-11.7	-56.6
Electrical beat FWHM (Hz)	59.1k	430k
Temporal width (ps)	5.8	8.57
TBP	1.13	1.06
NO OPTICAL AMPLIFYING, NO OPTICAL FILTERING (FIGS. 3 TO 6) ABSOLUTE BETTER VALUES OF THE FIGURES OF MERIT		
Maximum optical power (mW)	2.1	0.15
Maximum optical FWHM (nm/GHz)	6.3/814	9.1/1229

As mentioned before, these devices are planned to be used for mm-wave and sub-THz generation. To evaluate the maximum frequency that could be synthesized with both OFCG, the absolute maximum optical FWHM of the devices (Maximum optical FWHM in Table I) along with their optical FWHM in the V-I point determined as optimum (Optical FWHM (without filtering) in Table I) are shown in Fig. 8. Signals up to 814 GHz (Maximum optical FWHM of Device A in Table I) and up to 1229 GHz (Maximum optical FWHM of Device B in Table I) can be synthesized provided a sufficient bandwidth photomixer [18-20].

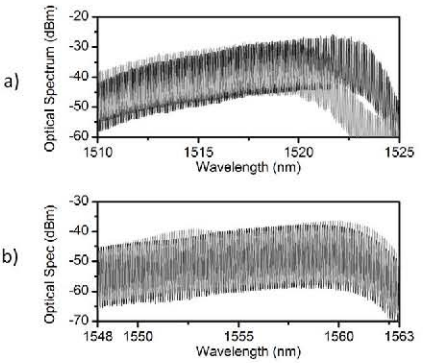

Fig. 8. Optical spectra showing the optical FWHM for the optimum V-I point (black line) and the absolute maximum optical FWHM (grey). Device A (a) and device B (b).

C. Algorithm for calculation of the Global Performance Maps of the devices as Optical Frequency Comb Generators

In the previous paragraphs we have performed a systematic and exhaustive analysis of two PMLLD to evaluate them as OFGCs for sub-THz generation that has included the evaluation of several parameters and a three steps process to identify the best operation points for them and characterize the performance of the devices for those points. This process is tedious and may take a lot of time that is not efficient when several devices of slightly different characteristics are to be evaluated.

In this sense, and with the aim to provide ourselves with a more efficient way to characterize different PMLLDs for mm-wave and sub-THz generation, we have developed an algorithm that provides directly with a Global Performance Map for the devices, in this case to evaluate their performance as OFCG. The algorithm gives a mark to each V-I point based on a criteria adapted to the actual application that will have the device. The criteria are user configurable. For the particular study presented in this work, and based on the detailed discussion described in the previous section, we are ready to define a criteria oriented to evaluate the optimum operation point of a PMLLD when considered as an OFCG. The resulting maps allow a direct and quantitative identification of the optimum V-I points for OFCG operation. Furthermore, the mark values can be referred to a common reference scale, allowing us to evaluate PMLLDs with different characteristics (i.e. gain regions, cavity structures). This provides us with a useful, fair and accurate comparison indicator across devices with different characteristics.

From the different figures of merit evaluated above, the Global Performance (GP) Indicator, i.e. the mark value assigned to each V-I point, is calculated as follows:

$$GP_i = \prod_j \left\{ \frac{MF_{ij} - \min\left(mMF_j\right)}{\max\left(MMF_j\right) - \min\left(mMF_j\right)} \right\}^{w_j} \quad (1)$$

where:

$$mMF_j = \left\{ \min\left(MF_{ij}\right) \right\}_{i=1}^{N} \quad (2)$$

$$MMF_j = \left\{ \max\left(MF_{ij}\right) \right\}_{i=1}^{N} \quad (3)$$

This is, the Global Performance indicator (GP_i) for a device i is computed as the product of all its figures of merit described above ($MF_{i,j}$), where each one is normalized between the minimum (2) and the maximum (3) figure of merit values for all the compared devices. An exponential weighting factor (w_j) is applied to each figure of merit normalized this way. The absolute value for this weighting factor accounts for the relevance of that figure for the intended application (OFCG in this case), and the sign discriminates if a higher value of the figure is preferred (positive sign) or a lower value is preferred (negative), as it is the case of the electrical FWHM for OFCG application. A product has been chosen instead of a sum to have a sharper identification of different performance areas.

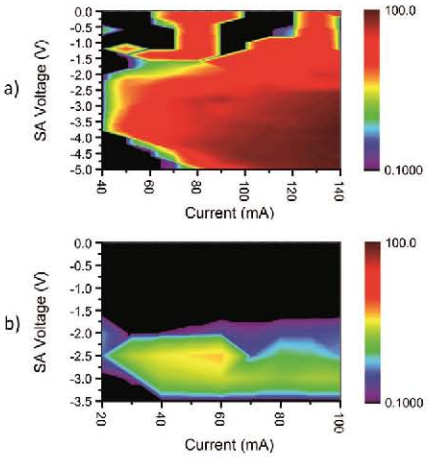

Fig. 9. OFCG performance maps for PMLLD A (a) and PMLLD B (b) using the same reference scale (logarithmic scale).

For this analysis, a w value of 1 has been chosen for optical power, electrical power and optical FWHM. Both, beat frequency and central wavelength, have been assigned with a weight of 0 (i.e. not relevant), while the electrical FWHM has a weight of -1.

The GP indicators for both devices under study, normalized to a common scale between 0 and 100, are presented in Fig. 9 in a logarithmic scale. Device A obtains a much better performance mark in this case, mainly because of the better electrical FWHM and especially because of the optical and electrical power that is able to deliver. It must be noted that if a higher weight is assigned to the optical span, which would be another possible scenario for the evaluation of an OFCG, device B would have a much higher mark, given the wide optical span it is able to provide (up to 1.2 THz).

III. Sub-THz Continuous Wave signals generation with Monolithic Optical Frequency Comb Generators based on Passively Mode-Locked Lasers

As mentioned in the introduction, the final objective of this work is to propose a systematic way to evaluate different PMLLD to be used as OFCG for mm-wave and sub-THz generation comparing two different PMLLD structures using a proposed Global Performance map. In this sense, the final step of this work must be the use of such devices for CW sub-THz photonic generation employing them as OFCG in an optical heterodyning scheme, and to compare the actual characteristics of the synthesized signals (quality) with the outcomes from the previous analysis.

As stated in the introduction, a PMLLD is suitable to be used as OFCG in any optical heterodyning setup based on the photomixing of two longitudinal modes from a multimode source, like those described on [18, 22, 23]. For the analysis presented here, the scheme reported in [22] based on optical filtering is used. In this case, the selection of the optical modes from the OFCG for sub-THz signal generation is attained by using high selectivity Fabry-Perot Tunable Fiber Filters while the photomixing is accomplished using a high bandwidth photodiode (50 GHz 3-dB bandwidth). Optical amplification with two EDFAs is used to have an optical power at the input of the photodiode equal to its maximum average optical input power (13 dBm). In this case the employed photomixer is the limiting factor because of its 50-GHz bandwidth and thus the analysis will be restricted to the synthesis of CW signals at ~60 and ~90 GHz. Nevertheless, the results at those mm-wave frequencies will be sufficient for the study of the electrical linewidth and spectral shape of the synthesized signals, and to determine the differences between the signals produced from both PMLLDs.

The bias conditions for the PMLLDs correspond to the optimum working points identified in the analysis from section II, this is, -4V and 140 mA for device A, and -2.5 V and 50 mA for device B. In Fig. 10, the optical spectra after the high selectivity filtering stage to select the longitudinal optical modes from the OFCG before photomixing, are represented. The optical spectrum corresponding to device A is depicted in black, while that from device B is presented in grey. For both devices the beating of the optical spectra displayed in solid trace will generate the ~60 GHz CW signal in the photodiode; and the spectra in dashed trace, the ~90 GHz CW signal. More

specifically, the generated frequencies will correspond to $n \cdot f_i$, where n is the number of modes of separation between the selected longitudinal modes, and f_i the fundamental frequency associated to each device (59.52 GHz and 89.28 GHz for device A; 59.96 GHz and 89.94 GHz for device B). The Side Mode Suppression Ratio (SMSR) for device A is around 12 dB and increases up to almost 20 dB for device B because of the higher frequency spacing.

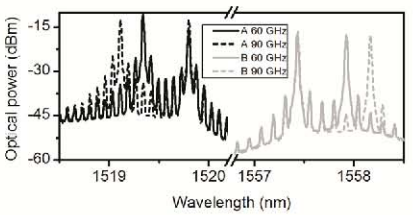

Fig. 10. Filtered optical spectra with the selected longitudinal optical modes for the generation of the sub-THz CW signal.

In Fig. 11, the normalized sub-THz signals synthesized with both monolithic OFCGs at ~60 and ~90 GHz are represented. The measurements are limited by the low power of the generated signals and especially by the low dynamic range of the measurement system mainly caused by the conversion losses of the harmonic mixers employed for the downconversion as well as the operation beyond the bandwidth of the photodiode. For device A, the electrical output powers corrected for the losses of the harmonic mixers are -42 dBm and -35 dBm for 60 GHz and 90 GHz, respectively. The signals generated with device B have an electrical power of -61 dBm (60 GHz) and -68 dBm (90 GHz).

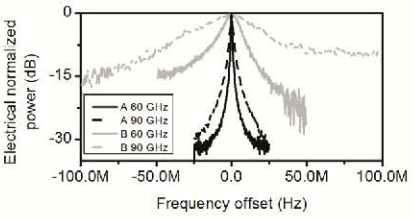

Fig. 11. Electrical spectra of the sub-THz CW signals generated after photomixing the optical spectra in Fig. 9 in a photomixer

The differences in the dynamic range for the different measurements has as a consequence that a fair comparison of the electrical performance should be based on the electrical linewidth rather than on the SSB noise [22]. Accordingly, the analysis of the performance of the photonically synthesized signals will be based mainly in the electrical FWHM. From the results of Fig. 11 we can see that device A provides a much narrower linewidth, performing a FWHM of 843 kHz at 60 GHz and 1.96 MHz 90 GHz. For its part, the sub-THz signals synthesized with device B present 10.5 MHz at 60 GHz and 32.2 MHz at 90 GHz. The increment in the linewidth as the frequency increases is within the expected range for a PMLLD [32].

Again, it must be noted that the maximum frequency of the synthesized signals is limited both by the bandwidth of the OFCGs (around 800 GHz and 1.2 THz of 3-dB bandwidth for our OFCG A and B, respectively) and by the photomixer bandwidth. The photodiode used in this experiment has a maximum optical input power of 20 mW and a 3-dB bandwidth of 50 GHz and it is clearly limiting the performance above 90 GHz regardless the high bandwidth available associated to our OFCGs. However, as previously mentioned, state of the art photomixers can reach values up to 1 THz in the case of Uni-Travelling-Carrier Photodiodes (UTC-PD) [18], Travelling-Wave Uni-Travelling-Carrier Photodiodes (TW-UTC-PD) [19] or n-i-pn-i-p superlattice photomixers [20]. Hence, the proposed scheme can be readily scaled to synthesize higher frequencies.

These results regarding the sub-THz CW photonic synthesis agree well with the systematic analysis and comparison presented in section II, and especially with the use of the defined GP indicators to evaluate the performance of PMLLD as OFCG for sub-THz signal synthesis when used in an optical heterodyning setup based in multimode source for CW sub-THz generation.

IV. Conclusion

This work provides with reference information of the performance of two different PMLLD topologies that can be used for the implementation of the next generation of integrated sub-THz CW photonic generation technology based on PICs. With this aim, two different PMLLDs are characterized and evaluated as monolithic OFCG for CW sub-THz generation.

Firstly, an exhaustive characterization and analysis of both devices is carried out. It is focused in the figures of merit of an OFCG. A specific characterization platform has been implemented for this, providing all the measurement data and computing a Global Performance (GP) map for each device that allows a direct identification of the optimum working points for an specific application (in this case OFCG), based on a quantitative analysis whose criteria is user configurable. The algorithm computes the GP indicator referred to a common scale for all the devices under study, allowing a fair an accurate comparison between devices with different characteristics.

Secondly, the devices have been employed in a sub-THz CW photonic synthesis scheme for the generation of signals at ~60 GHz and ~90 GHz. This allows validating the application of this kind of devices for sub-THz generation. The signals are

analyzed and evaluated in terms of electrical linewidth and the results for both devices serve us to validate the Global Performance predicted in the first part and validate the proposed systematic analysis and comparison between devices.

Device A, which has a one-QW straight Fabry Perot cavity, gets a better overall performance, and provides with narrower linewidth sub-THz synthesized signals than device B, which features a four-QW ring cavity. Nevertheless there are two important points where device B provides better features: the maximum optical span it can offer (up to 1.2 THz), and the advantages given by its cavity design (much higher integration potential in a PIC and more accurate fabrication of the cavity length).

ACKNOWLEDGMENT

We acknowledge COBRA Research Institute, Eindhoven University of Technology, the Netherlands for the fabrication of the ring lasers within the joint European platform for InP-based components and circuits, JePPIX.

REFERENCES

[1] P. H. Siegel, "Terahertz technology," Microwave Theory and Techniques, IEEE Transactions on, vol. 50, pp. 910-928, 2002.

[2] M. Tonouchi, "Cutting-edge terahertz technology," Nat Photon, vol. 1, pp. 97-105, 2007.

[3] C. Jansen, S. Wietzke, O. Peters, M. Scheller, N. Vieweg, M. Salhi, N. Krumbholz, C. Jördens, T. Hochrein, and M. Koch, "Terahertz imaging: applications and perspectives," Appl. Opt., vol. 49, pp. E48-E57, 2010.

[4] W. R. Tribe, D. A. Newnham, P. F. Taday, and M. C. Kemp, "Hidden object detection: security applications of terahertz technology," San Jose, CA, USA, 2004, pp. 168-176.

[5] P. H. Siegel, "Terahertz technology in biology and medicine," Microwave Theory and Techniques, IEEE Transactions on, vol. 52, pp. 2438-2447, 2004.

[6] P. F. Taday, "Applications of terahertz spectroscopy to pharmaceutical sciences," Philosophical Transactions of the Royal Society of London. Series A: Mathematical, Physical and Engineering Sciences, vol. 362, pp. 351-364, February 15, 2004 2004.

[7] R. Piesiewicz, T. Kleine-Ostmann, N. Krumbholz, D. Mittleman, M. Koch, J. Schoebel, and T. Kurner, "Short-Range Ultra-Broadband Terahertz Communications: Concepts and Perspectives," Antennas and Propagation Magazine, IEEE, vol. 49, pp. 24-39, 2007.

[8] "A new phase for THz," Electronics Letters, vol. 47, pp. 1255-1255, 2011.

[9] R. S. Tucker, "Green Optical Communications; Part I: Energy Limitations in Transport," Selected Topics in Quantum Electronics, IEEE Journal of, vol. 17, pp. 245-260, 2011.

[10] R. S. Tucker, "Green Optical Communications; Part II: Energy Limitations in Networks," Selected Topics in Quantum Electronics, IEEE Journal of, vol. 17, pp. 261-274, 2011.

[11] H. W. Hubers, "Terahertz Heterodyne Receivers," Selected Topics in Quantum Electronics, IEEE Journal of, vol. 14, pp. 378-391, 2008.

[12] [T. Nagatsuma, "Generating millimeter and terahertz waves," Microwave Magazine, IEEE, vol. 10, pp. 64-74, 2009.

[13] M. Feiginov, C. Sydlo, O. Cojocari, and P. Meissner, "Resonant-tunnelling-diode oscillators operating at frequencies above 1.1 THz," Applied Physics Letters, vol. 99, pp. 233506-3, 2011.

[14] S. Preu, "Tunable, continuous-wave Terahertz photomixer sources and applications," J. Appl. Phys., vol. 109, p. 061301, 2011.

[15] A. Masaaki, A. Ryota, S. Hiroshi, K. Ikufumi, I. Tadashi, M. Katsuhiko, and I. Hiromasa, "Ultrabroadband THz Field Detection beyond 170THz with a Photoconductive Antenna," in CLEO 2008, 2008, p. CTuX6.

[16] X. Leijtens, "JePPIX: the platform for Indium Phosphide-based photonics," Optoelectronics, IET, vol. 5, pp. 202-206, 2011.

[17] L. A. Coldren, S. C. Nicholes, L. Johansson, S. Ristic, R. S. Guzzon, E. J. Norberg, and U. Krishnamachari, "High Performance InP-Based Photonic ICs - A Tutorial," Journal of Lightwave Technology, vol. 29, pp. 554-570, 2011.

[18] S. Ho-Jin, N. Shimizu, T. Furuta, K. Suizu, H. Ito, and T. Nagatsuma, "Broadband-Frequency-Tunable Sub-Terahertz Wave Generation Using an Optical Comb, AWGs, Optical Switches, and a Uni-Traveling Carrier Photodiode for Spectroscopic Applications," Lightwave Technology, Journal of, vol. 26, pp. 2521-2530, 2008.

[19] E. Rouvalis, C. C. Renaud, D. G. Moodie, M. J. Robertson, and A. J. Seeds, "Traveling-wave Uni-Traveling Carrier Photodiodes for continuous wave THz generation," Opt. Express, vol. 18, pp. 11105-11110, 2010.

[20] S. Preu, F. H. Renner, S. Malzer, G. H. Döhler, L. J. Wang, M. Hanson, A. C. Gossard, T. L. J. Wilkinson, and E. R. Brown, "Efficient terahertz emission from ballistic transport enhanced n-i-p-n-i-p superlattice photomixers," Applied Physics Letters, vol. 90, p. 212115, 2007.

[21] P. Acedo, H. Lamela, S. Garidel, C. Roda, J. P. Vilcot, G. Carpintero, I. H. White, K. A. Williams, M. Thompson, W. Li, M. Pessa, M. Dumitrescu, and S. Hansmann, "Spectral characterisation of monolithic modelocked lasers for mm-wave generation and signal processing," Electronics Letters, vol. 42, pp. 928-929, 2006.

[22] A. R. Criado, P. Acedo, G. Carpintero, C. de Dios, and K. Yvind, "Observation of phase noise reduction in photonically synthesized sub-THz signals using a passively mode-locked laser diode and highly selective optical filtering," Opt. Express, vol. 20, pp. 1253-1260, 2012.

[23] E. Rouvalis, M. J. Fice, C. C. Renaud, and A. J. Seeds, "Optoelectronic detection of millimetre-wave signals with travelling-wave uni-travelling carrier photodiodes," Opt. Express, vol. 19, pp. 2079-2084, 2011.

[24] S. Pengbo, N. J. Gomes, P. A. Davies, P. G. Huggard, and B. N. Ellison, "Analysis and Demonstration of a Fast Tunable Fiber-Ring-Based Optical Frequency Comb Generator," Lightwave Technology, Journal of, vol. 25, pp. 3257-3264, 2007.

[25] A. R. Johnson, Y. Okawachi, J. S. Levy, J. Cardenas, K. Saha, M. Lipson, and A. L. Gaeta, "Chip-based frequency combs with sub-100 GHz repetition rates," Opt. Lett., vol. 37, pp. 875-877, 2012.

[26] G. Carpintero, M. G. Thompson, R. V. Penty, and I. H. White, "Low Noise Performance of Passively Mode-Locked 10-GHz Quantum-Dot Laser Diode," Photonics Technology Letters, IEEE, vol. 21, pp. 389-391, 2009.

[27] Y. K. Chen, M. C. Wu, T. Tanbun-Ek, R. A. Logan, and M. A. Chin, "Multicolor single-wavelength sources generated by a monolithic colliding pulse mode-locked quantum well laser," Photonics Technology Letters, IEEE, vol. 3, pp. 971-973, 1991.

[28] J. Hasch, E. Topak, R. Schnabel, T. Zwick, R. Weigel, and C. Waldschmidt, "Millimeter-Wave Technology for Automotive Radar Sensors in the 77 GHz Frequency Band," Microwave Theory and Techniques, IEEE Transactions on, vol. 60, pp. 845-860, 2012.

[29] E. Rouvalis, M. J. Fice, C. C. Renaud, and A. J. Seeds, "Millimeter-Wave Optoelectronic Mixers Based on Uni-Traveling Carrier Photodiodes," Microwave Theory and Techniques, IEEE Transactions on, vol. 60, pp. 686-691, 2012.

[30] T. Yasui, S. Yokoyama, H. Inaba, K. Minoshima, T. Nagatsuma, and T. Araki, "Terahertz Frequency Metrology Based on Frequency Comb," Selected Topics in Quantum Electronics, IEEE Journal of, vol. 17, pp. 191-201, 2011.

[31] D. Eliyahu, R. A. Salvatore, and A. Yariv, "Noise characterization of a pulse train generated by actively mode-locked lasers," Journal of the Optical Society of America B-Optical Physics, vol. 13, pp. 1619-1626, Jul 1996.

[32] D. Eliyahu, R. A. Salvatore, and A. Yariv, "Effect of noise on the power spectrum of passively mode-locked lasers," Journal of the Optical Society of America B-Optical Physics, vol. 14, pp. 167-174, Jan 1997.

[33] K. Yvind, D. Larsson, L. J. Christiansen, J. Mork, J. M. Hvam, and J. Hanberg, "High-performance 10 GHz all-active monolithic modelocked semiconductor lasers," Electronics Letters, vol. 40, pp. 735-737, 2004.

A. R. Criado (S'09) received his BSc and MSc on Telecommunication Engineering from Universidad Carlos III de Madrid (Spain) in 2009 and his MRes on Advanced Electronics Systems from Universidad Carlos III (Spain) in 2011.
He has been involved in research tasks on laser diagnostics for fusion plasmas, specifically electronic density measurement using two color multichannel laser interferometry, and he worked as collaborator researcher during 2009 and 2010 in the National Fusion Laboratory in CIEMAT (Spain).
From 2009, he works toward his PhD in the field of low noise photonic generation and homodyne/heterodyne detection of mm-waves and sub-THz signals at Universidad Carlos III de Madrid.

C. de Dios received her M.S. degree in Applied Physics and Electronics from the Universidad Complutense of Madrid. Then, she joined the private sector as a Technical Consultant for Hewlett-Packard. Since 2002, she has been a member of the Optoelectronics and Laser Technology Group at the Universidad Carlos III de Madrid, where she obtained her MRes in 2004 and her Doctorate in 2010 for her work in ultrafast pulsed diode lasers and nonlinear pulse compression. Now, she is an assistant professor at the Electronics Technology Department, in this same university. Her research interests are high-speed optical communications, pulsed semiconductor laser sources, nonlinear optical phenomena and sub-terahertz and millimeter wave photonic signal synthesis and detection.

P. Acedo (M'99) received his bachelor degree on Telecommunication Engineering in 1993 from the Universidad Politécnica de Madrid, and his Doctorate (with honors) from the Universidad Carlos III de Madrid in 2000 for his work on heterodyne two color laser interferometry for fusion plasma diagnostics at the Stellarator TJ-II, (Laboratorio Nacional de Fusión, CIEMAT, Madrid) and Tokamak C-Mod (Plasma Science and Fusion Centre, Massachusetts Institute of Technology). In 2002 he was appointed as Assistant Professor by Universidad Carlos III de Madrid where he has continued with the development of scientific instrumentation systems for fusion plasma diagnostics and biomedical applications. He has been also involved in research on high speed semiconductor laser devices for microwave and millimeter-wave generation and processing. Currently his interests in this line are the development of integrated active photonic antennas for mm-wave and THz generation and detection.

G. Carpintero (M'10) received the Ph.D. degree from the Universidad Carlos III de Madrid, Madrid, Spain in 1999. From 2003 he is Associate Professor of the Electronic Technology Department at Universidad Carlos III de Madrid. From 2006 to 2009, has been a regular visiting scholar at the Engineering Department of the University of Cambridge, involved with quantum dot mode-locked lasers. He has authored or coauthored a number of papers on semicondctor lasers and microwave photonics. His current research interests include mode-locked lasers, optical frequency synthesis, photonic integrated circuits and photonic enabled broadband wireless systems.
Guillermo Carpintero is also member of the Optical Society of America.

K. Yvind received the M.Sc.E. and Ph.D. degree in 1999 and 2003 from the Research Center for Communication, Optics and Materials (COM) at the Technical University of Denmark. He is currently associate professor and group leader for Nanophotonic Devices at DTU Fotonik. His working areas cover a broad range of topics from design, cleanroom fabrication and testing of optical devices in InP, GaAs and silicon.

4

IET, Electronics Letters (published 10/2012)

Selected publication 4	
Citation	**A. R. Criado**, C. de Dios, G. H. Döhler, S. Preu, S. Malzer, S. Bauerschmidt, H. Lu, A. C. Gossard, and P. Acedo, "Ultra-narrow linewidth CW sub-THz generation using GS based OFCG and n-i-pn-i-p superlattice photomixers," Electronics Letters, vol. 48, no. 22, pp. 1425–1426, 2012.
JCR impact factor	0.965
Submitted	04/09/ 2012
Published	25/10/2012
Comments	Copyright (c) 2012 IEEE. Personal use of this material is permitted. However, permission to use this material for any other purposes must be obtained from the IEEE by sending a request to pubs-permissions@ieee.org. Featured article in Electronics Letters vol.48, no. 22. Inside View. See IET, Electronics Letters featured "Inside view" (published 10/2012)

Table VI-4 Selected publication 4. Summary of publication information

CHAPTER VI

Ultra narrow linewidth CW sub-THz generation using GS based OFCG and n-i-pn-i-p superlattice photomixers

Á. R. Criado, C. de Dios, G. H. Döhler, S. Preu, S. Malzer, S. Bauerschmidt, H. Lu, A. C. Gossard and P. Acedo

We report on the photonic synthesis of ultra narrow linewidth Continuous Wave (CW) sub-THz signals using a Gain-Switching (GS) based Optical Frequency Comb Generator (OFCG), selective optical filtering and a n-i-pn-i-p superlattice photomixer. This setup provides continuous tunability with a tuning resolution in the range of 0.1 Hz at 120 GHz and Full Width at Half Maximum (FWHM) of the generated signals below the limits of the measurement setup (<10 Hz). The advantages of this system make it a great candidate for applications requiring extremely low phase noise and continuous tunability, such as high resolution spectroscopy in the sub-THz and THz range.

Introduction: The sub-THz generation technology has dramatically advanced in the last years given the potential applications in the sub-THz and THz frequency ranges [1] and the great research effort invested on this field. Nowadays, there exist commercially available solutions for sub-THz generation. For photonically generated THz radiation, however, the provided linewidths are not narrow enough for many applications such as high resolution spectroscopy [1] and there is still an important need of ultra narrow sub-THz generation systems with continuous tunability. In this letter, we present a compact system for the photonic synthesis of ultra narrow linewidth Continuous Wave (CW) sub-THz signals using a Gain-Switching (GS) based Optical Frequency Comb Generator (OFCG), selective optical filtering and a n-i-pn-i-p superlattice photomixer. This system meets the abovementioned issues that currently exist in commercial systems regarding Full Width Half Maximum (FWHM) of the synthesized sub-THz signals and the tunability resolution required for these ultra narrow linewidths.

Experimental setup: The ultra narrow linewidth CW sub-THz generation scheme comprises three main parts: OFCG, selective optical filtering stage, and a high bandwidth photomixer. The OFCG employed in this work (Fig. 1) is based on the phase modulation of a GS Discrete Mode (DM) diode laser [2] to obtain a relatively wide span (~140GHz, see Fig. 2) using a scheme without the need of additional non-linear elements usually associated to standard OFCG, thus allowing for a very compact, potentially low-cost and energy efficient OFCG. The GS regime is achieved by modulating the DM, which is biased at 60 mA, with a 28 dBm RF reference. In this case, f_{REF}=10 GHz. The optical output from the DM is delivered to a $LiNbO_3$ phase modulator (PM, Fig. 1). The PM is driven with f_{REF}, which is properly phase trimmed with an electrical phase shifter (PS) to achieve optimum flatness of the optical output of the OFCG [2].

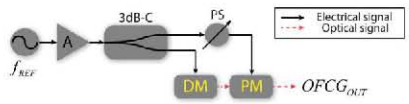

Fig. 1 *OFCG basic scheme. A: electrical amplifier; 3dB-C: 3-dB coupler; DM: Discrete Mode Laser; PS: electrical phase shifter; PM: optical phase modulator.*

The optical output of the OFCG is shown in Fig.2. This output spectrum is introduced in the selective optical filtering scheme [3]. This scheme allows us to extract two longitudinal modes of the optical spectrum with the desired frequency spacing, in order to beat them in the high bandwidth photomixer. Further details on this selective optical filtering setup can be found in [3].

The high bandwidth photomixer employed to beat the two optical frequencies with the desired frequency separation is a n-i-pn-i-p superlattice photomixer [4]. This photomixer has been packaged in order to provide an optical fiber connection, bias input and direct sub-THz free space output by the use of a hyperhemispherical silicon lens coupled to the planar antenna integrated with the photomixer. This allows a direct way to beat the two optical modes and radiate the sub-THz signal in a single packaged device [1].

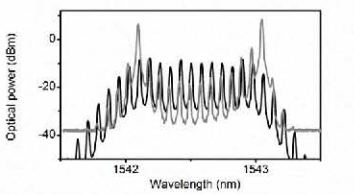

Fig. 2 *Optical spectra of the OFCG output (black trace) and n-i-pn-i-p superlattice photomixer input (grey trace).*

Experimental results: The synthesized sub-THz CW signals are evaluated in terms of electrical spectra (i.e. electrical FWHM) and tunability. For this purpose, the sub-THz signal emitted by the photomixer is collected with a 115 GHz corrugated circular horn antenna. No parabolic mirrors were used to improve the coupling of the quasi-optical beam to the horn. The horn antenna feeds a 90-140 GHz harmonic mixer that is connected to an Electrical Spectrum Analyzer (ESA).

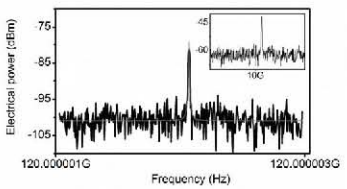

Fig. 3 *Synthesized signal at 120 GHz. Measured (black trace) and Lorentzian fit (grey trace). Inset: reference signal measured with similar dynamic range (same axis).*

As an example of the generated signals, a 120 GHz synthesized signal spectrum, corrected for the harmonic mixer losses (~45 dB), is shown in Fig.3. It has been generated with an average optical input power delivered to the n-i-pn-i-p photomixer of 13 mW. The measurement has been accomplished using a Resolution Bandwidth (RBW) of 10 Hz and the minimum frequency span allowed by the ESA at this frequency range (2.1 kHz). The measured FWHM of the 120 GHz signal is ~10 Hz, which corresponds with the RBW of the ESA. Thus, the actual FWHM for the synthesized signal is ≤10 Hz. For comparison purposes, the reference RF signal at f_{REF}=10 GHz is measured with a similar dynamic range (Fig.3, inset). The measured FWHM of the reference is also ≤10 Hz.

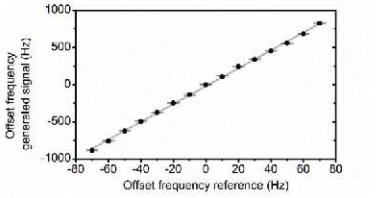

Fig. 4 *Continuous tunability. Measured data (average values: black dots; standard deviation: black caps); and linear fit (grey trace).*

The continuous tunability of the reported system is achieved by tuning f_{REF} (fine continuous tuning) and selecting the desired optical modes using the selective filtering stages (coarse discrete tunability in f_{REF} steps). To characterize the continuous tunability characteristics of the system (fine tuning), the reference signal has been tuned in 10 Hz steps to get frequency steps of the sub-THz signal (~120 Hz) within the frequency readout accuracy of the ESA. The results are shown in Fig. 4 with the minimum frequency span of the ESA (2.1 kHz). The standard deviation of the measurement set (sub-THz frequency) is between 5 and 10 Hz and the linear fit gives a R-square value of 0.999. It must be noted that we are in the frequency accuracy and frequency resolution limits of the ESA, so it cannot be determined whether the standard deviation is due to the system itself or due to the uncertainty associated to the measurement setup. The employed reference RF generator allows 0.01 Hz steps, which would be translated to a tuning resolution of the 120 GHz signal in the range of 0.1 Hz (10^{-12}).

Concerning the power of the synthesized sub-THz signals, it must be noted that the coupling of the divergent THz beam emitted by the photomixer to the horn antenna can be strongly improved using parabolic mirrors with matched numerical apertures. Furthermore, for these photomixers, the generated power is proportional to the square of the optical input power ($P_{THz} \propto P_{OPT}^2$) so the use of higher optical power (i.e. optical amplification) would allow higher power sub-THz signals. In this sense, the heterodyning of just two modes in a photomixer, as employed in this work, is more efficient than direct harmonic generation [5] as all the optical power is concentrated in the desired frequency components [3].

The maximum synthesized frequency is limited by the optical span of the OFCG and the bandwidth of the photomixer. The first can be expanded by the use of already reported techniques (i.e. non-linear fiber [6], non-linear loops [7], and use of more intensity and phase modulators [8] or FWM [8]). The photomixer used in this work features a working bandwidth in excess of 1 THz [4]. So this scheme can be used for higher frequencies synthesis straightforwardly.

Conclusion: We report on the photonic synthesis of ultra narrow linewidth Continuous Wave (CW) sub-THz signals using a Gain-Switching (GS) based Optical Frequency Comb Generator (OFCG), selective optical filtering and a n-i-pn-i-p superlattice photomixer. This compact setup provides continuous tunability with a tuning resolution in the range of 0.1 Hz at 120 GHz and Full Width at Half Maximum (FWHM) of the generated signals below the limits of the measurement setup (<10 Hz). The advantages of this system make it a great candidate for applications requiring extremely low phase noise, such as high resolution spectroscopy in the sub-THz and THz range.

Acknowledgments: Work supported by the Spanish Ministry of Science and Technology through the project TEC2009-14525-C02-02. The work by A.R. Criado has been supported by the Spanish Ministry of Science and Technology under the FPI Program, Grant# BES2010-030290.

Á. R. Criado, C. de Dios and P. Acedo (Electronics Technology Department, Universidad Carlos III de Madrid, Leganés, Madrid 28911 Spain).

E-mail: acriado@ing.uc3m.es

G. H. Döhler and S. Bauerschmidt (Max Planck Institute for the Science of Light, Guenther-Scharowsky-Str. 1/ Bldg. 24, 91058 Erlangen, Germany).

S. Preu and S. Malzer (Lehrstuhl für Angewandte Physik, Friedrich-Alexander-Universität Erlangen-Nürnberg, 91058 Erlangen, Germany).

H. Lu and A. C. Gossard (Materials Dept. University of California, Santa Barbara, Santa Barbara, CA USA)

References

1 Preu, S., Döhler, G.H., Malzer, S., Wang, L.J., and Gossard, A.C.: 'Tunable, continuous-wave Terahertz photomixer sources and applications', *J. Appl. Phys,*2011, **109**, (6) p. 061301

2 Zhou, R., Latkowski, S., O'Carroll, J., Phelan, R., Barry, L.P., and Anandarajah, P.M.: '40nm wavelength tunable gain-switched optical comb source', *Opt. Express*, 2011, **19**, (26), pp. B415-B420

3 Criado, A.R., Acedo, P., Carpintero, G., de Dios, C., and Yvind, K.: 'Observation of phase noise reduction in photonically synthesized sub-THz signals using a passively mode-locked laser diode and highly selective optical filtering', *Opt. Express*, 2012, **20**, (2), pp. 1253–1260

4 Preu, S., Renner, F.H., Malzer, S., Döhler, G.H., Wang. L.J., Hanson, M., Gossard, A.C., Wilkinson, T.L.J., Brown, E.R., and Döhler, G.H.: 'Efficient terahertz emission from ballistic transport enhanced n-i-p-n-i-p superlattice photomixers', *Appl. Phys. Lett.*, 2007, **90**, (21), p. 212115

5 Xiao, S., Hollberg, L., and Diddams, S.A.: 'Low-noise synthesis of microwave and millimetre-wave signals with optical frequency comb generator', *Electron. Lett.*, 2009, **45**, (3), pp. 170–171

6 Anandarajah, P.M., Maher, R., Xu, Y.Q., Latkowski, S., O'Carroll, J., Murdoch, S.G., Phelan, R., O'Gorman, J., and Barry, L.P.: 'Generation of Coherent Multicarrier Signals by Gain Switching of Discrete Mode Lasers', *IEEE Photon. J.*, 2011, **3**, (1), pp. 112–122

7 de Dios, C., and Lamela, H.: 'Improvements to Long-Duration Low-Power Gain-Switching Diode Laser Pulses Using a Highly Nonlinear Optical Loop Mirror: Theory and Experiment', *J. Lightwave Technol.*, 2011, **29**, (5), pp. 700–707

8 Supradeepa, V.R., and Weiner, A.M.: 'Bandwidth scaling and spectral flatness enhancement of optical frequency combs from phase-modulated continuous-wave lasers using cascaded four-wave mixing'. *Opt. Lett.*, 2012, **37**, (15), pp. 3066–3068

5

IET, Electronics Letters featured "Inside view" (published 10/2012)

The previous letter had significant acceptance within the THz technology community and it is featured in the same issue of IET Electronics Letter in which is published. An interview to our group is included as part of this feature article ("Inside view"). It is included here because of the significant content of the answers when related to our vision of THz technology.

Selected publication 5	
Citation	D. Davies, "Inside View," Electronics Letters, vol. 48, no. 22, p. 1376, 2012.
JCR impact factor	0.965
Submitted	N/A
Published	25/10/2012
Comments	Copyright (c) 2012 IEEE. Personal use of this material is permitted. However, permission to use this material for any other purposes must be obtained from the IEEE by sending a request to pubs-permissions@ieee.org. Featured article in Electronics Letters vol.48, no. 22. Inside View.

Table VI-5 Selected publication 5. Summary of publication information

CHAPTER VI

www.uc3m.es/gotl
www.mpl.mpg.de/
www.lap.physik.uni-erlangen.de/
www.materials.ucsb.edu/ 'Ultra narrow linewidth CW sub-THz generation using GS based OFCG and n-i-pn-i-p superlattice photomixers', Á. R. Criado, C. de Dios, G. H. Döhler, S. Preu, S. Malzer, S. Bauerschmidt, H. Lu, A. C. Gossard and P. Acedo

An international team of researchers has developed a photonic sub-THz source with excellent signal quality, tunability and stability. Members of the Spanish arm of the team talk to us about the potential and challenges of photonic sub-THz generation

Why the interest in sub-terahertz generation?

The reason is basically the high number of applications identified in the sub-THz and THz domains, some from several decades ago, like spectroscopy applications, especially in the radioastronomy field. Others have become more extensively used in recent years, like imaging forsecurity and biomedical applications and short-distance high-data rate communications. Moreover, new applications are appearing every year, including in art and structure conservation and even holography. Maybe the most exciting application that may appear in the near future is high sensitivity, low phase noise THz heterodyne systems, for example for radioastronomy receivers.

What are the limitations of current approaches?

There are two bottlenecks common to all compact sub-THz generation systems: power and maximum frequency of operation. There are also limitations that only exist for some approaches. Up to now, upconversion using Schottky multipliers has been the solid state solution with best performance in terms of power, so it used to be the preferred commercially available sub-THz generation system.

However, photonic generation is able to provide unique features that cannot be offered by other alternatives, in tunability range and especially remote distribution and generation. You can distribute your optical source signal through optical fibre with very low losses (0.2 dB/km), EMI immunity and low cost to one or several remote photomixers where the THz generation is performed. However the output power is still lower than that achievable by electronic approaches based on multiplication. But, now that photonic systems are able to match or even surpass electronic systems in terms of signal quality, the photonic approach is a great candidate to fulfil THz users' requirements.

What have you achieved in the work reported in your Letter?

We have developed a photonic sub-THz source with all the advantages of photonic THz generation, which matches or even surpasses the signal quality, tunability and stability of the best commercially available electronic solutions. The system has good potential for commercial solutions because it provides all the characteristics required by the market; very high signal performance (unique for a photonic solution) and a simple and compact scheme with a continuous and ultra-high resolution tunability covering the whole frequency range. It is also low cost, has low energy consumption, is highly stable and reliable with good linewidth and phase noise characteristics.

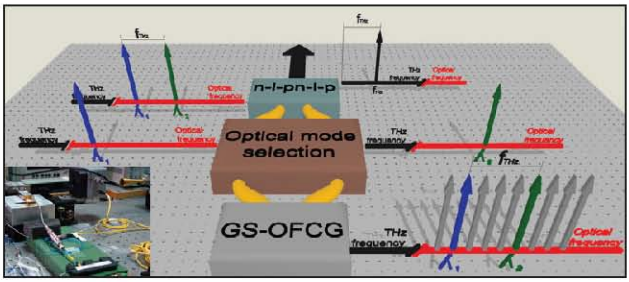

ABOVE: A schematic view of how the frequencies are generated and processed through the setup. Inset: The experimental setup with the complete gain switching (GS)-OFCG (bottom-left) and the n-i-pn-i-p photomixer (top-right)
Bottom: Members of the team from Spain (left) and Germany (right). From left to right: Pablo Acedo, Á. Rubén Criado, Cristina de Dios, Gottfried Döhler, Stefan Malzer, Sascha Preu. Not pictured here, the team also includes S. Bauerschmidt (Germany) and the US members, from UCSB: H. Lu and A. C. Gossard

What were the breakthrough elements in the work?

Our generation scheme consists of three main parts: the optical source, the optical mode selection scheme, and the sub-THz photomixer. For the last three years we have been working with several alternatives for each part. We finally arrived at a compact, cost-effective and high performance multimode source, providing continuous tunability and great mode coherence. Together with the n-i-pn-i-p superlattice photomixers provided by our colleagues in Germany, these were the two key factors in reaching the final scheme.

This work was a collaboration across three countries and four institutions. What did each part of the team bring to the project?

We began our collaboration about a year ago, when G.H. Döhler came to Universidad Carlos III de Madrid (UC3M) as a visitor under the Excellence Chair Programme. He and his colleagues in Germany (both at Max Planck Institute for the Science of Light and University of Erlangen) designed and developed the photomixer devices. As these structures contain ErAs as an essential ingredient, they are grown in the group of A.C. Gossard from University of California, Santa Barbara (UCSB), who pioneered growth and applications of layers containing ErAs. UC3M implement the optical source and mode selection scheme and set up the complete system. Collaboration between the groups allows us to cover the whole chain, from photomixer manufacturing and optical source development to system level implementation.

What applications of this work are you expecting to see and what are the longer term goals your team is moving toward?

Applications like high resolution spectroscopy or THz local oscillators that depend on a high quality signal. We are now working with a spin-off of UC3M - Luz WaveLabs – for the development of a commercial THz source based on our scheme. Providing higher THz frequencies and power and a wider frequency range will be top of our list of priorities.

A key issue is downsizing and integration of the components to come up with a small and cost efficient prototype system. Beyond that, the longer term goal is improving the system to arrive at a commercial solution and cost-effective approaches for optical frequency comb generators with optical tunability well above 1 THz. In addition, in THz detection, our aim is heterodyne systems that make use of our low-phase noise photonic local oscillator.

CHAPTER VI

6

IEEE/MTTS, Transactions on Terahertz Science and Technology (submitted 12/2012)

Selected publication 6	
Citation	**Á. R. Criado**, C. de Dios, G. H. Döhler, S. Preu, S. Malzer,H. Lu, A. C. Gossard and P. Acedo, "Continuous wave sub-THz photonic generation with ultra-narrow linewidth, ultra-high resolution, full frequency range coverage and high long-term frequency stability," IEEE Transactions on Terahertz Science and Technology, submitted 12/2012
JCR impact factor	N/A
Submitted	12/ 2012
Published	N/A
Comments	Copyright (c) 2012 IEEE. Personal use of this material is permitted. However, permission to use this material for any other purposes must be obtained from the IEEE by sending a request to pubs-permissions@ieee.org.

Table VI-6 Selected publication 6. Summary of publication information

CHAPTER VI

Continuous wave sub-THz photonic generation with ultra-narrow linewidth, ultra-high resolution, full frequency range coverage and high long-term frequency stability

Á. R. Criado, *Student Member, IEEE*, C. de Dios, E. Prior, G. H. Döhler, S. Preu, S. Malzer, H. Lu, A. C. Gossard, and P. Acedo, *Member, IEEE*

***Abstract*—We report on a photonic system for generation of high quality Continuous Wave (CW) sub-THz signals. The system consists on a Gain-Switching-based Optical Frequency Comb Generator (GS-OFCG), a two-optical-modes selection mechanism and a n-i-pn-i-p superlattice photomixer. As mode selection mechanism, both selective tunable optical filtering using Fabry-Perot Tunable Filters (FPTF) and Optical Injection Locking (OIL) are evaluated. The performance of the reported system surpasses in orders of magnitude the performance of any commercially available optical mm-wave and sub-THz generation system in a great number of parameters. It matches and even overcomes those of the best commercially available electronic THz generation systems. The performance parameters featured by our system are: linewidth <10 Hz at 120 GHz, complete frequency range coverage (60-140 GHz) with a resolution in the order of 0.1 Hz at 120 GHz (10^{-12} of generated frequency), and high long term frequency stability (5 Hz deviation over one hour). Most of these values are limited by the measurement instrumentation accuracy and resolution, thus the actual values of the system could be better than the reported ones. The frequency can be extended straightforwardly up to 1 THz extending the OFCG frequency span. This system is compact, robust, reliable, and offers a very high performance, especially suited for sub-THz photonic Local Oscillators and high resolution spectroscopy.**

***Index Terms*—Optical Frequency Comb, THz Local Oscillator, narrow linewidth THz generation, THz photonic generation, Optical Injection Locking**

Manuscript received December 12, 2012. Work supported by the Spanish Ministry of Science and Technology through the project TEC2009-14525-C02-02. The work by Á.R. Criado has been supported by the Spanish Ministry of Science and Technology under the FPI Program, Grant# BES2010-030290.

Á. R. Criado, C. de Dios, E. Prior and P. Acedo are with the Electronics Technology Department, Universidad Carlos III de Madrid, Leganés, Madrid 28911 Spain (e-mail: acriado@ing.uc3m.es).

G. H. Döhler is with the Max Planck Institute for the Science of Light, Guenther-Scharowsky-Str. 1/ Bldg. 24, 91058 Erlangen, Germany.

S. Preu and S. Malzer are with the Lehrstuhl für Angewandte Physik, Friedrich-Alexander-Universität Erlangen-Nürnberg, 91058 Erlangen, Germany.

H. Lu and A.C. Gossard are with the Materials Dept. University of California, Santa Barbara, Santa Barbara, CA USA

I. Introduction

The study of the sub-THz and THz frequency ranges has experienced a great development in the last years [1]. There is a great number of emerging applications in this frequency range, namely, imaging (for security [2] and biomedical [3] purposes among others), short-range high data-rate communications [4] and spectroscopy [5], [6]. Nevertheless, spectroscopy applications have been the ones that have driven the THz development since the 70´s due to their importance in radioastronomy [7]. Even today, it remains the main field of application within the THz range, widely used in security [2], material identification and inspection [8], biomedicine [9] and radioastronomy [10], [11].

Nowadays, the THz research focus is mainly oriented to generation and detection systems that would allow full exploitation of all these applications. This requires the development of technologies providing compactness, reasonable cost, stability, robustness and room temperature operation. Specifically, if the application is related to Continuous Wave (CW) spectroscopy, generation systems must feature narrow linewidth and continuous tunability with a tuning resolution below the linewidth of the species under test. Moreover, a robust and reliable system with high long-term stability and frequency accuracy is desirable to properly accomplish frequency sweep operation and provide customer satisfaction.

The existing THz generation technologies can be classified in three groups: electronic upconversion, THz oscillators and optical downconversion. The electronic upconversion aims to push the frequency limits from the mm-wave region up to the THz region, while the optical downconversion relies mainly on Difference Frequency Generation (DFG) to generate signals down to the THz range [7]. The THz oscillators make use of several technologies and are able to directly generate THz radiation.

Among the compact sources able to generate coherent THz radiation with the different approaches mentioned above, the following technologies should be highlighted: electronic upconversion using Schottky multipliers [12]; direct THz

generation with Resonant Tunneling Diodes (RTD) [13] or THz Quantum Cascade Lasers (THz-QCL) [14], and optical downconversion based on DFG using photomixers.

Schottky multipliers are a commercial solution capable of providing high performance THz signals up to 2.7 THz with a narrow linewidth (Hz range), comparatively good power levels (around 100 μW at 1 THz), and continuous tunability within a limited frequency range determined by the employed waveguides [12]. However, the generation relies on a radiofrequency (RF) reference that is multiplied; this worsens the linewidth and phase noise performance as the multiplication order increases [15].

RTDs operating up to 1.1 THz have been demonstrated [13] and they are a promising technology with high integration potential. However, the generated CW signal shows a wider linewidth (in the order of 10 MHz [16]) and the tunability is very limited (about 4% of the central frequency [17]). THz-QCLs provide a very high signal power (up to 140 mW in CW operation [18]), but they hardly operate below 2 THz (the minimum demonstrated frequency is 0.8 THz, achieved by applying external magnetic fields [7]). They also need cryogenic cooling to offer the mentioned high power in the THz range [19]. Moreover, they can only provide narrow linewidths (in the range of 100´s Hz) by making use of complex Phase Locked Loop systems [20], and have a very limited tunability, with a record value of 8.6% (330 GHz) around the center frequency by mechanical means [21].

THz generation from DFG in photomixers, although it offers a slightly lower power than other solutions (up to 24 □W at 0.914 THz) [22], is able to offer continuous tunability over a large frequency range (up to 1.53 THz for photodiode-based photomixers) in compact systems [23]. Additionally, they offer the possibility of distributing the optical signal using optical fiber with very low losses (0.2 dB/km) and Electromagnetic Interference (EMI) immunity to one or several remote photomixers where the THz generation is accomplished. This means that the mixing process can be carried out remotely. This is a really interesting feature for remote spectroscopy, remote sensing and Local Oscillator (LO) distribution in radioastronomy heterodyne receivers [11]. With respect to the integration potential, a great effort is placed today and Photonic Integrated Circuits (PICs) for sub-THz generation have been already implemented [24].

In this scenario, the electronic upconversion using Schottky diodes and the optical downconversion using DFG with photomixers are the most suitable approaches for a compact and good performance source below 2 THz. There exist commercial solutions for both technologies [12], [25] but nowadays Schottky diodes are preferred because of their better characteristics in terms of output power, linewidth, frequency resolution, long term stability and frequency accuracy.

In this work we are going to discuss a DFG based system for narrow linewidth, large frequency coverage for sub-THz and frequency equal to the frequency spacing between those modes. Hence, a simplified DFG scheme consists of an optical source providing the two required optical frequencies and a photomixer. There are several ways to obtain the two optical modes. Two single-mode lasers can be used, offering continuous tunability. However, in order to obtain a narrow-linewidth THz signal, the lasers have to be very well stabilized in frequency and they have to be locked between each other by complex Optical Phase Locked Loops (OPLL) to attain coherence between the optical lines. Even in those cases, the linewidth and tunability resolution of the synthesized THz signal is typically in the MHz range [25]. If a two-mode laser is used, it can offer much better mode coherence, hence a better linewidth performance without OPLLs, but there is no tunability or it is very limited [26]. More interesting are the multimode sources (i.e. Optical Frequency Comb Generators (OFCG)), such as Mode-Locked Laser Diodes (MLLD) [27] or tunable OFCGs. An OFCG presents high coherence between longitudinal modes, and the linewidth and phase noise characteristics of the synthesized signals can be very good, but an additional stage for the selection of the two modes is required. MLLDs can be integrated as PICs but the frequency tunability of the generated signal is discrete, in frequency steps corresponding to the spacing between modes [28]. Tunable benchtop OFCGs are able to provide tunability of the frequency spacing between modes and then, continuous tunability over the whole range, overcoming the issue presented by MLLDs. Between the tunable OFCGs, some schemes based on Gain Switching (GS) [29], [30] have been recently reported, featuring a more compact and cost-effective setup than other benchtop OFCGs, as fewer components are employed to produce an equivalent optical span, all of them reliable and commercially available.

When a multimode OFCG source is considered, a mode selection stage is often included in the system to provide coarse frequency tunability. For this block of the system, two basic approaches can be followed. The first one is selective optical filtering, using Arrayed Waveguide Gratings (AWG) [31] or high-selective Fabry-Perot tunable filters (FPTF) [27], [28], [30], [32]. An alternative mode selection mechanism is the use of Optical Injection Locking (OIL) techniques [33].

Every DFG system is completed with the photomixing device responsible for the photonic-to-RF frequency conversion. Devices based on p-i-n structures are preferred to photoconductors due to their higher available output power, although they offer a lower bandwidth, around 1.53 THz [23]. Examples of these p-i-n devices are Uni-Travelling-Carrier photodiodes (UTC-PD) [31], Travelling-Wave Uni-Travelling-Carrier (TW-UTC-PD) [23] and n-i-pn-i-p superlattice photomixers [30], [34], [35]. The latter take advantage of a superlattice of p-i-n diodes allowing for independent optimization of both transit and RC times, thus overcoming the trade-off usually present in most high-bandwidth photodiodes.

frequency range coverage from 60 to 140 GHz with potential extension to several hundreds of GHz and optical fiber distribution) and is able to match and even surpass the linewidth, tunability resolution and frequency stability of the best available electronic THz sources (i.e. Schottky multiplier chains). This is achieved with a compact and simple scheme that is also able to provide a robust and reliable system.

The system is a DFG scheme consisting of a GS based OFCG, a selective filtering stage and a n-i-pn-i-p superlattice photomixer. Both optical filtering using FPTF [30] and OIL are evaluated and compared to determine the most suitable optical filtering method. The sub-THz output signal is evaluated in terms of linewidth, power, tunability resolution and range, and power and frequency stability. The resulting system and its performance make it a potential candidate for high resolution CW spectroscopy able to compete with the best electronic THz commercially available systems.

II. Optical Multimode Source: Gain-Switching-based Optical Frequency Comb Generator

A. Principle of operation

One of the more compact and efficient schemes for the generation of multimode sources (Optical Frequency Combs) relies on the use of a laser under GS modulation as seed [29]. As it can be seen in Fig. 1, a basic version of a Gain Switching based OFCG (GS-OFCG) consists of a Discrete Mode (DM) laser that is modulated under GS regime and then phase modulated with a driving signal synchronized in phase with the GS modulating signal [30].

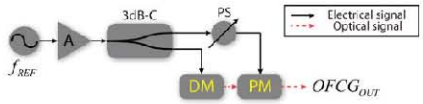

Fig. 1. Scheme of the GS-based OFCG. 3dB-C (3 dB electrical splitter), DM (Discrete Mode laser), PS (Electrical Phase Shifter), PM (Optical Phase Modulator).

B. Performance

In order to characterize the phase noise degradation of the RF reference signal (f_{REF}) after passing through the GS-OFCG and its non-linear mechanisms, in Fig. 2 is shown the Single Side-Band (SSB) noise of both the reference signal (directly measured at the output of the RF amplifier, *A*, in Fig. 1) and the photodetected output of the GS-OFCG ($OFCG_{OUT}$ in Fig. 1). The parameters of the GS modulation are I_{DM} = 60 mA, f_{REF} = 10 GHz and P_{REF} = 27 dBm. The measurement floor is shown (Displayed Average Noise Level, DANL). Both signals are measured with the same dynamic range and amplification chain. There is no significant degradation at low and high frequency offsets (below 100 kHz and above 10 MHz). However, two differences are observed. Firstly, a spurious signal at about 9 kHz that is present in the reference does not spurious signal, a certain degradation of the actual signal can be observed. One possible explanation for this is the high power applied to the optical phase modulator. Nevertheless, it is not significant at all as can be concluded by the Root-Mean-Square (RMS) integrated jitter values over the 20 kHz-80 MHz frequency region. The values are 70.97 fs for the reference signal and 76.05 fs for the OFCG-GS output. The DANL has a jitter of 25 fs. The Full Width at Half Maximum (FWHM) of both signals have the same value of about 4 Hz (measured with a RBW = 1 Hz) (Fig. 2, inset), which basically corresponds to the Local Oscillator of the Electrical Spectrum Analyzer (ESA) rather than to the employed reference signal.

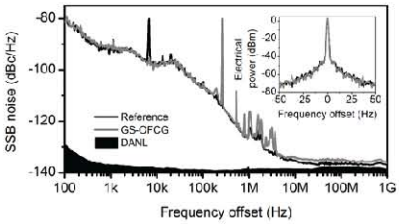

Fig. 2. SSB noise measurements for Fig.1. Inset: measured electrical spectra for both signals. Black trace: reference signal at 10 GHz; grey trace: photodetected OFCG output at 10 GHz. Four samples average for each trace (see text for details).

For the characterization of the GS-OFCG we investigated the evolution of the optical spectra with respect to changes in the modulation power (P_{REF}), in the phase difference between both GS and phase modulating signals ($\Delta\varphi_{MOD}$) and in the bias current of the DM laser (I_{DM}, see Fig.1).

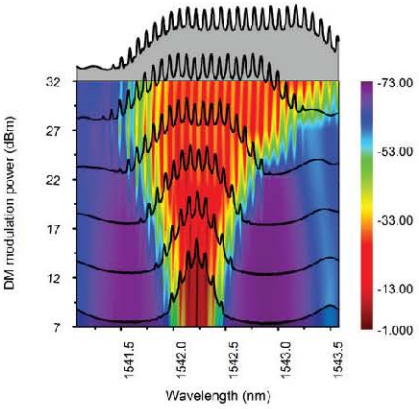

Fig. 3. OFCG optical spectra (Z axis: optical power (dBm)). Evolution with

The optical spectra of the GS-OFCG, as a function of P_{REF}, are shown in Fig. 3. As expected, higher values of P_{REF} provide a wider optical comb, and a flat comb with up to 23 lines (10 GHz apart) within a 10 dB bandwidth can be generated. However, the maximum value of P_{REF} is limited by the maximum modulating power the DM and the PM can admit. In our case, this value corresponds to approximately 32 dBm.

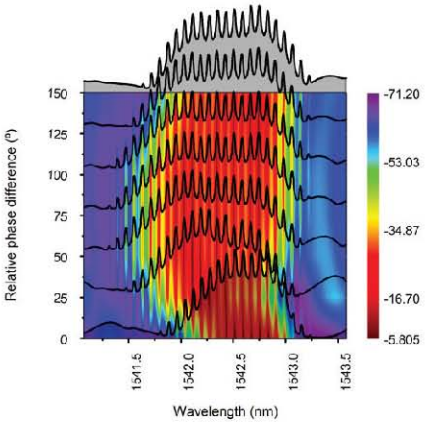

Fig. 4. OFCG optical spectra (Z axis: optical power (dBm)). Evolution with the relative phase difference between the DM modulation signal and the optical phase modulator driving signal.

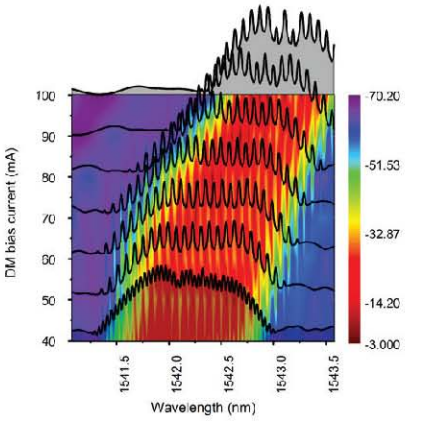

Fig. 5. OFCG optical spectra (Z axis: optical power (dBm)). Evolution with the bias modulation of the DM laser.

The evolution of the GS-OFCG with the change in Δ_{MOD} is the GS-OFCG output. This is the reason why an electrical phase trimmer or phase shifter (PS) is required in the scheme of the GS-OFCG (see Fig.1).

Finally, Fig. 5 shows how the optical spectra change with I_{DM}. In this case, it is clearly shown how the spectra evolve from GS modulation (lower I_{DM}) to linear modulation (higher I_{DM}), when the effect of the PM is dominant and the phase modulation side bands appear. It is important to note that the value I_{DM} has to be carefully selected to provide proper GS regime and maximize the optical span [36].

C. GS-OFCG Continuous Tunability

The tunability of the GS-OFCG (frequency spacing between modes) is basically limited by the bandwidth of its components. The DM laser employed in this work has a usable bandwidth of around 20 GHz, thus being able to theoretically provide GS operation up to that frequency. In our case, the limiting factor is the PM, with a bandwidth around 10 GHz (the *PS* and power amplifier *A* (Fig. 1) have a bandwidth of 18 GHz).

For our GS-OFCG scheme, the frequency spacing between modes (f_{REF}) can be tuned directly using the reference CW generator. Nevertheless, due to the dependence on Δ_{MOD}, significant frequency detuning values (above 10 MHz), require a re-tuning of Δ_{MOD}. In this work, manual re-tuning has been used, although a control loop using a voltage-controlled electrical phase shifter would provide automatic control of this parameter.

D. Optical Comb Frequency Span

The basic GS-OFCG presented in this paper includes up to 23 modes within a 10 dB-bandwidth for a 220 GHz frequency span. An increase in the number of modes can be accomplished by increasing the modulation depth of the signal inducing the GS regime in the DM laser and/or the phase modulator RF input (see Fig. 3). However, these devices have a maximum input power that determines the maximum optical span that a basic GS-OFCG, like that on Fig. 1, is able to provide.

Nevertheless, there exist many techniques to broaden the optical span of an OFCG that can be added to the basic GS-OFCG scheme of Fig. 1 in order to provide a GS-OFCG with an optical span above 1 THz. Recent works on the expansion of OFCG consider the use of cascaded phase modulators and intensity modulator elements [37], resulting in a flat optical spectra exceeding 3 THz [38]. Other techniques are based on polarization modulation [39]. Another approach is the exploitation of the nonlinear propagation of light travelling along special highly nonlinear optical fibers [40]. Interferometric nonlinear propagation of light has also been studied as shapers for pulsed optical sources. Results on the capability of Sagnac interferometers to expand the optical spectra have also been reported [41], showing a good potential as a new OFCG expander technique. Hence, it is clear that the

of the presented system to the THz domain straightforwardly.

III. Selection of two optical modes: High-Selectivity Fabry-Perot Tunable Optical Fiber Filters

A. Principle of operation

One of the most widely used methods to select the two required optical modes from a multimode source in DFG schemes is to use selective filtering. This can be accomplished with Arrayed Waveguided Gratings (AWGs) [31], or high-selective Fabry-Perot Tunable Filters (FPTF) [27], [28], [30], [32]. In this section we are going to evaluate the use of the second type of components (FPTF) for mode selection. It is important to note that in the case of selective filtering optical gain is usually needed to compensate the insertion losses of the filters [27]. Fig. 6 shows the experimental scheme for the generation of THz signals using FPTF.

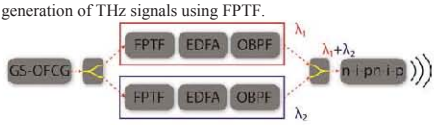

Fig. 6. THz photonic generation scheme using selective optical filtering. OFCG: Gain-Switched Comb Generator; FP-TF: Fabry-Perot Tunable Filter; EDFA: Erbium Doped Fiber Amplifier; OBPF: (optional) Optical Band-Pass Filter.

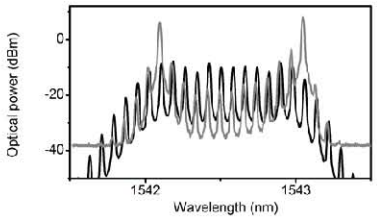

Fig. 7. Measured optical spectrum at the photomixer input using selective optical filtering (grey trace, see Fig. 6). OFCG spectrum (black trace).

A typical optical spectrum, after FPTF filtering and prior to photomixing (see Fig. 6) is shown in Fig. 7. The optical bandwidth (FWHM) of the used FPTF is about 6 GHz at 1550 nm, thus having a Side Mode Suppression Ratio (SMSR) of about 13 dB for a frequency spacing of 10 GHz. It can be also seen from Fig. 7 that there is an increase in the noise floor due to the Amplified Spontaneous Emission (ASE) of the Erbium Doped Fiber Amplifier (EDFA) required to compensate for filters insertion losses.

B. Long Term Stability

Given the high selectivity of the employed FPTF (Q = 3000), a bias voltage value of around 8 mV applied to the piezoelectric transducer (PZT) of the FPTF, detunes its center frequency by 10 GHz. This requires highly stable voltage

The driving voltage of the FPTF is provided in this case by a commercial voltage source (Agilent E3631A) with a resolution of 1 mV. Alternatively, a custom made dual channel DC voltage source has been designed and implemented, featuring a resolution of 20 µV and theoretical output stability in the range of a few ppm/ºC [42].

The long term stability (60 min) of the FPTFs is tested using both voltage sources. Fig. 8 shows both the wavelength drift and the room temperature drift. The wavelength drift has been measured at the output of the FPTF, using a white light source as input. From Fig. 8, it can be seen that there is a significant correlation between the room temperature drift and the voltage drift (i.e. wavelength drift). The best results are obtained with the custom made DC source, with a wavelength drift of around 0.2 nm (25 GHz) in one hour. The results conclude that a short term operation is possible with free-running FPTF, but high long term stability would require very accurate temperature control or preferably control loops for the FPTFs. The latter solution requires a very precise electronic design due to voltage values below 1 mV. Control loops for this Q-factor range have been demonstrated [43].

Finally, it must be noted that the drift of the center frequency of the FPTFs is translated to the THz synthesized signal as power drifts. However, the filters´ drift have no impact in the linewidth or phase noise of the THz signal [27].

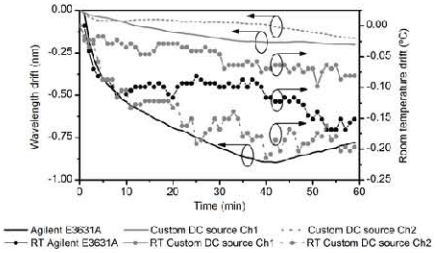

Fig. 8. Long term stability of the high selective FPTF. Wavelength drift (line traces) and room temperature drift (line + symbol traces). Black traces (commercial voltage source Agilent E3631A), grey traces (custom DC source, channels 1 and 2).

IV. Selection of two optical modes: Optical Injection Locking

A. Principle of operation

Another mechanism of optical mode selection from a multimode source is Optical Injection Locking (OIL) [33]. The desired optical mode of the source is injected to a slave laser, which acts both as filter and amplifier, in the sense that it is able to filter the injected mode and to provide with optical gain at the same time. As the optical gain is only applied to the selected optical mode, better values of noise floor and SMSR are achieved. When the process is performed over the two

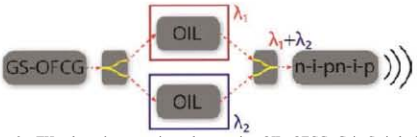

Fig. 9. THz photonic generation scheme using OIL. OFCG: Gain-Switched Comb Generator; OIL: Optical Injection Locking.

A typical optical spectrum at the input of the photomixer (Fig.11) is shown in Fig. 10. When comparing with Fig. 7, it can be clearly seen that a higher SMSR (around 30 dB) and much lower values of the noise floor are obtained for same output power. This SMSR value has a negligible effect in the phase noise of the sub-THz generated signal[44].

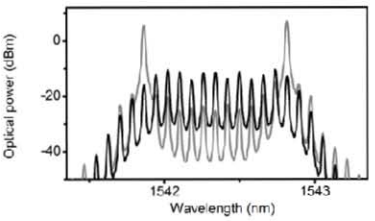

Fig. 10. Measured optical spectrum of photomixer input using OIL (grey trace) and OFCG spectrum (black trace).

B. Locking behavior

In the mode selection using optical filtering, the operation consists on tuning the center frequency of the two filters on the selected optical modes (e.g. using a voltage source to control the filters). At a first glance, the OIL seems to be a much more complex scheme. Nevertheless, we will show that the operation requirements are not very complex compared to optical filtering and performance is much better.

When the OFCG is injected into the slave laser (in this case a DFB laser), both current and especially temperature control of the DFB allow centering the slave on the selected mode from the OFCG. If the optical signal after OIL is photodetected in an ESA, the beat note between the adjacent modes of the OFCG and the slave appears. Usually, the baseband is monitored. In our case, due to the availability of adjacent modes from the OFCG, it is more convenient to monitor the region around f_{REF}. Fig. 11 shows how the beat note around 10 GHz evolves as the slave laser wavelength is centered on the selected optical mode from the master laser (GS-OFCG). Proper OIL can be identified when the noise floor drastically reduces and the peak frequency (f_{REF}) increases, as it can be seen in Fig. 11.

Nevertheless, OIL is only possible for a certain amount of injected power. In this work, we will use the injection maps to evaluate the Injected Ratio per optical Mode (IRm) that is the ratio of the slave power to the power of the selected optical and IRm) is shown in Fig. 12, where the expected V-shaped map for OIL can be observed. It must be noted that, although a wider tuning range of OIL is obtained with lower IRm, a high amount of injected power eventually produces unstable operation. Then, IRm values around 25-35 dB are preferred for our application. The estimated frequency to temperature tuning ratio for the employed DFBs is around 27.2 MHz/Ω, referred to the standard 10 kΩ thermistor included in the butterfly packages of both DM and DFB lasers.

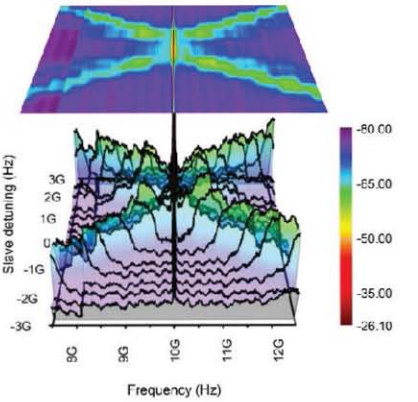

Fig. 11. OIL beat note around 10 GHz (Span = 5 GHz). (Z axis: electrical power (dBm)). Evolution of the electrical spectra with the frequency detuning of the slave laser. The IRm used is 35 dB.

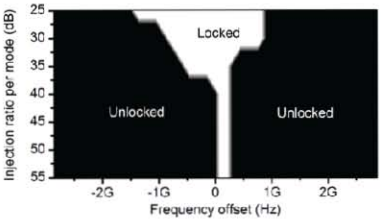

Fig. 12. Locking region map. Locking state (locked/unlocked) as a function of the frequency detuning between master and slave lasers and as a function of the IRm parameter.

C. Long Term Stability

In order to characterize the long term stability of the mode selection mechanism based on OIL, the beat note of the output of the slave laser (see Fig. 11) is monitored with respect to the time in the locked state. In Fig. 13 we monitored the OIL over time. It remained locked over the measured period of 1 hr.

lasers and the locking range (2 GHz at IRm = 25 dB). Regular laboratory-grade laser diode controllers have stability specifications of 40 ppm in current and 0.01 ºC in temperature control over 24 hours [45]. This can be translated for our setup into a 24-hour stability of 0.005 mA and 5 □ (around 150 MHz), amply within the OIL locking range. So, the system should remain stable for days as long as normal conditions in the setup are kept.

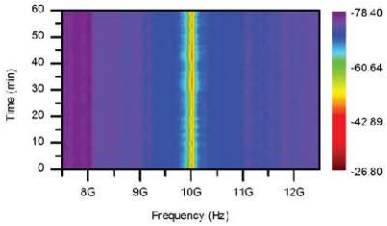

Fig. 13. OIL beat note under locked state. (Z axis: electrical power (dBm)). Evolution of the electrical spectra with time (see text for details).

V. Photomixer: n-i-pn-i-p superlattice photomixer

The photomixer used in this THz photonic synthesis system is a n-i-pn-i-p superlattice photomixer [34]. A packaged version has been used, with a FC/APC optical input and a BNC bias input. The fiber-coupled photomixer consists of a three period n-i-pn-i-p superlattice photodiode that is coupled to a logarithmic-periodic broadband antenna. It covers a frequency range from below 100 GHz to about 1.4 THz (c.f. Fig. 14 and ref [22]]). The chip (i.e. the photomixer antenna) is attached to a hyperhemispherical lens to provide a free space THz output.

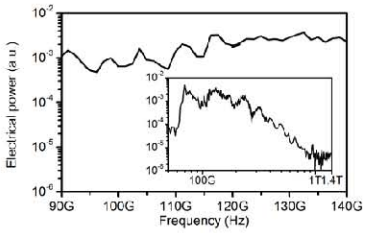

Fig. 14. Frequency response of the n-i-pn-i-p superlattice photomixer (packaged version). Inset: whole frequency response of the photomixer (X-axis is Frequency (Hz) and Y-Axis is Electrical power (a.u.). The generated photocurrent is 0.5 mA.

The frequency response of the n-i-pn-i-p photomixer in the operation frequency range is depicted in Fig. 14, which also shows the whole operation bandwidth of the device in excess of 1 THz (Fig. 14, inset).

–235.5 μA, at a bias voltage of -1.6 V. Safe long-term operation of this device is expected for a photocurrent up to -2-3 mA where the thermal load within the device is still low. Thus much higher optical power (and up to 100 times higher THz output power) could be used for this work, but as the objectives were not associated to high power generation, we kept the working point far below the maximum power.

VI. CW sub-THz Generation: experimental results

A. Experimental setup

From the characterization of the two mode selection mechanisms of sections III and IV, it can be concluded that OIL provides higher performance since it offers better mode selectivity, higher optical power associated to the selected modes, less noisy optical spectra and a much better long term stability. The CW sub-THz generated signals and their characterization are presented in this section, where OIL has been used as mode selection mechanism. The experimental setup is depicted in Fig. 9. Due to the limitations in our available electrical characterization measurement system (ESA), the results are limited up to frequencies of 140 GHz.

B. Ultra-narrow linewidth performance

The CW sub-THz signal generated at 120 GHz is shown in Fig. 15. The span and resolution bandwidth (RBW) are the minimum allowed by the ESA at this frequency range (2.1 kHz and 10 Hz, respectively). The measured FWHM of the generated mm-wave signal is 10 Hz (Fig. 15), which corresponds to the employed RBW, thus we can conclude that the actual FWHM is ≤10 Hz.

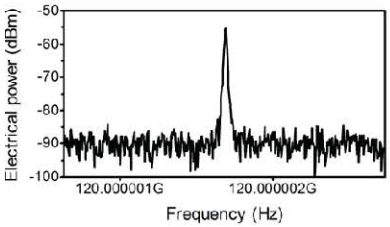

Fig. 15. Sub-THz generated signal at 120 GHz. Span = 2.1 kHz, RBW = 10 Hz, sweep time = 63 s.

This result shows that the OIL mechanism does not degrade the phase noise or FWHM of the sub-THz generated signal, providing in this sense a mode selection scheme as good as just optical filtering, where no degradation in the THz signal is produced [30], [32].

C. Ultra-high resolution tunability with complete frequency range coverage

The THz frequency delivered by the system at the output of

complete and quasi-continuous frequency coverage of the 60-140 GHz band of our THz photonic generation system is achieved in two complementary ways. The coarse tunability (in f_{REF} steps) is given by the selection of the different optical modes from the GS-OFCG using one of the two previously analyzed mode selection mechanisms. The fine tuning is accomplished by detuning f_{REF}. In this case, the detuning of the THz signal corresponds to n times the frequency change of f_{REF}.

In Fig. 16, the coarse tunability within the F band (90-140 GHz) is shown. It must be noted that the minimum selectable frequency is f_{REF}, while the maximum selectable frequency is limited by both the GS-OFCG optical span and the bandwidth of the photomixer.

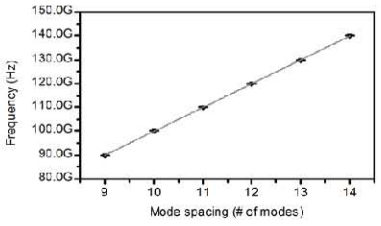

Fig. 16. Coarse tunability of f_{THz} (f_{REF} = 10 GHz). X axis: n (number of optical modes spacing); Y axis: THz output frequency, f_{THz}. Measured data (average values: black dots; standard deviation: black caps); and linear fit (grey trace). Electrical spectra measurement parameters: span = 2.1 kHz, RBW = 30 Hz, sweep time = 7 s.

In Fig. 17, the fine tunability with 1.2 GHz steps (of f_{THz}) is shown. This detuning has been chosen as it is the maximum range of tunability within the fine tunability range, that is, higher detuning would correspond to coarse tunability as the needed fine tunability range for complete continuous tunability is ± 5 GHz of f_{THz} detuning for a f_{REF} of 10 GHz. This maximum range of fine tunability (1.2 GHz f_{THZ} steps corresponds to a f_{REF} detuning of 100 MHz for n = 12) requires, as previously explained in section II, the PS to maintain the GS-OFCG characteristics and also the mode selection mechanism (see Fig. 10-13) has to be readjusted to re-lock the slave lasers.

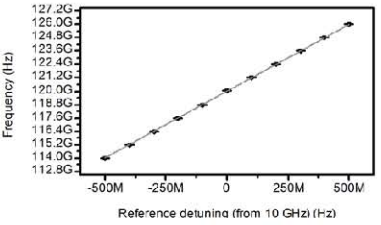

values: black dots; standard deviation: black caps); and linear fit (grey trace). Electrical spectra measurement parameters: span = 2.1 kHz, RBW = 30 Hz, sweep time = 7 s.

Fig. 18 shows a finer tunability characteristic of our system, in this case for very low frequency detuning values (120 Hz steps of f_{THZ}). For this lower tuning range, there is neither need of PS adjustments nor OIL re-locking, as the frequency detuning is within the locking range. Due to the limited frequency accuracy readout of the ESA at this frequency range [46], smaller values of frequency detuning cannot be properly measured.

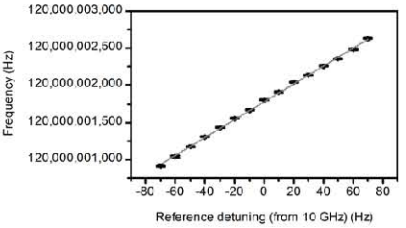

Fig. 18. Fine tunability, 120 Hz steps of f_{THZ} (f_{REF} = 10 GHz). X axis: detuning of f_{REF}; Y axis: THz output frequency, f_{THz}. Measured data (average values: black dots; standard deviation: black caps); and linear fit (grey trace). Electrical spectra measurement parameters: span = 2.1 kHz, RBW = 30 Hz, sweep time = 7 s.

The average values of the standard deviations of the set of samples of Fig. 16 to 20 are summarized in Table I. The coefficient of determination (R^2) of the linear fit of the data is also included. Almost a perfect linear behavior is achieved. Standard deviations in the range of the RBW (30 Hz for the tunability test) and below the frequency readout accuracy are obtained. Thus, and due to the ESA limitations, we cannot conclude whether these fluctuations in the values are due to the system itself, or due to measurement instrumentation uncertainty [46].

TABLE I
ULTRA-HIGH RESOLUTION CONTINUOUS TUNABILITY

Range	Average standard deviation (Hz)	R^2 linear fit
Coarse (10 GHz steps of f_{THz})	22.27	1
Fine (1.2 GHz steps of f_{THz})	21.53	1
Fine (120 Hz steps of f_{THz})	7.31	0.99985

Simultaneous control of the coarse and fine tunability allows the synthesis of signals without dead regions and with full coverage of the whole frequency range under study (60-140 GHz). Moreover, higher synthesized THz frequencies mean less PS adjustments to maintain the GS-OFCG characteristics as the detuning of f_{REF} required for a same THz frequency change is smaller.

Finally, the tuning resolution of the synthesized signal is $f_{THZ\ RES} = n \cdot f_{REF\ RES}$, where $f_{REF\ RES}$ is the resolution of the

GHz (tuning resolution of 10^{-12} over the center frequency).

D. High long-term frequency stability

The frequency stability of the synthesized THz signal is measured as a function of the time. As expected from the stability analysis of the OIL mechanism (section IV), the synthesized THz signals feature an excellent long term stability. The electrical spectra variation of the sub-THz signal over one hour is measured. It has also been measured over the minimum span (2.1 kHz), with a RBW of 30 Hz (in order to acquire more data in one hour). The variation of both peak frequency and peak power with respect to time is summarized in Table II. The power stability and especially the frequency stability are excellent. Their characterization has been again limited by the ESA, particularly for the power variation measurement, as the power accuracy in an ESA at high frequencies is low and its uncertainty is several dB´s higher than the reported standard deviation (1.5 dB) [47].

TABLE II
LONG-TERM STABILITY (1 HOUR)

Parameter	Mean value	Standard deviation
Peak frequency	120000001684.26 Hz	5.2 Hz
Peak power	-55.38 dBm	1.5 dB

Finally, the frequency stability is also studied through its Allan deviation [48]. Overlapped Allan deviation has been used and the results are shown in Fig. 20. The type of noise of the fluctuations is between white FM and Flicker FM [48]. Nevertheless, as the measurement instrumentation is not accurate enough for our system, we cannot confirm whether the noise is due to the system itself or due to the measurement system (as is the case of the tunability analysis).

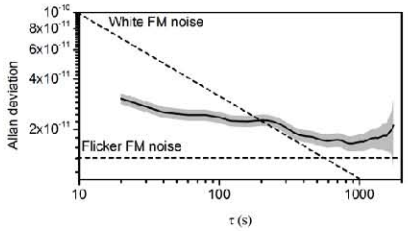

Fig. 20. Overlapped Allan deviation of the fractional frequency of the signal at 120 GHz. Black trace: overlapped Allan deviation; grey: error region.

VII. CONCLUSION

In this work, we have reported on a photonic system for generation of high quality CW sub-THz signals. The system is based on a Gain-Switching-based Optical Frequency Comb Generator (GS-OFCG), an optical mode selection mechanism and a n-i-pn-i-p superlattice photomixer. As mode selection mechanism, both selective tunable optical filtering using Fabry-Perot Tunable Filters (FPTF) and Optical Injection with respect to long term frequency and power stability. The resulting system offers sub-THz signals with linewidth values < 10 Hz at 120 GHz, complete frequency range (60-140 GHz) coverage with a resolution in the order of 0.1 Hz at 120 GHz (10^{-12} of the generated frequency), and excellent long term frequency stability (5 Hz deviation over one hour). Most of these reported values are limited by the instrumentation accuracy and resolution, thus the actual values of the system could be below the data given in this paper. The frequency can be extended straightforwardly up to 1 THz. This scheme is compact, robust, and reliable. The excellent performance is particularly well suited for sub-THz photonic Local Oscillators and high resolution spectroscopy.

REFERENCES

[1] T. Nagatsuma, "Generating millimeter and terahertz waves," *IEEE Microwave Magazine*, vol. 10, no. 4, pp. 64–74, 2009.

[2] W. R. Tribe, D. A. Newnham, P. F. Taday, and M. C. Kemp, "Hidden object detection: security applications of terahertz technology," in *SPIE 2004. Proceedings of SPIE*, 2004, 1st ed., vol. 5354, pp. 168–176.

[3] E. Pickwell and V. P. Wallace, "Biomedical applications of terahertz technology," *Journal of Physics D: Applied Physics*, vol. 39, no. 17, pp. R301–R310, Sep. 2006.

[4] R. Piesiewicz, T. Kleine-Ostmann, N. Krumbholz, D. Mittleman, M. Koch, J. Schoebel, T. Kurner, and E. Felder, "Short-Range Ultra-Broadband Terahertz Communications: Concepts and Perspectives," *IEEE Antennas and Propagation Magazine*, vol. 49, no. 6, pp. 24–39, 2007.

[5] P. H. Siegel, "Terahertz technology," *IEEE Transactions on Microwave Theory and Techniques*, vol. 50, no. 3, pp. 910–928, 2002.

[6] A. G. Davies, A. D. Burnett, W. Fan, E. H. Linfield, and J. E. Cunningham, "Terahertz spectroscopy of explosives and drugs," *Materials Today*, vol. 11, no. 3, pp. 18–26, Mar. 2008.

[7] E. Bründermann, H.-W. Hübers, and M. F. Kimmitt, *Terahertz Techniques*. Springer. Springer Series in Optical Sciences, Vol. 151, 2012, p. 383.

[8] R. E. Miles, X.-C. Zhang, H. Eisele, and A. Krotkus, "Terahertz Frequency Detection and Identification of Materials and Objects," in *Terahertz Frequency Detection and Identification of Materials and Objects*, 2007, p. 364.

[9] P. F. Taday, "Applications of terahertz spectroscopy to pharmaceutical sciences," *Philosophical Transactions of the Royal Society of London. Series A: Mathematical, Physical and Engineering Sciences*, vol. 362, no. 1815, pp. 351–364, Feb. 2004.

[10] P. F. Goldsmith and D. C. Lis, "Early Science Results From the Heterodyne Instrument for the Far Infrared (HIFI) on the Herschel Space Observatory," *IEEE Transactions on Terahertz Science and Technology*, vol. 2, no. 4, pp. 383–392, Jul. 2012.

[11] I. Cámara Mayorga, A. Schmitz, T. Klein, C. Leinz, and R. Gusten, "First In-Field Application of a Full Photonic Local Oscillator to Terahertz Astronomy," *IEEE Transactions on Terahertz Science and Technology*, vol. 2, no. 4, pp. 393–399, Jul. 2012.

[12] Virginia Diodes Co., "Virginia Diodes Co. Multipliers," 2012. [Online]. Available: http://vadiodes.com/. [Accessed: 12-Feb-2012].

[13] M. Feiginov, C. Sydlo, O. Cojocari, and P. Meissner, "Resonant-tunnelling-diode oscillators operating at frequencies above 1.1 THz," *Applied Physics Letters*, vol. 99, no. 23, pp. 233503–233506, 2011.

[14] R. Köhler, A. Tredicucci, F. Beltram, H. E. Beere, E. H. Linfield, A. G. Davies, D. A. Ritchie, R. C. Iotti, and F. Rossi, "Terahertz semiconductor-heterostructure laser.," *Nature*, vol. 417, no. 6885, pp. 156–9, May 2002.

[16] M. Asada, "Theoretical analysis of spectral linewidth of terahertz oscillators using resonant tunneling diodes and their coupled arrays," *Journal of Applied Physics*, vol. 108, no. 3, p. 034504, 2010.
[17] S. Suzuki, M. Asada, A. Teranishi, H. Sugiyama, and H. Yokoyama, "Fundamental oscillation of resonant tunneling diodes above 1 THz at room temperature," *Applied Physics Letters*, vol. 97, no. 24, p. 242102, 2010.
[18] B. S. Williams, "Terahertz quantum-cascade lasers," *Nature Photonics*, vol. 1, no. 9, pp. 517–525, Sep. 2007.
[19] M. a. Belkin, F. Capasso, F. Xie, A. Belyanin, M. Fischer, A. Wittmann, and J. J. Faist, "Room temperature terahertz quantum cascade laser source based on intracavity difference-frequency generation," *Applied Physics Letters*, vol. 92, no. 20, p. 201101, 2008.
[20] D. Rabanus, U. U. Graf, M. Philipp, O. Ricken, J. Stutzki, B. Vowinkel, M. C. Wiedner, C. Walther, M. Fischer, and J. Faist, "Phase locking of a 1.5 Terahertz quantum cascade laser and use as a local oscillator in a heterodyne HEB receiver.," *Optics Express*, vol. 17, no. 3, pp. 1159–68, Feb. 2009.
[21] Q. Qin, J. L. Reno, and Q. Hu, "MEMS-based tunable terahertz wire-laser over 330 GHz," *Optics Letters*, vol. 36, no. 5, p. 692, Feb. 2011.
[22] S. Preu, G. H. Döhler, S. Malzer, L. J. Wang, and a. C. Gossard, "Tunable, continuous-wave Terahertz photomixer sources and applications," *Journal of Applied Physics*, vol. 109, no. 6, pp. 061301–01 – 061301–56, 2011.
[23] E. Rouvalis, C. C. Renaud, D. G. Moodie, M. J. Robertson, and A. J. Seeds, "Continuous Wave Terahertz Generation From Ultra-Fast InP-Based Photodiodes," *IEEE Transactions on Microwave Theory and Techniques*, vol. 60, no. 3, pp. 509–517, Mar. 2012.
[24] Y. R. Huang, H. P. Chen, P. C. Chiu, J. I. Chyi, B. H. Wang, S. Y. Chen, and C. K. Sun, "Propagation, Resonance, and Radiation on Terahertz Optoelectronic Integrated Circuits," *IEEE Photonics Journal*, vol. 4, no. 3, pp. 1–1, 2012.
[25] Toptica Photonics, "Toptica Photonics. THz CW," 2012. [Online]. Available: http://www.toptica.com. [Accessed: 12-Feb-2012].
[26] P. Acedo, H. Lamela, S. Garidel, C. Roda, J. P. Vilcot, G. Carpintero, I. H. White, K. A. Williams, M. Thompson, W. Li, M. Pessa, M. Dumitrescu, and S. Hansmann, "Spectral characterisation of monolithic modelocked lasers for mm-wave generation and signal processing," *Electronics Letters*, vol. 42, no. 16, pp. 928–929, 2006.
[27] A. R. Criado, P. Acedo, G. Carpintero, C. de Dios, and K. Yvind, "Observation of phase noise reduction in photonically synthesized sub-THz signals using a passively mode-locked laser diode and highly selective optical filtering," *Optics Express*, vol. 20, no. 2, pp. 1253–1260, Jan. 2012.
[28] A. R. Criado, C. de Dios, P. Acedo, G. Carpintero, and K. Yvind, "Comparison of Monolithic Optical Frequency Comb Generators based on Passively Mode-Locked Lasers for Continuous Wave mm-Wave and sub-THz generation," *Journal of Lightwave Technology*, vol. 20, no. 2, pp. 1253–1260, Jan. 2012.
[29] R. Zhou, S. Latkowski, J. O'Carroll, R. Phelan, L. P. Barry, and P. M. Anandarajah, "40nm wavelength tunable gain-switched optical comb source," *Optics Express*, vol. 19, no. 26, pp. B415–20, Dec. 2011.
[30] A. R. Criado, C. de Dios, G. H. Döhler, S. Preu, S. Malzer, S. Bauerschmidt, H. Lu, A. C. Gossard, and P. Acedo, "Ultra narrow linewidth CW sub-THz generation using GS based OFCG and n-i-pn-i-p superlattice photomixers," *Electronics Letters*, vol. 48, no. 22, pp. 1425–1426, 2012.
[31] S. Ho-Jin, N. Shimizu, T. Furuta, K. Suizu, H. Ito, T. Nagatsuma, H. Song, and S. Member, "Broadband-Frequency-Tunable Sub-Terahertz Wave Generation Using an Optical Comb, AWGs, Optical Switches, and a Uni-Traveling Carrier Photodiode for Spectroscopic Applications," *Journal of Lightwave Technology*, vol. 26, no. 15, pp. 2521–2530, 2008.
[32] C. de Dios, A. R. Criado, G. H. Döhler, S. Preu, S. Malzer, S. [illegible] p-n-i-p Superlattice Photomixers," in *International Topical Meeting on Microwave Photonics. MWP 2012*, 2012.
[33] E. Rouvalis, C. C. Renaud, D. G. Moodie, M. J. Robertson, and A. J. Seeds, "Traveling-wave Uni-Traveling Carrier photodiodes for continuous wave THz generation," *Optics express*, vol. 18, no. 11, pp. 11105–10, May 2010.
[34] S. Preu, F. H. Renner, S. Malzer, G. H. Döhler, L. J. Wang, M. Hanson, a. C. Gossard, T. L. J. Wilkinson, E. R. Brown, and G. H. Döhler, "Efficient terahertz emission from ballistic transport enhanced n-i-p-n-i-p superlattice photomixers," *Applied Physics Letters*, vol. 90, no. 21, p. 212115, 2007.
[35] S. Bauerschmidt, S. Preu, S. Malzer, G. H. Döhler, L. J. Wang, H. Lu, and A. C. Gossard, "<title>Continuous wave terahertz emitter arrays for spectroscopy and imaging applications</title>," 2010, p. 76710D–76710D–11.
[36] P. P. Vasil'ev, I. H. White, and J. Gowar, "Fast phenomena in semiconductor lasers," *Reports on Progress in Physics*, vol. 63, p. 1997, 2000.
[37] R. Wu, V. R. Supradeepa, C. M. Long, D. E. Leaird, and A. M. Weiner, "Generation of very flat optical frequency combs from continuous-wave lasers using cascaded intensity and phase modulators driven by tailored radio frequency waveforms," *Optics Letters*, vol. 35, no. 19, pp. 3234–3236, Sep. 2010.
[38] M. Song, R. Wu, V. Torres-Company, and A. M. Weiner, "Programmable Microwave Photonic Phase Filters With Large Time-Bandwidth Product Based on Ultra- Broadband Optical Frequency Comb Generation," in *IEEE International Topical Meeting on Microwave Photonics. MWP 2012, 2012*, 2012.
[39] C. He, S. Pan, R. Guo, Y. Zhao, and M. Pan, "Ultraflat optical frequency comb generated based on cascaded polarization modulators," *Optics Letters*, vol. 37, no. 18, pp. 3834–3836, Sep. 2012.
[40] V. R. Supradeepa and A. M. Weiner, "Bandwidth scaling and spectral flatness enhancement of optical frequency combs from phase-modulated continuous-wave lasers using cascaded four-wave mixing," *Optics Letters*, vol. 37, no. 15, pp. 3066–3068, Aug. 2012.
[41] C. de Dios and H. Lamela, "Improvements to Long-Duration Low-Power Gain-Switching Diode Laser Pulses Using a Highly Nonlinear Optical Loop Mirror: Theory and Experiment," *Journal of Lightwave Technology*, vol. 29, no. 5, pp. 700–707, Mar. 2011.
[42] M. Egan, "The 20-Bit DAC Is the Easiest Part of a 1-ppm-Accurate Precision Voltage Source," *Analog Dialogue*, vol. 44, no. 04, 2010.
[43] L. L. Wang and T. Kowalcyzk, "A Novel Locking Technique for Very Narrow Tunable Optical Filters With Sub-GHz 3-dB Bandpass," *IEEE Photonics Technology Letters*, vol. 22, no. 17, pp. 1267–1269, Sep. 2010.
[44] M. P. van Exter, S. J. M. Kuppens, and J. P. Woerdman, "Excess phase noise in self-heterodyne detection," *IEEE Journal of Quantum Electronics*, vol. 28, no. 3, pp. 580 – 584, 1992.
[45] ILX Lightwave Co., "Tech Note: Typical Output Stability of the LDC-3724B," 2012.
[46] Anritsu Co., "MS2668C Spectrum Analyzer Operation Manual Vol. 1," 2007.
[47] Agilent Technologies, "Product Note. Agilent PSA High-Performance Spectrum Analyzer Series. Amplitude Accuracy." 2006.
[48] W. J. Riley, *NIST Special Publication 1065: Handbook of Frequency Stability Analysis*. National Institute of Standards and Technology (NIST), 2008.

Á. R. Criado (S'09) received his BSc and MSc on Telecommunication Engineering from Universidad Carlos III de Madrid (Spain) in 2009 and his MRes on Advanced Electronics Systems from Universidad Carlos III (Spain) in 2011.

He has been involved in research tasks on laser diagnostics for fusion plasmas and he worked as [illegible]

From 2009, he works toward his PhD in the field of low noise photonic generation and homodyne/heterodyne detection of mm-waves and sub-THz signals at Universidad Carlos III de Madrid.

C. de Dios received her M.S. degree in Applied Physics and Electronics from the Universidad Complutense of Madrid. Then, she joined the private sector as a Technical Consultant for Hewlett-Packard. Since 2002, she has been a member of the Optoelectronics and Laser Technology Group at the Universidad Carlos III de Madrid, where she obtained her MRes in 2004 and her Doctorate in 2010 for her work in ultrafast pulsed diode lasers and nonlinear pulse compression. Now, she is an assistant professor at the Electronics Technology Department, in this same university. Her research interests are high-speed optical communications, pulsed semiconductor laser sources, nonlinear optical phenomena and sub-terahertz and millimeter wave photonic signal synthesis and detection.

E. Prior received her BSc and MSc on Telecommunication Engineering from Universidad Carlos III de Madrid (Spain) in 2012. From 2011, she has been involved in research and development tasks related to Microwave Photonics and Radio over Fiber, in both transmission and receiver systems. She currently works on pulsed operation (Gain Switching) on VCSELs at Universidad Carlos III de Madrid.

G. H. Döhler received his Ph.D. in physics from the Technical University in Munich (Germany) in 1968. He has worked with the Max-Planck-Institute in Stuttgart and with HP-Labs in Palo Alto, before taking a position as Professor at the University of Erlangen-Nürnberg (Germany). After retiring he joined the Max Planck Institute for the Science of Light in 2009. Most of his research has been devoted to experimental and theoretical investigations of transport and optical properties of superlattices, nanostructures, nanodevices and quantum dots. Most recently he has worked on femtosecond transport in nanostructures and its application to THz emitters. He has (co)-authored more than 400 publications including many reviews, book chapters, and patents. G. H. Döhler is the recipient of the Walter-Schottky-Prize of the German Physical Society 1984. In 2004 a Sarojini Damodaran Fellowship by the Tata Institute of Fundamental Research (Mumbai) was awarded to him and in 2011 a Chair of Excellence by the University Carlos III in Madrid.

S. Preu received the Diploma degree and the Ph.D. degree in physics (*summa cum laude*) from the Univ. of Erlangen-Nuremberg, Erlangen, Germany, in 2005 and 2009, respectively. From 2004 to 2010, he was with the Max Planck Institute for the Science of Light, Erlangen, Germany. During 2010–2011, he worked at the Materials and Physics Department, University of Santa Barbara, CA. Currently, he is at the Chair of Applied Physics, University Erlangen-Nuremberg, Erlangen, Germany. His research interests focus on the development of semiconductor-based THz sources and detectors. He also works on applications of THz radiation, in particular spectroscopy, and the characterization of novel THz optics and materials such as whispering gallery mode resonators and graphene.

S. Malzer received his PhD in semiconductor physics in 1991 in Erlangen, Germany. He has been a staff member at the Institute of condensed matter physics at the University of Erlangen. There, he has been involved in III-V- optoelectronic research projects on quantum dots, high speed opto-electronics, and THz devices. Currently, his research focus is in the THz-generation by photomixing in semiconductor nanostructures and applications of CW THz tunable devices. He is co-

H. Lu received her B. S. degree in Chemistry from University of Science and Technology of China, and Ph.D in Chemistry from the City University of New York in 2007. Her Ph. D research was focused on intersubband transitions of wide bandgap II-VI semiconductors grown by MBE. She is currently working in University of California at Santa Barbara (UCSB) as a project scientist. Her current research areas include using and developing MBE growth techniques for synthesis of materials and material structures, and characterization and processing for fundamental understanding and device applications, especially applications in thermoelectrics. Other research interests include two dimensional electron gas for electronic spin states control and rare earth-V compounds in III-V semiconductors for ultrafast photoconductive switches and THz based technology. Dr. Lu has coauthored in more than 40 papers in refereed journals.

A. C. Gossard (SM'88–F'01–LF'12) is Professor of Materials and Electrical and Computer Engineering at University of California, Santa Barbara. His special interests are molecular beam epitaxy, the growth of quantum wells and superlattices, and their applications to high performance electrical and optical devices. Dr. Gossard is a fellow of the American Physical Society, AAAS, and a member of the National Academy of Engineering, and the National Academy of Sciences.

P. Acedo (M'99) received his bachelor degree on Telecommunication Engineering in 1993 from the Universidad Politécnica de Madrid, and his Doctorate (with honors) from the Universidad Carlos III de Madrid in 2000 for his work on heterodyne two color laser interferometry for fusion plasma diagnostics at the Stellarator TJ-II, (Laboratorio Nacional de Fusión, CIEMAT, Madrid) and Tokamak C-Mod (Plasma Science and Fusion Centre, Massachusetts Institute of Technology). In 2002 he was appointed as Assistant Professor by Universidad Carlos III de Madrid where he has continued with the development of scientific instrumentation systems for fusion plasma diagnostics and biomedical applications. He has been also involved in research on high speed semiconductor laser devices for microwave and millimeter-wave generation and processing. Currently his interests in this line are the development of integrated active photonic antennas for mm-wave and THz generation and detection.

CHAPTER VI

7

IEEE, Photonics Technology Letters

(published 07/2012)

Selected publication 7	
Citation	**Á. R. Criado**, C. de Dios, and P. Acedo, "Characterization of Ultra-Nonlinear SOA in a Heterodyne Detector Configuration With Remote Photonic Local Oscillator Distribution," IEEE Photonics Technology Letters, vol. 24, no. 13, pp. 1136–1138, Jul. 2012.
JCR impact factor	2.191
Submitted	01/02/2012
Published	01/07/2012
Comments	Copyright (c) 2012 IEEE. Personal use of this material is permitted. However, permission to use this material for any other purposes must be obtained from the IEEE by sending a request to pubs-permissions@ieee.org.

Table VI-7 Selected publication 7. Summary of publication information

CHAPTER VI

Characterization of Ultra Non Linear SOA in a heterodyne detector configuration with remote Photonic Local Oscillator distribution

A. R. Criado, *Student Member, IEEE,* C. de Dios and P. Acedo, *Member, IEEE*

***Abstract*— A heterodyne receiver scheme based on electro-optical (EO) downconversion is introduced. The local oscillator (LO) and the retrieved intermediate frequency (IF) signals are remotely distributed over fiber to/from a single Ultra Non Linear semiconductor optical amplifier device (SOA) that acts as a highly nonlinear mixer device, enhancing the downconversion performance of the system. The photonic LO is generated modulating a DFB under Gain Switching (GS) eliminating the need of external elements and the polarization dependency. We evaluate the performance of the downconversion up to frequencies much higher than the bandwidth of the devices (15 GHz). Results show broadband heterodyne detection performance of the system. The presented scheme offers advantages in terms of compactness, cost efficiency and can be easily scaled to remotely reach multiple receivers in scalable detection arrays.**

***Index Terms*—Microwave photonics, heterodyne receiver, optical mixing, Semiconductor Optical Amplifier,**

I. Introduction

MICROWAVE photonics has allowed to overcome many of the limitations related to traditional electronic systems in terms of bandwidth, electromagnetic interference (EMI) immunity and power losses, becoming a fundamental technology for signal distribution, broadband communications and optical signal processing [1, 2]. Among the variety of new technologies that have recently arisen following this approach [2], the study of photonic heterodyne receivers in the GHz range is an important field of study, for which the development of an optoelectronic mixer would be advantageous, allowing direct downconversion of the received RF signal to an intermediate frequency (IF) modulated on an optical carrier for further distribution and processing. Such component and their associated functionality could be directly integrated in the photonic local oscillator distribution architectures that are common place today in Radar and other fields [3].

Several optical mixing schemes have been already introduced considering elements as Mach-Zehnder modulators [4], electro-absorption modulators [5] or dual-mode monolithic laser sources [6]. These configurations have shown polarization dependence or low conversion efficiencies. These drawbacks have somehow hidden the advantages of these photonic schemes. Recently, Semiconductor Optical Amplifiers (SOA) have also been proposed as optoelectronic mixers [7-10].

Optical mixing using SOAs is usually accomplished in all-optical [9, 10] configurations, but also Electro-Optical (EO) schemes have been recently reported [7, 8]. In the EO approach, which is the most interesting in terms of obtaining a photonic heterodyne mixer, one of the electrical signals involved (i.e. the local oscillator (LO) or the radio-frequency (RF)) is modulated onto an optical carrier that is delivered to the optical input of the SOA. The other electrical signal is directly applied to the electrical port of the SOA modulating its bias voltage. Both down-conversion [8] and up-conversion [7] have been reported. These studies [7, 8] focus on the use of SOA-based EO mixing schemes for modulated RF signal distribution using Radio over Fiber (RoF) techniques. All the reported systems use polarization-dependent external modulators, and provide with sufficient mixing efficiency only in a limited range of frequencies [8].

In this work, we present the detailed study of a new scheme for electro-optical (EO) downconversion using a SOA where the LO and the retrieved IF signals are remotely distributed over fiber to/from a single COTS Ultra Non Linear SOA (XN-SOA) that acts as a mixer device in the RF detection front-end. The photonic LO is generated modulating a DFB under Gain Switching (GS) operation and the RF electrical signal is directly applied to the mixer (SOA). This eliminates the requirement of other optical components (e.g. external modulators and polarization controllers) and the subsequent polarization dependency, thus having a dramatically improvement in complexity, size, cost, energy efficiency and compactness of the system. Downconversion ratios up to -5.65 dB have been obtained in a wide frequency range (from 2 to 15 GHz), showing a broadband performance of the proposed heterodyne optoelectronic receiver. These results are specially promising for the development of scalable antenna arrays with photonic distribution of LO.

Manuscript received February 01, 2012. Work supported by the Spanish Ministry of Science and Technology through the project TEC2009-14525-C02-02. The work by A.R. Criado has been supported by the Spanish Ministry of Science and Technology under the FPI Program, Grant# BES2010-030290.

A. R. Criado, C. de Dios and P. Acedo are with the Electronics Technology Department, Universidad Carlos III de Madrid, Leganés, Madrid 28911 Spain (e-mail: cdios@ing.uc3m.es).

II. ELECTRO-OPTICAL MIXING SETUP

The scheme introduced in this work is depicted in Fig. 1. The LO signal (f_{LO}) is applied to a DFB diode laser (QPhotonics QDFBLD-1550-50) that works under GS conditions. This approach permits the modulation of the optical carrier without external modulators. The photonic LO produced has an optical frequency comb-like spectra [11] that is distributed to the heterodyne receiver using a fiber link (Fig.1a). The LO is then coupled to the optical input of the Ultra Nonlinear SOA (CIP SOA-XN-OEC-1550), where the EO mixing process takes place when the RF electrical signal (f_{RF}) introduced in the electrical port of the XN-SOA modulates its biasing point. The XN-SOA device has a small signal gain of 20dB at bias at 150 mA and a maximum saturated optical power of 13 dBm. The obtained IF appears modulating the optical carrier at the output of the XN-SOA (Fig. 1c) and is recovered at the end of the optical downlink using a high bandwidth photodiode (u2t XPDV2120R) followed by a low-pass filter. This scheme is cost effective and takes advantage of the additional non-linearities of the mixer and its polarization independence.

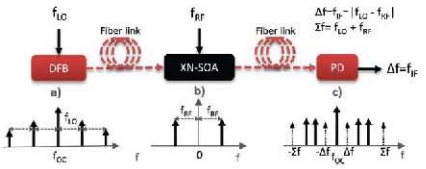

Fig. 1. EO mixing concept using an Ultra Non Linear SOA. (a) Optical output of GS DFB laser; (b) electrical signal modulating the XN-SOA bias; (c) optical output of the XN-SOA (only sum and difference terms are represented)

III. EXPERIMENTAL RESULTS

A. Characterization of the optoelectronic devices

The electronic frequency response of the transmission coefficients for the XN-SOA and the DFB are measured (Fig. 2). In both cases we obtain a 3-dB bandwidth below 2 GHz. These preliminary results may lead to the wrong assumption that the proposed system will show an operational upper frequency limit in that range, but that it is not the case as it will be demonstrated later. In this sense, we have to keep in mind that we are using both DFB laser and XN-SOA in non-linear regimes (GS and saturation, respectively).

To illustrate this later point, in Fig. 2 (bottom) we show that for the optical input power values considered in our study (P_{in}> 1.5mW) the transmission parameters of the XN-SOA remain constant when its operating current is higher than 100mA. This demonstrate that the SOA is working under saturation condition; increasing its non-linear behavior and phenomena as cross-gain modulation (XGM) are enhanced [12]. These are the operating points of interest for the EO downconversion scheme.

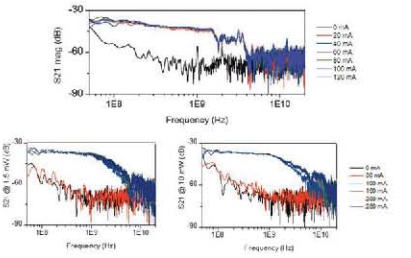

Fig. 2. Electro-optical transmission coefficients for GS DFB (top), and bias-modulated XN-SOA for 1.5mW and 10 mW optical input power (bottom).

B. Ultra-Non-Linear SOA performance as EO mixer

The parameter we have used to evaluate the performance of the system has been the downconversion ratio, defined for optoelectronics mixers as the ratio between the electrical power of the downconverted signal at f_{IF} (output of the photodiode) and the electrical power of the RF signal present after mixing at f_{RF} [9]. The downconversion efficiency map for a wide frequency range is depicted in Fig 3 (top) for the system described in Fig.1. Also in Fig. 3 (bottom) the same map is shown for the case where the LO is applied to the electrical port of the SOA to allow a comparison with previously published results [8].

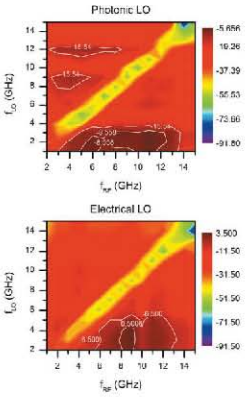

Fig. 3. Down-conversion ratio for the GS DFB as photonic LO (top) and for the bias modulated XN SOA as electrical LO (bottom).Contour lines represent 3dB and 10dB bandwidth.

An analysis of the frequency dependence of the downconversion ratio has been performed sweeping both f_{LO} and f_{RF} up to 15GHz. The bias current applied to the DFB is 40 mA, for an average optical power around 5 mW. The XN-SOA is biased at 150 mA (saturation) and shows an average optical output power of 10 mW. Regardless of the relatively high power introduced into the fiber, nonlinear effects in the

fiber are not of relevance as the transmission lengths involved are small (<500 m).

The results shown in Fig.3 demonstrate some reciprocity in the behavior of the scheme. The maximum downconversion ratio when a photonic LO is used reaches -5.65 dB. This value is smaller than the one obtained when the LO is applied to the electrical port of the SOA (3.5dB); however, the optimum downconversion area is flatter and wider with a photonic LO. These regions with better conversion ratios appear for RF frequencies in the ~4 to 13 GHz range and LO frequencies below 4 GHz. The latter frequency limit for the LO is probably associated to the direct modulation bandwidth of the DFB under GS operation (Fig. 2, top). However, this limitation does not hold for the RF frequency as the system behaves properly even for frequencies much higher than the 3 dB bandwidth of the transmission coefficients for the SOA shown in section II (Fig. 2, bottom). This demonstrates the advantages of the use of a highly nonlinear SOA as presented in this work, since it can be used as an optoelectronic mixer well above its linear 3 dB modulation bandwidth showing broadband performance as a downconversion mixer. When both frequencies (LO and IF) are close to each other, the conversion ratio falls as expected (homodyne operation). Finally, and besides the demonstrated reciprocity of this system, we have observed also the possibility of using it for up-conversion [7]. This will be key to obtain a low cost, compact and polarization independent bidirectional system.

In order to complete the characterization of the optoelectronic mixer, in Fig. 4 we show the evolution of the downconversion ratio for a photonic LO scheme versus the XN-SOA bias current at a given operation point (f_{LO}=9.1 GHz, f_{RF}=8 GHz). It can be seen that for saturated operation of the XN-SOA (above 100 mA), the downconversion ratio presents an almost constant value. This is advantageous, since other optoelectronic mixing approaches do not show this stable performance under variations in the operation point of the SOA [8]. This confirms again the importance of operating the XN-SOA in its high non-linear region to improve the mixing features of the device.

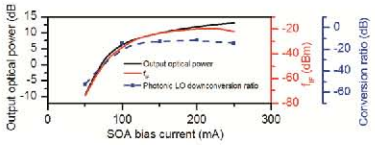

Fig. 4. Current dependence of the downconversion ratios (blue dashed), the average optical output power of the XN-SOA (solid black) and the power of the remotely recovered IF electrical signal (solid red).

IV. Conclusions

A RF heterodyne receiver scheme based on electro-optical (EO) downconversion using a single COTS Ultra Non Linear SOA (XN-SOA) without the use of any external modulator has been presented. The performance of the system has been evaluated under remote fiber distribution of a photonic LO to the heterodyne receiver and optical retrieval of the IF signal. Downconversion has been experimentally observed in a wide range of frequencies showing a broadband operation. The dependence of the downconversion ratio on the bias current applied to the XN-SOA has also been studied, showing an almost constant value for saturated operation, what is an advantage over other mixing approaches that do not show this stability under variations in the operation point of the SOA. The proposed scheme presents reciprocity as it also behaves properly when the LO is electrically applied to the XN-SOA bias voltage.

This optoelectronic mixer could find applications in scalable antennas arrays to remotely process the received signal as the LO can be remotely delivered to the RF receiver (where the RF signal is directly applied to the SOA electrical port) and the IF retrieved using optical fiber. The final scheme will result in a very compact system, with low transmission losses, lightweight and EMI immunity, valid for a relatively wide frequency range (4 to 13 GHz).

References

[1] A. J. Seeds and K. J. Williams, "Microwave Photonics," Lightwave Technology, Journal of, vol. 24, pp. 4628-4641, 2006.

[2] J. Marti and J. Capmany, "Microwave photonics and radio-over-fiber research," Microwave Magazine, IEEE, vol. 10, pp. 96-105, 2009.

[3] N. Breuil, M. Dispenza, L. Morvan, A. M. Fiorello, S. Tonda, D. Dolfi, M. Varasi, and J. Chazelas, "New optical modulation schemes applied to local oscillator distribution in radar systems," in Microwave Photonics, 2004. MWP'04. 2004 IEEE International Topical Meeting on, 2004, pp. 119-122.

[4] T. Kuri, H. Toda, and K. Kitayama, "Dense wavelength-division multiplexing millimeter-wave-band radio-on-fiber signal transmission with photonic downconversion," Lightwave Technology, Journal of, vol. 21, pp. 1510-1517, 2003.

[5] B. Hraimel, Z. Xiupu, and W. Ke, "Photonic Down-Conversion of Millimeter Wave Multiband Orthogonal Frequency Division Multiplexing Ultra-Wideband Using Four Wave Mixing in an Electro-Absorption Modulator," Lightwave Technology, Journal of, vol. 28, pp. 1987-1993, 2010.

[6] P. Acedo, H. Lamela, and C. Roda, "Optoelectronic up-conversion using compact laterally mode-locked diode lasers," Photonics Technology Letters, IEEE, vol. 18, pp. 1888-1890, 2006.

[7] J. Palací, G. Villanueva, and J. Herrera, "EAM-SOA millimeter-wave frequency up-converter for radio-over-fiber applications," Optics Communications, vol. 284, pp. 98-102, 2011.

[8] C. Bohémond, A. Sharaiha, T. Rampone, and H. Khaleghi, "Electro-optical radiofrequency mixer based on semiconductor optical amplifier," Electronics Letters, vol. 47, pp. 331-333, 2011.

[9] S. Jun-Hyuk, C. Chang-Soon, K. Young-Shik, C. Yong-Duck, K. Jeha, and C. Woo-Young, "SOA-EAM frequency up/down-converters for 60-GHz bi-directional radio-on-fiber systems," Microwave Theory and Techniques, IEEE Transactions on, vol. 54, pp. 959-966, 2006.

[10] C. Bohémond, P. Morel, A. Sharaiha, T. Rampone, and B. Pucel, "Experimental and Simulation Analysis of the Third-Order Input Interception Point in an All-Optical RF Mixer Based on a Semiconductor Optical Amplifier," Lightwave Technology, Journal of, vol. 29, pp. 91-96, 2011.

[11] P. M. Anandarajah, R. Maher, Y. Q. Xu, S. Latkowski, J. O'Carroll, S. G. Murdoch, R. Phelan, J. O'Gorman, and L. P. Barry, "Generation of Coherent Multicarrier Signals by Gain Switching of Discrete Mode Lasers," Photonics Journal, IEEE, vol. 3, pp. 112-122, 2011.

[12] N. K. Dutta and Q. Wang, Semiconductor optical amplifiers. Singapore ; Hackensack, NJ: World Scientific Pub., 2006.

CHAPTER VI

8

IEEE/OSA, Journal of Lightwave Technology (published 04/2013)

Selected publication 8	
Citation	C. de Dios, **Á. R. Criado** E. Prior and P. Acedo, "Enhancing the Performance of Electro-Optical Heterodyne Receivers using Gain Switched Photonic Local Oscillators," Journal of Lightwave Technology, vol. 31, no. 8 pp. 1331-1336, April 2013.
JCR impact factor	2.784
Submitted	06/11/2012
Published	15/04/2013
Comments	Copyright (c) 2013 IEEE. Personal use of this material is permitted. However, permission to use this material for any other purposes must be obtained from the IEEE by sending a request to pubs-permissions@ieee.org.

Table VI-8 Selected publication 8. Summary of publication information

CHAPTER VI

Enhancing the Performance of Electro-Optical Heterodyne Receivers Using Gain Switched Photonic Local Oscillators

Cristina de Dios, A. Rubén Criado, *Student Member, IEEE*, Estefanía Prior, and Pablo Acedo, *Member, IEEE*

***Abstract*—The performance of a Gain Switched (GS) optical source used as a Photonic Local Oscillator (PLO) in an Electro-Optical (EO) heterodyne receiver is experimentally evaluated and compared to the use of a traditional linearly modulated PLO. The EO heterodyne receiver used is based on an Ultra Nonlinear Semiconductor Optical Amplifier (XN-SOA) that provides a compact, cost effective and energy efficient receiver with a remote distribution of both PLO and Intermediate Frequency (IF) signals and a direct 50-ohms input for the Radiofrequency (RF) component. The comparison between both GS and linearly modulated PLO is made in terms of the conversion efficiency (conversion ratio); linearity (1-dB compression point) and noise (integrated RMS timing jitter). The analysis results in a significant improvement of the evaluated figures of merit when using a Gain Switched PLO.**

***Index Terms*—Electro-optical receiver, gain switching, heterodyne receiver, photonic local oscillator.**

I. Introduction

PROCESSING of radiofrequency (RF) signals in the optical domain has become one of the most active research fields [1], [2]. This is mainly due to the advantages that the optical approach offers, such as high bandwidth capabilities, Electromagnetic Interference (EMI) immunity, extremely low transmission losses when using optical fibers and the possibilities of including signal processing features, like True Time Delay (TTD) [3]. Another key advantage is the availability of a wide variety of high performance, compact and low cost photonic devices in the telecom wavelength range, suitable for their use in Microwave Photonics and Radio over Fiber (RoF) systems [1], [2].

Among the variety of new technologies that have been reported [1], [2], the investigation of photonic heterodyne receivers in the GHz range is an important field of study, for which the development of an optoelectronic mixer is a key element. Several optical mixing schemes have been already introduced based on elements as Mach–Zehnder modulators [4], electro-absorption modulators [5] or dual-mode monolithic laser sources [6]. The photonic heterodyne receivers can be combined with the use of remote photonic distribution of Local Oscillators (LO) and Intermediate Frequencies (IF) architectures that are becoming common place in the last years [7]. Combination of such architectures and a photonic receiver able to perform directly the mixing of the LO (distributed over optical fiber) and the RF with high sensitivity [7] will lead to flexible and scalable solutions for RoF heterodyne receivers.

Recently, Semiconductor Optical Amplifier (SOA) have been also proposed as optoelectronic mixers [8]–[11]. They are versatile, compact and reliable low cost devices. The mixing process using a SOA can be accomplished in all optical [11] or Electro-Optical (EO) configuration. In the EO mixing, only one of the electrical signals, the local oscillator (LO) or the radio-frequency (RF), is modulated on an optical carrier. The other electrical signal modulates the SOA bias voltage [8], [10]. Both downconversion [10] and upconversion [9] have been reported, considering an electrical LO.

The most straightforward Photonic LO (PLO) to be used in such architectures is based on the linear amplitude modulation of the power emitted by a diode laser, either using direct modulation or via an external modulator, being this later approximation polarization dependent and more complex in terms of component count. In addition to these two, if special operating regimes of the diode lasers are also considered, other ways of generating a PLO can be accomplished. The use of the Gain Switching (GS) technique is one of them [12], [13]. It is based on the direct modulation of diode lasers under specific bias current, modulation and frequency conditions to obtain picosecond optical pulses in the temporal domain. In the frequency domain, it shows a comb-like spectrum, different to the one offered by a linear PLO. Using this type of PLO, a good conversion efficiency has been reported in a EO heterodyne configuration [8].

In this work we present a detailed study of a scheme for EO downconversion where the PLO and the retrieved IF are remotely distributed over fiber to a single Commercial Off the Shelf (COTS) Ultra Nonlinear SOA (XN-SOA) that acts as a mixer device [8]. Several figures of merit are evaluated to study the quality of the detection such as the conversion efficiency, the linearity (1 dB compression factor) and the phase noise influence through the root mean square (RMS) integrated jitter. In order to provide a reference for one of the potential applications of this EO receiver, this last figure of merit is evaluated according to the jitter requirements of ITU-T G.709 standard for Optical Transport Networks (OTN) [14], [15]. The dependence

This work was supported in part by the Spanish Ministry of Science and Technology through the project TEC2009-14525-C02-02. The work of A. R. Criado has been supported by the Spanish Ministry of Science and Technology under the FPI Program, Grant # BES2010-030290.

The authors are with the Electronics Technology Department, Universidad Carlos III de Madrid, Leganés, Madrid 28911, Spain (e-mail: cdios@ing.uc3m.es).

Fig. 1. Optical spectra of the DFB under linear and GS modulation.

of the performance of the EO heterodyne receiver with the mixer element (XN-SOA) operating conditions (i.e., bias current) and with the RF frequency is also considered.

All these parameters are evaluated considering two PLO scenarios. The first one is a linear directly modulated Distributed Feedback (DFB) laser diode and the second is a GS pulsed optical source, based on the same device, and emitting the same average optical power. The two schemes are polarization independent and are applied to the same EO heterodyne receiver. Results show that under the figures of merit considered, the GS PLO offers better results, with a conversion ratio up to -15 dB, a linear behavior in the whole analyzed frequency range and an enhanced RMS integrated jitter performance.

II. Photonic Local Oscillator

As mentioned in the introduction, the influence of the PLO scheme used in an EO mixing architecture is one of the main objectives of this work. In this sense, we have considered two possibilities: a linear PLO, which is the commonly used LO scheme, and a GS based PLO. In the next paragraphs we discuss the use of the Gain Switching technique in the framework of PLO for EO mixing.

Gain Switching (GS) is a direct and straightforward technique typically used to obtain picosecond optical pulses from semiconductor laser sources. Such gain switched optical pulses inherit many advantages that compact semiconductor devices provide, chiefly the frequency tunability, possibility for high repetition rates and their low cost nature [16]–[18]. Although it can be applied to any diode laser (Commercial Off the Shelf, COTS, devices), it is more advantageous to use it in single mode diode lasers, since they will be less affected by dispersion and nonlinearities when propagating through an optical fiber. Also, studies have shown that they offer better quality pulsed regime [13]. Hence, for our study of a local oscillator based on a GS optical source, we will consider a COTS DFB device emitting at 1550 nm (QPhotonics 1550-50).

Fig. 1 details a typical GS experimental scheme, where a laser diode is biased with I_{bias}, and modulated at a frequency f_{LO} with a modulation depth P_m, being these the three control parameters of the pulsed regime for a given device. By changing these parameters, the pulses at the output change in width, power, repetition rate and shape.

This temporal pulsed regime has a translation in the frequency domain, where several modes separated by the repetition rate frequency appear around the original modes of the diode laser under GS in a comb-like optical spectrum. This can be also observed in the downconverted electrical spectrum recovered by an electronic spectrum analyzer after detection in a fast photodiode.

In order to start the comparison of both schemes for our PLO (linear and GS modulations) the output optical spectra from the same DFB laser under both operation modes have been experimentally studied using the same modulation frequency. This is shown in Fig. 2. In order to provide a fair comparison between the two strategies, we fix the same average optical power, 8 dBm, in both cases. This value has been chosen in order to ensure adequate linear optical propagation trough an optical fiber [8]. The parameters for GS operation are $I_{bias} = 65$ mA, modulation power of $P_m = 16$ dBm and modulation frequency $f_{LO} = 12$ GHz. For the linear modulation the frequency is also 12 GHz, with a $P_m = 4$ dBm which is the maximum value for modulation within the linear region. The I_{bias} was slightly changed to 61 mA in order to provide exactly the same average output power as in the GS case (8 dBm) avoiding the addition of extra elements in one of the scenarios such as optical attenuators.

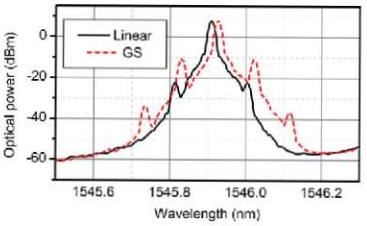

Fig. 2. Optical spectra of the DFB under linear and GS modulation.

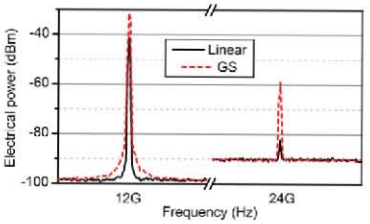

Fig. 3. Electrical spectra of the DFB under linear and GS modulation. The first (12 GHz) and second harmonic (24 GHz) are shown. $\mathbf{RBW = 100}$ kHz, $\mathbf{Span = 10}$ MHz.

As expected, under GS operation, not only the primary typical side bands corresponding to an amplitude modulated signal appear around the laser main mode as it happens under linear sinusoidal modulation (Fig. 2, continuous line), but also several side modes, separated by the applied modulation frequency f_{LO}, appear (dashed line). The shift towards longer wavelengths is caused by the different bias current. A minor asymmetry is also perceived in the GS optical spectrum, which is in well agreement with the expected behavior under this modulation regime [19].

The outputs from both schemes are downconverted using a photodiode and the output spectra observed in an electric spectral analyzer (ESA). For both cases a main peak appears at the modulation frequency (12 GHz) as well as several high orders harmonics. In Fig. 3 we show a comparison between the

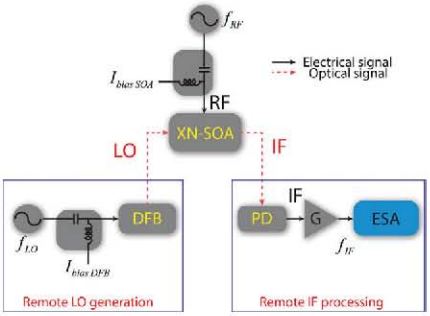

Fig. 4. Experimental setup of the EO receiver based on a XN-SOA using PLO.

fundamental and first harmonic of the GS recovered spectrum (dashed line) and the linearly modulated one (continuous line). The power at the fundamental harmonic is significantly higher for the GS case (around 10 dB bigger). The power for the second harmonic is also much higher in the GS case as compared to the power of the first harmonic in the linear case, that happens to be very small (**−85** dBm). In the GS case, the optical power is related to signal, while in the linear case, a high amount of it is DC optical power not carrying any modulation information.

Hence, though the same optical power is being distributed, its spectral distributions are different. The next section will evaluate the implications of this fact in the performance of these sources as PLO in an EO heterodyning scheme.

III. Electro-Optical Heterodyne Receiver

The EO heterodyne receiver under study in the present work is described in Fig. 4. The PLO reaches the optical input of the XN-SOA device (CIP SOA-XN-OEC-1550) where the mixing process takes place. The retrieved IF signal is modulated onto an optical carrier in the same mixing process in the XN-SOA, and is distributed via optical fiber to the Remote IF processing stage (Fig. 4). This IF signal is detected using a high bandwidth photodiode (u2t XPV2020R) that performs the optical to electronic conversion and makes the IF electronic signal available [8]. As we can see in this Fig. 4 the RF signal is directly applied to the bias port of the mixing element, the XN-SOA, that comes in a 7-PIN SMA-connector butterfly package with a 50-ohm RF input used to introduce both the bias current and the RF signal to the device (Fig. 4). The special nonlinear characteristics of the XN-SOA element considered offer a high efficient mixing in a compact, polarization independent scheme [8].

IV. Experimental Results

The scheme of Fig. 4 has been used to evaluate the several figures of merit considered to characterize the performance of the EO heterodyne receiver described previously and the influence of the two PLO schemes (GS and linear modulations). A bias-tee (65 kHz–20 GHz bandwidth) allows to introduce the bias current and the direct modulation (linear or GS) to the DFB laser. A bias-tee (65 kHz–20 GHz bandwidth) is also employed in the XN-SOA to introduce the bias current and bias modulation (i.e., RF signal). Both currents are provided by two laser diode drivers. In the remote IF processing stage, a high bandwidth photodiode (u2t XPV2020R, 50 GHz 3-dB bandwidth) performs the conversion of the IF signal from the optical to the electrical domain. A low noise 2–40 GHz preamplifier (Cernex CBL02403050-01) is used before detection in an ESA.

As stated previously, the figures of merit under study are the conversion efficiency, the linearity using the 1-dB compression point and the phase noise via the RMS integrated jitter performance of the system. This latter is of major importance since it characterizes the temporal stability of the recovered IF and it is critical in, for example, photonic signal distribution in Radar systems and Optical Transport Networks (OTN) [15].

A. Conversion Efficiency

The figure of merit considered to evaluate the efficiency of the EO heterodyne receiver is the downconversion ratio, defined for optoelectronics mixers as the ratio between the electrical power of the downconverted signal at f_{IF} (output of the photodiode) and the electrical power of the RF signal present after mixing at f_{RF} [11]. Electrical losses and the effect of the auxiliary 2–40 GHz preamplifier (Cernex CBL02403050-01, G in Fig. 4) included in the setup have been calibrated and the reported values are corrected from these effects.

Fig. 5 details the experimental results obtained after the characterization of the conversion ratio of the EO heterodyne receiver for both a linear and GS PLO and for several XN-SOA bias points versus the RF frequency.

When the XN-SOA is biased at the smallest operating current, below its gain threshold (50 mA, Fig. 5), and the GS PLO (red triangles) is considered, proper mixing behavior can be observed for almost the whole range of RF frequencies under study (5 GHz to 15 GHz). The conversion ratio increases from **−29** dB for 5 GHz to a maximum of **−17** dB at 11 GHz. When using the linearly modulated PLO (black squares), mixing behavior is not achieved for most of the range, and when it is present, the downconversion ratio is as small as **−28** dB (at 14 GHz).

When the XN-SOA is biased at higher operating current (150 mA), the mixer performance improves and the heterodyning is observable for the whole RF range and for the two PLO considered. If this operating current is increased even further, the device conversion efficiency somehow stabilizes above 250 mA, being always higher for the GS LO in approximately 11–12 dB. It can be appreciated that as the XN-SOA current increases, the conversion ratios at lower RF frequencies (below 10 GHz) have a slightly greater increment than for frequencies higher than 10 GHz. When the XN-SOA is biased at 450 mA, the GS LO offers a maximum of **−15** dB conversion efficiency at 8 GHz, and it shows a very stable behavior for the whole RF range, except for the value at 12 GHz. This is an expected result as 12 GHz is the frequency of the PLO signal and for this IF frequency (RF frequency slightly detuned to 11.9 GHz, i.e., IF frequency is 100 MHz) the RF preamplifier (G in Fig. 4) is out of its frequency working range (2–40 GHz). In the view of these results, it can be clearly seen that there is an 11–12 dB

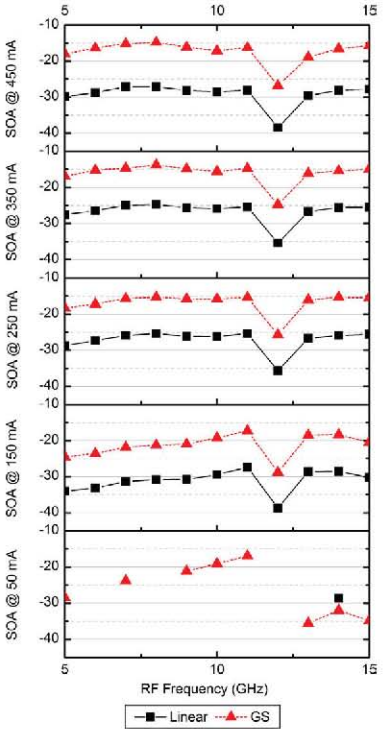

Fig. 5. Downconversion ratio (dB) for both linearly modulated (black squares) and GS modulated (red triangles) PLO under different bias point of the XN-SOA.

difference between the conversion ratios of both PLO schemes. This corresponds to the difference in modulation power that is applied between the two PLO schemes to guarantee that they emit the same average power. Under these conditions, the GS PLO is able to transport much more LO modulation information under the same average optical power. This higher LO power is transferred to the mixing process in a more efficient way.

B. Linearity

The linearity of the system has been studied through the 1-dB compression point. In order to do so, the power of the LO is kept constant while the power of the RF signal is increased. The input RF power for which the recovered IF signal did not increase linearly with the power of this RF signal by 1 dB, was identified as the 1-dB compression point.

The RF frequency was swept from 5 GHz to 15 GHz and its power from 1 dBm to 16 dBm, as 16 dBm is the maximum input power specified by the manufacturer for the RF port of the XN- SOA. The 1 dB compression point was not observable, so, within the range considered, the system is linear for all the bias operating points studied for the SOA mixer (50, 150, 250, 350 and 450 mA) and for the two types of PLO under evaluation (linearly and GS modulated), being the maximum RF input power specifications of the XN-SOA the limiting factor.

C. Noise: RMS Integrated Timing Jitter

In order to analyze the noise added by the complete EO receiver (i.e., PLO, XN-SOA and IF retrieving stage) in the downconversion process, the phase noise is evaluated through the RMS integrated jitter. The analysis of this figure of merit is important in order to evaluate the influence of the additional nonlinearities added by the GS process. The well-known standard defining OTN, ITU-T G.709 [14], is used as a reference of an actual potential application.

OTN is the current standard for optical networks with high capacity. It is based in the experience with SONET/SDH networks and was the result of the increasing need of higher line rates, new features such as optical channel management and Forward Error Correction (FEC), and global orientation [20].

There exist three different line rates in OTN: OTN1 (2.66 Gbps), OTN2 (10.7 Gbps) and OTN3 (40 Gbps). Given the operation bandwidth of our EO receiver (5–15 GHz), OTN2 frame is chosen as a restrictive limit to evaluate our noise results. The jitter requirements for OTN interfaces are defined in ITU-T G.8251 [15]. Wideband integration range is chosen instead of narrowband in order to provide a more complete view of eventual spurious signals far from the carrier. In OTN2, the wide band is defined from 20 kHz to 80 MHz [15], and this is the integration range used in our jitter analysis. The maximum allowed RMS integrated jitter in this band in order to ensure proper OTN operation is 49.93 ps. This reference value is shown in all the graphs of Fig. 6 as a dashed line.

Fig. 6 shows the RMS integrated jitter measurements for the bias current conditions of the XN-SOA previously considered with the exception of that below threshold (150, 250, 350 and 450 mA) and for a frequency range from 5 to 11 GHz. No data is shown above 12 GHz as the detected Signal to Noise Ratio (SNR) was not enough for the phase noise analyzer to perform a proper phase noise analysis. Following the trend of the analysis of other figures of merit, the EO receiver using a linearly modulated PLO only works properly for the whole frequency range at higher bias current of the XN-SOA (above 350 mA). Nevertheless, the EO mixer works properly for GS PLO for all the experimental conditions studied in this analysis and it is important to note that in all cases, the measured jitter is almost one order of magnitude better than in the case of the linearly modulated PLO. This is a significant result as it demonstrates that the use of a GS PLO, that includes some non-linear nature in its generation [12], does not degrade the noise performance of the system.

As the RMS integrated jitter covers a wide frequency range, it includes both the low frequency offset noise (mainly due to phase noise), and the high frequency offset noise (interpreted as floor noise, i.e., Noise Figure). The improvement on the noise performance when using a GS PLO instead of a linearly modulated one has its origin in the fact that under GS regime, a

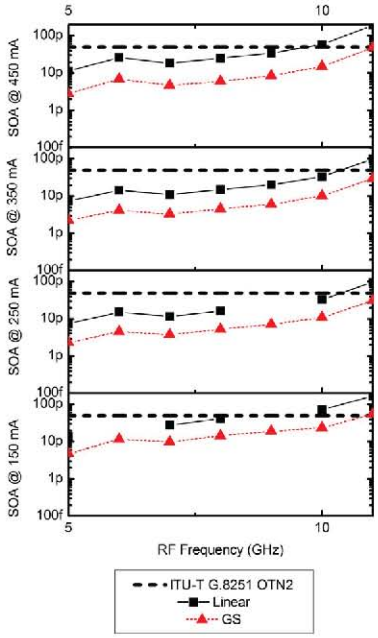

Fig. 6. RMS jitter (s) integrated over the band 20 kHz–80 MHz (OTN2 protocol) for both linearly modulated (black squares) and GS modulated (red triangles) PLO under different bias point of the XN-SOA.

much higher modulation current is applied to the laser. At the receiver, this results in a higher SNR, or equivalently a better Noise Figure of the system that is directly translated into a better noise performance, especially at higher frequency offsets.

Finally, it is worth mentioning that for the GS PLO, the RMS integrated jitter requirements for OTN2 are met for all the analyzed cases, while the linearly modulated PLO fails to do it for RF frequencies above 9 GHz for the smaller bias current (150 mA) and above 10–11 GHz for higher bias current applied to the XN-SOA (above 250 mA).

V. Conclusion

We have evaluated in detail the performance of an Electro-Optical (EO) heterodyne receiver based on an Ultra Nonlinear SOA (XN-SOA) considering several figures of merit. The scheme shows moderate conversion ratios, good linearity and a reduced root mean square (RMS) integrated jitter. However, its behavior can be significantly improved when the Photonic LO is based on a pulsed optical source as a Gain Switching (GS) DFB diode laser instead of the traditionally employed linearly modulated DFB. This pulsed regime can be induced in any diode laser, even commercially available, and permits a more efficient distribution of the same amount of optical power, where the energy transmitted is related to the LO modulation signal rather than lost in DC optical power. The performance of the receiver improves for all the figures of merit considered. The downconversion ratio increases by 11–12 dB for all RF frequency values considered and the several XN-SOA working points under study. The RMS integrated jitter is reduced by one order of magnitude, showing values that are well below the jitter requirements of ITU-T G.709 OTN standard [14] for the whole RF frequency range. The reported EO heterodyne receiver, along with the use of a Photonic LO based on GS allows for a cost-effective, compact, polarization-independent and scalable solution with enhanced performance for applications requiring LO and IF remote distribution.

References

[1] A. J. Seeds and K. J. Williams, "Microwave photonics," *J. Lightw. Technol.*, vol. 24, no. 12, pp. 4628–4641, 2006.

[2] J. Marti and J. Capmany, "Microwave photonics and radio-over-fiber research," *IEEE Microw. Mag.*, vol. 10, pp. 96–105, Jun. 2009, no..

[3] P. Berger, J. Bourderionnet, F. Bretenaker, D. Dolfi, and M. Alouini, "Time delay generation at high frequency using SOA based slow and fast light," *Opt. Exp.*, vol. 19, no. 22, pp. 21180–21188, Oct. 2011.

[4] T. Kuri, H. Toda, and K. Kitayama, "Dense wavelength-division multiplexing millimeter-wave-band radio-on-fiber signal transmission with photonic downconversion," *J. Lightw. Technol.*, vol. 21, no. 6, pp. 1510–1517, Jun. 2003.

[5] B. Hraimel, "Photonic down-conversion of millimeter wave multiband orthogonal frequency division multiplexing ultra-wideband using four wave mixing in an electro-absorption modulator," *J. Lightw. Technol.*, vol. 28, no. 13, pp. 1987–1993, Jul. 2010.

[6] P. Acedo, H. Lamela, and C. Roda, "Optoelectronic up-conversion using compact laterally mode-locked diode lasers," *IEEE Photon. Technol. Lett.*, vol. 18, no. 17–20, pp. 1888–1890, 2006.

[7] N. Breuil, M. Dispenza, L. Morvan, A. M. Fiorello, S. Tonda, D. Dolfi, M. Varasi, and J. Chazelas, "New optical modulation schemes applied to local oscillator distribution in radar systems," in *Proc. MWP*, 2004, pp. 119–122.

[8] Á. R. Criado, C. de Dios, and P. Acedo, "Characterization of ultra-nonlinear SOA in a heterodyne detector configuration with remote photonic local oscillator distribution," *IEEE Photon. Technol. Lett.*, vol. 24, no. 13, pp. 1136–1138, Jul. 2012.

[9] J. Palaci, G. Villanueva, and J. Herrera, "EAM-SOA millimeter-wave frequency up-converter for radio-over-fiber applications," *Opt. Commun.*, vol. 284, no. 1, pp. 98–102, Jan. 2011.

[10] C. Bohemond, A. Sharaiha, T. Rampone, and H. Khaleghi, "Electro-optical radiofrequency mixer based on semiconductor optical amplifier," *Electron. Lett.*, vol. 47, no. 5, pp. 331–333, 2011.

[11] S. Jun-Hyuk, C. Chang-Soon, K. Young-Shik, C. Yong-Duck, K. Jeha, C. Woo-Young, J. H. Seo, C. S. Choi, Y. S. Kang, Y. D. Chung, J. Kim, and W. Y. Choi, "SOA-EAM frequency up/down-converters for 60-GHz bidirectional radio-on-fiber systems," *IEEE Trans. Microw. Theory Tech.*, vol. 54, no. 2, pp. 959–966, 2006.

[12] P. P. Vasil'ev, I. H. White, and J. Gowar, "Fast phenomena in semiconductor lasers," *Reports Progr. Phys.*, vol. 63, p. 1997, 2000.

[13] S. M. Riecke, H. Wenzel, S. Schwertfeger, K. Lauritsen, K. Paschke, R. Erdmann, and G. Erbert, "Picosecond spectral dynamics of gain-switched DFB lasers," *IEEE J. Quantum Electron.*, vol. 47, no. 5, pp. 715–722, May 2011.

[14] ITU-T, *Interfaces for the Optical Transport Network (OTN)*, ITU-T Rec. G.709/Y.1331 2001.

[15] ITU-T, *The Control of Jitter and Wander Within the Optical Transport Network (OTN)*, ITU-T Rec. G.8251 2001.

[16] H. Shams, A. Kaszubowska-Anandarajah, P. Perry, and L. Barry, "Demonstration and optimization of an optical impulse radio ultra-wideband distribution system using a gain-switched laser transmitter," *J. Opt. Netw.*, vol. 8, no. 2, p. 179, Jan. 2009.

[17] K. Taira, T. Hashimoto, and H. Yokoyama, "Two-photon fluorescence imaging with a pulse source based on a 980-nm gain-switched laser diode," *Opt. Exp.*, vol. 15, no. 5, p. 2454, Mar. 2007.
[18] H. Liu, C. Gao, J. Tao, W. Zhao, and Y. Wang, "Compact tunable high power picosecond source based on Yb-doped fiber amplification of gain switch laser diode," *Opt. Exp.*, vol. 16, no. 11, pp. 7888–7893, 2008.
[19] C. de Dios and H. Lamela, "Improvements to long-duration low-power gain-switching diode laser pulses using a highly nonlinear optical loop mirror: Theory and experiment," *J. Lightw. Technol.*, vol. 29, no. 5, pp. 700–707, 2011.
[20] Agilent Technologies, Application Note: 1379. An Overview of ITU-T G. 709, 2001.

C. de Dios received the M.S. degree in applied physics and electronics and the M.Res. in 2004 and Doctorate in 2010 for her work in ultrafast pulsed diode lasers and nonlinear pulse compression, from the Universidad Complutense of Madrid, Madrid, Spain.

She then joined the private sector as a Technical Consultant for Hewlett-Packard. Since 2002, she has been a member of the Optoelectronics and Laser Technology Group at the Universidad Carlos III de Madrid. Currently, she is an Assistant Professor at the Electronics Technology Department in this same university. Her research interests are high-speed optical communications, pulsed semiconductor laser sources, nonlinear optical phenomena and sub-terahertz and millimeter wave photonic signal synthesis and detection.

A. R. Criado (S'09) received the B.Sc. and M.Sc. (2009) n telecommunication engineering and the M.Res. degree on advanced electronics Systems from Universidad Carlos III de Madrid, Madrid, Spain, in 2011, where he is currently working toward the Ph.D. degree in the field of low noise photonic generation and homodyne/heterodyne detection of mm-waves and sub-THz signals.

He has been involved in research tasks on laser diagnostics for fusion plasmas, specifically electronic density measurement using two color multichannel laser interferometry, and he worked as collaborator researcher during 2009 and 2010 in the National Fusion Laboratory in CIEMAT (Spain).

E. Prior received the B.Sc. and M.Sc. degrees in telecommunication engineering from Universidad Carlos III de Madrid, Madrid, Spain, in 2012.

Since 2011, she has been involved in research and development tasks related to Microwave Photonics and Radio over Fiber, in both transmission and receiver systems. She currently works on pulsed operation (gain switching) on VCSELs at Universidad Carlos III de Madrid.

P. Acedo (M'99) received the B.S. degree on telecommunication engineering in 1993 from the Universidad Politécnica de Madrid, Madrid, Spain, and the Doctorate (hons) from the Universidad Carlos III de Madrid, Spain, in 2000 for his work on heterodyne two color laser interferometry for fusion plasma diagnostics at the Stellarator TJ-II, (Laboratorio Nacional de Fusión, CIEMAT, Madrid) and Tokamak C-Mod (Plasma Science and Fusion Centre, Massachusetts Institute of Technology).

In 2002 he was appointed as Assistant Professor by Universidad Carlos III de Madrid where he has continued with the development of scientific instrumentation systems for fusion plasma diagnostics and biomedical applications. He has been also involved in research on high speed semiconductor laser devices for microwave and millimeter-wave generation and processing. Currently his interests in this line are the development of integrated active photonic antennas for mm-wave and THz generation and detection.

9

Hindawi, Advances on Optical Technologies (published 09/2012)

Selected publication 9	
Citation	**Á. R. Criado**, J. Montero-de-Paz, C. de Dios, L. E. García, D. Segovia, and P. Acedo, "Photonic Heterodyne Pixel for Imaging Arrays at Microwave and mm-wave Frequencies," Advances on Optical Technologies
JCR impact factor	N/A
Submitted	27/06/2012
Published	09/2012
Comments	Special issue: "Microwave Photonics"

Table VI-9 Selected publication 9. Summary of publication information

CHAPTER VI

Research Article

Photonic Heterodyne Pixel for Imaging Arrays at Microwave and MM-Wave Frequencies

Á. R. Criado,[1] J. Montero-dePaz,[2] C. de Dios,[1] L. E. García,[2] D. Segovia,[2] and P. Acedo[1]

[1] *Electronics Technology Department, Universidad Carlos III de Madrid, 28911 Leganés, Spain*
[2] *Grupo de Radiofrecuencia (GRF), Universidad Carlos III de Madrid, 28911 Leganés, Spain*

Correspondence should be addressed to P. Acedo, pag@ing.uc3m.es

Received 27 June 2012; Accepted 13 September 2012

Academic Editor: Borja Vidal

The use of photonic heterodyne receivers based on semiconductor optical amplifiers to be used in imaging arrays at several GHz frequencies is evaluated. With this objective, a 3×3 imaging array based on such photonic pixels has been fabricated and characterized. Each of the receiving optoelectronic pixels is composed of an antipodal linear tapered slot antenna (LTSA) that sends the received RF signal directly to the electrical port of a semiconductor opticalamplifier (SOA) acting as the optoelectronic mixer. Both the local oscillator (LO) and the intermediate frequency (IF) signals are directly distributed to/from the array pixels using fiber optics, that allows for remote LO generation and IF processing to recover the image. The results shown in this work demonstrate that the performances of the optoelectronic imaging array are similar to a reference all-electronic array, revealing the possibility of using this photonic architecture in future high-density, scalable, compact imaging arrays in microwave and millimeter wave ranges.

1. Introduction

Microwave photonics and radio-over-fiber (RoF) techniques have been used in antenna arrays for some years now typically associated with local oscillator (LO) distribution and remote intermediate frequency (IF) processing [1]. The advantages usually associated with the use of such techniques are the high bandwidth capabilities, the electromagnetic interference (EMI) immunity, the extremely low transmission losses when using optical fibers, and the possibilities of including signal processing features, like true local time delay (TTD) [2] or optical beam forming [3]. Their advantages are also associated with the availability of optical/photonic devices in the telecom wavelength range which, due to the growth of the optical communications in the last decades, provide us with high-performance, wide-variety, compact, and low-cost (COTS) optical components suitable for its use in microwave photonics and RoF.

Following this trend, new functionalities based on photonic processing of RF are becoming available to be incorporated into arrays beyond optical signal distribution. In this sense, a major contribution to obtain high-density receiving arrays based on photonic techniques would be the obtaining of a photonic heterodyne receiver able to perform directly the mixing of the LO (photonically distributed) and the received RF with high sensitivity. This all-optical pixel would reduce the several electrooptical (EO) conversions typical to conventional RoF systems and would be able to be integrated directly into the mature optical signal distribution architectures already available. In order to obtain such heterodyne optoelectronic RF detector, several mixing techniques have been already proposed using components as Mach-Zehnder modulators [4], electroabsorption modulators [5], or dual-mode monolithic laser sources [6] that show polarization dependence or low conversion efficiencies. Recently, semiconductor optical amplifiers (SOAs) have also been proposed as optoelectronic mixers [7–10]. Optical mixing using SOAs has been demonstrated both in all-optical [9, 10] and electrooptical (EO) configurations [7, 8]. In the EO approach, which is the most interesting in terms of obtaining a photonic heterodyne mixer, one of the electrical signals involved (i.e., the local oscillator (LO) or the radio-frequency (RF)) is modulated onto an optical carrier that is delivered to the optical input of the SOA. The other electrical

signal is directly applied to the electrical port of the SOA modulating its bias voltage. Both downconversion [8] and upconversion [7] have been reported.

One of the fields these all-optical pixel-based receiving arrays will have a great impact on is microwave and millimeter wave imaging. These techniques have been successfully demonstrated for a variety of applications like nondestructive testing [11], medical imaging [12], and security applications [13]. Usually these systems, working either in near field or far field, have their pixel elements multiplexed in the RF level into a single receiver to obtain reasonable size systems. Recently, a portable real-time camera at 24 GHz based on this strategy has been reported [14], but although the speed is reasonably good (22 frames per second) the resolution (24×24 pixels) is still far to be the required for the applications mentioned above, especially if we address the necessity of obtaining a portable (low-size and -weight) device.

In this sense, the incorporation of all-optical RF receiving pixel-based photonic mixing techniques [15] to imaging arrays will have a major impact on the resulted size, weight, and power consumption of the system. The high integration potential associated to PICs (photonic integrated circuits) [16] allows also for the integration on the same substrate of all the required functionalities necessary to process RF frequencies in the optical domain. Nowadays, several high-functionality PICs have already been reported [17], especially for optical communication purposes, demonstrating that the technology is already mature to implement other functionalities.

With this aim, in this work we present a three by three element (3×3) imaging array based on a heterodyne optoelectronic pixel based on an electrooptical (EO) ultra nonlinear mixer using an ultra nonlinear semiconductor optical amplifier (XN-SOA) [15]. This XN-SOA EO mixer presents a direct RF electrical input provided by an antipodal linear tapered slot antenna (LTSA) [18]. The LO is optically introduced at the optical input of the XN-SOA, and the IF is also optically delivered at its output, allowing for remote photonic LO generation and remote IF processing over optical fiber. Both, the mixing scheme and the used antenna make up a compact, low-cost, and flexible receiving heterodyne antenna that offers good scalability properties for imaging array applications. In this work, first imaging results using the heterodyne optoelectronic pixel 3×3 array are presented. Although the imaging system presented in this paper works at a relatively low frequency (13 GHz), the high bandwidth associated to the photonic components already available for optical communications opens the possibility to scale the presented architecture to higher (millimeter wave) frequencies.

2. Description and Characterization of the Heterodyne Optoelectronic Pixel for Imaging Arrays

2.1. Heterodyne Optoelectronic Pixel Fundamentals. The core of the reported photonic imaging array is an ultra nonlinear semiconductor optical amplifier (XN-SOA) based heterodyne pixel receiver that makes our system compact and cost-effective. The scheme is depicted in Figure 1 [15]. The LO signal (f_{LO}) is applied to a distributed feedback (DFB) diode laser (QPhotonics QDFBLD-1550-50) that works under gain switching conditions [19], allowing for the modulation of the optical carrier without external modulators. The photonic LO produced has an optical frequency comb-like spectra [15] that is distributed to the heterodyne receiver using a fiber link (Figure 1(a)). The LO is then coupled to the optical input of the ultra nonlinear SOA (CIP SOA-XN-OEC-1550), where the EO mixing process takes place when the RF electrical signal (f_{RF}) introduced into the electrical port of the XN-SOA modulates its bias point. The XN-SOA device has a small signal gain of 20 dB at 150 mA bias current and a maximum saturated optical output power of 13 dBm. The obtained IF appears modulating the optical carrier at the output of the XN-SOA (Figure 1(c)) and is recovered at the end of the optical downlink using a high bandwidth photodiode (u2t XPDV2120R) followed by a low-pass filter. This scheme is cost-effective and takes advantage of the additional nonlinearities of the mixer and its polarization independence compared to other schemes already proposed [7, 8].

It is important to note in this scheme that no external modulator is used for the photonic LO generation and neither a laser nor an external modulator is needed for modulating the RF signal onto an optical carrier for the mixing process. Moreover, no optical coupler is required to add the optical signals containing LO and RF prior to the SOA input, as it is typical to previous reported schemes [9]. In this way, most devices usually employed in typical RoF architectures are avoided, thus having a much more compact and cost-effective configuration, allowing for easier integration onto a single PIC. The proposed approach, with the LO and the IF distributed over fiber, results in an especially suitable strategy for scaled and flexible signal distribution in large array applications.

2.2. Heterodyne Optoelectronic Pixel Description. The optoelectronic heterodyne pixel incorporates to the EO mixing scheme described above for heterodyne RF detection, a broadband antenna to provide the XN-SOA with an impedance as constant as possible along its broad working band. For this reason an antipodal linear tapered slot antenna (LTSA) [18] has been selected (Figure 2). As a substrate, Rogers Duroid 5880, with $\varepsilon r = 2.2$ and 0.787 mm thickness, has been chosen. In Figure 2, we see how the antenna collects the RF signal that is directly delivered to the bias port of the XN-SOA of Figure 1. The optical signal at the output of the XN-SOA, that contains the IF, is delivered over optical fiber to the remote IF-processing stage, where a photodiode performs the conversion from optical to electrical domain.

2.3. Heterodyne Optoelectronic Pixel Characterization. The characterization of the heterodyne pixel must include both the evaluation of the performances of the photonic mixing scheme (Figure 1) and the antenna (Figure 2). The parameter

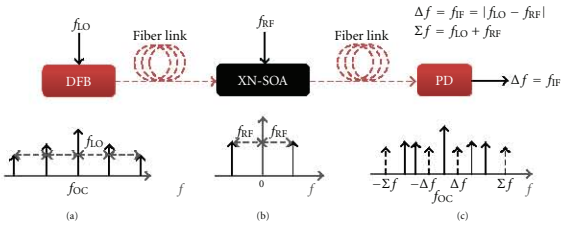

Figure 1: EO mixing concept using an ultra nonlinear SOA. (a) Optical output of GS DFB laser; (b) electrical signal modulating the XN-SOA bias; (c) optical output of the XN-SOA (only sum and difference terms are represented).

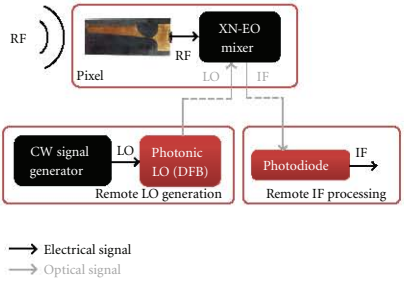

Figure 2: Heterodyne photonic receiving antenna setup.

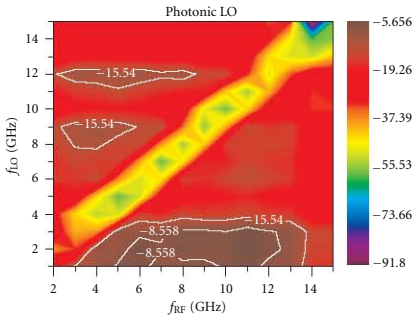

Figure 3: Downconversion ratios in dB for the photonic mixer. Contour lines represent 3 dB and 10 dB bandwidth.

we have used to evaluate the performance of the photonic mixer has been the downconversion ratio (Figure 3), defined for optoelectronics mixers as the ratio between the electrical power of the downconverted signal at f_{IF} (output of the photodiode) and the electrical power of the RF signal present after mixing at f_{RF} [9]. An analysis of the frequency dependence of the downconversion ratio has been performed sweeping both f_{LO} and f_{RF} up to 15 GHz. The bias current applied to the DFB is 40 mA, for an average optical power around 5 mW. The XN-SOA is biased at 150 mA (saturation) and shows an average optical output power of 10 mW. The regions with better (higher) conversion ratios appear for RF frequencies in the ∼4 to 13 GHz range and LO frequencies below 4 GHz. When both frequencies (LO and IF) are close to each other, the conversion ratio falls as expected (homodyne operation).

As mentioned before, the broadband antenna design selected for the receiver pixels is an antipodal LTSA [18] that includes a number of corrugations in order to make the beam symmetric and improve its radiation pattern [20]. The characterization of the antenna started with the measurement of the reflection coefficient. In Figure 4, we show the reflection coefficient for the LTSA demonstrating a working frequency band from 7 GHz to 20 GHz with the

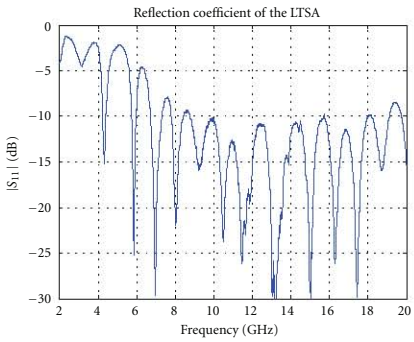

Figure 4: Measured reflection coefficient of the manufactured LTSA.

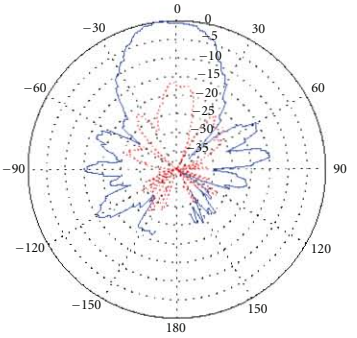

(a)

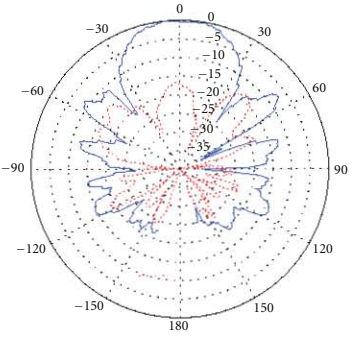

(b)

Figure 5: Antipodal LTSA radiation pattern (measured at 13 GHz).

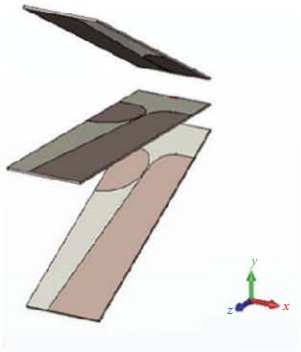

Figure 6: 3 × 1 Subarray based on antipodal LTSAs.

Figure 7: Picture of the actual 3 × 3 array inside the anechoic chamber.

desired relatively constant impedance presented to the XN-SOA over frequency. Also the radiation pattern has been measured, as shown in Figure 5, where such radiation pattern at 13 GHz is displayed as an example of how each of the elements of the array radiates. This antenna has a directivity in the whole band around 9 dBi-10 dBi.

3. Imaging Array Description and Experimental Setup

The final objective of this work is to validate the use of the introduced optoelectronic pixel for heterodyne RF detection in imaging arrays incorporating the advantages of remote photonic LO and IF distribution and the high integration capability of photonic circuits. For this reason, a 3 × 3 element array has been designed and fabricated based on the pixel described above to proof the concept. The 3 × 3 array design is based on three 3 × 1 subarray elements as shown in Figure 6, where we can see the LTSA radiant elements chosen for the pixels. Upper and lower elements are tilted 30° with respect to the central element in order to scan different directions and provide faster scanning capabilities. The final array built is shown in Figure 7, where we can see the actual appearance of the array made of the subarrays of Figure 5. A 130 × 110 × 70 mm PVC box has been designed to hold the complete array and provide the desired tilt to the antennas. Each horizontal subarray (Figure 6) is formed by 3 LTSAs printed on a 110 × 100 mm Rogers Duroid 5880 substrate separated 30 mm from each other. Each subarray

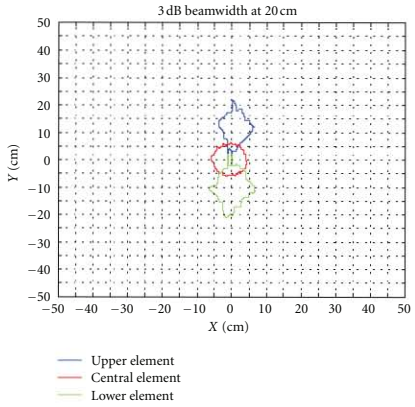

Figure 8: Beam spot diameter at 20 cm from the subarray from Figure 6. Working frequency 13 GHz.

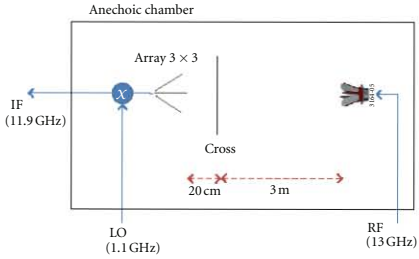

Figure 9: Imaging experiment (see text for details).

has been manufactured with a LPKF ProtoLaser S laser milling machine.

As mentioned briefly in the introduction, microwave imaging arrays (cameras) can be operated either in near field (higher spatial resolution) or far field. If the later is the case (far field imaging), the spatial resolution is fixed by the spot size of the array elements individual beams. In Figure 8, we show the measured spot diameter for the subarray shown in Figure 6 at 20 cm of the antenna (inside an anechoic chamber). These measurement results show 10 cm spot diameters (3 dB) for 13 GHz RF frequency. It is important to highlight that this spot diameter for the antenna elements that fixes the spatial resolution of the imaging system can be improved by increasing the operating frequency, as the types of antennas we are planning to use at higher frequencies present similar radiation patterns. In this situation, it is basically the operation frequency the

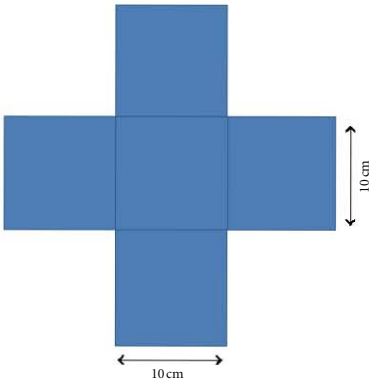

Figure 10: Metallic target for the imaging experiment.

parameter that fixes the spatial resolution of the system (beam diameter).

In order to evaluate the imaging performances of the array, an imaging experiment has been carried out (Figure 9). The working frequency has been chosen using the down-conversion ratios map of Figure 3 for optimum performance of the heterodyne photonic pixels (f_{RF} = 13 GHz, f_{LO} =1.1 GHz). The 11.9 GHz IF (intermediate frequency) is remotely recovered for each pixel with a high-speed photodiode). In Figure 9, we can see how a transmitter element (horn) illuminates at the designated frequency (13 GHz) a metallic object placed 3 m from the emitter (horn) and 20 cm from the 3 × 3 imaging array. It is important to note here that these are the conditions used to evaluate the spot diameter for the independent elements of the array (10 cm, Figure 8), which will limit the spatial resolution of the system. For the results shown in the next section, the metallic object chosen for the imaging experiment is an aluminum cross of 300 mm × 300 mm dimensions shown in Figure 10. Its dimensions are in the order of magnitude of the beam size.

4. Experimental Results

The images obtained for the object of Figure 10 are shown in Figures 11 and 12 using two different receiving pixels. As a preliminary step, and to separate the influence of the use of an optoelectronic pixel from the actual imaging capabilities of the array built, the array for Figure 7 is equipped with a set of electronic mixers, including RF preamplification, to evaluate the actual spatial resolution of the array. The results obtained are shown in Figure 11, where we can see that the cross is resolved through the simultaneous recovery of the amplitude signals for each pixel of the array. In this sense, it is important to note again that the beam diameter at 20 cm of the array is 10 cm, limiting the spatial resolution as can be extracted from Figure 11.

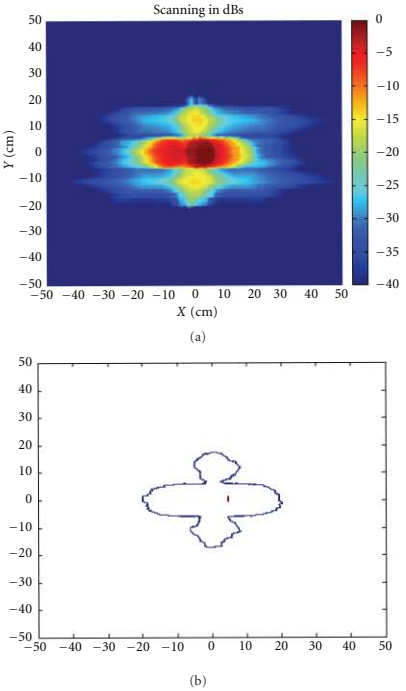

Figure 11: Results from the scanning of the object shown in Figure 10 with the 3 × 3 array using an electronic mixer for heterodyne detection. (a): power difference measured for each pixel with and without the cross (in dB). (b): −10 dB contour for the results shown on (a).

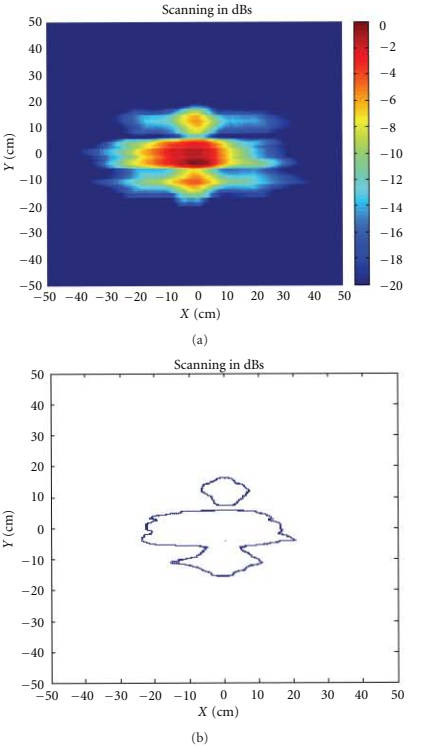

Figure 12: Results from the scanning of the object shown in Figure 10 with the 3 × 3 array using an optoelectronic mixer for heterodyne detection with remote LO and IF distribution. (a): power difference measured for each pixel with and without the cross (in dB). (b): −10 dB contour for the results shown on (a).

The scanning results obtained for the optoelectronic heterodyne pixel array are shown in Figure 12. We can observe that the image obtained is similar to the one recovered using electronic pixels (Figure 11). It must be noted at this point that, in this case, both the LO and IF are optically distributed using fiber optics to/from the array, eliminating the necessity of further electronics in the individual pixels. In this sense, this photonic-based imaging array presents evident advantages associated with its lower weight, lower power consumption EMI immunity, and flexibility, along with the integration capabilities associated with the possibility of implementing the XN-SOA and optical distribution fibers as photonic integrated circuits.

5. Conclusions

Microwave and millimeter wave imaging techniques have demonstrated their capacities in several and important application fields. In order to introduce the well-known advantages of microwave photonics and radio-over-fiber techniques in this emerging field, in this work we have designed, implemented, and tested an imaging array based on a photonic heterodyne receivers. The objective is to take advantage of the already well-known advantages of photonic local oscillator distribution in antenna arrays and the introduction of a novel optoelectronic mixer to reduce even further the electronic components count at the antenna front-end, reducing thus power consumption, space, and cost at the expenses of a little less sensitivity. The photonic setup chosen, based on an XN-SOA in EO configuration, reduces also the optical elements typical to other optoelectronic mixers schemes (using external modulators, polarization control optics, etc), allowing for further

integration of the different optoelectronic components in photonic integrated circuits (PICs).

The results shown demonstrate the possibility of using this approximation for imaging arrays in the GHz band, but, even more important, they open the possibility to scale this architecture (once that has been validated) to higher frequencies (100 GHz). This further step is associated with the high bandwidth of the photonic components already available in the market for optical communications. In this sense, preliminary work of 100 GHz imaging arrays are already being under development.

References

[1] J. Marti and J. Capmany, "Microwave photonics and radio-over-fiber research," *Microwave Magazine, IEEE*, vol. 10, pp. 96–105, 2009.

[2] P. Berger, J. Bourderionnet, F. Bretenaker, D. Dolfi, and M. Alouini, "Time delay generation at high frequency using SOA based slow and fast light," *Optics Express*, vol. 19, pp. 21180–21188, 2011.

[3] L. Jofre, C. Stoltidou, S. Blanch et al., "Optically beamformed wideband array performance," *IEEE Transactions on Antennas and Propagation*, vol. 56, no. 6, pp. 1594–1604, 2008.

[4] T. Kuri, H. Toda, and K. I. Kitayama, "Dense wavelength-division multiplexing millimeter-wave-band radio-on-fiber signal transmission with photonic downconversion," *Journal of Lightwave Technology*, vol. 21, no. 6, pp. 1510–1517, 2003.

[5] B. Hraimel, X. Zhang, and K. Wu, "Photonic down-conversion of millimeter wave multiband orthogonal frequency division multiplexing ultra-wideband using four wave mixing in an electro-absorption modulator," *Journal of Lightwave Technology*, vol. 28, no. 13, Article ID 5473097, pp. 1987–1993, 2010.

[6] P. Acedo, H. Lamela, and C. Roda, "Optoelectronic up-conversion using compact laterally mode-locked diode lasers," *IEEE Photonics Technology Letters*, vol. 18, no. 17, pp. 1888–1890, 2006.

[7] J. Palací, G. Villanueva, and J. Herrera, "EAM-SOA millimeter-wave frequency up-converter for radio-over-fiber applications," *Optics Communications*, vol. 284, no. 1, pp. 98–102, 2011.

[8] C. Bohémond, A. Sharaiha, T. Rampone, and H. Khaleghi, "Electro-optical radiofrequency mixer based on semiconductor optical amplifier," *Electronics Letters*, vol. 47, no. 5, pp. 331–333, 2011.

[9] J. H. Seo, C. S. Choi, Y. S. Kang, Y. D. Chung, J. Kim, and W. Y. Choi, "SOA-EAM frequency up/down-converters for 60-GHz Bi-directional radio-on-fiber systems," *IEEE Transactions on Microwave Theory and Techniques*, vol. 54, no. 2, pp. 959–966, 2006.

[10] C. Bohémond, P. Morel, A. Sharaiha, T. Rampone, and B. Pucel, "Experimental and simulation analysis of the third-order input interception point in an all-optical rf mixer based on a semiconductor optical amplifier," *Journal of Lightwave Technology*, vol. 29, no. 1, Article ID 5638116, pp. 91–96, 2011.

[11] S. Kharkovsky and R. Zoughi, "Microwave and millimeter wave nondestructive testing and evaluation," *IEEE Instrumentation and Measurement Magazine*, vol. 10, no. 2, pp. 26–38, 2007.

[12] T. Henriksson, N. Joachimowicz, C. Conessa, and J. C. Bolomey, "Quantitative microwave imaging for breast cancer detection using a planar 2.45 GHz system," *IEEE Transactions on Instrumentation and Measurement*, vol. 59, no. 10, pp. 2691–2699, 2010.

[13] D. M. Sheen, D. L. McMakin, and T. E. Hall, "Three-dimensional millimeter-wave imaging for concealed weapon detection," *IEEE Transactions on Microwave Theory and Techniques*, vol. 49, no. 9, pp. 1581–1592, 2001.

[14] M. T. Ghasr, M. A. Abou-Khousa, S. Kharkovsky, R. Zoughi, and D. Pommerenke, "Portable real-time microwave camera at 24 GHz," *IEEE Transactions on Antennas and Propagation*, vol. 60, no. 2, pp. 1114–1125, 2012.

[15] Á. R. Criado, C. de Dios, and P. Acedo, "Characterization of Ultra Non Linear SOA in a heterodyne detector configuration with remote Photonic Local Oscillator distribution," *IEEE Photonics Technology Letters*, vol. 24, no. 13, pp. 1136–1138, 2012.

[16] X. Leijtens, "JePPIX: the platform for Indium Phosphide-based photonics," *Optoelectronics, IET*, vol. 5, pp. 202–206, 2011.

[17] S. Ristic, A. Bhardwaj, M. Rodwell, L. Coldren, and L. Johansson, "An optical phase-locked loop photonic integrated circuit," *Journal of Lightwave Technology*, vol. 28, no. 4, pp. 1–1, 2009.

[18] K. S. Yngvesson, T. L. Korzeniowski, Y. S. Kim, E. L. Kollberg, and J. F. Johansson, "Tapered slot antenna—a new integrated element for millimeter—wave applications," *IEEE Transactions on Microwave Theory and Techniques*, vol. 37, no. 2, pp. 365–374, 1989.

[19] C. De Dios and H. Lamela, "Improvements to long-duration low-power gain-switching diode laser pulses using a highly nonline optical loop mirror: theory and experiment," *Journal of Lightwave Technology*, vol. 29, no. 5, Article ID 5678610, pp. 700–707, 2011.

[20] J. B. Rizk and G. M. Rebeiz, "Millimeter-wave Fermi tapered slot antennas on micromachined silicon substrates," *IEEE Transactions on Antennas and Propagation*, vol. 50, no. 3, pp. 379–383, 2002.

CHAPTER VI

10

Preprint A

Selected preprint A	
Citation	**Á. R. Criado** et al., "Zero-bias mm-wave optoelectronic heterodyne detection with np-i-pn THz detector and ultra-narrow linewidth sub-THz photonic Local Oscillator,"
JCR impact factor	N/A
Submitted	N/A
Published	N/A
Comments	

Table VI-10 Selected preprint A. Summary of preprint information

CHAPTER VI

Zero-bias mm-wave optoelectronic heterodyne receiver with a np-i-pn quasi-ballistic detector and ultra-narrow linewidth sub-THz photonic Local Oscillator

A. R. Criado, Author, Author, Author, …

***Abstract*—We report on a novel scheme for electro-optical (EO) heterodyne detection based on a np-i-pn quasi-ballistic THz detector and a ultra-narrow linewidth photonic local oscillator (LO). The THz detector is based in a new design concept for homodyne/heterodyne detection and is fabricated from a symmetric n+p+-i-p+n+ In0.53(Ga1-x Alx)0.47As-layer structure. The photonic LO is able to provide all the advantages of photonic THz generation (i.e. whole frequency range coverage, optical fiber distribution) and matching or even surpassing the signal quality of the best available electronic systems for sub-THz generation (e.g. Schottky multipliers): generated linewidth ≤ 10 Hz, frequency resolution of 0.1 Hz and excellent power and frequency stability. The first implementation of this np-i-pn detector is evaluated in both sub-THz direct and heterodyne receiving schemes, demonstrating zero-bias operation capabilities and excellent linearity. This EO heterodyne receiver is a promising candidate for systems with improved dynamic range in the sub-THz range, especially for those applications where remote THz operation is desirable, due to the zero-bias operation of the np-i-pn THz detectors and the photonic LO distribution.**

***Index Terms*—THz Local Oscillator, narrow linewidth THz generation, THz photonic generation, THz heterodyne detection, THz receivers, np-i-pn photomixers.**

I. Introduction

THE THz frequency region (0.1-10 THz) has remain mostly unexplored until the last decades, when the technological capabilities have permitted the development of suitable enough generation and detection devices allocated in this frequency region [1], [2]. First research results in the frequency region that today is known as THz region dates back to the first decades of 20th century [3], when research on the Far Infrared (FIR) covered a certain part of the high THz region, mostly by the use of thermal sources such as the mercury arc lamp [4] and incoherent detector as the radiometer [5]. Crucial advances and concepts still used today were accomplished during subsequent decades as the 20th century passed by, both in generation (Backward Oscillator (BWO) [6], gyrotron [7], Golay cell [11], bolometer [12] or Schottky diodes [13]). Nevertheless, until 1970´s, the THz research remained basically unexplored and with only a few groups dedicated to this field. In the 1970´s, techniques as Time Domain Spectroscopy (TDS) [14] and the appearance of a leading application in the THz range, Radioastronomy [15], stimulated the research effort in the THz region. Since them, popularity, number of potential applications and the research investment in the THz range has grown exponentially until today.

Among the significant amount of generation and detection technology developed until now [2], only a few have been successfully launched as commercial products. This is basically related to the fact that high reliability, ease of operation, compactness and cost have yet a great room for improvement and be able to provide full explotation capabilities to a wide range of users interested in the THz range.

From the electronic approach, the best available compact generation solution is based in electronic upconversion using Schottky multipliers [16]. They provide reasonable power levels (around 100μW at 1 THz), high quality signals (phase noise, electrical linewidth in the Hz range), and continuous tunability with high resolution (Hz range); but they are not able to cover the whole frequency range, and are limited by the waveguide bandwidth ranges [16]. The other commercial approach for generating THz waves is based in optical downconversion by photomixing two optical frequencies with frequency spacing equal to the desired generated THz frequency. The non-linear process within the photomixer provides the difference term in the THz range [17]. These photonic techniques are able to provide unique features such as distribution of the optical signal through optical fiber (Electromagnetic Immunity, EMI; very low losses, 0.2 dB/km, lightweight and low cost), thus allowing remote THz generation. Moreover some schemes [18] permit whole frequency coverage capabilities. However, the commercially available photonic THz synthesizers have traditionally featured a signal quality much below their electronic

even surpassing the electronic systems are promising to integrate the advantages of both approaches in commercial systems.

A common bottleneck for all these compact THz synthesizers (both electronic but especially the photonic ones), is the generated power and thus the dynamic range of the whole THz system. This issue has driven the pursuit of a solution from two different perspectives: the first one related to increasing the output power in generation and the second one improving the sensitivity of the receiver system.

In photonic systems, the current trends to increase the output power are related to emitter arrays or Large Area Emitters (LAE). Much less attention has been paid up to now to the receiver approach, where the development has a significant technological delay with respect to photonic generation technology. However, the research focus is changing towards this direction, both by increasing the sensitivity of THz receivers in direct detection [21], and by the attainment of heterodyne systems in the THz range [21–23]. In this sense, the capabilities of photonic systems regarding optical fiber transport are especially useful for remote local oscillator (LO) distribution in heterodyne systems [24]. These receivers, where the LO is provided photonically and the received signal is in the electrical range, are known as electro-optical (EO) or optoelectronic heterodyne receivers. Extensive work has been reported about them in the microwave region, where Microwave Photonics and Radio-over-Fiber (RoF) fields have taken advantage of these configurations [25], [26].

In the THz range, only a few research groups have reported THz EO heterodyne receivers, and to the best of our knowledge, only two have used photodiode devices [21], [23]. The THz detector elements that have been used as EO mixer are: Uni-Traveling Carrier photodiode (UTC-PD) [21], UTC-PD with Travelling-Wave design (TW-UTC-PD) [23] and Photoconductive Antennas (PCA) [27–29].

In this work, we present an EO sub-THz heterodyne receiver using a THz detector based in a new design concept: the np-i-pn quasi-ballistic THz detector [30]. The EO heterodyne receiver is completed by the use of a photonic LO providing ultra-narrow linewidth, full frequency range coverage, and ultra-high frequency resolution [18].

The detector, whose design is specifically made for heterodyne and homodyne detection [30], is fabricated from a symmetric n+p+-i-p+n+ In0.53(Ga1-x Alx)0.47As-layer structure. In this work, we report on the successful application of this detector to EO heterodyne detection using the first implemented samples of this novel design.

The performance of this THz detector will be evaluated in two parts. First, the np-i-pn quasi-ballistic THz detector is evaluated in a direct detection scheme where the measured sub-THz signal comes in an optical carrier (i.e. direct detection of the photonic LO). The detected power and its dependence on both the THz detector bias voltage and the optical power of the LO is provided photonically [18] and the measured sub-THz signal is generated using a mm-wave synthesizer. This scheme is evaluated through the conversion losses and its dependence on both LO optical power and THz detector bias voltage; and through its linearity.

The presented scheme provides two major advantages over already reported EO heterodyne schemes: zero-bias operation capabilities of this new THz detector concept; and usage of a photonic sub-THz synthesizer with excellent phase noise and tunability performance, especially suitable for LO operation.

This EO heterodyne receiver is a promising candidate for high signal quality systems with improved dynamic range in the sub-THz range, especially for those applications where remote THz operation is desirable, due to the zero-bias operation of the np-i-pn THz detectors and the photonic LO distribution.

II. MM-WAVE HETERODYNE ELECTRO-OPTICAL RECEIVER

The block diagram of the EO heterodyne receiver is depicted in Fig. 1. The np-i-pn THz detector acts as mixer. One of the inputs is photonically delivered to the active area of the np-i-pn, in this case the LO (LO, Fig. 1). The other input, which is the measured (M, Fig. 1) sub-THz signal, is applied to the terminals of the detector. The first samples of this detector, which are those evaluated in this work, have a ground-signal-ground (GSG) contact pad as interface for characterization purposes. Nevertheless, free-space coupling of the M signal using a planar antenna could be done straightforwardly in future implementations of the samples [17]. After mixing the sub-THz signal contained in the photonic LO with the sub-THz M signal, an intermediate frequency (IF) signal is generated in the np-i-pn that will be detected in an electrical spectrum analyzer (ESA, Fig. 1).

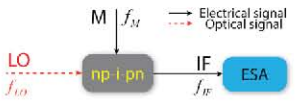

Fig. 1. EO heterodyne receiver scheme. LO: photonic LO; np-i-pn: np-i-pn quasi-ballistic THz detector; M: measured sub-THz signal; IF: detected IF signal; ESA: electrical spectrum analyzer.

A. Sub-THz ultra-narrow linewidth photonic Local Oscillator

The employed photonic LO is based in optical downconversion using photomixing. The two required optical modes are extracted from an optical multimode source, i.e Optical Frequency Comb Generator, based on Gain Switching pulsed operation (GS-OFCG, Fig. 2). The optical mode selection is based in Optical Injection Locking (OIL, Fig. 2) [31] rather than selective optical filtering [18]. This sub-THz

capabilities (≤ 10 Hz), a complete frequency range coverage and a frequency resolution of 0.1 Hz at 120 GHz [18]. The use of OIL adds to this scheme additional stability features, with frequency and power stabilities over one hour of 5 Hz and 1.5 dB, respectively. The signal quality and tunability characteristics of this sub-THz synthesizer make it an excellent choice for a LO in a receiving scheme.

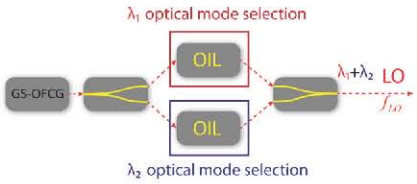

Fig. 2. Ultra-narrow linewidth photonic sub-THz LO. GS-OFCG: Gain-Switched Optical Frequency Comb Generator; OIL: Optical Injection Locking stage; LO sub-THz frequency: $|f_2-f_1|$.

B. *np-i-pn quasi-ballistic THz detectors*

As InGaAs with sufficiently low dark conductivity, suitable for photoconducting heterodyne detection is difficult to fabricate, we have developed a new detector concept based on quasi-ballistic transport [30]. Here we are reporting on its first implementation and application in the sub-THz frequency range.

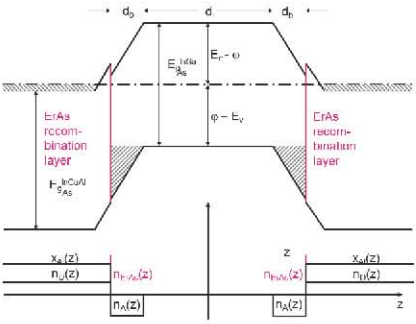

Fig. 3. Layer structure diagram of the np-i-pn quasi-ballistic THz detector [30].

The detector is fabricated from a symmetric n+p+-i-p+n+ In0.53(Ga1-x Alx)0.47As-layer structure as shown in Fig. 3. Although the full report on this device will be published elsewhere [30], we can briefly summarized its key design features as follows:

- The layer thickness and the acceptor density in the p+-conductance.
- Due to the symmetric design at zero bias the central i-InGaAs layer is field-free. Under illumination the photo-generated electrons escape symmetrically into the n+layers by diffusion on the sub-ps scale.
- The thin barrier resulting from the p-doping in combination with the ErAs layer enables fast tunnelling recombination of the photo-generated holes with electrons from the n+-layers on the ns scale. Hence, the photocurrent at zero bias should be zero.
- At low applied voltage the additional drift favours escape of the electrons in field direction, yielding a photocurrent saturating corresponding to the full electron generation rate a few 100 mV. This implies high responsivity up to high frequencies.
- If the optical power and the applied voltage are modulated at THz frequencies f_1 and f_2, respectively, the amplitude of the signal observed at the difference frequency $f_{IF} = f_1 - f_2$ is proportional to the product of the amplitudes of the two signals.

III. Direct mm-Wave Optoelectronic Detection

The np-i-pn THz detector is firstly evaluated in direct detection under sub-THz optical illumination. This is, only applying the photonic LO of Fig. 1 to the device, measuring at its output the electrical signal at the LO frequency. The detected LO electrical power is analyzed as a function of both np-i-pn bias voltage and LO optical power.

A. *Experimental setup*

The experimental setup for the direct detection scheme is shown in Fig. 4. The np-i-pn detector is illuminated with the photonic LO using a vertical lensed fiber (lightwave probe). The distance of the lensed fiber to the probe is used to estimate the optical power coupled into the active area of the device. A GSG RF probe (50 GHz bandwidth) is connected to the device and it is used as both input for the bias voltage and output for the electrical detected signal. The bias voltage is provided by a voltage source/pA meter in order to monitor the current generated by the np-i-pn. After the RF probe, a bias-tee (BT1, Fig. 4, 40 GHz bandwidth) is used to separate both signals. Finally, the detected signal is measured using an harmonic mixer in the 40-60 GHz band connected to an ESA.

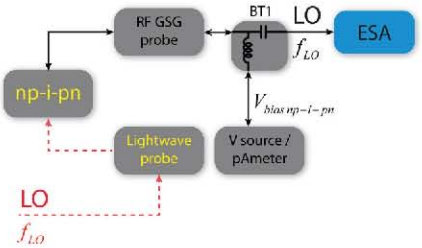

Fig. 4. Sub-THz direct detection scheme. LO: photonic LO of Fig. 2; Lightwave probe: vertical lensed fiber lightwave probe; np-i-pn: np-i-pn quasi-ballistic THz detector; RF GSG probe: 50 GHz RF GSG probe (125 um pitch); BT1: 75 kHz-40 GHz bias-tee; ESA: electrical spectrum analyzer.

B. *Experimental results*

The electrical spectrum of the detected LO signal (f_{LO} = 50 GHz) at the output of the np-i-pn is shown in Fig. 5. Span of 2 kHz and minimum allowed resolution bandwidth (RBW) of 10 Hz are used. The Full Width at Half Maximum (FWHM) or 3-dB linewidth of the detected signal is ~10 Hz, which corresponds to the employed RBW. Thus, the actual value, as reported in [18] is ≤10 Hz.

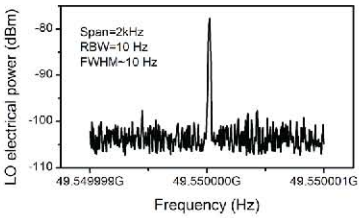

Fig. 5. LO detected electrical signal. Span= 2 kHz, RBW=10 Hz, sweep time=60 s.

The peak power of the detected LO electrical signal for different bias voltages and optical illumination power is mapped in Fig. 6. In this Fig. 6, also the cuts of the map at 2.4 mW of LO optical power and at 0 V bias voltage are represented as top and right insets, respectively. It can be seen that the detected electrical power changes only within a range of 3-4 dB for the whole range of bias voltage (-0.5 to 0.5 V). A more detailed representation of this is shown in Fig. 7, where also the bars related to the random uncertainty in the measurement set are represented. This shows that the variation of the detected power as a function of the bias

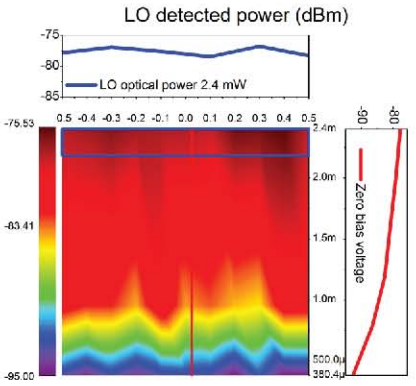

Fig. 6. Z-axis: LO detected electrical power (dBm). X-axis: bias voltage of the np-i-pn (V). Y-axis: LO optical power (W). Top inset: cut of the map at maximum LO optical power (2.4 mW). Right inset: cut of the map at zero bias voltage.

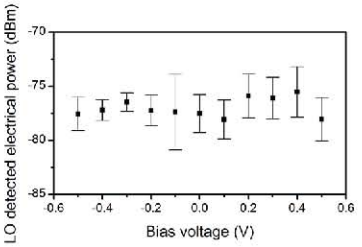

Fig. 7. LO detected electrical power as a function of the np-i-pn bias voltage. Uncertainty bars represent random uncertainty of the measurement set (they do not instrumentation uncertainty). Optical LO power is 2.4 mW.

Finally, the right inset of Fig, 6 (i.e. LO detected electrical power at zero bias) is represented along with the photocurrent variation in Fig. 8. In this figure, it is shown how the detected electrical power has a linear dependence with the LO optical power (in logarithmic scale), with a coefficient of determination R^2 of 0.998 and a slope of 1.02 (LO detected electrical signal, dBm, to LO optical power, dBm). Moreover, this linear fit is perfectly linear within the uncertainty range of the measurement. The generated photocurrent is also depicted in Fig. 8, showing a linear trend dependence with the

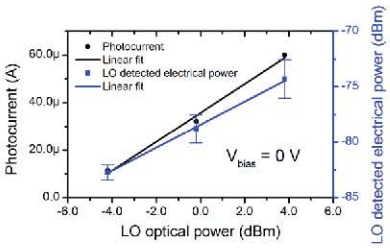

Fig. 8. LO detected electrical power and generated photocurrent as a function of the LO optical power. Uncertainty bars represent random uncertainty of the measurement set. Bias voltage np-i-pn is 0 V. Photocurrent linear fit (slope=6 uA/dBm, R^2=0.992); LO detected electrical power linear fit (slope=1.02 dBm/dBm, R^2=0.998).

IV. Heterodyne mm-wave optoelectronic detection

The fundamental part of this work is devoted to analyze the performance of the np-i-pn THz detector in an EO heterodyne receiver scheme (Fig. 1). The performance analysis covers two aspects: conversion ratio and linearity. The conversion ratio is analyzed along with its dependence with both np-i-pn bias voltage and LO optical power. The detected IF power is measured as a function of both M signal power and np-i-pn bias voltage, allowing for an exhaustive analysis of the linearity of the detector as a function of these two parameters.

A. Experimental setup

The experimental setup for the sub-THz EO heterodyne receiver scheme of Fig. 1 is shown in Fig. 9. The photonic LO and the GSG RF probe are placed in the same way than in the direct detection scheme of section III (Fig. 4). However, the scheme changes after the RF probe. The experimental arrangement has to permit delivering both np-i-pn bias voltage and M signals to the np-i-pn THz detector, while allowing the extraction of the IF signal. This is accomplished by the use of two cascaded bias-tee (BT1, BT2, Fig. 9). The first one (BT1), connected to the RF probe, has an AC bandwidth of 70 kHz to 40 GHz. The M signal is delivered by the AC port of this first bias-tee (BT1) through a 50 GHz synthesizer, while the IF and bias voltage signals go through the DC port of BT1. Due to the bandwidth of BT1, the IF signal is attenuated when passing through the DC port. These losses are measured and corrected for the analysis. A second bias-tee (BT2), with an AC bandwidth of 7 kHz-12.5 GHz is connected to the DC port of BT1, allowing the separation between the IF and the bias voltage. Finally, the IF signal is monitored in an ESA (Fig. 9). The bias voltage is provided by a voltage source/pA meter that

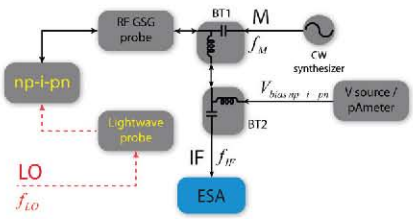

Fig. 9. Sub-THz EO heterodyne detection scheme. LO: photonic LO of Fig. 2; Lightwave probe: vertical lensed fiber lightwave probe; np-i-pn: np-i-pn quasi-ballistic THz detector; RF GSG probe: 50 GHz RF GSG probe (125 um pitch); BT1: 75 kHz-40 GHz bias-tee; BT2: 7 kHz-12.5 GHz bias-tee; ESA: electrical spectrum analyzer.

The LO frequency has been chosen to be 49.8 GHz (f_{LO} = 49.8 GHz) and the IF frequency 5 MHz (f_{IF} = 5 MHz). This way, the frequency of the M signal is set to $f_M = f_{LO} + f_{IF}$. The IF frequency has been chosen as a trade-off between the IF path losses and the sensitivity of the ESA at different frequencies (better above 1 MHz).

B. Experimental results

The electrical spectrum of the IF signal is shown in Fig. 10. The same measurement parameters of Fig. 5 are used. As in Fig. 5, the FWHM is ≤10 Hz. Nevertheless, two sidebands appears in the IF signal. These are spurious sidebands (70 Hz) that come from the M received signal at ~50 GHz.

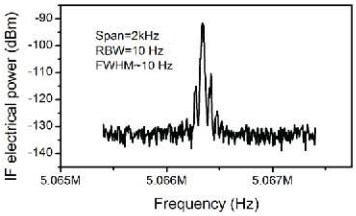

Fig. 10. IF detected electrical signal. Span= 2 kHz, RBW=10 Hz, sweep time=60 s.

The conversion ratio is mapped as a function of both np-i-pn bias voltage and LO optical power in Fig. 11. The losses of the system are calibrated and the reported values are corrected for these losses.

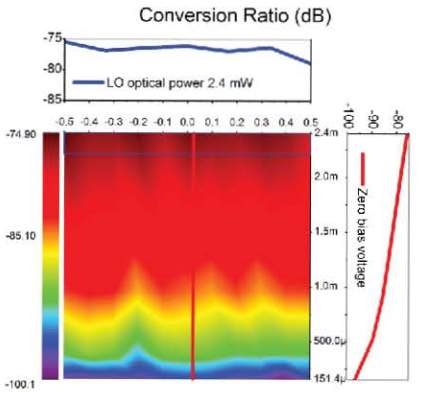

Fig. 11. Z-axis: Conversion ratio (dB). X-axis: bias voltage of the np-i-pn (V). Y-axis: LO optical power (W). Top inset: cut of the map at maximum LO optical power (2.4 mW). Right inset: cut of the map at zero bias voltage.

The top inset of Fig. 11 shows the cut of the map for the maximum applied LO optical power (2.4 mW). It can be seen that this conversion ratio has a slightly decreasing trend from lower to higher voltages. The highest conversion ratio (-74.9 dB) is achieved for -0.5 V, and it decreases as the voltage increases down to -79 dB for a bias voltage of 0.5 V. The right inset shows the cut of the map for zero bias voltage, and it can be seen how the conversion ratio decreases as the LO optical power decreases. This cut at zero bias voltage is represented with uncertainty bars in Fig. 12, where also the generated photocurrent is shown. The results of Fig. 12 show a quadratic dependence of the conversion ratio with the LO optical power, i.e. linear fit with 2.13 dB/dBm slope, with a coefficient of determination R^2 of 0.988. According to this quadratic relationship, the photocurrent also shows a quadratic dependence with the LO optical power, with a coefficient of determination R^2 of 0.996. From this it can be concluded that the LO optical power and the detected signal at the IF port have a linear dependence in direct detection (Fig. 8) and quadratic dependence in heterodyne detection (Fig. 12).

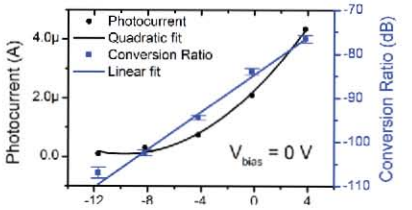

Fig. 12. Conversion ratio and generated photocurrent as a function of the LO optical power. Uncertainty bars represent random uncertainty of the measurement set. Bias voltage np-i-pn is 0 V. Photocurrent quadratic fit (R^2=0.996); conversion ratio linear fit (slope=2.13 dB/dBm, R^2=0.988).

The map in Fig. 13 contains the IF detected electrical peak power as a function of both the bias voltage of the detector and M signal power. Again the cuts for maximum M signal power (-3 dBm) and for zero bias voltage are represented as top and right insets, respectively. The detected IF power as a function of the bias voltage shows a similar behavior as in Fig. 11, with better performance (i.e. higher IF signal power) for lower bias voltages (-77.9 dBm for -0.5 V).

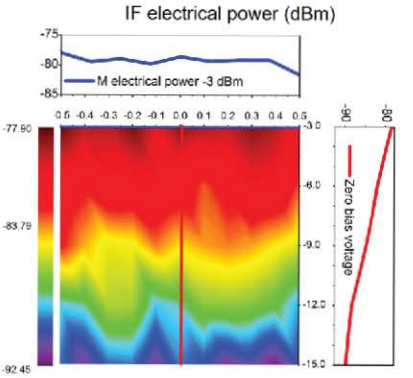

Fig. 13. Z-axis: IF electrical power (dB). X-axis: bias voltage of the np-i-pn (V). Y-axis: M electrical power (dBm). Top inset: cut of the map at maximum M electrical power (- 3 dBm). Right inset: cut of the map at zero bias voltage.

The cut at zero bias voltage for the IF electrical power is represented in Fig. 14. A perfect linear fit is obtained within the uncertainty region. The linear fit gives a slope of 1.01 (dBm IF power to dBm LO power) and a coefficient of determination of 0.998. Thus, the linearity of the detector under the EO heterodyne receiving scheme is excellent.

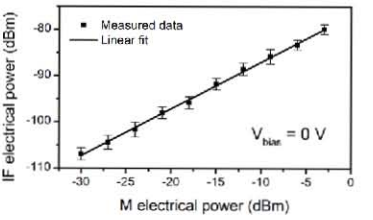

Fig. 14. IF electrical power as a function of M electrical power. Uncertainty

V. Conclusion

A novel scheme for electro-optical (EO) heterodyne detection based on a np-i-pn quasi-ballistic THz detector and a ultra-narrow linewidth photonic local oscillator (LO) is presented. The THz detector is based in a new design concept for homodyne/heterodyne detection and is fabricated from a symmetric n+p+-i-p+n+ In0.53(Ga1-x Alx)0.47As-layer structure. The photonic LO is able to provide all the advantages of photonic THz generation (i.e. whole frequency range coverage, optical fiber distribution) and matching or even surpassing the signal quality of the best available electronic systems for sub-THz generation (e.g. Schottky multipliers): generated linewidth ≤ 10 Hz, frequency resolution of 0.1 Hz and excellent power and frequency stability. The first implementation of this np-i-pn detector is evaluated in both sub-THz direct and heterodyne receiving schemes at 50 GHz, demonstrating zero-bias operation capabilities and excellent linearity. This EO heterodyne receiver is a promising candidate for high signal quality systems with improved dynamic range in the sub-THz range, especially for those applications where remote THz operation is desirable, due to the zero-bias operation of the np-i-pn THz detectors and the photonic LO distribution.

References

[1] P. H. Siegel, "Terahertz technology," *IEEE Transactions on Microwave Theory and Techniques*, vol. 50, no. 3, pp. 910–928, 2002.

[2] E. Bründermann, H.-W. Hübers, and M. F. Kimmitt, *Terahertz Techniques*. Springer. Springer Series in Optical Sciences, Vol. 151, 2012, p. 383.

[3] Luz WaveLabs and A. R. Criado, "Luz WaveLabs. THz resources: THz history," 2012. [Online]. Available: http://www.luzwavelabs.com.

[4] H. Rubens and R. W. Wood, "Focal isolation of long heat-waves," *Philosophical Magazine*, vol. 21, p. 249, 1911.

[5] E. F. Nichols, "A method for energy measurements in the infrared spectrum and the properties of the ordinary ray in quartz for waves of great wavelength," *Physical Review*, vol. 4, 1897.

[6] P. Guenard, O. Doehler, B. Epsztein, and R. Warnecke, "New UHF tubes with wide electronic tuning range," *Comptes Rendus de l'Académie des Sciences*, vol. 235, 1952.

[7] R. Q. Twiss, "Radiation transfer and the possibility of negative absorption in radio astronomy," *Australian Journal of Physics*, vol. 11, p. 564, 1958.

[8] R. H. Pantell, "The design and characteristics of a megawatt space-harmonic traveling-wave tube," *Proceedings of the Institute of Radio Engineers*, vol. 48–53, p. 1146, 1959.

[10] C. H. Cartwright, "Radiation thermopiles for use at liquid-air temperatures," *Review of Scientific Instruments*, vol. 4, p. 382, 1933.

[11] M. J. E. Golay, "A pneumatic infra-red detector," *Review of Scientific Instruments*, vol. 18, p. 347, 1947.

[12] D. H. Andrews, W. F. Bruksch, W. T. Zeigler, and E. R. Blanchard, "Attenuated superconductors I. For measuring infra-red radiation," *Review of Scientific Instruments*, vol. 13, p. 281, 1942.

[13] D. T. Young and J. C. Irvin, "Millimeter frequency conversion using Au-n-type GaAs Schottky barrier epitaxial diodes with a novel contacting technique," *Proceedings of the IEEE*, vol. 53, p. 2130, 1965.

[14] A. M. Nicolson, "Broad-band microwave transmission characteristics from a single measurement of the transient response," *Instrumentation and Measurement, IEEE Transactions on*, vol. 17, p. 395, 1968.

[15] R. W. Wilson, K. B. Jefferts, and A. A. Penzias, "Carbon monoxide in the Orion nebula," *Astrophysics Journal*, vol. 161, p. L43, 1970.

[16] Virginia Diodes Co., "Virginia Diodes Co. Multipliers," 2012. [Online]. Available: http://vadiodes.com/. [Accessed: 12-Feb-2012].

[17] S. Preu, G. H. Döhler, S. Malzer, L. J. Wang, and a. C. Gossard, "Tunable, continuous-wave Terahertz photomixer sources and applications," *Journal of Applied Physics*, vol. 109, no. 6, pp. 061301–01 – 061301–56, 2011.

[18] A. R. Criado, C. de Dios, G. H. Döhler, S. Preu, S. Malzer, S. Bauerschmidt, H. Lu, A. C. Gossard, and P. Acedo, "Ultra narrow linewidth CW sub-THz generation using GS based OFCG and n-i-pn-i-p superlattice photomixers," *Electronics Letters*, vol. 48, no. 22, pp. 1425–1426, 2012.

[19] Toptica Photonics, "Toptica Photonics. THz CW," 2012. [Online]. Available: http://www.toptica.com. [Accessed: 12-Feb-2012].

[20] Emcore Co., "Emcore Co. CW THz system," 2012. [Online]. Available: www.emcorephotonicsystems.com. [Accessed: 12-Feb-2012].

[21] T. Nagatsuma, A. Kaino, S. Hisatake, K. Ajito, H.-J. Song, A. Wakatsuki, Y. Muramoto, N. Kukutsu, and Y. Kado, "Continuous-wave Terahertz Spectroscopy System Based on Photodiodes," *PIERS*, vol. 6, no. 4, pp. 390–394, 2010.

[22] A. J. Seeds, G. Aeppli, K. Balakier, A. G. Davies, M. Fice, E. H. Linfield, O. Mitrofanov, M. Natrella, M.Pepper, E. Rouvalis, and C. C. Renaud, "Coherent Terahertz Systems," in *International Topical Meeting on Microwave Photonics. MWP 2012*, 2012.

[23] E. Rouvalis, M. J. Fice, C. C. Renaud, and A. J. Seeds, "Millimeter-Wave Optoelectronic Mixers Based on Uni-Traveling Carrier Photodiodes," *IEEE Transactions on Microwave Theory and Techniques*, vol. 60, no. 3, pp. 686–691, 2012.

[24] I. Cámara Mayorga, A. Schmitz, T. Klein, C. Leinz, and R. Gusten, "First In-Field Application of a Full Photonic Local Oscillator to Terahertz Astronomy," *IEEE Transactions on Terahertz Science and Technology*, vol. 2, no. 4, pp. 393–399, Jul. 2012.

[25] J. Marti and J. Capmany, "Microwave photonics and radio-over-fiber research," *IEEE Microwave Magazine*, vol. 10, no. June, pp.

[26] A. R. Criado, C. de Dios, and P. Acedo, “Characterization of Ultra-Nonlinear SOA in a Heterodyne Detector Configuration With Remote Photonic Local Oscillator Distribution,” *IEEE Photonics Technology Letters*, vol. 24, no. 13, pp. 1136–1138, Jul. 2012.

[27] F. L. Constantin, “Phase-Coherent Heterodyne Detection in the Terahertz Regime With a Photomixer,” *IEEE Journal of Quantum ElectronicsQuantum Electronics*, vol. 47, no. 11, pp. 1458–1462, Nov. 2011.

[28] T. Yasui, S. Yokoyama, H. Inaba, K. Minoshima, T. Nagatsuma, and T. Araki, “Terahertz Frequency Metrology Based on Frequency Comb,” *IEEE Journal of Selected Topics in Quantum Electronics*, vol. 17, no. 1, pp. 191–201, Jan. 2011.

[29] H. Füser, R. Judaschke, M. Bieler, and H. Füser, “High-precision frequency measurements in the THz spectral region using an unstabilized femtosecond laser,” *Applied Physics Letters*, vol. 99, no. 12, p. 121111, 2011.

[30] G. H. Döhler, S. Malzer, and S. Preu, “[Unpublished].”

[31] C. de Dios, A. R. Criado, G. H. Döhler, S. Preu, S. Malzer, S. Bauerschmidt, L. E. García, P. Acedo, and D. Segovia, “Sub-THz and THz Photonic Generation with Continuous Tunability Using Gain Switching based Optical Frequency Comb Generators and n-i-p-n-i-p Superlattice Photomixers,” in *International Topical Meeting on Microwave Photonics. MWP 2012*, 2012.

11

Preprint B

Selected preprint B	
Citation	**Á. R. Criado et al.,** "Sub-THz optoelectronic heterodyne receiver based on np-i-pn quasi-ballistic THz receiver and ultra-low phase noise sub-THz photonic Local Oscillator,"
JCR impact factor	N/A
Submitted	N/A
Published	N/A
Comments	

Table VI-11 Selected preprint B. Summary of preprint information

CHAPTER VI

Sub-Thz optoelectronic heterodyne receiver based on np-i-pn quasi-ballistic detector and ultra-low phase noise sub-THz photonic Local Oscillator

Author, Author, Author, Author, Author,

We report on a sub-THz optoelectronic heterodyne receiver based on a np-i-pn quasi-ballistic THz receiver and an ultra-low phase noise CW sub-THz photonic Local Oscillator (LO). The employed THz receiver is a new detector design concept based on quasi-ballistic transport and fabricated from a symmetric n+p+-i-p+n+ In0.53(Ga1$_x$ Al$_x$)0.47As-layer structure. The sub-THz photonic Oscillator is based on an ultra-low phase noise sub-THz generator that features an electrical FWHM≤10 Hz, frequency resolution of 0.1 Hz (both at 120GHz), excellent frequency stability and continuous tunability. The downconversion performance of the receiving system is evaluated by the analysis of the Conversion Ratio, Signal-to-Noise Ratio (SNR) and Noise Floor for LO and sub-THz Measurement (M) signals at around 110 GHz. This receiver scheme is a promising candidate for the improvement of the sensitivity in the sub-THz range by the use of optoelectronic techniques.

Introduction: Due to the significative and increasingly number of potential applications in the sub-THz and THz ranges [1], the last decade has witnessed a great advance in the development of technology for this frequency range. Several compact room-temperature generation systems are even commercially available, although they have great room to improve and provide system quality comparable to other frequency ranges [2]. Furthermore, there exists a bottleneck regarding the output power of these generation systems that is limiting the dynamic range of sub-THz technology. While one approach to overcome this limitation is improving the output power using array systems, an alternative is working from the detector point of view. Traditionally, less attention has been paid to sub-THz receiver development, and is currently becoming the research trend to provide higher dynamic range sub-THz systems, by using higher sensitivity detectors [3] and especially by the use of heterodyne receivers [4, 5], where optoelectronic approaches [6, 7] are able to provide remote distribution of the sub-THz Local Oscillator (LO) as major advantage [4]. In this work, we present a novel scheme of sub-THz optoelectronic heterodyne receiver. It comprises a np-i-pn quasi-ballistic THz receiver, which is based on a new receiver design concept for heterodyne THz detection, and an ultra-low phase noise CW sub-THz photonic LO, which was recently reported as a system capable of surpass the signal quality, resolution and stability of any commercially available photonic THz generation solution [2].

Experimental setup: The scheme of our sub-THz optoelectronic heterodyne receiver is depicted in Fig. 1. The photonic LO used here is that reported in our previous work [2]. Key features of this photonic LO include a sub-THz electrical linewidth below 10 Hz, continuous tunability with a frequency resolution of 0.1 Hz (both parameters at around 120 GHz) and excellent frequency stability. In this receiver scheme, the LO is not provided as a mm-wave signal, but as an optical one containing two optical frequencies separated by the sub-THz LO frequency, this is, is not photomixed before entering the detector. This offers a great advantage that is the possibility of remote distribution of the LO with very low losses (0.2 dB/km), EMI immunity and additional signal processing features inherited from Microwave Photonics field [4].

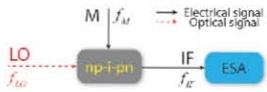

Fig. 1 *Sub-THz optoelectronic heterodyne receiver scheme.*

As InGaAs with sufficiently low dark conductivity, suitable for photoconducting heterodyne detection is difficult to fabricate, we have developed a new detector concept based on quasi-ballistic transport [8]. The detector is fabricated from a symmetric n+p+-i-p+n+ In0.53(Ga1$_x$ Al$_x$)0.47As-layer structure. Here we are reporting on its first implementation and application in the sub THz frequency range. Further details on this device will be reported elsewhere [8].

The downconversion process in our heterodyne receiver scheme takes place in the np-i-pn detector, which acts as an optoelectronic mixer, where the photonic LO and the received Measurement THz signal (M) are mixed and an Intermediate Frequency (IF) signal is obtained at its output.

Fig.2 shows the experimental setup of the EO heterodyne receiver. The photonic LO is coupled to the active area of the device using a lensed fiber. The sub-THz M signal, the IF signal and the bias voltage are connected to/from the np-i-pn detector by its GSG pad, where a RF probe is connected. The separation of these three signals is performed by two cascaded bias-tee with different lower cut-off frequency. The sub-THz M signal is generated by a 75-110GHz mm-Wave multiplier, the bias voltage by a voltage source/pAmeter that allows measuring the device current and the IF signal is monitored in an Electrical Spectrum Analyzer (ESA in Fig.1, Fig. 2).

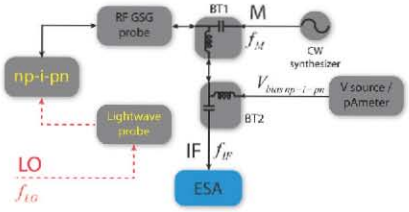

Fig. 2 *Sub-THz EO heterodyne detection scheme. LO: photonic LO of Fig. 2; Lightwave probe: vertical lensed fiber lightwave probe; np-i-pn: np-i-pn quasi-ballistic THz detector; RF GSG probe: 50 GHz RF GSG probe (125 um pitch); BT1: 75 kHz-40 GHz bias-tee; BT2: 7 kHz-12.5 GHz bias-tee; ESA: electrical spectrum analyzer.*

In the setup of Fig. 2, f_{LO} is set to 109.89 GHz and the sub-THz M signal from the mm-Wave multiplier is set to f_M=f_{LO}-f_{IF}. The IF signal frequency is chosen to be around 960 kHz (f_{IF}=*960 kHz)*, as it is an optimum trade-off between the frequency response of the IF path losses and the ESA sensitivity at different frequencies. It is worth mention to say that the measurement system is limited to 40 GHz (bias-tee, RF probe, coaxial connectors), so the losses of the M path are as high as 32 dB. Additionally, due to the use of two bias-tee to separate the different signals (BT1 and BT2), the IF path has 6.5 dB of losses at 960 kHz. These limitations of the measurement setup also limit the dynamic range of the obtained IF signal, thus the analysis presented here.

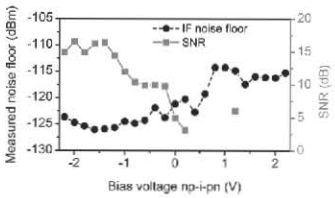

Fig. 3 *Measured noise floor and SNR of the IF signal as a function of np-i-pn bias voltage.*

Fig. 3 shows both the measured noise floor at f_{IF} and the Signal-to-Noise Ratio (SNR). It can be seen that for bias voltages above 0.2 V, the IF signal cannot be detected, except for an isolated point (1.2 V).

The limited dynamic range does not allow to state if this is because a worse Conversion Ratio (CR), because of a higher dark current, or both. Nevertheless, it can be clearly seen that optimum SNR and noise floor values are obtained at bias voltage in the range of -1.4 to -2.2 V. The lowest noise floor is obtained for -1.6 V and the highest SNR values for -1.4, -1.6 and -2 V. The noise floor values given in Fig. 3 are not corrected for system losses.

The CR (i.e. downconversion ratio) is defined as the ratio of the power of the IF signal to the power of the sub-THz M signal. The CR values as a function of the bias voltage of the np-i-pn THz detector are depicted in Fig. 4. The CR values are corrected for the system losses. Maximum CR is achieved for -2 V (-74 dB). This bias voltage value also provides maximum SNR as depicted in Fig. 3.

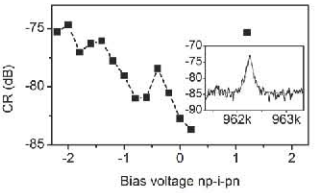

Fig. 4 *Conversion Ratio of the optoelectronic downconversion as a function of np-i-pn bias voltage. Inset:IF electrical spectrum. RBW:100 Hz, Span: 2 kHz, 55 traces average.*

The electrical spectrum of the IF signal is also shown in Fig. 5 (inset) at a bias voltage of -1.6 V and calibrated for the losses of the system. The used RBW is 100 Hz and the span is 2 kHz. 55 traces average is employed. The measured FWHM of this signal corresponds approximately to the RBW (i.e. 100 Hz).

Conclusion: In this work, we have presented a novel scheme of sub-THz optoelectronic heterodyne receiver. It is formed by two key components: an ultra-low phase noise sub-THz photonic LO [2] and a np-i-pn quasi-ballistic THz detector based on a new concept design for heterodyne detection [8]. The first implementation of these detectors are used in this heterodyne receiver scheme and the overall performance of the receiver is analysed by the noise floor, SNR at IF frequencies and the CR. The dependence of these parameters with the bias voltage is also studied. Maximum SNR values of 16 dB and CR of -74 dB for sub-THz heterodyne detection at ~110 GHz are obtained. This analysis is strongly limited by the limitations of the employed measurement system, specified up to frequencies of 40 GHz. Our sub-THz heterodyne optoelectronic receiver offers a major advantage associated to the optical fiber distribution of the sub-THz LO, and has a promising potential for the development of high sensitivity and improved dynamic range sub-THz systems.

References

1. Tonouchi M (2007) Cutting-edge terahertz technology. Nature Photonics 1(2):97–105

2. Criado AR, De Dios C, Döhler GH, Preu S, Malzer S, Bauerschmidt S, Lu H, Gossard AC, Acedo P (2012) Ultra narrow linewidth CW sub-THz generation using GS based OFCG and n-i-pn-i-p superlattice photomixers. Electronics Letters 48(22):1425–1426

3. Preu S, Kim S, Verma R, Burke PG, Sherwin MS, Gossard a. C (2012) An improved model for non-resonant terahertz detection in field-effect transistors. Journal of Applied Physics 111(2):024502

4. Davies D (2012) Inside View. Electronics Letters 48(22):1376

5. Seeds AJ, Aeppli G, Balakier K, et al (2012) Coherent Terahertz Systems. International Topical Meeting on Microwave Photonics. MWP 2012

6. Rouvalis E, Fice MJ, Renaud CC, Seeds AJ (2012) Millimeter-Wave Optoelectronic Mixers Based on Uni-Traveling Carrier Photodiodes. IEEE Transactions on Microwave Theory and Techniques 60(3):686–691

7. Nagatsuma T, Kaino A, Hisatake S, Ajito K, Song H-J, Wakatsuki A, Muramoto Y, Kukutsu N, Kado Y (2010) Continuous-wave Terahertz Spectroscopy System Based on Photodiodes. PIERS 6(4):390–394

8. Döhler GH, Malzer S, Preu S [Unpublished].

Appendix I

THz HISTORY

1

Appendix I. THz history

This appendix is devoted to introduce the history of THz technology in a graphic way (infography) to give the reader a quick overview of the evolution of the THz technology during the 20th century. The "when" and "how" it began and the key advances through are presented, both in generation and detection techniques and devices.

As said, this THz history review is presented as an infography where each page covers one decade or half a decade. The structure is as follows: a temporal line is marked with the years in which representative research advances were accomplished. Above the temporal line, these advances are briefly described including the year, authorship, and bibliographical reference about the work. Below the temporal line, the main actors in THz research in that temporal span are introduced. Finally, the generation and detection technologies used in the correspondent temporal span are also included as a guide on how THz research has been evolving within the last century.

It must be highlighted that most of this THz history infography is a summary of the first chapter of the book Terahertz Techniques[21], a very comprehensive introduction and reference guide to THz technology. The lack of an extensive description of photonic generation technology in the abovementioned reference is solved through several additions that are made for the sake of completeness. References used in this infography are added at the end of the Appendix.

1899

Point contact diode detector @ 60 GHz[3]

J.C. Bose

He worked up to 60 GHz and constructed several devices for this frequency range (prisms, lenses, polarizers...). His metal coherer was an earlier version of the modern diodes (it presented similar I-V curves). He investigated the sensitivity to electric radiation of different metal contact

1897

Radiometer in the FIR range
First "Residual ray". Emission at 9 μm[2]

E. F. Nichols

A radiometer for measurements in the FIR range is developed for these experiments. A wave at 9 μm, reflected from a crystalline quartz due to lattice vibrations, is detected with the new radiometer. After that, Nichols and Rubens found longer wavelength emissions

1893

FIR spectroscopy of rock salt, sylvine and fluorite prisms[1]

H. Rubens, B. W. Snow

They accomplished spectroscopy in rock salt (NaCl), sylvine (KCl) and fluorite (CaF2) in the "great wavelength" range (FIR)

Rubens, Heinrich
1865, Germany - 1922, Germany

Technische Hochscule Berlin-Charlottenburg
Universität Berlin

Bose, Jagadish Chandra
1858, India - 1937, India

University of Cambridge
Presidency College

Nichols, Ernest Fox
1869, USA - 1924, USA

Colgate University
Dartmouth College
Columbia University
MIT

Generation

"Residual rays"

Detection

Radiometer
"Primitive" diode

60 GHz to 6 THz
is unexplored

1904

Electrical conductivity dependance on reflectivity[7]

E. Hagens, H. Rubens

They empirically found that any pure metal at FIR regime has a reflectivity above 99%. This demostrated that any pure metal-based reflecting system has no significant losses in this frequency range

1900

Planck´s Radiation Law[4,5,6]

M. Planck, H. Rubens, F. Kurlbaum

In this decade the radiation from hot bodies and especially its wavelength variation became an important concern. The most important model for this was based in the blackbody, an ideal source. Unfortunately, the experimental data did not agree with the theory. Nevertheless, Rubens and Kurlbaum, making use of a residual ray spectrometer, were able to obtain the required experimental data that allow Planck to write the Radiation Law the same day he received the data from Rubens

1900 — 1910

Planck, Max

1858, Germany - 1947, Germany

University of Kiel
University of Berlin
University of Göttingen
Kaiser-Wilhelm-Gesellschaft

Generation

"Residual rays"

Detection

Radiometer

The research interest was directed to low frequencies due to Marconi´s experiments in low-freq communications

1911

Quartz mercury arc lamp[9]

H. Rubens, R. W. Wood

The quartz mercury arc lamp was able to emit very long wavelength radiation (210 and 324 μm). This thermal source is still the only source capable of generating radiation at those frequencies (in the 30-50 THz range)

1910

First blazed diffraction grating[8]

R. W. Wood

The grating achieved efficiencies around 75% for the first order even beyond 3 THz. The diffraction gratings are largely used nowadays in tunable lasers

Generation
Mercury arc lamp
Residual rays

Detection
Radiometer

1927

Rotational levels of gases in the FIR[12]

R. M. Badger

Badger studied the rotational level of gases such as hydrogen-chloride, discovering one of the major applications of the spectroscopy in this frequency range: the study of rotational levels.

1924

Hertzian oscillator down to 92 μm[11]

G. Arkediewa

This Russian scientist achieve emission down to 92 um using a Hertzian oscillator

1923

Joining the FIR and microwave range: the Hertzian oscillator[10]

J.D. Tear, E. F. Nichols

A Hertzian oscillator is used to generate wavelengths down to 220 μm. This generation range overlapped with the emission of the mercury arc lamp up to 420 μm

1920 — 1930

Tear J. D.

National Electric Light Association

Generation

Hertzian oscillator
Mercury arc lamp
Residual rays

Detection

Radiometer

American researchers got more involved in this decade in IR and FIR radiation studies. University of Michigan and California Institute of Technology consolidated as top FIR research centers

1934

Prelude of the microwave spectroscopy[15]

V. Cleeton, N.H. Williams

The molecular absoprtion of the ammonia was measured using a coherent source in the microwave range (split-anode magnetron at a wavelength of 1.1 cm)

1933

Cooled thermopile for FIR detection[14]

C.H. Cartwright

A detector with a responsivity one order of magnitude better than the available ones was developed

1930

Materials absorption in the FIR range[13]

C.H. Cartwright

Cartwright was one of the major contributors to FIR technology in this decade. He studied the absorption of 25 materials in the FIR range to find a suitable material for a detector, with high absorption in the FIR range and low in lower wavelengths

Generation
Hertzian oscillator
Mercury arc lamp
Residual rays

Detection
Thermocouples
Thermopiles
Bolometers

The detectors technology in the FIR range is improved in this decade

A great work in gas spectroscopy is also carried out

1947

The "Golay" detector[18,19]

H.A. Zahl, M.J.E. Golay,

In 1938, Zahl patented a "pneumatic cell detector". One year later, he and Golay patented a "System for detecting sources of radiant energy". In 1946, they published the "Pneumatic heat detector". One year later, Golay individually published the "Pneumatic infra-red detector"

1944

Klystron in a crystal harmonic generator radiates at 60 GHz[17]

R. Beringer

The spectra of the oxygen is experimentally measured in this frequency range

1942

First cooled bolometer[16]

D.H. Andrews, W.F. Bruksch, W.T. Zeigler, E.R. Blanchard

The bolometer was cooled at superconducting region (4.4 K) using liquid helium. In 1946, Andrews achieved proper operation of the bolometer at 14.3 K, where the cooling system with liquid hydrogen was more easily available

1940 — 1950

Golay, Marcel J. E.
1902, Switzerland - 1989, USA

Bell Laboratories
University of Chicago
US Army Signal Corps
Perkin-Elmer

Generation

- Hertzian oscillator
- Klystron + crystal harmonic gen
- Mercury arc lamp
- Residual rays

Detection

- Thermocouples
- Cooled thermopiles and bolometers
- Golay cell

Despite the WWII, there was significant research in this decade

DC detection is substituted by AC synchronous detection using choppers

1954

Submillimeter-wave spectroscopy[22]

C.A. Burrus, W. Gordy

Gordy´s group became very important in this and later decades in the development of the mm and sub-mm frequency technology. They reached the sub-mm using a silicon crystal multiplier driven by a centimeter-wave klystron

1952

270 GHz using magnetron harmonics[21]

J.A. Klein, J.H.N. Loubser, A.H. Nethercot, C.H. Townes

The magnetron harmonic generation for mm-waves began to be employed in 1949. In 1952, 270 GHz is achieved with this technique

1952

First Backward Wave Oscillator (BWO) or Carcinotron[20]

P. Guenard, O. Doehler, B. Epsztein, R. Warnecke

This high power (mW range at 1 THz) source is demonstrated for the first time in 1952. It offers a limited electronic tunability (~10%).

1950 — 1955

Gordy, Walter
1909, USA - 1985, USA

Mary Hardin-Baylor College
California Institute of Technology
MIT Radiation Laboratory
Duke University

The extension of the microwaves into the mm and sub-mm region became very significant in this decade

The research group of Gordy at Duke University (in 1990 moved to Ohio University) is still one of the most important groups in the sub-mm region. One of his 75 PhD students, Dehmelt, won the Nobel Prize in Physics in 1989

Generation
- BWO
- Hertzian oscillator
- Klystron + crystal harmonic gen
- Magnetron harmonics
- Mercury arc lamp
- Residual rays

Detection
- Thermocouples
- Cooled thermopiles and bolometers
- Golay cell
- Silicon crystal

1959

First photoconductive detector in the THz domain[26]

S.J. Fray, J.F.C. Oliver

The photoconductor was made with germanium doped with antimony. A spectroscopy setup demonstrated the functionality of the detector from 50 to 118 µm

1959

Carbon bolometer[25]

W.S. Boyle, K.F. Rogers

The new design operated cooled by liquid helium and used the core of a carbon composition resistor. This detector improved the SNR of all existing detectors

1958

High-power Gyrotron[23,24]

R.Q. Twiss, Pantell, R.H.

The theoretical work of Twiss will lead to the first gyrotron demonstration at microwave domain in 1959 in USA by Pantell

1955 — 1960

Pantell, Richard H.
1927, USA -

Stanford University
IEEE Life Fellow

Development of Fourier Trasform Spectroscopy in this decade

Solar and lunar radiation spectroscopy in the THz range is published in 1955[27]

Generation
- BWO
- Gyrotron
- Klystron + crystal harmonic gen
- Magnetron harmonics
- Mercury arc lamp

Detection
- Carbon bolometer
- Golay cell
- Cooled thermopiles
- Photoconductor

1969

Time Domain Spectroscopy[31]

A.M. Nicolson

Also in this decade the TDS is demonstrated for the first time in the THz regime

1965

Honeycomb Schottky diode[30]

D.T. Young, J.C. Irvin

The semiconductor development is rapidly growing. Young and Irvin designed a honeycomb structure for a Schottky diode. The diode was able to downconvert 58.3 GHz signals with 6 dB of conversion loss

1964

First THz laser[29]

A. Crocker, H.A. Gebbie, M.F. Kimmitt

This first THz laser was based in a water vapor laser

1963

Dispersive Fourier-Transform Spectroscopy[28]

J.E. Chamberlain, J.E. Gibbs, H.A. Gebbie

This is the first demostration of the DFTS. The DFTS uses the transmission and reflection coefficients of solids, liquids and gases (obtained by direct measurements of amplitude and phase) to obtain their optical coefficients

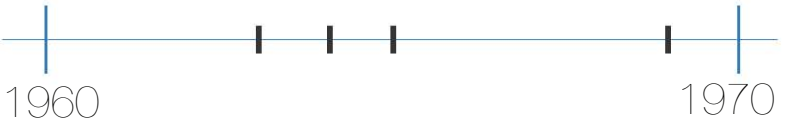

Richards, Paul Linford

University of California Berkeley
National Academy of Sciences
American Academy of Arts and Science

The number of publications, research groups and conferences at FIR range increases significantly

Detectors are largely improved: pyroelectric detectors, new bolometer designs (n-InSb electron[32], Ge[33]), the Ge:Ga photoconductor[34], and a Josephson effect-based detector[35]

Generation
- BWO
- Gyrotron
- Klystron + crystal harmonic gen
- Magnetron harmonics
- Mercury arc lamp

Detection
- Schottky diodes
- Bolometers
- Golay cell
- Photoconductor
- Pyroelectric detector

1971

First THz TDS results[38]

K.H. Yang, P.L. Richards, Y.R. Shen

These first TDS results were accomplished using as harmonic generator a Nd:glass laser in a EO LiNbO3 crystal. Pulses of 2 ps were produced

1970

Interestellar CO measured using a heterodyne 115 GHz receiver[37]

R.W. Wilson, K.B. Jefferts, A.A. Penzias

Heterodyne receivers using Schottky diodes become very popular, especially in Astronomy. Also Schttky diodes are used as harmonic mixers in the generation with a klystron as source. The CO transition was detected from nine gallactic sources, including the Orion nebula

1970

Optically pumped THz Gas laser[36]

T.Y. Chang, T.J. Bridges

A Q-switched CO2 laser was used to pump a CH3F laser. Lines at 452, 496 and 541 um were generated. The THz gas laser will be a very important and largely used high power (100 mW range) generator

High altitude observatories, and advances in both generators and receivers (especially heterodyne receivers) has as a consequence a large amount of astronomical research in the THz region

Generation
- THz Gas laser
- BWO
- Gyrotron
- SHG
- Schottly diodes

Detection
- Schottly diodes
- Bolometers
- Golay cell
- Photoconductor
- Pyroelectric detector

Mixers
- Schottly diodes

1979

First Superconductor-Insulator-Superconductor (SIS) mixer[40]

G.J. Dolan, T.G. Phillips, D.P. Woody

Demonstration of SIS mixing at 115 GHz is achieved. This first SIS maked use of superconducting Pb in 1 um2 area juntions

1975

FIR imaging become popular [39]

D.H. Barker, D.T. Hodges, T.S. Hartwick

The FIR imaging applications begin to grow. At the time, astronomy is the main (and almost unique) application, but industrial, militar and medical applications began to be suggested

Schottky diodes experimented a great development. They are largely used in generation as harmonic mixers for frequency multiplication, and in detection as both direct detectors and mixers for heterodyne detectors

Gunn and IMPATT diodes are developed in this decade

Generation
- THz Gas laser
- BWO
- Gyrotron
- SHG
- Schottly diodes for frequency mult.

Detection
- Schottly diodes
- Bolometers
- Golay cell
- Photoconductor
- Pyroelectric detector

Mixers
- Schottly diodes
- SIS mixers

1989

First Hot Electron Bolometer (HEB) mixer[43]

E.M. Gershenzon, M.E. Gershenzon, G.N. Goltsman, A.M. Lyulkin, A.D. Semenov, A.V. Sergeev

The HEB was able to work as thermal detector in a wide range in the IR and THz domain, but the significant advantage is that is also able to work as mixer

1984

Photoconductive switch[42]

D.H. Auston, K.P. Cheung, P.R. Smith

It was known in this decade that an ultra-short optical pulse incident to a photoconductor or a EO crystal can generate THz pulses. The highest frequency of the THz pulses depends on the optical pulse width and also in the electron mobility for the photoconductors. Photoconductors were able to provide higher power at expense of less THz frequency. Auston developed a photoconductive switch with a improved THz power output

1984

First Free Electron Laser[41]

L.R. Elias, J. Hu, G. Ramian

It covered from 0.3 to 0.77 THz with 10 kW of peak power. This kind of sources are room-building size. Several FELs were installed in this decade in several countries

The first THz and FIR on-board systems are developed and employed in the Infrared Astronomical Satellite (1983) and in Kuiper Airbone Observatory (1986)

A large amount of new applications in the FIR and THz are discovered in this decade. This produces a huge growth in this research field. This growth has not yet stopped.

There is an important need of higher power to achieve better sensitivities and be able to resolve the spectral lines in astronomy and upper atmospheric applications.

Availability and development of computer science make the FT spectroscopy more easily available

Generation
- FEL
- THz Gas laser
- BWO
- Gyrotron
- SHG
- Schottly diodes

Detection
- Schottly diodes
- Bolometers
- Golay cell
- Photoconductor
- Pyroelectric detector

Mixers
- Schottly diodes
- SIS mixers
- HEB

1998

Uni-Travelling-Carrier Photodiode (UTC-PD)[46]

Y. Muramoto, K. Kato, M. Mitsuhara, O. Nakajima, Y. Matsuoka, N. Shimizu, T. Ishibashi

A photodiode with a new structure (UTC) is developed, demonstrating a bandwidth of 70 GHz. The UTC is the first of several PD structures for sub-THz operation and was always linked to the development of the photonic CW sub-THz generation techniques

1995

First THz TDS imaging experiment[45]

B.B. Hu, M.C. Nuss

The signal in each point is downconverted and processed in real time in a DSP. Actually, a unique detector in a motorized stage is used to scan the samples

1994

The Quantum Cascade Laser[44]

J. Faist, F. Capasso, D. L. Sivco, C. Sirtori, A. L. Hutchinson, A. Y. Cho

The quantum confinement determines the wavelength, that could go from mid-infrared to the submillimeter wave region. Altough the THz QCL will appear in 2002, this is actually the birth of the QCL technology

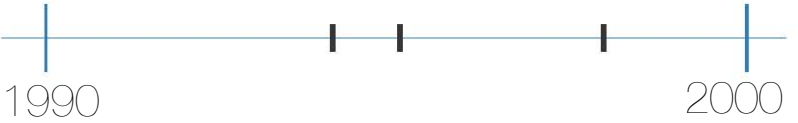

Faist, Jerome

ETH Zurich
University of Neuchâtel
Bell Laboratories

The optical techniques for signal generation were used from the appearance of the laser (mainly optical heterodyning)[47]. In this decade, the development of the optical communications and the higher bandwidth photomixers (photodiodes) produce a huge development of the photonic techniques for sub-THz and THz generation and detection that will continue up to nowadays

Generation
- THz-QCL
- THz Gas laser
- BWO
- Gyrotron
- SHG
- Schottly diodes

Detection
- Schottly diodes
- Bolometers
- Golay cell
- Photoconductor
- Pyroelectric detector
- UTC photodiodes

Mixers
- Schottly diodes
- SIS mixers
- HEB


State of the Art
2000

Appendix I Infography references

1. RUBENS, H. & SNOW, B. W. On the refraction of rays of great wavelength in rock salt, sylvine, and fluorite. Philosophical Magazine 35, (1893).
2. NICHOLS, E. F. A method for energy measurements in the infrared spectrum and the properties of the ordinary ray in quartz for waves of great wavelength. Physical Review 4, (1897).
3. BOSE, J. C. On a Self-Recovering Coherer and the Study of the Cohering Action of Different Metals. Proceedings of the Royal Society 65, (1899).
4. PLANCK, M. Über eine Verbesserung der Wienschen Spektralgleichung (On an Improvement of Wien's Equation for the Spectrum). Verhandlungen der Deutschen Physikalischen Gesselschaft 2, 202–204 (1900).
5. PLANCK, M. Zur Theorie des Gesetzes der Energieverteilung im Normalspektrum (On the Theory of the Energy Distribution Law of the Normal Spectrum). Verhandlungen der Deutschen Physikalischen Gesselschaft 2, 237 (1900).
6. RUBENS, H. & KURLBAUM, K. Über die Emission langwelliger Wärmestrahlen durch den schwarzen Körper bei verschiedenen Temperaturen. Sitzungsberichte der Koniglich Preussischen Akademie der Wissenschaften zu Berlin 2, (1900).
7. HAGEN, E. & RUBENS, H. On some relations between the optical and the electrical qualities of metals. Philosophical Magazine 7, 157 (1904).
8. WOOD, R. W. The echelette grating for the infrared. Philosophical Magazine 20, 770 (1910).
9. RUBENS, H. & WOOD, R. W. Focal isolation of long heat-waves. Philosophical Magazine 21, 249 (1911).
10. NICHOLS, E. F. & TEAR, J. D. Joining the infra-red and electric-wave spectra. The Astrophysical Journal 61, 17 (1925).
11. ARKADIEWA, A. G. Short electromagnetic waves of wave-length up to 92 um. Nature 113, 640 (1924).
12. BADGER, R. M. Absolute intensities in the hydrogen-chloride rotation spectrum. Proceedings of the National Academy of Sciences USA 13,(6) 408 (1927).
13. CARTWRIGHT, C. H. Black bodies in the extreme infra-red. Physical Review 35, 415 (1930).
14. CARTWRIGHT, C. H. Radiation thermopiles for use at liquid-air temperatures. Review of Scientific Instruments 4, 382 (1933).
15. CLEETON, V. & WILLIAMS, N. H. Electromagnetic waves of 1.1 cm wave-length and the absorption spectrum of ammonia. Physical Review 45, 234 (1934).
16. ANDREWS, D. H., BRUKSCH, W. F., ZEIGLER, W. T. & BLANCHARD, E. R. Attenuated superconductors I. For measuring infra-red radiation. Review of Scientific Instruments 13, 281 (1942).
17. BERINGER, R. The absorption of one-half centimeter electromagnetic waves in oxygen. Physical Review 70, 53 (1946).

18. ZAHL, H. A. & GOLAY, M. J. E. Pneumatic heat detector. Review of Scientific Instruments 17, 511 (1946).

19. GOLAY, M. J. E. A pneumatic infra-red detector. Review of Scientific Instruments 18, 347 (1947).

20. GUENARD, P., DOEHLER, O., EPSZTEIN, B. & WARNECKE, R. New UHF tubes with wide electronic tuning range. Comptes Rendus de l'Académie des Sciences 235, (1952).

21. KLEIN, J. A., LOUBSER, J. H. N., NETHERCOT, A. H. & TOWNES, C. H. Magnetron harmonics at millimeter wavelengths. Review of Scientific Instruments 23, 78 (1952).

22. BURRUS, C. A. & GORDY, W. Submillimeter wave spectroscopy. Physical Review 93, 897 (1954).

23. TWISS, R. Q. Radiation transfer and the possibility of negative absorption in radio astronomy. Australian Journal of Physics 11, 564 (1958).

24. PANTELL, R. H. The design and characteristics of a megawatt space-harmonic traveling-wave tube. Proceedings of the Institute of Radio Engineers 48-53, 1146 (1959).

25. BOYLE, W. S. & ROGERS, K. F. Performance characteristics of a new low-temperature bolometer. Journal of the Optical Society of America 49, 66 (1959).

26. FRAY, S. J. & OLIVER, J. F. C. Photoconductive detector of radiation of wavelength greater than 50 um. Journal of Scientific Instruments 36, 195 (1959).

27. SINTON, W. M. Observation of solar and lunar radiation at 1.5 millimeters. Journal of the Optical Society of America 45, 975 (1955).

28. CHAMBERLAIN, J. E., GIBBS, J. E. & GEBBIE, H. A. Refractometry in the far infra-red using a twobeam interferometer. Nature 198, 874 (1963).

29. CROCKER, A., GEBBIE, H. A., KIMMITT, M. F. & MATHIAS, L. E. S. Stimulated emission in the far infrared. Nature 201, 250 (1964).

30. YOUNG, D. T. & IRVIN, J. C. Millimeter frequency conversion using Au-n-type GaAs Schottky barrier epitaxial diodes with a novel contacting technique. Proceedings of the IEEE 53, 2130 (1965).

31. NICOLSON, A. M. Broad-band microwave transmission characteristics from a single measurement of the transient response. Instrumentation and Measurement, IEEE Transactions on 17, 395 (1968).

32. PUTLEY, E. H. Impurity photoconductivity in n-type InSb. Proceedings of Physical Society 76, 802 (1960).

33. LOW, F. J. Low temperature germanium bolometer. Journal of the Optical Society of America 51, 1300 (1961).

34. MOORE, W. J. & SHENKER, H. A high-detectivity gallium-doped germanium detector for the 40–120 um region. Infrared Physics 5, 99 (1965).

35. GRIMES, C. C., RICHARDS, P. L. & SHAPIRO, S. Josephson-effect far-

infrared detector. Applied Physics 39, 3905 (1968).

36. CHANG, T. Y. & BRIDGES, T. J. Laser action at 452, 496, and 541 μm in optically pumped CH3F. Optics Communications 1,(9) 423–426 (1970).

37. WILSON, R. W., JEFFERTS, K. B. & PENZIAS, A. A. Carbon monoxide in the Orion nebula. Astrophysics Journal 161, L43 (1970).

38. YANG, K. H., RICHARDS, P. L. & SHEN, Y. R. Generation of far-infrared radiation by picosecond light pulses in LiNbO3. Applied Physics Letters 19, 320 (1971).

39. BARKER, D. H., HODGES, D. T. & HARTWICK, T. S. Far infrared imagery. Proceedings SPIE 67, 27 (1975).

40. DOLAN, G. J., PHILLIPS, T. G. & D.P.WOODY. Low-noise 115-GHz mixing in superconducting oxidebarrier tunnel junctions. Applied Physics Letters 34, 347 (1979).

41. ELIAS, L. R., HU, J. & RAMIAN, G. The UCSB electrostatic accelerator free electron laser: First operation. Nuclear Instruments and Methods in Physics Research A237, 203 (1984).

42. AUSTON, D. H. H., CHEUNG, K. P. P. & SMITH, P. R. R. Picosecond photoconducting Hertzian dipoles. Applied Physics Letters 45,(3) 284 (1984).

43. GERSHENZON, E. M., GERSHENZON, M. E., GOLTSMAN, G. N., LYULKIN, A. M., SEMENOV, A. D. & SERGEEV, A. V. On the limiting characteristics of high-speed superconducting bolometers. Soviet Physics : Technical Physics 34, 195 (1989).

44. FAIST, J., CAPASSO, F., SIVCO, D. L., SIRTORI, C., HUTCHINSON, A. L. & CHO, A. Y. Quantum Cascade Laser. Science 264,(5158) 553–556 (1994).

45. HU, B. B. & NUSS, M. C. Imaging with terahertz waves. Optics Letters 20,(16) 1716 (1995).

46. MURAMOTO, Y., KATO, K., MITSUHARA, M., NAKAJIMA, O., MATSUOKA, Y., SHIMIZU, N. & ISHIBASHI, T. High-output-voltage, high speed, high efficiency uni-travelling-carrier waveguide photodiode. Electronics Letters 34,(1) 122 (1998).

47. HALL, J. L. Optical heterodyne measurement of Neon Laser´s millimeter wave difference frequency. Applied Physics Letters 10,(5) 152 (1967).

Appendix II

mm-wave, sub-THz and THz technology.

Sources and detectors: state-of-the-art

(November, 2012)

1

mm-wave, sub-THz and THz generation technologies

There exist a significant number of technologies for the generation of sub-THz and THz radiation. They can be organized by any of the figures of merit of a generated THz wave (see Table VII1 to Table VII24.). In this general overview, a classification criterion based on the source technology is used. This classification allows allocating any THz generation technology in one of the following three groups:

- Electronic upconversion. An electronic source in the microwave or sub-THz regime is multiplied up to the THz range.
- Direct THz generators/THz oscillators. These sources are able to directly generate radiation at THz frequencies without the use of upconversion or downconversion.
- Optical downconversion. The optical frequency components of one or several optical sources are downconverted to the THz frequency domain.

In Figure 76, the different technologies for THz generation covered in this overview are represented following this criterion. Moreover, the ability of producing Continuous Wave (CW) and/or pulsed THz radiation is also depicted in Figure 76.

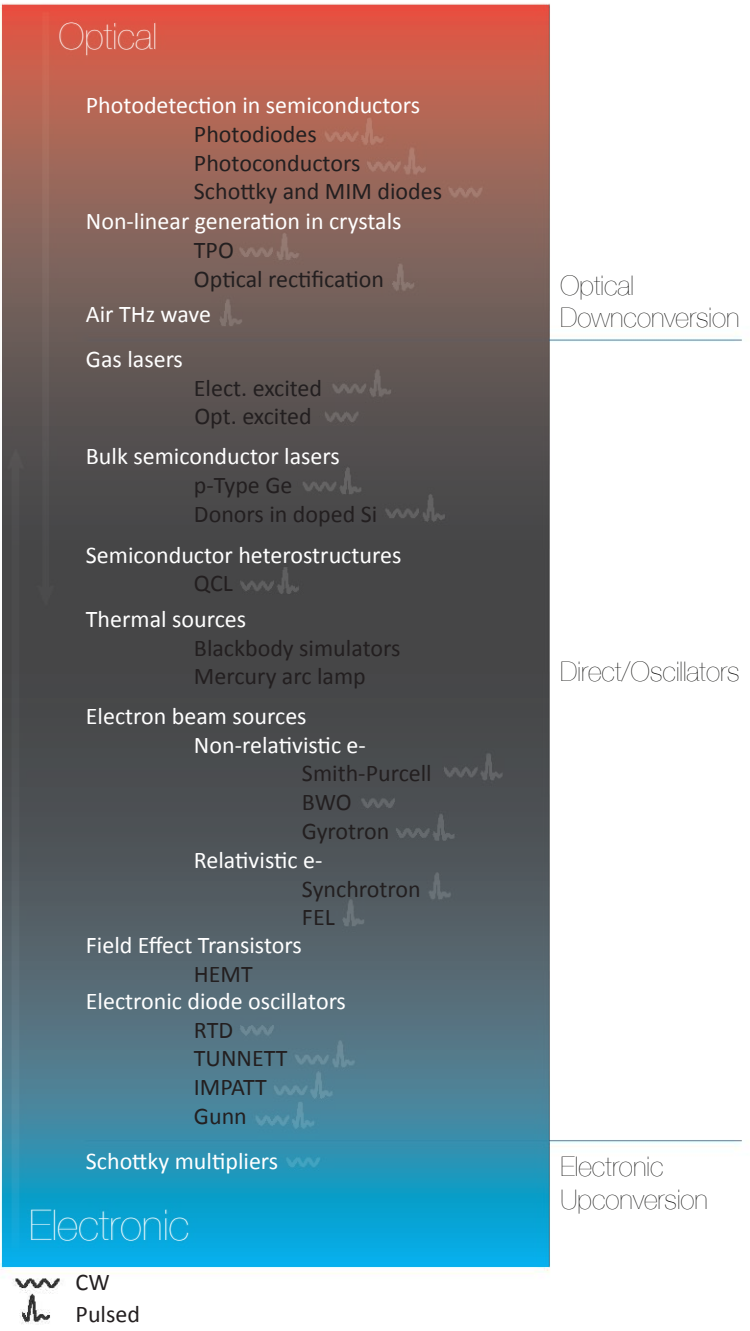

Figure 76 THz generation technology map. The sources are classified as a function of the source technology employed: electronic upconversion, direct generation and optical downconversion. Furthermore, the CW and pulsed generation capabilities of each source are shown

Throughout this section 2.1, these THz technologies are briefly described following the sorting criterion of Figure 76, i.e. frequency of the source technology: electronic upconversion, direct generation (from "electronic-like" sources to "optical-like" sources), and optical downconversion.

A summary of the state-of-the-art performance is included for each technology. The parameters included in these summaries are described below:

- Pulsed/CW. Ability to produce pulsed and/or CW radiation.
- Maximum power. Maximum output power demonstrated for a given technology.
- Frequency range. Frequency range in which it is possible to generate signals.
- Tunability. Tunability capabilities around the center frequency. Also tunability characteristics (continuous or discrete) are considered.
- Minimum FWHM. Minimum Full Width at Half Maximum (FWHM) of the generated CW signals demonstrated with the analyzed technology. Because of the difficulty of measuring phase noise at high frequencies, most investigations only report on the FWHM as an indicator of the phase noise performance.
- Minimum size. Minimum size in which the given technology has been implemented.
- Coherent/incoherent. Coherent sources are defined here as those having a significant degree of both temporal and spatial coherence in the generated signals. Further details on temporal and spatial coherence of EM waves can be found in[117].
- Cooling. Cooling requirements. Room temperature (RT) operation is defined here for those systems where no cooling is needed, or just Thermo Electric Coolers (TEC), heatsinks or thermal pads are required.

1.1 Electronic upconversion

1.1.1 Schottky Barrier Diodes

The harmonic generation of THz waves from a microwave source reference is typically accomplished by Schottky Barrier Diodes (SBD) as they are

currently the best electronic multipliers at high frequencies[267]. A chain of SBDs, used as frequency doublers or triplers is used to multiply a reference signal that is provided by microwave sources such as Backward Wave Oscillators (BWO), IMPATT or Gunn diodes (Table VII1).

They can be divided into two groups: varactors and varistors, the latter ones providing higher frequency operation[118]. The CW THz sources based in SBDs are commercially available from a few years to now, being the most widely used in several applications in the THz range[268].

Their main limitations are the low output power and its tunability range. The latter is limited and determined by the bandwidth of the waveguides employed. To overcome this and cover wide frequency ranges, several multiplier chains covering different frequency ranges can be used[119,169].

Parameter	Schottky diodes
Pulsed/CW	CW
Maximum power (CW)/ Pulse energy (pulsed)	Around 100 μw at 1 THz, 10 μW at 2 THz, 1 μW at 2.7 THz[118]
Frequency range (THz)	Microwave to 2.85 THz[119]
Tunability	Continuous over range limited by metallic waveguides (typically few 100´s GHz maximum)
Minimum FWHM (CW)	Dependent on reference source. Phase noise increases by 20log(N) and frequency drifts by N. N is the harmonic number
Minimum size (range)	Integrated
Coherent/Incoherent	Coherent
Cooling	Room Temperature (RT)

Table VII1 Performance summary of THz generation based on harmonic generation with Schottky Barrier Diodes

1.2 Direct THz generation and THz oscillators

1.2.1 Electronic diode oscillators

In this section, the performance of the main THz oscillators based on diodes is summarized. In these devices, like in lower-frequency versions, a DC

current provided to the device is upconverted to an AC signal. The devices treated here are:

- Gunn diodes.
- Impact Ionization Avalanche Transit-Time (IMPATT) diodes.
- Tunnel Injection Transit-Time (TUNNETT) diodes.
- Resonant Tunneling Diodes (RTD).

Similar operating diodes would include (just named here for their lower significance): Mixed Tunneling or Thermionic Emission and Avalanche Multiplication (MITATT) and Thermionic Emission Over a Barrier (BARRITT)[269].

The Impact Ionization Avalanche Transit Time (IMPATT) and Gunn diodes can be used in high frequency microwave circuits (<140 GHz) to implement oscillators and also for amplification purposes[270]. Although they are usually employed as sources for multipliers given their limited maximum frequency, some approaches using harmonics have been reported[271]. Moreover, operation up to the several hundreds of GHz using micrometric channel lengths has been theoretically analyzed[272], although experimental attempts are not yet successful and further optimization is required[272] (Table VII2).

It is especially interesting the integration of these devices into planar structures to implement Monolithic Microwave Integrated Circuits (MMIC)[273] in the lower THz band (below 500 GHz).

Parameter	Gunn and IMPATT diodes
Pulsed/CW	Pulsed/CW[78]
Maximum power (CW)/ Pulse energy (pulsed)	Around 30 mW at 100 GHz[78]
Frequency range (THz)	Microwave up to 140 GHz[78]. 480 GHz using harmonics[271]
Tunability	Limited, around 20-30% of Center Frequency (CF)[21]
Minimum FWHM (CW)	Several kHz. Needs PLL to achieve Hz range linewidths[274].
Minimum size (range)	Integrated[274]
Coherent/Incoherent	Coherent
Cooling	Room Temperature (RT). Cooling increases output

Table VII2 Performance summary of THz generation based on IMPATT and Gunn Diodes

The Tunnel Injection Transit-Time (TUNNETT) diodes present improved characteristics over IMPATT or Gunn diodes, especially in terms of maximum

generated frequency[79] and noise[275,276]. Nevertheless, their development has stacked since 2008, when the maximum frequency was achieved[79], despite the fact of predicted operation up to 1 THz[276]. In fact, the last published work about these diodes is dated from 2010[277] (Table VII3).

Parameter	TUNNETT diode
Pulsed/CW	Pulsed/CW[278]
Maximum power (CW)/ Pulse energy (pulsed)	0.1 nW at 706 GHz[79]
Frequency range (THz)	Microwave to 706 GHz[79]
Tunability	Limited (up to ~100 GHz at 650 GHz)[275]
Minimum FWHM (CW)	Around 100 kHz (at 355 GHz)[278]
Minimum size (range)	Integrated
Coherent/Incoherent	Coherent
Cooling	RT, special heatsinks (diamond)[278]

Table VII3 Performance summary of THz generation based on TUNNETT diodes

In the last years, the best performance on THz diodes has been achieved by Resonant Tunneling Diodes (RTD). The RTDs working principle is the quantum mechanical tunneling that allow electrons to achieve certain energy states. RTDs are relatively new devices that can oscillate up to 1.1 THz[81], although operation up to 2-3 THz in a short-term future is expected[121]. Their performance, especially in terms of frequency and integration potential make them promising devices for THz generation, although they present the same issue associated to the majority compact-size THz sources: limited output power (Table VII4).

Parameter	RTD
Pulsed/CW	CW[80,81]
Maximum power (CW)/ Pulse energy (pulsed)	Around 7 μW at 1 THz[80]
Frequency range (THz)	Microwave[279] to 1.1 THz[81]
Tunability	Limited to around 4% CF (using bias voltage)[80]
Minimum FWHM (CW)	Around 10 MHz[122]
Minimum size (range)	Integrated
Coherent/Incoherent	Coherent
Cooling	RT

Table VII4 Performance summary of THz generation based on RTDs

1.2.2 Plasmonic Field-effect Transistors (FET)

Although the electron decay time of FETs has been traditionally the limit factor of the maximum frequency of these devices, in the last years the identification of operation well above the theoretical bandwidth has produced a significant research effort in the use of FETs for both generation and detection of THz waves[157]. In order to achieve 1 THz and above operation, plasmonic operation has to be produced in the device, thus requiring extremely short gate dimensions or cryogenic cooling[165]. Nevertheless, detection has a much better performance (even better than widely used solutions) and offers a much higher potential than generation (see 2.2.2.1b).

The HEMTs are one of the FETs with more potential. They include a heterojunction of two materials with different bandgap and are mainly based on GaAs, InGaAs and InP materials. The main application field of HEMTs is as amplifiers in MMICs, where they have shown gain capabilities from microwave region[280] up to 480 GHz[281], with some predictions of operation above 1 THz[282]. Nevertheless, they have been already used for THz generation[82–84] and detection[83,85,86]. They show broadband emission over several hundreds of GHz, up to 6.5 THz[82]. In this broadband emission, there are some resonances due to plasma wave excitations[84]. In summary, their performance seems to be more adequate for amplification (HEMTs) and detection rather than for generation purposes (Table VII5).

Parameter	HEMTs
Pulsed/CW	Broadband emission over 100´s GHz[83]
Maximum power (CW)/ Pulse energy (pulsed)	0.1 μW (integrated over emission spectrum)[82]
Frequency range (THz)	Microwave to 6.5 THz[82]
Tunability	Medium. The resonance can be tuned over several 100´s GHz[84]
Minimum FWHM (CW)	The resonance have around 1 THz FWHM[283]
Minimum size (range)	Integrated
Coherent/Incoherent	Incoherent
Cooling	RT

Table VII5 Performance summary of THz generation based on HEMTs

1.2.3 Electron beam sources

The sources included under this category make use of an electron beam to generate THz radiation. They are:

- Sources based in non-relativistic electrons:
    - Smith-Purcell source.
    - Backward Wave Oscillator (BWO).
    - Gyrotron
- Sources based in relativistic electrons:
    - Synchrotron.
    - Free Electron Laser (FEL)

The Smith-Purcell structure can be easily described as a THz "whistle"[87]. An electron beam passes by a conducting material grating, in which the kinetic energy of the electron is converted into oscillation. The oscillation frequency depends on the electron velocity, the grating period and the incidence angle with the grating[21]. This source was developed under exclusive license of Vermont Photonics with the commercial name of Smith-Purcell Tunable Terahertz Source™ (TTS)[87]. Recently, new approaches have been theoretically proposed based on superradiation (SP) from two electron pre-bunched beams[284] (Table VII6).

Parameter	Smith-Purcell source
Pulsed/CW	Pulsed/CW[87]
Maximum power (CW)/ Pulse energy (pulsed)	Around 1 μW (CW)[87]
Frequency range (THz)	0.3 to 3THz[87]
Tunability	Continuous over range limited by metallic waveguides (typically few 100´s GHz maximum)[87]
Minimum FWHM (CW)	N/A
Minimum size (range)	Benchtop/Room[87]
Coherent/Incoherent	Coherent[285]
Cooling	RT[87]

Table VII6 Performance summary of THz generation based on Smith-Purcell sources

In the case of the BWO, an electron beam is generated between the cathode and the anode of the BWO, which behaves like a vacuum diode. An external magnetic field collimates the electrons into a slow-wave structure where the kinetic energy is transferred to generate the THz signal. The operation principle is similar to a travelling-wave oscillator[21]. The need of a magnetic field of significant strength obstructs its miniaturization. Nevertheless, some planar structures based on diamond have been attempted at frequencies of 300 GHz[286]

(Table VII7).

Parameter	BWO
Pulsed/CW	CW (multiline)
Maximum power (CW)/ Pulse energy (pulsed)	Up to 2 mW at 1.25 THz[88]
Frequency range (THz)	0.1 to 1.4 THz[88]
Tunability	Continuous over a limited range (around 10% CF)[21,88]
Minimum FWHM (CW)	Around 10-20 MHz. <1 kHz with locking techniques (even several PLLs)
Minimum size (range)	Benchtop. Planar for low frequency ones (300 GHz)
Coherent/Incoherent	Coherent
Cooling	RT with water cooling

Table VII7 Performance summary of THz generation based on Backward Wave Oscillator (BWO)

In a gyrotron, an electron beam is injected into a resonant cavity where a strong magnetic field is applied to make the electrons oscillate. The oscillation frequency is determined by the magnetic field amplitude and the electron mass. Thus, the gyrotron behaves more stable at low electron velocities, where the electrons mass do not experiment relativistic effects[21] (Table VII8).

Parameter	Gyrotron
Pulsed/CW	Pulsed/CW[287]
Maximum power (CW)/ Pulse energy (pulsed)	400 W at 1 THz (μs pulse)[89], and 250 W at 1 THz (CW)[21]
Frequency range (THz)	Microwave to 1.4 THz[21,89,90]
Tunability	Continuous over a wide range (by magnetic field)[21]
Minimum FWHM (CW)	Around 1 MHz at 1 THz[287]
Minimum size (range)	Room[90]
Coherent/Incoherent	Coherent
Cooling	RT with water cooling

Table VII8 Performance summary of THz generation based on Gyrotrons

The basic working principle of the sources based on relativistic electrons is the acceleration of electrons at a velocity close to the speed of light. Under this state, the electron emits electromagnetic radiation due to the acceleration. Moreover, the emitted power increases dramatically when the electron velocity is

close to the speed of light (Larmor´s formula)[288]. The electromagnetic emission can cover from the X-rays to the mm-waves, in pulsed form (usually pulse bunches)[143].

The synchrotrons basically can be categorized depending on the cavity where the electrons are accelerated in ring and linear structures. The emission can be both incoherent and coherent, and in this latter case the power is much higher[21] (Table VII9).

Parameter	Synchrotron (Coherent Radiation(CSR))	Synchrotron
Pulsed/CW	Pulsed (long pulse, bunch)[143]	
Maximum power (CW)/ Pulse energy (pulsed)	60 mW average power from 0.1 to 1.5 THz[91]	
Frequency range (THz)	0.1 to 3 THz	
Tunability	N/A	
Minimum FWHM (CW)	N/A	
Minimum size (range)	Building	
Coherent/Incoherent	Coherent (just for CSR)	
Cooling	RT with water cooling. Additional electron cooling mechanisms can be needed: stochastic cooling[289] and electron cooling[290]	

Table VII9 Performance summary of THz generation based on CSR

In a FEL, the relativistic electron beam passes through a periodic structure called undulator or wiggler, where spontaneous emission occurs. If a cavity is formed between the start and the end of the undulator, the cavity gain and resonance produce coherent emission. They can provide very high power at the expense of huge facilities and electric and magnetic fields[21] (Table VII10).

Parameter	FEL
Pulsed/CW	Pulsed (macropulses formed by micropulses
Maximum power (CW)/ Pulse energy (pulsed)	Up to 15 kW pulsed. 10 GW in UV[92]
Frequency range (THz)	0.12 to UV[92]
Tunability	N/A
Minimum FWHM (CW)	N/A
Minimum size (range)	Building
Coherent/Incoherent	Coherent

Cooling	RT with water cooling. Additional electron cooling mechanisms can be needed: stochastic cooling[289] and electron cooling[290]

Table VII10 Performance summary of THz generation based on FEL

1.2.4 Thermal sources

The thermal sources were the first devices from which radiation in the THz domain was detected:

- Blackbody simulators.
- Mercury arc lamp.

Blackbody-like sources include the Nernst Glower, the Globar and the gas mantle. They are incoherent sources that have an emission spectrum similar to that of the Blackbody (Table VII11).

Parameter	Blackbody simulators
Pulsed/CW	Blackbody like (exponential in freq, no CW), relatively uniform between 1-20 um
Maximum power (CW)/ Pulse energy (pulsed)	Very similar to blackbody emission[94]
Frequency range (THz)	1-38 μm
Tunability	None
Minimum FWHM (CW)	N/A
Minimum size (range)	cm
Coherent/Incoherent	Incoherent
Cooling	RT with air/heatsink/TEC cooling

Table VII11 Performance summary of THz generation based on Blackbody simulators

Between the different lamp sources, the mercury arc lamp emits radiation in the THz range. The radiation is incoherent and has several lines in the 200-650 μm range (Table VII12).

Parameter	Mercury arc lamp
Pulsed/CW	Several lines[93]
Maximum power (CW)/ Pulse energy (pulsed)	100-400 mW per line (10 nm)[93]

Frequency range (THz)	200-650 μm[93]
Tunability	None
Minimum FWHM (CW)	N/A
Minimum size (range)	Around 10 cm[93]
Coherent/Incoherent	Coherent
Cooling	RT with air/heatsink/TEC cooling

Table VII12 Performance summary of THz generation based on mercury arc lamps

1.2.5 Semiconductor heterostructures: Quantum Cascade Lasers (QCL)

The Quantum Cascade Laser (QCL) is a revolutionary semiconductor laser structure that was demonstrated for the first time in 1994 in the IR domain[95]. It has three fundamental differences with respect to a conventional diode laser: a QCL is a unipolar device as only electrons are involved in the laser phenomenon; a QCL is a intersubband device as the laser process takes place between conduction bands called subbands; and many photons can be generated by a single electron as a cascade scheme is used[21].

Although the wavelength emission was predicted to be configured by the quantum confinement using the same heterostructure material in the first QCL publication[95], the QCL emitting in the THz region would appear few years later in 2002[96].

QCL are very promising THz sources. They are able to emit a high output power (in excess of 100 mW) providing both pulsed (even Gain-Switching for THz amplifying purposes[291] has been achieved) and CW operation. Nevertheless, they only are able to emit down to 2 THz (although operation down to 0.8 has been achieved applying external magnetic fields)[21]. Some other drawbacks are their limited tunability and the cryogenic operation. The main tunability methods use mechanical means[124], like MEMs[125] and wire-lasers[126]. Very fine tunability (10 GHz) can be obtained with current or temperature control. Regarding the need of cryogenic cooling, it must be said that RT operation has been achieved in the medium IR[292], but not yet in the THz range. The closest approach consists on mixing the emission of the QCL with an injected IR laser in the QCL itself, producing a THz output at RT in the nW range[123] (Table VII13).

Parameter	THz QCL
Pulsed/CW	Pulsed/CW[97]

Maximum power (CW)/ Pulse energy (pulsed)	140 mW (CW)[21]
Frequency range (THz)	0.8 THz to 4.9 THz
Tunability	Limited (8.6% of CF)[125]
Minimum FWHM (CW)	Several MHz unlocked[293], <100 Hz with locking techniques[294]
Minimum size (range)	Integrated
Coherent/Incoherent	Coherent
Cooling	Yes (cryogenic, mainly liquid He cryostat or mechanical cooler)[97]

Table VII13 Performance summary of THz generation based on THz QCLs

1.2.6 Semiconductor bulk lasers

The lasing mechanism at THz range is very difficult because the smallest bandgaps in typical semiconductors materials are equivalent to photon frequencies (>18 THz), and because obtaining a population inversion at room temperature is not possible due to thermal effects[21]. However, there exist some mechanisms to obtain lasing between Landau levels at THz frequencies from a bulk semiconductor structure, such as the use of external magnetic and electric fields[99] or optical pumping[99]. The two main semiconductor bulk lasers are:

- p-Type Germanium lasers.
- Silicon-doped optically excited.

Parameter	p-Type Ge lasers
Pulsed/CW	Pulsed (mode locking)/CW(several emission lines)[98]
Maximum power (CW)/ Pulse energy (pulsed)	40 W peak power (pulsed), 1 mW (CW)[21]
Frequency range (THz)	1 THz to 4.5 THz
Tunability	Yes, using magnetic field (around 0.6 THz/T)[21]
Minimum FWHM (CW)	<1 MHz[98]
Minimum size (range)	Several mm[98]
Coherent/Incoherent	Coherent
Cooling	Yes (cryogenic, mainly liquid He at 4K)[295]

Table VII14 Performance summary of THz generation based on p-Type Ge Lasers

In p-Type Ge lasers, streaming motion and population inversion of electrons between Landau levels is achieved by means of an external magnetic field, whose strength allows tunability of the THz radiation (Table VII14).

Silicon doped with certain donors is also able to lase at THz frequencies due to some impurities transitions (G, C and E lines of Ga)[99] under optical excitation[21] (Table VII15).

Parameter	Doped Silicon optically excited lasers
Pulsed/CW	Pulsed/CW (multiline or single line depending on donor)[99]
Maximum power (CW)/ Pulse energy (pulsed)	Around 2.5 kW peak power (pulsed)[21,99]
Frequency range (THz)	1-2 THz and 3.5-7 THz[21,99]
Tunability	Limited. By compression or magnetic field[21]
Minimum FWHM (CW)	Around 30 GHz[296]
Minimum size (range)	Several mm[99]
Coherent/Incoherent	Coherent
Cooling	Yes (cryogenic, mainly mechanical cryocooler below 30k)[99]

Table VII15 Performance summary of THz generation based on doped Silicon optically excited lasers

1.2.7 Gas lasers

The gas lasers emitting at THz frequencies can be divided into two groups:

- Electrically excited: H_2O, D_2O, NH_3, OCS, H_2S, SO_2, DCN and HCN
- Optically excited: CH_3OH, CH_2F_2, HCOOH.

The THz emission in electrically excited gas lasers is due to population inversion between rotational levels of vibrational states of the gas compounds, achieved by the electric excitation of the gas tubes[21].Between the electrically excited gas lasers, only DCN and HCN are useful sources. H_2O gas lasers have a huge emission range from 1-40 THz, but their very limited power makes them impractical sources (Table VII16).

Parameter	Elect. excited Gas lasers
Pulsed/CW	Pulsed/CW (multiline)[21]

Maximum power (CW)/ Pulse energy (pulsed)	600 mW strongest line (CW), 1 kW peak power (pulsed)[21]
Frequency range (THz)	0.9-1.5 THz
Tunability	None
Minimum FWHM (CW)	Around 100 kHz[297]
Minimum size (range)	Several meters[21]
Coherent/Incoherent	Coherent
Cooling	RT with air/water cooling[298]

Table VII16 Performance summary of THz generation based on electrically excited gas lasers

In an optically excited gas laser, the vibrational states of the molecules are achieved by optical pump, usually a CO_2 laser. The gas lasers pumped by a CO_2 laser have been the main CW narrow linewidth sources for many years since its first demonstration in 1970[299] until some years ago. They need stabilization of both power and frequency[26]. Today, they are still used, especially in radioastronomy[26] and fusion plasma diagnostics[11] applications (Table VII17).

Parameter	Opt. excited Gas lasers
Pulsed/CW	CW (multiline)[21]
Maximum power (CW)/ Pulse energy (pulsed)	Around 100 mW strongest lines[21]
Frequency range (THz)	0.15-8 THz[26]
Tunability	None
Minimum FWHM (CW)	Around 1 kHz with locking techniques[21]
Minimum size (range)	Several meters[21]
Coherent/Incoherent	Coherent
Cooling	RT with air/water cooling[298]

Table VII17 Performance summary of THz generation based on optically excited gas lasers

1.3 Optical downconversion

1.3.1 THz wave air photonic generation

The THz wave air photonic generation is a recent technology for the generation and detection of pulsed THz radiation. Its main advantage is the high frequency that can be achieved, as high as 60 THz[100–103]. The operation principle relies on the creation of a gas plasma region by optical excitation trough an ultrafast pulse. Emission of THz pulsed radiation from frequency components contained in the optical excitation mixed in air plasma is due to nonlinear processes (i.e. ponderomotive force or Four-Wave Mixing (FWM))[100–102].

One of the main advantages of this method is the wide spectral coverage from 0.2 to >60 THz (using sub-20 fs pulses), only limited by the pulse width of the optical excitation. This is a great advantage over photomixing in non-linear crystals or semiconductors, where phonon absorption, carrier lifetime and dispersion also limit the maximum achievable frequency[100]. Another advantage is the high electric field of the generated pulses[101] (Table VII18).

Parameter	THz Air wave photonic generation
Pulsed/CW	Pulsed[102]
Maximum power (CW)/ Pulse energy (pulsed)	Around 400 kV/cm
Frequency range (THz)	0.2->60 THz[102]
Tunability	N/A
Minimum FWHM (CW)	N/A
Minimum size (range)	Table
Coherent/Incoherent	Coherent
Cooling	RT

Table VII18 Performance summary of THz generation based on THz wave air photonic generation

1.3.2 THz generation in non-linear crystals

1.3.2.1 THz Optical Parametric Oscillator (THz OPO or TPO)

An optical beam is introduced in a cavity that contains a monolithic

grating made from a non-linear crystal. In order to be able to use high power near-IR lasers, usually LiNbO3 and Nd:YAG are employed. Due to the three-wave mixing in the crystal, THz radiation is emitted with a certain angle. Phase matching is required to obtain THz output. Continuous tunability can easily be achieved by rotating both cavity and grating together respect to the optical beam[21].

CW THz radiation is obtained by the use of CW lasers as optical pump, such as Yb:YAG laser (1030 nm). Alternatively, if a pulsed optical pump is used (usually Q-switched nanosecond Nd:YVO4 laser), THz pulsed output is obtained.

Parameter	TPO
Pulsed/CW	Pulsed/CW[21]
Maximum power (CW)/ Pulse energy (pulsed)	Around 9.12 μW at 1.75 THz[104,105]
Frequency range (THz)	0.7-5.9 THz[21,300]
Tunability	Continuous over a wide range (can be a few THz)[104]
Minimum FWHM (CW)	Around 1 MHz[105]
Minimum size (range)	Table
Coherent/Incoherent	Coherent
Cooling	RT

Table VII19 Performance summary of THz generation based on TPOs

1.3.2.2 Optical rectification in crystals

The generation of THz emission due to optical rectification is based on second order nonlinear processes present in some materials. A train of ultrafast optical pulses is directed to the mentioned material in which Difference Frequency Generation (DFG) occurs due to second order nonlinearities. The different frequency components of the optical pulse train are mixed to generate frequency emission in the THz range[107]. The maximum synthesized frequency depends on the optical pulse width, among other parameters, as all THz pulsed setups based on optical downconversion. The most common optical source is a fs Ti:Shappire mode-locked lasers, which provides pulse widths down to 5 fs.

The pulsed THz setups based on downconversion used to be employed in pump-probe, generation-detection schemes, like Electro-Optical Sample detection (EOS), where the same optical train is used both in generation and detection with a delay between them. This allows for a coherent detection system in which the controlled variation of the delay permits to sample the output

pulse and reconstruct them. The delay usually is implemented with mechanical delay lines, but much better results in terms of Signal-to-Noise Ratio (SNR)[137] and especially speed[254] have been demonstrated using optical phase modulators (Single-Sampling-Point (SSP) technique) in CW coherent detection systems[137,254].

The materials that can be used for optical rectification are: dielectric crystals, semiconductors or organic materials. In this section, the performance described in Table VII20 is focus on crystals, specifically the most used one: ZnTe. Nevertheless, several materials have been also used, such as GaAs, InP, CdTe, Gap, BBO and $LiTaO_3$[107].

Parameter	Optical rectification in crystals
Pulsed/CW	Pulsed
Maximum power (CW)/ Pulse energy (pulsed)	0.8 μJ (500 fs pulse)[106]
Frequency range (THz)	0.5-3 THz (useful range due to the power, but frequency components up to 100 THz)[107]
Tunability	N/A
Minimum FWHM (CW)	N/A
Minimum size (range)	Table
Coherent/Incoherent	Coherent
Cooling	RT

Table VII20 Performance summary of THz generation based on optical rectification in crystals

1.3.3 Photomixing in semiconductors

The photomixing process occurs when an optical signal containing two or more optical frequencies is delivered to a device that is capable to act as a mixer at optical frequencies. The output contains both the sum and difference frequency terms, although usually the sum term is well above the response of the photomixer and it is not present at the output[107].

If the optical excitation is pulsed, all the frequency components (in a wide range) are mixed together, giving as a result also a pulsed signal, but downconverted to THz frequencies. As it will be explained below, a fs-range optical pulse is capable to produce a broadband signal with frequency components up to the THz range when downconverted [21,107,301].

Alternatively, when only two optical frequencies are mixed in the photomixer, the same process occurs, and the frequency difference term appears at the output of the photomixer as a CW signal. When the frequency spacing

between the optical frequencies can be selected, a great tunability potential is offered, even covering the full range from microwaves to THz region[116]. This CW generation process by photomixing is called Difference Frequency Generation (DFG)[21,107] and it is also identified in the literature as Optical Heterodyne Generation (OHG)[108].

1.3.3.3 Photomixing in electronic diodes

Although the photomixing for CW THz generation is mainly accomplished in photoconductors and photodiodes, there are some other methods using electronic diodes:

- Photomixing in Schottky diodes using sideband generation.
- Photomixing in Metal-Insulator-Metal (MIM) diodes.

Nevertheless, these two systems were mainly used several years ago, and now have been clearly surpassed by the performance, compactness and lower cost of photomixing in photoconductors and photodiodes.

In the sideband generation with Schottky diodes[109], a high power (>10 mW) THz gas laser is mixed in the diode with a microwave signal to generate several sidebands around the emission lines of the THz gas laser. The main problems are the limited operation range, due to the maximum microwave frequency that can be used; and that usually the only sideband that offers enough power is the first one, being higher orders not useful[21] (Table VII21).

Parameter	Sideband generation with Schottky diodes
Pulsed/CW	CW (multiline)
Maximum power (CW)/ Pulse energy (pulsed)	55 μW at 1.6 THz[109]
Frequency range (THz)	0.5-3 THz[21]
Tunability	Limited around the gas laser lines. In those ranges tunability of GHz given by microwave source. Also limited by waveguides band-width[109]
Minimum FWHM (CW)	Dependent on gas laser and microwave source. At least several kHz with locking techniques[21]
Minimum size (range)	Table
Coherent/Incoherent	Coherent
Cooling	RT

Table VII21 Performance summary of THz generation based on sideband generation with Schottky diodes

The photomixing in MIM diodes has the same operation principle that CW photomixing in photoconductors and photodiodes: two optical frequencies are mixed in the MIM diode to obtain a signal with a frequency equal to the frequency spacing between the two optical lines.

The main attempts have been accomplished by the use of two CO_2 lasers in the mid-IR region. Third order generation has been also reported, where the two optical frequencies are mixed together with a microwave signal. In this case much lower power is obtained[21] (Table VII22).

Parameter	Photomixing in MIM diodes
Pulsed/CW	CW
Maximum power (CW)/ Pulse energy (pulsed)	1 μW[21]
Frequency range (THz)	0.5-3 THz[21]
Tunability	Very limited as the CO_2 lasers have MHz range tunability. Higher tunability if using third order, but limited to microwave source range[21]
Minimum FWHM (CW)	Dependent on lasers and microwave source
Minimum size (range)	Table
Coherent/Incoherent	Coherent
Cooling	RT

Table VII22 Performance summary of THz generation based on photomixing in MIM diodes

1.3.3.4 Photodetection in photoconductors

THz generation by photomixing in photoconductors can be pulsed, using fs-range pulsed optical sources, and also CW, using DFG. The maximum achievable frequency depends on both the optical pulse width and the photoconductor carrier lifetime[116].

The most suitable and widely used material for photoconductors is Low Temperature Grown GaAs(LT-GaAs)[116]. The LT-GaAs is used with optical sources in the 800 nm range, such as fs Ti:Sapphire lasers[108] or Er-doped fiber lasers[241] for pulsed THz generation, and near infrared CW lasers, such as 850 nm CW laser diodes, for CW THz generation[242–244] (Table VII23).

However, it is especially interesting the pursue of the operation in the telecom range wavelength, in order to take advantage of the great number of compact, low cost and high performance Commercially available Off-The-Shelf (COTS) optical devices. With this motivation, photoconductors operating in the

1500 nm range have been recently developed. These photoconductors are made of LT InGaAs/InAlAs on InP multilayer quantum well[110,127–130].

Parameter	Photomixing in photoconductors
Pulsed/CW	Pulsed/CW
Maximum power (CW)/ Pulse energy (pulsed)	2 μW at 1 THz[108]
Frequency range (THz)	0-3 THz[21]
Tunability	Dependent on optical source. Can be very wide and continuous
Minimum FWHM (CW)	Dependent on optical source. Can be very narrow (Hz range)[132]
Minimum size (range)	Integrated. Compact devices packaged in cm[110,111]
Coherent/Incoherent	Coherent
Cooling	RT

Table VII23 Performance summary of THz generation based on photomixing in photoconductors

1.3.3.5 Photodetection in p-i-n photodiodes

The maximum operation frequency of photoconductors basically depends (without taking into account the optical excitation) on the carrier lifetime (transit time) associated to the photomixer. In the case of p-i-n diodes, it depends both on the transit time and RC roll-offs of the device[107,116], existing a trade-off between both[107]. This is the main reason of the lower maximum frequency of p-i-n photodiodes when compared to photoconductors.

However, photodiodes present several advantages over photoconductors that make them a promising technology for THz generation: first; they have higher gain (unity quantum efficiency at sufficiently low frequencies[116]); second, they need lower applied voltage between contacts; and third, the thermal effects are lower, thus higher optical power can be applied and higher THz power can be obtained[116].

There exist basically three kinds of devices based on p-i-n structures[116]:

- p-i-n diodes. They have a limited bandwidth, thus having low output power even at intermediate frequencies. They are surface illuminated devices, where the optical signal is perpendicular to the generated current. An improved design of p-i-n diodes are the Travelling-Wave (TW) PDs. These are edge-illuminated devices with a waveguide structure where optical and electronic signals travel in the same direction. As the waveguide can be designed as lumped elements, it can be matched to the output impedance,

and the RC frequency bandwidth is greatly improved[248].

- Photodiodes with electron transport only. In these diodes, the photocurrent is basically generated only by electrons. As the velocity of the holes is less than that of electrons, higher frequencies can be achieved. This operation principle is followed by the Uni-Travelling Carrier Photodiode (UTC-PD)[113,114], Travelling-Wave Uni-Travelling Carrier Photodiode (TW-UTC-PD)[112], and n-i-pn-i-p superlattice photomixers[115,116]. Also by other modifications over UTC-PD: Near-Ballistic UTC (NBUTC)[249] and Modified UTC (MUTC)[250]. The main advantage of the UTC structures is that they are able to provide a higher maximum output power[247].

- Ballistic transport p-i-n structures. The electrons are accelerated trough a large region, obtaining higher carrier velocities. This is the case of n-i-pn-i-p superlattice photomixers[115,116].

In the case of n-i-pn-i-p photomixers, the trade-off between transit time and RC roll-offs has been overcome by the use of superlattice structure, allowing for independent design of both.[116] This is a promising result for the development of higher frequency photodiodes.

As the limited THz output power is one of the main concerns in compact THz technology, great effort is currently placed in photodiodes, as they are expected to generate higher THz power. In this sense, 24 μW at 1.06 THz has been achieved[112] and around 300 μW is theoretically predicted with the limitations of space charge effects and heating of the device[247].

It must be noted that PDs have been successfully integrated with planar antennas, both resonant[112] and broadband (i.e. log-periodic[112], log-spiral[116]). In the first case, they have higher output power but tunability around 20% of the center frequency, while in the latter case they are able to cover the whole range[21].Moreover, they have also been integrated in InP substrates[251], in this case achieving lower bandwidth values around 100 GHz (Table VII24).

Parameter	Photomixing in p-i-n photodiodes
Pulsed/CW	Pulsed[252]/CW
Maximum power (CW)/ Pulse energy (pulsed)	24 μW at 1.06 THz[108]
Frequency range (THz)	0-1.6 THz[131]
Tunability	Dependent on optical source. Can be continuous and covering the whole range[21]
Minimum FWHM (CW)	Dependent on optical source. Can be very narrow (Hz range)[132]
Minimum size (range)	Integrated. Compact devices packaged in cm[116]

Coherent/Incoherent	Coherent
Cooling	RT

Table VII24 Performance summary of THz generation based on p-i-n photodiodes

2

mm-wave, sub-THz and THz detection technologies

In the previous section, the different THz generation technologies were firstly classified depending on source technology (see Figure 76). For this overview of the THz detection technologies, this first classification is made depending on the pulsed or continuous temporal behavior of the detected THz wave (Figure 77).

Two main groups will be covered in pulsed THz detection. The first one is the coherent detection of fs-ps THz pulses using pump-probe schemes. This is the case of the TDS measurement systems. The second is the direct detection of ns-scale THz pulses.

Among the CW THz detection, direct and heterodyne detection is differentiated. Thermal detectors, electronic rectifiers and photodetectors are presented as direct detectors. For the case of heterodyne detection, both electronic and Electro-Optical (EO) mixers are covered.

As in the generation technology section, a performance table summarizing the main figures of merit of the detectors is included for each technology (Table VII26 to Table VII42). It must be noted that some devices have been allocated in several groups as they can be used for various detection schemes. The figures of merit included in these summarizing tables are described below:

- Frequency range. Frequency range in which it is possible to detect signals with a given technology.
- Coherence. In a coherent receiver, the detected signal is phase-correlated with the emitted signal, thus, it has a constant relative phase with respect to the generated signal (under no changes in the path). Coherent receivers allow measuring not only amplitude, but also the phase changes of the received signal with

respect to a reference.

- Minimum size. Minimum size in which the given technology has been implemented.
- NEP. Signal power that is required at the input to obtain a Signal-to-Noise Ratio (SNR) equal to unity at the output of a detector in 1 Hz bandwidth[21].
- Frequency bandwidth. Bandwidth of detection around the specified center frequency.
- Cooling. Cooling requirements. Room temperature (RT) operation is defined here for those systems where no cooling is needed, or just Thermo Electric Coolers (TEC), heatsinks or thermal pads are required.

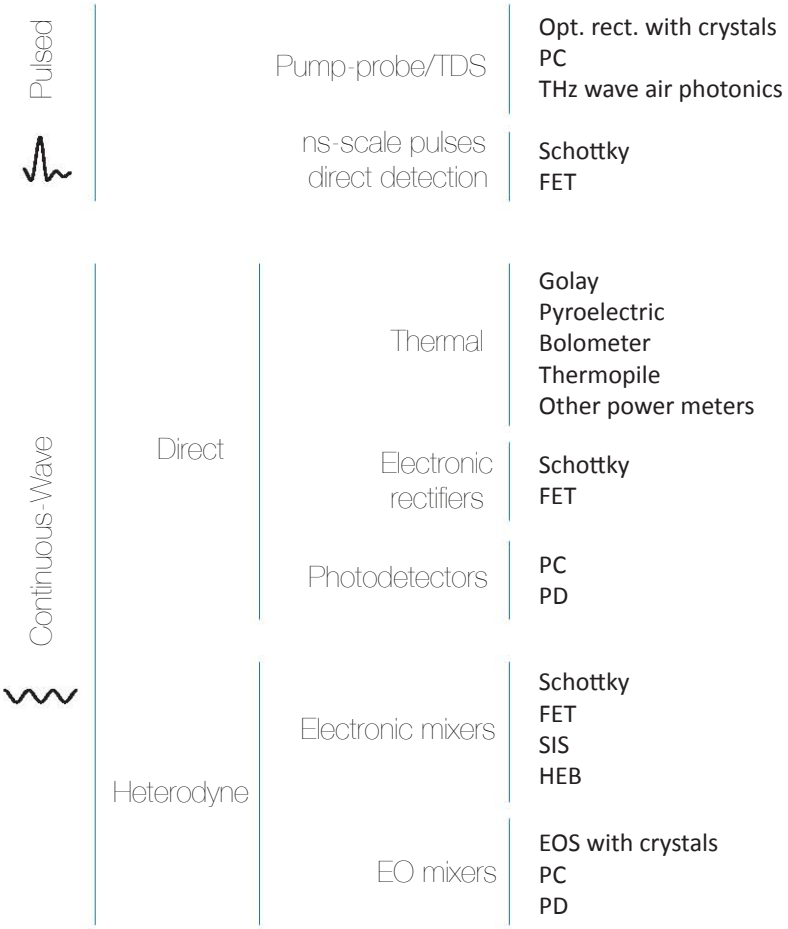

Figure 77 THz detection technology map

2.1 Detection of pulsed THz radiation

2.1.1 Pump-probe / Time Domain Spectroscopy schemes

Time Domain Spectroscopy (TDS) is a widespread scheme for broadband frequency spectroscopy in the THz range. It consists on a pulsed THz emitter, a THz detector and a method to introduce an optical delay between the fs laser beams used for generation and detection. The emitter always uses a fs laser to produce the THz pulse, and can be based on optical rectification in crystals or photomixing in a photoconductor (see section 2.1.3). The detector also makes use of the same fs laser. It converts the received THz radiation to a DC current that corresponds to a time sample of the THz pulse (homodyne operation). Usually, the bias voltage or optical signal are modulated (normally in amplitude[107] but also in phase[254]) with a low frequency signal to increase the sensitivity using lock-in detection. In order to measure different samples of the received THz pulse and recover it, a controlled delay has to be applied between the fs-laser beam in generation and detection. As the same fs-laser is used coherently in generation and detection, this scheme is also known as pump-probe scheme. Further details on TDS can be found, for instance, on Sakai[107] and Jepsen[139].

2.1.1.6 Electro-optical sampling (EOS) detection with crystals

Some birefringent crystals, like $LiTaO_3$ or ZnTe[21] are sensitive to THz radiation that is able to change the birefringence characteristics of the crystal depending on the time and its electric field strength. This way, if a fs laser passes through the crystal synchronized to the THz radiation, its polarization changes. This change in the polarization state allows measuring each sample of the THz pulse.

The limiting factor of the maximum detected frequency is given by the difference between group velocities of both the optical and THz pulse while passing through the crystal. The length of the crystal determines the tradeoff between dispersion (shorter crystal) and modulation induced in the crystal (larger crystal, more sensitivity)[107] (Table VII25).

Parameter	EOS in crystals
Frequency range (THz)	0->120 THz[140]
Coherent/Incoherent	Coherent
Minimum size (range)	Benchtop/Table in TDS scheme

Cooling	RT

Table VII25 Performance summary of THz pulsed detection based on EOS in crystals

2.1.1.7 Photoconductors

The THz detection of pulsed radiation using photoconductors follows the inverse process of the generation of pulsed radiation using photomixing in photoconductors (see section 2.1.3). The fs optical beam falls upon the photoconductor gap, where photocarriers are generated. The incident THz pulse accelerates the photocarriers and a photocurrent is generated and measured in the bias port of the photoconductor[107].

Although the response in detection depends, as in generation, on the optical pulse width and carrier lifetime of the photoconductor, astonishing detection bandwidth up to 170 THz has been achieved, with theoretical predicted operation up to 200 THz[141] using 5 fs lasers. Nevertheless, commercial systems have bandwidth in the order of a few THz (complete TDS systems)[142] (Table VII26).

Parameter	Pulsed detection with photoconductors
Frequency range (THz)	0->170 THz[140]
Coherent/Incoherent	Coherent
Minimum size (range)	Benchtop/Table in TDS scheme
Cooling	RT

Table VII26 Performance summary of pulsed THz detection based on photoconductors

2.1.1.8 THz Wave Air Photonics detection

The THz wave air photonics provides with novel pump-probe schemes for both generation and detection of THz pulses. Some details have been already commented previously (see 2.1.3.1). In detection there are three basic schemes[102].

When an interaction between the THz wave and the fs optical beam is achieved in a gaseous media or laser induced plasma, third order processes appear giving as a result an optical wave (fluorescence) at half wavelength of that of the fs optical beam excitation. The field amplitude of this generated optical wave is proportional to the fs optical beam field and the THz field. In order to have coherent detection, one of the mixing components has to dominate, and this is achieved with a minimum pulse energy of the fs optical probe beam, from which the air is broken down[100]. Thus, this method is called THz-air-breakdown coherent detection (THz-ABCD). This is maybe the most significant of the three

schemes, as it achieves the highest detected frequency.

The other two schemes are THz-radiation-enhanced emission of fluorescence (THz-REEF) and THz Wave Enhanced Acoustics (TEA). Further details can be found in[100,102] (Table VII27).

Parameter	THz wave air photonics
Frequency range (THz)	0.2->60 THz[102]
Coherent/Incoherent	Coherent
Minimum size (range)	Benchtop/Table (complete scheme)
Cooling	RT

Table VII27 Performance summary of pulsed THz detection based on THz wave air Photonics

2.1.2 ns-scale pulse detection

Asides from pump-probe schemes for coherent detection of fs-ps pulses, some of the devices that will be described in this section are capable of directly detect slower THz pulses. Only some of them have bandwidth enough to detect these THz pulses, usually in the ns range (several GHz bandwidth).

Some of the devices that have been reported for detection of ns-scale pulses are FETs[146] or Schottky diodes[144,145] (that will be described later with more detail).

2.2 Detection of CW THz radiation

2.2.1 Direct detection

2.2.1.1 Thermal detectors

In these detectors, the radiation absorbed heats the device and some physical variation in the device properties is measured. They are characterized by a wide detection frequency range (usually covering both THz and far-IR regions) and very slow operation at room temperature, although it can be increased by cryogenic cooling[21]. They were the first devices used for detection (see *Appendix I. THz history*) and are still widely used for power measurement in this frequency

range. In this group are included: Golay cells[21,147,148], pyroelectric detectors[21,147,149], bolometers[21,149,150] and thermopiles[21,151,152].

a Golay detector

The Golay detector is one of the first and more widely used detectors for decades. The radiation impinges in a gas cell. The heating of the gas produces a movement in a flexible mirror or membrane[21] (Table VII28).

Parameter	Golay cell
Frequency range (THz)	0.04-15 THz[147]
Coherent/Incoherent	Coherent[149]
Minimum size (range)	Integrated[148]
NEP (W/(Hz)$^{1/2}$)	$2{\cdot}10^{-10}$ [21]
Frequency bandwidth (Hz)	Around 20 Hz
Cooling	RT[21]

Table VII28 Performance summary of CW THz detection based on thermal detection: Golay cell

b Pyroelectric detector

Some materials (best ones from triglycine sulfate (TGS) group) experiment a change in the dipole moment and electrical charge under a change of temperature due to the incident THz radiation. If a capacitor-like structure is used, this change can be measured. The pyroelectric detectors are also available from several decades ago and together with the Golay cells and bolometers is one of the most widely used thermal detectors. As the equivalent circuit is a RC scheme, the frequency response and sensitivity of the pyroelectric detectors depends on the load resistance. The frequency response can reach the range of 100´s MHz. The Noise Equivalent Power (NEP) is about one order of magnitude worse than Golay cells, but as they are more insensitive to environmental noise, are able to provide even better sensitivity[21] (Table VII29).

Parameter	Pyroelectric detector
Frequency range (THz)	0.1-280 THz[147]
Coherent/Incoherent	Coherent[149]
Minimum size (range)	Mm range[21]
NEP (W/(Hz)$^{1/2}$)	Around $2{\cdot}10^{-9}$ [21]

Frequency bandwidth (Hz)	Around 100 MHz[21].
Cooling	RT[21]

Table VII29 Performance summary of CW THz detection based on thermal detection: pyroelectric detectors

c Bolometers

The principle of operation of a bolometer is based on the use of a thermistor to measure the heating associated to the incoming THz radiation. The thermistor chip used to be heavily doped with a semiconductor like Si or Ge to obtain higher temperature coefficient, thus higher sensitivity.

In order to increase the time response, cryogenic cooling or reduction of the thermal mass can be employed. The first is the case of superconducting bolometers that can work to temperatures as low as 0.95 K, obtaining dramatic improvements on NEP values. Astonishing NEP values in the range of $3{\cdot}10^{-19}$ $(W/(Hz)^{1/2})$[302] have been reported. Moreover, the cooling allow reaching high frequency bandwidth values as high as 25 GHz[21]. When the size is reduced, there appear problems related to the absorption of the light and the robustness of the devices. This last case corresponds to room-temperature microbolometers[21] and bolometers[150]. At room temperature, they present worse NEP values, reaching 10^{-10} $W/(Hz)^{1/2}$ with frequency bandwidths of 25 MHz. A way to increase the sensitivity at room temperature of micro bolometers and bolometers is the use of array schemes[21] (Table VII30).

A novel and interesting approach for power sensing based on bolometers includes the use of Dielectric Rod Waveguides (DRW)[303], which are nowadays one of the best devices to guide millimeter waves with low losses[68,71].

Parameter	Bolometer
Frequency range (THz)	THz-FIR[21]
Coherent/Incoherent	Coherent[149,150]
Minimum size (range)	Integrated (microbolometers)[21]
NEP $(W/(Hz)^{1/2})$	Around 10^{-17} (superconducting)[21]
Frequency bandwidth (Hz)	Up to 25 GHz (superconducting)[21]
Cooling	RT for microbolometers and cryogenic cooling for superconducting[21]

Table VII30 Performance summary of CW THz detection based on thermal detection: bolometers

d *Thermopiles*

A thermopile is a set of thermocouple junction pairs connected in series. The change in temperature results in electromotive force in the junction contact, generating a voltage difference proportional to the temperature gradient. To set up the thermopile, several thermocouples are connected in series to increase the sensitivity, and an absorber to filter the non-desired frequency ranges of detection is used. As the thermocouples only measure the temperature gradient, a temperature reference has to be included in the thermopile[21] (Table VII31).

Parameter	Thermopile
Frequency range (THz)	THz to far-IR(depends on absorber) [21]
Coherent/Incoherent	N/A
Minimum size (range)	Integrated[151]
NEP (W/(Hz)$^{1/2}$)	Around $3{\cdot}10^{-10}$ [151,152]
Frequency bandwidth (Hz)	Up to 100 Hz[151,152]
Cooling	RT[21,151,152]

Table VII31 Performance summary of CW THz detection based on thermal detection: thermopiles

e *Other power meters*

The accurate power measurement in the THz domain is challenging, mainly because the responsivity of thermal detectors is not accurately know for a particular frequency. Usually, blackbody emitters (see 2.1.2.4) are used for calibration of thermal detectors, but they are not able to provide enough accuracy[21]. The accurate absolute power measurement is a requirement for applications of THz metrology and instrumentation[147].

Between the power meters reported in the THz range, it can be highlighted the following ones: calorimetric power meters[304] and those based on photoacoustic effects[21].

2.2.1.2 Electronic rectifiers

A rectifier is a device that is able to generate a DC current from an AC excitation. Due to a nonlinear relationship between the bias voltage and the generated current, the AC excitation is downconverted to DC due to self-mixing mechanisms. In this sense, a rectifier can also be used as mixer for downconversion to an intermediate frequency (IF) in a heterodyne system[21].

Schottky diodes and FETs are largely used as rectifiers in the microwave

region since decades, and one of the approaches for THz detection is the extension of these devices to higher frequencies. They are replacing detection solutions based on thermal detection as they are able to provide similar NEP values (but not similar to superconducting bolometers), room-temperature operation and higher frequency bandwidth[134]. However, their maximum operation frequency is at last term limited by parasitic effect and the difficult of manufacturing devices within the sub-μm range[21,165].

a Schottky diodes

Schottky diodes are the most commonly used THz rectifiers and they are commercially available, featuring a high performance[153,154]. One of the characteristic of most of the state-of-the-art Schottky diodes rectifiers in the THz range is the zero bias operation[153,154]. To provide differential impedance suitable for proper operation without the need of bias voltage has the advantage of reducing (even eliminating) the shot noise, thus dramatically reducing the total noise, whose main component is in this way just the thermal noise[155]. This noise reduction is essential to reduce the NEP parameter down to values similar to those of Golay cells and RT bolometers. Moreover, the zero-bias operation is much more convenient for antenna-coupled devices[147]. They are usually made with GaAs and InGaAs[155] (Table VII32).

Parameter	Schottky diodes (rectifier operation)
Frequency range (THz)	From microwave to 1.7 THz[154]
Coherent/Incoherent	Coherent
Minimum size (range)	Planar, integrated[155]
NEP (W/(Hz)$^{1/2}$)	$3{\cdot}10^{-12}$ at 639 GHz[305], $20{\cdot}10^{-12}$ in the 750-1100 GHz band[154], and $30{\cdot}10^{-12}$ at 1 THz[155]
Frequency bandwidth (Hz)	Theoretically (from response time) around 1 THz [154,156]
Cooling	RT[155]

Table VII32 Performance summary of CW THz direct detection based on Schottky diodes

b Plasmonic Field-effect Transistors (FET)

There are several FET structures that can be divided in two groups depending on their operation principle: non-resonant and resonant. The non-resonant FETs have an operation bandwidth limited by the electron transit time and can achieve up to 600 GHz[157] with a broadband frequency response. In the case of resonant devices, much larger operation frequencies (>14 THz[158]) are achieved, with a band-limited frequency response given by the resonance. As the plasma waves velocities are much larger (in the order of 10^{10} m/s) than electron

drift velocities, the excitation of plasma resonances lead to much higher operation frequencies. Resonant operation begins to occur approximately at 1 THz for Si and GaAs based devices[165]. The plasma fundamental frequency is directly proportional to the square root of the gate voltage and inversely proportional to the gate length. This way, a short enough gate (sub-μm) can provide a plasma resonance cavity in the transistor, while the gate voltage provides certain tunability in the resonance[157,306]. Resonant devices with more reasonable gate dimensions can be implemented, at the expense of cryogenic colling[165].

As a summary, resonant FETs provide less frequency response (up to about 600 GHz) but more ease of fabrication and RT operation. Resonant devices need very small gate dimensions and/or cryogenic cooling, but they are able to work (in band-limited response) above 1 THz.

Although nowadays they provide with NEP values a few orders of magnitude worse that state-of-the-art Schottky diodes, the predicted limit for direct non-resonant detection in FETs is as low as $7{\cdot}10^{-13}$ W/(Hz)$^{1/2}$ [165].

Reported FET structures for THz detection include: GaAs/AlGaAs and GaN/AlGaN heterostructure FETs (HFET)[157,307], GaAs/AlGaAs High Electron Mobility Transistors (HEMT)[158], Modulation-doped FETs (MODFET)[134], grating-gate plasmonic FETs[308,309], Si Complementary metal–oxide–semiconductor FETs (CMOS)[159–161,310], Si FinFETs[156], Si FETs[166] or even graphene-based FET structures[311], among others.

Especially interesting is the case of a 1 kPixel CMOS Terahertz camera operating at video rate (25fps)[160]. The camera uses a 1024 elements array and all the needed circuitry to provide a fully working camera at THz frequencies. The reported device was able to work up to 1 THz, but higher frequency operation is expected[160] (Table VII33).

Parameter	FET (rectifier operation)
Frequency range (THz)	Up to 1 THz (non-resonant)[159] and up to 14 THz (resonant, harmonics)[158].
Coherent/Incoherent	Coherent[134]
Minimum size (range)	Integrated[157]
NEP (W/(Hz)$^{1/2}$)	$50{\cdot}10^{-12}$ [161]
Frequency bandwidth (Hz)	Very wide for non-resonant operation, about 0.6 THz for resonant[158]
Cooling	RT, but can operate with cryogenic cooling to plasmonic effect enhancement[165]

Table VII33 Performance summary of CW THz direct detection based on FETs

2.2.1.3 Photodetectors

Photodetectors are devices that do not respond to thermal variations, as is the case of thermal detectors, but to the interaction of photons with electrons in the material[21]. This is why they are also known as quantum detectors[147]. There are two kinds of photodetectors: photoconductors and photodiodes.

c Photoconductors

The THz detection with photoconductors below 2 THz began with GaAs devices. GaAs is sensitive to near infrared optical wavelengths (around 800 nm). The appearance of Low Temperature grown GaAs (LT-GaAs), was a major advance for THz technology, given the short carrier lifetime of this material that made it especially suitable for THz detection and generation[107]. The maximum operation frequency of a photoconductor is determined by the photo-generated carrier transit time and/or the carrier recombination time. The carrier recombination time can be reduced by reducing the distance gap between the electrodes or applying a higher bias voltage[246]. Examples of CW THz receivers using LT-GaAs photoconductors (i.e. using wavelength around 800-850 nm) can be found in Verghese[243] or Gregory[244].

Nevertheless, the detection of CW was introduced later than pulsed operation. This is because the differences between pulsed and CW radiation. If the same average optical power is considered, fs pulses with MHz range repetition rates have much higher peak power values, but also the semiconductor has much more time to recover from the excited into dark state, given the repetition rate. This is the main reason why the CW detection with photoconductors was delayed until the technology was developed[163].

The advent of the telecom technologies in the optical domain has driven the development of photoconductors for operation with optical wavelengths at 1550 nm, in order to take advantage of wide variety of compact, reliable, high performance, low cost and commercially available optical devices at this wavelength region. However, much worse power performance in emission is achieved with PCs at these wavelenghts[127,128,130,133,163] (Table VII34).

Parameter	PC (CW operation)
Frequency range (THz)	Up to 4 THz[130,163]
Coherent/Incoherent	Coherent[163,256]
Minimum size (range)	Planar, antenna coupled[127]
NEP (W/(Hz)$^{1/2}$)	$4{\cdot}10^{-14}$ with GaAs[21]
Frequency bandwidth (Hz)	50 MHz[21]

Cooling	RT, but cooling can improve performance of some materials[21]

Table VII34 Performance summary of CW THz direct detection based on photoconductors

d Photodiodes

Between the several photodiode structures reported for THz emission (section 2.1.3.3c), up to now, only two have been successfully used for detection: TW-UTC-PD[171,172] and UTC-PD[164]. Between these two only UTC-PD[164] has been reported to work as direct detector. In this PhD work, a new photodiode-like detector is reported to properly work for heterodyne detection: the np-i-pn quasi-ballistic THz detector.

As seen on section 2.1.3.3c, generation based on PD provides much higher power than photoconductors, so they use to be the preferred choice for state-of-the-art THz generation schemes based on DFG on semiconductors[25,163]. However, in detection, photoconductors are preferred for direct detection. This is because of the operation behavior of typical photodiodes which does not allow coherent direct detection. Their operation as square-law detectors (in direct detection) is difficult and non-linear regions in the forward bias voltage region have to be used (diode operation. This has been only reported by Nagatsuma *et al.*[164]. In this case, and due to the square-law detector nature, coherent detection systems like those used with photoconductors[127,254] cannot be employed.

In the only already reported results on direct detection using a photodiode at sub-THz regime[164] (asides from the work presented in this PhD about direct detection of a photonic LO, see chapter 3), the NEP is not reported, but the noise floor of the measurements does (-110 dBm). Some assumptions have to be made to have an estimation of the NEP: first, the reported power is over 1 Hz (normalized power); second, the ESA and measurement system (preamplifier) are not limiting the noise performance of the instrumentation measurement system; and third, the measurement system has an input impedance of 50 Ω (what is the case in almost all ESAs). If the used instrumentation was limiting the noise measurement, the NEP for the photodiode will be equal or less than the computed NEP. A value of -110 dBm/Hz corresponds to 0.2 fA^2/Hz in a 50 Ω measurement system. In a photodiode, the NEP is equal to the noise current divided by the responsivity[312]. Although the responsivity is not reported, values in the order of 0.3 A/W are given for similar devices[172]. With these values, the estimated NEP would be $4.7 \cdot 10^{-8}$ $W/(Hz)^{1/2}$ or less (Table VII35).

Parameter	PD (CW operation)
Frequency range (THz)	Up to 350 GHz[164]
Coherent/Incoherent	Incoherent[163]

Minimum size (range)	Planar, antenna coupled[164]
NEP (W/(Hz)$^{1/2}$)	NA, estimated NEP ≤ $4.7 \cdot 10^{-8}$ [164]
Frequency bandwidth (Hz)	NA. Should be several GHz[172].
Cooling	RT[164]

Table VII35 Performance summary of CW THz direct detection based on photodiodes

2.2.2 Heterodyne detectors

In the heterodyne detection, the THz detector is used as mixer. Two signals, the THz radiation (or measurement signal, M) and a LO with a frequency close to this THZ radiation, are mixed to obtain an IF signal at lower frequencies.

In order to be able to mix, the detector must have a non-linear relationship between the generated current and detector voltage, i.e. V-I curve. Thus, the mixer V-I curve can be expressed as a power series[21]:

$$I(V) = k_0 + k_1 V + k_2 V^2 + \ldots = \sum_{i=0}^{\infty} k_i V^i \qquad (55)$$

Depending on the order of the significant terms of equation (55), several mixing terms will appear. However, the most important are the sum term and especially the difference term (i.e. IF). Additional higher order terms are of special interest to analyze the quality of a mixer in terms of the spurious signals generated[264].

Mixers have two different ways to react to the received signals (M and LO). The first one is that of square-law mixers or power mixers. In this case, the detector is sensitive to the total power of the sum of both M and LO signals, but not to the individual fields as they are not fast enough to follow both fields. They have enough bandwidth for the IF signal but not for responding directly to the LO or M fields. Typical square-law detectors are thermal detectors like Hot Electron Bolometers (HEB).

The second type of mixers are those able to react to the individual fields M and LO. They are called switch mixers[21]. The IF power has a component proportional to the product of M and LO amplitudes. It must be noted that this multiplicative component used to be very low, like in Schottky diodes, but can be higher (desired scenario) in some state-of-the-art FET mixers[134]. Other switch mixers are Superconductor-Insulator-Superconductor (SIS) mixers[21]. As the IF power will depend in the mixing components, a higher multiplicative term is much convenient than lower multiplicative terms or additive terms in order to provide higher mixer input (basically through higher LO power) and higher

sensitivity in the receiver[134].

All these mixers can be used as rectifiers in direct detection, although the achieved NEP values used to be worse than in other direct detectors.

We can made another mixer classification based in the received signals M and LO. The most typical mixers are electronic, with both M and LO signals are in the THz range. This is the approach most widely used and with better performance. Between electronic mixer, some of them have two inputs, one for each received signal (M and LO), like some three-terminal FETs[165], and other have only one input two-terminal devices), thus M and LO signals have to be coupled before entering the mixer. This is the case of Schottky diodes, for instance.

Another approach, is the mixing of an M signal in the THz domain with a LO modulated onto an optical carrier, i.e. photonic LO. This is called Electro-Optical (EO) mixing. The great advantage of this is the possibility of remote distribution using optical fiber of the LO. This is the receiver approach on which this PhD work is focused. This offers great scalability, flexibility, light weight and cost reduction in the receiver design.

The inception of the EO mixing is dated back from 1970, where it was accomplished in an Avalanche Photodetector (APD) at 100 MHz[313]. Also in this work, the use of a photonic LO like those currently used in EO mixing at THz regime is predicted, this is, the use of two optical modes with a frequency spacing equal to the LO frequency[313]. This technique was still used in APDs during 1980´s[314]. However, the EO mixing demonstrated its great potential especially in the last years in Microwave Photonics field, with M signals at microwave frequencies[261].

The EO mixing has been reported only a few times in the THz frequency region, mainly due to the lack of EO mixers in the THz domain, or due to their high conversion losses. Between these works on EO heterodyne detection, some of them use PCs, and only two groups have used photodiode-like structures. In this thesis a new device for EO heterodyne THz mixing is reported. These devices for EO mixing will be described with detail in following subsections.

For this section, mixer temperature noise will be evaluated instead of NEP in the summary tables, as this is a value more commonly reported in heterodyne detection. Further information on the relationship between both parameters can be found in the last chapter of[21].

2.2.2.1 Electronic mixers

a Schottky diodes

Schottky diodes are the preferred option nowadays for heterodyne detection in the THz range. Although they have the same limitations associated

to the bandwidth than if used as multipliers, they are able to work up to high frequencies (up to 5 THz) with very good conversion losses (below 9 dB for 500 GHz)[77] One of the most popular Schottky structures for mixers is the honeycomb design[21].

There are basically three parameters that can be tuned in a Schottky diode to optimize its behavior as mixer: doping density of the epitaxial layer, thickness of the epitaxial layer and area of the anode[21]. A careful design of these parameters has to be accomplished to obtain a tradeoff between hot-electron noise, series resistance and shunt capacitance.

Regarding the DSB temperature noise (more details on DSB temperature noise can be found on Bründermann[21]), they provide with good values, from 400 K at 100 GHz to 15000 K at 900 GHz[77], but worse than other mixers such as HEB or SIS mixers[21]. To the contrary of these mixers, cooling effect in Schottky mixers in not very significant (up to 30%) mainly due to the doping values[21].

The two advantages of Schottky mixers over other electronic THz mixers is their room temperature operation and high IF bandwidth[169] (Table VII36).

Parameter	Schottky mixers (CW operation)
Frequency range (THz)	Up to 5 THz[21,167]
Coherent/Incoherent	Coherent[21]
Minimum size (range)	Planar, antenna coupled[21]
Frequency bandwidth (Hz)	Up to 120 GHz[168]
Conversion losses (dB)	<9 dB below 500 GHz[77]
Noise temperature	Around 1000 K at 600 GHz. Around 80000 K at 5 THz[21,77]
Cooling	RT, but cooling can improve performance up to 30%[21]

Table VII36 Performance summary of CW THz heterodyne detection based on Schottky diodes

b *Plasmonic Field-effect Transistors (FET)*

The general description of the available FET detectors in the THz range, both resonant and non-resonant, was presented in section 2.2.2.1. Some of these FET detectors have been successfully used for heterodyne detection, especially non-resonant ones[134,166].

FETs are currently becoming a prolific research field, given their room temperature operation and potential NEP values (although they are worse than Schottky mixers yet). Also the mixing capabilities are a very interesting feature of these devices, especially in the range below 600 GHz (Table VII37).

Parameter	Schottky mixers (CW operation)
Frequency range (THz)	Up to 650 GHz[166]
Coherent/Incoherent	Coherent[134,165]
Minimum size (range)	Planar, antenna coupled[134,165]
Frequency bandwidth (Hz)	<20 GHz estimated[134,165], 24 MHz demonstrated[166]
Conversion losses (dB)	Theoretical about 35 dB at 600 GHz, demonstrated 63 dB[166]
Noise temperature	Theoretical limit about 880 K (with 10 μW LO)[165]
Cooling	RT, but can operate with cryogenic cooling to plasmonic effect enhancement[165]

Table VII37 Performance summary of CW THz heterodyne detection based on Schottky diodes

c *Superconductor-Insulator-Superconductor (SIS)*

SIS mixers were the first practical mixers for the THz region, and they appear, leaded by the radioastronomy application, in late 1970´s[315]. A SIS mixer consists of two layers of superconductor material with a thin insulator film between them (in the order of 20 Å. The usually employed superconductor is Nb for mixers up to 0.7 THz and NbTiN for frequencies up to 1.3 THz

They provide with high bandwidth, in the order of several GHz, and noise temperature about 10-100 times better than Schottky diodes. As a drawback, they need to be cryogenically cooled down to 4 K, what has limited them basically to radioastronomy applications[167] (Table VII38).

Parameter	SIS
Frequency range (THz)	Up to 1.4THz[21,169]
Coherent/Incoherent	Coherent[21]
Minimum size (range)	Planar, antenna coupled[21]
Frequency bandwidth (Hz)	4-8 GHz[21]
Conversion losses (dB)	~13 dB at 1 THz[21,77]
Noise temperature	<100 K at 600 GHz[21,167] 260 K at 1 THz[316]
Cooling	Cryogenic cooling at 4.2 K[21,167]

Table VII38 Performance summary of CW THz heterodyne detection based on SIS mixers

d Hot Electron Bolometers (HEB)

HEBs are thermal detectors tan can be used as mixers. As any thermal detector, they have a limited response time. HEBs have to be cryogenically cooled in order to increase their bandwidth at least to IF frequencies of a few GHz. However, they are not able to provide as high bandwidth as other electronic mixers.

They can be used up to approximately 5.2 THz. They have slightly worse noise temperature than SIS in the band where both operate, but much better than Schottky diodes. Their main advantage is that the needed LO power for optimum operation is very small, in the order of 1 μW.

In radioastronomy applications, they are the most widely used mixer above 1.3 THz[21] (Table VII39).

Parameter	HEB
Frequency range (THz)	Up to 5.2THz[21,167]
Coherent/Incoherent	Coherent[21]
Minimum size (range)	Planar, antenna coupled[21,167]
Frequency bandwidth (Hz)	2-4 GHz[21,167]
Conversion losses (dB)	~1 dB at 1 THz[170]
Noise temperature	400 K at 600 GHz. 3800 K at 5.2 THz[21]
Cooling	Cryogenic cooling at few K[21,167]

Table VII39 Performance summary of CW THz heterodyne detection based on HEB mixers

2.2.2.2 Electro-optical mixers

a Electro-Optical sampling (EOS) with crystals

Heterodyne detection of CW signals using EOS is not a wide spread technique for EO CW THz mixing, as its main field of application is in pulsed TDS schemes.

However some experiments have been reported for EO heterodyne detection using this technique[56]. The figures of merit of a receiver/mixer, such as NEP or noise temperature are not provided. A comparison with PCs is available in the literature, and the results suggest that this technique achieves much lower dynamic range than mixing with PCs[56] (Table VII40).

Parameter	EOS with crystals (CW operation)
Frequency range (THz)	N/A
Coherent/Incoherent	Coherent[56]
Minimum size (range)	Cm range[56]
Frequency bandwidth (Hz)	N/A
Conversion losses (dB)	N/A
Noise temperature	N/A
Cooling	RT[56]

Table VII40 Performance summary of CW THz heterodyne detection based on EOS with crystals

b Photoconductors

Among the limited number of work on EO THz heterodyne detection nowadays, PCs are the most usually employed devices. They have been used for heterodyne detection demonstrating coherent capabilities[138], and also in metrology applications with OFCGs[55–57,59,60] (Table VII41).

Parameter	PC (CW operation)
Frequency range (THz)	Demonstrated up to 100 GHz[55–57,59,60,138]
Coherent/Incoherent	Coherent[138]
Minimum size (range)	Planar, antenna coupled[138]
Frequency bandwidth (Hz)	Around 830 MHz[138]
Conversion losses (dB)	N/A
Noise temperature	N/A
Cooling	RT[138]

Table VII41 Performance summary of CW THz heterodyne detection based on PCs

Up to now, they have been demonstrated in THz heterodyne receivers with M signals in the order of 100 GHz[55–57,59,60,138]. The IF signal with higher frequency reported is around 850 MHz[138]. Besides this, higher M frequencies should be readily achievable at the expense of higher conversion losses, and also higher IF frequencies should be achieved by proper IF output design (bias-Tee, coaxial IF output).

The use of PDs under heterodyne schemes with M signals in the THz region was firstly reported in 2010, using a UTC-PD in a homodyne receiver up to 420 GHz[164]. After that, extensive work of another group on this topic has been also reported, in this case using a TW-UTC-PD[171,172] in heterodyne detection at 100 GHz with IF signals in the order of 50 kHz.

In this thesis, the first results of heterodyne detection of a new THz detector are presented. This detector is based in a new concept especially designed for homodyne/heterodyne detection: the np-i-pn quasi-ballistic THz detector. Heterodyne detection with 110 GHz M signals and 1 MHz IF signals has been obtained (Table VII42).

Parameter	PD (CW operation)
Frequency range (THz)	Demonstrated up to 420 GHz (homodyne detection)[164], and 110 GHz (heterodyne detection)
Coherent/Incoherent	Coherent[211]
Minimum size (range)	Planar, antenna coupled[138]
NEP (W/(Hz)$^{1/2}$))	NA, estimated NEP ≤ $4.7 \cdot 10^{-8}$ [164,172]
Frequency bandwidth (Hz)	Around 1 MHz (Chapter 3)
Conversion losses (dB)	32 dB[172]
Noise temperature	N/A
Cooling	RT[211]

Table VII42 Performance summary of CW THz heterodyne detection based on PDs

Appendix III

On the basics of nonlinear optics

1

Appendix III. On the basics of nonlinear optics

In this appendix we are going to discuss the origin of nonlinear effects in crystals and optical fibers as a theoretical background for the discussion on nonlinear effects for OFCG expansion techniques presented in chapter II. Let us start this discussion with the well known set of Maxwell equations defined below[4,230,231,317], assuming the absence of extraneous charges and currents as we are focusing on dielectrics[231].

$$\nabla \times \mathbf{E} = -\frac{1}{c}\frac{\partial \mathbf{B}}{\partial t} \tag{56}$$

$$\nabla \times \mathbf{B} = \frac{1}{c}\frac{\partial \mathbf{D}}{\partial t} \tag{57}$$

$$\nabla \cdot \mathbf{D} = 0 \tag{58}$$

$$\nabla \cdot \mathbf{B} = 0 \tag{59}$$

Where the electric displacement field ***D*** is defined as follows[317]:

$$\mathbf{D} = \varepsilon_0 \mathbf{E} + 4\pi \mathbf{P} = \varepsilon \mathbf{E} \tag{60}$$

being ***E*** is the electric field, ***P*** the polarization field and ε is the electric permittivity. A general definition of the polarization field ***P*** is given by (61), where χ.is the electrical susceptibility tensor.

$$\mathbf{P} = \chi \mathbf{E} \tag{61}$$

However, when an EM field with sufficiently high amplitude is considered, the bound electrons present an anharmonic motion, and the polarization field ***P*** is no longer linear with the electric field ***E***[318]**.** In this case, if small variations in ***P*** are assumed, the Taylor expansion gives an equation for ***P*** that includes a linear ($\boldsymbol{P}_L$) and a nonlinear term ($\boldsymbol{P}_{NL}$)[317].

$$\mathbf{P} = \mathbf{P}_L + \mathbf{P}_{NL} \tag{62}$$

$$\mathbf{P}_L = \int \chi^{(1)}\left(t - t'\right)\mathbf{E}\left(t'\right)dt' \tag{63}$$

$$\begin{aligned}\mathbf{P}_{NL} &= \int \chi^{(2)}\left(t - t_1, t - t_2\right) : \mathbf{E}\left(t_1\right)\mathbf{E}\left(t_2\right)dt_1 dt_2 + \\ &+ \int \chi^{(3)}\left(t - t_1, t - t_2, t - t_3\right) \vdots \mathbf{E}\left(t_1\right)\mathbf{E}\left(t_2\right)\mathbf{E}\left(t_3\right)dt_1 dt_2 dt_3 + \ldots\end{aligned} \tag{64}$$

The linear term (63) is given by the first order susceptibility $\chi^{(1)}$, while the nonlinear term (64) is related to the second ($\chi^{(2)}$), third ($\chi^{(3)}$) and higher orders of electric susceptibility. Although orders higher than three can be experimentally found[231], they are related to very specific applications, and most nonlinearities can be included in either second ($\chi^{(2)}$) or third order ($\chi^{(3)}$) susceptibilities.

As we are considering an optical field with different frequency components, we can define the electric field ***E*** as a sum of monochromatic waves:

$$\mathbf{E} = \sum_i \mathbf{E}_i \exp\left(i\mathbf{k}_i\mathbf{r} - 2\pi f_i t\right) + c.c. \tag{65}$$

And taking the Fourier transform of equations (63) and (64), the polarization field ***P*** as a function of frequency can be written according to the following equations:

$$\mathbf{P}_L\left(f\right) = \chi^{(1)}\left(f_i\right)\mathbf{E}\left(f_i\right) \tag{66}$$

$$\begin{aligned}\mathbf{P}_{NL}\left(f\right) &= \chi^{(2)}\left(f; f_i, f_j\right) : \mathbf{E}\left(f_i\right)\mathbf{E}\left(f_j\right) + \\ &+ \chi^{3}\left(f; f_i, f_j, f_k\right) \vdots \mathbf{E}\left(f_i\right)\mathbf{E}\left(f_j\right)\mathbf{E}\left(f_k\right) + \ldots\end{aligned} \tag{67}$$

where $f_{i,j,k}$ are the input frequency components to the nonlinear medium and f is the sum of the frequency components associated to the susceptibility tensor $\chi^{(n)}$ (i.e. $f = f_i + f_j$ for $\chi^{(2)}$, and $f = f_i + f_j + f_k$ for $\chi^{(3)}$). This frequency component f is the new generated frequency due to the nonlinear process, as the polarization vector $\boldsymbol{P}$ is the source of the electric field $\boldsymbol{E}$ according to the non-linear wave equation (68), which is derived from the propagation of light waves under certain assumptions using the Maxwell equations[231].

$$\nabla\times\left(\nabla\times\mathbf{E}\right)-\frac{1}{c^2}\frac{\partial^2\mathbf{E}}{\partial t^2}=\frac{4\pi}{c^2}\left(\frac{\partial^2\mathbf{P}_L}{\partial t^2}+\frac{\partial^2\mathbf{P}_{NL}}{\partial t^2}\right) \tag{68}$$

Depending on the value of these frequencies, the nonlinear processes associated to second and third order can be classified in several groups that can be found elsewhere (chapter II).

The explanation above gives answer to how new frequencies are generated due to non-linear processes. Furthermore, it is demonstrated how after some calculations[317,318], the effective refractive index n of the nonlinear media has a term that is proportional to the product of the second order susceptibility and the electric field ($\propto \boldsymbol{E}\cdot\chi^{(2)}$); and also a term proportional to the product of the third order susceptibility and the squared electric field ($\propto \boldsymbol{E}^2\cdot\chi^{(3)}$).

From equation (60), the electric permittivity ε can be obtained from:

$$\varepsilon=\frac{\varepsilon_0\mathbf{E}+4\pi\mathbf{P}}{\mathbf{E}} \tag{69}$$

where $\boldsymbol{P}$ is given by equation (62). The dielectric permittivity ε can be expressed as a function of its real and imaginary parts. The real part is associated to the refraction index n, while the imaginary part is related to the absorption index α, according to equation (70):

$$\varepsilon=\left(n+i\alpha c/2\omega\right)^2 \tag{70}$$

From (69) and (70), the refraction index can be expressed as a function of the different electrical susceptibilities·$\chi^{(n)}$. The term related to the second order susceptibility $\chi^{(2)}$ is given by the Pockels effect (linear EO effect), and it is proportional to the electric field $\boldsymbol{E}$ passing through the nonlinear medium. The term related to the third order susceptibility $\chi^{(3)}$ originates from the Kerr effect (quadratic EO effect) and it is proportional to the squared electric field $\boldsymbol{E}^2$ (see Figure 78). In equation (71) the refraction index n is represented as a function of the EO coefficients, associated to $\chi^{(2)}$ (Pockels) and $\chi^{(3)}$ (Kerr) effects.

$$n(\mathbf{E}) = n - \frac{1}{2}k_{Pockels}n^3\mathbf{E} - \frac{1}{2}k_{Kerr}n^3\mathbf{E}^2 \qquad (71)$$

The two last terms on (71) are the nonlinear refraction index terms, which usually are encompassed in the n_2 term, called nonlinear refractive index. The Pockels effect occurs basically in crystals, while the Kerr effect appears in optical fiber (silica).

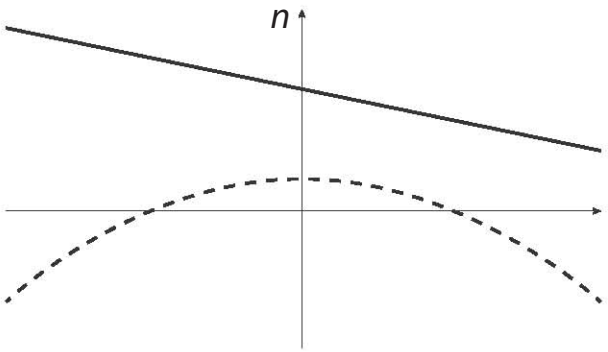

Figure 78 Refraction index n as a function of the electric field $\boldsymbol{E}$. Solid line: Pockels effect (linear EO effect, associated to second order susceptibility $\chi^{(2)}$); dashed line: Kerr effect (quadratic EO effect, associated to third order susceptibility $\chi^{(3)}$)

Appendix IV

Phase Noise measurement

1

Appendix IV. Phase Noise measurement

1.1 Introduction

In this appendix, the basics of the phase noise and its measurement will be summarized, trying to synthetize the information of several sources along with some aspects of the know-how phase noise measurement acquired during this work.

First of all, a theoretical description of both phase and amplitude noises will be presented. This will show that the measurement of the phase noise independently of the amplitude noise is not trivial. After that, the main schemes for phase noise measurement will be described. Finally, further details on the phase noise measurement in specific devices, like amplifiers or mixers will be briefly discussed.

1.2 Noise in the frequency domain

To begin our analysis, the theoretical description of a monochromatic signal modulated in phase and amplitude is described. The contents of this section are basically a summary of part of a very comprehensive work about phase noise measurement techniques in lasers by Scott et al[319]. The concepts of the noise spectral densities and noise-to-carrier power ratio are also defined.

1.2.1 Theoretical description of the modulated signal

The expression for a double-sideband large-carrier AM current signal with carrier power P_c in a 1-Ω system is:

$$\begin{aligned} i_{AM}(t) &= \sqrt{2P_c}\left[1+m\cos\left(\omega_m t\right)\right]\cos\left(\omega_0 t\right) \\ &= \sqrt{2P_c}\,\mathrm{Re}\left\{e^{i\omega_0 t}+\frac{m}{2}\left(e^{i(\omega_0+\omega_m)t}+e^{i(\omega_0-\omega_m)t}\right)\right\} \\ &= \sqrt{2P_c}\,\mathrm{Re}\left\{e^{i\omega_0 t}\left[1+\frac{m}{2}\left(e^{i\omega_m t}+e^{-i\omega_m t}\right)\right]\right\} \end{aligned} \tag{72}$$

Where m is the modulation index, ω_0 the carrier frequency and ω_m the modulation frequency.

In the same system, a PM modulated signal can be expressed as follows:

$$\begin{aligned} i_{PM}(t) &= \sqrt{2P_c}\cos\left[\omega_0 t+\beta\sin\left(\omega_m t\right)\right] \\ &= \sqrt{2P_c}\,\mathrm{Re}\left\{e^{i\omega_0 t}e^{i\beta\sin(\omega_m t)}\right\} \\ &= \sqrt{2P_c}\,\mathrm{Re}\left\{e^{i\omega_0 t}\sum_{n=-\infty}^{\infty}J_n\left(\beta\right)e^{in\omega_m t}\right\} \end{aligned} \tag{73}$$

Being J_n Bessel functions of the first order and β the peak phase deviation or phase modulation index. When the small modulation index approximation is taken ($\beta << 1$), the Bessel functions are simplified according to:

$$J_n\left(\beta\right)\approx\begin{cases}1;n=0\\ \pm\beta/2;n=\pm1\\ 0;\left|n\right|>1\end{cases} \tag{74}$$

and then the equation (73) can be expressed by the following equation:

$$i_{PM}(t) \approx \sqrt{2P_c}\,\mathrm{Re}\left\{e^{i\omega_0 t} + \frac{\beta}{2}\left(e^{i(\omega_0+\omega_m)t} - e^{i(\omega_0-\omega_m)t}\right)\right\}$$
$$= \sqrt{2P_c}\,\mathrm{Re}\left\{e^{i\omega_0 t}\left[1 + \frac{\beta}{2}\left(e^{i\omega_m t} - e^{-i\omega_m t}\right)\right]\right\} \quad (75)$$

1.2.2 Single Sideband and Double Sideband Signal

It is interesting to obtain an expression for the Single Sideband (SSB) modulated signal in order to clearly identify spectral noise components. A SSB modulated signal (Figure 79) is composed of the carrier power component P_c at the carrier frequency ω_0, and a noise power component P_n at frequency $\omega_0 + \omega_m$ that we will take as a noise power component. Only the noise at the upper band SSB is considered here:

$$i(t) = \mathrm{Re}\left\{e^{i\omega_0 t}\left(\sqrt{2P_c} + \sqrt{2P_n}e^{i\omega_m t}\right)\right\} \quad (76)$$

The SSB noise component can be expanded to analyze the contribution of each kind of modulation:

$$\sqrt{2P_n}e^{i\omega_m t} = \sqrt{2P_n}\left(\cos\omega_m t + i\sin\omega_m t\right)$$
$$= \sqrt{\frac{P_n}{2}}\left[\underbrace{\left(e^{i\omega_m t} + e^{-i\omega_m t}\right)}_{AM} + \underbrace{\left(e^{i\omega_m t} - e^{-i\omega_m t}\right)}_{PM}\right] \quad (77)$$

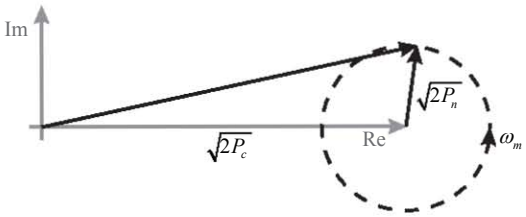

Figure 79 Carrier and SSB noise phasors

Comparing the expressions of a AM and PM modulated signal (equations (72) and (75)) to those in (77), the terms associated to each modulation are identified. The AM component is in phase with the carrier while the PM component is in quadrature. The terms at the lower band cancel out while those

at the upper band remain (see (77)). In this case, the contribution of AM and PM components is identical.

Nevertheless, the contribution of the AM and PM noise in an actual carrier is not equal as it could be thought by the above SSB signal analysis. This is because the other sideband (in this case the lower sideband), has some effect at the same offset frequency. Both lower and upper SSB are oscillating at $\pm\omega_m$ respectively, but they have some phase offset ψ. When both sidebands are taken into account (i.e. the entire modulated signal with both upper and lower noise bands), this phase offset determines if the superposition gives pure AM, pure PM or a mix of both modulations. The double sideband signal (DSB, the entire modulated signal) is given then by (78).

$$\begin{aligned} i_{DSB}(t) &= \sqrt{2P_n}\left[e^{i\left[(\omega_0+\omega_m)t+\psi\right]} + e^{i(\omega_0-\omega_m)t}\right] \\ &= \sqrt{2P_n}\left[\cos(\omega_0 t+\psi/2)\cos(\omega_m t+\psi/2)\right. \\ &\left.+i\sin(\omega_0 t+\psi/2)\cos(\omega_m t+\psi/2)\right] \\ &= 2\sqrt{2P_n}\cos(\omega_m t+\psi/2)e^{i(\omega_0 t+\psi/2)} \end{aligned} \tag{78}$$

This DSB signal, (78), has an amplitude phasor coefficient stationary around the carrier frequency ω_0 and oscillates in magnitude at the offset frequency ω_m. It must be noted that the phase angle ψ determines the amount of amplitude and phase noise contribution to the mixed signal.

1.2.3 Phase and amplitude Noise

In order to measure the phase and amplitude noise, one of the usual schemes is to downconvert the signal to baseband in order to analyze it using an Electrical Spectrum Analyzer (ESA). In this case, the RF signal is mixing with a local oscillator (LO). If a controlled phase shift θ is introduced to the LO signal, the contribution of AM-FM noise can be separated. The intermediate frequency (IF) signal follows the expression:

$$\begin{aligned} i_{IF}(t) &= i_{RF}(t)\,i_{LO}(t) \\ &= \sqrt{2P_{LO}}\cos(\omega_0 t+\theta)\left[\sqrt{2P_C}\cos\omega_0 t\right. \\ &\left.+2\sqrt{P_n}\cos(\omega_m t+\psi/2)\cos(\omega_0 t+\psi/2)\right] \end{aligned} \tag{79}$$

which after low pass filtering can be expressed as:

$$i_{IF}(t) = \sqrt{P_{LO}P_c}\cos\theta + 2\sqrt{P_{LO}P_n}\cos(\omega_m t + \psi/2) \times \left[\underbrace{\cos\theta\cos(\psi/2)}_{AM} + \underbrace{\sin\theta\sin(\psi/2)}_{PM}\right] \quad (80)$$

As the AM noise component is in phase, it can be identify with the first term between graves in (80); while the quadrature term gives the PM noise component. If the LO phase can be adjusted and set to $\theta = \pi/2$, only PM noise component remains. It is important to note that the DC term also depends on the phase offset between RF and LO, and is zero for $\pi/2$, so it is usually used for stabilization of this phase offset in PM noise measurements to have only PM noise contribution in the measurement. Alternatively, when $\theta = 0$, only AM noise is present in the measured signal.

The analysis presented in this section is very important as it demonstrates that the AM and PM noise components can be isolated from each other for its measurement when a downconversion scheme with controlled phase offset is used.

1.2.4 SSB Noise-to-carrier Power Ratio

The discussion above establishes the theoretical background for a proper understanding of the AM and PM noise of a signal. In this section, the definitions of the phase noise of a signal for an actual measurement are presented.

The expression below describes a general current signal with both amplitude ($\varepsilon(t)$) and phase fluctuations ($\phi(t)$)[320]. This is equivalent to a signal amplitude and phase noise modulation given by equations (72) and (73), respectively:

$$i(t) = \left[I_0 + \varepsilon(t)\right]\sin\left[\omega_0 t + \phi(t)\right] \quad (81)$$

The basic tool to describe the of phase noise is the spectral density of phase fluctuations $S_\phi(f_m)$.

$$S_\phi(f_m)\left[\frac{rad^2}{Hz}\right] = \frac{\Delta\phi_{RMS}{}^2(f_m)}{BW}$$
$$S_\phi(f_m)\left[\frac{dBr}{Hz}\right] = 20\log\frac{\Delta\phi[rad]}{1[rad]} \quad (82)$$

Where $\Delta\phi_{RMS}^{2}(f_m)$ is the RMS power of the phase fluctuations $\phi(t)$ measured at the offset frequency from the carrier f_m, and BW is the measurement bandwidth.

Nevertheless, the magnitude that is usually measured is the so-called SSB noise-to-carrier power ratio ($\mathscr{L}(f_m)$).

$$\mathscr{L}(f_m)\left[\frac{W}{W}\right] = \frac{P_{SSB}}{P_c}$$
$$\mathscr{L}(f_m)\left[\frac{dBc}{Hz}\right] = P_{SSB}[dB] - P_c[dB] \tag{83}$$

$\mathscr{L}(f_m)$, normally expressed in *dBc/Hz*, represents half the spectral density of phase fluctuations $S_\phi(f_m)$ (84) only when the phase fluctuations are small enough ($\phi(t) << 1\ rad$) to assume the linear approximation of the Bessel function (74).

$$\mathscr{L}(f_m)\left[\frac{dBc}{Hz}\right] = S_\phi(f_m)\left[\frac{dBr}{Hz}\right] - 3\,dB \tag{84}$$

However, in order to normalize the usage of this definition, IEEE has defined $\mathscr{L}(f_m)$, according to (84) even when the small modulation restriction is not fulfilled[319,321].

The frequency stability of a signal is caused by the contribution of causal and random effects[320]. The causal components comprise long term effects given by frequency drifts and short term effects basically given by spurious signals. The random components are short term effects that are determined by the phase noise.

Nevertheless, usually the phase noise is the most significant component of the frequency stability, and they can be directly related according to (85)[320].

$$S_{\Delta f}(f_m) = f_m^{\,2} \cdot S_\phi(f_m) \tag{85}$$

where both spectral densities are in natural units.

1.3 Phase noise measurement

1.3.1 Measurement schemes

There are five basic schemes to measure the phase noise of a signal [320,322]:

- Spectrum analyzer measurement
- Use of delay line discriminator
- Quadrature technique
- Use of FM discriminator
- Direct digital measurement

In this part, a brief description of each one will be made. Furthermore, several tables providing a clear and comprehensive comparison of all the methods can be found in [322].

1.3.1.1 Spectrum analyzer measurement

This is the most direct and extended scheme for phase noise measurement. The RF signal to analyze (Source Under Test, SUT) is simply introduced in an ESA, where the signal is internally downconverted and its power spectrum is plotted as a function of the frequency. The phase noise is extracted by means of applications working with the device to compute on-line the phase noise or by off-line algorithms.

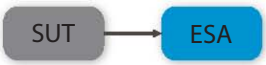

Figure 80 Spectrum analyzer measurement of phase noise

1.3.1.2 Use of delay line discriminator

The delay line discriminator demodulates SUT, giving an output signal proportional to the FM noise. This FM noise can be related with the PM (phase) noise.

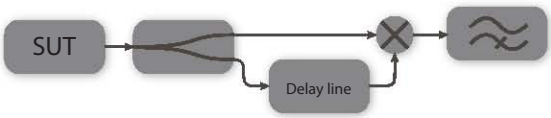

Figure 81 Delay line discriminator method

The RF signal is split into two branches to implement a FM receiver. One of the branches is delayed and then both are mixed in a double balanced mixer. The output from the mixer is a DC voltage that it is a function of the phase difference between both signals. RF amplification is usually needed to drive the mixer as a linear phase detector.

1.3.1.3 Quadrature technique

In the quadrature technique, the signal to be measured is mixed with a reference source (with a phase noise much lower of that of the signal). The resulting IF signal is measured again using an ESA. It is very common to implement a closed loop to phase-lock the signals in quadrature and measure only phase noise (see 4.2.3).

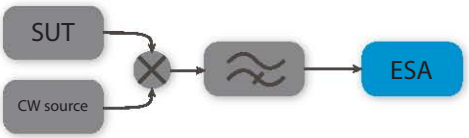

Figure 82 Quadrature technique

1.3.1.4 Use of FM discriminator

This method is similar to the previous one, but the resulting IF signal is not directly measured but passed through a FM discriminator where it is demodulated.

Figure 83 FM discriminator method

The FM discriminator design determines the performance of this technique. In this method, the FM noise is measured, so a conversion between FM and PM noise is required as in method *a*.

1.3.1.5 Direct digital measurement

The direct digital measurement is a direct method where the signal is digitized in a computer or FPGA where is analyzed using Fourier transform algorithms. The analog to digital conversion limits the bandwidth in a severe way. For this reason, this method is only used with very low frequencies signals, where it performs a very low cost solution; or combined with the quadrature

technique to extend the bandwidth of the signal that can be measured, where the performance of this method grows dramatically.

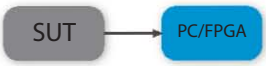

Figure 84 Direct digital measurement

1.3.1.6 Comparison tables

In Feher[320] and Owen[322], all this methods are compared from several points of view, namely, by application, overall performance, speed, ease of calibration, what they measure, performance limitations, reference oscillator requirement and other complications.

It is especially interesting to find in these tables that the ESA direct measurement, although is the most widely extended method, has severe limitations for some kind of applications, like very low phase noise signals, unstable sources or low frequency offsets. Moreover, its overall performance is amongst the worst of the comparison. Thus, the signal to be measured and application must be analyzed prior measurement to determine if the ESA direct method would be enough, or more complex phase noise measurement schemes are needed.

1.3.2 Phase noise sources

Noise sources can be categorized in several ways. In a first step, they can be divided based on how they contribute to the overall phase noise into parametric (multiplicative) and additive sources, as it is depicted in Figure 85.

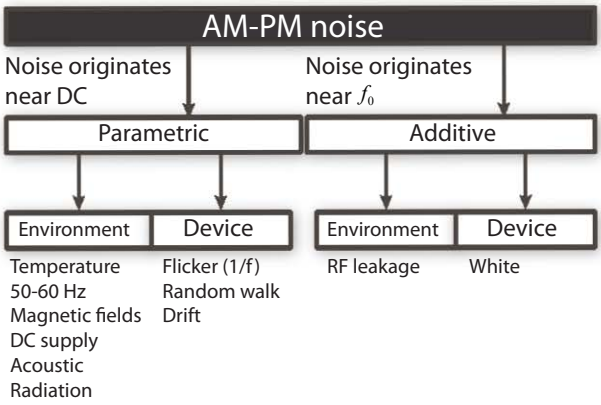

Figure 85 Classification of phase and frequency noise. Adapted from Boudot *et al.*[323]

A noise source contributes as a function of $f_m^{-\alpha}$, where f_m is the frequency offset and $-\alpha$ an exponential factor describing the slope (in dB/decade) of the frequency dependence of the noise. Thus, the SSB noise $S_\phi(f_m)$ can be written as a function of these terms, (86).

$$S_\phi(f_m) \approx \sum_{\alpha=0}^{n} b_\alpha f_m^{-\alpha} = b_0 + b_1 f_m^{-1} + b_2 f_m^{-2} + b_3 f_m^{-3} + \ldots \quad (86)$$

Being b_α weighting parameters associate to each slope (α) term. When $\alpha = 0$, the noise is additive as phase noise and when $\alpha = 2$ is additive as frequency noise, given the relation between phase and frequency noise (85). This way, the noise source is considered multiplicative in phase noise for $\alpha > 1$, and for $\alpha > 3$ in frequency noise[322,324] (see Figure 86). Moreover, the value of α allows to estimate the nature of the noise source, i.e. Flicker, random walk…[324–326].

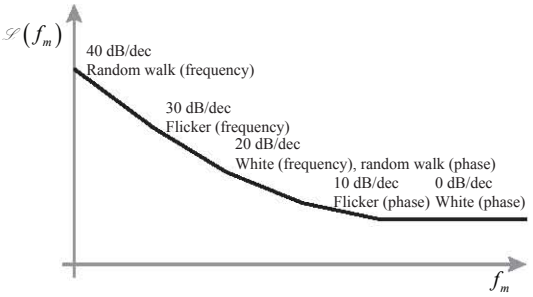

Figure 86 Classification of phase and frequency noise sources from the slopes of $\mathscr{L}(f_m)$

The effect of both additive and parametric noise in the total phase noise $\mathscr{L}(f_m)$ (or alternatively $S_\phi(f_m)$) given by (86) can be seen in Figure 87. The parametric noise effect is especially critical near the carrier (f_1 in Figure 87) and the most significant effect is the masking of both desired signals near the carrier and Intermediate Frequency (IF) signals when downconverting. It increases the corner frequency between white and Flicker (or higher order) noise. The multiplicative noise has its origin at baseband, and is up-converted around the carrier in most two-port devices such as amplifiers, mixers, multipliers, dividers, filters phase-locked-loop synthesizers[327]. In the case of oscillators, this noise is strongly dependent on the Q factor associated to the oscillator[120,328].

The additive noise sources can also affect signals by masking at any frequency offset (Figure 87). In this case, the total white noise has to be high and/or the signal power (f_2) very low to appear as a significant effect.

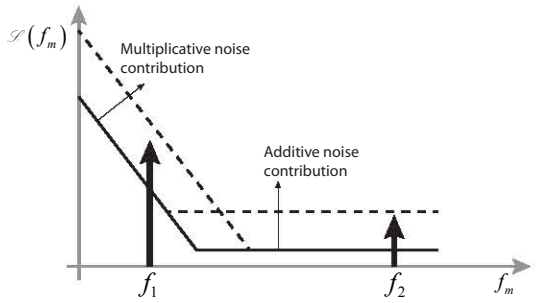

Figure 87 Effect on the phase noise spectrum of additive and multiplicative noise sources

Usually the measurements of phase noise will cover until a frequency offset where the phase noise becomes white (i.e. $\alpha = 0$).

1.3.3 Phase noise measurement in specific devices

1.3.3.1 Phase noise in RF amplifiers

The phase noise at the output of an amplifier can be approximated by a model containing just white and flicker terms (i.e. $\alpha = 0$ and $\alpha = 1$, respectively)[323,329]. This model is described by (87):

$$S_{\phi AMP}(f_m) = b_0 + \frac{b_{-1}}{f_m} \tag{87}$$

where b_0 is the component associated to white noise and b_{-1} that related to Flicker noise. Usually, the white noise component is associated to the introduced Noise Figure (NF), which is the degradation in Signal to Noise Ratio (SNR) at the output of the device for a given input.

The parameter b_0 depends on three parameters: NF, thermal noise (kT_0) and input power (P_0); according to (88).

$$b_0 = \frac{NFkT_0}{P_0} \tag{88}$$

On the other hand, b_{-1} is a constant to be determined for each device:

$$b_{-1} = C \tag{89}$$

It is important to highlight that under small signal operation, the phase noise addition is mainly given just by the white noise term (90)[330]. In large signal regime, not only the Flicker term becomes significant, but also the NF can increase and stop being a constant value[323]. Nevertheless, the small signal regime is the common assumption when computing the phase noise addition of an amplifier.

$$S_{\phi AMP}\left(f_m\right) \approx b_0 = \frac{FkT_0}{P_0} \tag{90}$$

The relation between thermal noise and input power in (90) is the Signal to Noise Ratio (SNR) at the input of the amplifier. It can be seen that the phase noise addition of the amplifier is directly given by an increment (in dB) of the white noise by the NF value.

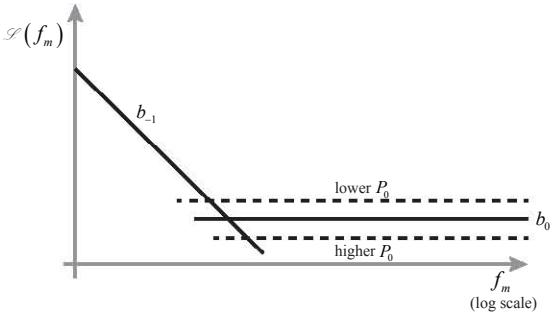

Figure 88 $\mathscr{L}(f_m)$ of a single amplifier

Furthermore, it is interesting to analyze the case where several amplifiers are set in cascade or parallel configuration.

When several (m) amplifiers are in cascade, the NF of b_0 (88) is given by the Friis equation for the NF[323]:

$$F = F_1 + \sum_{n=2}^{m} \frac{F_n}{\prod_{n'=1}^{n-1} G_{n'}{}^2} \tag{91}$$

where G is the gain of the n amplifier.

The Flicker term is just the sum of all the Flicker terms of the cascaded amplifiers[323]:

$$b_{-1} = \sum_{n=1}^{m} b_{-1n} \tag{92}$$

For the general case of small signal, the white noise is almost the same, while for large signal conditions the Flicker term of all the amplifiers sum up, as it is described in Figure 89.

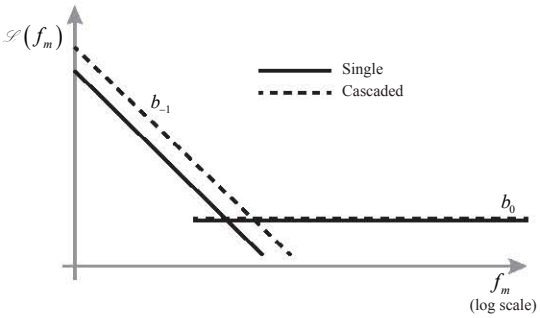

Figure 89 $\mathscr{L}(f_m)$ of several cascaded amplifiers. Comparison with single amplifier case

Another scheme, which is basically found only in audio applications, is that of m amplifiers in parallel. In this case, the white noise term remains the same as in the case of one amplifier, while the Flicker term decreases by a factor of m according to (93)[323]:

$$b_{-1} = \frac{1}{m} b_{-1n} \tag{93}$$

This is a very important result especially for low frequency applications, where the white noise can be maintained at the same level while reducing the Flicker noise. The effect is illustrated in Figure 90.

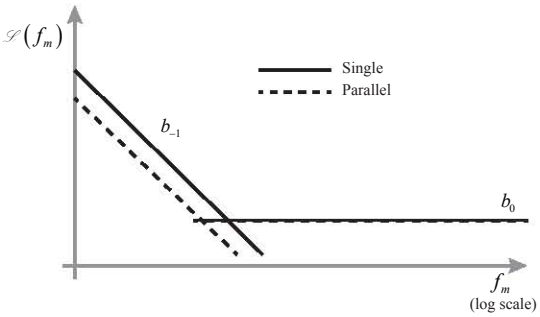

Figure 90 $\mathscr{L}(f_m)$ of several amplifiers in parallel. Comparison with single amplifier case

1.3.3.2 Phase noise in RF mixers

The mixing process is a nonlinear process. This requires that most of mixer devices have to be driven in large signal or non-linear states to perform the mixing. For that reason, as opposite to the amplifier case, the Flicker term of the phase noise must be always taken into account[264].

In this work, it has been assumed a simplified phase noise model for a mixer similar to that described in (87) for the amplifier. Nevertheless, it is very common in the literature to provide information of the noise of a mixer just in terms of its NF, thus just in terms of the white noise of the phase noise. Although this makes sense because the NF becomes variable under large signal and non-linear regime of the device[330], and it can estimate the contribution to the phase noise under non-linear regime, the author of this document maintains that a detailed analysis must include all terms of the phase noise and not just the white noise term, described by the NF. This is because, as stated in Figure 86, the slope of the phase noise can provide us with valuable information about the noise source of a device.

1.3.3.3 Phase noise in RF multipliers and dividers

As any other two-port device, a frequency multiplier or divider can contribute to the phase noise with both additive and multiplicative noise, as it has been described for both amplifiers and mixers. However, a general rule that always apply for all multipliers and dividers is that the additive (white) noise increases in the case of the multipliers and decreases in the case of dividers.

Being N the harmonic (for multiplication) or the sub-harmonic (for dividers), the contribution to the overall phase noise is a factor N for the multiplicative devices and a factor $1/N$ for the dividers (in natural units)[331,332]. In logarithmic scale, the contribution of a multiplier is given by (94).

$$20\log(N) \tag{94}$$

This result is especially relevant for our work, as it allows us to know how the all-electronic techniques for THz generation based on multipliers chains significantly degrade the phase noise, what is not the case with the DFG photonic architecture developed in this thesis work, which directly inherits the phase noise of the reference.

In the case of frequency dividers, the contribution to the phase noise is given by (95).

$$20\log\left(\frac{1}{N}\right) \tag{95}$$

1.4 Phase noise and Timing Jitter

The detailed description of timing jitter and its relationship with the phase noise spectrum have been extensively studied in the literature[120,188,324,326,329,333–339]. In this appendix, only the basic relationship between phase noise and timing jitter is presented.

The timing jitter is the variation of the period or the zero crossings of a signal. As the zero crossings has to be referenced, there exists several definitions of timing jitter[337–339]. Usually, the timing jitter is expressed as absolute timing jitter and cycle-to-cycle (or period) timing jitter. The first one is the sum of the variations of all the periods from the average. The second one is the variance of each period from the average[188], and it is illustrated in Figure 91.

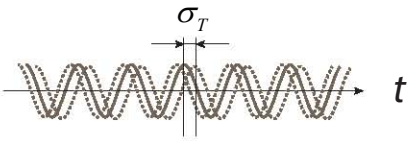

Figure 91 Cycle-to-cycle (period) timing jitter

The cycle-to-cycle timing jitter is usually expressed as the root mean square (RMS) value. In this case, it can be related to the phase noise spectrum as follows[340]:

$$\sigma_T^{RMS} = \frac{1}{2\pi f_c}\sqrt{2\int_0^{\infty} \mathscr{L}(f)df} \tag{96}$$

The RMS cycle-to-cycle jitter is the most commonly used expression for the timing jitter. In order to have reference values and limits for the timing jitter, for some applications and standards[340], the integration limits are defined for a specific frequency range. In this case, the expression for the RMS cycle-to-cycle timing jitter becomes:

$$\sigma_T^{RMS} = \frac{1}{2\pi f_c}\sqrt{2\int_{f_1}^{f_2} \mathscr{S}(f)df} \tag{97}$$

It is important to note that timing jitter is a temporal magnitude, while the SSB noise is a density representation of the phase fluctuations, which in turn are directly related to timing jitter.

Appendix V

UNCERTAINTY

1

Appendix V. Uncertainty

1.1 Introduction

Precision, resolution and accuracy are parameters of a measurement determined basically by the instrument employed and the measurement technique and conditions. These parameters are taken into account in most experiment designs to choose the proper setup or instrumentation, and in subsequent data analysis stages to interpret and understand the measurements. Nevertheless, uncertainty is a parameter sometimes forgotten or avoided, especially on those fields not closely related to metrology.

The objective of this appendix is to explain the importance of the estimation of uncertainties, briefly summarizing its general principles and the estimation process for the two existing categories of uncertainties: Type A and Type B. The full description of the expression and evaluation of uncertainties in measurements is defined in the ISO guide *The Guide to the expression of Uncertainty in Measurement*, also known as GUM[341]. Further reading and comprehensive guides about uncertainty estimation can be found in [341–353]

In order to state the importance of the uncertainty in the experimental measurement process and also to explain more clearly how it is estimated, a practical example related to the work described in this document is presented. Specifically, the estimation of the uncertainty associated to the measurement of an electrical spectrum using an Electrical Spectrum Analyzer (ESA) is developed at the end of this appendix.

1.2 Estimation of uncertainty

1.2.1 Uncertainty, error and tolerance of a measurement

First of all, the differences between uncertainty, error and tolerance must be clarified, as they are often confused.

The objective of a measurement is to determine the value of a measurand. There is no perfect measurement, in the sense that a measurement is always an approximation of the actual value of a measurand. This difference between the measurement and the actual value of the measurand is the measurement error. The measurement errors arise from random processes and/or from systematic sources. Given the random component of the error, it can be within a range from the actual value of the measurand. This range is what is known as the uncertainty of a measurement.

The tolerance of the value of a measurand is the permitted range in which it can lie. It must be noted that in order to be able to ensure that the value is within the tolerance range, the uncertainty associated to its measurement must be much smaller (at least four times smaller[346]). Moreover, when a tolerance is referred to the instrumentation, it can be seen as a component of the uncertainty of the measurement made with it.

1.2.2 Why estimating uncertainty?

There are several reasons for estimating uncertainty and consider it in the measurement processes. Some of them are listed below:

- Regulation and standard. Testing and Calibration laboratories are required to estimate and report the uncertainty associated to their measurements according to ISO/IEC 17025[347].
- Validation and interpretation of the measurement. The knowledge of the uncertainty or at least its consideration should lead to a proper interpretation of the meaning of the data acquired during a measurement, as well as its validity.
- Allow comparison. The availability of the uncertainty values allows checking the validity of different set of measurements done by different laboratories or with different equipment.

1.2.3 Types of errors and sources of uncertainty

The errors can be categorized as random or systematic. The random errors have as source the random distribution of the magnitudes under measurement, thus being statistical fluctuations of the measurements repeated under the same experimental setup. They are given by unknown sources or the instrumentation employed.

The systematic errors are reproducible when a measurement is made a number of times using the same experimental scheme. They are deterministic and if its source is identified –which is usually difficult-, they should be subtracted from the measurements, as they are just a bias of the measured values.

In the case of uncertainty, it is divided into Type A and Type B by the GUM[341]. Both types will be discussed later. What we have to clarify first is that the estimation of uncertainty is computed from the chain of sources of uncertainty present in a system. In some cases, the random component of the uncertainty of a stage of the chain is seen as a systematic component by the following stage, for example, the uncertainty of an instrument, given by a random and systematic component, is considered as systematic when estimating the uncertainty of the measurements done with it. This is the reason why the uncertainty is divided by it evaluation method and not by the nature (random or systematic) of its components.

1.2.4 Estimation method

Both Type A and Type B sources of uncertainty are estimated from the standard deviations (s_i) associated to them. The values of standard deviation s_i are obtained and computed in different ways according to the Type and nature associated to the source of uncertainty, as it will be explained later in this chapter. At this point, it is important to define the standard uncertainty u_i that is obtained from the standard deviation s_i using a sensitivity coefficient w_i, (98).

$$u_i = w_i \cdot s_i \tag{98}$$

All the uncertainty components (both Type A and Type B) are then combined to give the overall uncertainty estimated for a measurement by the combined standard uncertainty u_c:

$$u_c = \sqrt{\sum_{i=1}^{N} u_i^{\,2}} \tag{99}$$

Where N is the number of sources of uncertainty, and all the standard

uncertainty quantities are given in the same units.

In some cases, in order to meet some requirements or regulations associated to the application, it is employed the expanded uncertainty (U) rather than the combined standard uncertainty (u_c). The expanded uncertainty is just the result of multiply the combined standard uncertainty by a coverage factor k.

$$U = k \cdot u_c \tag{100}$$

One of the most usual cases is the combined standard uncertainty following a normal distribution. In this cases, k is directly related with the confidence level required for the uncertainty (e.g. $k = 2$ and $k = 3$ for confidence levels 95% and 99.7%, respectively).

1.3 Method of evaluation Type A

As previously said, when every sample of a set of data is measured under the same conditions (experimental setup, environment conditions...), it has a random variation between samples. The estimation of the uncertainty of this set of data is done using the method of evaluation Type A.

The probability distribution function of one set of n samples measured under identical conditions is usually assumed to be a normal distribution. In this case, the standard deviation s of that set is obtained with the expression:

$$s = \sqrt{V} \tag{101}$$

$$V = \frac{\sum_{k=1}^{n} \left(x_k - \overline{x_k} \right)^2}{n-1} \tag{102}$$

Where x_k is the sample, n the number of samples of the data set, $/x_k$ the average value and V the variance.

In order to increase the reliability of the results, it is recommended to repeat the measurement of the set of samples n' times. In this case, the standard deviation can be estimated from a previous result of the standard deviation of one of the sets, rather than use (103) and (104) for the $n{\cdot}n$' samples[349]. This is because sometimes the whole raw data is not available for all the sets and they are only described by its average value and standard deviation. Thus, the estimated

standard deviation is basically the standard deviation of the mean of all the data sets. It is expressed as:

$$s_i = \frac{s}{\sqrt{n'}} \tag{103}$$

The standard uncertainty is directly the estimated standard deviation:

$$u_i = s_i \tag{104}$$

Nevertheless, in the case of a small value of n', the reliability of the results decreases. In order to provide a security bound to compensate this smaller reliability, a coverage factor can be used for the expanded uncertainty. When there is only a significant source of uncertainty, this coverage factor is based on a t-Student distribution. In the case of several significant sources of uncertainty coexisting, Welch-Satterwaite equation can provide the coverage factor[346].

$$U = k \cdot u_i \tag{105}$$

1.4 Method of evaluation Type B

Type B evaluation method is used for sources of uncertainty that can be considered as systematic. The uncertainty associated with the calibration of measurement equipment is also evaluated as Type B.

When possible, it is desirable to correct a systematic error that has been identified. However, sometimes the source of systematic error is difficult to identify, in this case, the error has to be considered as a source of uncertainty, and an equivalent standard deviation has to be determined (or estimated):

$$s_i = s_{est} \tag{106}$$

The uncertainty associated to measurement equipment is usually given as a lower and upper bound in the calibration certificate or specifications of the instrument. This range, which usually is given with symmetric bounds ($\pm s_{specifications}$), is what is considered as standard deviation for uncertainty estimation:

$$s_i = s_{specifications} \tag{107}$$

When the range is asymmetric, an equivalent range can be used, where the central value of the range is the mean value between the upper and lower bound and $s_{specifications}$ is half the difference between upper and lower bounds.

The probability distribution of the uncertainty within this range can be different. For Type B uncertainties, the considered probability distributions are normal, rectangular, triangular and U-shaped. The standard uncertainty u_i is computed according (98) using a weight w_i that is defined by the distribution considered.

For normal distributions, the weight factors are $w_i=1/2$ and $w_i=1/3$ when the range is provided with a confidence level of 95% and 99.7%, respectively. When the confidence level is not defined in the specifications or calibration certificate, 95% is considered.

One of the most usual distributions is the rectangular, which can be considered when there is no information about the distribution of the provided bounds[346]. In this case $w_i=1/sqrt(3)$.

Triangular and U-shaped distributions are not frequently used. For example, U-shaped distributions are applied in RF impedance mismatch measurements[346,349]. The weight factors are $w_i=1/sqrt(2)$. for the U-shaped distribution and $w_i=1/sqrt(6)$ for the rectangular.

1.5 Summary

A summary on the previous equations and considerations can be found in Table VII43:

Estimation of uncertainty	
Standard deviation	s_i
Standard uncertainty	$u_i = w_i \cdot s_i$
Combined standard uncertainty	$u_c = \sqrt{\sum_{i=1}^{N} u_i^2}$

Expanded uncertainty	$U = k \cdot u_i$
TYPE A UNCERTAINTIES (MEASUREMENT SAMPLES)	
Estimated standard deviation	$s_i = \frac{s}{\sqrt{n'}}$
Standard uncertainty	$u_i = s_i$
TYPE B UNCERTAINTIES (CALIBRATION SPECIFICATION OF INSTRUMENTATION)	
Estimated standard deviation	$s_i = s_{specifications}$
Standard uncertainty	$u_i = w_i \cdot s_i$
	$w_i = 1/2$ (95%)
Normal distribution:	$w_i = 1/3$ (99.7%)
Rectangular distribution:	$w_i = 1/\sqrt{3}$
Triangular distribution:	$w_i = 1/\sqrt{6}$
U-shaped distribution:	$w_i = 1/\sqrt{2}$

Table VII43. Uncertainty estimation summary

1.6 A practical case: estimation of the uncertainty of the power level measurement of an Electrical Spectrum Analyzer

In order to give an idea of the importance of uncertainty estimation, a practical case is presented. The uncertainty associated to the electrical power

of a signal measured using an ESA is presented. Special considerations about uncertainty estimation in ESA measurements can be found in several Application Notes from Agilent Technologies[344,350], Briaire[351] or Bertocco[354].

1.6.1 The measurement

A 15 GHz signal is measured in an ESA Anritsu MS2668C. Thirty traces are measured. As the averaging function of the ESA does not give the standard deviation, the traces are independently acquired and processed to obtain both the average trace and its associated standard deviation (0.5 dB). The signal comes from a photodiode fed by a low optical power of a semiconductor laser, resulting in an electrical signal with a minimum value of -83 dBm in the measurement span (1 GHz).

1.6.2 Estimation of uncertainty

Several significant sources of uncertainty are present in this measurement.

The uncertainty associated with the random variation between the 30 measured traces is evaluated using Type A evaluation method. As only one measurement set is performed, $n' = 1$ and $n = 30$. The estimation result is presented in Table VII44.

Type A	
Estimated standard deviation	$s_A = \frac{s}{\sqrt{n'}} = \frac{0.5}{\sqrt{1}} = 0.5\,dB$
Standard uncertainty	$u_A = s_A = 0.5\,dB$

Table VII44. Type A uncertainty estimation

Type B sources of uncertainty are given by the ESA power level uncertainty, as the frequency uncertainty is not considered here. The associated standard deviation of the sources of uncertainty can be found in both the calibration certificate and the specifications of the user manual There exist a lot of sources of uncertainty in an ESA, but for a specific measurement only a few of them are significant. For this measurement, the sources considered and their uncertainties under the measurement parameters described in 5.6.1 can be seen in Table VII45. The probability distribution of the uncertainty range specified by the manufacturer is assumed to be a normal distribution defined with a 95% confidence level ($w_i = 1/2$).

Type B		
Reference level and amplitude (IF gain)	$s_{B1} = 0.4\,dB$	$u_{B1} = 0.2\,dB$
Reference level and amplitude (RBW switching)	$s_{B2} = 0.3\,dB$	$u_{B2} = 0.15\,dB$
Reference level and amplitude (input attenuator)	$s_{B3} = 0.3\,dB$	$u_{B3} = 0.15\,dB$
Reference level and amplitude (Frequency response)	$s_{B4} = 4\,dB$	$u_{B4} = 1.5\,dB$
Reference level and amplitude (Scale fidelity)	$s_{B5} = 1.5\,dB$	$u_{B5} = 0.75\,dB$

Table VII45. Type B uncertainty estimation

The Type B uncertainty is computed according to equation (99):

$$u_B = \sqrt{\sum_{i=1}^{5} u_i^{\,2}} = \sqrt{0.2^2 + 0.15^2 + 0.15^2 + 2^2 + 0.75^2} = 2.156 \tag{108}$$

The combined uncertainty is given by:

$$u_C = \sqrt{u_A^{\,2} + u_B^{\,2}} = 2.21 \tag{109}$$

And finally, in order to report the overall uncertainty with a confidence level of 95% (assuming normal distribution of the combined uncertainty), an appropriate coverage factor must be applied in order to ensure the uncertainty to be within the reported range.

$$U = k \cdot u_c = 2 \cdot 2.21 = 4.42\,dB \tag{110}$$

So, the measurement will have a uncertainty of ±4.42 dB.

In the view of this result, it can be concluded that the uncertainty associated to a common measurement like the analyzed here, is much higher than expected at a first view. Thus, although a detailed estimation of uncertainty according the ISO specification is not usually required; an overall estimation is very important in the understanding of the measurements in order to properly

validate the results and eventually compare them.

Appendix VI

Laser Characterization Platform

1

Appendix VI. Laser Characterization Platform

1.1 Introduction

A Semiconductor Laser Characterization Platform (SLCP) has been implemented to provide a tool for systematic and exhaustive characterization of semiconductor lasers. This software-hardware platform makes use of LabVIEW software to control different equipment of the laboratory and to process, analyze and save the raw data, plots and a pdf report automatically. The SLCP is described in this Appendix.

1.2 Functionality

The SLCP performs sweeps in both bias current and saturable absorber voltage within a user-defined range and stepping. If the laser does not have a saturable absorber, the measurements are done for just one voltage value.

Several optical and electrical parameters are measured and systematically mapped and plotted in different ways to provide a comprehensive view of the dynamics of the device.

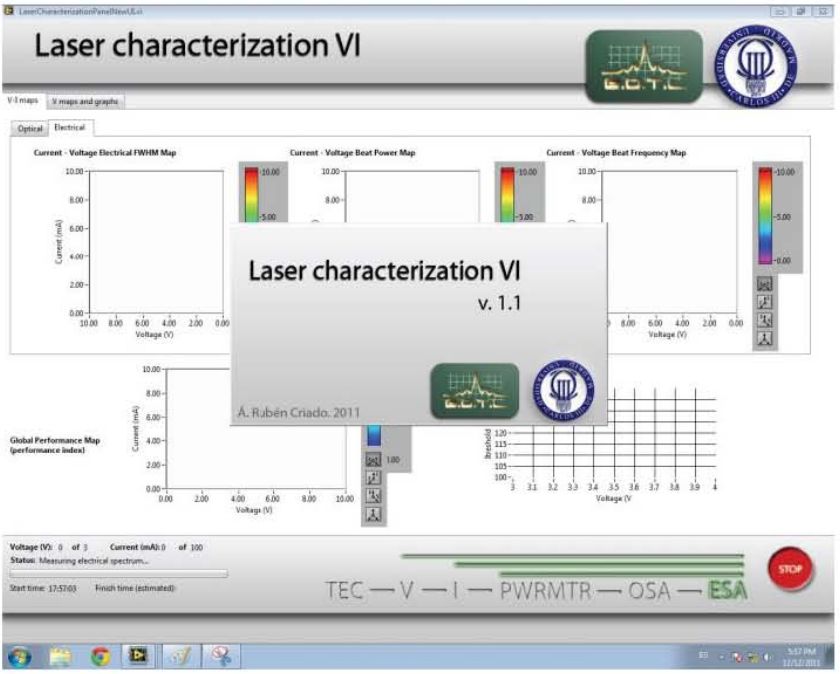

Figure 92 User Interface (UI) of the Semiconductor Laser Characterization Platform (SLCP)

Finally, the raw data, plots, maps and a pdf report are automatically saved.

Configuration

At execution, a dialogue window prompts to ask the user to introduce the configuration of the different devices and parameters of the setup.

- General. Device denomination, comments of the measurement, user, and directory to save (data, figures and report).
- Equipment configuration. Configuration parameters of the equipment used and controlled by the SLCP (i.e. voltage source, current source, optical power meter, ESA and OSA). Furthermore, the ESA preamplifier can be chosen from a list to correct for the Noise Figure (NF) in the SSB measurements.
- Setup configuration. Coupling ratios between OSA and ESA outputs. The coupling ratios are automatically corrected in the acquired data.

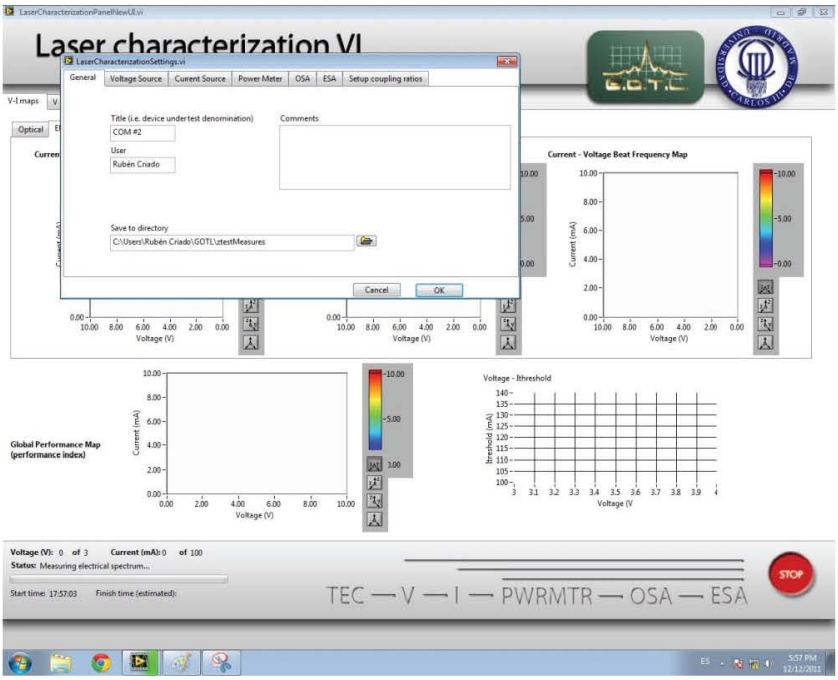

Figure 93 Configuration dialogue window

1.2.1 Current measurements

For each value of the voltage applied to the saturable absorber, the bias current is sweep and the following parameters are measured in each current value:

- Optical measurements. Optical power, optical FWHM, central wavelength, optical spectra, estimation of the threshold current (2nd derivative algorithm).
- Electrical measurements. Electrical power, electrical beat power, electrical beat frequency, electrical beat FWHM.

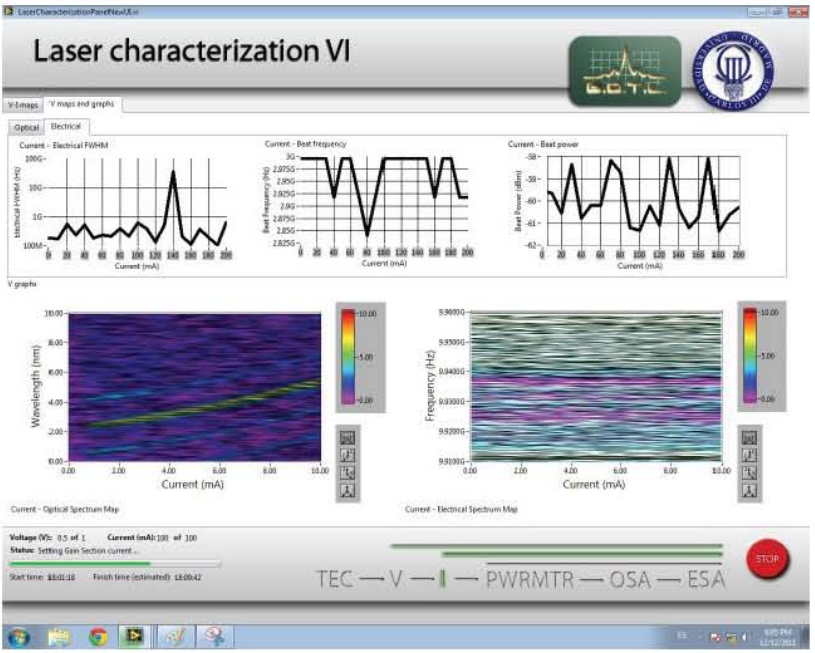

Figure 94 Current sweep for a fixed voltage value. Optical and Electrical Spectra maps, and electrical parameters plots are shown

1.2.2 Current-Voltage measurements

The previous optical and electrical measurements for the whole bias current range are performed for a range of saturable absorber voltage values. Once all current and voltage values are measured, the optical and electrical parameters are mapped as a function of bias current and saturable absorber voltage.

1.2.3 Global Performance maps

After accomplishing the previous measurements, the data is analyzed, and a Global Performance (GP) index is assigned for each Current-Voltage pair. The algorithm to assign this index is user configurable, and will weight each parameter with a certain value depending on the target application for what the GP index is calculated. More details on this algorithm can be found in[228].

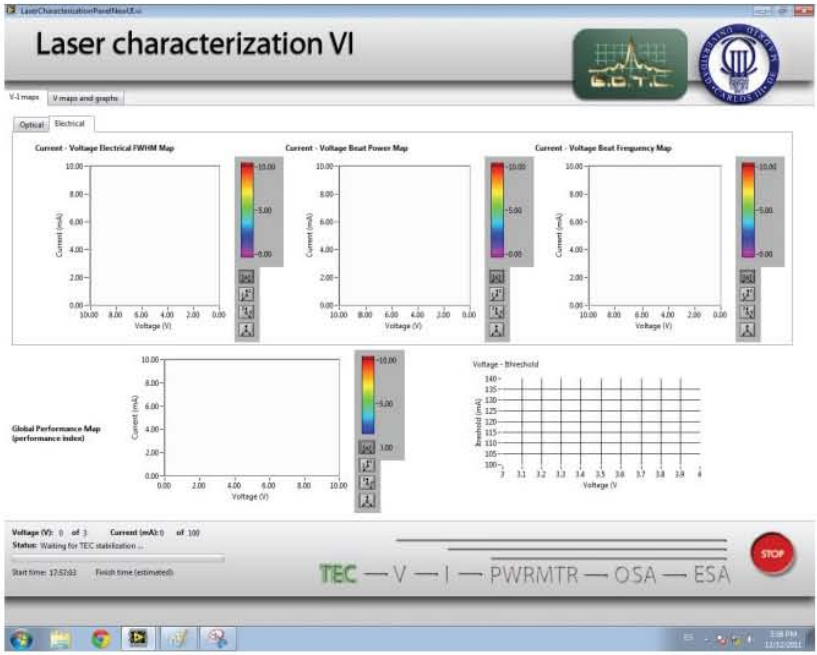

Figure 95. Voltage-Current maps, threshold current estimation and Global Performance map.

1.2.4 Generation of reports and data saving

The pdf report is automatically generated and saved in the directory defined by the user. The report contains (Figure 96): a) cover; b) user data, measurement and equipment parameters; c) optical and electrical measurements sweeping current (one page dynamically created for each voltage point); d) Voltage-Current maps; e) Global Performance Map and threshold current estimation.

Both the raw data and the images of the plots and maps are saved with a defined nomenclature to easy sorting and search of the files. The name format is: "dateVoltage_Description.extension".

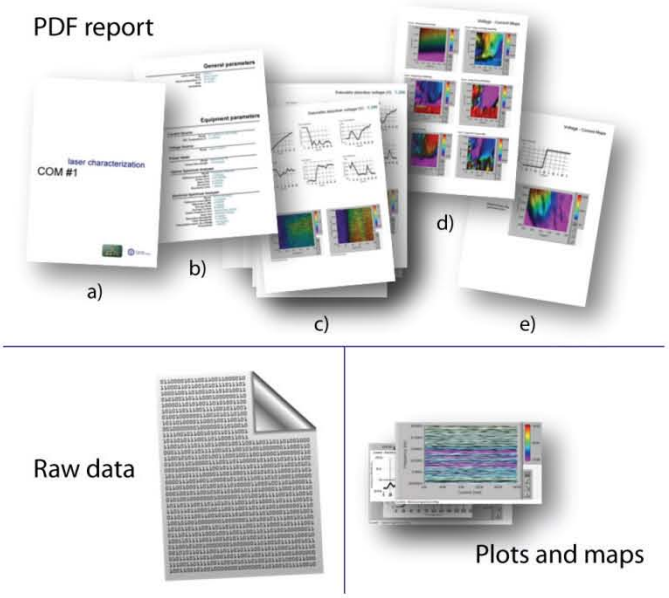

Figure 96 Saving process. PDF report, Raw data and Plots and maps

1.3 User interface

The UI has been modified to provide the user with an improved appearance. All the buttons and sections have been customized with custom-made graphs (see Figure 97).

The bottom part also provides information to the user about the measurement status. In the right part (Figure 97), an measurement flow graph indicates the measurement process and what is being measured at the moment. This info ins complemented with the text indicator (Status).

In the left region, the start time and the expected finish time is shown to the user both in numerical and progress bar forms. Moreover, the progress bar has been integrated in LabVIEW icon of the task bar of Windows 7, which also shows the progress of the measurement. The current and voltage values that are being measured are shown, as well as the total current and voltage values to finish the measurement.

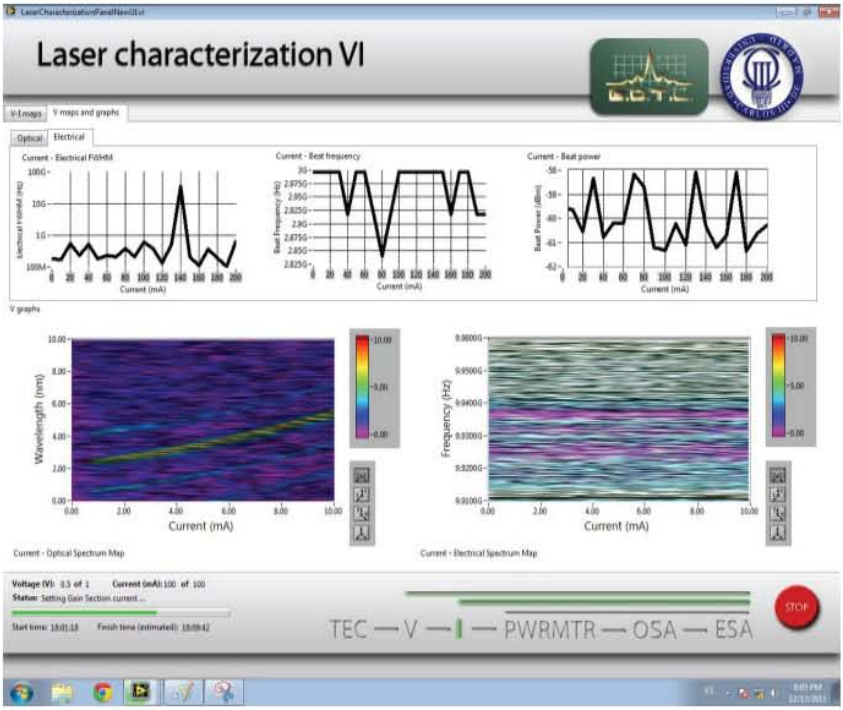

Figure 97 Header of the SLCP

List of Acronyms

AE	Antenna Emitter
AML	Active Mode Locking
ASE	Amplified Stimulated Emission
AWG	Arrayed Waveguide Grating
BWO	Backward Wave Oscillator
COTS	Commercial Off-The-Shelf
CR	Conversion Ratio
CW	Continuous Wave
DFG	Difference Frequency Generation
DFWM	Degenerate Four Wave Mixing
DM	Discrete Mode
ECE	Electron Cyclotron Emission
EM	Electromagnetic
EMI	Electromagnetic Interference
EO	Electro Optical
EOR	Electro Optical Rectification
EOS	Electro Optical Sampling
ESA	Electrical Spectrum Analyzer
FEL	Free Electron Laser
FET	Field Effect Transistor
FIR	Far Infrared
FPTF	Fabry-Perot Tunable Filter
FTS	Fourier Transform Spectroscopy
FWHM	Full Width at Half Maximum
FWM	Four Wave Mixing
GS	Gain Switching
GS-LO	Gain Switching Local Oscillator
GS-OFCG	Gain Switching Optical Frequency Comb Generator

HEB	Hot Electron Bolometer
HML	Hybrid Mode Locking
IEEE	Institute of Electrical and Electronics Engineers
IF	Intermediate Frequency
IMPATT	Impact Ionization Avalanche Transit-Time
LAE	Large Area Emitter
LO	Local Oscillator
LT-GaAs	Low-Temperature grown GaAs
M	Measurement frequency
MIM	Metal Insulator Metal
ML	Mode Locking
MLLD	Mode-Locked Laser Diode
MUTC	Modified Uni Travelling Carrier
NBUTC	Near Ballistic Uni Travelling Carrier
NEP	Noise Equivalent Power
NLSE	Non Linear Schrödinger Equation
OFCG	Optical Frequency Comb Generator
OHG	Optical Heterodyne Generation
OIL	Optical Injection Locking
OPLL	Optical Phase Locked Loop
OSA	Optical Spectrum Analyzer
PC	Photoconductor
PCF	Photonic Crystal Fiber
PD	Photodiode
PIC	Photonic Integrated Circuit
PML	Passive Mode Locking
PMLLD	Passively Mode Locking Laser Diode
QCL	Quantum Cascade Laser

RF	Radiofrequency
RMS	Root Mean Square
RT	Room Temperature
RTD	Resonant Tunneling Diode
SBS	Stimulated Brillouin Scattering
SHG	Second Harmonic Generation
SIS	Superconductor-Insulator-Superconductor
SMSR	Side Mode Suppression Ratio
SNR	Signal to Noise Ratio
SOA	Semiconductor Optical Amplifier
SPM	Self Phase Modulation
SR	Superradiance
SRS	Stimulated Raman Scattering
SSB	Single Side Band
ST	Schawlow-Townes
SVE	Slow-Varying Envelope
TBP	Time Bandwidth Product
TDS	Time Domain Spectroscopy
TEC	Thermo Electric Cooler
THG	Third Harmonic Generation
THz-QCL	Terahertz Quantum Cascade Laser
TPO	Terahertz Optical Parametric Oscillator
TUNNETT	Tunnel Injection Transit-Time
TW-UTC-PD	Travelling Wave Uni Travelling Carrier Photodiode
UTC-PD	Uni Travelling Carrier Photodiode
VNA	Vector Network Analyzer
WDM	Wavelength Division Multiplexing
XN-SOA	Ultra Nonlinear Semiconductor Optical Amplifier

XPM	Cross Phase Modulation

References

1. Hertz, H. *Electric Waves: Being Researches on the Propagation of Electric Action with Finite Velocity Through Space*. 278 (1893).

2. Tesla, N. U.S. Patent 0,645,576. (1900).

3. Yuste, A. P. & Salazar, M. Scanning our Past from Madrid: Leonardo Torres Quevedo. *Proceedings of the IEEE* **93,(7)** 1379–1382 (2005).

4. Maxwell, J. C. *A treatise on electricity and magnetism*. (1873).

5. Capri, A. Z. *Quips, quotes, and quanta: an anecdotal history of physics*. (2007).

6. Planck, M. Über eine Verbesserung der Wienschen Spektralgleichung (On an Improvement of Wien's Equation for the Spectrum). *Verhandlungen der Deutschen Physikalischen Gesselschaft* **2,** 202–204 (1900).

7. Einstein, A. Über einen die Erzeugung und Verwandlung des Lichtes betreffenden heuristischen Gesichtspunkt. *Annalen der Physik* **17,(6)** 132–148 (1905).

8. Whitaker, A. *The New Quantum Age: From Bell's Theorem to Quantum Computation and Teleportation*. (2011).

9. Gould, R. G. The LASER, Light Amplification by Stimulated Emission of Radiation. in *The Ann Arbor Conference on Optical Pumping, the University of Michigan* 128 (1959).

10. Maiman, T. H. Stimulated optical radiation in ruby. *Nature* **187,(4736)** 493–494 (1960).

11. Siegel, P. H. Terahertz technology. *IEEE Transactions on Microwave Theory and Techniques* **50,(3)** 910–928 (2002).

12. Nagatsuma, T. Generating millimeter and terahertz waves. *IEEE Microwave Magazine* **10,(4)** 64–74 (2009).

13. Redo-Sanchez, A. & Xi-Cheng, Z. Terahertz Science and Technology Trends. *IEEE Journal of Selected Topics in Quantum Electronics* **14,(2)** 260–269 (2008).

14. Zomega Terahertz Corporation. *The Terahertz Wave eBook*. (2012).

15. Tribe, W. R., Newnham, D. A., Taday, P. F. & Kemp, M. C. Hidden object detection: security applications of terahertz technology. in *SPIE 2004. Proceedings of SPIE* (Hwu, R. J.) **5354,** 168–176 (SPIE, 2004).

16. Siegel, P. H. Terahertz technology in biology and medicine. *IEEE Transactions on Microwave Theory and Techniques* **52,(10)** 2438–2447 (2004).

17. Naval Air Systems Command & Naval Air Warfare Center. *Electronic Warfare and Radar Systems Engineering Handbook*. (2007).

18. Piesiewicz, R., Kleine-Ostmann, T., Krumbholz, N., Mittleman, D., Koch, M., Schoebel, J., Kurner, T. & Felder, E. Short-Range Ultra-Broadband Terahertz Communications: Concepts and Perspectives. *IEEE Antennas and Propagation Magazine* **49,(6)** 24–39 (2007).

19. Bushburg, J., Seibert, A., Leidholdt, E. & Boone, J. *The Essential Physics of Medical Imaging*. (Lippincott Williams & Wilkins, 2002).

20. Luhmann, N. C. & Peebles, W. A. Instrumentation for magnetically confined

fusion plasma diagnostics. *Review of Scientific Instruments* **55,(3)** 279 (1984).

21. Bründermann, E., Hübers, H.-W. & Kimmitt, M. F. *Terahertz Techniques*. 383 (Springer. Springer Series in Optical Sciences, Vol. 151, 2012).

22. Fice, M. J., Rouvalis, E., Van Dijk, F., Accard, A., Lelarge, F., Renaud, C. C., Carpintero, G. & Seeds, A. J. 146-GHz millimeter-wave radio-over-fiber photonic wireless transmission system. *Optics Express* **20,(2)** 1769–1774 (2012).

23. Huang, K.-C. & Wang, Z. *Millimeter Wave Communication Systems*. (2011).

24. Kuo, F. M., Shi, J. W., Shao-Ning, W., Nan-Wei, C., Po-Tsung, S., Chun-Ting, L., Wen-Jr, J., Er-Zih, W., Chen, J. & Sien, C. W-Band Wireless Data Transmission by the Integration of a Near-Ballistic Unitraveling-Carrier Photodiode With a Horn Antenna Fed by a Quasi-Yagi Radiator. *IEEE Electron Device Letters* **30,(11)** 1167–1169 (2009).

25. Renaud, C. C., Ponnampalam, L., Pozzi, F., Rouvalis, E., Moodie, D., Robertson, M. & Seeds, A. J. Photonically enabled communication systems beyond 1000 GHz. in *2008 International Topical Meeting on Microwave Photonics jointly held with the 2008 Asia-Pacific Microwave Photonics Conference* 55–58 (IEEE, 2008). doi:10.1109/MWP.2008.4666633

26. Huebers, H.-W., Richter, H., Pavlov, S., Semenov, A., Tredicucci, A., Mahler, L., Beere, H. & Ritchie, D. Laser local oscillators for heterodyne receivers beyond 2 terahertz. *Frequenz* **62,(5-6)** 111–117 (2008).

27. Withington, S. Terahertz astronomical telescopes and instrumentation. *Philosophical transactions. Series A, Mathematical, physical, and engineering sciences* **362,(1815)** 395–401; discussion 401–2 (2004).

28. Cámara Mayorga, I., Schmitz, A., Klein, T., Leinz, C. & Gusten, R. First In-Field Application of a Full Photonic Local Oscillator to Terahertz Astronomy. *IEEE Transactions on Terahertz Science and Technology* **2,(4)** 393–399 (2012).

29. Wolfe, S. M., Button, K. J., Waldman, J. & Cohn, D. R. Modulated submillimeter laser interferometer system for plasma density measurements. *Applied Optics* **15,(11)** 2645 (1976).

30. Jepsen, P. U., Møller, U. & Merbold, H. Investigation of aqueous alcohol and sugar solutions with reflection terahertz time-domain spectroscopy. *Optics Express* **15,(22)** 14717 (2007).

31. Garin, B. M., Parshin, V. V., Polyakov, V. I., Rukovishnikov, A. I., Serov, E. A., Mocheneva, O. S., Jia, C. C., Tang, W. Z. & Lu, F. X. *Dielectric Properties and Applications of CVD Diamonds in the Millimeter and Terahertz Ranges. Recent Advances in Broadband Dielectric Spectroscopy NATO Science for Peace and Security Series B: Physics and Biophysics* pp 79–87 (2013).

32. Vaks, V., Domracheva, E., Sobakinskaya, E. & Chernyaeva, M. Upgrading the sensitivity of spectroscopy gas analysis with application of supersonic molecular beams. *Journal of Applied Physics* **111,(7)** 074903 (2012).

33. Taday, P. F. Applications of terahertz spectroscopy to pharmaceutical sciences. *Philosophical Transactions of the Royal Society of London. Series A: Mathematical, Physical and Engineering Sciences* **362,(1815)** 351–364 (2004).

34. Kim, K. W., Kim, K.-S., Kim, H., Lee, S. H., Park, J.-H., Han, J.-H., Seok, S.-H.,

Park, J., Choi, Y., Kim, Y. Il, Han, J. K. & Son, J.-H. Terahertz dynamic imaging of skin drug absorption. *Optics Express* **20,(9)** 9476 (2012).

35. Du, S. Q., Li, H., Xie, L., Chen, L., Peng, Y., Zhu, Y. M., Dong, P. & Wang, J. T. Vibrational frequencies of anti-diabetic drug studied by terahertz time-domain spectroscopy. *Applied Physics Letters* **100,(14)** 143702 (2012).

36. Pickwell, E. & Wallace, V. P. Biomedical applications of terahertz technology. *Journal of Physics D: Applied Physics* **39,(17)** R301–R310 (2006).

37. Tonouchi, M. Cutting-edge terahertz technology. *Nature Photonics* **1,(2)** 97–105 (2007).

38. Synview GmbH. Synview. THz Non Destructive Testing systems. (2013). at <http://www.synview.com/> [Last accessed: 02/2013]

39. Trex Enterprise. Trex Enterprise. Passive imaging for security. (2012). at <http://www.trexenterprises.com/Products and Services/Sensors/security.html> [Last accessed: 02/2012]

40. Miles, R. E., Zhang, X.-C., Eisele, H. & Krotkus, A. Terahertz Frequency Detection and Identification of Materials and Objects. in *Terahertz Frequency Detection and Identification of Materials and Objects* 364 (Springer, 2007).

41. Nagel, M., Först, M. & Kurz, H. THz biosensing devices: fundamentals and technology. *Journal of Physics: Condensed Matter* **18,(18)** S601–S618 (2006).

42. Chahat, N., Zhadobov, M., Sauleau, R. & Alekseev, S. I. New Method for Determining Dielectric Properties of Skin and Phantoms at Millimeter Waves Based on Heating Kinetics. *IEEE Transactions on Microwave Theory and Techniques* **60,(3)** 827–832 (2012).

43. Recur, B., Guillet, J.-P., Bassel, L., Fragnol, C., Manek-Hönninger, I., Delagnes, J. C., Benharbone, W., Desbarats, P., Domenger, J.-P. & Mounaix, P. Terahertz radiation for tomographic inspection. *Optical Engineering* **51,(9)** 091609 (2012).

44. Vaks, V. High-Precise Spectrometry of the Terahertz Frequency Range: The Methods, Approaches and Applications. *Journal of Infrared, Millimeter, and Terahertz Waves* **33,(1)** 43–53 (2011).

45. Vaks, V. L., Domracheva, E. G., Sobakinskaya, E. A., Chernyaeva, M. B. & Maslennikova, A. V. Using the methods and facilities of nonsteady-state spectroscopy of the subterahertz and terahertz frequency ranges for noninvasive medical diagnosis. *Journal of Optical Technology* **79,(2)** 66 (2012).

46. Bakhtiari, S., Liao, S., Elmer Ii, T., x201C, Sami, x201D, Gopalsami, N. S., Raptis, A. C. & Elmer, T. A Real-time Heart Rate Analysis for a Remote Millimeter Wave I–Q Sensor. *Biomedical Engineering, IEEE Transactions on* **58,(6)** 1839–1845 (2011).

47. Globus, T., Woolard, D., Khromova, T., Crowe, T., Bykhovskaia, M., Gelmont, B., Hesler, J. & Samuels, A. THz-spectroscopy of biological molecules. *Journal of Biological Physics* **29,(2-3)** 89–100 (2003).

48. Palací, J., Bockelt, A. & Vidal, B. SOA-based optical processing for terahertz time-domain spectroscopy. *Electronics Letters* **48,(10)** 593 (2012).

49. Oh, T. I., You, Y. S. & Kim, K. Y. Two-dimensional plasma current and optimized terahertz generation in two-color photoionization. *Optics Express* **20,(18)** 19778 (2012).

50. Palací, J., Bockelt, A. & Vidal, B. Terahertz radiation shaping based on optical spectrum modulation in the time domain. *Optics Express* **20,(21)** 23117 (2012).

51. Rius, E., Prigent, G., Happy, H., Dambrine, G., Boret, S. & Cappy, A. Wide- and narrow-band bandpass coplanar filters in the W -frequency band. *IEEE Transactions on Microwave Theory and Techniques* **51,(3)** 784–791 (2003).

52. Wang, X., Cui, Y., Sun, W., Ye, J. & Zhang, Y. Terahertz polarization real-time imaging based on balanced electro-optic detection. at <http://apps.webofknowledge.com/full_record.do?product=UA&search_mode=GeneralSearch&qid=21&SID=1C7OL3jjG4l5ph4A5iB&page=1&doc=1>

53. Xu, Z. & Lam, E. Y. Image reconstruction using spectroscopic and hyperspectral information for compressive terahertz imaging. at <http://apps.webofknowledge.com/full_record.do?product=UA&search_mode=GeneralSearch&qid=17&SID=1C7OL3jjG4l5ph4A5iB&page=1&doc=1>

54. Yeom, S., Lee, D.-S., Jang, Y., Lee, M.-K. & Jung, S.-W. Real-time concealed-object detection and recognition with passive millimeter wave imaging. *Optics Express* **20,(9)** 9371 (2012).

55. Yokoyama, S., Nakamura, R., Nose, M., Araki, T. & Yasui, T. Terahertz spectrum analyzer based on a terahertz frequency comb. *Optics Express* **16,(17)** 13052–13061 (2008).

56. Yasui, T., Nakamura, R., Kawamoto, K., Ihara, A., Fujimoto, Y., Yokoyama, S., Inaba, H., Minoshima, K., Nagatsuma, T. & Araki, T. Real-time monitoring of continuous-wave terahertz radiation using a fiber-based, terahertz-comb-referenced spectrum analyzer. *Optics Express* **17,(19)** 17034–17043 (2009).

57. Yasui, T., Yokoyama, S., Inaba, H., Minoshima, K., Nagatsuma, T. & Araki, T. Terahertz Frequency Metrology Based on Frequency Comb. *IEEE Journal of Selected Topics in Quantum Electronics* **17,(1)** 191–201 (2011).

58. Yokoyama, S., Yokoyama, T., Hagihara, Y., Araki, T. & Yasui, T. A distance meter using a terahertz intermode beat in an optical frequency comb. *Optics Express* **17,(20)** 17324–17337 (2009).

59. Yasui, T., Kabetani, Y., Saneyoshi, E., Yokoyama, S. & Araki, T. Terahertz frequency comb by multifrequency-heterodyning photoconductive detection for high-accuracy, high-resolution terahertz spectroscopy. *Applied Physics Letters* **88,(24)** 241104 (2006).

60. Füser, H., Judaschke, R., Bieler, M. & Füser, H. High-precision frequency measurements in the THz spectral region using an unstabilized femtosecond laser. *Applied Physics Letters* **99,(12)** 121111 (2011).

61. Xue, K., Li, Q., Li, Y.-D. & Wang, Q. Continuous-wave terahertz in-line digital holography. *Optics Letters* **37,(15)** 3228 (2012).

62. Agladze, N. I. & Sievers, a J. Holographic Fourier transform spectrometer for terahertz region. *Optics letters* **35,(5)** 664–6 (2010).

63. Anthony, J., Leonhardt, R., Leon-Saval, S. G. & Argyros, A. THz propagation

in kagome hollow-core microstructured fibers. *Optics Express* **19,(19)** 18470–18478 (2011).

64. Chen, D. & Chen, H. A novel low-loss Terahertz waveguide: Polymer tube. *Optics Express* **18,(4)** 3762–3767 (2010).

65. Doradla, P., Joseph, C. S., Kumar, J. & Giles, R. H. Characterization of bending loss in hollow flexible terahertz waveguides. *Optics Express* **20,(17)** 19176 (2012).

66. Hu, B., Wang, Q. J. & Zhang, Y. Broadly tunable one-way terahertz plasmonic waveguide based on nonreciprocal surface magneto plasmons. *Optics Letters* **37,(11)** 1895 (2012).

67. Huang, Y. R., Chen, H. P., Chiu, P. C., Chyi, J. I., Wang, B. H., Chen, S. Y. & Sun, C. K. Propagation, Resonance, and Radiation on Terahertz Optoelectronic Integrated Circuits. *IEEE Photonics Journal* **4,(3)** 1–1 (2012).

68. Lioubtchenko, D., Dudorov, S., Mallat, J., Tuovinen, J. & Raisanen, A. V. Low-loss sapphire waveguides for 75-110 GHz frequency range. *IEEE Microwave and Wireless Components Letters* **11,(6)** 252–254 (2001).

69. Li, G., Jin, Z., Xue, X., Lin, X., Ma, G., Hu, S. & Dai, N. Terahertz coherent control of surface plasmon polariton propagation in subwavelength metallic hole arrays. *Applied Physics Letters* **100,(19)** 191115 (2012).

70. Kitagawa, J., Kodama, M., Koya, S., Nishifuji, Y., Armand, D. & Kadoya, Y. THz wave propagation in two-dimensional metallic photonic crystal with mechanically tunable photonic-bands. *Optics Express* **20,(16)** 17271–17280 (2012).

71. Pousi, J. P., Lioubtchenko, D. V., Dudorov, S. N. & Raisanen, A. V. High Permittivity Dielectric Rod Waveguide as an Antenna Array Element for Millimeter Waves. *IEEE Transactions on Antennas and Propagation* **58,(3)** 714–719 (2010).

72. Sun, C.-K. Subwavelength plastic fiber for terahertz wave guiding. in *SPIE 2006. Proceedings of SPIE* (2006).

73. Wang, Z., Liu, H., Huang, N., Sun, Q. & Wen, J. Efficient terahertz-wave generation via four-wave mixing in silicon membrane waveguides. *Optics Express* **20,(8)** 8920 (2012).

74. Preu, S., Malzer, S., Döhler, G. H., Zhao, Q. Z., Hanson, M., Zimmerman, J. D., Gossard, a. C., Wang, L. J. & Döhler, G. H. Interference between two coherently driven monochromatic terahertz sources. *Applied Physics Letters* **92,(22)** 221107 (2008).

75. Grainger, W. F., Juanola-Parramon, R., Ade, P. A. R., Griffin, M., Liggins, F., Pascale, E., Savini, G. & Swinyard, B. Demonstration of spectral and spatial interferometry at THz frequencies. *Applied Optics* **51,(12)** 2202 (2012).

76. Wang, X., Hou, L. & Zhang, Y. Continuous-wave terahertz interferometry with multiwavelength phase unwrapping. *Applied Optics* **49,(27)** 5095–102 (2010).

77. Virginia Diodes Co. Virginia Diodes Co. Mixers. (2012). at <www.vadiodes.com> [Last accessed: 02/2012]

78. Insight Product Co. Insight Product Co. Gunn and IMPATT diodes. at

<http://www.insight-product.com/products3.htm> [Last accessed: 02/2012]

79. Nishizawa, J., Płotka, P., Kurabayashi, T. & Makabe, H. 706-GHz GaAs CW fundamental-mode TUNNETT diodes fabricated with molecular layer epitaxy. *physica status solidi (c)* **5,(9)** 2802–2804 (2008).

80. Suzuki, S., Asada, M., Teranishi, A., Sugiyama, H. & Yokoyama, H. Fundamental oscillation of resonant tunneling diodes above 1 THz at room temperature. *Applied Physics Letters* **97,(24)** 242102 (2010).

81. Feiginov, M., Sydlo, C., Cojocari, O. & Meissner, P. Resonant-tunnelling-diode oscillators operating at frequencies above 1.1 THz. *Applied Physics Letters* **99,(23)** 233503–233506 (2011).

82. Meziani, Y. M., Nishimura, T., Handa, H., Knap, W., Otsuji, T., Sano, E., Popov, V. V., Coquillat, D. & Teppe, F. Room temperature generation of terahertz radiation from dual grating gate HEMT's. in *2008 33rd International Conference on Infrared, Millimeter and Terahertz Waves* 1–2 (IEEE, 2008). doi:10.1109/ICIMW.2008.4665540

83. El Fatimy, A., Teppe, F., Dyakonova, N., Knap, W., Seliuta, D., Valušis, G., Shchepetov, A., Roelens, Y., Bollaert, S., Cappy, A. & Rumyantsev, S. Resonant and voltage-tunable terahertz detection in InGaAs⁄InP nanometer transistors. *Applied Physics Letters* **89,(13)** 131926 (2006).

84. El Fatimy, a., Dyakonova, N., Meziani, Y., Otsuji, T., Knap, W., Vandenbrouk, S., Madjour, K., Theron, D., Gaquiere, C., Poisson, M. a., Delage, S., Prystawko, P., Skierbiszewski, C. & Théron, D. AlGaN/GaN high electron mobility transistors as a voltage-tunable room temperature terahertz sources. *Journal of Applied Physics* **107,(2)** 24504 (2010).

85. Coquillat, D., Nadar, S., Teppe, F., Dyakonova, N., Boubanga-Tombet, S., Knap, W., Nishimura, T., Otsuji, T., Meziani, Y. M., Tsymbalov, G. M. & Popov, V. V. Room temperature detection of sub-terahertz radiation in double-grating-gate transistors. *Optics express* **18,(6)** 6024–32 (2010).

86. Macario, J., Shireen, R., Schuetz, C. a. & Prather, D. W. Development of Electro-Optic Phase Modulator for 94 GHz Imaging System. *Journal of Lightwave Technology* **27,(24)** 5698–5703 (2009).

87. Mross, M., Lowell, T., Durant, R. & Kimmitt, M. Performance characteristics of a Smith-Purcell Tunable Terahertz Source. *Journal of Biological Physics* **29,(2-3)** 295–302 (2003).

88. Insight Product Co. Insight Product Co. BWO. at <http://www.insight-product.com/submmbwo3.htm> [Last accessed: 02/2012]

89. Bratman, V., Kalynov, Y. & Manuilov, V. Large-Orbit Gyrotron Operation in the Terahertz Frequency Range. *Physical Review Letters* **102,(24)** (2009).

90. Sabchevski, S. P. & Idehara, T. Design of a Compact Sub-Terahertz Gyrotron for Spectroscopic Applications. *Journal of Infrared, Millimeter, and Terahertz Waves* (2010). doi:10.1007/s10762-010-9668-2

91. Feikes, J., Von Hartrott, M., Ries, M., Schmid, P., Wüstefeld, G., Hoehl, A., Klein, R., Müller, R. & Ulm, G. Metrology Light Source: The first electron storage ring optimized for generating coherent THz radiation. *Physical Review*

Special Topics - Accelerators and Beams **14,(3)** (2011).

92. Ackermann, W., Asova, G., Ayvazyan, V., Azima, A., Baboi, N., Bähr, J., Balandin, V., Beutner, B., Brandt, A., Bolzmann, A., Brinkmann, R., Brovko, O. I., Castellano, M., Castro, P., Catani, L., Chiadroni, E., Choroba, S., Cianchi, A., et al. Operation of a free-electron laser from the extreme ultraviolet to the water window. *Nature Photonics* **1,(6)** 336–342 (2007).

93. Advanced Radiation Co. Advanced Radiation Co. Mercury arc lamp. (2012). at <http://www.arc-lamps.com/pdf/HP-Mercury_shortArc-hsa200.pdf> [Last accessed: 02/2012]

94. Accetta, J. S. & Shumaker, D. L. *The Infrared and Electro-Optical Systems Handbook*. (SPIE, 1993).

95. Faist, J., Capasso, F., Sivco, D. L., Sirtori, C., Hutchinson, A. L. & Cho, A. Y. Quantum Cascade Laser. *Science* **264,(5158)** 553–556 (1994).

96. Köhler, R., Tredicucci, A., Beltram, F., Beere, H. E., Linfield, E. H., Davies, A. G., Ritchie, D. A., Iotti, R. C. & Rossi, F. Terahertz semiconductor-heterostructure laser. *Nature* **417,(6885)** 156–9 (2002).

97. Williams, B. S. Terahertz quantum-cascade lasers. *Nature Photonics* **1,(9)** 517–525 (2007).

98. Chamberlin, D. R., Bründermann, E. & Haller, E. E. Narrow linewidth intervalence-band emission from germanium terahertz lasers. *Applied Physics Letters* **83,(1)** 3 (2003).

99. Hübers, H.-W., Pavlov, S. G. & Shastin, V. N. Terahertz lasers based on germanium and silicon. *Semiconductor Science and Technology* **20,(7)** S211–S221 (2005).

100. Dai, J., Liu, J. & Zhang, X.-C. Terahertz Wave Air Photonics: Terahertz Wave Generation and Detection With Laser-Induced Gas Plasma. *IEEE Journal of Selected Topics in Quantum Electronics* **17,(1)** 183–190 (2011).

101. Bartel, T., Gaal, P., Reimann, K., Woerner, M. & Elsaesser, T. Generation of single-cycle THz transients with high electric-field amplitudes. *Optics Letters* **30,(20)** 2805 (2005).

102. Dai, J., Clough, B., Ho, I.-C., Lu, X., Liu, J. & Zhang, X.-C. Recent Progresses in Terahertz Wave Air Photonics. *IEEE Transactions on Terahertz Science and Technology* **1,(1)** 274–281 (2011).

103. Thomson, M. D., Blank, V. & Roskos, H. G. Terahertz white-light pulses from an air plasma photo-induced by incommensurate two-color optical fields. *Optics Express* **18,(22)** 23173 (2010).

104. Li, Z., Bing, P., Yao, J., Xu, D. & Zhong, K. High-powered tunable terahertz source based on a surface-emitted terahertz-wave parametric oscillator. *Optical Engineering* **51,(9)** 091605 (2012).

105. Sowade, R., Breunig, I., Cámara Mayorga, I., Kiessling, J., Tulea, C., Dierolf, V. & Buse, K. Continuous-wave optical parametric terahertz source. *Optics Express* **17,(25)** 22303 (2009).

106. You, D., Jones, R. R., Bucksbaum, P. H. & Dykaar, D. R. Generation of high-

power sub-single-cycle 500-fs electromagnetic pulses. *Optics Letters* **18,(4)** 290 (1993).

107. Sakai, K. *Terahertz Optoelectronics*. 400 (Springer. Topics in Applied Physics, Vol. 97, 2005).

108. Fice, M. J., Rouvalis, E., Ponnampalam, L., Renaud, C. C. & Seeds, A. J. Telecommunications technology-based terahertz sources. *Electronics Letters* **46,(26)** S28 (2010).

109. Kurtz, D. S., Hesler, J. L., Crowe, T. W. & Weikle, R. M. Submillimeter-wave sideband generation using varactor Schottky diodes. *IEEE Transactions on Microwave Theory and Techniques* **50,(11)** 2610–2617 (2002).

110. Menlo Systems Co. Menlo Systems Co. TERA15 antennas. (2012). at <http://www.menlosystems.com/home/products/thz-solutions/> [Last accessed: 02/2012]

111. Han, S.-P., Kim, N., Ko, H., Ryu, H.-C., Park, J.-W., Yoon, Y.-J., Shin, J.-H., Lee, D. H., Park, S.-H., Moon, S.-H., Choi, S.-W., Chun, H. S. & Park, K. H. Compact fiber-pigtailed InGaAs photoconductive antenna module for terahertz-wave generation and detection. *Optics Express* **20,(16)** 18432 (2012).

112. Rouvalis, E., Renaud, C. C., Moodie, D. G., Robertson, M. J. & Seeds, A. J. Traveling-wave Uni-Traveling Carrier photodiodes for continuous wave THz generation. *Optics express* **18,(11)** 11105–10 (2010).

113. Ito, H., Furuta, T., Kodama, S., Watanabe, N. & Ishibashi, T. InP/InGaAs uni-travelling-carrier photodiode with 220 GHz bandwidth. *Electronics Letters* **35,(18)** 1556–1557 (1999).

114. Hiroshi, I., et al., Ito, H., Nakajima, F., Furuta, T. & Ishibashi, T. Continuous THz-wave generation using antenna-integrated uni-travelling-carrier photodiodes. *Semiconductor Science and Technology* **20,(7)** S191 (2005).

115. Preu, S., Renner, F. H., Malzer, S., Döhler, G. H., Wang, L. J., Hanson, M., Gossard, a. C., Wilkinson, T. L. J., Brown, E. R. & Döhler, G. H. Efficient terahertz emission from ballistic transport enhanced n-i-p-n-i-p superlattice photomixers. *Applied Physics Letters* **90,(21)** 212115 (2007).

116. Preu, S., Döhler, G. H., Malzer, S., Wang, L. J. & Gossard, a. C. Tunable, continuous-wave Terahertz photomixer sources and applications. *Journal of Applied Physics* **109,(6)** 061301–01 – 061301–56 (2011).

117. Born, M. & Wolf, E. *Principles of Optics: Electromagnetic Theory of Propagation, Interference and Diffraction of Light*. 986 (Cambridge University Press, 1999).

118. Virginia Diodes Co. Virginia Diodes Co. Multipliers. (2012). at <http://vadiodes.com/> [Last accessed: 02/2012]

119. Insight Product Co. Insight Product Co.THz synthesizers. (2012). at <http://www.insight-product.com/thz_synth3.html> [Last accessed: 02/2012]

120. Scherer, D. The Art of Phase Noise Measurement. in *RF & Microwave Measurement Symposium and Exhibition* (1983).

121. Feiginov, M., Sydlo, C., Cojocari, O. & Meissner, P. Operation of resonant-tunnelling-diode oscillators beyond tunnel-lifetime limit at 564 GHz. *EPL*

(Europhysics Letters) **97,(5)** 58006 (2012).

122. Asada, M. Theoretical analysis of spectral linewidth of terahertz oscillators using resonant tunneling diodes and their coupled arrays. *Journal of Applied Physics* **108,(3)** 034504 (2010).

123. Belkin, M. a., Capasso, F., Xie, F., Belyanin, A., Fischer, M., Wittmann, A. & Faist, J. J. Room temperature terahertz quantum cascade laser source based on intracavity difference-frequency generation. *Applied Physics Letters* **92,(20)** 201101 (2008).

124. Gmachl, C. Tunable Terahertz Lasers: A wrench of wavelength. *Nature Photonics* **3,(12)** 683–684 (2009).

125. Qin, Q., Reno, J. L. & Hu, Q. MEMS-based tunable terahertz wire-laser over 330 GHz. *Optics Letters* **36,(5)** 692 (2011).

126. Qin, Q., Williams, B. S., Kumar, S., Reno, J. L. & Hu, Q. Tuning a terahertz wire laser. *Nature Photonics* **3,(12)** 732–737 (2009).

127. Sartorius, B., Schlak, M., Stanze, D., Roehle, H., Künzel, H., Schmidt, D., Bach, H.-G., Kunkel, R. & Schell, M. Continuous wave terahertz systems exploiting 1.5 microm telecom technologies. *Optics Express* **17,(17)** 15001–7 (2009).

128. HHI Fraunhofer. HHI Fraunhofer. PCA detector modules. (2012). at <www.hhi.fraunhofer.de> [Last accessed: 02/2012]

129. Emcore Co. Emcore Co. CW THz system. (2012). at <www.emcorephotonicsystems.com> [Last accessed: 02/2012]

130. BATOP GmbH. BATOP GmbH. THz Photoconductive Antennas. (2012). at <www.batop.de> [Last accessed: 02/2012]

131. Rouvalis, E., Renaud, C. C., Moodie, D. G., Robertson, M. J. & Seeds, A. J. Continuous Wave Terahertz Generation From Ultra-Fast InP-Based Photodiodes. *IEEE Transactions on Microwave Theory and Techniques* **60,(3)** 509–517 (2012).

132. Criado, A. R., De Dios, C., Döhler, G. H., Preu, S., Malzer, S., Bauerschmidt, S., Lu, H., Gossard, A. C. & Acedo, P. Ultra narrow linewidth CW sub-THz generation using GS based OFCG and n-i-pn-i-p superlattice photomixers. *Electronics Letters* **48,(22)** 1425–1426 (2012).

133. Toptica Photonics. Toptica Photonics. THz CW. (2012). at <http://www.toptica.com> [Last accessed: 02/2012]

134. Preu, S., Kim, S., Verma, R., Burke, P. G., Vinh, N. Q., Sherwin, M. S. & Gossard, A. C. Terahertz Detection by a Homodyne Field Effect Transistor Multiplicative Mixer. *IEEE Transactions on Terahertz Science and Technology* **2,(3)** 278–283 (2012).

135. Davies, D. Inside View. *Electronics Letters* **48,(22)** 1376 (2012).

136. Seeds, A. J., Aeppli, G., Balakier, K., Davies, A. G., Fice, M., Linfield, E. H., Mitrofanov, O., Natrella, M., M.Pepper, Rouvalis, E. & Renaud, C. C. Coherent Terahertz Systems. in *International Topical Meeting on Microwave Photonics. MWP 2012* (2012).

137. Schoenherr, D., Sydlo, C., Feiginov, M., Meissner, P., Hartnagel, H. L.

& Gobel, T. Continuous-wave terahertz system with electro-optical terahertz phase control. *Electronics Letters* **44,(14)** 863–864 (2008).

138. Constantin, F. L. Phase-Coherent Heterodyne Detection in the Terahertz Regime With a Photomixer. *IEEE Journal of Quantum ElectronicsQuantum Electronics* **47,(11)** 1458–1462 (2011).

139. Jepsen, P. U., Cooke, D. G. & Koch, M. Terahertz spectroscopy and imaging - Modern techniques and applications. *Laser & Photonics Reviews* **5,(1)** 124–166 (2011).

140. Kübler, C., Huber, R., Tübel, S. & Leitenstorfer, A. Ultrabroadband detection of multi-terahertz field transients with GaSe electro-optic sensors: Approaching the near infrared. *Applied Physics Letters* **85,(16)** 3360 (2004).

141. Masaaki, A., Ryota, A., Hiroshi, S., Ikufumi, K., Tadashi, I., Katsuhiko, M. & Hiromasa, I. Ultrabroadband THz Field Detection beyond 170THz with a Photoconductive Antenna. in *CLEO 2008. Conference on Lasers and Electro-Optics 2008* (Optical Society of America, 2008). at <http://www.opticsinfobase.org/abstract.cfm?URI=CLEO-2008-CTuX6>

142. Menlo Systems Co. Menlo Systems. THz solutions. (2012). at <http://www.menlosystems.com/home/products/thz-solutions/> [Last accessed: 02/2012]

143. Carr, G. L., Martin, M. C., McKinney, W. R., Jordan, K., Neil, G. R. & Williams, G. P. High-power terahertz radiation from relativistic electrons. *Nature* **420,(6912)** 153–6 (2002).

144. Laperashvili, T., Kvitsiani, O., Imerlishvili, I. & Laperashvili, D. Terahertz pulse detection by the GaAs Schottky diodes. in *SPIE Photonics Europe* 77281K–77281K–8 (2010). doi:10.1117/12.854048

145. Semenov, A., Cojocari, O., Hübers, H.-W., Klushin, A. & Müller, A.-S. Application of Zero-Bias Quasi-Optical Schottky-Diode Detectors for Monitoring Short-Pulse and Weak Terahertz Radiation. *IEEE Electron Device Letters* **31,(7)** 674–676 (2010).

146. Preu, S., Lu, H., Sherwin, M. S. & Gossard, A. C. Detection of nanosecond-scale, high power THz pulses with a field effect transistor. *Review of Scientific Instruments* **83,(5)** 053101 (2012).

147. Popovic, Z. & Grossman, E. N. THz Metrology and Instrumentation. *IEEE Transactions on Terahertz Science and Technology* **1,(1)** 133–144 (2011).

148. Jiang, C., McConney, M. E., Singamaneni, S., Merrick, E., Chen, Y., Zhao, J., Zhang, L. & Tsukruk, V. V. Thermo-Optical Arrays of Flexible Nanoscale Nanomembranes Freely Suspended over Microfabricated Cavities as IR Microimagers. *Chemistry of Materials* **18,(11)** 2632–2634 (2006).

149. Wilk, R. Continuous wave Terahertz spectrometer with coherent detection. *Bulletin of the Polish Academy of Sciences. Technical Sciences* **58,(4)** 13–716 (2010).

150. Cherednichenko, S., Hammar, A., Bevilacqua, S., Drakinskiy, V., Stake, J. & Kalabukhov, A. A Room Temperature Bolometer for Terahertz Coherent and Incoherent Detection. *IEEE Transactions on Terahertz Science and Technology* **1,(2)** 395–402 (2011).

151. Schilz, J. & PerkinElmer Optoelectronics GmbH. Thermoelectric Infrared Sensors (Thermopiles) for remote temperature measurements; pyrometry. (2000). at <http://www.tuhh.de/mt/ftir/lib/RemoteTemperature/pyrometry.pdf> [Last accessed: 02/2013]

152. Dexter Research Center Inc. Introduction to Thermopile Detectors. (2006).

153. ACST GmbH. Advanced Compound Semiconductor Technologies (ACST). Zero bias Schottky detectors. (2012).

154. Virginia Diodes Co. Virginia Diodes Co. Detectors. (2012). at <http://vadiodes.com/> [Last accessed: 02/2012]

155. Sydlo, C., Cojocari, O., Schçnherr, D., Goebel, T., Meissner, P. & Hartnagel, H. L. Fast THz detectors based on InGaAs Schottky Diodes. *Frequenz* **62,(5-6)** (2008).

156. Stillman, W., Donais, C., Rumyantsev, S., Shur, M., Veksler, D., Hobbs, C., Smith, C., Bersuker, G., Taylor, W. & Jammy, R. Silicon FINFETs as detectors of Terahertz and sub-Terahertz radiation. *International Journal of High Speed Electronics and Systems* **20,(01)** 27–42 (2011).

157. Knap, W., Kachorovskii, V., Deng, Y., Rumyantsev, S., Lü, J.-Q., Gaska, R., Shur, M. S., Simin, G., Hu, X., Khan, M. A., Saylor, C. A. & Brunel, L. C. Nonresonant detection of terahertz radiation in field effect transistors. *Journal of Applied Physics* **91,(11)** 9346 (2002).

158. Wang, L., Chen, X.-S., Hu, W.-D., Wang, J., Wang, J., Wang, X.-D. & Lu, W. The plasmonic resonant absorption in GaN double-channel high electron mobility transistors. *Applied Physics Letters* **99,(6)** 063502 (2011).

159. Al Hadi, R., Sherry, H., Grzyb, J., Baktash, N., Zhao, Y., Ojefors, E., Kaiser, A., Cathelin, A. & Pfeiffer, U. A broadband 0.6 to 1 THz CMOS imaging detector with an integrated lens. in *2011 IEEE MTT-S International Microwave Symposium* 1–4 (IEEE, 2011). doi:10.1109/MWSYM.2011.5972870

160. Sherry, H., Grzyb, J., Zhao, Y., Hadi, R. Al, Cathelin, A., Kaiser, A. & Pfeiffer, U. A 1kpixel CMOS camera chip for 25fps real-time terahertz imaging applications. in *2012 IEEE International Solid-State Circuits Conference* 252–254 (IEEE, 2012). doi:10.1109/ISSCC.2012.6176997

161. Ojefors, E., Baktash, N., Zhao, Y., Hadi, R. Al, Sherry, H. & Pfeiffer, U. R. Terahertz imaging detectors in a 65-nm CMOS SOI technology. in *2010 Proceedings of ESSCIRC* 486–489 (IEEE, 2010). doi:10.1109/ESSCIRC.2010.5619749

162. Boppel, S., Lisauskas, A., Krozer, V. & Roskos, H. G. Performance and performance variations of sub-1 THz detectors fabricated with 0.15 [micro sign] m CMOS foundry process. *Electronics Letters* **47,(11)** 661 (2011).

163. Sartorius, B., Schlak, M., Stanze, D., Roehle, H., Kuenzel, H., Schmidt, D., Bach, H.-G., Kunkel, R. & Schell, M. Continuous wave terahertz systems exploiting 1.5 mu m telecom technologies. *Journal of Infrared, Millimeter, and Terahertz Waves* **33,(4)** 405–417 (2012).

164. Nagatsuma, T., Kaino, A., Hisatake, S., Ajito, K., Song, H.-J., Wakatsuki, A., Muramoto, Y., Kukutsu, N. & Kado, Y. Continuous-wave Terahertz Spectroscopy System Based on Photodiodes. *PIERS* **6,(4)** 390–394 (2010).

165. Preu, S., Kim, S., Verma, R., Burke, P. G., Sherwin, M. S. & Gossard, a. C. An improved model for non-resonant terahertz detection in field-effect transistors. *Journal of Applied Physics* **111,(2)** 024502 (2012).

166. Glaab, D., Boppel, S., Lisauskas, A., Pfeiffer, U., Öjefors, E. & Roskos, H. G. Terahertz heterodyne detection with silicon field-effect transistors. *Applied Physics Letters* **96,(4)** 042106 (2010).

167. Hubers, H. W. Terahertz Heterodyne Receivers. *IEEE Journal of Selected Topics in Quantum Electronics* **14,(2)** 378–391 (2008).

168. Erickson, N. R. & Goyette, T. M. 1.5 THz Low Noise Schottky-Diode Mixers. in *SOFIA workshop 2010* (2010).

169. Wild, W. Terahertz heterodyne technology for astronomy and planetary science. in *2007 Joint 32nd International Conference on Infrared and Millimeter Waves and the 15th International Conference on Terahertz Electronics (IRMMW-THz)* (2007). at <http://ieeexplore.ieee.org/xpl/articleDetails.jsp?tp=&arnumber=4516517&contentType=Conference+Publications&searchField=Search_All&queryText=Superconducting+detectors+andmixers+for+millimeter+and+submillimeter+astrophysics,>

170. Ekstrom, H., Karasik, B. S., Kollberg, E. L. & Yngvesson, K. S. Conversion gain and noise of niobium superconducting hot-electron-mixers. *IEEE Transactions on Microwave Theory and Techniques* **43,(4)** 938–947 (1995).

171. Rouvalis, E., Fice, M. J., Renaud, C. C. & Seeds, A. J. Optoelectronic detection of millimetre-wave signals with travelling-wave uni-travelling carrier photodiodes. *Optics express* **19,(3)** 2079–84 (2011).

172. Rouvalis, E., Fice, M. J., Renaud, C. C. & Seeds, A. J. Millimeter-Wave Optoelectronic Mixers Based on Uni-Traveling Carrier Photodiodes. *IEEE Transactions on Microwave Theory and Techniques* **60,(3)** 686–691 (2012).

173. Criado, A. R. Zero-bias mm-wave optoelectronic heterodyne detection with np-i-pn THz detector and ultra-narrow linewidth sub-THz photonic Local Oscillator. *Preprint* (2012).

174. Döhler, G. H., Malzer, S. & Preu, S. [Unpublished].

175. Criado, A. R. Sub-Thz optoelectronic heterodyne receiver based on np-i-pn quasi-ballistic THz receiver and ultra-low phase noise sub-THz photonic Local Oscillator. *Preprint* (2012).

176. Lee, Y.-S. *Principles of Terahertz Science and Technology*. 340 (Springer, 2009).

177. Virginia Diodes Co. Virginia Diodes. Waveguide feedhorns. (2012). at <http://vadiodes.com/VDI/pdf/waveguidechart200908.pdf> [Last accessed: 02/2012]

178. Virginia Diodes Co. Virginia Diodes. Waveguide designation. (2012). at <http://vadiodes.com/VDI/pdf/waveguidechart200908.pdf> [Last accessed: 02/2012]

179. Lioubtchenko, D., Tretyakov, S. & Dudorov, S. *Millimeter-Wave Waveguides*. 195 (2003).

180. Lioubtchenko, D. V. Dielectric Rod Waveguides. (2012). at <http://radio.aalto.fi/en/research/projects/dielectric_rod_waveguide_components/>

181. Generalov, A. A., Lioubtchenko, D. V. & Raisanen, A. V. Dielectric rod waveguide antenna for 220–325 GHz. in *2012 6th European Conference on Antennas and Propagation (EUCAP)* 3551–3553 (IEEE, 2012). doi:10.1109/EuCAP.2012.6205968

182. Marti, J. & Capmany, J. Microwave photonics and radio-over-fiber research. *IEEE Microwave Magazine* **10,(June)** 96–105 (2009).

183. Seeds, A. J. & Williams, K. J. Microwave Photonics. *Journal of Lightwave Technology* **24,(12)** 4628–4641 (2006).

184. Tucker, R. S. Green Optical Communications — Part I : Energy Limitations in Transport. *IEEE Journal of Selected Topics in Quantum Electronics* **17,(2)** 245–260 (2011).

185. Wiener, N. Generalized harmonic analysis. *Acta Mathematica* **55,(1)** 117–258 (1930).

186. Eliyahu, D., Salvatore, R. A. & Yariv, A. Effect of noise on the power spectrum of passively mode-locked lasers. *JOSA B* **14,(1)** 167–174 (1997).

187. Herzel, F. An analytical model for the power spectral density of a voltage-controlled oscillator and its analogy to the laser linewidth theory. *IEEE Transactions on Circuits and Systems I: Fundamental Theory and Applications* **45,(9)** 904–908 (1998).

188. Poore, R. & Agilent Technologies. Overview on Phase Noise and Timing Jitter. (2001).

189. Podesta, J. J. *Phase noise cancellation in a mixer circuit: analysis using a random phase function*. 56 (1996).

190. Criado, A. R., Acedo, P., Carpintero, G., De Dios, C. & Yvind, K. Observation of phase noise reduction in photonically synthesized sub-THz signals using a passively mode-locked laser diode and highly selective optical filtering. *Optics Express* **20,(2)** 1253–1260 (2012).

191. Ho-Jin, S., Shimizu, N., Furuta, T., Wakatsuki, A., Nagatsuma, T. & Song, H.-J. Subterahertz noise signal generation using a photodetector and wavelength-sliced optical noise signals for spectroscopic measurements. *Applied Physics Letters* **93,(24)** 241113 (2008).

192. Friederich, F., Schuricht, G., Deninger, A., Lison, F., Spickermann, G., Haring Bolívar, P. & Roskos, H. G. Phase-locking of the beat signal of two distributed-feedback diode lasers to oscillators working in the MHz to THz range. *Optics Express* **18,(8)** 8621–8629 (2010).

193. Steed, R. J., Pozzi, F., Fice, M. J., Renaud, C. C., Rogers, D. C., Lealman, I. F., Moodie, D. G., Cannard, P. J., Lynch, C., Johnston, L., Robertson, M. J., Cronin, R., Pavlovic, L., Naglic, L., Vidmar, M. & Seeds, A. J. Monolithically integrated heterodyne optical phase-lock loop with RF XOR phase detector. *Optics Express* **19,(21)** 20048–20053 (2011).

194. Acedo, P., Lamela, H., Garidel, S., Roda, C., Vilcot, J. P., Carpintero, G., White, I. H., Williams, K. A., Thompson, M., Li, W., Pessa, M., Dumitrescu, M. & Hansmann, S. Spectral characterisation of monolithic modelocked lasers for mm-wave generation and signal processing. *Electronics Letters* **42,(16)** 928–

929 (2006).

195. Ho-Jin, S., Shimizu, N., Furuta, T., Suizu, K., Ito, H., Nagatsuma, T., Song, H. & Member, S. Broadband-Frequency-Tunable Sub-Terahertz Wave Generation Using an Optical Comb, AWGs, Optical Switches, and a Uni-Traveling Carrier Photodiode for Spectroscopic Applications. *Journal of Lightwave Technology* **26,(15)** 2521–2530 (2008).

196. Optical Comb Inc. Optical Comb Inc. at <http://www.optocomb.com/> [Last accessed: 02/2012]

197. Johnson, A. R., Okawachi, Y., Levy, J. S., Cardenas, J., Saha, K., Lipson, M. & Gaeta, A. L. Chip-based frequency combs with sub-100 GHz repetition rates. *Optics Letters* **37,(5)** 875 (2012).

198. Agrawal, G. P. & Dutta, N. K. *Semiconductor Lasers*. 616 (Kluwer Academic Pub, 1993).

199. Coldren, L. A. & Corzine, S. W. *Diode lasers and photonic integrated circuits*. 594 (Wiley, 1995).

200. Vasil´ev, P. *Ultrafast Diode Lasers: Fundamentals and Applications*. (Artech House Publishers, 1995).

201. Gallion, P. & Debarge, G. Quantum phase noise and field correlation in single frequency semiconductor laser systems. *IEEE Journal of Quantum Electronics* **20,(4)** 343–349 (1984).

202. Henry, C. Theory of the linewidth of semiconductor lasers. *IEEE Journal of Quantum Electronics* **18,(2)** 259–264 (1982).

203. De Dios, C. PhD dissertation.Generación de Pulsos Cortos mediante Diodos Láser Gain Switching. Estudio de Técnicas de Compresión Experimental basadas en Lazos Ópticos no Lineales NOLM. (2010).

204. Petermann, K. *Laser Diode Modulation and Noise*. (Kluwer Academic Publishers, 1991).

205. Yang, Z., Criado, A. R., Wonfor, A., Dijk, F. van, Acedo, P., Penty, R. V. & White, I. H. Tunable Directly Modulated Photonic Integrated Sub-Terahertz Transmitter. *Preprint* (2013).

206. Thorlabs. Thorlabs. Current and TEC laser control CLD1015. (2012). at <http://www.thorlabs.com/NewGroupPage9.cfm?ObjectGroup_ID=5882> [Last accessed: 01/2013]

207. Frank, M. J. in *Advances in Propability Distributions with Given Marginals* (Kluwer Academic Publishers, 1991). at <http://apps.webofknowledge.com/full_record.do?product=UA&search_mode=GeneralSearch&qid=2&SID=S2ng2@dM9d9f8OO2ElD&page=1&doc=1>

208. Black, E. D. An introduction to Pound-Drever-Hall laser frequency stabilization. *American Journal of Physics* **69,(1)** 79–87 (2000).

209. Drever, R. W. P., Hall, J. L., Kowalski, F. V, Hough, J., Ford, G. M., Munley, A. J. & Ward, H. Laser phase and frequency stabilization using an optical resonator. *Applied Physics B: Lasers and Optics* **31,(2)** 97–105 (1983).

210. Thorlabs. Thorlabs. Single frequency laser manual SFL1550S/SFL1550P. (2012).

at <http://www.thorlabs.com/NewGroupPage9.cfm?ObjectGroup_ID=4907> [Last accessed: 01/2013]

211. Stanze, D., Deninger, A., Roggenbuck, A., Schindler, S., Schlak, M. & Sartorius, B. Compact cw Terahertz Spectrometer Pumped at 1.5 μm Wavelength. *Journal of Infrared, Millimeter, and Terahertz Waves* **32,(2)** 225–232 (2010).

212. O'Carroll, J., Phelan, R., Kelly, B., Byrne, D., Smyth, F., Cardiff, B., Anandarajah, P. M. & Barry, L. P. Narrow linewidth discrete mode laser diodes for advanced modulation formats. in *Optical Fiber Communication Conference and Exposition (OFC/NFOEC), 2012 and the National Fiber Optic Engineers Conference* (2012).

213. Criado, A. R., Dios, C. de, Prior, E., Döhler, G. H., Preu, S., Malzer, S., Lu, H., Gossard, A. C. & Acedo, P. Continuous wave sub-THz photonic generation with ultra-narrow linewidth, ultra-high resolution, full frequency range coverage and high long-term frequency stability. *Submitted to IEEE Transactions on Terahertz Science and Technology* (2012).

214. Glauber, R. J., Hall, J. L. & Hänsch, T. W. The Nobel Prize in Physics 2005. (2005). at <http://www.nobelprize.org/nobel_prizes/physics/laureates/2005/> [Last accessed: 02/2012]

215. Schliesser, A., Picqué, N. & Hänsch, T. W. Mid-infrared frequency combs. *Nature Photonics* **6,(7)** 440–449 (2012).

216. Oppenheim, A. V., Willsky, A. S. & Nawab, S. H. *Signals and Systems*. 957 (Prentice Hall, 1997).

217. Sala, K., Kenney-Wallace, G. & Hall, G. E. CW autocorrelation measurements of picosecond laser pulses. *IEEE Journal of Quantum ElectronicsQuantum Electronics* **2,(9)** 990–996 (1980).

218. Vasil'ev, P. P., White, I. H. & Gowar, J. Fast phenomena in semiconductor lasers. *Reports on Progress in Physics* **63,** 1997 (2000).

219. Supradeepa, V. R. & Weiner, A. M. Bandwidth scaling and spectral flatness enhancement of optical frequency combs from phase-modulated continuous-wave lasers using cascaded four-wave mixing. *Optics Letters* **37,(15)** 3066–3068 (2012).

220. Bennett, S., Cai, B., Burr, E., Gough, O. & Seeds, A. J. 1.8-THz bandwidth, zero-frequency error, tunable optical comb generator for DWDM applications. *IEEE Photonics Technology Letters* **11,(5)** 551–553 (1999).

221. Dicke, R. Coherence in Spontaneous Radiation Processes. *Physical Review* **93,(1)** 99–110 (1954).

222. Guo, X., Williams, K. a., Olle, V., Wonfor, A., Penty, R. V. & White, I. H. Theoretical Model for Dicke Superradiance in a Semiconductor Laser Device. *IEEE Photonics Technology Letters* **23,(23)** 1817–1819 (2011).

223. Xia, M., Penty, R. V., White, I. H. & Vasil'ev, P. P. Femtosecond superradiant emission in AlGaInAs quantum-well semiconductor laser structures. *Optics Express* **20,(8)** 8755 (2012).

224. Boiko, D. L. & Vasil'ev, P. P. Superradiance dynamics in semiconductor laser

diode structures. *Optics Express* **20,(9)** 9501 (2012).

225. Jeffrey, A. *Handbook of mathematical formulas and integrals*. 589 (Elsevier, 2008).

226. Carpintero, G., Thompson, M. G., Penty, R. V & White, I. H. Low Noise Performance of Passively Mode-Locked 10-GHz Quantum-Dot Laser Diode. *IEEE Photonics Technology Letters* **21,(6)** 389–391 (2009).

227. Paschotta, R. Timing jitter and phase noise of mode-locked fiber lasers. *Optics Express* **18,(5)** 5041–5054 (2010).

228. Criado, A. R., De Dios, C., Acedo, P., Carpintero, G. & Yvind, K. Comparison of Monolithic Optical Frequency Comb Generators based on Passively Mode-Locked Lasers for Continuous Wave mm-Wave and sub-THz generation. *Journal of Lightwave Technology* **30,(19)** 3133–3141 (2012).

229. Saleh, B. E. A. & Teich, M. C. *Fundamentals of Photonics*. 1200 (John Wiley & Sons, 2007).

230. Agrawal, G. P. *Nonlinear Fiber Optics*. 648 (Academic Press, 2012).

231. Träger, F. *Springer Handbook of Lasers and Optics*. 1694 (Springer, 2012).

232. Yariv, A. & Yeh, P. *Photonics: Optical Electronics in Modern Communication*. 836 (Oxford University Press, 2007).

233. Acedo, P., Carpintero, G., Criado, A. R., De Dios, C. & Yvind, K. Photonic synthesis of continuous-wave millimeter-wave signals using a passively mode-locked laser diode and selective optical filtering. *Microwave and Optical Technology Letters* **54,(6)** 1416–1419 (2012).

234. Carpintero, G., Rouvalis, E., Lawniczuk, K., Fice, M., Renaud, C. C., Leijtens, X. J. M., Bente, E. A. J. M., Chitoui, M., Van Dijk, F. & Seeds, A. J. 95 GHz millimeter wave signal generation using an arrayed waveguide grating dual wavelength semiconductor laser. *Optics Letters* **37,(17)** 3657–3659 (2012).

235. Fukushima, S., Silva, C. F. C. F. C., Muramoto, Y. & Seeds, A. J. A. J. Optoelectronic millimeter-wave synthesis using an optical frequency comb generator, optically injection locked lasers, and a unitraveling-carrier photodiode. *Journal of Lightwave Technology* **21,(12)** 3043–3051 (2003).

236. Phase Matrix Inc. Phase Matrix. Quicksyn RF synthesizers. (2013). at <http://www.phasematrix.com/pages/Synthesizers.html> [Last accessed: 02/2013]

237. Eliyahu, D., Salvatore, R. A. & Yariv, A. Noise characterization of a pulse train generated by actively mode-locked lasers. *Journal of the Optical Society of America B-Optical Physics* **13,(7)** 1619–1626 (1996).

238. Song, M., Wu, R., Torres-Company, V. & Weiner, A. M. Programmable Microwave Photonic Phase Filters With Large Time-Bandwidth Product Based on Ultra- Broadband Optical Frequency Comb Generation. in *IEEE International Topical Meeting on Microwave Photonics. MWP 2012, 2012* (2012).

239. Zhou, R., Latkowski, S., O'Carroll, J., Phelan, R., Barry, L. P. & Anandarajah, P. M. 40nm wavelength tunable gain-switched optical comb source. *Optics Express* **19,(26)** B415–20 (2011).

240. Anandarajah, P. M., Maher, R., Xu, Y. Q., Latkowski, S., O'Carroll,

J., Murdoch, S. G., Phelan, R., O'Gorman, J. & Barry, L. P. Generation of Coherent Multicarrier Signals by Gain Switching of Discrete Mode Lasers. *IEEE Photonics Journal* **3,(1)** 112–122 (2011).

241. Menlo Systems Co. Menlo Systems Co. fs lasers. (2012). at <http://www.menlosystems.com/home/products/thz-solutions/> [Last accessed: 02/2012]

242. Verghese, S., McIntosh, K. A. & Brown, E. R. Highly tunable fiber-coupled photomixers with coherent terahertz output power. *IEEE Transactions on Microwave Theory and Techniques* **45,(8)** 1301–1309 (1997).

243. Verghese, S., McIntosh, K. A., Calawa, S., Dinatale, W. F., Duerr, E. K. & Molvar, K. A. Generation and detection of coherent terahertz waves using two photomixers. *Applied Physics Letters* **73,(26)** 3824 (1998).

244. Gregory, I. S., Tribe, W. R., Baker, C., Cole, B. E., Evans, M. J., Spencer, L., Pepper, M. & Missous, M. Continuous-wave terahertz system with a 60 dB dynamic range. *Applied Physics Letters* **86,(20)** 204104 (2005).

245. Gregory, I. S., Baker, C., Tribe, W. R., Bradley, I. V, Evans, M. J., Linfield, E. H., Davies, A. G. & Missous, M. Optimization of photomixers and antennas for continuous-wave terahertz emission. *IEEE Journal of Quantum ElectronicsQuantum Electronics* **41,(5)** 717–728 (2005).

246. Vidal, B., Nagatsuma, T., Gomes, N. J. & Darcie, T. E. Photonic Technologies for Millimeter- and Submillimeter-wave Signals. *Advances in Optical Technologies* **2012,** (2012).

247. Feiginov, M. N. Analysis of limitations of terahertz p-i-n uni-traveling-carrier photodiodes. *Journal of Applied Physics* **102,(8)** 84510 (2007).

248. Chiu, Y.-J. PhD dissertation.Sub-Terahertz Traveling-Wave Low-Temperature Grown-GaAs P-I-N Photodetector. (1999).

249. Shi, J.-W., Wu, Y.-S. & Lin, Y.-S. Near-Ballistic Uni-Traveling-Carrier Photodiode-Based V-Band Optoelectronic Mixers With Internal Up-Conversion-Gain, Wide Modulation Bandwidth, and Very High Operation Current Performance. *IEEE Photonics Technology Letters* **20,(11)** 939–941 (2008).

250. Campbell, J. C. J. C., Huapu, P., Zhi, L., Pan, H., Li, Z. & Abstract, A. High-Power High-Responsivity Modified Uni-Traveling-Carrier Photodiode Used as V-Band Optoelectronic Mixers. *Journal of Lightwave Technology* **28,(8)** 1184–1189 (2010).

251. Rouvalis, E., Chtioui, M., Tran, M., Lelarge, F., Van Dijk, F., Fice, M. J., Renaud, C. C., Carpintero, G. & Seeds, A. J. High-speed photodiodes for InP-based photonic integrated circuits. *Optics Express* **20,(8)** 9172 (2012).

252. Lisauskas, A., Reklaitis, A., Venckevičius, R., Kašalynas, I., Valušis, G., Grigaliūnaitė–Vonsevičienė, G., Maestre, H., Schmidt, J., Blank, V., Thomson, M. D., Roskos, H. G. & Köhler, K. Experimental demonstration of efficient pulsed terahertz emission from a stacked GaAs/AlGaAs p-i-n-i heterostructure. *Applied Physics Letters* **98,(9)** 091103 (2011).

253. Wood, C. D., Hatem, O., Cunningham, J. E., Linfield, E. H., Davies, A. G., Cannard, P. J., Robertson, M. J. & Moodie, D. G. Terahertz emission from metal-organic chemical vapor deposition grown Fe:InGaAs using 830 nm to

1.55 μm excitation. *Applied Physics Letters* **96,(19)** 194104 (2010).

254. Schoenherr, D., Sydlo, C., Feiginov, M., Meissner, P., Hartnagel, H. L. & Gobel, T. Single-sampling-point coherent detection in continuous-wave photomixing terahertz systems. *Electronics Letters* **45,(1)** 65–66 (2009).

255. Gobel, T., Schoenherr, D., Sydlo, C., Feiginov, M., Meissner, P., Hartnagel, H. L. L. & Göbel, T. Continuous-wave single-sampling-point characterisation of optoelectronic on-chip terahertz transceiver. *Electronics Letters* **45,(23)** 1171–1172 (2009).

256. Stanze, D., Göbel, T., Dietz, R. J. B. J. B., Sartorius, B., Schell, M. & Gobel, T. High-speed coherent CW terahertz spectrometer. *Electronics Letters* **47,(23)** 1292 (2011).

257. Hirata, A., Furuta, T., Ito, H., Nagatsuma, T. & Member, S. 10-Gb/s millimeter-wave signal generation using photodiode bias modulation. *Journal of Lightwave Technology* **24,(4)** 1725–1731 (2006).

258. Tsuchiya, M. & Hoshida, T. Nonlinear photodetection scheme and its system applications to fiber-optic millimeter-wave wireless down-links. *IEEE Transactions on Microwave Theory and Techniques* **47,(7)** 1342–1350 (1999).

259. Huapu, P., Zhi, L., Beling, A. & Campbell, J. C. Characterization of High-Linearity Modified Uni-Traveling Carrier Photodiodes Using Three-Tone and Bias Modulation Techniques. *Journal of Lightwave Technology* **28,(9)** 1316–1322 (2010).

260. Eblana Photonics. Eblana Photonics. (2012). at <http://www.eblanaphotonics.com/> [Last accessed: 02/2013]

261. Criado, A. R., De Dios, C. & Acedo, P. Characterization of Ultra-Nonlinear SOA in a Heterodyne Detector Configuration With Remote Photonic Local Oscillator Distribution. *IEEE Photonics Technology Letters* **24,(13)** 1136–1138 (2012).

262. Dios, C. de, Criado, A. R., Prior, E. & Acedo, P. Enhancing the Performance of Electro-Optical Heterodyne Receivers Using Gain Switched Photonic Local Oscillators. *Journal of Lightwave Technology* **31,(8)** 1331–1336 (2013).

263. Jun-Hyuk, S., Chang-Soon, C., Young-Shik, K., Yong-Duck, C., Jeha, K., Woo-Young, C., Seo, J. H., Choi, C. S., Kang, Y. S., Chung, Y. D., Kim, J. & Choi, W. Y. SOA-EAM frequency up/down-converters for 60-GHz bi-directional radio-on-fiber systems. *IEEE Transactions on Microwave Theory and Techniques* **54,(2)** 959–966 (2006).

264. Maas, S. A. *Microwave mixers*. 375 (Artech House Publishers, 1993).

265. Criado, A. R., Montero-dePaz, J., De Dios, C., García, L. E., Segovia, D. & Acedo, P. Photonic Heterodyne Pixel for Imaging Arrays at Microwave and MM-Wave Frequencies. *Advances in Optical Technologies* **2012,** (2012).

266. Leijtens, X. JePPIX: the platform for Indium Phosphide-based photonics. *IET Optoelectronics* **5,(5)** 202–206 (2011).

267. Saeedkia, D., Safavi-Naeini, S. & Paper, I. Terahertz Photonics: Optoelectronic Techniques for Generation and Detection of Terahertz Waves. *Journal of Lightwave Technology* **26,(15)** 2409–2423 (2008).

268. Mueller, E. R., Henschke, R., Robotham, J., Newman, L. A., Laughman, L. M., Hart, R. A., Kennedy, J. & Pickett, H. M. Terahertz local oscillator for the Microwave Limb Sounder on the Aura satellite. *Applied Optics* **46,(22)** 4907 (2007).

269. Haddad, G. I., East, J. R. & Kidner, C. Tunnel transit-time (TUNNETT) devices for terahertz sources. *Microwave and Optical Technology Letters* **4,(1)** 23–29 (1991).

270. Panda, A. K., Dash, G. N., Agrawal, N. C. & Parida, R. K. Studies on the characteristics of GaN-based Gunn diode for THz signal generation. in *2009 Asia Pacific Microwave Conference* 1565–1568 (IEEE, 2009). doi:10.1109/APMC.2009.5384399

271. Eisele, H. 480 GHz oscillator with an InP Gunn device. *Electronics Letters* **46,(6)** 422–423 (2010).

272. Íñiguez-de-la-Torre, A., Íñiguez-de-la-Torre, I., Mateos, J., González, T., Sangaré, P., Faucher, M., Grimbert, B., Brandli, V., Ducournau, G. & Gaquière, C. Searching for THz Gunn oscillations in GaN planar nanodiodes. *Journal of Applied Physics* **111,(11)** 113705 (2012).

273. Kosugi, T., Sugiyama, H., Murata, K., Takahashi, H., Hirata, A., Kukutsu, N., Kado, Y. & Enoki, T. A 125-GHz 140-mW InGaAs/InP composite-channel HEMT MMIC power amplifier module. *IEICE Electronics Express* **6,(24)** 1764–1768 (2009).

274. Zhong, C., Xu, J., Yu, Z. & Zhu, Y. Ka-Band Substrate IntegratedWaveguide Gunn Oscillator. *IEEE Microwave and Wireless Components Letters* **18,(7)** 461–463 (2008).

275. Plotka, P. Tunnett diode oscillators for mm-wave wideband communication and for terahertz electronics. in *Proceedings of the International Conference Mixed Design of Integrated Circuits and System, 2006. MIXDES 2006.* 52–57 (IEEE, 2006). doi:10.1109/MIXDES.2006.1706535

276. Nishizawa, J., Motoya, K. & Okuno, Y. GaAs TUNNETT Diodes. *IEEE Transactions on Microwave Theory and Techniques* **26,(12)** 1029–1035 (1978).

277. Balasekaran, S., Endo, K., Tanabe, T. & Oyama, Y. Patch antenna coupled 0.2THz TUNNETT oscillators. *Solid-State Electronics* **54,(12)** 1578–1581 (2010).

278. Eisele, H. 355 GHz oscillator with GaAs TUNNETT diode. *Electronics Letters* **41,(6)** 329 (2005).

279. Berger, P. R. & Thompson, P. E. Si/SiGe resonant interband tunnel diode with f/sub r0/ 20.2 GHz and peak current density 218 kA/cm/sup 2/ for K-band mixed-signal applications. *IEEE Electron Device Letters* **27,(5)** 364–367 (2006).

280. CREE Co. CREE Co. HEMT. (2012). at <www.cree.com> [Last accessed: 02/2012]

281. Deal, W. R., Mei, X. B., Radisic, V., Leong, K., Sarkozy, S., Gorospe, B., Lee, J., Liu, P. H., Yoshida, W., Zhou, J., Lange, M., Uyeda, J. & Lai, R. Demonstration of a 0.48 THz Amplifier Module Using InP HEMT Transistors. *IEEE Microwave and Wireless Components Letters* **20,(5)** 289–291 (2010).

282. Lai, R., Mei, X. B., Deal, W. R., Yoshida, W., Kim, Y. M., Liu, P. H., Lee,

J., Uyeda, J., Radisic, V., Lange, M., Gaier, T., Samoska, L. & Fung, A. Sub 50 nm InP HEMT Device with Fmax Greater than 1 THz. in *2007 IEEE International Electron Devices Meeting* 609–611 (IEEE, 2007). doi:10.1109/IEDM.2007.4419013

283. Knap, W., Lusakowski, J., Parenty, T., Bollaert, S., Cappy, A., Popov, V. V. & Shur, M. S. Terahertz emission by plasma waves in 60 nm gate high electron mobility transistors. *Applied Physics Letters* **84,(13)** 2331 (2004).

284. Zhang, Y., Dong, L. & Zhou, Y. Enhanced coherent terahertz Smith-Purcell superradiation excited by two electron-beams. *Optics Express* **20,(20)** 22627–22635 (2012).

285. Urata, J., Goldstein, M., Kimmitt, M., Naumov, A., Platt, C. & Walsh, J. Superradiant Smith-Purcell Emission. *Physical Review Letters* **80,(3)** 516–519 (1998).

286. Dayton, J. A., Mearini, G. T. & Kory, C. L. Diamond-based sub millimeter backward wave oscillator. in *Fifth IEEE International Vacuum Electronics Conference (IEEE Cat. No.04EX786)* 71–72 (IEEE, 2004). doi:10.1109/IVELEC.2004.1316203

287. Dumbrajs, O. & Nusinovich, G. S. Effect of technical noise on radiation linewidth in free-running gyrotron oscillators. *Physics of Plasmas* **4,(5)** 1413 (1997).

288. Williams, G. P. Filling the THz gap—high power sources and applications. *Reports on Progress in Physics* **69,(2)** 301–326 (2006).

289. Blaskiewicz, M., Brennan, J. & Severino, F. Operational Stochastic Cooling in the Relativistic Heavy-Ion Collider. *Physical Review Letters* **100,(17)** (2008).

290. Nagaitsev, S., Broemmelsiek, D., Burov, A., Carlson, K., Gattuso, C., Hu, M., Kroc, T., Prost, L., Pruss, S., Sutherland, M., Schmidt, C., Shemyakin, A., Tupikov, V., Warner, A., Kazakevich, G. & Seletskiy, S. Experimental Demonstration of Relativistic Electron Cooling. *Physical Review Letters* **96,(4)** (2006).

291. Jukam, N., Dhillon, S. S., Oustinov, D., Madeo, J., Manquest, C., Barbieri, S., Sirtori, C., Khanna, S. P., Linfield, E. H., Davies, A. G. & Tignon, J. Terahertz amplifier based on gain switching in a quantum cascade laser. *Nature Photonics* **3,(12)** 715–719 (2009).

292. Mohan, A., Wittmann, A., Hugi, A., Blaser, S., Giovannini, M. & Faist, J. Room-temperature continuous-wave operation of an external-cavity quantum cascade laser. *Optics Letters* **32,(19)** 2792 (2007).

293. Hübers, H.-W., Pavlov, S. G., Semenov, A. D., Köhler, R., Mahler, L., Tredicucci, A., Beere, H. E., Ritchie, D. A. & Linfield, E. H. Terahertz quantum cascade laser as local oscillator in a heterodyne receiver. *Optics Express* **13,(15)** 5890 (2005).

294. Rabanus, D., Graf, U. U., Philipp, M., Ricken, O., Stutzki, J., Vowinkel, B., Wiedner, M. C., Walther, C., Fischer, M. & Faist, J. Phase locking of a 1.5 Terahertz quantum cascade laser and use as a local oscillator in a heterodyne HEB receiver. *Optics Express* **17,(3)** 1159–68 (2009).

295. Choi, H. K. *Long-Wavelength Infrared Semiconductor Lasers*. 395 (Wiley-Interscience, 2004).

296. Pavlov, S., Hübers, H.-W., Hovenier, J., Klaassen, T., Carder, D., Phillips, P., Redlich, B., Riemann, H., Zhukavin, R. & Shastin, V. Stimulated Terahertz Stokes Emission of Silicon Crystals Doped with Antimony Donors. *Physical Review Letters* **96,(3)** (2006).

297. Strauch, R. G. Technique for measurement of HCN-laser linewidth. *Electronics Letters* **5,(11)** 246 (1969).

298. Kiseliov, V. K., Kuleshov, E. M. & Lapty, V. K. Research of the Gas HCN- Laser of Terahertz Frequency Band with Anomalous Secondary Emission Hollow Cathode. in *2006 International Workshop on Laser and Fiber-Optical Networks Modeling* 127–130 (IEEE, 2006). doi:10.1109/LFNM.2006.252000

299. Chang, T. Y. & Bridges, T. J. Laser action at 452, 496, and 541 μm in optically pumped CH3F. *Optics Communications* **1,(9)** 423–426 (1970).

300. Li, S., Liu, H., Huang, N., Sun, Q. & Li, X. High efficiency terahertz-wave photonic crystal fiber optical parametric oscillator. *Applied Optics* **51,(22)** 5579 (2012).

301. Auston, D. H. H., Cheung, K. P. P. & Smith, P. R. R. Picosecond photoconducting Hertzian dipoles. *Applied Physics Letters* **45,(3)** 284 (1984).

302. Karasik, B. S., Olaya, D., Pereverzev, S., Gershenson, M. E., Kawamura, J. H., McGrath, W. R. & Sergeev, A. V. Record-Low NEP in Hot-Electron Titanium Nanobolometers. *IEEE Transactions on Applied Superconductivity* **17,(2)** 293–297 (2007).

303. Generalov, A. A., Lioubtchenko, D. V., Mallat, J. A., Ovchinnikov, V. & Raisanen, A. V. Millimeter-Wave Power Sensor Based on Silicon Rod Waveguide. *IEEE Transactions on Terahertz Science and Technology* **2,(6)** 623–628 (2012).

304. Klaassen, T. O., Hovenier, J. N., Fischer, J., Jakob, G., Poglitsch, A. & Sternberg, O. THz calorimetry: an absolute power meter for TeraHertz radiation and the absorptivity of the Herschel Space Observatory telescope mirror coating. in *SPIE 2004. Proceedings of SPIE* **5354,(May 2010)** 159–167 (2004).

305. Brown, E., Young, A. C., Bjarnason, J. E., Zimmerman, J. D. & Gossard, A. C. Millimeter and sub-millimeter wave performance of an ErAs: InGaAs Schottky diode coupled to a single turn square spiral. *International Journal of High Speed Electronics and Systems* **17,(2)** 383–394 (2007).

306. Knap, W., Deng, Y., Rumyantsev, S. & Shur, M. S. Resonant detection of subterahertz and terahertz radiation by plasma waves in submicron field-effect transistors. *Applied Physics Letters* **81,(24)** 4637 (2002).

307. Rumyantsev, S. L., Deng, Y., Borovitskaya, E., Dmitriev, A., Knap, W., Pala, N., Shur, M. S., Levinshtein, M. E., Khan, M. A., Simin, G., Yang, J. & Hu, X. Low-frequency noise in GaN/AlGaN heterostructure field-effect transistors at cryogenic temperatures. *Journal of Applied Physics* **92,(8)** 4726 (2002).

308. Shur, M. Plasma wave terahertz electronics. **46,** (2010).

309. Dyer, G. C., Aizin, G. R., Reno, J. L., Shaner, E. A. & Allen, S. J. Novel Tunable

Millimeter-Wave Grating-Gated Plasmonic Detectors. *IEEE Journal of Selected Topics in Quantum Electronics* **17,(1)** 85–91 (2011).

310. Schuster, F., Videlier, H., Sakowicz, M., Teppe, F., Coquillat, D., Dupont, B., Siligaris, A., Dussopt, L., Giffard, B. & Knap, W. Imaging above 1 THz limit with Si-MOSFET detectors. in *35th International Conference on Infrared, Millimeter, and Terahertz Waves* 1–2 (IEEE, 2010). doi:10.1109/ICIMW.2010.5612547

311. Ryzhii, V. Terahertz Plasma Waves in Gated Graphene Heterostructures. *Japanese Journal of Applied Physics* **45,(No. 35)** L923–L925 (2006).

312. Kim, E. A primer on Photodiode Technology. at <http://home.sandiego.edu/~ekim/photodiode/pdtech.html#NEP> [Last accessed: 02/2013]

313. Davis, Q. V. & Kulczyk, W. K. Optical and electronic mixing in an avalanche photodiode. *Electronics Letters* **6,(2)** 25 (1970).

314. Seeds, A. J. & Lenoir, B. Avalanche diode harmonic optoelectronic mixer. *Optoelectronics, IEE Proceedings J* **133,(6)** 353–357 (1986).

315. Dolan, G. J., Phillips, T. G. & D.P.Woody. Low-noise 115-GHz mixing in superconducting oxidebarrier tunnel junctions. *Applied Physics Letters* **34,** 347 (1979).

316. Karpov, A., Miller, D. A., Stern, J. A., Bumble, B., LeDuc, H. G., Mehdi, I., Lin, R. H. & Zmuidzinas, J. Low Noise 1 THz SIS Mixer for Stratospheric Observatory: Design and Characterization. *IEEE Transactions on Applied Superconductivity* **21,(3)** 616–619 (2011).

317. Figura, C. C. PhD dissertation.Second Order Nonlinear Optics in Ionically Self-Assembled Thin Films. (2000).

318. Singh, S. P. & Singh, N. Nonlinear effects in optical fibers: Origin, management and applications. *Progress In Electromagnetics Research* **73,** 249–275 (2007).

319. Scott, R. P., Member, S., Langrock, C. & Kolner, B. H. High-dynamic-range laser amplitude and phase noise measurement techniques. *IEEE Journal of Selected Topics in Quantum Electronics* **7,(4)** 641–655 (2001).

320. Feher, K. *Telecommunications measurements, analysis, and instrumentation*. (Prentice Hall, 1987).

321. IEEE. 1139-1988 - IEEE Standard Definitions of Physical Quantities for Fundamental Frequency and Time Metrology. (1989). doi:10.1109/IEEESTD.1989.82404

322. Owen, D. Measurement Good Practice Guide No. 68: Good Practice Guide to Phase Noise Measurement. (2004).

323. Boudot, R. & Rubiola, E. Phase Noise in RF and Microwave Amplifiers. *arXiv* (2012).

324. Riley, W. J. *NIST Special Publication 1065: Handbook of Frequency Stability Analysis*. (National Institute of Standards and Technology (NIST), 2008).

325. International Radio Consultative Committee (C.C.I.R). *Characterization of Frequency and Phase Noise. Report 580 of the International Radio Consultative Committee (C.C.I.R)*. 142–150 (1986).

326. Sullivan, D. B., Allan, D. W., Howe, D. A. & Walls, F. L. NIST Technical Note 1337. Characterization of Clocks and Oscillators. (1990).

327. Agilent Technologies. Agilent's Phase Noise Measurement Solutions. (2011).

328. Scherer, D. Design Principles and Test Methods for Low Phase Noise RF and Microwave Sources. in *RF & Microwave Measurement Symposium and Exhibition*

329. Scherer, D. Generation of Low Phase Noise Microwave Signals. in *RF & Microwave Measurement Symposium and Exhibition* (1981).

330. Breitbarth, J. & Koebel, J. Additive (residual) Phase Noise Measurement of Amplifiers, Frequency Dividers and Frequency Multipliers. *Microwave Journal* **(June)** (2008).

331. Hittite Microwave Corp. Active Multipliers & Dividers to Simplify Measurements. *Microwave Journal* **November,** (2002).

332. Barret, C. Fractional/Integer - N PLL Basics. (1999).

333. Chandler, D. & Corning Frequency Control. Phase Jitter: Phase Noise and Voltage Controlled Crystal Oscillators.

334. Maxim. Tutorial 3631. Random Noise Contribution to Timing Jitter—Theory and Practice. (2005).

335. Renaudier, J., Lavigne, B., Gallion, P., Guang-Hua, D. & Member, S. Study of phase-noise properties and timing jitter of 40-GHz all-optical clock recovery using self-pulsating semiconductor lasers. *Journal of Lightwave Technology* **24,(10)** 3734–3742 (2006).

336. Demir, A. Computing Timing Jitter From Phase Noise Spectra for Oscillators and Phase-Locked Loops With White and 1/f Noise. *IEEE Transactions on Circuits and Systems I: Regular Papers* **53,(9)** 1869–1884 (2006).

337. Hajimiri, A., Limotyrakis, S. & Lee, T. H. Jitter and phase noise in ring oscillators. *IEEE Journal of Solid-State Circuits* **34,(6)** 790–804 (1999).

338. Hajimiri, A. & Lee, T. H. A general theory of phase noise in electrical oscillators. *IEEE Journal of Solid-State Circuits* **33,(2)** 179–194 (1998).

339. Demir, A., Mehrotra, A. & Roychowdhury, J. Phase noise in oscillators: a unifying theory and numerical methods for characterization. *IEEE Transactions on Circuits and Systems I: Fundamental Theory and Applications* **47,(5)** 655–674 (2000).

340. Maxim. Application Note 3359. Clock (CLK) Jitter and Phase Noise Conversion. (2004).

341. Bureau International des Poids et Measures (BIPM), J. *Evaluation of measurement data - Guide to the expression of Uncertainty in Measurement*. ((BIPM). JCGM, 2008).

342. Sánchez, C. *Análisis de errores*. (Ediciones de la Universidad Complutense, 1989).

343. Bell, S. A beginner´s Guide to Unvertainty of Measurement. Measurement Good Practice Guide No. 11. (2001).

344. Agilent Technologies. Application Note. AN 1316. Optimizing Spectrum

Analyzer Amplitude Accuracy. (2000).

345. European co-operation for Accreditation. EA 4-02. Expression of the Uncertainty of Measurement in Calibration. (2011).

346. Birch, K. *Estimating Uncertainties in Testing. Measurement Good Practice Guide No. 36*. (British Measurement and Testing Association, 2003).

347. ISO. ISO/IEC 17025:2005. General requirements for the competence of testing and calibration laboratories. (2005).

348. ISO. ISO/IEC Guide 98-1:2009. Uncertainty of measurement -- Part 1: Introduction to the expression of uncertainty in measurement. (2009).

349. United Kingdom Accreditation Service. M3003 The Expression of Uncertainty and Confidence in Measurement JH 2007.

350. Agilent Technologies. Product Note. Agilent PSA High-Performance Spectrum Analyzer Series. Amplitude Accuracy. (2006).

351. Briaire, J. & Vandamme, L. K. J. K. J. The influence of a digital spectrum analyzer on the uncertainty in 1/f noise parameters. *Microelectronics Reliability* **40,(11)** 1975–1980 (2000).

352. NIST. Uncertainty of Measurement Results. *http://physics.nist.gov/cuu/Uncertainty/index.html*

353. Smith, B. R. *Avoiding pitfalls in measurement uncertainty analysis.*

354. Bertocco, M., Sona, A. & Zanchetta, P. An Improved Method for the Evaluation of Uncertainty of Channel Power Measurement With a Spectrum Analyzer. *IEEE Transactions on Instrumentation and Measurement* **56,(4)** 1165–1170 (2007).

About the author

Ángel Rubén Criado Serrano received his Bachelor Degree and Masters Degree on Telecommunication Engineering from Universidad Carlos III de Madrid in 2009 and his Master on Advanced Electronics Systems from Universidad Carlos III (UC3M) in 2011. He joined UC3M Electronics Technology Department in 2007, where he was involved in research tasks on laser diagnostics for fusion plasmas, specifically electronic density measurement using two color multichannel laser interferometry. As part of this project, he also worked as collaborator researcher during 2009 and 2010 in the Laboratorio Nacional de Fusión in CIEMAT. From November 2009, he works toward his PhD in the field of ultra-low phase noise photonic generation of sub-THz and THz waves with ultra-narrow and continuous tunability; homodyne/heterodyne detection of mm-waves and sub-THz signals; and compact and tunable Optical Frequency Comb Generators at Universidad Carlos III de Madrid. He is also taking a Business Sciences Degree at UNED. He is currently starting the creation of a spin-off : Luz WaveLabs. This company will focus on the development of photonic solutions for low phase noise and continuous tunable THz generation. Furthermore, a wide variety of photonic and THz products and consulting services will be offered by Luz WaveLabs.

This PhD dissertation presents new photonic architectures and devices for generation and detection of sub-THz and THz waves.

The traditional issues of photonic THz generation are overcome through the design and implementation of a photonic THz synthesizer with frequency resolution, phase noise and stability performance more than one million times better than currently commercially available state-of-the-art photonic systems, and matching or even surpassing this performance with respect to state-of-the-art electronic THz generation systems. Additionally, the advantages of photonic techniques are mantained, namely, remote distribution using optical fiber, whole frequency range tunability and the use of telecom optical devices and components.

The barely explored field of Electro-Optical (EO) heterodyne THz detection, which permits higher sensitivity and the remote distribution of THz Local Oscillator (LO) signals with very low losses through several kilometers, is also covered in this document. The photonic THz synthesizer developed in this thesis is employed together with a novel THz detector acting as EO THz mixer to demonstrate EO heterodyne detection under zero bias voltage and with ultrahigh LO frequency resolution for the first time.

The results reported in this doctoral thesis validate the use of photonic techniques for state-of-the-art THz generation and for the implementation of remote EO heterodyne receivers capable of working unbiased.

Universidad Carlos III de Madrid
April 2013

NEW PHOTONIC ARCHITECTURES AND DEVICES FOR GENERATION AND DETECTION OF SUB-THZ AND THZ WAVES

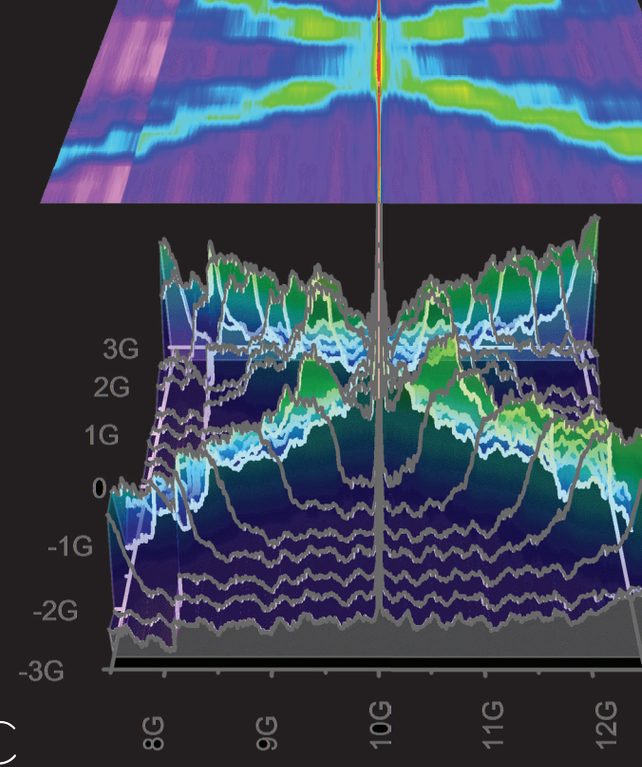

Doctoral thesis

NEW PHOTONIC ARCHITECTURES AND DEVICES FOR GENERATION AND DETECTION OF SUB-THZ AND THZ WAVES

Author: Ángel Rubén Criado Serrano
Supervisor: Pablo Acedo Gallardo